# *WFC3 Instrument Handbook*
# *for Cycle 33*

**STScI | SPACE TELESCOPE SCIENCE INSTITUTE**

# WFC3 Instrument Handbook

*Version 17.0* – December 2024
PDF version

## Wide Field Camera 3 Instrument Handbook for Cycle 33

## User Support

Please contact the HST Help Desk for assistance. We encourage users to access the new web portal where you can submit your questions directly to the appropriate team of experts.

- Web: http://hsthelp.stsci.edu
- E-mail: help@stsci.edu

## Additional Resources

Information and other resources are available from the STScI website:

- http://www.stsci.edu/hst/instrumentation/wfc3

## Revision History

| Version | Date | Editors |
| --- | --- | --- |
| 17.0 | December 2024 | Mariarosa Marinelli and Joel Green |
| 16.0 | January 2024 | Mariarosa Marinelli and Linda Dressel |
| 15.0 | February 2023 | Linda Dressel and Mariarosa Marinelli |
| 14.0 | January 2022 | Linda Dressel |
| 13.0 | January 2021 | Linda Dressel |
| 12.0 | December 2019 | Linda Dressel |
| 11.0 | January 2019 | Linda Dressel |
| 10.0 | May 2018 | Linda Dressel |
| 9.0 | January 2017 | Linda Dressel |
| 8.0 | January 2016 | Linda Dressel |
| 7.0 | January 2015 | Linda Dressel |
| 6.0 | January 2014 | Linda Dressel |

| 5.0 | December 2012 | Linda Dressel |
|-----|---------------|---------------|
| 4.0 | December 2011 | Linda Dressel |
| 3.0 | December 2010 | Linda Dressel |
| 2.1 | June 25, 2010 | Linda Dressel, Michael H. Wong, Cheryl Pavlovsky, Knox S. Long |
| 2.0 | January 2010 | Michael H. Wong, Cheryl Pavlovsky, Knox S. Long |
| 1.0 | December 2007 | Howard E. Bond and Jessica Kim Quijano |

## Citation

In publications, refer to this document as:

- Marinelli, M. & Green, J. 2024. "Wide Field Camera 3 Instrument Handbook, Version 17.0" (Baltimore: STScI)

# Acknowledgments

## Current WFC3 Science Instrument Team (2024)

Munazza Alam
Jay Anderson
Sylvia Baggett (Team Lead)
Varun Bajaj
Annalisa Calamida (Deputy)
Frederick Dauphin
Michele De La Pena
Linda Dressel
Joel Green
Ky Huynh
Harish Khandrika
Benjamin Kuhn
Jennifer Mack
Mariarosa Marinelli
Catherine Martlin
Peter McCullough
Anne O'Connor
Amanda Pagul
Aidan Pidgeon
Mitchell Revalski
Isabel Rivera
Sachindev Shenoy
Debopam Som

## All WFC3 Instrument Handbook Contributors

Munazza Alam, Jay Anderson, Sylvia Baggett, Varun Bajaj, Bruce Balick, John Biretta, Howard Bond, Ray Boucarut, Matthew Bourque, Gabriel Brammer, Jeremy Brett, Tom Brown, Howard Bushouse, Annalisa Calamida, Nicholas Collins, Colin Cox, Tomas Dahlen, Ilana Dashevsky, Tiffany Davis, Susana Deustua, Linda Dressel, Michael Dulude, Mario Gennaro, Mauro Giavalisco, Ron Gilliland, Heather Gunning, George Hartig, Bryan Hilbert, Robert J. Hill, Jason Kalirai, Diane Karakla, Harish Khandrika, Jessica Kim Quijano, Randy Kimble, Vera Kozhurina-Platais, Ben Kuhn, Martin Kümmel, Harald Kuntschner, Janice Lee, Matt Lallo, Knox Long, Olivia Lupie, Jennifer Mack, John MacKenty, Eliot Malumuth, Mariarosa Marinelli, André Martel, Catherine Martlin, Peter McCullough, Brian McLean, Jennifer Medina, Ivelina Momcheva, Mireia Montes-Quiles, Nikolay Nikolov, Kai Noeske, Cheryl Pavlovsky, Larry Petro, Aidan Pidgeon, Nor Pirzkal, Elizabeth Polidan, Manuel Quijada, Abhijith Rajan, Neill Reid, Adam Riess, Massimo Robberto, Barry Rothberg, Elena Sabbi, Kailash Sahu, Clare Shanahan, Kevin Stevenson, Massimo Stiavelli, Ben Sunnquist, Randal Telfer, Alex Viana, Nolan Walborn, Jeremy Walsh, Allen Welty, Tom Wheeler, and Mike Wong.

## Past Science Integrated Product/Instrument Team Members

Elizabeth Barker, Sylvia Baggett, Wayne Baggett, John Biretta, Howard Bond, Matthew Bourque, Ariel Bowers, Gabriel Brammer, Howard Bushouse, Tom Brown, Laura Cawley, Ed Cheng (GSFC), Tomas Dahlen, Ilana Dashevsky, Tiffany Davis, Susana Deustua, Michael Dulude, Meredith Durbin, Michael Fall, Don Figer, Julia Fowler, Mario Gennaro, Mauro Giavalisco, Ron Gilliland, Shireen Gonzaga, Catherine Gosmeyer, Heather Gunning, Derek Hammer, Christopher Hanley, George Hartig, Ron Henry, Bryan Hilbert, Robert Hill (GSFC), Jason Kalirai, Jessica Kim Quijano, Randy Kimble (GSFC), Pat Knezek, Aiden Kovacs, Vera Kozhurina-Platais, Ray Kutina, Janice Lee, Casey Lisse, Knox Long, Olivia Lupie (GSFC), John MacKenty, André Martel, Myles Mckay, Brian McLean, Jennifer Medina, Ivelina Momcheva, Kai Noeske, Heather Olszewski, Cheryl Pavlovsky, Larry Petro, Nor Pirzkal, Marc Rafelski, Abhijith Rajan, Neill Reid, Adam Riess, Massimo Robberto, Michael Robinson, Barry Rothberg, Russell Ryan, Elena Sabbi, Kailash Sahu, Clare Shanahan, Megan Sosey, Keven Stevenson, Massimo Stiavelli, Ben Sunqnuist, Alex Viana, Mike Wong

## The WFC3 Scientific Oversight Committee

Bruce Balick, University of Washington
Howard E. Bond, Space Telescope Science Institute
Daniela Calzetti, University of Massachusetts
C. Marcella Carollo, Institute of Astronomy, ETH, Zurich
Michael J. Disney, Cardiff University
Michael A. Dopita, Mt Stromlo and Siding Spring Observatories
Jay Frogel, AURA
Donald N. B. Hall, University of Hawaii
Jon A. Holtzman, New Mexico State University
Randy Kimble, NASA Goddard Space Flight Center (ex officio)
Gerard Luppino, University of Hawaii
Patrick J. McCarthy, Carnegie Observatories
John MacKenty, Space Telescope Science Institute (ex officio)
Robert W. O'Connell, University of Virginia (Chair)
Francesco Paresce, European Southern Observatory
Abhijit Saha, National Optical Astronomy Observatory
Joseph I. Silk, Oxford University
John T. Trauger, Jet Propulsion Laboratory
Alistair R. Walker, Cerro Tololo Interamerican Observatory
Bradley C. Whitmore, Space Telescope Science Institute
Rogier A. Windhorst, Arizona State University
Erick T. Young, University of Arizona

## Thanks

The editors thank Munazza Alam, Sylvia Baggett, Annalisa Calamida, Ky Huynh, Benjamin Kuhn, Jennifer Mack, and Aidan Pidgeon for providing valuable feedback and updates for this edition. Contributions to earlier editions were made by past and present members of the WFC3 Science Integrated Product/Instrument Team.

The assistance of HDox Lead Coordinator Jenna Ryon and HDox software expert Paul Mulgrew is greatly appreciated.

# Chapter 1: Introduction to WFC3

## Chapter Contents

# 1.1 New for Cycle 33

We have made the following updates to the WFC3 Instrument Handbook for this cycle:

- We updated information, plots, and references throughout the handbook based on the Instrument Science Reports (ISRs) released in 2024.
- We replaced Figures 2.2, 3.1, 3.2, 3.3, 3.4, 3.5, 5.10, 5.11, 5.20, and 9.1 with equivalent but higher resolution versions
- We added Section 3.3.4, as well as Figures 3.6, 3.7, and 3.8, to compare select WFC3/UVIS and WFC3/IR bandpasses with JWST/NIRCAM filters.
- We updated Figures 5.8, 5.9, 5.13, and 5.14 to include the most recent WFC3/UVIS calibration data.
- We used the latest version of the SMOV4 in-flight WFC/IR quantum efficiency correction in the new version of Figure 5.25.
- We updated Figure 5.31 to reflect the most recent analysis of WFC3/IR pixel populations.
- We color-code bright sources and their corresponding figure-8 ghosts in the updated Figure 6.13 .
- We discuss new analysis regarding the impact of x-CTE (serial CTE) in Section 6.9.
- We updated the estimated roll angle drift rate and translation in Sections 6.11.4 (UVIS) and 7.10.5 (IR).
- We revised Sections 6.11.5 and 7.10.6 to reflect that the Drift-And-SHift (DASH) observing method is unavailable in RGM.
- We added Table 7.11 to share WFC3/IR sensitivity loss rates for F098M and all five wide-band filters.
- We updated Sections 7.8 and 9.3 to reflect the new (2024) WFC3/IR time-dependent photometric calibration.
- We updated Figure 7.15 to include WFC3/IR blob positions as of May 2024.
- We used the latest (2021) calibration files to replace Figure 8.3, in which the UVIS G280 grism throughput (for the +1 and -1 orders) is plotted out to 800 nm.
- We added additional context regarding the 2020 calibration of the G280 grism to Section 8.2.
- We updated Section 8.6 to reflect new limitations to spatial scan rates (as of June 2024) due to RGM.
- The following changes have been made to Appendix E:
  - We added the Cycle 32 calibration plan and time span to Table E.1 (Section E.1).
  - We have added a summary of the WFC3 calibration plan for the current cycle in Section E.19.

# 1.2. Overview

The **Wide Field Camera 3 (WFC3)** is a fourth-generation imaging instrument. It was installed in the *Hubble Space Telescope (HST)* during Servicing Mission 4 (SM4) in May 2009. WFC3 saw first external light on June 24, 2009, following the cooling of its detectors. Servicing Mission 4 Observatory Verification (SMOV) activities were completed in late August 2009, and were followed by the Cycle 17 calibration and science programs (see Appendix 3.2 for the SMOV calibration plan and Appendix E.3 for the Cycle 17 calibration plan).

This *WFC3 Instrument Handbook* has been prepared by the WFC3 team at STScI. It is the basic technical reference manual for WFC3 observers. The information in this Handbook is intended to be useful for Cycle 33 Phase I proposers, for the subsequently selected General Observers (GOs) as they prepare their Phase II specifications, and for those analyzing WFC3 data. The *WFC3 Data Handbook* provides an overview of architecture, calibration, and analysis of WFC3 data. The *HST Primer* and the *HST Call for Proposals* also contain valuable information for proposers, and the *HST Call for Proposals* is the final authority on *HST* policy.

This edition of the *WFC3 Instrument Handbook* (Version 17.0) was written during the execution of the Cycle 32 calibration plan and the beginning of the Cycle 33 calibration plan (see Appendix E for cycle cadence and calibration programs). It supersedes Version 16.0, and includes results from analysis of most calibration programs executed through Cycle 32. See the Documents Archive for links to Instrument Handbooks from previous cycles.

The WFC3 instrument occupies *HST's* radial scientific-instrument bay, from where it obtains on-axis direct images. During SM4, the shuttle astronauts installed WFC3 in place of the long-serving Wide Field Planetary Camera 2 (WFPC2). WFPC2, in turn, was installed during SM1 in December 1993, to replace the original Wide Field/Planetary Camera (WF/PC1). WFC3, like WFPC2, contains optics that correct for the spherical aberration discovered in the *HST* primary mirror following launch of the telescope in April 1990.

WFC3 is designed to ensure that *HST* maintains its powerful imaging capabilities until the end of its mission, while at the same time advancing its survey and discovery capability through WFC3's combination of broad wavelength coverage, wide field of view, and high sensitivity. WFC3 also provides a good degree of redundancy for the Wide Field Channel of the Advanced Camera for Surveys (ACS) and has replaced some of the capabilities of the Near-Infrared Camera and Multi-Object Spectrometer (NICMOS).

A key feature of WFC3 is its panchromatic wavelength coverage. By combining two optical/ultraviolet CCDs with a near-infrared HgCdTe array, WFC3 is capable of direct, high-resolution imaging over the entire wavelength range from 200 to 1700 nm. In addition to a comprehensive range of wide-, intermediate-, and narrow-band filters for imaging, WFC3 is also equipped with multiple grating prisms (grisms) to allow for wide-field slitless spectroscopy. Together, these features ensure WFC3 has broad applicability to a variety of ongoing and cutting-edge astrophysical investigations.

WFC3 is a facility instrument. It was developed, constructed, characterized, and calibrated by an Integrated Product Team (IPT) led by NASA's Goddard Space Flight Center (GSFC), and composed of staff astronomers and engineers from GSFC, STScI, Ball Aerospace & Technologies Corp., the Jet Propulsion Laboratory (JPL), and other industrial contractors.

A Scientific Oversight Committee (SOC), selected by NASA from the international astronomical community and appointed in 1998, provided scientific advice for the design and development of WFC3 (for the list of SOC members, see Acknowledgements). The SOC's activities were in a range of areas, including: defining the key scientific goals and success criteria for WFC3; participating in project reviews; recommending an optimum set of filters and grisms for the instrument and the pixel scale and field of view of the detectors; participating in the selection of flight detectors; and advising on technical trade-off decisions in the light of the scientific goals of the instrument.

# 1.3 Key Features of WFC3

The optical design of WFC3 features two independent channels, one sensitive at ultraviolet (UV) and optical wavelengths, approximately 200 to 1000 nm (the **UVIS channel**), and the other sensitive at near-infrared (near-IR) wavelengths, approximately 800 to 1700 nm (the **IR channel**). A channel-selection mirror directs on-axis light from the HST optical telescope assembly (OTA) to the IR channel, or the mirror can be removed from the beam to allow light to enter the **UVIS channel**. This means that *simultaneous* observations with the UVIS and IR detectors are not possible. However, both UVIS and IR observations can be made *sequentially*, even during the same HST orbit.

The extended wavelength range, combined with high sensitivity, high spatial resolution, a large field of view, and a wide selection of spectral elements, makes WFC3 an extremely versatile instrument. Key features of WFC3 include:

- **UVIS channel**: two 2k × 4k CCDs; pixel scale 0.04 arcsec/pix; field of view 162 × 162 arcsec; wavelength range 200-1000 nm; S/N=10 in a 10-hour exposure (F606W filter) for a point source with $V$=29.2 (ABMAG).
- **IR channel**: 1k × 1k HgCdTe array; pixel scale 0.13 arcsec/pix; field of view 136 × 123 arcsec; wavelength range 800-1700 nm; S/N=10 in a 10-hour exposure (F160W) for a point source with $H$=27.9 (ABMAG).
- 62 wide-, medium-, and narrow-band filters in the UVIS channel.
- 15 wide-, medium-, and narrow-band filters in the IR channel.
- 1 grism in the UVIS channel (G280), and 2 grisms in the IR channel (G102 and G141).

In 2001, a "white paper" was prepared by the SOC and the Science IPT(see Acknowledgments for list of members). This report outlined some scientific areas anticipated to especially benefit from the capabilities of WFC3. These included searches for galaxies at redshifts up to $z$~10; studies of the physics of star formation in distant and nearby galaxies; investigations of resolved stellar populations down to faint levels in the UV, optical, and near-IR; and high-resolution imaging of objects in the solar system. Since installation, WFC3's panchromatic capabilities have allowed investigations of the assembly and evolution of galaxies; star birth, evolution, and death and its relation to the interstellar medium; individual and collective properties of small solar system bodies; and aurorae and meteorology of the outer planets. This report (Stiavelli, M., & O'Connell, R.W., eds., 2000, "*Hubble Space Telescope* Wide Field Camera 3, Capabilities and Scientific Program") can be found at: http://www.stsci.edu/~WFC3/resources/WFC3-WhitePaper-2001.pdf

WFC3 provides some overlapping capabilities with the near-infrared instruments on the James Webb Space Telescope (JWST). Both offer observing modes in the 0.6-1.7 um range. When considering which observatory to utilize, observers should consider their scientific requirements: (A) limiting sensitivity; (B) limiting spatial and spectral resolution; (C) temporal coverage and field of regard; (D) specific filters/bandpasses/grism modes; (E) scanning speed; (F) other efficiency factors as needed.

A brief review for observers considering differences between the observatories can be found in the JWST documentation: Guidelines for Proposals where JWST and HST Overlap in Capabilities. See Section 3.3.5 for a comparison of JWST/NIRCAM and WFC3 throughputs.

# 1.4 WFC3 Quick Reference Guide

The most important basic information about WFC3 can be found in this Handbook at the following locations:

- Table 5.1: instrument characteristics (field of view, pixel scale, detector parameters, etc.)
- Table 6.2: UVIS Channel Filters and Grism
- Figure 6.3 - Figure 6.10: system throughput plots for UVIS Filters
- Table 7.2: IR Channel Filters and Grisms
- Figure 7.2 - Figure 7.4: system throughput plots for IR Filters

> ✅ *Throughout this handbook, this symbol indicates information that is especially likely to be updated on the WFC3 website.*

# 1.5 Special Considerations for Cycle 33

## 1.5.1 Current Instrument Status

WFC3 is operating as expected on *HST*, with its detectors at nominal set points of –83°C (UVIS) and –128°C (IR). There are no significant anomalies in its performance.

## 1.5.2 Ongoing Calibration

At the time of this writing, Cycle 32 calibration observations have begun, and the majority of Cycle 31 calibration observations have concluded. Descriptions of the calibration plan for each cycle are given in Appendix E and on the WFC3 Calibration webpage.

Much of the analysis of the calibration programs from past cycles has already been documented in WFC3 Instrument Science Reports published on the WFC3 website; documentation of the remaining analysis is on-going.

Additional information will be released as part of WFC3 Space Telescope Analysis Newsletters (STANs) and other updates posted directly to the WFC3 website. To sign up for the STAN mailing list, please send a blank email to WFC3_NEWS-subscribe-request@MAILLIST.STSCI.EDU.

## 1.5.3 Special Capabilities

UVIS SHUTTER BLADE: The capability of commanding the UVIS shutter to use exclusively one of the two sides of the shutter blade in short exposures, resulting in less vibration and PSF smearing, was implemented early in cycle 21. This option will be made available to the observer when it is critical to the scientific success of a program (see Section 6.10.4). For short exposures, observers should avoid 0.7-s exposure times if possible, as the shutter timing jitter is significantly increased compared to 0.5-s or 1.0-s exposures (WFC3 ISR 2023-04).

UVIS POST-FLASH: The capability of adding a flash at the end of a UVIS exposure (post-flash) was implemented in Cycle 20, and APT began to issue diagnostic reports on exposures with inadequate or excessive flash in Cycle 23. Post-flash greatly increases the detection of faint sources in low background observations, where CTE losses would otherwise remove much or all of the flux from the sources. Most UVIS observers should consider using post-flash: it is useful for all UV, narrow-band, and relatively short medium- and wide-band exposures, reducing CTE losses to a level where the pixel-based CTE correction in the calibration pipeline functions best. The use of Charge Injection to mitigate CTE losses is not recommended (see Section 6.9.2). See Section 5.4.11, Section 6.9, and the WFC3 UVIS CTE webpage for further information on CTE and post-flash.

SPATIAL SCANS: The observing technique of spatial scanning was introduced for WFC3 in Cycle 19. (See Sections 6.11.3, 7.10.4, and 8.6.) Spatial scan mode was added to the ETC for UVIS and IR imaging and IR spectroscopy for cycle 24. This mode can be used to turn stars into well-defined streaks on the detector or to spread a stellar spectrum perpendicular to its dispersion. It is useful for:

- Observations requiring high temporal sampling and/or time resolution;

- High precision relative astrometric observations;
- Imaging and spectroscopy of sources brighter than possible via stare mode.

HST entered reduced gyro mode in June 2024. This change limits spatial scan speeds to 5 arcseconds, a notable reduction from 3-gyro mode. For more details, please see the HST Reduced Gyro Mode Primer.

# 1.6 Sources of Further Information

Table 1.1 provides a guide to online documents containing further information about HST, the proposal process, and data analysis.

**Table 1.1: Useful documents**

| Purpose | Document or resource |
|---|---|
| General observatory information | The Hubble Space Telescope Primer |
| Phase I proposals | HST Proposal Opportunities and Science Policies<br><br>Hubble Space Telescope Call for Proposals |
| Phase II programs | Phase II Proposal Instructions<br><br>Astronomer's Proposal Tool (APT) for Phase I and II preparations |
| Data analysis and instrument characteristics | Wide Field Camera 3 webpage (for general information and updates)<br><br>WFC3 Instrument Handbook (this handbook)<br><br>WFC3 Data Handbook<br><br>Space Telescope Analysis Newsletter (STANs):<br><br>• See web archive of past STANs<br>• To join the STAN mailing list, please send a blank email to WFC3_NEWS-subscribe-request@MAILLIST.STSCI.EDU<br><br>WFC3 Instrument Science Reports (ISRs)<br><br>HST Post-Observation Resources<br><br>Data analysis:<br><br>• WFC3 Data Analysis - landing page<br>• WFC3 Jupyter Notebooks - Github repository of tutorials<br><br>DrizzlePac:<br><br>• DrizzlePac - website landing page<br>• DrizzlePac Handbook - detailed documentation<br>• ReadTheDocs - software package documentation |

Proposers who desire more detailed information about WFC3 capabilities may also seek further assistance as described in the next section.

# 1.7 The WFC3 Instrument Team at STScI

STScI's team of scientific and technical staff support the design, development, operation, calibration, and documentation of WFC3. See the Acknowledgments for a list of current team members.

STScI also maintains a Help Desk to provide answers quickly to any *HST*- and WFC3-related questions. Please refer all questions regarding WFC3 and HST to the Help Desk, as follows:

- Web portal: http://hsthelp.stsci.edu
- E-mail: help@stsci.edu

See the Cycle 33 *HST Call for Proposals* for additional contact information for STScI.

# Chapter 2: WFC3 Instrument Description

**Chapter Contents**

# 2.1 Optical Design and Detectors

The optical design of WFC3 was driven by the need to provide a large field of view and high sensitivity over a broad wavelength range, excellent spatial resolution, and stable and accurate photometric performance. WFC3 features two independent imaging cameras: the **UV/Visible channel (UVIS)** and the **near-infrared channel (IR)**. Figure 2.1 shows a schematic diagram of the instrument's optical and mechanical layout.

On-axis light coming from the HST optical telescope assembly (OTA) is intercepted by the flat 45° WFC3 pick-off mirror (POM) and is directed into the instrument. For IR observations, the Channel Select Mechanism (CSM) then diverts the light into the IR channel; for UVIS observations, the CSM mirror is moved out of the incoming beam's path, which allows the light to enter the UVIS channel. As a result of this design, only a single channel, either UVIS or IR, can be used at any one time. Although it is possible to switch between them fairly quickly, only one channel switch per visit is permitted to minimize the total number of CSM moves (see Section 10.3.1 for channel switching instrument overhead times).

WFC3 uses two different types of detectors. The UVIS channel contains two butted 4096 × 2051 thinned, back-illuminated e2v Ltd. (formerly Marconi) CCD detectors to support imaging between 200 and 1000 nm. The IR channel uses a 1024 × 1024 Teledyne (formerly Rockwell Scientific) HgCdTe detector array and covers the near-infrared between 800 and 1700 nm. Optical elements (anamorphic aspherical correctors) in each channel correct separately for the ~1/2 wave spherical aberration of the HST primary mirror. Both channels also have internal flat-field illumination sources.

The primary characteristics of the two channels are summarized in Table 2.1.

Figure 2.1: Schematic optical layout of the WFC3 instrument. Note that for schematic simplicity, the incoming OTA beam and POM have been rotated into the plane of the optical diagram.
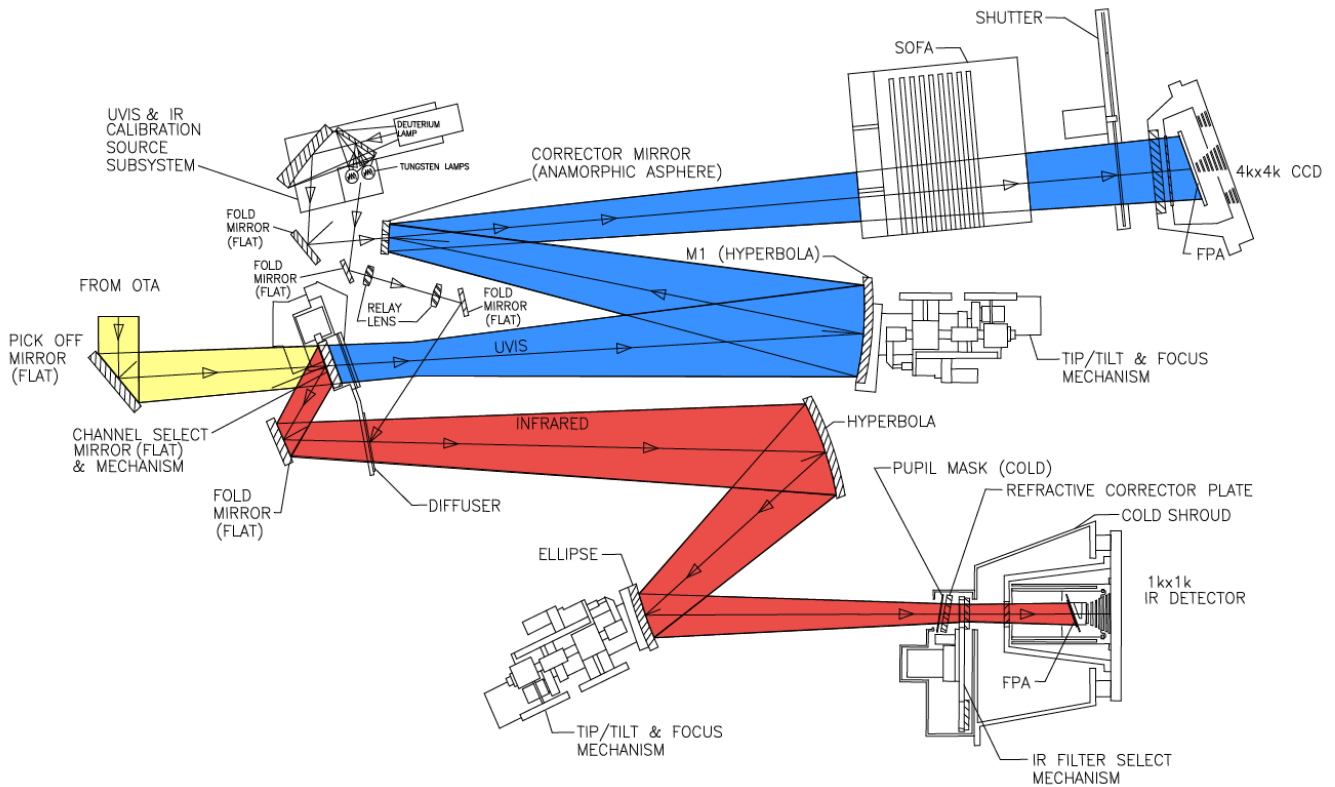


In Figure 2.1, the actual incoming OTA beam direction is into the page and then reflected by the POM into the instrument. Yellow indicates light from the OTA, which is sent into WFC3 by the pick-off mirror. The CSM then either allows light to pass into the UVIS channel (blue path), or directs light into the IR channel (red path). Mechanisms and optics in both channels allow for focus and alignment, and correct for the OTA spherical aberration. Filters and grisms are contained in the UVIS Selectable Optical Filter Assembly (SOFA) and the IR Filter Select Mechanism (FSM). The UVIS channel has a mechanical shutter, while the IR channel is shuttered electronically by the detector. Light is detected by either the UVIS CCDs or the IR focal-plane array. A separate subsystem provides flat-field illumination for both channels.

Table 2.1: Characteristics of the two WFC3 channels.

| Channel | f-ratio | Detector type | Spectral range (nm) | Detector pixel format | Pixel scale (arcsec) | Field of view (arcsec) |
|---------|---------|---------------|---------------------|-----------------------|----------------------|------------------------|
| UVIS | 31 | CCD | 200-1000 | 2 × 2051 × 4096 | 0.0395 × 0.0395 | 162 × 162 |
| IR | 11 | HgCdTe | 800-1700 | 1014 × 1014 | 0.135 × 0.121 | 136 × 123 |

## 2.2 Field of View and Geometric Distortions

WFC3 replaced WFPC2, Hubble's first large-area camera that included corrections for the spherical aberration of the *HST* primary mirror. The appearance of the HST focal plane following SM4 in 2009 is shown in Figure 2.2.

WFC3 images are subject to geometric distortions. These result primarily from the tilt of the focal plane relative to the optical axis (required for constant focus across the detectors; see Figure 2.1), which leads to a modest elongation of the field of view in both channels. In the UVIS detector, most of the distortion runs approximately parallel to the diagonal direction of the CCD, while in the IR channel the distortion is parallel to the sides of the detector. As a result, the UVIS field projected onto the sky is shaped like a rhombus, with an acute angle between the x- and y-axes of the detector of approximately 86.1°. The IR channel projected onto the sky is rectangular, with an aspect ratio of about 0.90. Individual pixels projected onto the sky have the same geometry; thus the UVIS pixels are rhomboidal, measuring 0.0395 arcsec on each side, while the IR pixels are rectangular, measuring 0.135 × 0.121 arcsec.

Although the WFC3 IR and UVIS detectors appear co-aligned in Figure 2.2, IR alignment activities have confirmed that the two detector centers are actually offset by 4.8 arcsec. The diameter of the outer black circle, projected onto the sky, is about 28 arcminutes.

For further discussion of geometric distortions in WFC3, see Appendix B.

**Figure 2.2:** The *HST* focal-plane layout, showing the instrument complement following SM4.
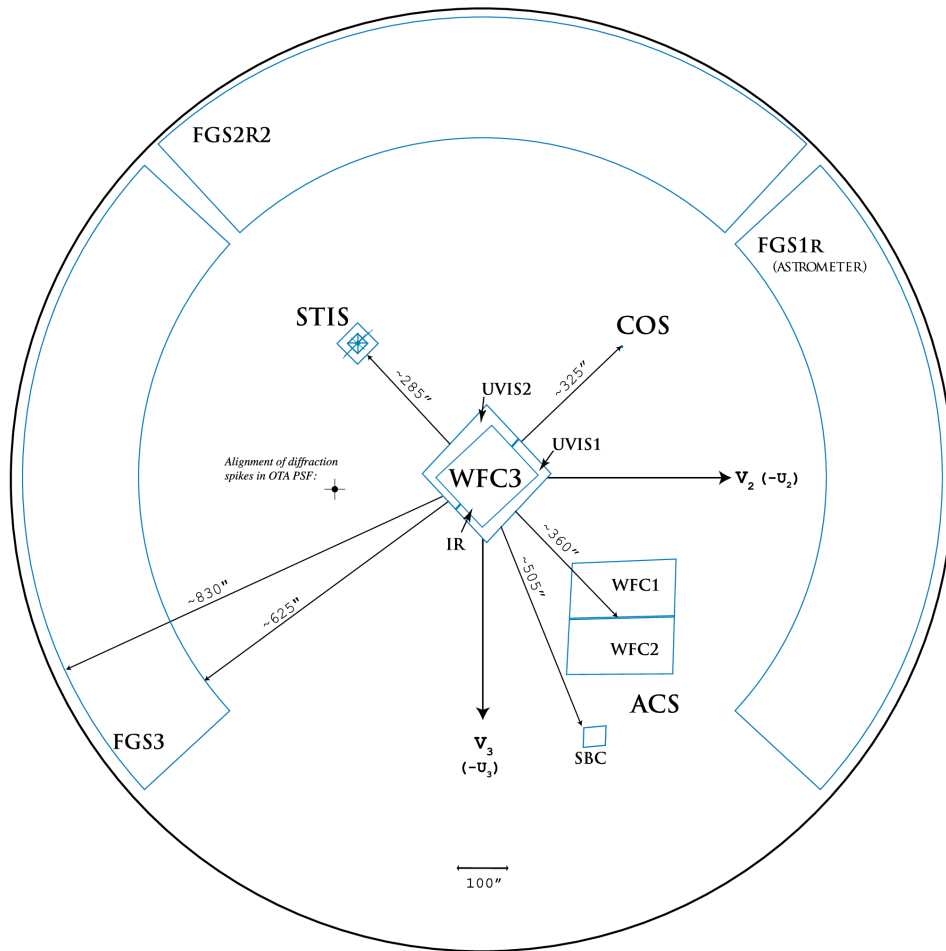
# 2.3 Spectral Elements

## 2.3.1 The Filter Selection Process

Both WFC3 channels are equipped with a broad selection of spectral elements. These elements were chosen on recommendation of the WFC3 Scientific Oversight Committee (SOC; see Acknowledgements for list of members), following a lengthy process with wide scientific and community input. Initial community suggestions and advice were considered at the WFC3 Filter Selection Workshop, held at STScI on July 14, 1999. Other input came from the WFC3 Science White Paper (see Section 1.3 in this handbook for details), from a suite of SOC-developed test proposals representing a broad range of current astronomical investigations, and from statistics of historical filter use in previous *HST* imaging instruments. The filter sets were chosen to fully cover the wavelength regimes of both WFC3 channels with a range of bandwidths, while complementing the filter sets available in ACS and NICMOS.

Based upon the SOC recommendations, the WFC3 Integrated Product Team (IPT; see Section 1.2) developed detailed specifications for the vendors who designed and manufactured the filters. The final flight spectral elements were fully characterized, evaluated by the IPT and SOC, approved for flight, and installed into the filter wheels.

## 2.3.2 Filter and Grism Summaries

The filter sets in both channels include wide-, medium-, and narrow-band filters, as well as low-dispersion grisms (one in the UVIS channel, two in the IR channel) for slitless spectroscopy. The wide- and medium-band filters include popular passbands used in extragalactic, stellar, and solar-system astronomy, as well as passbands similar to those already used in other *HST* instruments for photometric consistency and continuity. The classical *UBVRIJH*, Strömgren, and Washington systems are reproduced, along with the filters of the Sloan Digital Sky Survey (SDSS). In addition, several extremely wide-band filters have been included in both channels, for ultra-deep imaging.

The UVIS channel has a selectable optical filter assembly (SOFA) that contains a stack of 12 filter wheels housing a total of 48 elements: 42 full-frame filters, 5 quad filters, and 1 UV grism. Each wheel also has an open, or empty, slot. For UVIS observations, the appropriate wheel is rotated to place the chosen filter into the light path, and the other eleven wheels are rotated to place the open slot in the light path. Only a single filter can be used at a time. Since the simultaneous insertion of two filters would result in significant defocus, the ground system does not provide the capability of crossing two filters.

There are also a total of 36 different narrow-band passbands in the UVIS channel, consisting of 16 full-field filters and 5 quad filters. Quad filters are 2 × 2 mosaics occupying a single filter slot; each one provides four different bandpasses, at the cost of each one covering only about 1/6 of the field of view. The narrow-band filters provide the capability for high-resolution emission-line imaging in many of the astrophysically important transitions, as well as the methane absorption bands seen in planets, cool stars, and brown dwarfs.

The IR channel has a single filter wheel (FSM, or Filter Select Mechanism) housing 17 elements: 15 filters and 2 grisms; an 18th slot contains an opaque element (or BLANK). For IR observations, the requested single element is rotated into the light beam. The FSM is a bidirectional wheel and always takes the shortest path to a new filter position. The filter wheel and all of its filters are housed, along with the HgCdTe detector package, in a cold shroud maintained at –35°C, a thermally-isolated enclosure which reduces the thermal loads and background emission onto the detector.

In addition to the wide and medium-band filters, the IR channel includes six narrow-band filters, which likewise sample the most important planetary, stellar, and nebular spectral features in the near-IR.

Finally, wide-band filters with similar wavelength coverage to those of the grism dispersers are available. These allow direct images in the same spectral ranges covered by the grisms. They are used to accurately identify spectroscopic sources and for wavelength calibration. WFC3 contains no ramp filters or polarizers, unlike ACS or WFPC2.

Tables 6.2 and 7.2 provide a complete summary of the filters available for imaging with the UVIS and IR channels, respectively. Filter+WFC3+*HST* system throughput curves are presented in Section 6.5 (UVIS) and Section 7.5 (IR), as well as in Appendix A. Graphical representations of the UVIS and IR filter wheels are shown in Figures 2.3 and 2.4. Meanwhile, Figure 3.2 shows the overall integrated system throughputs of WFC3 compared to other instruments.

## Figure 2.3: UVIS Filter Wheels
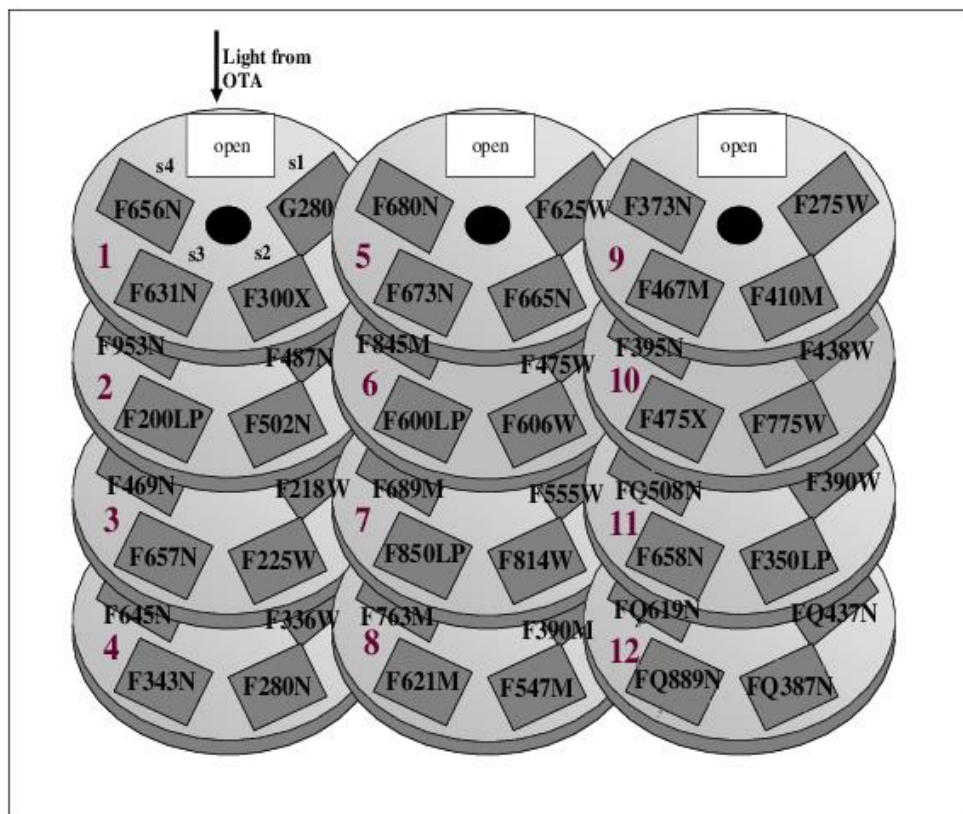
**Figure 2.4: IR Filter Wheel**
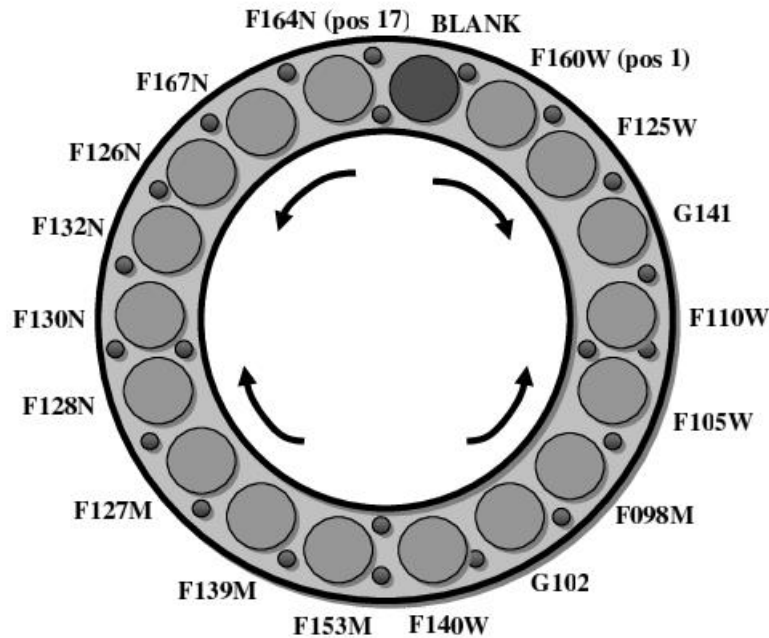


## 2.3.3 Shutter Mechanism

Integration times in the UVIS channel are controlled via a mechanical shutter blade very similar in design to the ACS/WFC shutter. Sitting directly behind the SOFA, the WFC3 UVIS shutter is a rotating disk about 12 inches in diameter; it is divided into four 90° quadrants, with alternating quadrants providing the blocking (i.e., there are two open and two closed positions). When the shutter is in the closed position initially, a commanded move of 90° places it into an open configuration; at the end of the exposure, another move of 90° places the shutter back into a closed position. Although the shutter can be operated in either a clockwise or counterclockwise direction, the current flight software always moves the blade in the same direction.

For very short exposure times in the UVIS channel, there are minor issues with exposure time non-uniformity (Section 6.7.1) and blurring due to shutter-induced vibration (Section 6.10.4).

There is no mechanical shutter in the IR channel; instead, the detector provides electronic shuttering. Dark-current measurements are obtained by using the BLANK, an opaque aluminum blocker in the filter wheel. The blank is also in place whenever the IR channel is not in use, such as during slews, Earth occultations and South Atlantic Anomaly (SAA) passages (when high energy particles are most likely to strike the telescope).

## 2.4 Detector Read-Out Modes and Dithering

The detectors in both channels offer full-frame and subarray readout capability; see Section 5.3 and Section 6.4.4 for UVIS, or Section 7.4.4 and Section 7.7 for IR. The UVIS channel also allows 2 × 2 and 3 × 3 on-chip binning of full-frame images (see Section 6.7.2).

Additionally, a variety of dithering patterns can be requested using the Astronomer's Proposal Tool ( APT) software. Predefined patterns have been established to address common requirements, such as sub-pixel dithering to improve PSF sampling or dithering to achieve large areal coverage while also sampling the inter-chip gap in UVIS, or avoid self-persistence or blob artificacts in IR (see Appendix C ).

The post-observation pipeline software, `calwf3`, carries out appropriate calibration of data taken in all of these configurations, and offers the option of reconstructing dithered images with a "drizzling" algorithm. For more information regarding the reduction and calibration pipeline maintained by STScI, see Appendix E.2 of this handbook. Chapter 3 of the *WFC3 Data Handbook* also details how WFC3 data are calibrated.

Image drizzling can be optimized using functions and modules in the DrizzlePac software package. If the dither pattern incorporates non-integer pixel offsets, it can effectively improve the sampling of the point-spread function (PSF). The software can also handle mosaicked images according to a set of rules or associations, rectifying them onto a Cartesian pixel coordinate system.

# Chapter 3: Choosing the Optimum HST Instrument

**Chapter Contents**

# 3.1 Overview

This chapter addresses the general questions that arise when observers choose between proposing to use WFC3 or one or more of the other imaging instruments that are available on *HST*. After Servicing Mission 4 (SM4), the observatory was its highest level of capability: both the Space Telescope Imaging Spectrograph (STIS) and the Wide Field Channel of the Advanced Camera for Surveys (ACS/WFC) were repaired and new instruments, including WFC3, were installed.

In choosing between instruments for particular projects, observers should carefully evaluate the capabilities of WFC3 and compare them to those of the other *HST* instruments, in the context of their own scientific goals. There is some intentional redundancy between WFC3, ACS, STIS, and the Cosmic Origins Spectrograph (COS) to provide a degree of protection against degradation or failure of the instruments. However, the instruments largely complement one another, and therefore it is likely that one instrument will be preferred for any given science program. Therefore, observers do need to give careful consideration to instrument capabilities in order to optimize their observations. They should refer to the *HST Call for Proposals* for any policy issues, while the *HST Primer* contains additional comparison information, especially the Scientific Instruments Comparison section.

# 3.2 Choosing Between Instruments

The primary factors to consider in choosing the preferred instrument are areal coverage, spatial resolution, wavelength coverage, sensitivity, and availability of specific spectral elements. Table 3.1 lists the primary characteristics of the imaging instruments currently available on *HST*.

For some research programs, the instrument choice may be dictated by the need for a particular spectral element. In this regard, WFC3 offers considerable capability thanks to its broad complement of wide-, medium-, and narrow-band filters both at UV/optical and near-IR wavelengths, as well as one UV grism and two near-IR grisms for slitless spectroscopy.

For studies at optical wavelengths, the trade-offs to consider when deciding between WFC3/UVIS and ACS/WFC include pixel size, field of view and, to some extent, throughput. WFC3 is generally preferable when angular resolution has higher priority than field of view, because of its finer pixel size (since ACS/HRC could not be repaired during SM4, WFC3 offers imaging at the finest pixel scale of any *HST* instrument at optical wavelengths). On the other hand, ACS/WFC has higher throughput than WFC3/UVIS at wavelengths longward of ~400 nm (see Figure 3.2), and hence may be the best choice when the highest possible sensitivity at such wavelengths is crucial. However, considerations of degraded charge transfer efficiency (CTE) should be kept in mind, since ACS has endured the high-radiation space environment for more than seven years longer than WFC3 has.

At UV wavelengths, WFC3/UVIS is the only imager on *HST* to offer a large field of view combined with high throughput. However, its spectral coverage does not extend shortward of 200 nm, whereas ACS/SBC and STIS/FUV-MAMA both reach down to 115 nm (STIS/NUV-MAMA reaches 160 nm), and also offer finer spatial sampling (see Section 3.3.3). Thus, WFC3 will be the choice whenever both large field of view and coverage down to 200 nm are required (e.g., multi-wavelength surveys). However, if observations at extreme far-UV wavelengths are necessary, or if the highest available spatial sampling at UV wavelengths is a primary requirement, then ACS/SBC or the STIS UV channels should be considered.

> ⚠ Warning: ACS/WFC (as well as WFC3/IR) may not be offered for new programs in Cycle 33; please refer to the Cycle 33 Call for Proposals for the most up-to-date information.

Table 3.1: Comparison of wavelength coverage, pixel scales, and fields of view of *HST*'s imaging instruments.

| Instrument | Wavelength coverage (nm) | Pixel size (arcsec) | Field of View (arcsec) |
|---|---|---|---|
| ACS SBC | 115 – 170 | 0.032 | 34 × 31 |
| STIS FUV-MAMA | 115 – 170 | 0.024 | 25 × 25 |
| STIS NUV-MAMA | 165 – 310 | 0.024 | 25 × 25 |
| **WFC3 UVIS** | **200 – 1000** | **0.04** | **162 × 162** |
| STIS CCD | 250 – 1100 | 0.05 | 52 × 52 |
| ACS WFC | 370 – 1100 | 0.05 | 202 × 202 |
| **WFC3 IR** | **800 – 1700** | **0.13** | **136 × 123** |

# 3.3 Comparison of WFC3 with Other HST and JWST Imaging Instruments

## 3.3.1 Wavelength Coverage

The WFC3 UVIS channel is similar in design to the Wide Field Channel (WFC) of the ACS. There are, however, a few differences. While ACS/WFC is unable to detect wavelengths shorter than about 370 nm (i.e., shortward of the *B* band), WFC3/UVIS has excellent sensitivity extending down to 200 nm. The design trade-offs adopted to achieve this extended UV wavelength coverage (primarily the CCD coating and the use of aluminum coatings for the reflective optics) lead to a reduced sensitivity of WFC3 at longer optical wavelengths compared to that of ACS/WFC. WFC3/UVIS has no sensitivity in the far-UV region below 200 nm. The far-UV is covered by three MAMA detectors in ACS and STIS.

## 3.3.2 Field of View

Figure 3.1 illustrates the fields of view, at the same scale, for the *HST* imaging instruments onboard *HST* in 2024. Note that the pixel scale of the WFC3 UVIS channel is 20% finer in comparison to the ACS/WFC, obtained at the cost of covering only about 64% of the area of the ACS field of view.

Figure 3.1: Schematic diagram comparing relative sizes of the fields of view for *HST* imaging instruments. Successive lines of text underneath each field of view give the field size in pixels, the pixel scale in arcsec/pixel, and the field size in arcsec. Detector footprints are rendered as rectangular in the diagram and thus do not include the effects of geometric distortion. For a more accurate depiction of detector footprints including geometric distortions and relative *HST* focal plane locations, see Figure 2.2.



**WFC3/UVIS**
2 × 2051 × 4096
0.04″/pix
162″ × 162″

**WFC3/IR**
1014 × 1014
0.13″/pix
136″ × 123″

**ACS/WFC**
2 × 2048 × 4096
0.05″/pix
202″ × 202″

**ACS/SBC**
1024 × 1024
0.032″/pix
34″ × 31″

**STIS/MAMA**
1024 × 1024
0.025″/pix
25″ × 25″

**STIS/CCD**
1024 × 1024
0.05″/pix
52″ × 52″
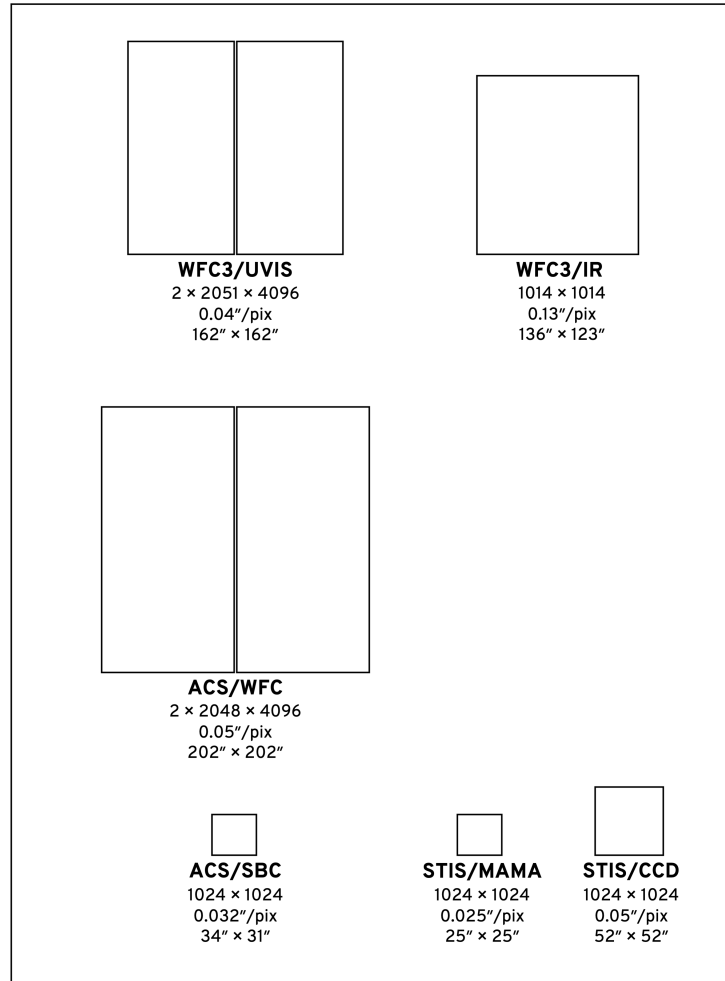
Table 3.1 presents a comparison of the wavelength coverage, pixel scale, and field of view of WFC3 and of the other *HST* imaging instruments that are currently available.

> ⚠ Warning: ACS/WFC (as well as WFC3/IR) may not be offered for new programs in Cycle 33; please refer to the Cycle 33 Call for Proposals for the most up-to-date information.

## 3.3.3 Detector Performance

Table 3.2 summarizes the on-orbit measurements of read-out noise and dark current for the WFC3 detectors, and compares them with the parameters for the other currently available *HST* imaging detectors. Chapter 5 gives more detailed information about the detectors in both channels. Chapter 9 discusses sensitivities, limiting magnitudes, and exposure times.

Table 3.2: Characteristics of *HST* CCD and HgCdTe imaging detectors currently available.

| Detector | Read-out noise (e⁻ rms) | Dark current (e⁻/pix/s) | Mean well Depth (e⁻) |
|---|---|---|---|
| **WFC3/UVIS** | **3.1–3.2** | **0.003** | **63,000-72,000** |
| ACS/WFC | 4.8 | 0.0062 | 84,700 |
| STIS/CCD | 5.4 (gain=1), 7.7 (gain=4) | 0.009 | 114,000 |
| **WFC3/IR** | **~12.0**[1] | **0.05** | **77,900** |

[1] WFC3/IR read noise is for a 16-read linear fit. WFC3/IR double sampling read noise is 20.2–21.4 e⁻.

## 3.3.4 System Throughputs and Discovery Efficiencies

Figure 3.2 plots the measured on-orbit system throughputs of the two WFC3 channels as functions of wavelength, compared to those of ACS, NICMOS, and WFPC2. These curves include the throughput of the OTA, all of the optical elements of the instruments themselves, and the sensitivities of the detectors. Throughputs were calculated at the central wavelength (the "pivot wavelength"; see footnote 3 in Table 6.2) of each wide-band filter of each instrument.

As Figure 3.2 shows, WFC3 offers a unique combination of high sensitivity and wide spectral coverage ranging from the UV to the near-IR. WFC3 extends and complements, over a large field of view, the optical performance of ACS/WFC at wavelengths shorter than ~400 nm and longer than 1000 nm. The good degree of functional redundancy with ACS will help ensure that the unique scientific capabilities of *HST*, at optical wavelengths, will remain available until the end of its mission.

Another quantity that is useful when comparing different instruments, especially in the context of wide-angle surveys, is the "discovery efficiency," defined as system throughput times area of the field of view as projected onto the sky. In Figure 3.3 we plot the discovery efficiencies of the *HST* imaging instruments, again vs. wavelength. Note that the y-axis is now logarithmic. This figure dramatically illustrates the enormous gains that WFC3 offers, compared to current *HST* instruments, both in the optical/UV below 400 nm, and in the near-IR.

Finally, we present WFC3's strengths by including detector noise and thus showing how its efficiency, wide wavelength coverage, and large field of view apply to general problems: the limiting point-source magnitude reached in 10 hours of observing time (Figure 3.4); and the time needed to survey a sky area about 9 times larger than the Hubble Ultra Deep Field, to a limiting ABMAG of 26 (Figure 3.5).

Figure 3.2: System throughputs of optical/infrared imaging instruments on *HST* as functions of wavelength. The plotted quantities are end-to-end throughputs, including filter transmissions, calculated at the pivot wavelength of each wide-band filter of each camera. Plot reproduced from Figure 2.1 of the ACS Instrument Handbook (Ryon, Stark, et al. 2023).
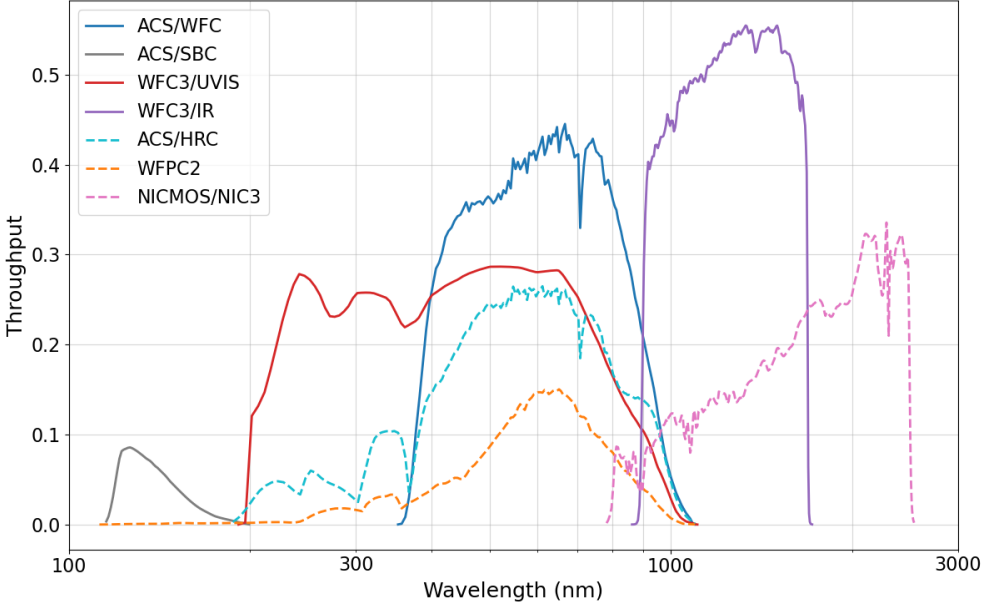
Figure 3.3: Discovery efficiencies of optical/infrared *HST* imaging instruments, including those verified on-orbit for WFC3. Discovery efficiency is defined as the system throughput (plotted in Figure 3.2) multiplied by the area of the field of view. Note that the y-axis is now logarithmic. Plot reproduced from Figure 2.2 of the ACS Instrument Handbook (Ryon, Stark, et al. 2023).
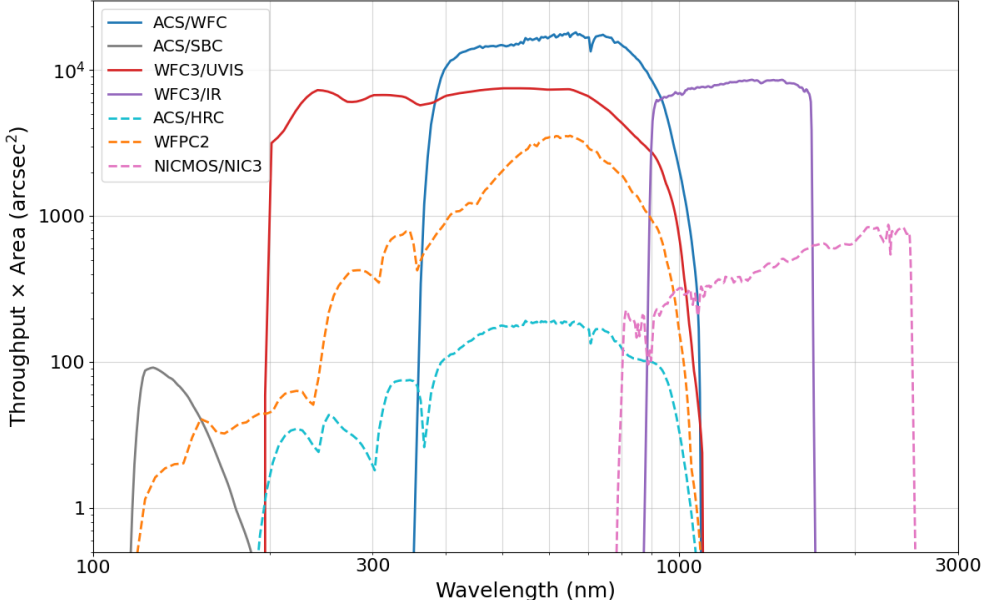
**Figure 3.4:** Limiting point-source magnitudes reached by optical/infrared *HST* imaging instruments in 10 hours. (Performance of WFC3/UVIS, as well as ACS/WFC, has declined slightly from the early on-orbit level shown here due to increasing CTE losses.)
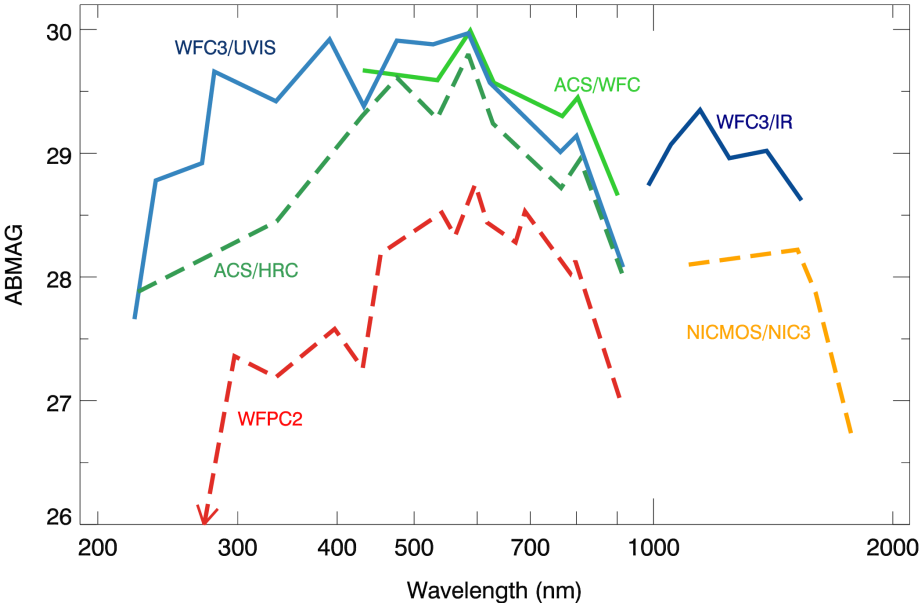
**Figure 3.5:** Time needed for optical/infrared *HST* imaging instruments to survey a wide sky area to a limiting extended (1 arcsec$^2$) ABMAG of 26. (WFC3/UVIS performance has declined slightly from the early on-orbit level shown here due to increasing CTE losses.)
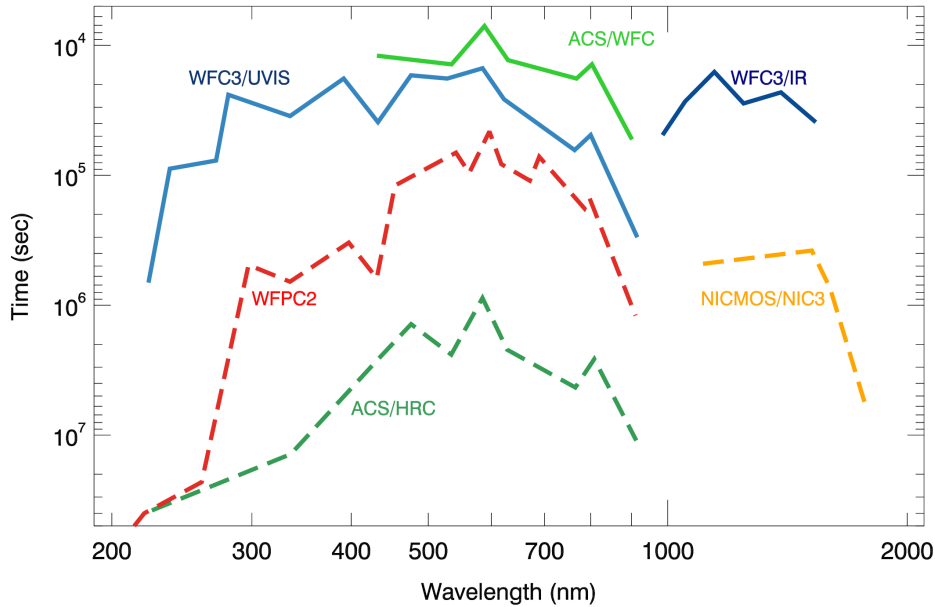


## 3.3.5 Comparison of HST/WFC3 and JWST/NIRCAM

Although they have different capabilities, JWST/NIRCam has significant wavelength overlap with WFC3 in both UVIS and IR bandpasses. Here we compare the filter coverage of the two observatory instruments.

Figure 3.6 plots the measured on-orbit system throughputs of the wide-band/long-pass filters for WFC3/UVIS channels as functions of wavelength, compared with two wide-band filters on NIRCam. UVIS works at shorter wavelengths than NIRCam but has less throughput at longer wavelengths. Their respective filter bandpasses are different in the central wavelength and span.

Figure 3.7 plots the measured on-orbit system throughputs of the wide-band/long-pass filters for WFC3/IR channels as functions of wavelength, compared with four wide/medium-band filters on NIRCam. The WFC3/IR filters generally broader and contain more overlap than the comparable NIRCam filters, except at the longest wavelengths. A similar comparison between medium/narrow-band filters for WFC3/IR and various NIRCam filers is shown in Figure 3.8.

**Figure 3.6:** System throughputs for four wide-band/long-pass WFC3/UVIS filters and two wide-band *JWST* NIRCAM filters, as functions of wavelength.
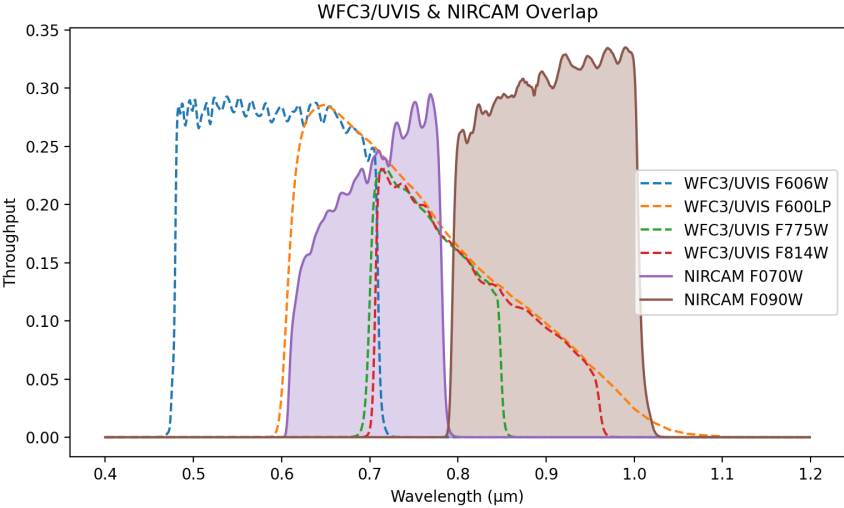
**Figure 3.7:** System throughputs for three wide-band WFC3/IR filters and four wide/medium-band *JWST* NIRCAM filters, as functions of wavelength.
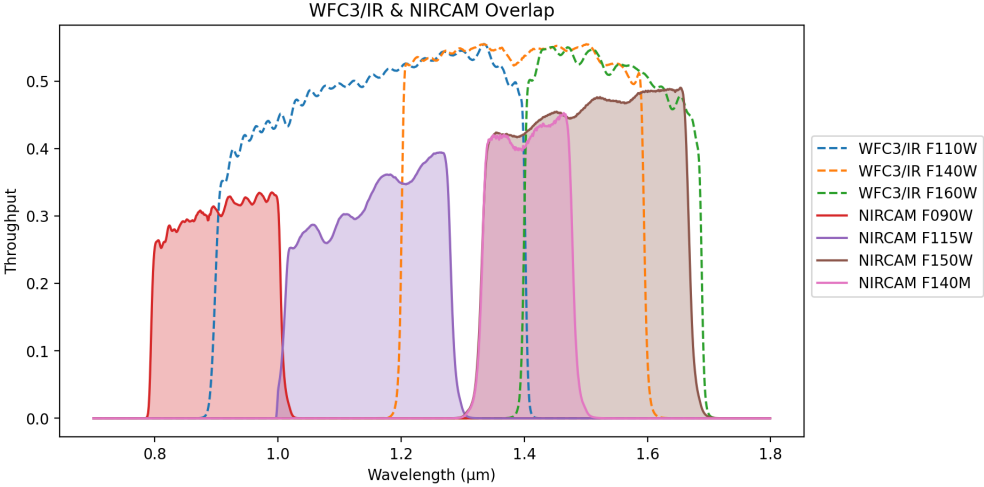
**Figure 3.8:** System throughputs for four medium/narrow-band WFC3/IR filters and five *JWST* NIRCAM filters, as functions of wavelength.
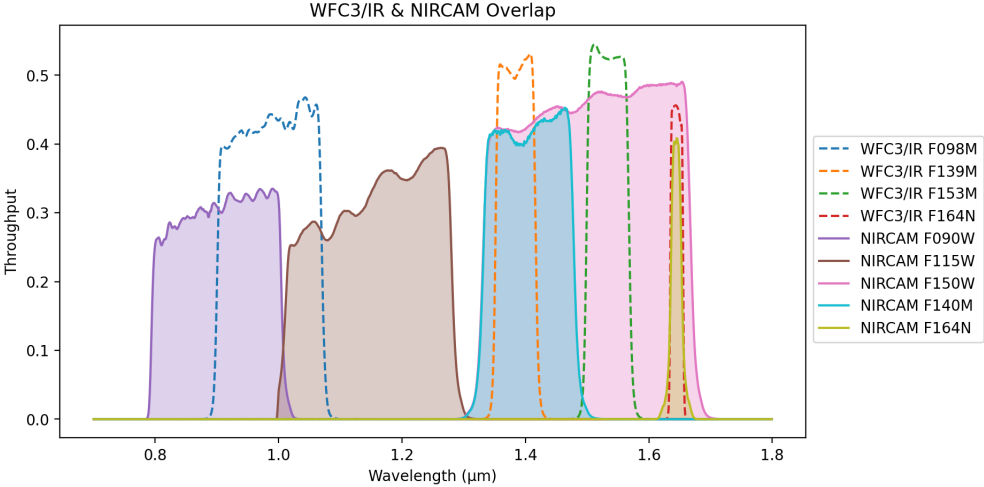
# Chapter 4: Designing a Phase I WFC3 Proposal

**Chapter Contents**

# 4.1 Phase I and Phase II Proposals

The first steps in preparing an *HST* program are to establish a set of science goals and to explore whether HST can be used to achieve those science goals. Once an observer has decided that *HST* can achieve the science goals, they must prepare a formal proposal.

In this chapter we give an overview of the steps that are taken in preparing an *HST* observing proposal that involves WFC3 observations. "**Phase I**" refers to the initial proposal that is reviewed by the Telescope Allocation Committee (TAC). The Phase I proposal presents the scientific justification for the project, lists the targets to be observed and the instrument(s) and spectral elements to be used, and includes a request for a specific number of spacecraft orbits. See the *HST Call for Proposals* and *HST Primer* for a full discussion of all policy issues and additional guidance.

The Phase I proposal does not contain many of the details that are actually required to carry out observations with *HST*. These are included in a "**Phase II**" proposal that will be needed if and after the proposal is recommended by the TAC and approved by the STScI Director. At that time, the *Phase II Proposal Instructions* (specifically Chapter 12 regarding the WFC3 instrument), will be a vital resource for users who have been awarded time.

The actual submission of proposals in both Phase I and Phase II is accomplished using the **Astronomer's Proposal Tool (APT)**; see http://apt.stsci.edu.

This chapter focuses on the steps for assembling the information needed to prepare a Phase I WFC3 proposal for submission using APT.

# 4.2 Preparing a Phase I Proposal

An *HST* program is a set of exposures specified so as to achieve one or more scientific objectives. We can break down the development of a WFC3 observing program, imaging and/or spectroscopic, into a six-step process. Often there is not one unique way in which to achieve the scientific objectives, and you must assess the trade-offs and feasibilities of multiple approaches. Furthermore, you will wish to use *HST* and WFC3 efficiently, in order to obtain as much science within as small an orbit allocation as possible. Therefore, you may need to iterate these steps in order to achieve a final feasible program that is also optimal.

In this chapter we introduce issues that you may need to consider in designing your observations. Later chapters in this handbook will present detailed information for your use. These six steps, and the considerations they entail, are described in the following subsections.

## 4.2.1 Which WFC3 Channel(s) and Filter(s)?

First, from your science requirements, determine the desired wavelength(s) of observation. Those requirements may include considerations of the spectral energy distribution (SED) of the target, or the required angular resolution, which also varies as a function of wavelength. Typically, if the wavelength of observation is less than 900 nm, then the WFC3 UVIS channel will be used; or if the wavelength is greater than 900 nm, then the WFC3 IR channel will be used. Your program may involve use of both channels.

The angular resolution, field of view, and sensitivity of the two channels differ appreciably, and may also influence your selection of the WFC3 channel(s) to use (see Chapter 2 for an overview of the UVIS and IR channels). Features of interest in the target's SED can be matched to the spectral resolution of the observation by selecting appropriate filters (see Chapter 6 for the UVIS channel, Chapter 7 for the IR channel, and Appendix A for detailed filter passbands), or grisms (see Chapter 8).

To match continuum features, wide-, medium-, and/or narrow-band filters may be selected, presenting the possibility of a trade-off between detector signal and spectral resolution. Note that the UVIS quad filters limit the field of view to about one sixth of the full field.

## 4.2.2 What Exposure Times?

Second, you should determine the exposure time and exposure sequences needed to achieve the required signal-to-noise ratio (SNR) with the chosen filter(s) or grism(s). A full discussion of exposure time calculation is presented in Chapter 9, but, as mentioned in that chapter, in most cases you will use the online Exposure Time Calculator (ETC). The SNR depends upon the target's incident flux and the noise from the background and detector sources. These sources include zodiacal light, detector dark current, and stray light from both Earth and bright targets in the field of view.

Having determined the basic exposure time necessary to achieve the required SNR, you will in most cases find it necessary to achieve that total exposure time through a sequence of shorter exposures (and/or the use of scan mode). For instance, if the exposure time is greater than the maximum orbital target visibility, it will be necessary to obtain a sequence of exposures. UVIS exposures exceeding 3,600 s require more than one exposure as do IR exposures greater than 2,800 s (see Chapter 6 and Chapter 7 for a fuller discussion).

Additional reasons to structure the total exposure time are described in the following paragraphs, as well as considerations specific to each of the two WFC3 channels.

## Dithering and Mosaicking

To mitigate the effects of flat-field calibration error, cosmic ray hits, and other residuals, a dither pattern is often employed for a given sequence of exposures. Using a dither pattern with sub-pixel displacement will also allow the point-spread function (PSF) to be better sampled. Users may design and specify a dither pattern, or use one of the pre-defined patterns already designed to sub-sample the PSF, to cover the UVIS inter-chip gap, or to mosaic a large field. The pre-defined sequences and information on designing custom patterns are presented in Appendix C of this handbook and in the *Phase II Proposal Instructions*. IR dither steps should be at least 10 pixels to avoid self-persistence or IR blob artifacts for sources that are larger than 5 pixels in size, but there is a corresponding tradeoff in pixel phase coherence for larger dithers (WFC3 ISR 2019-07).

## Bright Targets

For bright targets, a sequence of shorter exposures may be needed to avoid entering the non-linear or saturation regimes of the detectors (UVIS: Section 5.4 and Section 6.10 for UVIS; IR: Section 5.7 and Section 7.9). Bright objects do not cause safety concerns for either UVIS or IR observations with WFC3. Image persistence can be a concern for IR observations (as discussed in Section 7.9.4 and Appendix D) but is not a problem with the UVIS channel. Observers should consider ordering IR exposures in a way that reduces the impact of persistence from an exposure on subsequent exposures.

## UVIS Exposures

For UVIS observations, it will almost always be desirable to use multiple exposures to remove cosmic-ray impacts. Dithering is preferable to CR-SPLIT for the reasons discussed above under Dithering and Mosaicking. For observations with the UVIS channel of faint targets on low levels of background emission, the effects of charge transfer efficiency (CTE) during readout of the detector must be considered (see Sections 5.4.11 and 6.9). Post-flash, implemented for Cycle 20, reduces CTE losses.

## IR Exposures

For observations with the IR channel you must choose a readout method from the 12 available sample sequences, each of which may comprise from 1 to 15 non-destructive readouts. These include RAPID (linear), SPARS (linear), and STEP (linear-log-linear) sequences (see Chapter 7). The exposure time is dictated by the sequence chosen and whether a full array or subarray is used. The ability to remove cosmic-ray impacts will depend upon the sequence chosen.

## 4.2.3 Which Aperture or Subarray?

Next, from considerations of the target's angular size and structure, and of data volume, you should determine the WFC3 aperture or subarray you will use. The available UVIS apertures and subarrays are presented in Chapter 6, and those for the IR channel in Chapter 7.

In some cases, correct placement of an extended target within an aperture may require you to specify a special *HST* pointing and possibly the orientation of the field of view (which is determined by the spacecraft roll angle). Additional considerations may include detector imperfections such as the UVIS inter-chip gap (Section 5.2.2 and Section 6.3), diffraction spikes, filter ghost images (see Section 6.5.3 and Section 6.10.6), detector saturation (i.e. for "blooming" in a UVIS image along a detector column; Section 5.4.5), detector charge transfer (Section 6.9), distortion of the image ( Appendix B), or dispersion direction of the grism (see Chapter 8). Most of these aspects only need to be considered at the Phase II stage, unless they affect the number of orbits needed for the proposal or require a specific orientation. The latter must be justified in the Phase I proposal.

You can reduce the size of the image read out and thus the volume of data obtained by selecting a subarray. For the UVIS detector, on-chip binning of the pixels will also reduce the data volume, but at the expense of angular resolution (for more information about on-chip binning, see in particular Section 5.3 and Section 6.7). Reducing the data volume will reduce the overhead to read out and transfer images, which may be desirable in order to allow more images of the target of interest to be obtained during an *HST* orbit. During Phase II preparation, the location of the target can be specified with the POS TARG Special Requirement and the rotation of the image can be specified with the ORIENT Special Requirement. For more details regarding how to specify UVIS observations, see Section 6.2; for IR, see Section 7.2. In the Phase II Proposal Instructions, Section 6.2.2 gives detailed information on the relationship between detector coordinates, spacecraft coordinates, and ORIENT. **Note that any ORIENT requirement must be specified in the proposal Phase I proposal in the "Special Requirements" section** (see also the news section under the Phase I proposal instructions).

## 4.2.4 What Overheads and How Many *HST* Orbits?

Next, determine the overhead times required, in addition to the exposure times, in order to operate the spacecraft and the camera (see Chapter 10).

The spacecraft overhead includes the time needed for guide-star acquisition or re-acquisition at the beginning of each orbit. The camera overheads include time needed to change filters, change between the UVIS and IR channels, read out the exposure to the WFC3 data buffer, and transfer the images from the buffer to the *HST* science data storage. Note that overheads can accumulate quickly for sequences of short exposures, but these can sometimes be minimized by using small subarrays or by alternating short and long exposures. For Phase II proposals, the APT provides tools for detailed modeling of complete observation sequences.

Finally, you will add the overhead times to the exposure times to determine the total time needed for your program, which is what you will request in your Phase I proposal.

This total time is expressed as the (integer) number of *HST* orbits required to obtain the observations needed to achieve the proposed science goals.

## 4.2.5 Any Special Calibration Observations?

Most observers will not need to request special calibration observations. As a result of ground-based testing and regular on-orbit calibrations, WFC3 is well-characterized as described in this handbook and in more detail in the WFC3 Instrument Science Reports. Instrument characterization and calibration is maintained and improved as part of the ongoing calibration program conducted by STScI (Appendix E).

The main reasons an observer would need to consider special calibration observations are situations where a program requires greater precision than is provided through the standard calibration program. These additional observations must be justified in your Phase I proposal submission, and the orbits required to carry out the special observations must be included in the overall orbit allocation requested. Proposers are advised to discuss their need for special calibration observations with the helpdesk.

## 4.2.6 What is the Total Orbit Request?

Having determined the content of the science and supporting observations necessary to achieve your scientific objectives, you must finally determine the total amount of *HST* time to carry out those activities by including the appropriate amount of time for spacecraft and instrument overheads.

Detailed procedures for determining the total amount of time to request in your Phase I proposal are presented in Chapter 10.

# Chapter 5: WFC3 Detector Characteristics and Performance

**Chapter Contents**

# 5.1 Overview of this Chapter

The science return on any data can typically be enhanced if observers acquire a basic understanding of how the detectors operate, and of their individual characteristics and limitations. For the most demanding observations, such as imaging very faint or extremely bright sources, or for exposures using non-default parameters, an even deeper understanding of the detectors and their operation may be required. This chapter aims to provide both basic and in-depth information on the detectors used in both WFC3 channels. Sections 5.2-5.4 discuss the CCD detectors used in the UVIS channel, and Sections 5.5-5.7 discuss the infrared detector used in the IR channel.

Table 5.1 summarizes the basic characteristics of the flight CCD and IR detectors. For the CCDs, the information is either an average for the two chips, or the range of values for both of them. Results are based on ground measurements as well as on-orbit data acquired during 2009 and 2010 after WFC3 was installed in *HST*.

**Table 5.1: WFC3 Detector Characteristics**

| Characteristic | UVIS Channel CCDs | IR Channel Detector |
|---|---|---|
| Architecture | Teledyne CCD detectors. Thinned, backside illuminated, UV optimized, multi-phase pinned, buried/mini-channel, charge injection capability. | Teledyne HgCdTe infrared detector. MBE-grown, substrate removed, on Si CMOS Hawaii-1R multiplexer. |
| Wavelength Range | 200 to 1000 nm | 800 to 1700 nm |
| Pixel Format | 2 butted 2051 × 4096, 31-pixel gap (1.2") | 1024 × 1024 (1014 × 1014 active) |
| Pixel Size | 15 μm × 15 μm | 18 μm × 18 μm |
| Plate Scale | 0.040"/pixel | 0.13"/pixel |
| Field of View on Sky | Rhomboidal, 162" × 162" | Rectangular, 136" × 123" |
| Quantum Efficiency | 50–59% @ 250 nm[1] <br> 68–69% @ 600 nm <br> 47–52% @ 800 nm | 77% @ 1000 nm <br> 79% @ 1400 nm <br> 79% @ 1650 nm |
| Dark Count | ~11 e⁻/hr/pixel (median, projected to early 2023) | 0.048 e⁻/s/pixel (median) |
| Readout Noise | 3.1–3.2 e⁻ | 20.2–21.4 e⁻ (pair of reads) <br> 12.0 e⁻ (16-read linear fit) |
| Full Well[2] | 63,000–72,000 e⁻ | 77,900 e⁻ (mean saturation level) |
| Gain | 1.55 e⁻/DN | 2.3 e⁻/DN |

| ADC Maximum | 65,535 DN | 65,535 DN |
|---|---|---|
| Operating Temperature | 190 K | 145 K |

[1]Quantum efficiency at 250 nm does not include multiple-electron events, which lead to larger apparent efficiency in e.g., Figure 5.2.

[2]The IR full well value is based on fully-integrated instrument ground testing. Other CCD and IR parameters are derived from on-orbit data.

# 5.2 The WFC3 UVIS Channel CCD Detectors

## 5.2.1 Basics of CCD Operation

A charge-coupled device (CCD) is a silicon-based detector containing a two-dimensional array of summing wells called pixels, short for pixel elements. Each pixel accumulates electric charge in proportion to the number of photons striking that location on the detector. Physically, the summing wells are created by electric fields established at the depletion (charge-free) regions of the Si-SiO$_2$ metal-oxide-semiconductor (MOS) capacitors. In a typical three-phase CCD, the size of the depletion region is controlled by the voltage of three gates. The gates are arranged in parallel, with every third gate connected together.

At the end of an exposure, the voltages of the gates are changed with an appropriate clocking pattern, causing all charge packets to be sequentially transferred to the adjacent pixel, until they reach the readout circuitry at the detector's edge. The transfer of charges between pixels occurs in parallel, row by row, whereas the extraction of the "zeroth" row at the edge occurs along an external serial register, where each packet is serially transferred to an output amplifier at the detector corner.

## 5.2.2 The WFC3 CCDs

The WFC3 UVIS channel uses two CCD detectors fabricated by Teledyne (e2v at the time). Both CCDs are 2051 × 4096 devices with 15 × 15 μm square pixels. There are 2051 rows by 4096 columns, where the row/column definition follows the convention of having the parallel direction first and the serial direction second. Having the serial register along the long (4096 pixel) edge reduces the number of transfers required to read out a charge packet.

The WFC3 CCDs are three-phase devices, thinned and back-illuminated (back-thinned) to improve the sensitivity to UV light. Thinning refers to the removal of the thick substrate on which the chip is originally built and is done to improve shorter-wavelength efficiency (only those electrons generated in the vicinity of the gate structure can be collected efficiently). Back-illumination means that photons are focussed on the back side of the chip, rather than having to pass through the opaque gate structures implanted on the front side.

Similar to ACS, the WFC3 CCDs also have buried channels and are operated in multi-pinned phase (MPP) mode. The purpose of the buried channel, or mini-channel, is to improve CTE for targets with relatively low signal levels (~10K e⁻ or less) and reduce the dark current as well. The buried channels have the capability of injecting charges to fill in the traps and improve the CTE but this mode is not currently in use (Section 6.9.2). Further details of these features are given in Section 5.4.8.

The two WFC3 CCDs are aligned together along their long dimension to create a 2 × 1 mosaic. This butted configuration is equivalent to a 4102 × 4096 array, but with a gap of 31 ± 0.1 pixels between the two chips (1.2 arcsec on the sky). Figure 5.1 shows a picture of a CCD assembly similar to the flight detector.

The CCDs are cooled by a four-stage thermoelectric cooler (TEC) to a nominal temperature of 190 K. The detectors are packaged inside a cold enclosure, which is nearly identical to the one used for ACS, itself a scaled-up version of the STIS design. The package includes a second cooled window to reduce the radiative heat load.

The CCD focal plane is assembled on a molybdenum base disk, which provides some shielding from cosmic rays and also serves as the thermal sink path from the hot side of the TEC stack to the heat pipes (which carry the heat to the external radiator). The "cover" with the external window is about 1 cm thick and is made of "alloy 42" steel; it provides some protection from cosmic rays incident on the front side of the CCDs.

The WFC3 CCDs are quite similar to those used in the ACS Wide Field Channel (WFC). They have the same pixel size, nearly the same format (2051 × 4096 in WFC3, compared to 2048 × 4096 in ACS), the same orientation of the serial and parallel registers, similar technology (buried-channel, MPP operation), and nearly identical mechanical interfaces. The main differences of the WFC3 chips compared to those in ACS/WFC are:

- UV optimization of the WFC3 wavelength response
- Significantly lower readout noise for the WFC3 chips (~3.1- 3.2 e⁻ compared to 3.75-5.65 e⁻)
- 2051 rows instead of 2048
- Charge-injection capability for mitigation of degradation in CTE due to on-orbit radiation damage (not generally available for science observations; see Section 6.9.2)
- 31-pixel gap instead of 50
- Manufactured by e2V (formerly Marconi; Teledyne as of 2017); ACS chips were produced by Site.

An overview of the WFC3 CCD performance was given in Table 5.1.

Figure 5.1: Detector package similar to the WFC3/UVIS flight detector. The size of the 4k × 4k array is approximately 6 × 6 cm, and it consists of two butted 2051 × 4096 CCDs with a 31-pixel gap between them.
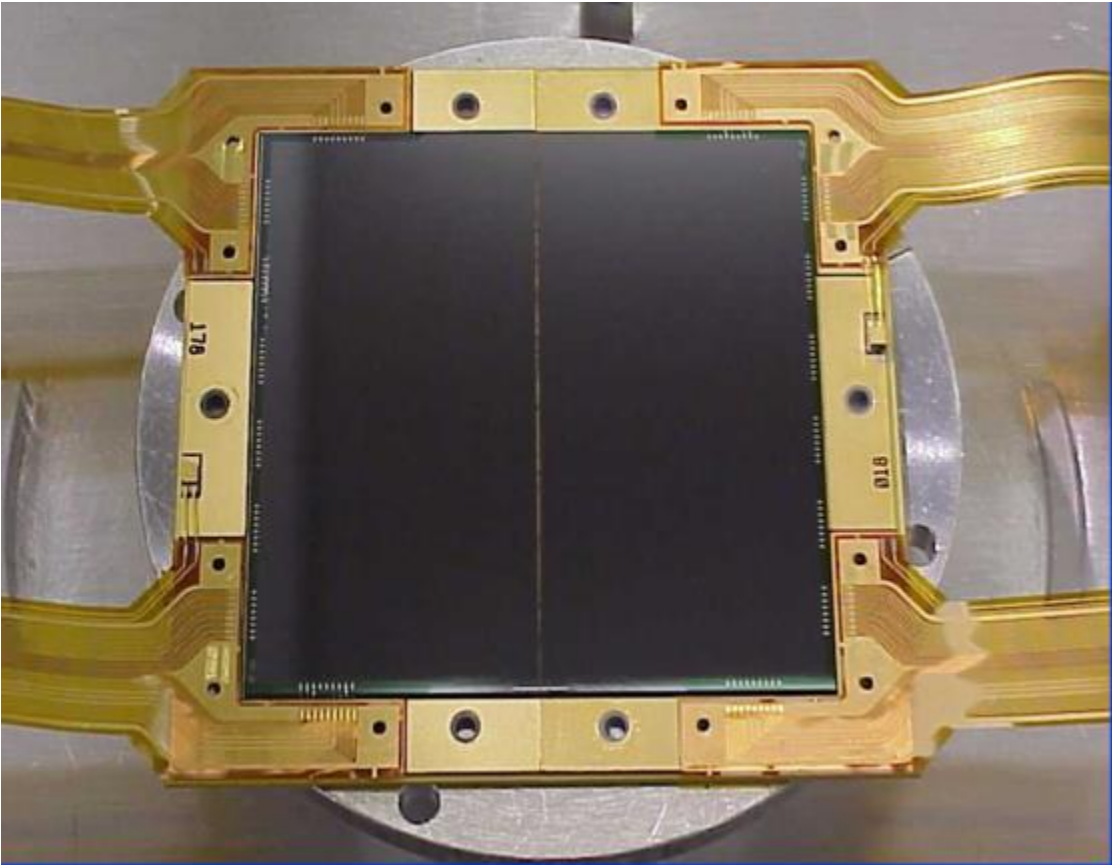
# 5.3 WFC3 CCD Readout Formats

## 5.3.1 Full-frame Readout

The WFC3 UVIS channel contains two CCD chips, each of which has two readout amplifiers. The amplifiers on chip 1 are designated A and B, and those on chip 2 as C and D. Although a chip (or part of a chip) may be read out through a single amplifier, the default and fastest readout mode employs all four amplifiers simultaneously, such that each amplifier reads out half of a chip.

A full-frame UVIS exposure produces a single FITS file in which the data from each of the two chips are stored in separate image extensions, along with associated error and data quality arrays for each image. For consistency with ACS, the image data from CCD chip 2 are stored in SCI array 1 (FITS extension 1) and the image data from CCD chip 1 are stored in SCI array 2 (FITS extension 4). Table 5.2 lists the chips, the associated amplifiers, and the FITS extensions of the science image data.

Each CCD chip contains 2051 × 4096 active pixels, but the raw images returned by the WFC3 electronics contain a larger number of pixels. This is due to the detector overscan: portions of the detector that are not exposed to light. Overscan regions are useful for characterizing detector electronics performance, and especially for measuring the bias level contained within an image. Serial overscan corresponds to a fixed number of unexposed pixels at each end of each serial shift register. Conversely, parallel overscan is generated by additional parallel shifting before or after all of the exposed rows of the detector have been read out. In principal, both serial and parallel overscan can be implemented either as physical overscan or virtual overscan. The physical overscan is a characteristic of the detector hardware, whereas virtual overscan is a software function, and the number of rows and columns of virtual overscan generated for an image is controllable via the readout timing pattern.

The WFC3 CCD overscan regions are described in more detail in Section 6.7, and dimensions for unbinned and binned exposures are specified in Table 6.10.

Table 5.2: WFC3 CCD Naming Conventions.

| CCD Chip | Amplifiers | Science Image FITS File Extension | Error Array FITS File Extension | Data Quality Array FITS File Extension |
|----------|-----------|-----------------------------------|---------------------------------|----------------------------------------|
| 1 | A, B | [SCI,2]=[4] | [ERR,2]=[5] | [DQ,2]=[6] |
| 2 | C, D | [SCI,1]=[1] | [ERR,1]=[2] | [DQ,1]=[3] |

## 5.3.2 Subarrays

The default CCD readout mode is to read all pixels of both chips, including all available overscan regions. It is also possible to restrict the readout to rectangular subarray regions. Only data from the area within the subarray are stored in buffer memory, and the rest of the image is discarded. The subarray can be chosen from several pre-defined configurations.

UVIS subarray images contain no virtual overscan data and serial physical overscan is present only if the defined subarray boundaries overlap the physical overscan columns on either end of the chips. Thus all corner subarrays contain physical overscan data, while centered subarrays do not (Table 6.1).

Subarrays are discussed in greater detail in Section 6.4.4.

## 5.3.3 On-Chip Binning

The UVIS CCDs also provide an on-chip binning capability, in which several adjacent pixels may be read out as a single pixel. The available choices are 2 × 2 and 3 × 3 on-chip binning. On-chip binning and subarrays can not be used simultaneously. See Section 6.4.4 for details on the use of on-chip binning in WFC3/UVIS observations. If on-chip binning is used, the overscan geometry is complicated by the need to truncate "odd" pixels, and each half of a row must be considered separately. As a result, depending on the binning mode, some science pixels adjacent to the overscan region may be binned together with overscan data. Details are given at the end of Section 6.7.2.

# 5.4 WFC3 CCD Characteristics and Performance

## 5.4.1 Quantum Efficiency

The quantum efficiencies (QEs) of the two WFC3 CCDs are plotted against wavelength in Figure 5.2. Here the QE is defined as electrons yielded per incident photon. The solid curves illustrate the QEs as measured at the Detector Characterization Laboratory (DCL) at Goddard Space Flight Center, slightly corrected downward by the TV3 ground tests. The plots demonstrate the high sensitivity of the CCDs in the UV down to 200 nm. On the other hand, the peak QE at ~600 nm is less than that of the ACS /WFC detectors (~85% at their peaks). The QE measurements were made with the detectors perpendicular to the incident light. As installed in WFC3, the CCDs are tilted by 21 degrees with respect to the normal. The nominal change in optical thickness is ~6%, but the QE variations, as measured at the DCL on similar devices, turn out to be negligible.

The integrated system throughput of WFC3 depends on many factors including the *HST* OTA, pickoff mirror, filter transmission functions, QE, etc. Based on ground measurements of these components, the intergrated system throughput was calculated and compared to the first on-orbit measurements during Servicing Mission/Orbital Verification in 2009. A 5 to 20% increase in the integrated system throughput was discovered, likely attributable to multiple components. The dashed curves represent the QE under the assumption that the entire flight correction is in the detector QE. For UV observations, UVIS2 achieves a higher sensitivity than UVIS1.

**Figure 5.2:** Quantum efficiency curves of the WFC3 UVIS 1 (blue) and UVIS 2 (orange) CCDs based on Goddard DCL measurements corrected by TV3 measurements (solid). The integrated system throughput of the UVIS detector was measured on-orbit to be higher than ground tests by 5–20%, and the dashed curves shows the QE under the assumption that this entire gain is due to the QE. In reality, some fraction of this gain is likely attributable to other *HST* and/or instrument components.
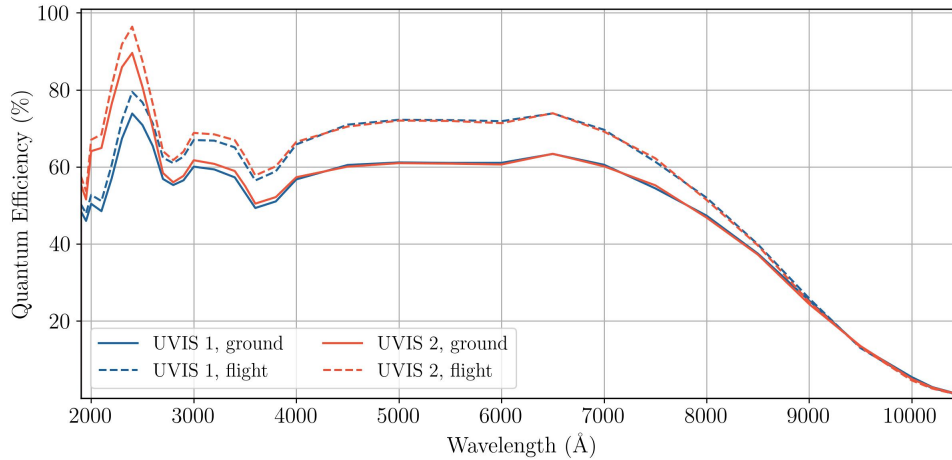


## 5.4.2 Multiple-Electron Events at Short Wavelengths

Like the ACS HRC and STIS CCDs (and unlike WFPC2), the WFC3 UVIS CCDs are directly sensitive to UV photons. In silicon, photons of energy higher than 3.65 eV (i.e., wavelength shorter than ~340 nm) can produce multiple electron-hole pairs when the energetic conduction-band electron collides with other valence-band electrons. At higher energies (energy above 3.65 eV, or wavelength below ~340 nm) the incident photons can directly extract more than one electron from the valence band. This effect (called "quantum yield") of a single photon producing more than one electron must be taken into account properly when estimating the noise level for short-wavelength observations.

Because the generation of multiple electrons is a random phenomenon, an extra noise term must be added to account for an observed variance larger than that associated with the normal Poisson distribution of incoming photons. The correction is theoretically about 1.7 e⁻/photon at 200 nm, decreasing linearly to 1.0 at 340 nm. Measurements of ground-based data, however, have indicated that the effect in the WFC3 chips is much less, 1.07 e⁻/photon at 218 nm and 1.03 e⁻/photon at 275 nm in broadband data (WFC3 ISR 2008-47) as well as monochromatic narrowband data (WFC3 ISR 2010-11). The cause for this is unclear, but may be due to charge sharing (Janesick, J.R., 2007, " Photon Transfer DM-->λ", SPIE, Bellingham, Washington, p 45-48).

Given the low level of quantum yield measured in the WFC3 data, neither the QE curves presented in Figure 5.2 nor the WFC3 Exposure Time Calculator (ETC) include the effects of quantum yield. The noise distortion from multiple electrons is not large compared to other contributions to the signal-to-noise ratio in the ultraviolet (see Section 9.2).

## 5.4.3 Flat Fields

Before launch, ground-based flats were obtained for all UVIS filters at an SNR of ~200 per pixel using an external optical stimulus (WFC3 ISR 2008-12). Because the overall illumination pattern of the ground-based flats did not precisely match the illumination attained on-orbit from the OTA, there are errors in these ground-based flats on large spatial scales. These errors were quantified by performing stellar photometry on rich stellar fields that were observed using large-scale dither patterns during SMOV and cycles 17-18 (2009-2011). In the on-orbit SMOV exposures, calibrated with the ground-based flats, the RMS difference between the average magnitude of a star and its magnitude in the first pointing varied from 1.5% to 4.5%, from the long to the short wavelengths (WFC3 ISR 2009-19).

The needed corrections to the ground-based flats are now well understood, including the treatment of expected window ghosts (see WFC3 ISR 2011-16 and Section 6.5.3). New reference files were delivered for all UVIS filters except the QUAD filters in December 2011 (WFC3 ISR 2013-10). The goal was to support photometry to ~1% accuracy over the full WFC3 UVIS field of view for most of the broadband filters (F336W, F390W, F438W, F555W, F606W, F775W, F814W), and to 2-3% accuracy for the remaining filters, for apertures of radius 0.4 arcsec. The actual accuracies of these flat fields were assessed via observations of bright *HST* standard stars on different portions of the detector in 8 filters to quantify any spatial variability in the photometry (WFC3 ISR 2015-18). For the UV filters, photometric residuals due to the crosshatch pattern in the flats (an artifact of the chip manufacturing process; see Figure 5.3) were found to be 1.8% rms and 6.7% peak-to-peak. Color differences between the blue *HST* standards and the average color of Omega Cen, which was used to compute inflight corrections to the ground flats, were found to account for offsets in the UV photometry of up to 5% between the two UVIS chips. Based on this analysis, an improved set of flat fields was generated and delivered to the *HST* archive to support the new chip-dependent calibration implemented in `calwf3` version 3.3 in February 2016 (see Section E.2).

A complete description of the new chip-dependent flat fields is given in WFC3 ISR 2016-04. Flats were computed using the TV3 ground flats and corrected for a large internal reflection or flare that arises due to the expected window ghosts (WFC3 ISR 2011-06). L-flats (low-frequency corrections to the ground flats) were derived from dithered observations of stars in the Omega Cen cluster, and account for low-frequency variations in sensitivity over the detector field of view. The three key differences of the 2016 set of flat field reference files with respect to the prior (2011) set are:

1. The star cluster observations were corrected for CTE (Charge Transfer Efficiency) effects before computing the L-flat;
2. The L-flat solutions were computed from photometry of stars dithered across a single chip only (i.e. they now exclude stars dithered between chips); and
3. The flats were independently normalized using the median value for each chip, rather than a small region on amplifier A. This changed the normalization by less than 1% for filters with pivot wavelengths longer than 400 nm.

The new UV flats are based on ground test data obtained in ambient conditions, and have been corrected for the ~3% sensitivity variations that correlate with a crosshatch pattern (on scales of 50 - 100 pixels) seen in the flats at short wavelengths. Figure 5.3 shows examples of bias-corrected ground-based flats for two wide-band filters. Both are displayed with an inverse greyscale stretch chosen to highlight features; the vignetting in the upper-right corner is not instrument-related but an artifact of the ground test optical stimulus. The crosshatch features in the UV flat field (F336W) are normal, due to the detection-layer structure in the CCDs; the level is typically <5% peak-to-peak compared to the rest of the flat.

During the time between anneals (when the UVIS detector is temporarily warmed; see Section 5.4.9), reductions in sensitivity ~1% to several percent develop in some pixels, especially at the bluer wavelengths (WFC3 ISR 2014-18). Reductions greater than 2-3% are rare in F438W and F814W (0.1% of the pixels), but occur in 3-10% of the pixels in F225W. About 90% of these pixels recover during an anneal, but the more strongly affected pixels can require more than one anneal to recover. Dithering of observations can mitigate the effect.

✓ *The latest information about UVIS flats can be found on the WFC3 UVIS Flats webpage.*

**Figure 5.3: WFC3/UVIS ground-based flat fields at F336W (top) and F555W (bottom).**
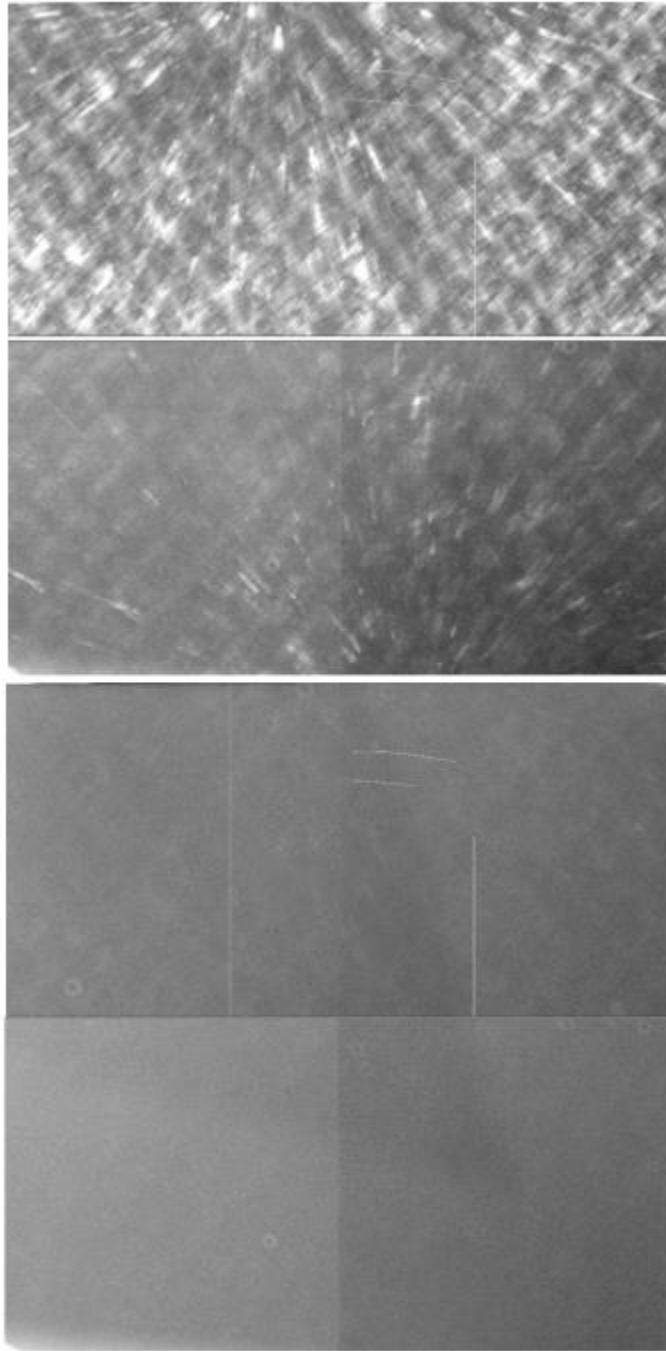


## 5.4.4 Long-Wavelength Fringing

Multiple reflections between the layers of a CCD detector can give rise to fringing, where the amplitude of the fringes is a strong function of the silicon detector layer thickness and the spectral energy distribution of the light source. Like most back-thinned CCDs, the WFC3 CCDs exhibit fringing at wavelengths longward of ~600-700nm (see Figure 5.4). The amplitude of the flat-field signal for monochromatic input increases gradually with wavelength and can reach levels of ± 50% at the longest CCD wavelengths (fringe amplitude is the envelope of the curve shown in Figure 5.5).

An analysis of fringing effects in *broadband-illuminated* ground flats longward of 600nm (WFC3 ISR 2010-04) has shown that F953N has the greatest fringe amplitude (~16%), followed by the quad filters FQ889N, FQ906N, FQ924N, and FQ937N (~10%). Other narrowband and quad filters have fringe amplitudes in the range of 0.5-4.6% (F656N, F658N, FQ672N, F673N, FQ674N, FQ727N, and FQ750N). Although fringing is generally weak at wavelengths shorter than 700 nm, the very narrow H-alpha filter (F656N) exhibits a fringe amplitude of up to several percent in flat fields acquired during ground testing (WFC3 ISRs 2008-17, 2008-46 and 2010-04).

Note, however, that the amplitudes of fringing listed here (and in WFC3 ISR 2010-04) should be used only as an estimate of the effect in science data. Fringing will be different for sources with spectral energy distributions (SEDs) which differ significantly from the calibration lamp used to generate the ground flat fields. For example, continuum sources in broad filters will effectively smooth out fringing effects, but that same filter can show strong fringes when illuminated by sources with strong spectral lines or SEDs much narrower than the filter bandpass. Conversely, for sources with SEDs similar to the calibration lamp, the fringes can be corrected by the flat-fielding process.

The fringe pattern has been shown to be very stable, as long as the wavelength of light on a particular part of the CCD stays constant, so fringing can be corrected if an appropriate flat field is available. The fringe pattern can also be modeled, either by interpolating between or combining monochromatic patterns previously obtained in the laboratory, or from theoretical calculations. For a detailed explanation of efforts to model the WFC3 fringe pattern, see Malumuth et al. (2003, *Proceedings of SPIE* 4854, Future EUV/UV and Visible Space Astrophysics Missions and Instrumentation, pp. 567–576) and "Fringing in the WFC3/UVIS Detector", presented by M. Wong at the 2010 STScI Calibration Workshop.

Figure 5.4: UVIS chip 1 (top) and chip 2 (bottom) fringe pattern for monochromatic illumination at 977 nm.
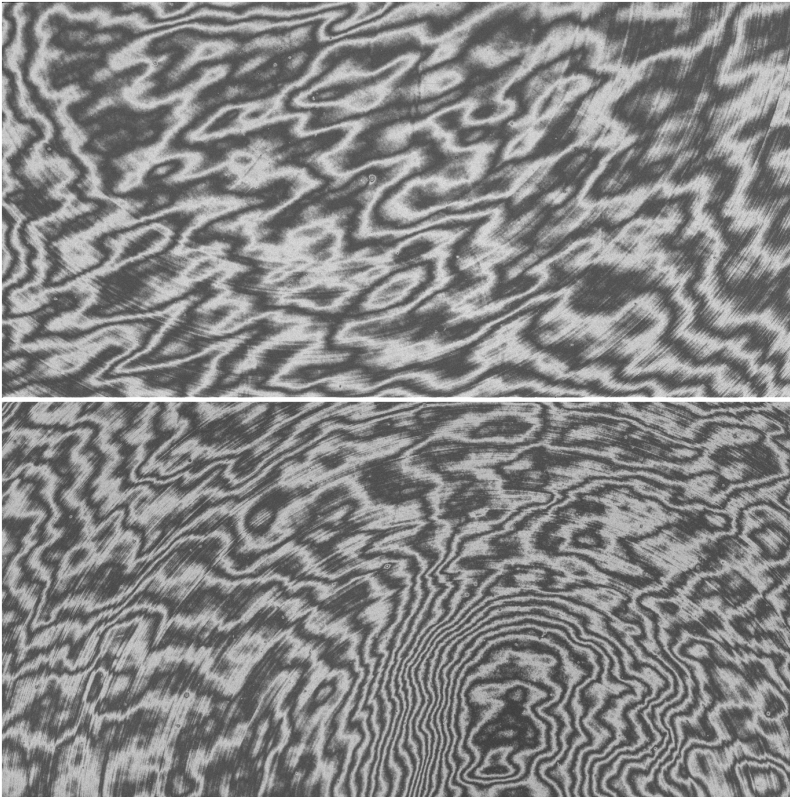
Figure 5.5: Flux (normalized to the mean of the image) as a function of wavelength for a single pixel, based on the Malumuth et al. (2003) model. Fringe phase (rapid oscillation) and fringe amplitude (curve envelope) vary as a function of wavelength. Due to wavelength averaging (even within narrow band filter bandpasses), actual WFC3 data exhibit peak to trough fringe amplitudes of < 30%.
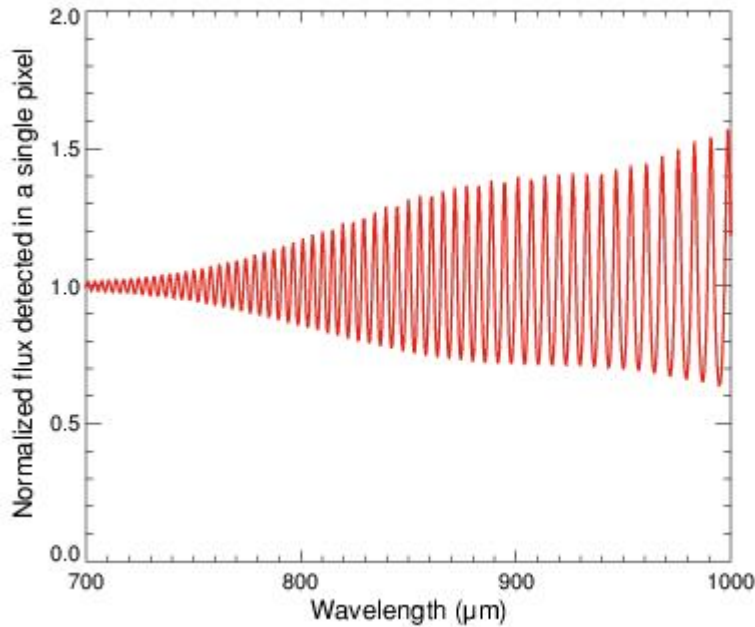


## 5.4.5 Linearity and Saturation

The dynamic range of a detector is limited either by the full-well capacity of the device or by the analog-to-digital converter (ADC) and gain setting that are used during readout to convert the accumulated charge into data numbers (DN). At the standard UVIS gain of ~1.5 e⁻/DN, saturation always occurs on chip unless binning is used, in which case saturation of the binned readout pixel can occur in the ADC; see Section 5.4.6 for the numerical limits on DN and electrons for unbinned and binned readouts. If saturation occurs on-chip, photometric information can still be recovered with reasonable accuracy, as described below. If the charge accumulated in a given (binned) readout pixel exceeds the ADC maximum, any additional charge does not result in any further increase in the DN and may, in cases of extreme saturation, result in values of zero. Extreme over-exposure is not expected to cause any long-term damage to the CCDs, so there are no bright-object limits for the WFC3 CCDs.

On-orbit observations have shown that on UVIS2, the onset of saturation varies from about 67000 to 72000 electrons per pixel over the CCD, while UVIS1 has a somewhat larger range of 63000 to 71000 electrons per pixel (WFC3 ISR 2010-10). The distribution of full well depth on the detector is shown in Figure 5.6. Once the charge exceeds the pixel full-well level, it can escape that pixel and spread into adjacent vertical pixels; as the signal continues to accumulate, these adjacent pixels themselves can accumulate charge up to full-well and leak into further adjacent vertical pixels, resulting in the "blooming," or charge overflow, effect. The multi-phased pinned (MPP; see Section 5.4.8) operation of the detectors, used to minimize surface dark current, constrains the blooming along the detector columns, so the blooming is only vertical and not horizontal. Photometric information well beyond saturation can be recovered for relatively isolated sources in unbinned images by defining a special aperture that encompasses all of the pixels that contain the bloomed charge. WFC3 ISR 2010-10 presents an algorithm that can be invoked for UVIS1 to regain full linearity to ~1% up to nearly 7 magnitudes past saturation. UVIS2 is linear with simple summation over the saturated pixels. Some small non-linearities (a few percent) have been detected at the lowest signal levels at greater distances from the amplifiers, but the behavior is consistent with CTE loss (Section 5.4.11) rather than a true non-linearity in the chips.

Figure 5.6: The distribution of full well depth, in electrons, for UVIS 1 (top half) and UVIS 2 (bottom half). The full well depth is the threshold at which charge begins to bloom for point sources.



Full Well Depth (electrons)
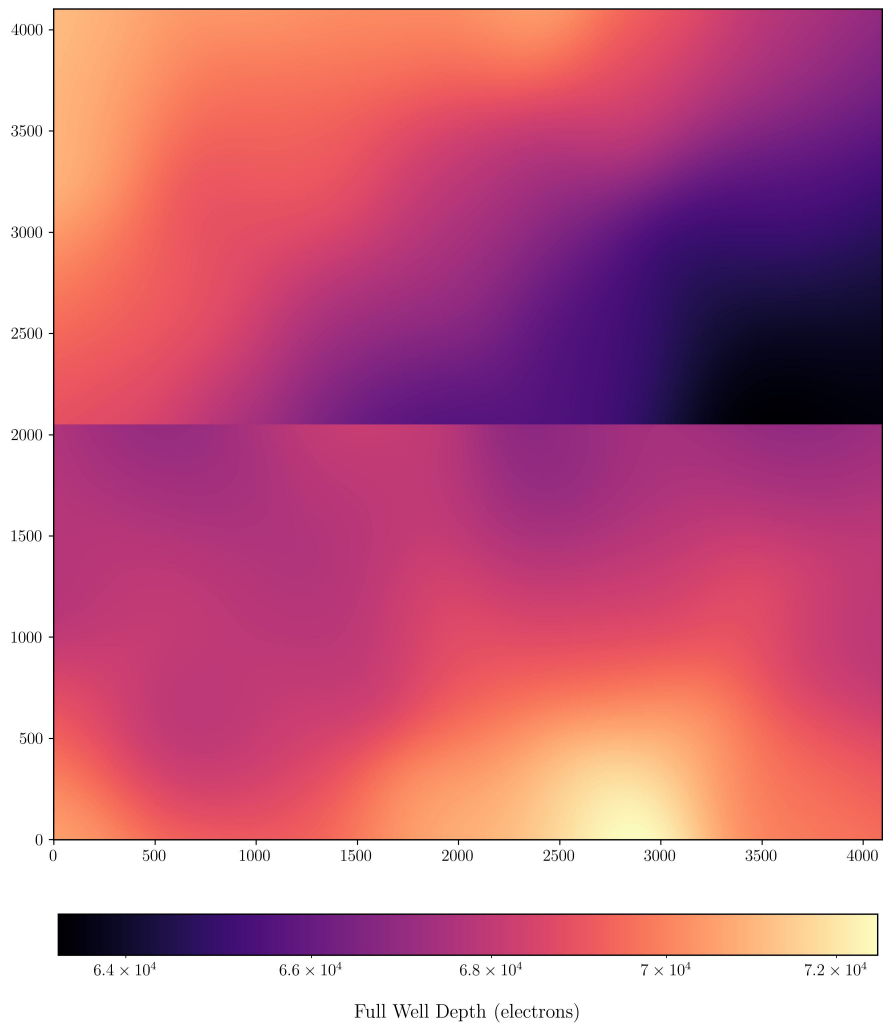
> ✅ FITS files showing the distribution of full well depth across both UVIS 1 and UVIS 2 are available for download at the Full Well Depth webpage.

## 5.4.6 Gain

Electrons that accumulate in the CCD wells are read out and converted to data numbers (DNs), often called Analog-to-Digital Units (ADUs), by the analog-to-digital converter (ADC). The conversion gain is defined as the number of electrons required to produce one DN. The ADC output is a 16-bit number, limiting the maximum DN that can be read out to $2^{16}$ - 1 or 65,535 for each readout pixel (single or binned detector pixel). Setting the conversion gain to unity, where one DN corresponded to one electron, would make it impossible to measure signals larger than 65,535 electrons. Adjusting the gain somewhat higher, so that multiple counts correspond to a single DN, allows larger numbers of electrons to be measured; however, the gain must also be low enough that it provides adequate sampling of the read noise.

For WFC3, the default gain has been set to ~1.5 e¯/DN. The maximum full well depth of the pixels on the WFC3/UVIS chips is ~72500 e¯ (Figure 5.6), which at the default gain corresponds to ~48000 DN, well below the ADC limit of 65,535 DN. If the pixels are binned 2 × 2 or 3 × 3, the binned pixels could reach flux levels of 4 or 9 times 48,000 DN, respectively, which would be truncated to 65,535 DN (~98,300 e¯) during readout. Although it is possible to operate the WFC3 CCD detector at gains of ~ 1, 1.5, 2, and 4 e¯/DN, only the gain of ~1.5 e¯/DN is supported. For unbinned readouts, this gain permits sampling of the entire dynamic range of the detectors, with negligible impact on the readout noise.

The on-orbit measured gain values for the WFC3 CCDs as of June 2022 are presented in Figure 5.7 and summarized in Table 5.3 (WFC3 ISR 2022-08). The gain is increasing slightly with the age of the detector, partially due to CTE degradation, but remains consistent over time to within 1-2%.

**Table 5.3: WFC3/UVIS Gains, as of June 2022.**

| CCD Chip | Amp | Gain(e¯/DN) |
|---|---|---|
| 1 | A | 1.587 |
| | B | 1.578 |
| 2 | C | 1.607 |
| | D | 1.592 |

**Figure 5.7: Gain stability measurements across all four amplifiers from October 2009 to June 2022 (WFC3 ISR 2022-08).**
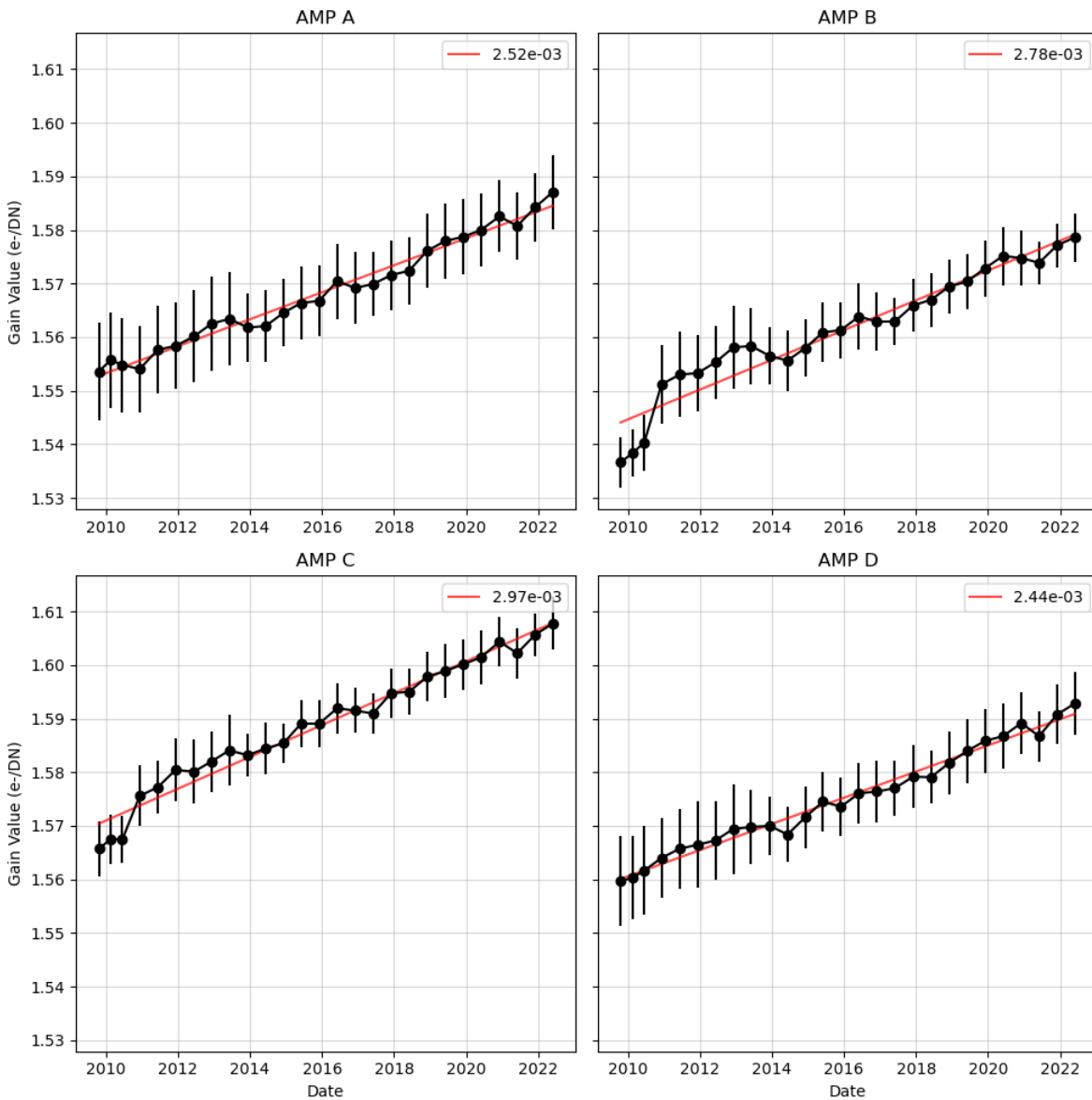


## 5.4.7 Read Noise

The read noise level in the science area pixels of bias frames for all of the amplifiers at the default gain setting was measured in 2009 during SMOV (WFC3 ISR 2009-26). Table 5.4 shows the results obtained at the default gain setting of 1.5 e⁻/DN. The read noise was found to be stable to 1%, 0.4%, 0.7%, and 0.8%, for amps A,B,C, & D, respectively, based on measurements through the end of August 2009. The read noise is monitored on a monthly cadence using full-frame UVIS bias images. An analysis of long-term trends showed the read noise increased by 0.06-0.075 electrons (0.01 electrons/year from 2009 to 2017; WFC3 ISR 2017-17).

Trend appear to be stable with no deviations or sudden changes. The increase in read noise is attributed to the on-going CTE degradation as well as a growing number of hot pixels; see Section 6.9 for more details.

Table 5.4: WFC3/UVIS readout noise (e⁻) and uncertainty for normal and binned modes in 2009.

|  | Amplifier A | | | | Amplifier B | | | | Amplifier C | | | | Amplifier D | | |
|---|---|---|---|---|---|---|---|---|---|---|---|---|---|---|---|
| Binning | 1 × 1 | 2 × 2 | 3 × 3 | | 1 × 1 | 2 × 2 | 3 × 3 | | 1 × 1 | 2 × 2 | 3 × 3 | | 1 × 1 | 2 × 2 | 3 × 3 |
| Mean | 2.91 | 3.11 | 3.22 | | 2.99 | 3.15 | 3.26 | | 2.90 | 2.99 | 3.09 | | 3.01 | 3.29 | 3.38 |
| Uncertainty | 0.03 | 0.02 | 0.04 | | 0.01 | 0.01 | <0.01 | | 0.02 | <0.01 | 0.01 | | 0.02 | 0.02 | <0.01 |

Analysis of the statistical behavior of the WFC3 ADCs showed some tendency for the least significant bit to be slightly biased at the readout speed adopted by the WFC3 electronics (WFC3 ISR 2005-27). However this effect is minor and does not degrade the photometric and noise characteristics of the WFC3/UVIS images.

## 5.4.8 Dark Current

The WFC3 CCDs, like most large-area scientific CCDs, operate with buried channels. Earlier generations of CCDs worked with surface channels, i.e., storing and transferring charges only along the surface of the semiconductor material. In these earlier devices, the Si-SiO2 interface between the detector material Si (p-doped conductor) and the surface layer of SiO2 (isolator) created significant charge traps, which limited both the charge transfer efficiency and the dark current (current measured without incident flux). In buried-channel devices, a shallow (~0.5 micron thick) n-type Si layer is implanted just below the surface between the p-doped Si and the $SiO_2$ surface, to store and transfer the collected signal charge away from the traps at the interface.

Dark current in WFC3 detectors is further reduced using MPP (multi-phased pinned) technology. The dark current generated at the Si-$SiO_2$ interface ultimately depends on two factors: the density of interface states and the density of free carriers (holes and electrons) that populate the interface. Electrons can thermally "hop" from the valence band to an interface state (sometimes referred to as a "mid-band state") and from there to the conduction band, producing a dark electron-hole pair. Free carriers also fill interface states and, if these states were completely populated, can suppress hopping and conduction, reducing the surface dark current at levels comparable to the bulk dark. Unfortunately, normal CCD operations deplete the interface of free carriers, maximizing dark current generation.

In MPP technology, the Si-SiO$_2$ interface is populated with holes that suppress the hopping conduction process. MPP mode is applied to the CCD by significantly biasing the array clocks negatively to invert (push electrons away from) the n-buried channel and "pin" the surface potential beneath each phase to substrate potential (hence the name multi-pinned phase). Biasing the array clocks in this manner causes holes from the p+ channel stops to migrate and populate the Si-SiO$_2$ interface, eliminating surface dark-current generation. Note that it is not possible to invert conventional CCDs in this way, as the sensor's full-well capacity would be annihilated since the potential wells within a pixel all assume the same level. To circumvent this difficulty in MPP CCD technology, an additional implant is included below one of the phases, allowing charge to accumulate in collecting sites when biased into inversion.

Besides eliminating surface dark current, MPP CCD technology offers additional advantages. For example, the charge transfer efficiency of a CCD generally degrades with decreasing operating temperature. MPP technology assists in the charge transfer process because it permits the use of higher operating temperatures.

The MPP CCD also eliminates residual image, a serious problem that has plagued low-signal-level CCD users for many years. Residual image, also known as quantum-efficiency hysteresis, results when the sensor is either overexposed or first powered up. Under these circumstances, electrons trapped at the Si-SiO$_2$ interface are slowly released into the pixel's potential well. Residual charge may take hours or even days before its level falls below the read-noise floor. Inverting the CCD causes holes to recombine immediately with the trapped residual electrons, eliminating remnant image effects during integration as well as readout.

During pre-flight tests, the CCD dark current was measured both in the cryogenic environment at the DCL, and in the instrument during thermal vacuum testing. The dark current levels have been regularly evaluated, e.g. during the 2004 thermal vacuum testing (WFC3 ISR 2005-13), early after installation in HST (WFC3 ISR 2009-16), and since then (WFC3 ISR 2014-04; WFC3 ISR 2016-08; WFC3 ISR 2019-10).

Like all CCDs operated in a low-earth-orbit radiation environment, the WFC3 CCDs are subject to radiation damage by energetic particles trapped in the radiation belts. Ionization damage and displacement damage are two types of impairment caused by protons in silicon. The MPP mode is very effective in mitigating the damage due to ionization, such as the generation of surface dark current due to the creation of new trapping states in the Si-SiO$_2$ interface. Although protons lose only a minor fraction of their total energy via non-ionizing energy loss, lattice displacement damage can cause significant performance degradation in CCDs by decreasing the charge transfer efficiency (CTE), increasing the average dark current, and introducing pixels with very high dark current (hot pixels). Displacement damage to the silicon lattice occurs mostly due to the interaction between low-energy protons and silicon atoms. The generation of phosphorous-vacancy centers introduces an extra level of energy between the conduction band and the valence band of the silicon. As described above, new energy levels in the silicon bandgap increase the dark current as they allow thermally generated charges to reach the conduction band. As a consequence, the dark current of CCDs operated in a radiative environment is predicted to increase with time.

The measured dark current, defined as the median level of the pixels below the hot pixel threshold (defined as 54 e-/hr), is shown in Figure 5.8. As expected, due to radiation damage the dark current has been slowly increasing over time. In November 2012, post-flash became available for use to reduce CTE losses by increasing the image background (Section 5.4.11). As a result, the measured dark current levels dropped (WFC3 ISR 2014-04): with post-flash, CTE losses are reduced, which in turn reduces the flux trailed out from hot pixels and cosmic ray hits due to delayed release of electrons, thereby decreasing the dark current as well as increasing the measured number of hot pixels (Section 5.4.9). Later, in November 2020, the post-flash level was increased from 12 to 20 e-/pixels to compensate for continuing CTE losses, resulting in another slight reduction in the measured dark current (and increase in hot pixels).

As of February 2016, with the introduction of `calwf3` version 3.3 into the calibration pipeline, CTE-corrected images and calibration files have been produced (WFC3 ISR 2016-08). The CTE correction helps return electrons that have trailed out of their original pixel back to the pixels they came from, which allows for a more accurate measurement of the dark current and hot pixel levels. The result is a further reduction in median dark current and a smaller dispersion than for darks without a CTE correction (compare Figure 5.9 versus Figure 5.8). The rate of increase is also somewhat less than for darks without a CTE correction and there is an increase in the measured number of hot pixels at that time (Section 5.4.9).

Reference file darks made from unflashed and flashed dark exposures have been analyzed to better quantify the effects of post-flash on the dark pixel population and the hot pixel population (WFC3 ISR 2019-10).

**Figure 5.8: Median dark current (e⁻/hr) of the WFC3/UVIS CCD 2 detector measured on orbit from June 2009 to October 2024, for non-CTE corrected darks ("blv_tmp" FITS files). Points are color-coded by post-flash levels for UVIS dark frames. Light and dark gray vertical shading indicates the monthly anneal periods. Vertical dashed lines mark some of the HST safing events within the past five years.**
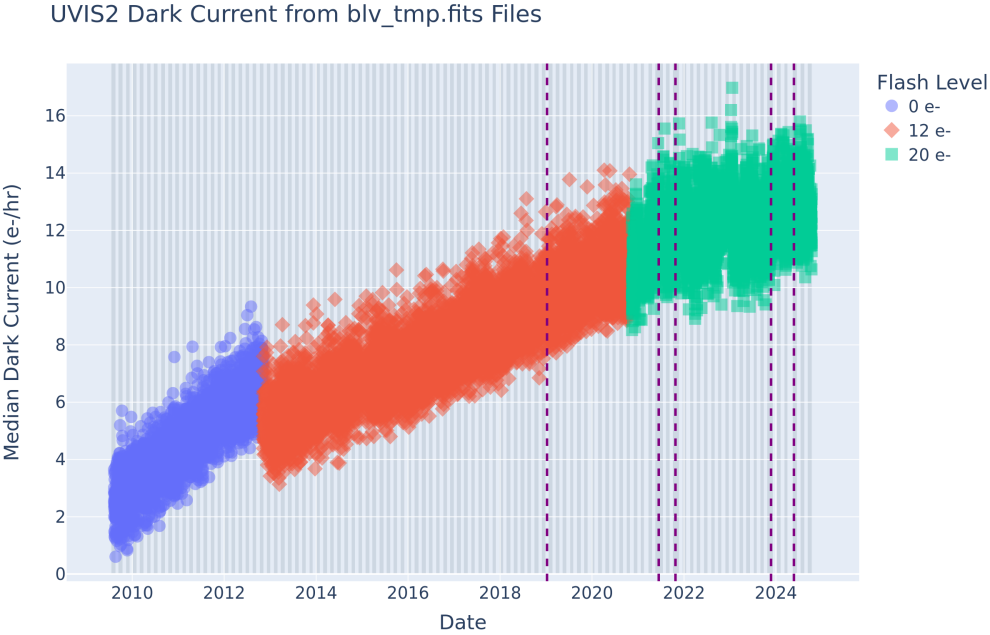
Figure 5.9: Median dark current of the WFC3/UVIS CCD 2 detector measured on orbit from June 2009 to October 2024, for CTE-corrected darks ("blc_tmp" FITS files). Points are color-coded by post-flash levels for UVIS dark frames. Light and dark gray vertical shading indicates the monthly anneal periods. Vertical dashed lines mark some of the HST safing events within the past five years.
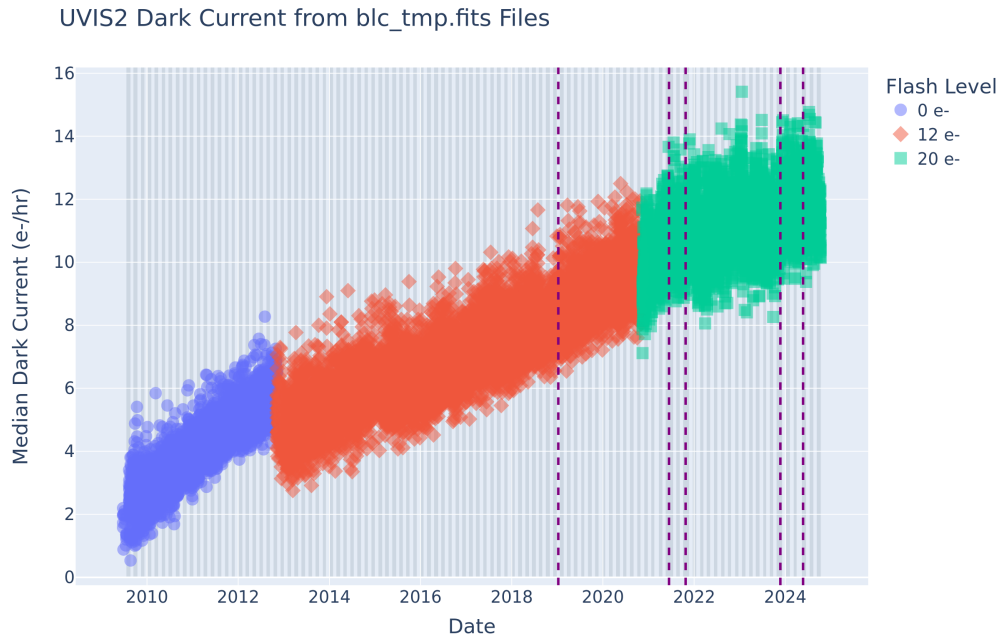


## 5.4.9 Bad Pixels

Three types of bad pixels are routinely monitored using on-orbit WFC3 data: hot pixels (higher than normal dark current), bad detector pixels (unstable, often with extremely low quantum efficiency), and sink (charge trap) pixels and their associated trails. All these pixels are flagged in the DQI array of the calibrated data with values 16, 4, and (since Feb 2016 with the installation of `calwf3` version 3.3) 1024, respectively (see also Appendix E and WFC3 ISR 2014-19).

On orbit, the number of hot pixels increases with time due to radiation damage, but is periodically partially reduced by annealing, when the UVIS detector is temporarily warmed to ~20°C. The number of sink pixels also grows over time, presumably because they are radiation-induced; unlike hot pixels, sink pixels appear to be unaffected by anneals. The extent of the sink pixel CTE trail to be flagged is based on the science image background: the lower the background is, the longer the sink pixel trail will be (WFC3 ISR 2014-19, WFC3 ISR 2014-22).

The bad detector pixel population, generally located along columns, is relatively constant. Bad detector pixels are shown for the upper chip (chip 1) and lower chip (chip 2) in Figure 5.10 and Figure 5.11, respectively. Note that a pair of bad columns passes near the center (reference pixel) of the subarray aperture UVIS2-C512C-SUB, which is at [282, 257] in the lower left corner of chip 2.

Figure 5.10: Bad detector pixels (DQI = 4) on the upper chip (chip 1) are in columns 1104, 2512, 2542, 2543, 2869, 3646, and 3667 in the flt image.
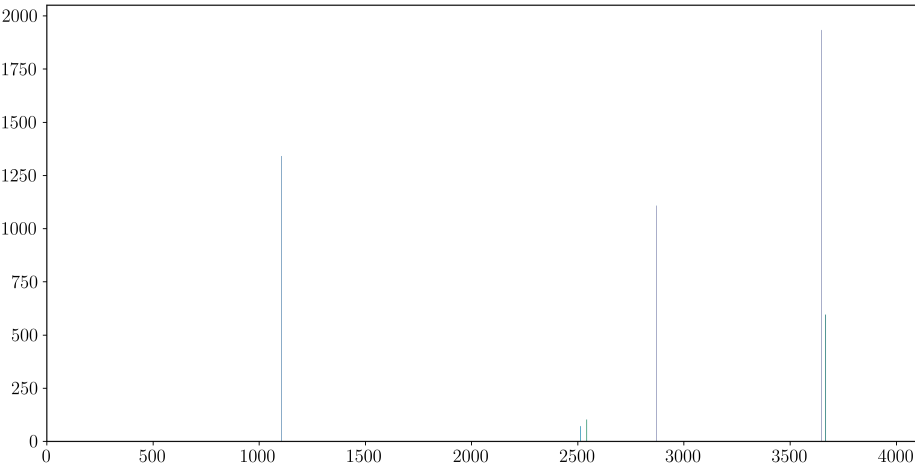
**Figure 5.11:** Bad detector pixels (DQI = 4) on the lower chip (chip 2) are in columns 223, 242, 243, 751, 1417, 1469, 2655, 2696, 2707, and 3915 in the flt image.
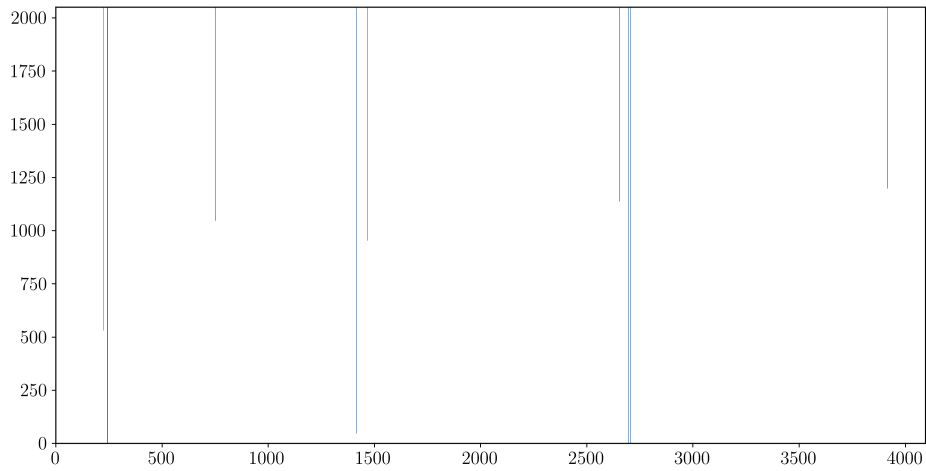


Figure 5.12 shows a histogram of superdarks taken at three different times after the anneal procedure on March 31, 2010: about 1 day (red line), 11 days (green line), and 26 days (blue line) later. Superdarks are created by averaging together approximately 5-15 dark exposures that are each 900-seconds long. These are the final reference files delivered to CRDS and used for UVIS data calibration in the calwf3 pipeline (see WFC3 ISR 2016-08 for more information on superdarks). The impact of on-orbit radiation damage can be seen in the increase in hot pixels between the three different times; radiation damage also produces an increase in dark current as well (see Section 5.4.8 ). The vertical line at 54 e-/hr (13.5 e-/pixel) represents the previously-implemented hot pixel threshold, which was based on the tail of the dark current distribution and 900-second dark frames from 2009. For data from 2012-2020, when post-flash levels were at 12 e-/pixel, the UVIS bad pixel table pipeline used the 13.5 electron threshold.

After increasing post-flash from 12 to 20 electrons in June 2020 to better mitigate CTE losses (WFC3 ISR 2020-08; WFC3 ISR 2021-03; WFC3 ISR 2021-06), it was observed that this ultimately led to a significant percentage of stable pixels being misflagged as unstable. To correct for this, in 2021 the WFC3 team implemented a formula into the pipeline to determine the hot pixel threshold; this formula is dependent on the post-flash level and dark current on the detector, and thus ensures a more accurate measurement of the unstable pixel population that is independent of future modifications to post-flash configurations (WFC3 ISR 2021-14).

**Figure 5.12:** Superdark histograms illustrate the increase in the number of hot pixels (>54 e–/hr) between anneal procedures. The March 31, April 11, and April 26 curves (red, green, and blue, respectively) are from 1-3 days after the anneal procedure, about mid-way between anneals, and about 1-3 days prior to the next anneal procedure.
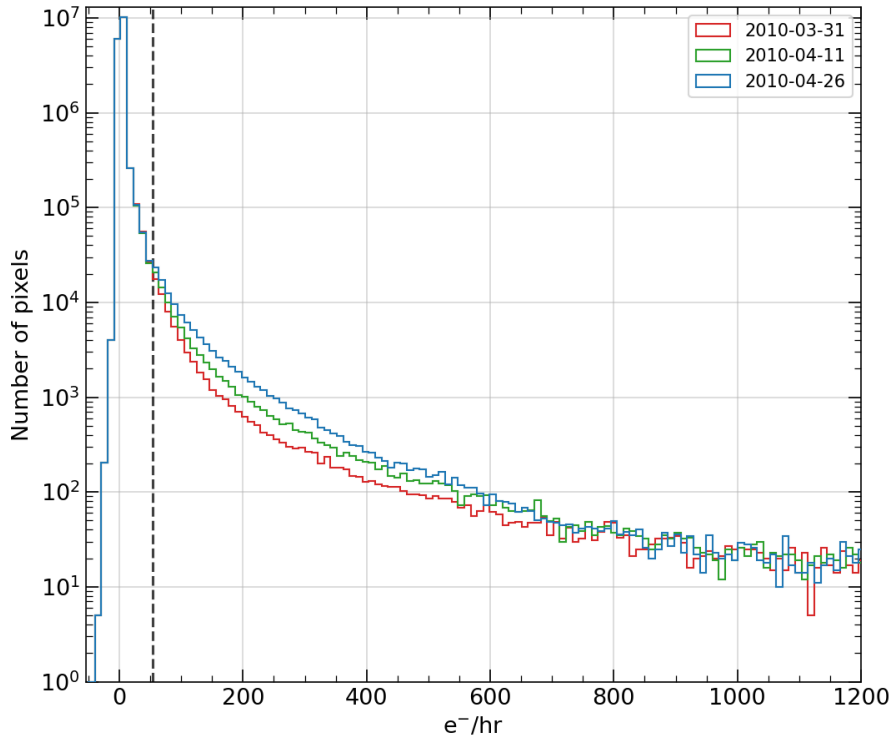


Figure 5.13 shows the number of hot pixels as a function of time since the installation of WFC3 on *HST* as measured using the non-CTE-corrected darks, while Figure 5.14 shows the same measurement made with the CTE-corrected darks which first became available in February 2016 (see WFC3 ISR 2016-08 and Section 5.4.8). Prior to Oct. 2009, WFC3 safings warmed the chips to 20°C, the temperature attained in the annealing procedure. Blue points indicate darks acquired with no post-flash; red and green points indicate darks that were acquired with post-flash (at levels of 12 e⁻/pix and 20 e⁻/pix, respectively), a change made to reduce CTE losses (Section 5.4.11). The increased background level introduced by post-flash reduces the trailing of electrons from hot pixels along columns during the readout, so more hot pixels are detected above the threshold, accounting for the discontinuity in the number of hot pixels at those transition points. Less trailing from hot pixels results in a corresponding drop in the measured dark rate as well (Section 5.4.8). The number of permanent hot pixels, i.e., pixels that the anneals are unable to fix, is growing by 0.03-0.1% per month whether using non-CTE-corrected darks or CTE-corrected darks (WFC3 ISR 2016-08).

Figure 5.13: Hot pixel growth for the WFC3/UVIS CCD 2 detector between anneals from June 2009 to October 2024, as measured from non-CTE-corrected darks ("blv_tmp" FITS files). Points are color-coded by post-flash levels for UVIS dark frames. Light and dark gray vertical shading indicates the monthly anneal periods. Vertical dashed lines mark some of the HST safing events within the past five years.
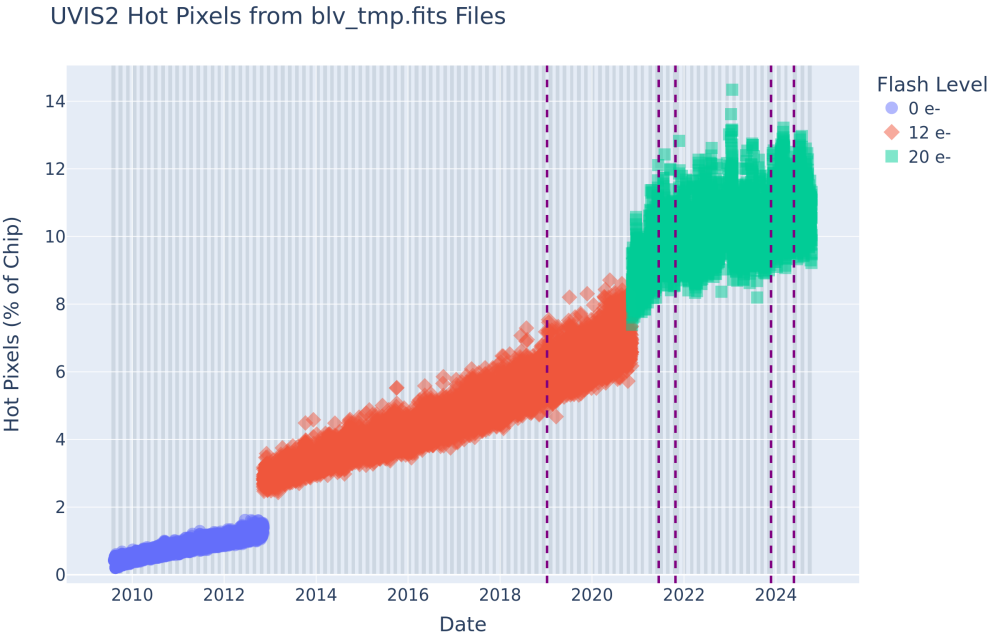
**Figure 5.14:** Hot pixel growth for the WFC3/UVIS CCD 2 detector between anneals from June 2009 to October 2024, as measured from CTE-corrected darks ("blc_tmp" FITS files). Points are color-coded by post-flash levels for UVIS dark frames. Light and dark gray vertical shading indicates the monthly anneal periods. Vertical dashed lines mark some of the HST safing events within the past five years.
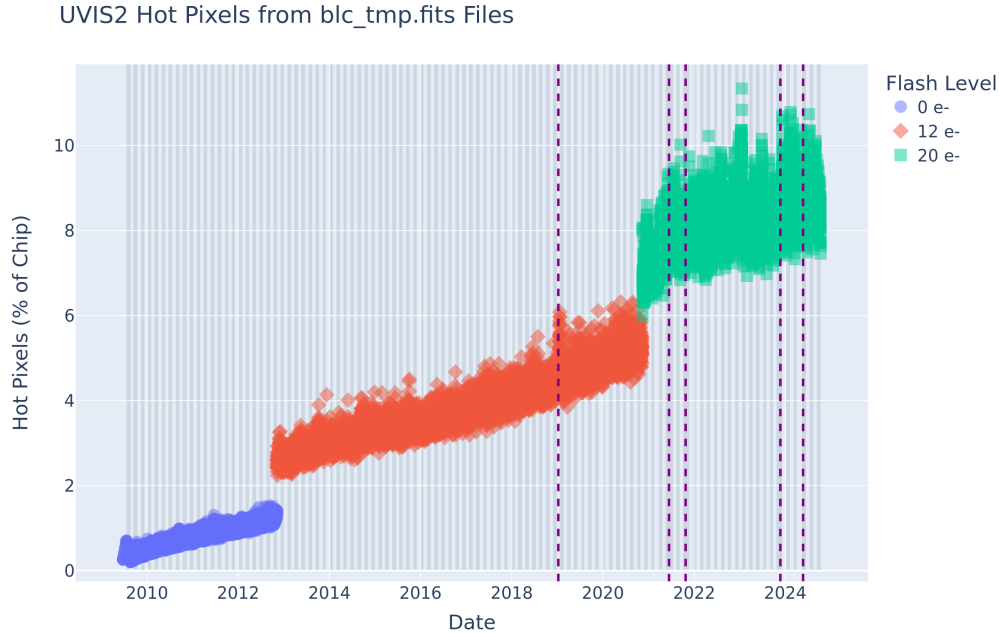


There are three significant differences between the measurements of hot pixels using the non-CTE-corrected darks (Figure 5.13) and using the CTE-corrected darks (Figure 5.14). With the pixel-based CTE correction, there is a tightening of the spread of the measurements of the percentage of hot pixels over time. The percentages and the growth rate are also lower for the CTE-corrected darks than for the un-corrected darks. These differences occur because the CTE correction algorithm helps return electrons that have trailed out of their original pixel back to their pixels of origin, which leads to additional (and more reliably) detected hot pixels. Since hot pixels are defined above a specific cut-off, when electrons trail into pixels they don't belong in, this adds additional noise to the hot pixel measurements by adding false positives or reducing a hot pixel below the cutoff level. The result is a larger spread in the measurements towards higher rates at a given date, as seen in the non-CTE-corrected measurements in Figure 5.13.

In 2018, a detailed study of pixel behavior over time in the UVIS CCDs showed that the vast majority of hot pixels are in fact quite stable and, as such, can be calibrated (WFC3 ISR 2018-15). A small portion of pixels are genuinely unstable and should not be used; some of these are hot and unstable while others are cold and unstable. The numbers of these unstable populations (< ~1% of chip) have remained nearly unchanged over the years (Figure 5.15). To allow the pipeline to handle the distinction between stable and unstable hot pixels, the UVIS bad pixel reference file now employs the flag of 32 in the Data Quality (DQ) array to mark unstable pixels. Hot pixels continue to be assigned the usual DQ flag of 16 (Table E.3). With the additional stability DQ flag, observers have enhanced control over which pixels to include, or exclude, from their analyses.

**Figure 5.15:** The number of pixels (as a percentage of the detector) as a function of type: hot, cold, stable, and unstable.
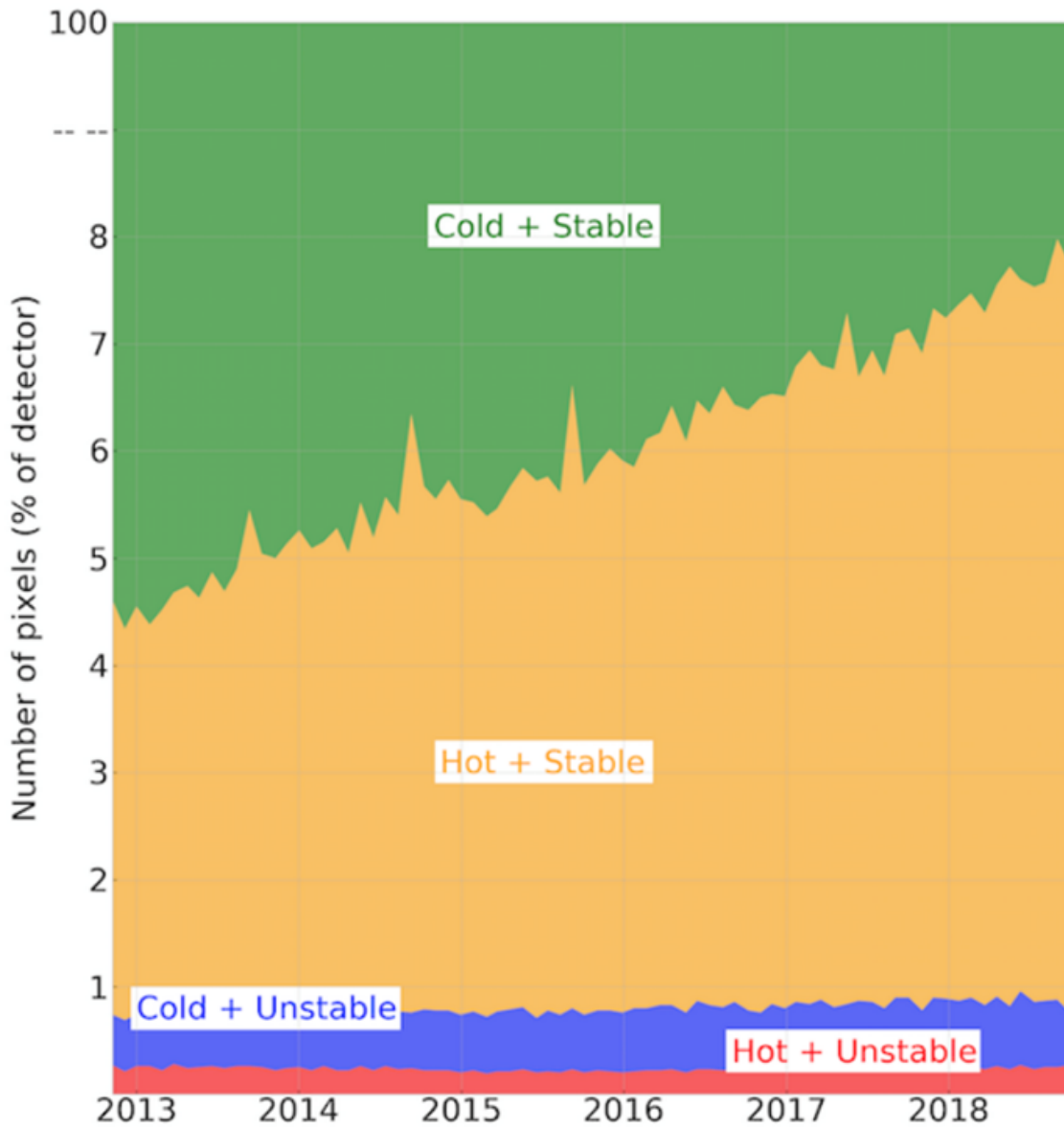


## 5.4.10 Cosmic Rays

The fraction of WFC3 pixels impacted by cosmic rays varies from 5% to 9% per chip during 1800 sec exposures in SAA-free orbits, providing a basis for assessing the risk that the target(s) in any set of exposures will be compromised. Observers seeking rare or serendipitous objects, as well as transients, may have stringent requirements on how many cosmic rays can be tolerated in an image combination. Assuming cosmic-rays affect 5-9% of a chip in 1800 sec, at least 4-5 images will be needed to ensure that fewer than 100 pixels will be hit in all images of the combination.

The flux deposited on a CCD from an individual cosmic ray depends less on the energy of the cosmic ray than on the distance it travels in the silicon substrate i.e. its direction of incidence. The electron deposition due to individual cosmic rays measured with ACS/WFC has a well-defined cutoff, with negligible events of less than 500 e⁻ and a median of ~1000 e⁻ (Figure 5.16). Similarly, the overall characteristics of the cosmic ray population appear nominal in WFC3. Miles et al. 2021 found that the rate of cosmic ray hits is ~1 hit per $cm^2$ $s^{-1}$, and a typical hit corresponds to ~2200 e⁻.

**Figure 5.16: Electron deposition by cosmic rays on ACS/WFC.**
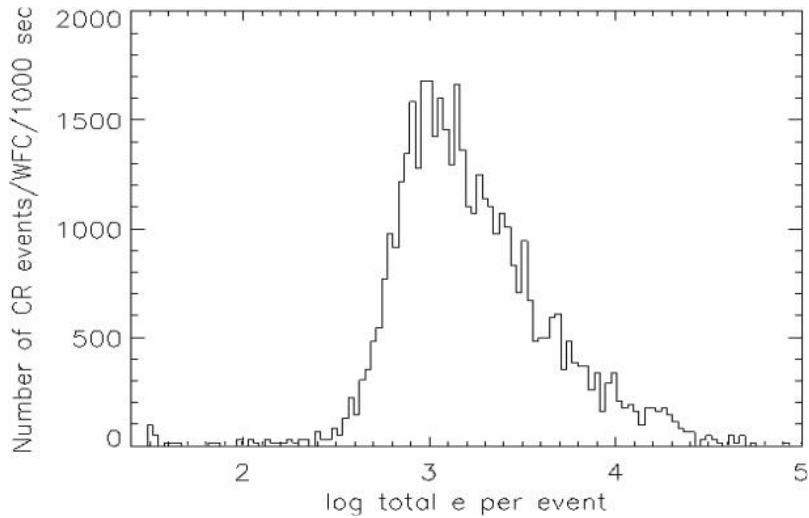


## 5.4.11 Charge Transfer Efficiency

Uniform response within each pixel and excellent charge transfer efficiency (CTE) are key to achieving accurate photometric performance. CTE is a measure of how effective the CCD is at moving charge from one pixel location to the next when reading out the chip. A perfect CCD would transfer 100% of the charge as it is shunted across the chip and then out through the serial register. In practice, small traps in the silicon lattice compromise this process by retaining electrons, and then releasing them at a later time. Depending on the trap type, the release time ranges from a few microseconds to several seconds. For large charge packets (many thousand electrons), losing a few electrons along the way is not a serious problem, but for smaller signals, it can represent a substantial fraction. The UVIS CCDs are large-format devices, similar in size to those in the ACS WFC, and thus require significantly more charge-shifting steps during readout, with more losses, than smaller devices like the STIS and WFPC2 CCDs. CTE inevitably declines over time as on-orbit radiation damage creates charge traps in the detector. Furthermore, WFC3 was installed during solar minimum, when the cosmic flux is greatest and radiation damage most rapid, so the UVIS detector experienced a steeper decline in CTE in its early years than the ACS WFC, which was deployed at a more favorable time (Baggett et al. 2011).

Several steps were taken in the design of WFC3 to reduce CTE losses on the UVIS detector. First, shielding (similar to ACS/WFC) has been used to protect the CCDs from the high-radiation space environment, thereby slowing the production of charge traps. Second, the WFC3 CCDs have been designed with a mini-channel (improved over ACS/WFC), which reduces the number of traps seen by small charge packets during read-out transfers. Third, the detector has a charge-injection capability (not generally available for science observations - see Section 6.9.2), which inserts charge electronically in equally spaced rows of pixels to fill the charge traps (WFC3 ISR 2011-02). Fourth, an operational mode has been developed to provide a flash of light from an LED at the end of an exposure to increase the background level in the exposure. Use of this post-flash mode is now strongly recommended for observations of faint objects when the background level is expected to be less than 20 e-/pixel. The rationale for using this mode was presented in MacKenty and Smith (2012). The state of the UVIS detector's CTE at that time is also discussed in Baggett et al. (2012). Given the current state of the CTE losses, the optimal background level (sky plus dark current plus post-flash if needed) is now 20 e-/pixel (see Section 6.9.2).

CTE is typically measured as a pixel-transfer efficiency, and would be unity for a perfect CCD. One way to measure CTE is via the Extended Pixel Edge Response (EPER) method, where a specialized readout takes flat-field exposures with a significant amount of overscan. Inefficient transfer of electrons in such exposures produces an exponential tail of charge into the overscan region. Analysis of EPER monitoring observations from 2009 through May 2020 showed a roughly linear decline of CTE over time (WFC3 ISR 2020-06). As expected, the EPER results show that the CTE has continued to decline with time and is steeper for the fainter signal levels. In addition, the trend of the linear fit residuals for the lowest EPER level show a periodicity which is anti-correlated with sunspot counts, i. e. solar activity (see Figure 5.17) This was not unexpected, given that the strength of the South Atlantic Anomaly, a region particularly damaging to instruments and through which HST must regularly pass, is also anti-correlated with the solar cycle.

**Figure 5.17:** Decline of EPER CTE over time in years as a function of illumination level (electrons) with over-plotted linear fits. Periodic deviations from the fits are anti-correlated with solar activity.
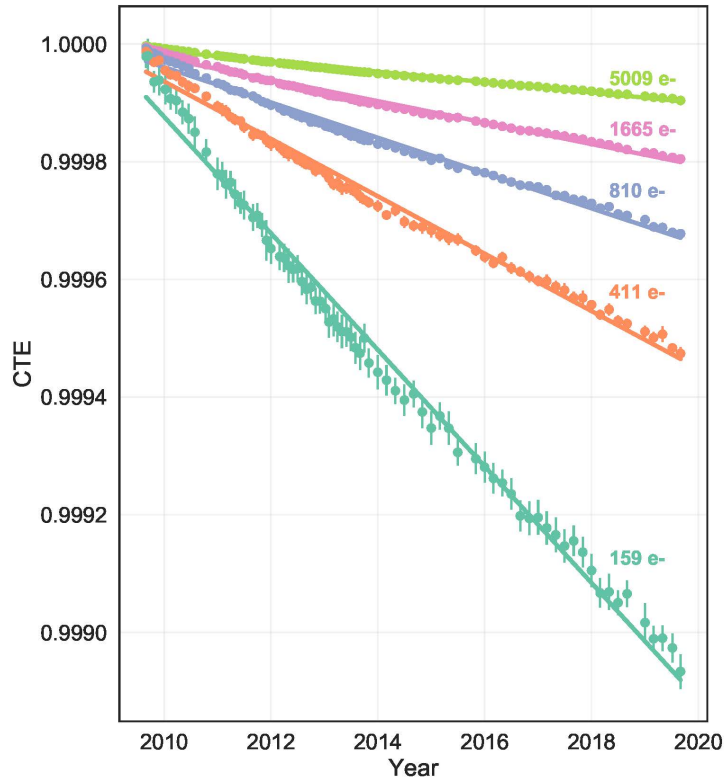


The CTE changes tracked with EPER testing provide a guide to likely evolution in time, but due to the specialized readout mode, cannot be directly interpreted to predict CTE loss as a function of target and background signal level in science images. Instead, occasional observations of stellar clusters are being used to monitor CTE losses. Early work in this area is shown in Figure 5.18 (Rajan et al., 2010 STScI Calibration Workshop). The figure illustrates how CTE affects stellar photometry for a stellar cluster as a function of the number of transfers along columns. The normalized ratio of stellar fluxes measured in a long exposure to fluxes measured in a short exposure is shown as a function of Y position on the detector for stars within a limited flux range. The ratio increasingly deviates from 1 at greater distances from the readout amplifiers because CTE losses are relatively greater for the short exposure, where the signal is smaller. Subsequent observations of stellar clusters have shown strong evolution of CTE on the UVIS CCDs, as expected from the commencement of on-orbit operations during the minimum of the solar cycle. See Section 6.9 for further monitoring of CTE using exposures of stellar clusters and advice to observers; the WFC3 CTE page contains updated information on CTE and links to relevant documents.

**Figure 5.18:** Normalized ratio of stellar fluxes measured in a long exposure of NGC 1850 to fluxes measured in a short exposure, shown as a function of Y position on the detector. Positions of 0 and 4096 reflect the location of the readout amplifiers. The ratio deviates from 1 due to the relatively greater CTE losses in the shorter (fainter) exposure.
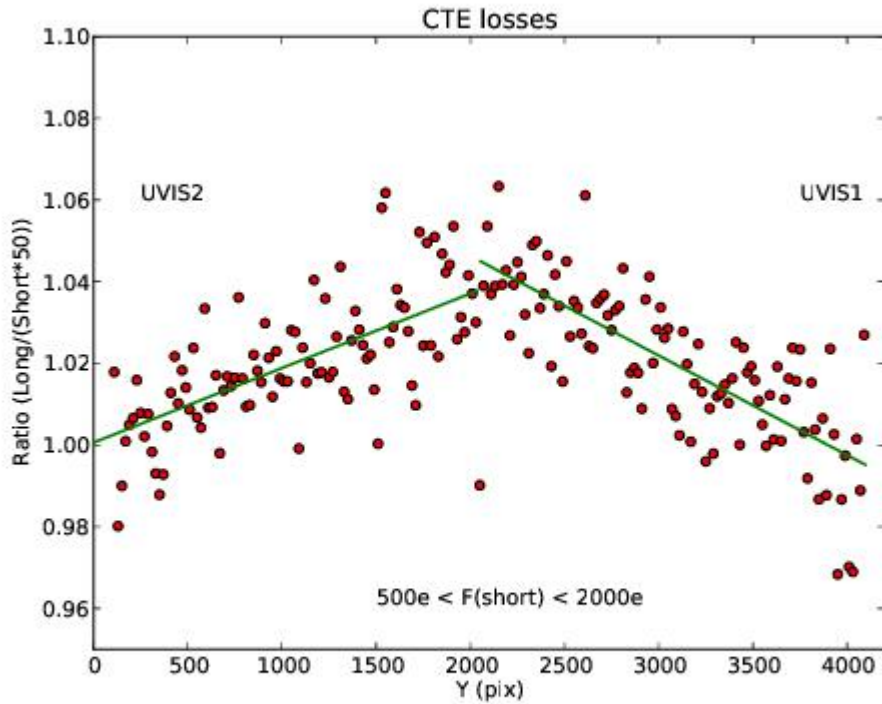


## 5.4.12 Crosstalk

Crosstalk, a type of electronic ghosting, is common in devices where two or more quadrants are read out simultaneously and WFC3 is no exception. Both the UVIS and IR channel exhibit low levels of crosstalk.

In the UVIS channel, point sources and extended targets generate a low-level, negative mirror images in the quadrant adjoining the target quadrant, on the same chip (i.e., crosstalk does not cross between the chips). The crosstalk effect is linear with flux and is stronger for targets in quadrant A or C. In a full-frame, unbinned, four-amp readout with a target in quadrant A or C, the crosstalk level is ~ -2 × 10$^{-4}$ that of the source; for a target in quadrant B or D, the crosstalk level is ~ -7 × 10$^{-5}$ that of the source (WFC3 ISR 2012-02). To within the errors, the crosstalk due to hot pixels and cosmic rays is the same as that due to point or extended sources. Figure 5.19, from WFC3 ISR 2009-03, illustrates the crosstalk effect as observed in an image taken during instrument ground tests.

The low-level effects of crosstalk can be mitigated by dithering: the mirror image nature of the crosstalk moves the features in a direction opposite to the target motion, i.e., they will appear to be transients and thus be removed during the drizzling procedure. Alternatively, crosstalk can be removed from single images by scaling the target image quadrant by the amp-dependent factor noted above, flipping the image about the y-axis, and subtracting it from the crosstalk image quadrant.

> ✅ An IDL routine that removes crosstalk, as described in WFC3 ISR 2012-02, can be obtained from the WFC3 Crosstalk webpage along with a Python implementation of the IDL code.

Figure 5.19: Crosstalk test frame (left), and 20-line average cuts through the target and crosstalk images (right). The image is displayed with a hard inverted greyscale stretch. The target was placed in quadrant C, and the crosstalk appears in quadrant D. The faint large ring in C offset from the primary target is an optical window ghost.
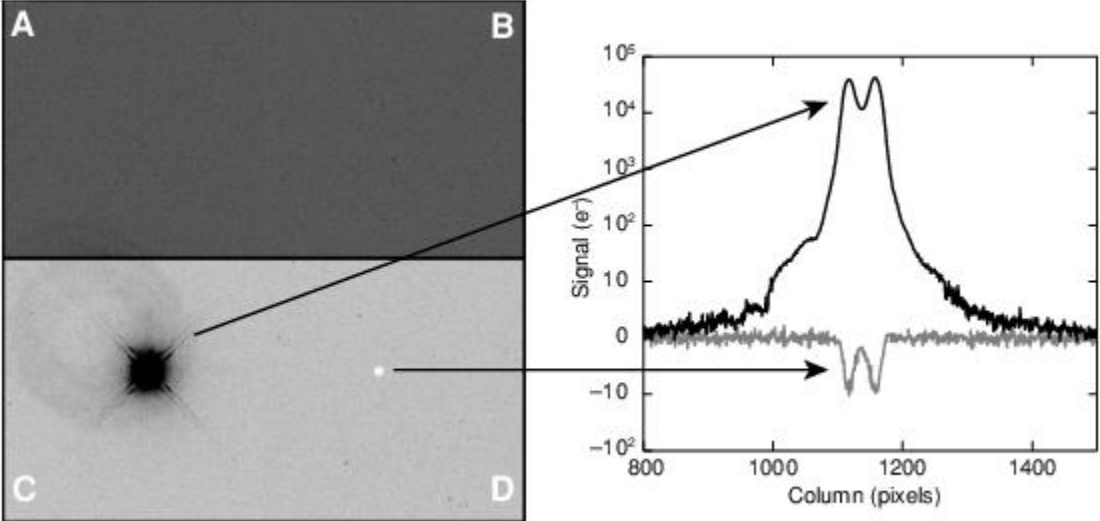
# 5.5 The WFC3 IR Channel Detector

## 5.5.1 Overview

The infrared channel of WFC3 employs a low-noise, high-QE, 1024 × 1024 pixel HgCdTe array manufactured by Teledyne Imaging Sensors (formerly Rockwell Science Center). The detector area sensitive to light is 1014 × 1014 pixels. Active cooling by a six-stage thermoelectric cooler (TEC) keeps the detector at a nominal operating temperature of 145 K. Although the IR detector is sensitive between 400 and 1700 nm, the detector coating is optimized for wavelengths longward of ~1000 nm, where the QE peaks (Figure 5.25). The IR channel filter set is also limited to wavelengths above 900 nm, making the IR channel complementary to the UVIS channel.

Compared to CCD detectors, IR detectors like the one used in the WFC3 IR channel have higher read noise and dark current. Unlike CCDs, however, IR detectors allow the accumulated signal in each pixel to be measured non-destructively multiple times. The capability to sample the signal multiple times during the integration can be exploited to reduce the effective read-out noise significantly as well as remove cosmic rays. IR exposures are called "ramps" due to this capability to sequentially read the detector as signal accumulates. IR detectors are also immune to the charge bleeding exhibited by CCDs at high signal levels. Saturation is still a concern, however, because pixels subject to the highest signal levels show higher dark-current rates ("image persistence" or afterglow) in subsequent exposures (WFC3 ISR 2010-17). Section 7.9.4 discusses the on-orbit characterization of persistence on the WFC3/IR detector and Appendix D summarizes ways to plan observations to minimize the impact of persistence.

The capability of multiple readouts and the absence of bleeding makes IR detectors able to perform very high dynamic-range observations. Non-destructive readouts also allow for the recovery of pixels affected by cosmic rays (CRs), because CR hits can be recognized and removed between adjacent reads. Unlike CCDs, IR detectors show minimal long-term on-orbit CTE degradation because they do not employ the charge transfer mechanism used in CCDs. IR detectors, however, are intrinsically non-linear. Nevertheless, at low and intermediate signal levels, the departure from linearity is quite modest and can be well calibrated by a low-order polynomial fit, whose parameters can in principle be determined for each pixel.

## 5.5.2 IR Detector Basics

In this section, we briefly describe the operational principles of the WFC3/IR detector. Figure 5.20 (adapted from McLean 1997, Electronic Imaging in Astronomy: Detectors and Instrumentation) shows the basic physical structure of the photovoltaic HgCdTe detector used in WFC3.

**Figure 5.20: Cross-section of a WFC3/IR detector (not to scale).**
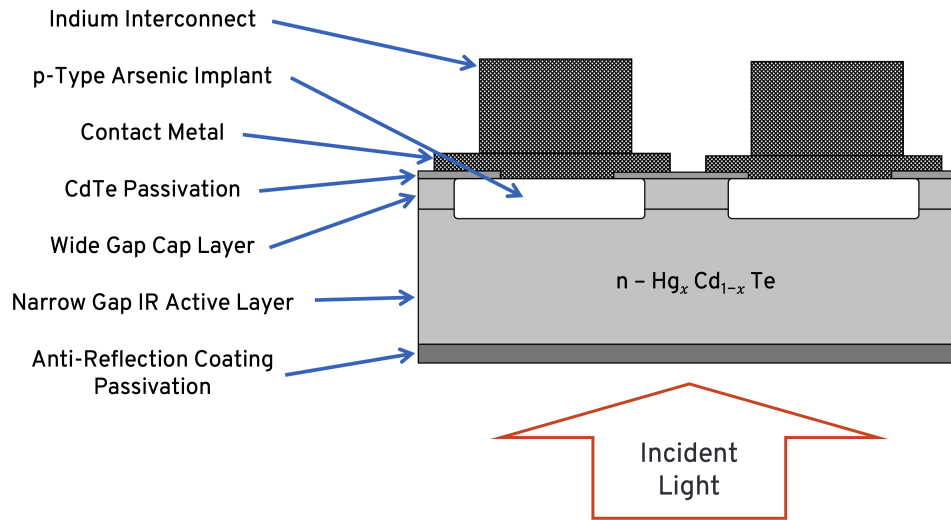


Infrared detectors used in astronomy today are basically two-dimensional arrays of p-n junctions working as photodetectors (photodiodes). In a p-n junction, negative charges migrate from the n-type doped material to saturate the unmatched covalent bonds of the adjacent p-type material. The displaced carriers establish an electric field across the junction, setting up an intermediate region depleted of free carriers. The depletion region is therefore both charged and highly resistive. The strength of the electric field and the size of the depletion region may be increased by applying an external electric field ("negative bias"). This biasing corresponds to the initial RESET applied at the beginning of an IR ramp. When an incident IR photon is absorbed by the photosensitive material, it creates a free electron-hole pair. The two photo-generated charges drift in the material and would eventually recombine. However, if the mobility of the charge carrier (a hole in an n-type material) is high enough, it will reach the depletion region before recombining and be swept to the other side of the junction by the electric field. There, in the p-type region, it will recombine with one of the electrons of the ionized holes, causing a reduction of the voltage across the junction. This change of voltage can be measured and, being proportional to the number of photo-generated charges, provides a direct measure of the photons captured on each pixel.

In the case of the WFC3 IR detector, the photosensitive material is made of HgCdTe grown with a molecular beam epitaxial (MBE) process on a ZnCdTe substrate. The fraction of Hg vs. Cd controls the long-wavelength cutoff of the material, whereas the doping material (As for the p-type, In for the n-type) creates the p-n junction. The MBE growth process is different from that used in the NICMOS detectors on *HST,* in which the HgCdTe was grown on sapphire in a liquid phase (PACE process). MBE growth on a ZnCdTe substrate is expected to provide a better lattice match to HgCdTe than sapphire, creating fewer defects and charge traps at the interface between the two materials. The MBE growth process is followed by the processing phase, in which the implants and contacts of each pixel are manufactured.

As usual with IR arrays, the readout circuitry is made on a separate CMOS chip (multiplexer or MUX), which is eventually hybridized to the detector with an indium contact for each pixel (Figure 5.21). After the two chips have been hybridized, the ZnCdTe substrate is removed to reduce the susceptibility of the device to cosmic-ray events which also increases the sensitivity at short wavelengths. The final chip therefore is a CMOS device connected through indium columns to a thin layer of HgCdTe photosensitive material.

**Figure 5.21: Basic "hybrid" structure of infrared array detectors (not to scale).**
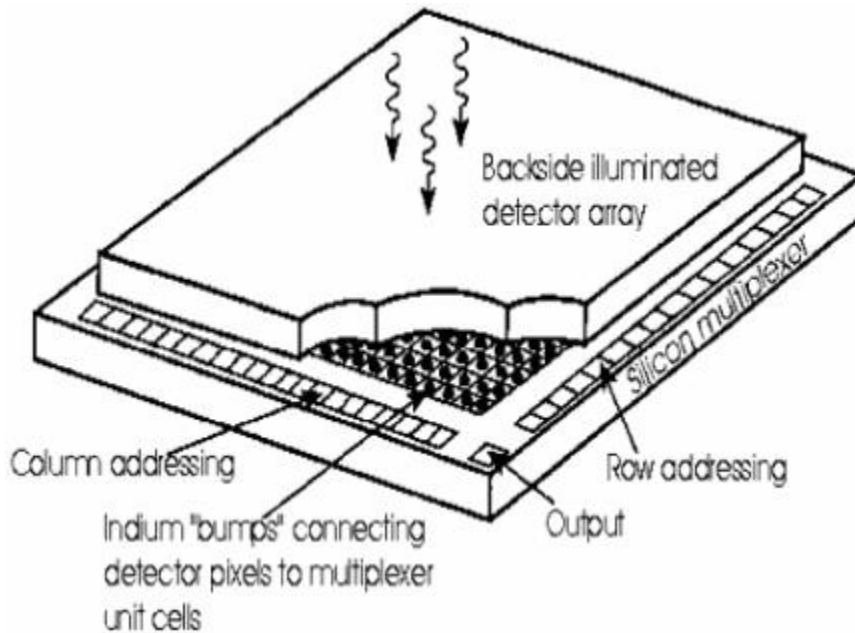


In the MUX, each pixel has its own dedicated readout circuitry (unit cell). In particular, the voltage change across the p-n junction is monitored by a field-effect transistor (FET) configured as a source-follower amplifier, which has gain of 1 and effectively decouples the detection process from the noisy readout circuitry. Two other FETs connect the pixel to the reset voltage and the output line. Figure 5.22 shows the equivalent circuit diagram for the WFC3 detector unit cell. Each WFC3 IR unit cell contains three transistors. For comparison, the NICMOS detectors had four transistors, whereas the latest generation of Hawaii-2RG detectors for JWST has seven transistors per unit cell. A higher number of transistors increases the versatility of the device. For example, on the NICMOS detectors it is possible to reset each individual cell, whereas on WFC3 detectors the reset is sent simultaneously to all cells on the same row. Note that since there are no potential barriers between pixels, pixels do not spill charges into nearby pixels when they reach a certain level ("blooming full well") of accumulated charges, as in typical multiphase CCDs. Therefore, IR detectors do not show "bleeding" along columns. Moreover, due to individual readout, bad pixels do not block the rest of the column as they do in a CCD.

**Figure 5.22: Equivalent circuit diagram of the WFC3/IR unit cell.**
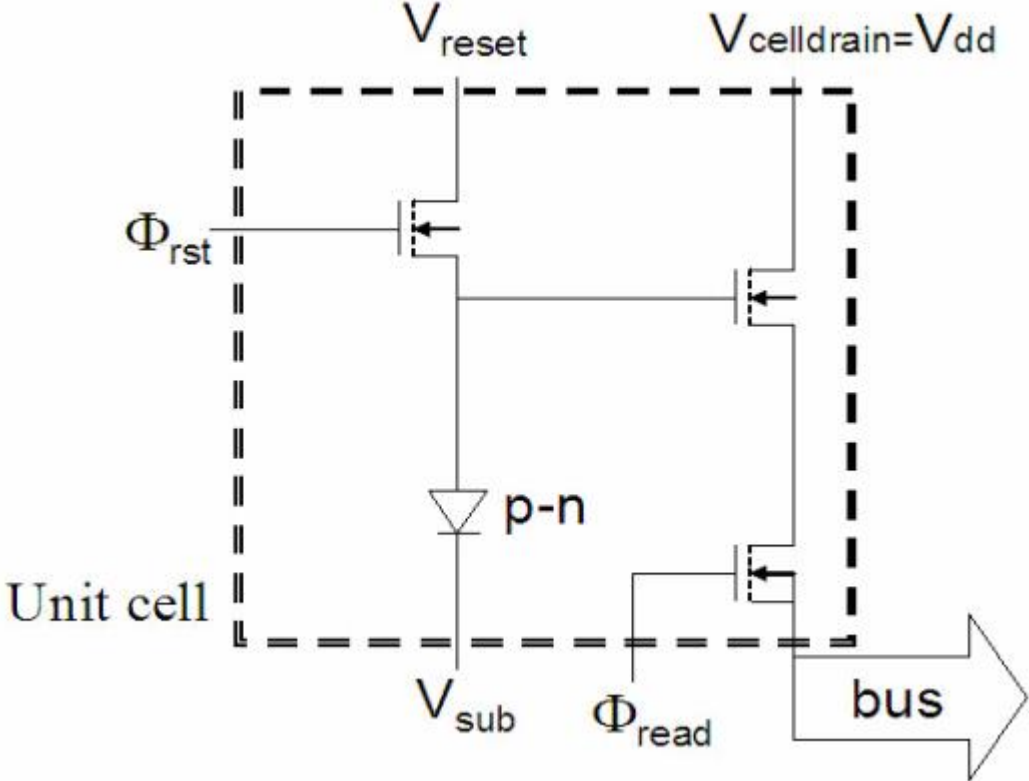
# 5.6 WFC3 IR Readout Formats

## 5.6.1 Full-Frame Readouts and Reference Pixels

The WFC3 IR detector contains 1024 × 1024 square pixels of 18 × 18 micron physical size. The detector is divided into four quadrants of 512 × 512 pixels, each of which is read out independently from its outer corner, as illustrated in Figure 5.23. The outermost rows are read first, proceeding along each row from the outermost column to the horizontal mid-point of the detector, and then continuing inwards on subsequent rows to the vertical mid-point.

**Figure 5.23:** Schematic layout of the WFC3 IR detector. The long (red) and short (blue) arrows indicate the direction of the fast and slow multiplexer clocking, respectively. In contrast to CCD "bucket-brigade" image-shifting to the output amplifier, the IR detector pixels are selected for readout in a raster pattern by multiplexer circuits.
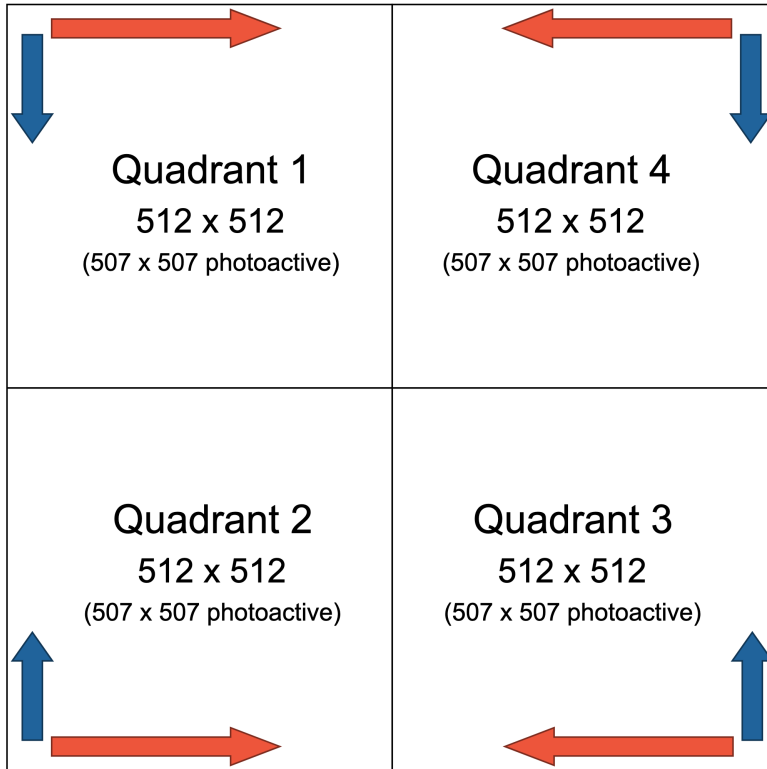


A major effort has been made to eliminate both the amplifier glow and bias drifts that affected the NICMOS detectors. For the former, WFC3 uses external amplifiers located in the immediate vicinity of the detector, rather than those directly on the multiplexer (which are also present, but are not activated in the WFC3 implementation). In regard to bias drifts, the WFC3 IR class of detectors is the first to use reference pixels: of the 1024 × 1024 pixels, only the inner 1014 × 1014 pixels are light-sensitive. The five outer rows and columns of pixels all around the array use fixed capacitances to provide constant-voltage reference values. There are two types of reference pixels: (1) the pixels on the outermost columns/rows that are connected to capacitors located outside of the unit cells and (2) the 4 inner rows/columns that are connected to capacitors created within their unit cells (Figure 5.24 ). The first type of reference pixel follows a 4× periodic pattern, providing 4 sequentially increasing voltage levels all within the range of the detector output signal. The second type of reference pixel, with the on-board capacitors, are identical by design and all provide nearly the same reference signal. The current version of the WFC3/IR data reduction pipeline uses only the inner, second type of reference pixels, as they provide a more robust statistical estimate of the variable detector bias.

The reference pixels track the low-frequency drift of the readout electronics and efficiently remove the "pedestal" variations that affected, for example, NICMOS data. Analysis of ground test data has shown that the reference pixel signal is also sensitive to the detector temperature and may therefore be used to assess the expected level of dark current during an exposure, independently from a reading of the detector temperature itself. Actual on-orbit experience indicates that detector temperature is very stable.

Full-frame exposures result in one raw 1024 × 1024 pixel image for each readout, which includes the 5 rows and columns of reference pixels on the periphery. After calibration, the reference pixels are trimmed off, leaving only the 1014 × 1014 arrays of light-gathering pixels.

Figure 5.24: Schematic layout of the light-sensitive pixels (dark green) and the reference pixels (light blue) at a corner of the WFC3/IR detector. The color-coding represents different values of the reference pixel capacitance.



1014 x 1014
active pixels

1014 x 5
reference pixels
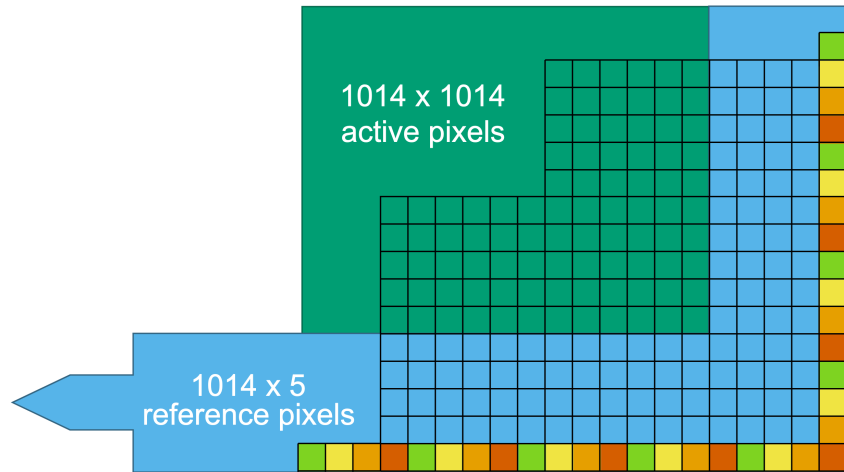
## 5.6.2 Subarrays

The default IR exposure mode is to read out the entire detector. It is also possible, however, to read out only a portion of the detector. WFC3 IR subarrays are implemented in four user-selectable sizes: 64 × 64, 128 × 128, 256 × 256, and 512 × 512 pixels. All subarrays are centered on the detector with an equal number of pixels in each quadrant, using each of the 4 detector amplifiers to read the subarray pixels contained in its quadrant (as occurs with full-frame readouts).

The 5-pixel wide bands of reference pixels that share rows or columns with the subarray are also included in subarray readouts. The reference pixels therefore come from the same detector rows and columns as the "live" portion of the subarray, with the 5 × 5 pixels at the subarray corners filled by the reference pixels at the corresponding corner of the detector.

Certain sequences of IR subarrays and sample sequences give rise to images containing a sudden low-level jump in the overall background level of the image, an effect that can be avoided by ensuring observations are taken from largest to smallest, in that order. For more discussion of this as well as the use of IR subarrays, see Section 7.4.4.

# 5.7 IR Detector Characteristics and Performance

## 5.7.1 Quantum Efficiency

The quantum efficiency (QE) of the flight IR detector, as measured at the Goddard Detector Characterization Lab (DCL), is shown as a solid curve in Figure 5.25.  The actual total system throughput of WFC3 depends on many factors including the *HST* OTA, pick off mirror, filter transmission functions, QE, etc. Based on ground measurements of these quantities, the total system throughput was calculated and compared to the first on-orbit measurements. A 5–20% increase in the total system throughput was discovered, attributed to multiple factors. The dashed curve represents the QE under the assumption that the entire flight correction is in the QE. Though this is admittedly unphysical given the realities of anti-reflection coatings and interpixel capacitance, computed total system throughputs are correct when the QE file is used in conjunction with the other optical components (pick off mirror, OTA, IR channel optics, and filters).

Figure 5.25: QE curve of the WFC3/IR detector from ground-based Goddard DCL measurements (solid). The total system throughput of the IR detector was measured on-orbit in SMOV4 (2009) to be higher than ground tests. The dashed curve shows the in-flight system throughput under the assumption that the entire observed gain is due to the QE. In reality, some fraction of this gain must reside in other *HST* and/or instrument components. This plot has been updated to use the latest version of the SMOV4 in-flight QE correction.
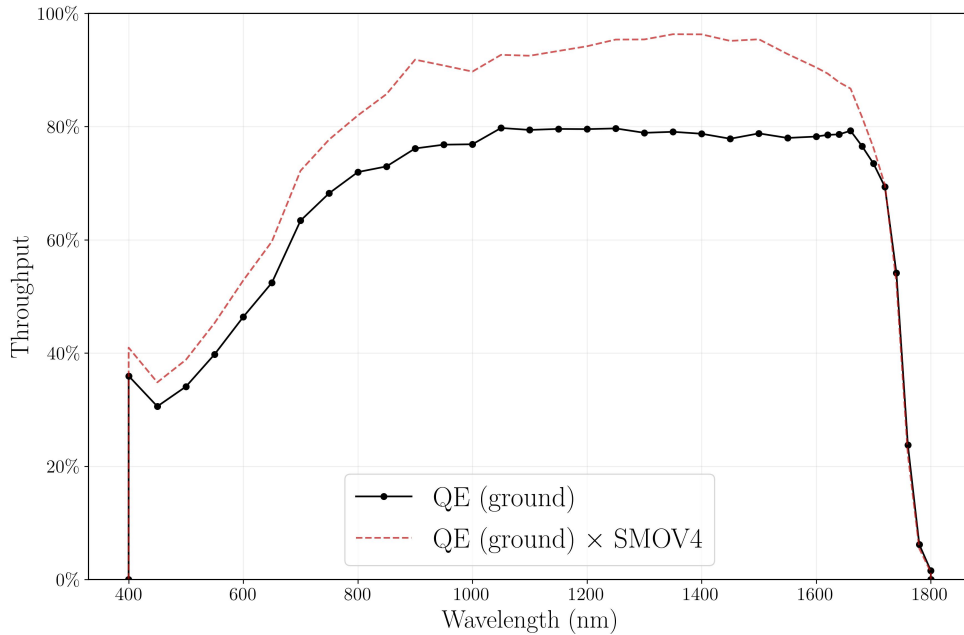


## 5.7.2 Dark Current

To avoid the complexity and limited lifetime of a stored-cryogen system, while at the same time providing the low operating temperatures required for dark-current and thermal-background reduction, the WFC3 IR detector is refrigerated with a six-stage TEC to a nominal operating temperature of 145 K. This is an unusually high operating temperature for near-IR detectors, and required tailoring the composition of the HgCdTe material for a long-wavelength cutoff at ~1700 nm. The higher band-gap associated with the short cutoff wavelength effectively limits both the intrinsic detector dark current and its sensitivity to the internal thermal background.

Direct thermal control of the detector (via a sensor integrated in the MUX that controls the 6-stage TEC current) provides typical thermal stability of < 50 mK. Tests made on similar detectors indicate that the residual dark-current variations can be largely calibrated and subtracted out using reference pixels.

WFC3 IR exposures taken with an aluminum blank in place, rather than a filter, provide a measure of the detector dark current. The dark current of the flight array has a skewed distribution, with a mode, median, and mean of 0.045, 0.048, and 0.048 e⁻/s/pixel respectively. The shifted mode is due to the asymmetry of the dark-current distribution among the pixels, characterized by a long tail of "hot pixels" randomly located across the detector. While the mean underlying dark current has been stable on-orbit (WFC3 ISR 2017-04; WFC3 ISR 2012-11), a small number of pixels (<4%) vary over time and are corrected in the calibration pipeline via time-dependent superdarks (WFC3 ISR 2019-04).

The histogram of dark current values, along with the cumulative dark-current distribution, i.e., the fraction of pixels with a dark current lower than a certain level, is shown in Figure 5.26; WFC3 ISR 2009-21 provides details on dark current calculations. Improved superdark reference files were created for all allowed full-frame and subarray modes using data collected during 2009-2013 (WFC3 ISR 2014-06). The signal-to-noise improved by a factor of 3-11 due to the use of a great deal more data, the use of a non-linearity correction, and the use of persistence masks. In 2019, updated WFC3 /IR dark calibration files were created for all allowed observing modes. Time-dependent pixels in these superdarks were generated in a cycle-by-cycle basis, allowing for improved calibration of those ~3.5% of detector pixels that have changed their dark current behavior since launch (WFC3 ISR 2019-04).

Note that in broad filters, the dominant background is not the dark current but zodiacal light, which at 0.3-1.0 e⁻/s/pixel is a factor of 10-20 times larger than the dark. The WFC3 ETC can be used to compute the zodiacal light contribution for a given pointing, in addition to providing thermal and dark current estimates (Sections 7.9.5 and 9.7).

**Figure 5.26: Histogram of the WFC3/IR detector dark current.**
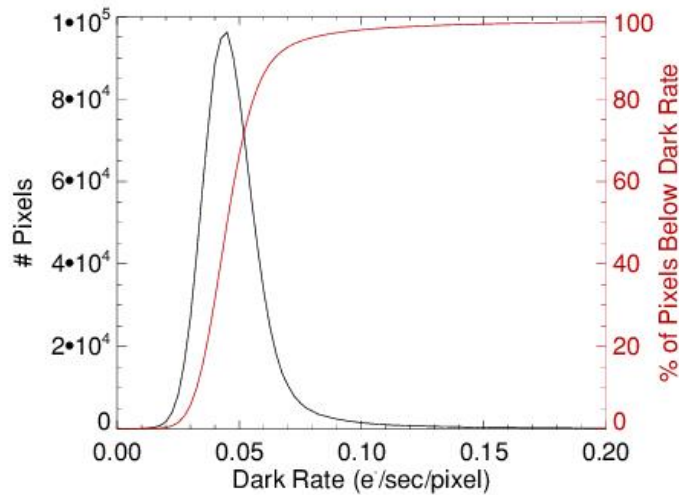


## 5.7.3 Read Noise

The IR detector has four independent readout amplifiers, each of which reads a 512 × 512 pixel quadrant. The four amplifiers generate very similar amounts of read noise. This is illustrated in Figure 5.27, which compares the correlated double sampling (CDS) read noise levels for the four quadrants of the detector. CDS read noise refers to the noise associated with subtracting a single pair of reads. These read noise values were derived from a series of RAPID ramps taken during SMOV testing, providing a measure of the total noise in a difference image. For short ramps, such as these RAPID ramps, the contribution of shot noise due to dark current accumulation is less than 0.01 e⁻ and the CDS read noise of the detector is between 20.2–21.4 e⁻ (left plot in Figure 5.27). By averaging over multiple reads, the effective noise of an IR ramp can be significantly reduced. As Figure 5.27 (below, right plot) illustrates, the effective noise in a SPARS200 ramp drops from ~20.0 e⁻ down to ~12.0 e⁻ (based on 2 reads plus zeroth read and 15 reads plus zeroth read, respectively). Similar reductions in noise can be achieved with other sample sequences (WFC3 ISR 2009-23).

**Figure 5.27:** Correlated double-sampling read noise values measured for each quadrant in forty RAPID ramps during early on-orbit SMOV testing in 2009 (left plot). The effective noise in a SPARS200 ramp as a function of the average number of reads +1 (i.e., including the zeroth read) is shown in the right plot.
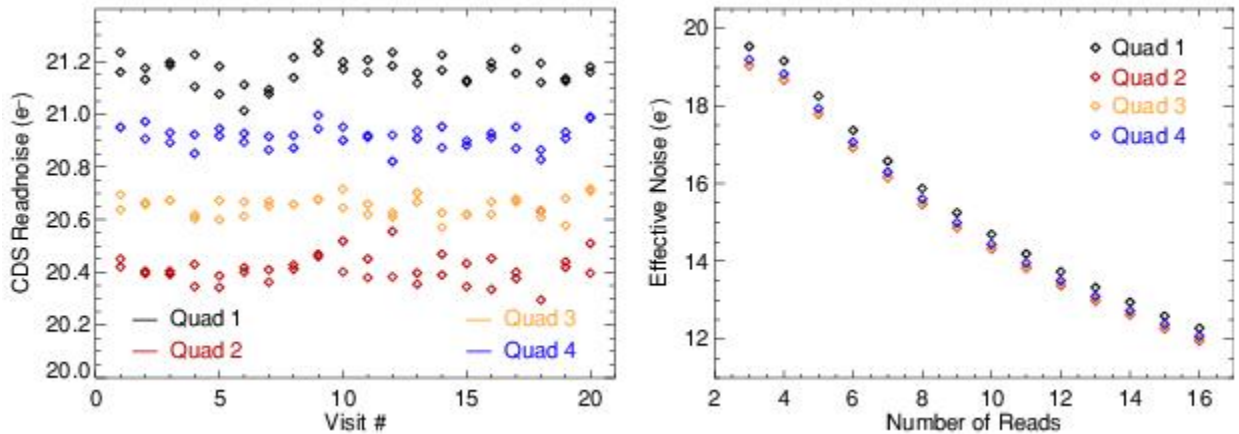


For some programs, read noise will not be an issue while for others, such as ultra-low-background observations, the read noise can be a non-negligible component of the noise floor. The relative contribution of read noise to the total noise will depend, of course, on infrared background levels as well (Section 7.9.5). The contribution to the read noise in WFC3 IR data due to digitization errors associated with the conversion from electrons to data numbers (DN) is negligible.

## 5.7.4 Flat Fields

Before launch, ground-based flats were obtained for the 15 imaging IR filters at a mean SNR of ~500 per pixel using an external optical stimulus (ISR 2008-28). Because the overall illumination pattern of the ground-based flats does not precisely match the illumination attained on-orbit from the OTA, there are errors in these ground-based flats on large spatial scales. These errors were initially measured by performing stellar photometry on rich stellar fields that were observed using large-scale dither patterns during SMOV and cycle 17 (ISR 2009-39). The errors were later determined more accurately by creating sky flats from thousands of on-orbit exposures, masking out astronomical sources and assuming filter-independent corrections. Initial flat field reference files corrected using these sky flats were delivered in December 2011 (ISR 2011-11).

These reference files were replaced in October 2020 with flats generated using a much larger set of in-flight data (ISR 2021-01). Six filters (F098M, F105W, F110W, F125W, F140W, and F160W) have sufficient signal-to-noise that the flats are now derived purely from in-flight data and are no longer dependent on the ground test data. For the remaining nine IR filters, the ground "P-flats" (pixel-to-pixel variation flats) were multiplied by a smooth correction derived from wavelength-interpolation using sensitivity residuals from the six primary filters. An accompanying set of delta flats (also known as "D-flats"; ISR 2021-10) was created for the six primary filters to correct for IR blobs at different epochs (Section 7.9.6). When two or more types of flats are available, they are multiplied together by `calwf3` to form a combined flat field correction image.

Figure 5.28 shows examples of bias-corrected P-flats computed from in-flight science observations acquired over ~10 years in the wide-band filters F110W (left) and F160W (right).

**Figure 5.28: Updated WFC3/IR pixel-to-pixel flats for F110W (left) and F160W (right).**
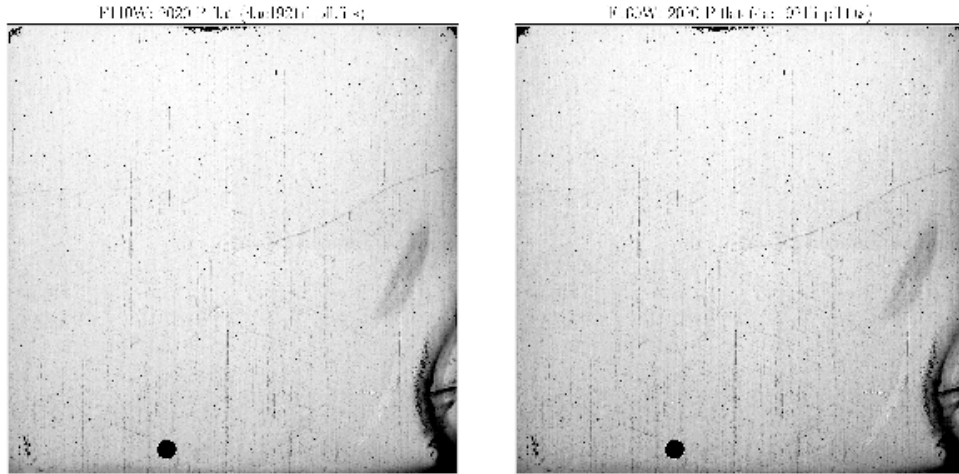


> ✓ The latest information about IR flats can be found on the WFC3 IR Flats webpage.

## 5.7.5 Linearity and Saturation

The WFC3 IR calibration program shows that the detector response is in fact (slightly) non-linear over the full dynamic range. This behavior is illustrated in Figure 5.29, which presents a plot of average counts as a function of time. The black diamonds are the measured average signal; a linear fit has been made to the signals up to ~25,000 electrons (solid red line). The dashed red line shows this best-fit line extended out to the total exposure time of the ramp. The blue horizontal line marks the level at which the counts deviate by more than 5% from linearity (about 78,000 electrons). For the purposes of non-linearity correction, the 5% nonlinearity level has been defined as "saturation."

**Figure 5.29:** Non-linear response of mean signal (electrons) as a function of time (sec), measured in Thermal Vacuum 3 ground testing of the WFC3/IR detector.
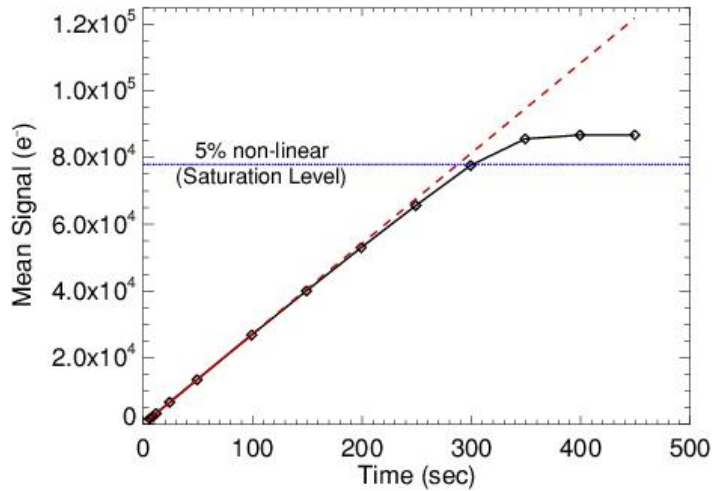


The linearity correction implemented in the WFC3/IR calibration pipeline corrects pixels over the entire dynamic range between zero and saturation. Once the pixel value exceeds the saturation threshold, the pixel is flagged as saturated in the data-quality array within the FITS file and no linearity correction is applied. Pixels driven heavily into saturation can begin to show decreasing readout values, such that their DN values fall back below the defined saturation threshold. To prevent a situation where a pixel is flagged as saturated in one or more readouts, but then not flagged in later readouts, the calibration processing system flags saturated pixels in all subsequent readouts for pixels that are found to be above the saturation threshold in any given readout.

Trials of non-linearity corrections have shown that a third-order fit to the measured linearity versus signal for each pixel provides a slightly better correction than the one currently implemented in the pipeline, with photometric results between short and long exposures more consistent by up to 0.5% (WFC3 ISR 2014-17).

## 5.7.6 Count Rate Non-Linearity

Previous HgCdTe detectors on *HST* have suffered from a count-rate dependent non-linearity (CRNL) and the WFC3-IR detector is no exception. An initial measurement of this effect was made by comparing the photometry of star clusters observed over a wide dynamic range and at overlapping wavelengths in the WFC3/IR and NICMOS and/or ACS/WFC detectors. We found a CRNL of ~1% per dex over a range of 10 magnitudes (4 dex) which was independent of wavelength (WFC3 ISR 2010-07). This measurement was confirmed using exposures that boosted count rates with Earth limb light (WFC3 ISR 2010-15) and observations of groups of stars observed with 2MASS (WFC3 ISR 2011-15). The impact of count-rate non-linearity is that photometry of faint (i.e., sky dominated) sources calibrated with WFC3/IR zeropoints will appear 0.04 +/-0.01 mag too faint. The effect is an order of magnitude smaller than the effect found for NICMOS, but large enough to potentially limit the accuracy of photometry.

In 2019, more precise measurements of CRNL were made by using a combination of comparisons of cluster star photometry between WFC3/IR and WFC3/UVIS and by using observed and synthetic magnitudes of white dwarfs (WFC3 ISR 2019-01). In this study, the measured range of CRNL was also extended to higher count rates by comparing magnitudes between the ground and WFC3/IR for LMC and Milky Way Cepheids. Combining these results with all previous measurements and those from the WFC3 grism provides a consistent and improved characterization of the CRNL of WF3/IR, of 0.75% +/- 0.06% per dex, with no apparent wavelength dependence, measured across 16 astronomical magnitudes. **This result should be used to correct IR photometry by using the difference in apparent flux (in dex) between where the WFC3/IR zeropoint is set (~12th mag) and the target source**. Fainter sources appear even fainter and thus must be corrected to be brighter.

## 5.7.7 Detector Cosmetics

The WFC3-IR detector's pixel population includes several flavors of anomalously responsive pixels: hot, cold, unstable, dead, and deviant in the zeroth read. Hot pixels, those showing excess charge, are defined as pixels with more than 100 times the average dark current. Cold pixels are inversely sensitive to incident photons and exhibit a negative slope when measured up the ramp (i.e., pixel value is lower in last frame up the ramp compared to first frame). The anomalous response of a cold pixel could be due to lower intrinsic QE in that pixel or to surface defects. Unstable pixels, as the name implies, are those that behave in an unpredictable fashion; that is, the signal up the ramp does not repeat reliably from ramp to ramp (Appendix 2, WFC3 ISR 2010-13 show examples). There are dead, or unbonded, pixels which do not respond to light (Figure 5.30). Overlapping the dead pixel population is the population of pixels that has bad zeroth read values, generally due to being short-circuited or unbonded (WFC3 ISR 2003-06).

In addition to randomly-distributed bad pixels, coherent regions of bad pixels exist in the IR detector (Figure 5.30). Pixels in the lower-right region (dubbed "wagon wheel") have lower than normal quantum efficiency. There are dead pixels near the detector edge and in the circular "death star" feature near the bottom. Pixels with deviant zeroth read are concentrated in the areas of the death star, the upper corners of the detector, and the quadrant boundaries. (The death star region is marked in the WFC3 FOV in APT to aid in observation planning.) WFC3 ISR 2008-28 describes the characterization of these defects based on ground-testing data; WFC3 ISR 2010-13 describes the various types of populations of bad pixels as observed on-orbit.

**Figure 5.30: IR Detector Cosmetic Defects**
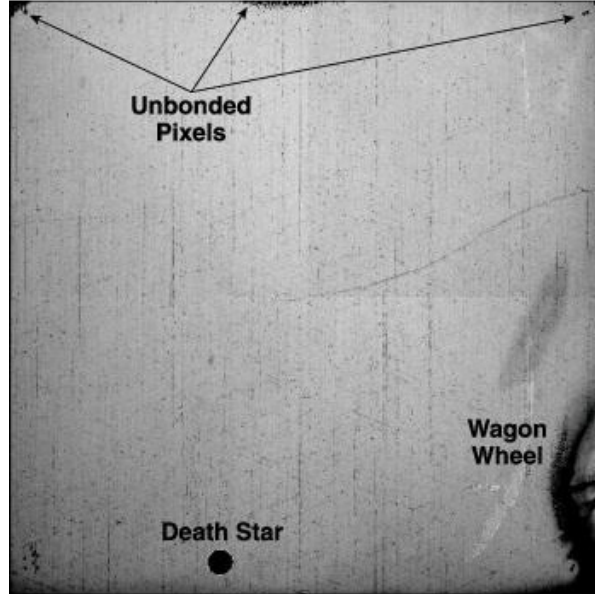


An in-depth study of the time-dependent behavior of the IR pixels (WFC3 ISR 2019-03) has shown that roughly 3.5% of pixels have experienced changes in their behavior since the installation of WFC3 on-orbit in May 2009. Such variations include normal pixels becoming hot, unstable pixels becoming stable, some pixels transitioning between different stable levels of dark current, other pixels alternating between two stable levels, and more. Figure 5.31, reproduced from WFC3 ISR 2024-02, shows the distribution of IR pixel behavior for the various combinations of cold (i.e. normal dark rate) and hot, stable and unstable states.

In general, the WFC3/IR detector shows an increase of only ~200 hot pixels per year (~0.02% of the detector). Prior to 2020, the unstable pixel population varied up to ~4000 pixels per year (~0.4% of the detector). It was observed that the unstable pixel population more than doubled between Cycle 27 and Cycle 28 (WFC3 ISR 2022-01), such that approximately ~3.35% detector pixels were classified as unstable (2.85% cold and 0.5% hot). However, WFC3 ISR 2024-02 found that this was due to an algorithmic discrepancies in the pipeline used for generating the bad pixel table; subsequent analysis showed that the actual flagged pixel percentage was <1% for Cycle 28, and that IR bad pixel populations remained stable through Cycles 29 and 30.

Calibration reference files in the past were insensitive to periods of pixel stability, simply permanently flagging as bad any pixels which spent any amount of time in a hot and/or unstable state. Now, time-variable pixel behavior is captured in the bad pixel tables and superdarks with a data quality flag of 32 to mark unstable pixels (as is now done for UVIS as well); e.g. unstable hot pixels are flagged with both '32' and '16' (hot) (Table E.3). As a result, users can reclaim stable pixels – even when hot – for their analyses; doing so can recover about 0.5% of the detector, which otherwise would have been thrown out. Likewise, the WFC3/IR bad pixel tables now track the time-variable bad pixel populations, which ensures that new bad pixels are flagged in a timely fashion and that the thousands of pixels which revert to a stable configuration are not flagged and discarded ( WFC3 ISR 2019-03, WFC3 ISR 2019-04).

Figure 5.31: Trends in the WFC3/IR pixel populations over time. The yellow area represents hot pixels that were found to be stable; while these are flagged as hot (DQ value 16) in observations, they are now successfully calibrated and do not necessarily need to be discarded from analyses. Pixels flagged as unstable (DQ value 32, blue and red areas) are not recommended for use.
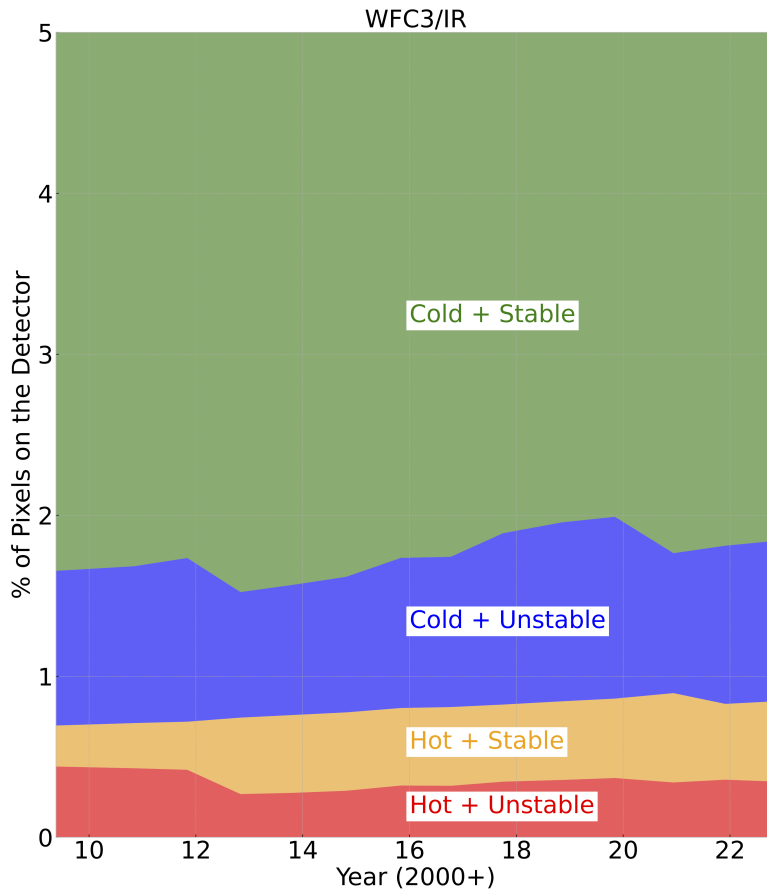


## 5.7.8 Crosstalk

As is common in devices with multiple amplifiers being read out simultaneously, the IR channel exhibits crosstalk: a bright source in one quadrant causing electronic ghosting in another quadrant. In the IR, the crosstalk manifests itself as a very low-level negative mirror image. In WFC3, amplifiers 1 and 2 are coupled (upper left and lower left quadrants; Figure 5.23) and amplifiers 3 and 4 are coupled (lower right and upper right quadrants). That is, sources in quadrant 1 generate crosstalk in quadrant 2, sources in quadrant 2 generate crosstalk in quadrant 1, and so on.

The level of the IR crosstalk is only $\sim 1e^{-06}$ that of the target flux (WFC3 ISR 2010-02); for unsaturated sources, the crosstalk is below the background noise. Once a source saturates, the crosstalk becomes visible at about the level of the background and remains constant as the voltage of the device is pinned.

## 5.7.9 Image Persistence

Image persistence is a common problem in HgCdTe and other types of IR arrays. Persistence manifests itself as ghost images or afterglows from earlier exposures. It was seen in NICMOS, and is also seen in a small but non-negligible fraction of the exposures taken with the Hawaii 1R detector that is the heart of the WFC3 IR channel.

Persistence is caused by traps that exist in the active regions of the reverse-biased diodes that make up the pixels of the detector. Resets, which occur at the end of multi-accum exposures (and during the process of flushing the detector when not observing with the IR channel), maximize the reverse bias of the diodes. Light impinging on the diode creates photo-electrons which cause the reverse bias to decrease. Changing voltages within the diode expose portions of the depletion region to free charge. Dislocations in these newly exposed regions trap charge. More traps are exposed for bright sources than for faint ones. This trapped charge is released in later exposures, resulting in after-images. The greater the saturation of the detector, the greater the number of traps and the greater the afterglow. Smith et al. 2008 (Proc. SPIE, 7021) has provided a very clear description of the physics of persistence and the effects in IR arrays.

The characteristics of persistence vary for different devices and device technologies, reflecting in part how traps are distributed within the diodes. Persistence in the WFC3 channel is primarily a function of the fluence (the total number of photo-electrons released) in an exposure, and secondarily a function of the amount of time the pixel is held at a high fluence level. As discussed by Long et al. 2012 (Proc. SPIE, 8442), the amount of persistence in the WFC3-IR detector is a non-linear function of the fluence. Persistence is observed mainly in situations where fluence levels approach or exceed saturation of the detector.

Several examples of persistence in WFC3 observations and strategies for avoiding persistence are described in Section 7.9.4. A description of a phenomenological model of persistence used to aid in removing the effects of persistence is given in the *WFC3 Data Handbook.*

Figure 5.32 shows the characteristic shape of persistence versus fluence as observed in a series of darks following an image of Omega Centauri which had been deliberately exposed to a level where many stars in the image were saturated. The first dark exposure took place a few minutes after the end of the Omega Centauri exposure and the last dark exposure took place about one orbit later ( WFC3 ISR 2013-07). The amount of persistence is fairly small until the exposure level reaches about half of full well and saturates near full well exposure. The persistence gradually decays with time from the first dark exposure (highest curve in figure) to the last dark exposure (lowest curve in figure).

**Figure 5.32: Persistence as a function of fluence ("stimulus" provided by exposure to Omega Centauri) observed over the detector in a subsequent series of darks (color coded).**
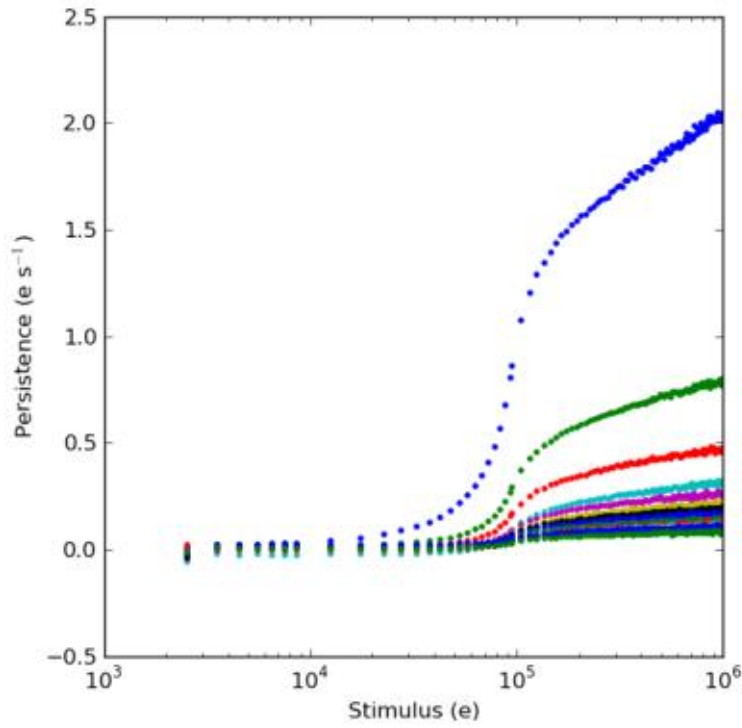


Persistence decays roughly as a power law with time, as illustrated in Figure 5.33, which is based on the data displayed in Figure 5.32. The different curves here show the decay for different levels of saturation, as measured in electrons. Persistence at low fluence levels decays more rapidly than persistence at high fluence levels. There are 3 curves for each level corresponding to the 3 times the experiment was repeated. The differences are partially due to the fact that different pixels were illuminated to different levels each time, but may also indicate some intrinsic variability that is not understood. For comparison, the dark current is about 0.05 electrons/sec. If one assumes that a power law describes persistence from 100 to 10,000 seconds after an exposure, then one concludes that about 3% of charge is trapped in an exposure that has a nominal fluence level of 100,000 electrons.

**Figure 5.33: Persistence as a function of time for pixels with selected (color coded) levels of fluence provided by exposure to Omega Centauri.**
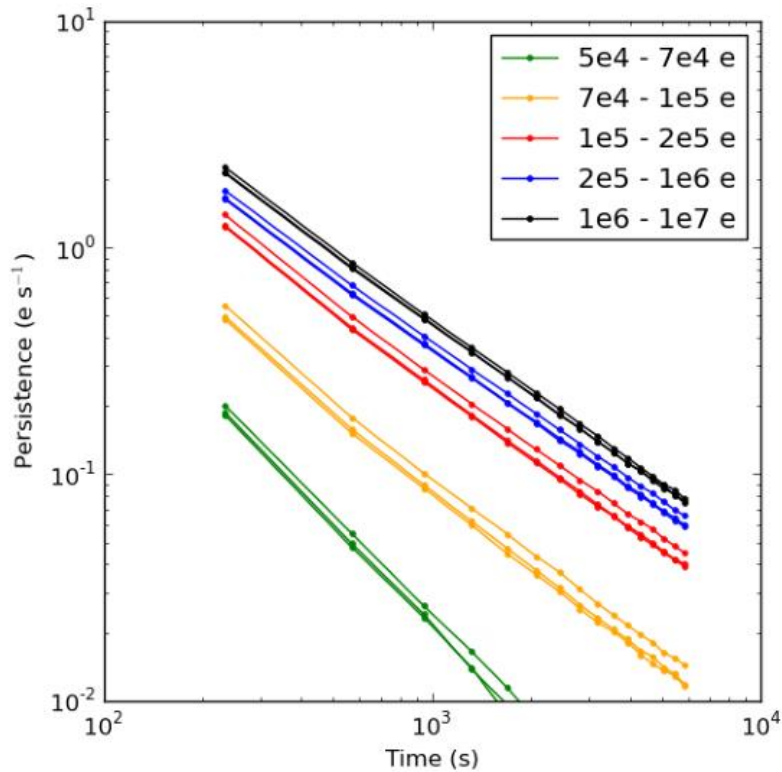


While fluence is the primary factor in determining how much persistence there will be after an observation, the amount of persistence actually depends on the time history of each pixel. Tests show that there is more persistence from a pixel exposed multiple times to the same brightness source (WFC3 ISR 2013-07) and the longer a pixel is held at a fixed flux level (WFC3 ISR 2013-06). This can be understood qualitatively as being due to the fact that traps have finite trapping times. A more accurate prediction of persistence has been achieved using an exposure-time dependent power law decay model (WFC3 ISR 2015-15) along with a "correction flat" that takes into account large-scale variations over the detector (WFC3 ISR 2015-16). Observers are cautioned that variability in persistence has been found in dark exposures taken within 1000 sec of a brief (274 sec) stimulus ( WFC3 ISR 2018-03).

MAST includes a search form that provides a persistence image for a specified exposure, produced by applying the persistence model to the preceding WFC3-IR exposures (see the *WFC3 Data Handbook*). Since the model is imperfect, the persistence image is intended as a guide to which pixels to flag in an exposure rather than as a reliable indicator of flux corrections.

# Chapter 6: UVIS Imaging with WFC3

## Chapter Contents

# 6.1 WFC3 UVIS Imaging

As described in Chapter 2, the optical design of WFC3 features two independent channels, each with its own set of optics, filters and grisms, and detectors. The **UVIS channel** is sensitive to UV and optical wavelengths (200-1000 nm), and the **IR channel** is sensitive to near-infrared wavelengths (800-1700 nm).

Only a single channel, either UVIS or IR, can be used at any one time. In other words, they cannot be used in parallel, but they can be used sequentially within the same orbit.

A schematic diagram showing the locations of the fields of view of the UVIS and IR detectors in the *HST* focal plane is shown in Figure 2.2.

This chapter describes the capabilities of the UVIS channel. The following chapter, Chapter 7, describes the IR channel. Detailed performance characteristics of the detectors used in both channels are given in Chapter 5 and summarized in Table 5.1.

# 6.2 Specifying a UVIS Observation

Using the Astronomer's Proposal Tool (APT), it is relatively simple to specify the parameters for a UVIS observation. Detailed documentation of the specifications can be found in the Phase II Proposal Instructions. The parameters available to General Observers for the UVIS channel are the following:

1. **Configuration**: always **WFC3/UVIS**
2. **Mode**: always **ACCUM**
3. **Aperture**: must be specified; see Section 6.4.4 and Section 6.4.5 for the dimensions, location, and reference point (target placement) of the full array and subarray apertures.
4. **Spectral Element**: must be specified for each exposure; see Section 6.5
5. **Optional Parameters**: the options include **FLASH** (to add a specified number of electrons per pixel to the image to reduce CTE losses; Section 6.9.2), **CR-SPLIT** (to split an exposure into a specified number of subexposures for cosmic ray rejection - but note that dithering provides improved calibrated science products over CR-SPLIT (see Appendix C), **BIN** (to perform on-chip binning by a specified number - but beware that this mode 1) increases the area affected by bad pixels and cosmic rays and 2) is not advantageous with post-flash; Section 6.4.4), **BLADE** (to minimize vibration effects in short <5 sec exposures by selecting shutter blade A; requires approval - see Section 6.10.4), and INJECT (to implement charge injection to reduce CTE losses - but the use of this option is not generally permitted for science observations; see Section 6.9.2 ).
6. **Special Requirements**: see the Phase II Proposal Instructions for details of Special Requirements related to the timing of visits and for dithering and mosaicking. Also available is the exposure-level Special Requirement **POS TARG** for offsetting the target from the default reference point of the aperture (see Section 6.4.3 for a discussion of the UVIS channel coordinate systems, Section 6.4.5 for reference points, and Appendix C for the POS TARGs associated with the WFC3 patterns).
7. **Number of Iterations and Time per Exposure**: the exposure time for the UVIS channel must be an integer multiple of 0.1 s, ranging from 0.5 to 3600 s, except that 0.6 s is not allowed ( Section 6.7.1) and 0.7 s is slightly less favorable than 0.5 s or > 0.8 s (WFC3 ISR 2023-04).

# 6.3 UVIS Channel Characteristics

In concept and functionality, as well as in many design details, the WFC3 UVIS channel is patterned after the ACS/WFC channel. The UVIS channel contains an optical train providing focus and alignment adjustments as well as a correction for the OTA spherical aberration, a filter-selection mechanism, a shutter mechanism, and a CCD detector assembly (which uses the same camera-head design as ACS/WFC). The channel is supported by a thermal-control subsystem and also by control and data-handling electronics subsystems.

As described in Section 5.2.2, the detectors in the WFC3 UVIS channel are two 4096 × 2051 pixel CCDs, butted together to yield a 4096 × 4102 light-sensitive array with a ~31 pixel (1.2 arcsec) gap. The gap can be filled in by using appropriate telescope dithering strategies (see Section 6.11.1 and Appendix C). The plate scale is approximately 0.04 arcsec per pixel, providing a good compromise between adequate sampling of the PSF and a wide field of view. Geometric distortions introduced by the WFC3 optics cause the nominally square detector to map onto the sky as a rhombus, about 162 arcsec on each side.

Upon the start of on-orbit operation in 2009, the UVIS CCDs had excellent CTE. As discussed in Section 5.4.11, the on-orbit radiation environment damages the CCDs over time and causes degraded CTE (charge transfer efficiency); in addition, the CTE degraded somewhat more than expected over the first few years of operation due to the solar minimum at the time. Observers with exposures with low sky backgrounds should use the post-flash mode (implemented in 2012) to avoid large CTE losses (Section 6.9.2).

# 6.4 UVIS Field Geometry

## 6.4.1 Field of View and Pixel Size

As described above, the UVIS channel uses two 4096 × 2051 CCDs, butted together to yield a 4096 × 4102 array with a ~31 pixel (1.2 arcsec) gap. Because the detector is tilted around its diagonal axis 21° with respect to the incident beam, the field of view projected onto the sky is rhombus-shaped, 162 arcsec on a side, with an angle of 86.1° between the sides at amplifiers B and C (Figure 6.1). The pixels projected onto the sky are also rhomboidal, ~0.04 arcsec on a side.

## 6.4.2 Geometric Distortion

Distortions due to the WFC3 optics cause the nominally square field of view of the UVIS detector to map onto the sky as a rhombus with small higher order distortion. Geometric distortions in both channels are discussed in more detail in Appendix B.

Distortion must be taken into account when exposures are flat-fielded, photometrically calibrated, used for astrometric measurements, or combined with other dithered exposures. The AstroDrizzle software from the DrizzlePac package appropriately carries out those operations; a combination of routines and functions available through DrizzlePac can be used to optimize the combination of dithered exposures.

## 6.4.3 Coordinate Systems

There are three different coordinate systems defined for use with the CCDs in the UVIS channel, each tailored to specific purposes. They are shown in Figure 6.1 and are as follows:

- **Data image-based system** (Axis1, Axis2; units of pixels)
- **Proposal POS TARG system** (Xpos, Ypos; units of arcsec)
- ***HST*-based system** (V2, V3 or U2, U3; units of arcsec)

The **image-based coordinate system** (Axis1, Axis2, as shown in Figure 6.1) is an orthogonal system of detector pixel readouts. Axis1 is aligned with the detector data rows and Axis2 with the columns. It is used by the calibration pipeline and other data-analysis software and is sometimes also referred to as the user frame. When a detector image is displayed on a computer screen, this system has the X-axis (Axis1) increasing to the right and the Y-axis (Axis2) increasing to the top of the screen, with 1 being the conventional index of the first pixel in both axes. For WFC3/UVIS, each chip has its own origin and Axis1, Axis2 system. The image-based coordinate system is used in most figures in this handbook, as well as in the aperture definitions available in the Science Instrument Aperture File.

Figure 6.1: Diagram of UVIS apertures, illustrating the fiducial points of the full-detector apertures (UVIS, UVIS1, UVIS2, and UVIS-CENTER), and the outlines of the 2K x 2K, 1K x 1K, and 512 x 512 subarray apertures. Positions of the four readout amplifiers are indicated (A, B, C, and D). The regions imaged by the UVIS detector are shaded in blue, and regions imaged by the IR detector are shaded in red. The POSition TARGet (POS TARG) coordinate system for the UVIS-CENTER aperture is shown with its origin at that aperture's fiducial point. The POS TARG coordinate systems for other apertures are not shown in this diagram, but are oriented the same as the UVIS-CENTER aperture, with each aperture's origin at the corresponding fiducial point. U2 = –V2 and U3 = –V3.
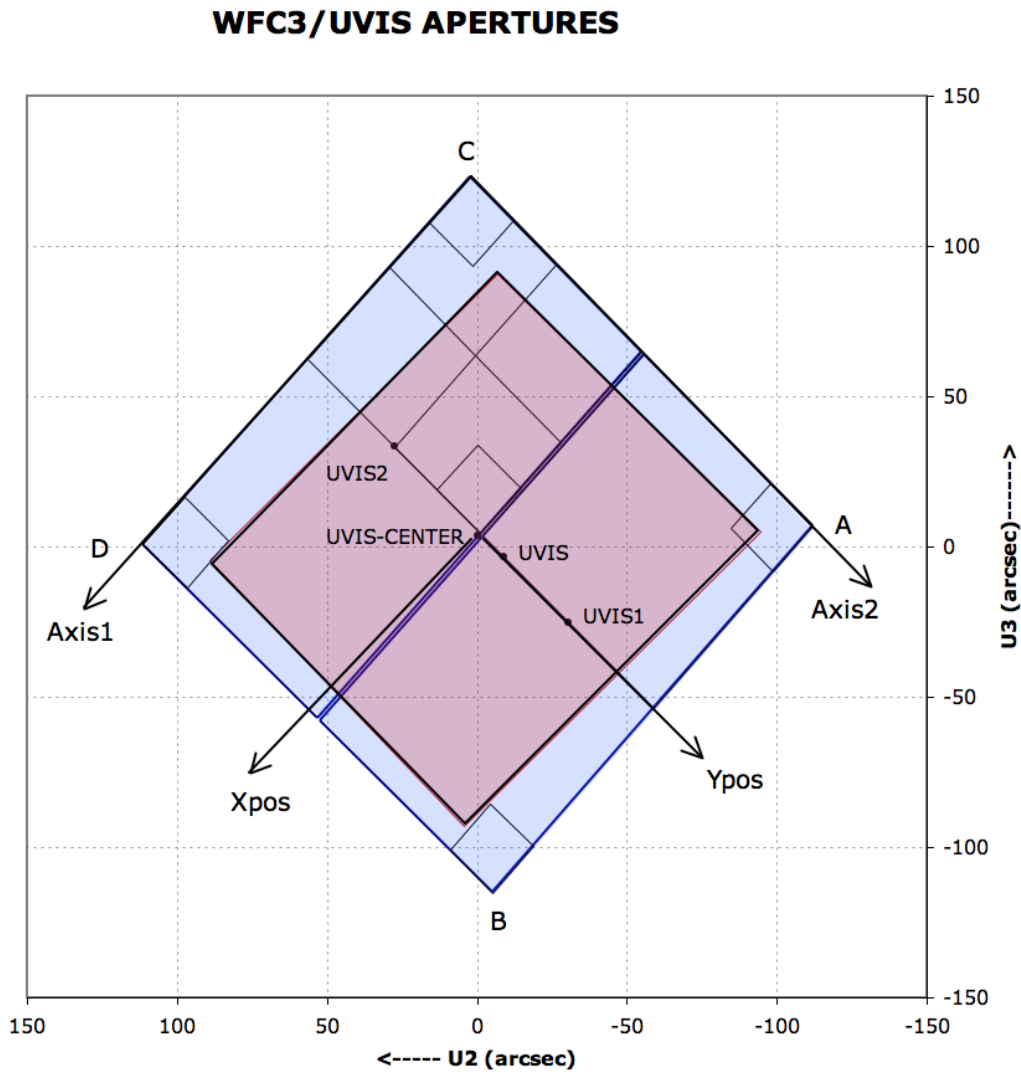


The origin of this coordinate system is context specific. Logical or image coordinates have the origin at the lower left corner of the image, even for subarray images or images containing overscan data. These coordinates are shown as the "Image X,Y" coordinates in DS9. Physical or CCD coordinates have their origin at the lower left corner of the chip's light sensitive area. Thus, pixels to the left of the science area within the physical overscan area (see Figure 6.20) actually have negative coordinates in the physical image-based system. These physical coordinates are displayed as "Physical X,Y" coordinates in DS9, which determines the coordinates using the LTV1 and LTV2 FITS

header keywords. The lengths of the axes, in pixels, are stored in the FITS header keywords NAXIS1 and NAXIS2.

The **POS TARG reference frame**, sometimes referred to as the spacecraft system, is used for specifying the placement of an astronomical target relative to the aperture reference point (sometimes called the fiducial point) in the instrument field of view. Its units are arcseconds. For the UVIS channel, the POS TARG system is defined such that the POS TARG Y axis is parallel to Axis2 at the reference point of the aperture in use. The POS TARG X axis is orthogonal to the POS TARG Y axis; *it is not parallel to Axis1 due to geometric distortion*.

As is the case for other *HST* instruments, the POS TARG origin is defined to be at the reference point (fiducial point) of the user-selected UVIS aperture (such as the geometric center of a particular chip, or the optimum center of a quadrant, etc.; see Table 6.1 below for the names of the various UVIS channel apertures). Figure 6.1 illustrates the POS TARG reference frame for the "UVIS" aperture, whose center is near the middle of the WFC3 UVIS field of view; the POS TARG directions are indicated by arrows labeled Xpos and Ypos.

The *HST*-based, or vehicle (V2, V3), system is an orthogonal reference frame tied to the telescope and is used operationally for alignment, pointing, and slewing purposes. The V1 axis lies along the optical axis while V2,V3 run parallel and perpendicular, respectively, to the solar-array rotation axis (see Figure 2.2). Note that the (undistorted) diagonals of the WFC3 CCD detector run along the V2,V3 directions. Because WFC3 is on-axis, the origin of the V2,V3 system lies near the center of the WFC3 field of view. However, the V2,V3 (and U2, U3) coordinate axes have been shifted for clarity in Figure 6.1. *HST* observers may be more familiar with the U2,U3 coordinate system than V2,V3; for example, the specification of the ORIENT angle Special Requirement in APT uses the position angle of the U3 axis. The U2,U3 coordinates are defined as U2 = –V2 and U3 = –V3, and are marked in Figure 6.1. Observations of an astrometric field are made to locate the detector in the (V2, V3) system (WFC3 ISR 2009-35).

A fourth coordinate system (the **detector-based reference frame** in pixel units) is described here for completeness, but observers are unlikely to encounter this system other than in technical documents created during the development and ground-testing of WFC3. The detector-based system (Xdet, Ydet) is used by the flight software for commanding the detectors. It is a right-handed system based upon the orientation of the CCD serial registers, with its origin at Amplifier A (the four amplifiers are in the outer corners of the detectors, as shown in Figure 6.1). The +Xdet and +Ydet axes map to the –Axis2 and +Axis1 axes, respectively. Unlike the image-based Axis1, Axis2 system, the detector system is 0-indexed. Parallel shifting is performed along constant Xdet, and serial shifting is done along the constant Ydet direction (Section 6.7.2).

## 6.4.4 Subarrays and On-Chip Binning

While the default WFC3 UVIS readout mode is full-frame (i.e., both CCD chips), subarrays may be employed to read out and store only a portion of a CCD. Subarrays may be used, for example, in cases where the full-field data-volume and/or instrument-overhead requirements would overly constrain the observations. There are also circumstances in which on-chip binning may be desirable, although note that when post-flash is necessary to mitigate CTE, binned mode is no longer advantageous (as discussed below). Both subarray and binned mode have implications for the inclusion of physical overscan information in the readout, as listed in Table 6.1 and discussed in Section 6.7.2.

## Subarrays

Since 2010 (Cycle 18), a wide range of subarray sizes have been available: 512 × 512, 1k × 1k, and 2k × 2k. User-defined subarrays, and subarrays that span quadrant boundaries, are no longer supported. Subarrays are invoked via the appropriate Aperture parameter in the Phase II observing proposal; these apertures contain the string "SUB" in their names. Figure 6.2 shows the supported subarrays. See Section 6.4.5 and Table 6.1 for the reference points (default target positions) of these apertures.

**Figure 6.2: WFC3/UVIS subarrays. See text for reasons to prefer quadrant C. Full names of the subarrays are given in Table 6.1.**
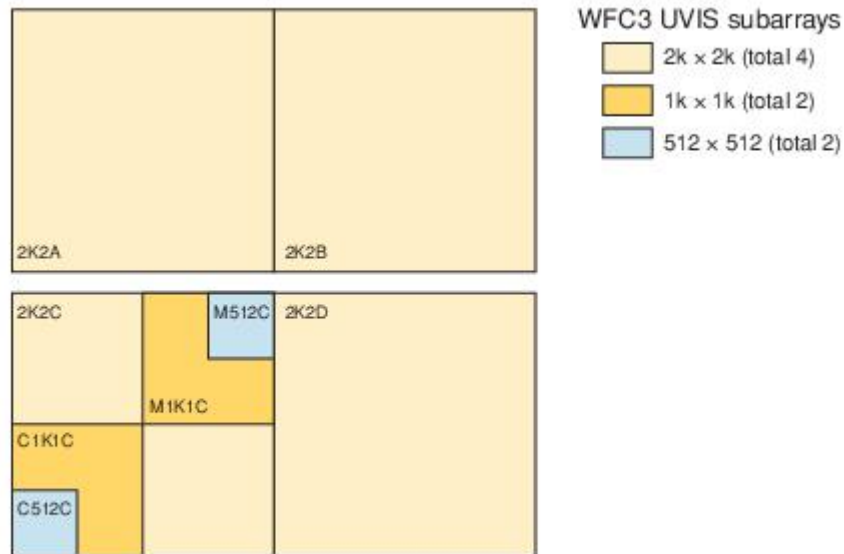


The lower left quadrant (amp C, CCD chip 2) was chosen as the preferred site for most of the subarrays for a number of reasons. The CCD focal plane is tilted around the diagonal from amp C to amp B (upper right quadrant; see Figure 6.20 for amplifier locations), so non-linear geometric distortion is greatest (Figure B.1) and PSFs are less well focused (WFC3 ISR 2013-11) near the A and D amplifiers. Bright stars imaged in the D quadrant form figure-eight ghosts that appear mostly in the D and A quadrants (see Figure 4 in WFC3 ISR 2011-16). The quantum efficiency below 3000 Angstroms is markedly higher on chip 2 (amp C and D) than it is on chip 1 (Figure 5.2). Note that full-quadrant subarrays have been defined for all four quadrants so that observers can use them to automatically align exposures made with continuum filters to exposures made with the quad filter apertures (discussed below; see Table 6.1). If not using quad filters, observers who want to make observations with a single-quadrant aperture (e.g., to reduce the time used for buffer dumps of short exposures) should consider choosing the UVIS2-2K2C-SUB aperture rather than the subarray apertures in the other quadrants for the reasons outlined earlier in this paragraph.

For the special case of quad filters (which are optical elements that provide four different bandpasses, one bandpass per WFC3 UVIS quadrant), the observer must select one of the "QUAD" Aperture values in the Phase II proposal, in conjunction with the desired quad filter via the filter parameter. This combination of quad aperture and quad filter ensures that the target is automatically placed in the correct quadrant for imaging with the requested quad bandpass. Furthermore, specification of the subarray quad aperture (UVIS-QUAD-SUB) instructs the ground system to read out only the 2k × 2k quadrant of interest. If "-SUB" is omitted from the quad aperture name (i.e., UVIS-QUAD, UVIS-QUAD-FIX), the target is positioned in the proper quadrant for the bandpass requested in the filter parameter, but the entire frame, both CCDs, is still read out. Table 6.1 indicates which apertures place the target at the geometric center of the subarray, and which apertures place it at a substantial offset from the center. See the *Phase II Proposal Instructions* for updates in aperture definitions at the beginning of a new cycle.

Use of any quad filter aperture, full-frame or subarray, is fully supported. However, if data volume and overhead time are not an issue, the observer is encouraged to allow full-frame readouts of quad-filter exposures, enabling serendipitous discoveries in the other quadrants of the image as well as enrichment of the *HST* data archive.

**On-Chip Binning**

The BIN optional parameter may be used in the observing proposal (see Section 6.2) to specify that the CCDs be read out in binned mode. Legal values for the parameter are NONE (the default), or 2 or 3, for 2× 2 and 3 × 3 on-chip binning, respectively. On-chip binning is only allowed with full-frame readouts; it may not be used in conjunction with any subarray mode. To perform on-chip binning, multiple rows are parallel-shifted into the serial register, which is shifted multiple pixels at a time into a single output pixel, which is then read once. **For the reasons discussed below, on-chip binning has not been useful for most programs, especially since the introduction of post-flash.**

One advantage of on-chip binning is that it reduces the readout noise: a 2 × 2 or 3 × 3 binned pixel contains approximately the same amount of read noise as a single pixel in an unbinned readout (see Section 5.4.7), but 4 times or 9 times the signal. However, binning increases the fraction of the image affected by cosmic rays and by the ever-increasing number of hot pixels (see Section 5.4.9). Moreover, if the background in an exposure is so low that read noise is a significant concern, then CTE losses, which are also ever-increasing over time, will make faint sources difficult or impossible to detect. CTE losses can be reduced by using post-flash to increase the background by a selected number of electrons per unbinned pixel (see Section 6.2), ideally bringing the total background up to a level of ~20 electrons/pixel (see Section 6.9). Note that the post-flash is applied before the readout, so if binning and post-flash were to be used together, a post-flash of 20 electrons per pixel would put 80 electrons into a 2 × 2 binned pixel, and 180 electrons into a 3 × 3 binned pixel, with an accompanying increase in noise. The reduction in read noise due to binning would then have a minor effect on the overall signal-to-noise (Section 9.6), not worth the disadvantages of binning.

On-chip binning does reduce the data volume, which affects the management of buffer dumps. Buffer dumps of unbinned full frame exposures can be done in parallel to the exposures only for exposure times of 348 sec or longer. Shorter unbinned exposures require serial buffer dumps, using up valuable time during an orbit. Use of the binned modes can reduce or eliminate the time devoted to serial buffer dumps during an orbit, and thus increase the number of exposures that can be fit into an orbit. For example, the number of 100 sec exposures that can be executed in a typical orbit is 6 for unbinned data, 12 for 2 × 2 binned data, and 19 for 3 × 3 binned data. This gain is, of course, achieved at the expense of spatial resolution of the already under-sampled PSF (see Section 6.6.2), at the cost of increasing the area affected by bad pixels and cosmic rays, as well as at the cost of a reduced signal-to-noise for images requiring post-flash. The optimum way to reduce data dumping time is to take unbinned exposures in a subarray large enough to contain the target.

In addition, binning affects the overscan data associated with an exposure. At the frame edges, some science and overscan pixels are binned together. Section 6.7.2 gives details concerning the rows and columns affected by binning mixed science and overscan data.

## 6.4.5 Apertures

The **APERTURE** parameter in the Phase II observing proposal defines two quantities: the active **region** of the detector to be read out (full frame or subarray), as well as the positioning of the target within the region (**reference point**). The default is to place the target at the reference point (also called the fiducial point) of the chosen aperture, but a **POS TARG** Special Requirement may be added to offset the target from this position.

With regard to pointing *HST*, there are two types of apertures: "**fixed**" and "**optimum**." The fixed positions have reference points near the geometric center of the aperture in question, and, as the name implies, their locations will remain fixed in image-based coordinates for the life of the instrument. The "optimum" apertures have reference points that are offset from the geometric center (if the need arises) so as to avoid any known CCD features (e.g., bad column, quad filter edge effects) that might compromise the observation of a target at that position. The locations of the "optimum" aperture reference points—in both the image-based coordinate system and the spacecraft V2,V3 coordinate system—may change over time as the characteristics and the characterization of the CCD evolve.

> ✓ *For updates on subarray and aperture definitions, check the* Science Instrument Aperture File (SIAF) page.

The choice of optimum or fixed aperture depends on the program's objectives and target. For a very small target, or one which easily fits into the aperture's field of view, the optimum aperture's reference point is defined to ensure that the target center does not fall on known problematic areas of the detector. The WFC3 website and STAN will announce changes in optimum aperture definitions. On the other hand, when the observer needs precise control of the position of the target on the detector, fixed apertures should be used. Fixed apertures are therefore appropriate when target position relative to detector edges is important, or when mosaics are being designed with edges requiring positional accuracies of better than 10 arcsec or so. The available WFC3 UVIS apertures ( Table 6.1) include both fixed and optimum versions for the primary locations: near the center of the full two-chip detector (UVIS and UVIS-FIX), and at the center of each chip (UVIS1 and UVIS2, and UVIS1-FIX and UVIS2-FIX). The aperture UVIS-CENTER places the target in or on the edge of the interchip gap; although it is not a FIX aperture, a change in the definition of this aperture is not expected.

**For faint targets, users are cautioned against using the apertures UVIS or UVIS-FIX, which put the target near the center of the array.** In these regions, CTE losses are high due to the large number of pixel transfers required to read out the detector. For full-frame exposures, users may wish to instead use apertures UVIS2-C512C-CTE or UVIS2-C1K1C-CTE. These apertures were introduced for Cycle 23 (Oct 2015). The UVIS*CTE apertures place the target near the C amplifier at the same reference positions as the optimum aperture subarrays UVIS2-C512C-SUB and UVIS2-C1K1C-SUB, respectively, and will read out the full 2-chip frame.

There are fixed and optimum apertures for use with the quad filters. Because the filter wheel assembly is necessarily offset from the focal plane, the edges between quad filters are blurred at the focal plane, producing regions with contributions from multiple quad filter passbands (Figure 6.8). The UVIS-QUAD-SUB apertures (redefined for cycle 20, Oct 2012) and UVIS-QUAD apertures have reference points centered within the useful single-passband regions, while the UVIS-QUAD-FIX apertures have reference points at the geometric centers of the quadrants (closer to the filter edge effects). In programs where targets are placed in different quadrants, the choice of quad aperture will affect the size of offsets and may require new guide star acquisition, as described in Section 10.2.

Subarray apertures pictured in Figure 6.2 are all "optimum"; no "fixed" apertures are available for these subarrays. The reference points for these apertures have initially been defined near the geometric center of the subarray, except for the 2K2 apertures, where the reference points match those of the UVIS-QUAD apertures.


**Table 6.1: Predefined apertures for WFC3/UVIS (see also the** Phase II Proposal Instructions**).**

| Aperture | Over-scan[1] | Region | Reference (fiducial) point |
|---|---|---|---|
| UVIS | P, V | Full detector | Optimum point near center (displaced from interchip gap) of full two-CCD field of view |
| UVIS-CENTER | P, V | Full detector | Geometric center of full two-CCD field of view |
| UVIS-FIX | P, V | Full detector | Near geometric center (displaced from interchip gap) of full two-CCD field of view |
| UVIS1 | P, V | Full detector | Optimum point near center of CCD Chip 1 |
| UVIS1-FIX | P, V | Full detector | Geometric center of CCD Chip 1 |
| UVIS2 | P, V | Full detector | Optimum point near center of CCD Chip 2 |
| UVIS2-FIX | P, V | Full detector | Geometric center of CCD Chip 2 |
| UVIS-IR-FIX | P, V | Full detector | Pointing matched to IR-FIX aperture in Table 7.1 |
| G280-REF[2] | P, V | Full detector | Reference point for undispersed exposures (coincides with reference point of exposures made with the G280 grism) |
| UVIS-QUAD | P, V | Full detector | Optimum point in the quadrant corresponding to the selected quadrant filter (offset from the center of the quadrant toward the nearest corner of the detector by about 8 to 10 arcsec in X and in Y; see Figure 6.8) |
| UVIS-QUAD-FIX | P, V | Full detector | Geometric center of quadrant corresponding to selected quadrant filter |
| UVIS2-C1K1C-CTE | P, V | Full detector | Same as UVIS2-C1K1C-SUB (see below), for better CTE performance |
| UVIS2-C512C-CTE | P, V | Full detector | Same as UVIS2-C512C-SUB (see below), for better CTE performance |
| UVIS-QUAD-SUB | P | 2047 × 2050 on the quadrant corresponding to selected quadrant filter | Same as UVIS-QUAD (optimum point in the relevant quadrant) starting in Cycle 20 in Oct 2012 (prior to that, the reference point was the geometric center of the quadrant) |

| | | | |
|---|---|---|---|
| UVIS1-2K2A-SUB UVIS1-2K2B-SUB UVIS2-2K2C-SUB UVIS2-2K2D-SUB | P | 2047 × 2050 | Optimum point for the corresponding quadrant filter FQ* (for matching N,M,W filter exposures to UVIS-QUAD or UVIS-QUAD-SUB aperture exposures), about 14 arcsec from the center of the 2k × 2k subarray.<br><br>If not pairing with FQ* quadrant filter exposures, UVIS2-2K2C-SUB is preferred (Section 6.4.4). |
| UVIS2-M1K1C-SUB | none | 1024 × 1024, quadrant C near detector center | Optimum point near center of 1k × 1k subarray |
| UVIS2-C1K1C-SUB | P | 1025 × 1024, near Amplifier C | Optimum point near center of 1k × 1k subarray |
| UVIS2-M512C-SUB | none | 512 × 512, quadrant C near detector center | Optimum point near center of 512 × 512 subarray |
| UVIS2-C512C-SUB | P | 513 ×512, near amplifier C | Optimum point near center of 512 × 512 subarray |

[1] "P" indicates aperture includes physical overscan, "V" indicates aperture includes virtual overscan.

[2] See Section 8.2 for information on the use of the G280-REF aperture.

# 6.5 UVIS Spectral Elements

## 6.5.1 Filter and Grism Summary

An overview of the UVIS spectral elements was given in Section 2.3. This section gives further details of the UVIS filters and grism. Table 6.2 contains a complete listing of the available spectral elements in the UVIS channel. Figures 6.3 through 6.10 show the effective throughput curves, including the filter transmission convolved with the OTA, WFC3 optics, and detector response. All of the UVIS filters are contained in a multi-wheel mechanism—identical to the mechanism on WFPC2—called the Selectable Optical Filter Assembly (SOFA). Values in Table 6.2 have been calculated for UVIS chip 1.

More detailed information on the throughput curves of all of the filters is given in Appendix A; in particular, Section A.2.1 describes how to generate tabular versions of the throughput curves using `stsynphot`. All measurements of the UVIS filters which involve wavelengths, as tabulated in Table 6.2 and plotted in Figures 6.3 through 6.10 and in Appendix A, were done in air. The data have been converted to vacuum wavelengths using the formula given by D. C. Morton (1991, *ApJS* **77**, 119). It should also be noted that the laboratory measurements were done at a temperature of 20°C, whereas the UVIS filters are operated on orbit at 0°C. The temperature difference may lead to wavelength shifts that are no more than 1.4 Å in the worst cases, according to the filter manufacturing specifications.

The UVIS filters have been chosen to cover a wide variety of scientific applications, ranging from color selection of distant galaxies to accurate photometry of stellar sources and narrow-band imaging of nebular gas. The set includes several very wide-band filters for extremely deep imaging, filters that match the most commonly used filters on WFPC2 and ACS (to provide continuity with previous observations), the SDSS filters, and filters that are optimized to provide maximum sensitivity to various stellar parameters (e.g., the Strömgren and Washington systems, and the F300X filter for high sensitivity to the stellar Balmer jump). There are a variety of narrow-band filters, which allow investigations of a range of physical conditions in the interstellar medium, nebulae, and solar system. A few of the narrow-band filters are also provided with slightly redshifted wavelengths, for use in extragalactic applications. Finally, there is a UV grism that provides slitless spectra with useful dispersion covering 2000–8000 Å (although the grism transmission spans the full wavelength range of the CCD).

Table 6.2: WFC3/UVIS Filters and Grism. The pivot wavelength, width and peak system throughput listed values are for UVIS chip1, except for the quad filters (see text for more details).

| Name[1] | Description[2] | Pivot[3] $\lambda_p$ (Å) | Width[4] (Å) | Peak System Throughput |
|---|---|---|---|---|
| UVIS Long-Pass (LP) and Extremely Wide (X) Filters | | | | |
| F200LP | Clear | 4971.9 | 5881.1 | 0.28 |

| F300X | Extremely wide UV; grism reference | 2820.5 | 707.3 | 0.16 |
|---|---|---|---|---|
| F350LP | Long pass | 5873.9 | 4803.7 | 0.29 |
| F475X | Extremely wide blue | 4940.7 | 2057.2 | 0.28 |
| F600LP | Long pass | 7468.1 | 2340.1 | 0.29 |
| F850LP | SDSS z′ | 9176.1 | 1192.5 | 0.11 |
| UVIS Wide-Band (W) Filters | | | | |
| F218W | ISM feature | 2228 | 330.7 | 0.04 |
| F225W | UV wide | 2372.1 | 467.1 | 0.09 |
| F275W | UV wide | 2709.7 | 405.3 | 0.12 |
| F336W | U, Strömgren u | 3354.5 | 511.6 | 0.2 |
| F390W | Washington C | 3923.7 | 894 | 0.25 |
| F438W | WFPC2 B | 4326.2 | 614.7 | 0.24 |
| F475W | SDSS g′ | 4773.1 | 1343.5 | 0.27 |
| F555W | WFPC2 V | 5308.4 | 1565.4 | 0.29 |
| F606W | WFPC2 Wide V | 5889.2 | 2189.2 | 0.29 |
| F625W | SDSS r′ | 6242.6 | 1464.6 | 0.28 |
| F775W | SDSS i′ | 7651.4 | 1179.1 | 0.23 |
| F814W | WFPC2 Wide I | 8039.1 | 1565.2 | 0.23 |
| UVIS Medium-Band (M) Filters | | | | |
| F390M | Ca II continuum | 3897.2 | 204.3 | 0.22 |
| F410M | Strömgren ν | 4109 | 172 | 0.26 |
| FQ422M | Blue continuum | 4219.2 | 111.7 | 0.18 |
| F467M | Strömgren b | 4682.6 | 200.9 | 0.28 |
| F547M | Strömgren y | 5447.5 | 650 | 0.27 |
| F621M | 11% passband | 6218.9 | 609.5 | 0.29 |
| F689M | 11% passband | 6876.8 | 684.2 | 0.25 |
| F763M | 11% passband | 7614.4 | 708.6 | 0.21 |
| F845M | 11% passband | 8439.1 | 794.3 | 0.14 |
| UVIS Narrow-Band (N) Filters | | | | |

| | | | | |
|---|---|---|---|---|
| FQ232N | [C II] 2326 | 2432.2 | 34.2 | 0.04 |
| FQ243N | [Ne IV] 2425 | 2476.3 | 36.7 | 0.05 |
| F280N | Mg II 2795/2802 | 2832.9 | 42.5 | 0.06 |
| F343N | [Ne V] 3426 | 3435.1 | 249.1 | 0.2 |
| F373N | [O II] 3726/3728 | 3730.2 | 49.6 | 0.18 |
| FQ378N | z ([O II] 3726) | 3792.4 | 99.3 | 0.19 |
| FQ387N | [Ne III] 3868 | 3873.7 | 33.6 | 0.16 |
| F395N | Ca II 3933/3968 | 3955.2 | 85.2 | 0.22 |
| FQ436N | Hγ 4340 + [O III] 4363 | 4367.2 | 43.4 | 0.18 |
| FQ437N | [O III] 4363 | 4371 | 30 | 0.19 |
| F469N | He II 4686 | 4688.1 | 49.7 | 0.2 |
| F487N | Hβ 4861 | 4871.4 | 60.4 | 0.25 |
| FQ492N | z (Hβ) | 4933.4 | 113.5 | 0.25 |
| F502N | [O III] 5007 | 5009.6 | 65.3 | 0.26 |
| FQ508N | z ([O III] 5007) | 5091 | 130.6 | 0.22 |
| FQ575N | [N II] 5754 | 5757.7 | 18.4 | 0.21 |
| FQ619N | $CH_4$ 6194 | 6198.5 | 60.9 | 0.25 |
| F631N | [O I] 6300 | 6304.3 | 58.3 | 0.25 |
| FQ634N | 6194 continuum | 6349.2 | 64.1 | 0.24 |
| F645N | Continuum | 6453.6 | 84.2 | 0.24 |
| F656N | Hα 6562 | 6561.4 | 17.6 | 0.23 |
| F657N | Wide Hα + [N II] | 6566.6 | 121 | 0.25 |
| F658N | [N II] 6583 | 6584 | 27.6 | 0.25 |
| F665N | z (Hα + [N II]) | 6655.9 | 131.3 | 0.25 |
| FQ672N | [S II] 6717 | 6716.4 | 19.4 | 0.21 |
| F673N | [S II] 6717/6731 | 6765.9 | 117.8 | 0.25 |
| FQ674N | [S II] 6731 | 6730.7 | 17.6 | 0.23 |
| F680N | z (Hα + [N II]) | 6877.6 | 370.5 | 0.25 |
| FQ727N | $CH_4$ 7270 | 7275.2 | 63.9 | 0.2 |
| FQ750N | 7270 continuum | 7502.5 | 70.4 | 0.18 |

| FQ889N | CH$_4$ 25 km-agt[5] | 8892.2 | 98.5 | 0.1 |
|---|---|---|---|---|
| FQ906N | CH$_4$ 2.5 km-agt[5] | 9057.8 | 98.6 | 0.09 |
| FQ924N | CH$_4$ 0.25 km-agt[5] | 9247.6 | 91.6 | 0.08 |
| FQ937N | CH$_4$ 0.025 km-agt[5] | 9372.4 | 93.3 | 0.07 |
| F953N | [S III] 9532 | 9530.6 | 96.8 | 0.05 |
| UVIS Grism (G) | | | | |
| G280[6] | UV grism | Useful range: 2000–8000 Å | | 0.17 |

1. The spectral-element naming convention is as follows for both the UVIS and IR channels. All filter names begin with F, and grisms with G; if the filter is part of a four-element quad mosaic, a Q follows F. Then there is a three-digit number giving the nominal effective wavelength of the bandpass, in nm (UVIS channel) or nm/10 (IR channel). (For long-pass filters, the number is instead the nominal blue cut-off wavelength in nm.) Finally, for the filters, one or two letters indicate the bandpass width: X (extremely wide), LP (long pass), W (wide), M (medium), or N (narrow).
2. Filters intended for imaging in a red-shifted bandpass are given descriptions similar to the following: "z (Hα + [N II])".
3. "Pivot wavelength" is a measure of the effective wavelength of a filter (see Section 9.3 and Tokunaga & Vacca 2005, PASP, **117**, 421). It is calculated here based on the integrated system throughput. Filter transmissions were measured in air, but the equivalent vacuum wavelengths are reported in this table.
4. Widths listed are passband rectangular width, defined as the equivalent width divided by the maximum throughput within the filter bandpass. Equivalent width is the integral with respect to wavelength of the throughput across the filter passband.
5. km-agt (km-amagat) is a unit of vertical column density, equal to $2.69 \times 10^{24}$ molecules/cm$^2$.
6. See Chapter 8 for UVIS Grism details.

Most of the UVIS filters, as well as the UVIS grism, are full-sized elements that cover the entire UVIS field of view. However, in order to provide a larger number of bandpasses, there are five sets of "quad" filters, identified with "FQ" in the filter name, where each bandpass covers ~1/6 of the WFC3 UVIS field of view (i.e., each bandpass covers less than half of a single CCD chip). The quad filters are discussed in more detail below.

The UVIS channel is designed to be used with a single filter or grism in the light path. Unfiltered imaging, or imaging through a combination of two filters (from two different SOFA wheels), although possible in principle, would lead to significantly degraded image quality and has not been tested; thus these options are not permitted. The F200LP filter provides a clear fused silica element that approximates unfiltered imaging.

While the red blocking in the WFC3 UV filters is generally very good, resulting in negligible red leaks for hot objects (typically far less than 1% for targets with effective temperature $T_{eff} > 10{,}000$ K), the red leak can become significant in some filters for cooler targets (e.g., ~10% in F225W for a star with $T_{eff} = 5000$ K). More details are available in Section 6.5.2; Table 6.5 in that section tabulates red-leak values as a function of stellar effective temperature.

**Figure 6.3:** Integrated system throughput of the WFC3 UVIS long-pass and extremely wide filters for UVIS1 (UVIS chip1) at the reference epoch of June 26, 2009. The throughput calculations include the *HST* OTA, WFC3 UVIS-channel internal throughput, filter transmittance, and the QE of the UVIS flight detector, and a correction factor to account for the gain sensitivity seen in SMOV4 on-orbit observations vs TV3 ground tests. Throughputs below ~3200 Å contain contributions at the measured rate from all detected electrons, including minor contribution from UV multiple electrons.

Figure 6.4: Integrated system throughput of the WFC3 UVIS wide-band filters with pivot wavelength < 4000 Å (top panel) and with pivot wavelength > 4000 Å (bottom panel) for UVIS1 at the reference epoch of June 26, 2009. The throughput calculations include the *HST* OTA, WFC3 UVIS-channel internal throughput, filter transmittance, and the QE of the UVIS flight detector, and a correction factor to account for the gain sensitivity seen in SMOV4 on-orbit observations vs TV3 ground tests. Throughputs below ~3200 Å contain contributions at the measured rate from all detected electrons, including minor contribution from UV multiple electrons.

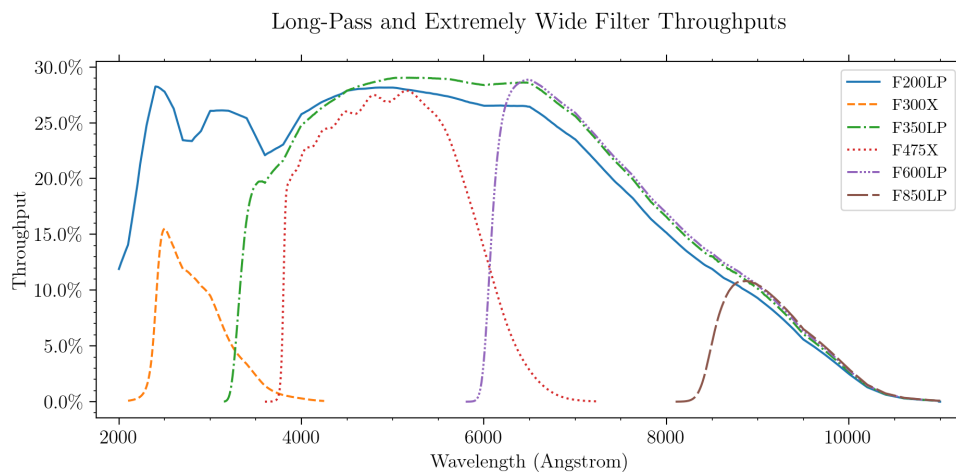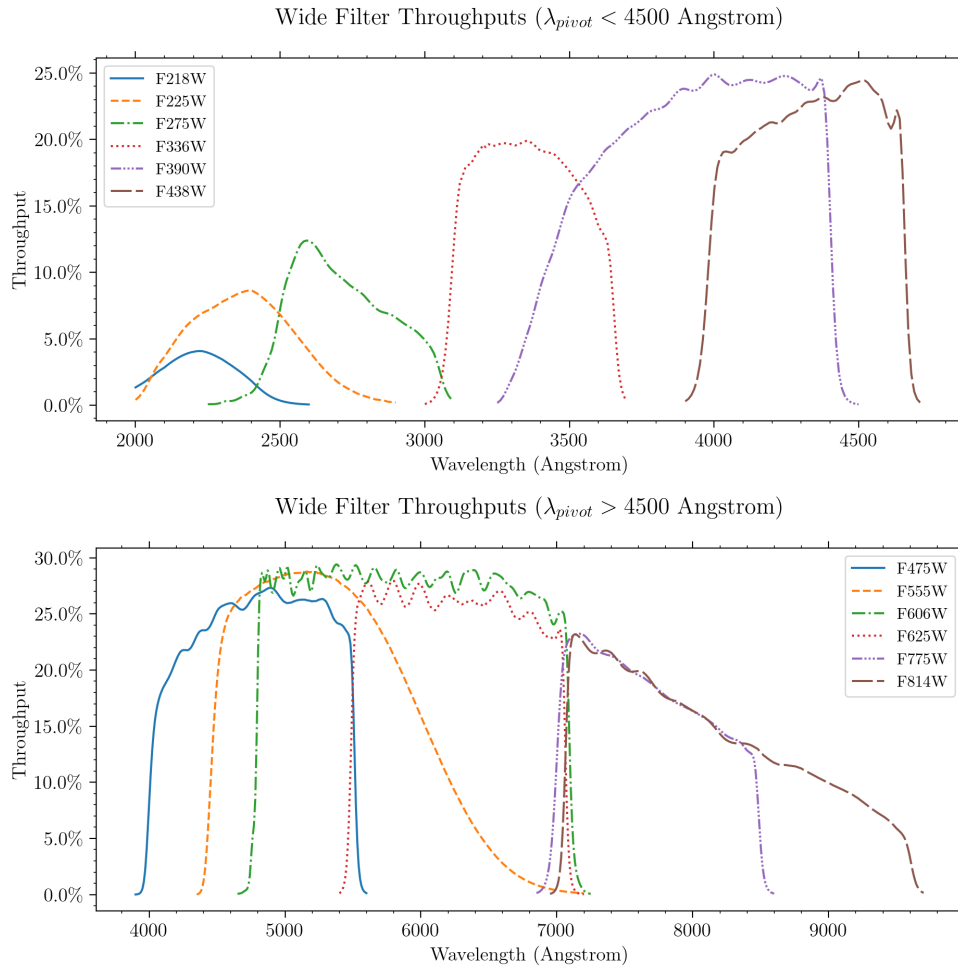**Figure 6.5:** Integrated system throughput of the WFC3 UVIS medium-band filters for UVIS1 at the reference epoch of June 26, 2009. The throughput calculations include the *HST* OTA, WFC3 UVIS-channel internal throughput, filter transmittance, and the QE of the UVIS flight detector, and a correction factor to account for the gain sensitivity seen in SMOV4 on-orbit observations vs TV3 ground tests.
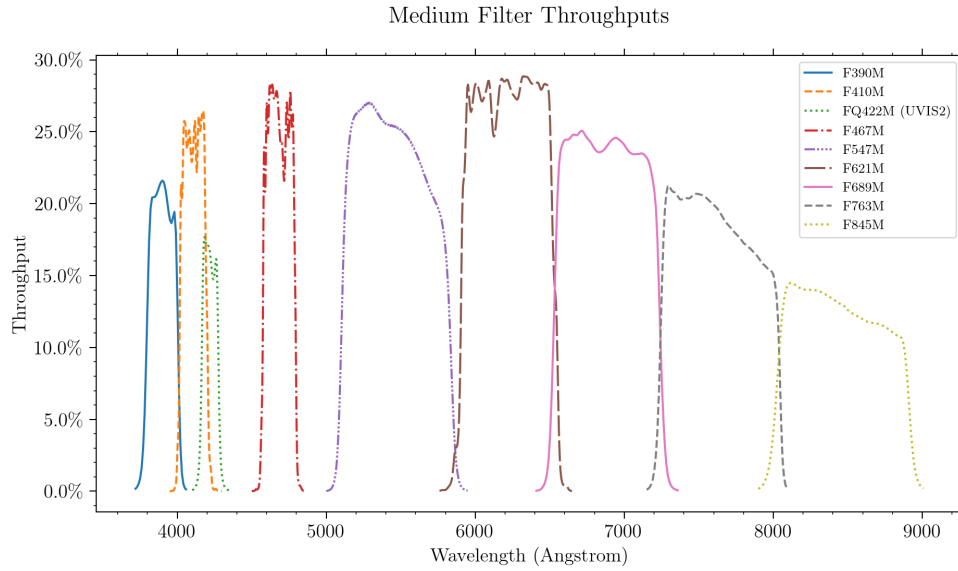
**Figure 6.6:** Integrated system throughput of the WFC3 UVIS narrow-band filters with pivot wavelength < 4000 Å for UVIS1 at the reference epoch of June 26, 2009. The throughput calculations include the *HST* OTA, WFC3 UVIS-channel internal throughput, filter transmittance, and the QE of the UVIS flight detector, and a correction factor to account for the gain sensitivity seen in SMOV4 on-orbit observations vs TV3 ground tests. Throughputs below ~3200 Å contain contributions at the measured rate from all detected electrons, including minor contribution from UV multiple electrons.
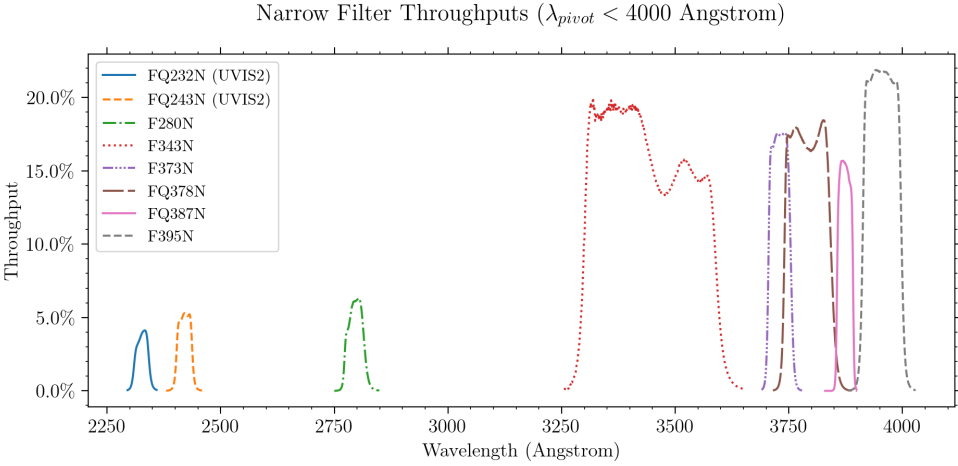
**Figure 6.7:** Integrated system throughput of the WFC3 UVIS narrow-band filters with 4000 Å < pivot wavelength < 5500 Å. The throughput calculations include the HST OTA, WFC3 UVIS-channel internal throughput, filter transmittance, and the QE of the UVIS flight detector, and a correction factor to account for the gain sensitivity seen in SMOV4 on-orbit observations vs TV3 ground tests.



Narrow Filter Throughputs (4000 Angstrom < $\lambda_{pivot}$ < 5500 Angstrom)

**Figure 6.8:** Integrated system throughput of the WFC3 UVIS narrow-band filters with 5500 Å < pivot wavelength < 6600 Å for UVIS1 at the reference epoch of June 26, 2009. The throughput calculations include the HST OTA, WFC3 UVIS-channel internal throughput, filter transmittance, and the QE of the UVIS flight detector, and a correction factor to account for the gain sensitivity seen in SMOV4 on-orbit observations vs TV3 ground tests.



Narrow Filter Throughputs (5500 Angstrom < $\lambda_{pivot}$ < 6600 Angstrom)

**Figure 6.9:** Integrated system throughput of the WFC3 UVIS narrow-band filters with 6000 Å < pivot wavelength < 7500 Å for UVIS1 at the reference epoch of June 26, 2009. The throughput calculations include the HST OTA, WFC3 UVIS-channel internal throughput, filter transmittance, and the QE of the UVIS flight detector, and a correction factor to account for the gain sensitivity seen in SMOV4 on-orbit observations vs TV3 ground tests.



Narrow Filter Throughputs (6600 Angstrom < $\lambda_{pivot}$ < 7500 Angstrom)

**Figure 6.10:** Integrated system throughput of the WFC3 UVIS narrow-band filters with pivot wavelength > 7500 Å for UVIS1 at the reference epoch of June 26, 2009. The throughput calculations include the HST OTA, WFC3 UVIS-channel internal throughput, filter transmittance, and the QE of the UVIS flight detector, and a correction factor to account for the gain sensitivity seen in SMOV4 on-orbit observations vs TV3 ground tests.
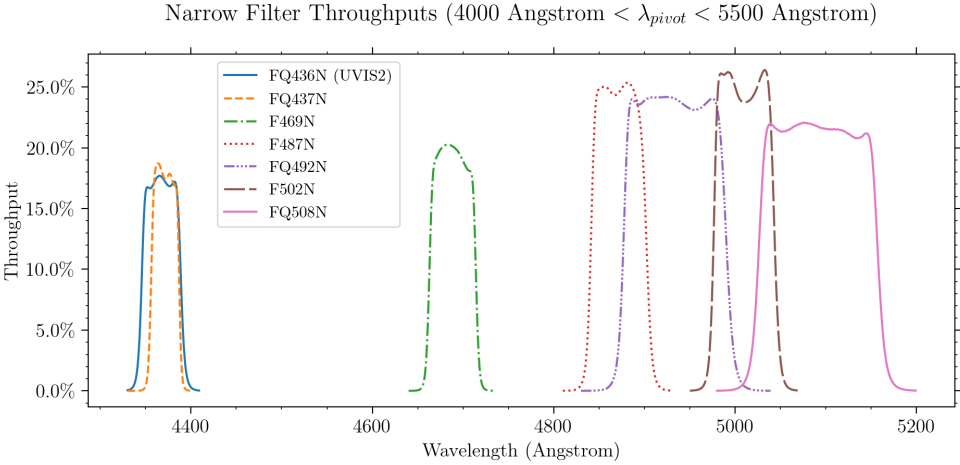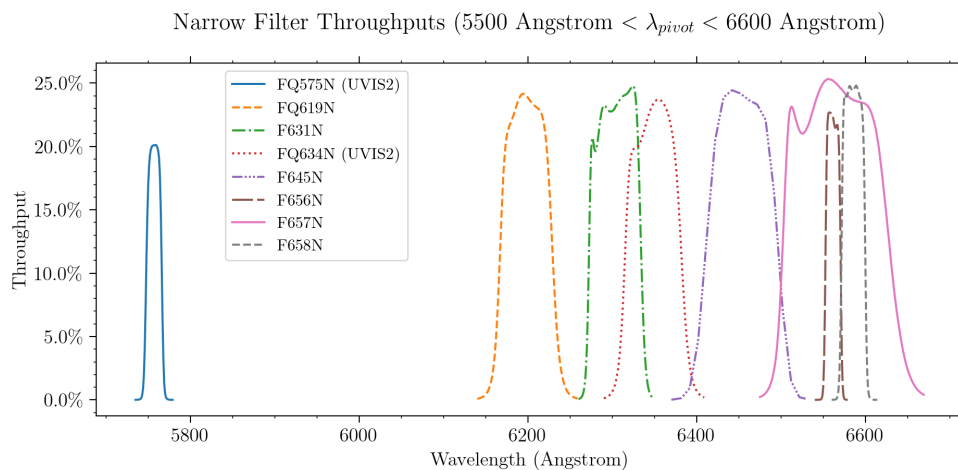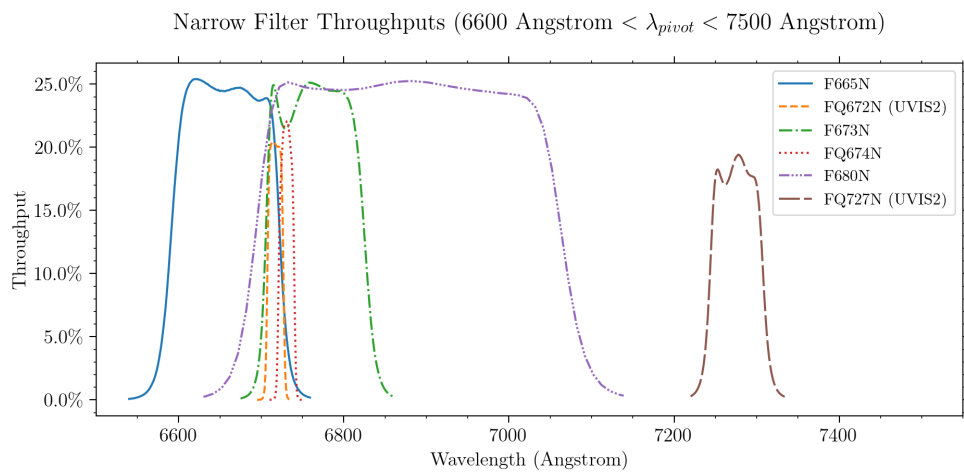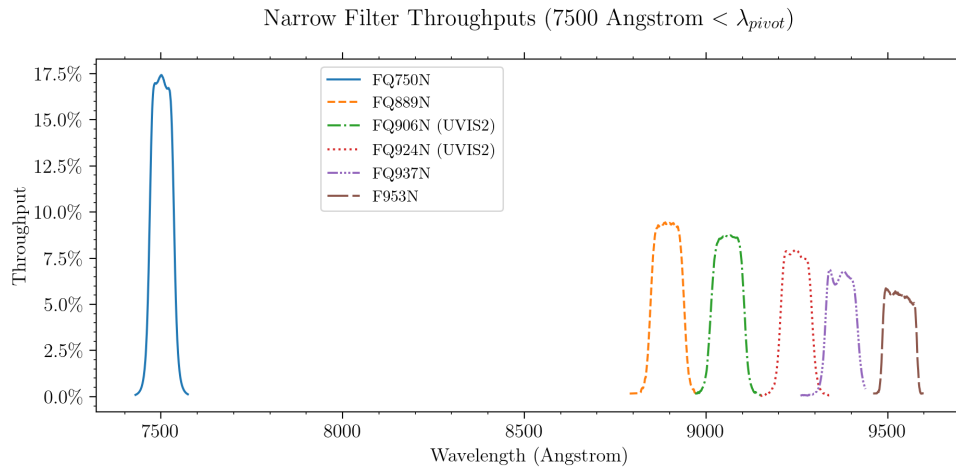


## UV Filters

As mentioned earlier, the WFC3 UVIS optics and CCDs have been optimized for UV imaging. As such, the UV filters play a key role and considerable effort has been made to procure filters with the best possible characteristics, including maximum throughput, maximum out-of-band blocking, and minimal ghosts.

The UV filters include the shortest-wavelength F218W, intended for studies of the ISM absorption feature; the wide F225W and F275W for broad-band UV imaging; the Strömgren u (F336W) and Washington C (F390W) for stellar astrophysics; the extremely wide F300X for very deep imaging; and narrow bands such as F280N (Mg II) and the quad filters FQ232N and FQ243N ([C II] and [Ne IV]).

## Ultra-Wide Filters

The selection of extremely wide (X) and long-pass (LP) filters is suited for deep imaging of faint sources. The ultra-wide F200LP filter is simply a fused-silica element with a UV-optimized anti-reflection coating which covers the UVIS channel's entire spectral range (2000 - 10000 Å). The F200LP filter is analogous to the clear filter on STIS.

WFC3's maximum sensitivity to hot sources can be obtained by subtracting an F350LP image from an F200LP, thereby creating a very broad ultraviolet bandpass. In Figure 6.11, the blue curve shows the filter transmission for the F200LP filter for UVIS2 at the reference epoch of June 26, 2009, and the black curve shows the effective transmission for a F200LP minus F350LP difference image. For redder targets, some additional calibration may be necessary to account for differences in the transmission of the two filters longward of ~4500 Å.

The F850LP filter is part of the Sloan Digital Sky Survey (SDSS) *griz* filter set, and is the reddest of the ultra-wide filters.

**Figure 6.11:** Sensitivity of F200LP-F350LP compared to other UV filters (F225W, F275W and F300X) for UVIS2 at the reference epoch of June 26, 2009. Light grey curves show blackbody functions for 20,000 and 50,000 K.
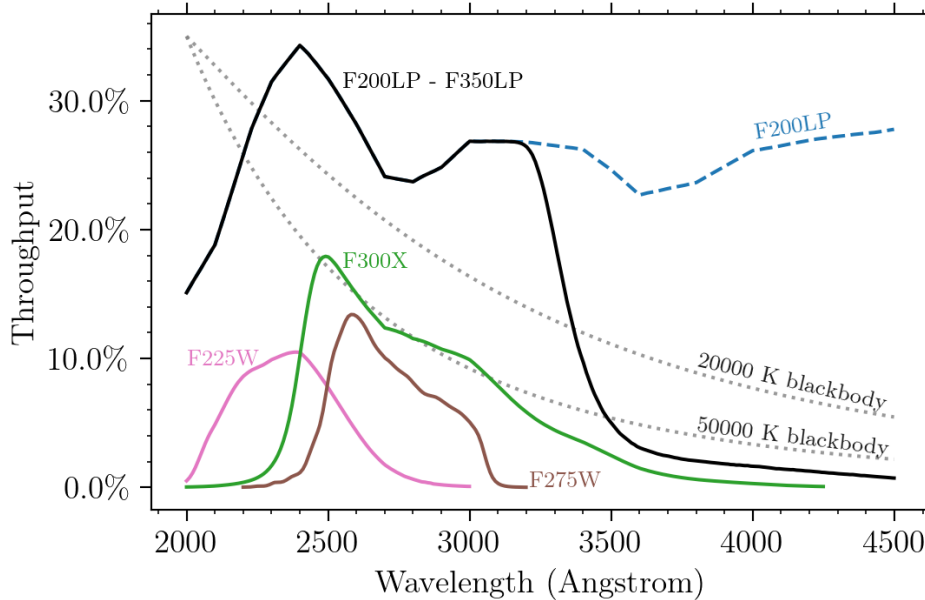


## Wide-Band Filters

The most commonly used WFPC2 and ACS wide filters are also included in the WFC3 filter set. In addition to a wide V-band filter (F606W), there is the Johnson-Cousins BVI set (F438W, F555W, F814W).
The Sloan Digital Sky Survey (SDSS) *griz* filter set (F475W, F625W, F775W, F850LP) is designed to provide high throughput for the wavelengths of interest and excellent rejection of out-of-band wavelengths. These filters provide wide, non-overlapping filter bands that cover the entire range of CCD sensitivity from blue to near-IR wavelengths.

## Medium-Band Filters

The medium-band filters include the Strömgren set (*u*, *v*, *b*, and *y*), as well as some continuum bands needed for use with narrow-band imaging (F390M, FQ422M). The four 11% passband filters were added to the WFC3 UVIS set in order to cover the ~ 6000 - 9000 Å wavelength region with equal-energy filters. The "11%" refers to the filter bandwidths, which are ~11% of the central wavelength.

## Narrow-Band Filters

The WFC3 UVIS channel contains 36 different narrow-band filters, covering a variety of species and most of the astrophysically interesting transitions, including Hα, Hβ, Hγ, He II, C II], [N II], [O I], [O II], [O III], [Ne IV], [Ne V], [S II], and Ca II. The methane absorption bands seen in planets, cool stars, and brown dwarfs are also covered.

Cosmological emission lines can be detected across a range of redshifts within the bandpasses of the narrow-band filters. Table 6.3 lists the redshifts that can be probed using the specified narrow emission lines (hence, no entries for broad absorption bands or continuum or "off" bands). These redshift ranges are offered as a guide; exact values depend on the wavelengths of the filter cutoffs. Filter cutoffs used in Table 6.3 were defined using the passband rectangular widths (defined in Footnote [4] of Table 6.2). However, passband cutoffs were not centered on the filter pivot wavelengths $\lambda_p$ (defined in Section 9.3), because red leaks shift the pivot wavelengths to longer wavelengths by 1-9% in some of the ultraviolet filters. Instead, the central wavelength for each filter was determined by maximizing the wavelength-integrated product of a rectangular passband of the specified width with the actual system throughput for the filter. In the most extreme case (FQ232N), the pivot wavelength of 2413 Å is more than two bandpass widths to the red of the rectangular passband equivalent central wavelength (2326 Å).

Table 6.3: Nominal redshift ranges for WFC3/UVIS narrow-band filters.

| Filter | Description | Pivot $\lambda_p$ (Å) | Width (Å) | Line Rest Wavelength (Å) | Minimum cz (km/sec) | Maximum cz (km/sec) |
|---|---|---|---|---|---|---|
| FQ232N | [C II] 2326 | 2432.2 | 34.2 | 2326 | -2191 | 2191 |
| FQ243N | [Ne IV] 2425 | 2476.3 | 36.7 | 2425 | -2843 | 1607 |
| F280N | Mg II 2795/2802 | 2832.9 | 42.5 | | | |
| F343N | [Ne V] 3426 | 3435.1 | 249.1 | 3426 | -10763 | 11113 |
| F373N | [O II] 3726/3728 | 3730.2 | 49.6 | 3727 | -1689 | 2333 |
| FQ378N | z ([O II] 3726) | 3792.4 | 99.3 | 3727 | 1247 | 9210 |
| FQ387N | [Ne III] 3868 | 3873.7 | 33.6 | 3869 | -907 | 1728 |
| F395N | Ca II 3933/3968 | 3955.2 | 85.2 | | | |
| FQ436N | Hγ 4340 + [O III] 4363 | 4367.2 | 43.4 | 4340 | 414 | 3384 |
| FQ437N | [O III] 4363 | 4371 | 30 | 4363 | -412 | 1649 |
| F469N | He II 4686 | 4688.1 | 49.7 | 4686 | -1388 | 1811 |
| F487N | Hβ 4861 | 4871.4 | 60.4 | 4861 | -1252 | 2448 |
| FQ492N | z (Hβ) | 4933.4 | 113.5 | 4861 | 968 | 7998 |
| F502N | [O III] 5007 | 5009.6 | 65.3 | 5007 | -1754 | 2138 |
| FQ508N | z ([O III] 5007) | 5091 | 130.6 | 5007 | 1120 | 8964 |
| FQ575N | [N II] 5754 | 5757.7 | 18.4 | 5755 | -344 | 594 |
| FQ619N | CH$_4$ 6194 | 6198.5 | 60.9 | | | |

| | | | | | | |
|---|---|---|---|---|---|---|
| **F631N** | [O I] 6300 | 6304.3 | 58.3 | 6300 | -1156 | 1604 |
| **FQ634N** | 6194 continuum | 6349.2 | 64.1 | | | |
| **F645N** | Continuum | 6453.6 | 84.2 | | | |
| **F656N** | Hα 6562 | 6561.4 | 17.6 | 6563 | -448 | 375 |
| **F657N** | Wide Hα + [N II] | 6566.6 | 121 | 6563 | -2709 | 2818 |
| **F658N** | [N II] 6583 | 6584 | 27.6 | 6583 | -519 | 756 |
| **F665N** | z (Hα + [N II]) | 6655.9 | 131.3 | 6563 | 1311 | 7295 |
| **FQ672N** | [S II] 6717 | 6716.4 | 19.4 | 6717 | -402 | 446 |
| **F673N** | [S II] 6717/6731 | 6765.9 | 117.8 | 6725 | -847 | 4413 |
| **FQ674N** | [S II] 6731 | 6730.7 | 17.6 | 6731 | -437 | 365 |
| **F680N** | z (Hα + [N II]) | 6877.6 | 370.5 | 6563 | 5833 | 22781 |
| **FQ727N** | $CH_4$ 7270 | 7275.2 | 63.9 | | | |
| **FQ750N** | 7270 continuum | 7502.5 | 70.4 | | | |
| **FQ889N** | CH4 25 km-agt | 8892.2 | 98.5 | | | |
| **FQ906N** | $CH_4$ 2.5 km-agt | 9057.8 | 98.6 | | | |
| **FQ924N** | $CH_4$ 0.25 km-agt | 9247.6 | 91.6 | | | |
| **FQ937N** | $CH_4$ 0.025 km-agt | 9372.4 | 93.3 | | | |
| **F953N** | [S III] 9532 | 9530.6 | 96.8 | 9531 | -1494 | 1557 |

### Quad Filters

The WFC3 UVIS channel contains five quad filters: each is a 2 × 2 mosaic of filter elements occupying a single filter slot, with each quadrant providing a different bandpass (typically narrow-band, although there are also several bandpasses intended for continuum measurements). The five quad filter sets on WFC3 significantly increase the number of available narrow-band filters. The WFC3 quad filters are listed in Table 6.4 with their readout amplifiers. The pivot wavelength, equivalent width and peak system throughput for these filters (see Table 6.2) were calculated by using the filter curves updated in October 2020: these are based on the original UVIS filter curves, aperture corrections and in-flight corrections (for more details see WFC3 ISR 2021-04).

A quadrant nominally covers only 1/4 of the WFC3 total field of view or about 80"× 80", although edge effects (Figure 6.12) result in a useable field of about 1/6 of the field of view. The filter edges are out of focus on the focal plane, so light from multiple passbands reaches the detector in those areas.

In programs where targets are placed in different quadrants during a single orbit, spacecraft maneuvers may be large enough to force a new guide star acquisition. Guide star acquisition overheads are described in Section 10.2.

Table 6.4: Quad filter names and positions (identified by readout amplifier).

| Filter | Readout Amplifier | | Filter | Readout Amplifier | | Filter | Readout Amplifier | | Filter | Readout Amplifier |
|---|---|---|---|---|---|---|---|---|---|---|
| FQ232N | C | | FQ436N | D | | FQ619N | A | | FQ750N | B |
| FQ243N | D | | FQ437N | A | | FQ634N | C | | FQ889N | A |
| FQ378N | B | | FQ492N | B | | FQ672N | D | | FQ906N | C |
| FQ387N | A | | FQ508N | A | | FQ674N | B | | FQ924N | D |
| FQ422M | C | | FQ575N | C | | FQ727N | D | | FQ937N | B |

**Figure 6.12:** Quad filter edge effects (indicated by brackets). QUAD-FIX apertures have reference points in the center of each quadrant. Starting in Oct 2010 (Cycle 18), QUAD and 2K2-SUB apertures have had reference points in the center of the areas unaffected by filter edge effects. QUAD-SUB apertures initially had quadrant-centered reference points, but match the reference points in the QUAD apertures as of Oct 2012 (Cycle 20).
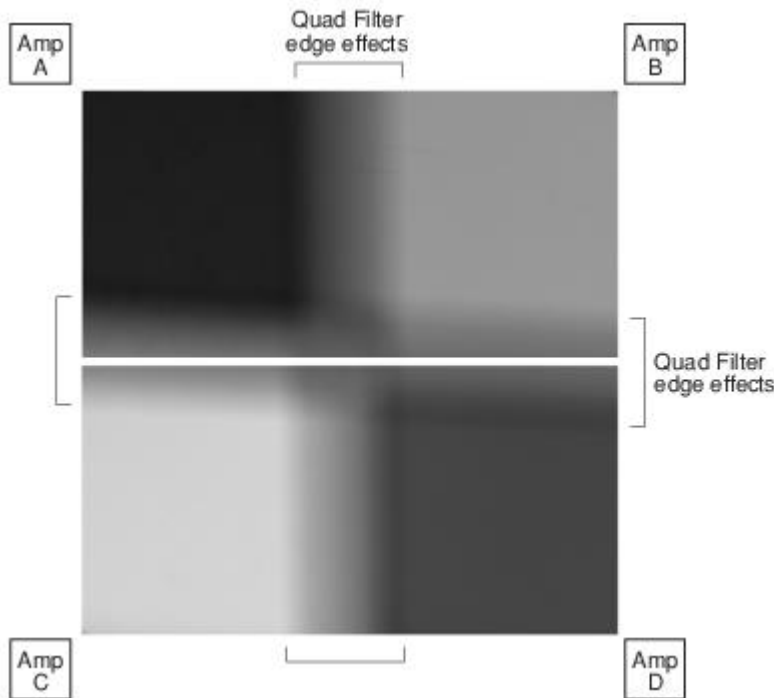


### Grism

The UVIS channel has a UV grism (G280), a spare element from WF/PC-1. It provides slitless spectra with a dispersion of about 14 Å/pix and a spectral resolution of about 70 over the 2000 - 8000 Å wavelength range, but with transmission in the zeroth order over the entire response of the CCD (see Figure 8.3). At wavelengths longer than ~ 4000 Å, however, reduced sensitivity and overlapping orders may complicate analysis. Typically, a grism observation is accompanied by a direct image, for source identification and wavelength zero-point calibration; an ideal filter for the identification image is the F300X discussed above. Chapter 8 discusses WFC3 slitless spectroscopy in detail.

## 6.5.2 Filter Red Leaks

The design and manufacture of the UV filters was based on a careful balance of the in- and out-of-band transmissions: in general, higher in-band transmission results in poorer suppression of out-of-band transmission, and vice versa. The WFC3 filters represent an attempt to achieve an optimum result, maximizing the in-band transmission while keeping the out-of-band transmission as low as possible in order to minimize red leaks.

Table 6.5 below summarizes the red-leak levels for the WFC3 UV filters. The table lists the fraction of the total signal that is due to flux longward of 4000 Å, as a function of effective temperature. This was calculated by convolving a blackbody of the given $T_{eff}$ with the system throughput in the listed

filter. As can be seen from the table, red leaks should not be an issue for observations of any objects taken with F275W or F336W. The other UV filters have some red leaks, whose importance depends on stellar temperature. The red leaks in F218W and F300X, for example, exceed ~1% for objects cooler than ~6000 K, while in F225W the red leak reaches ~1% for objects with even cooler temperatures. The most extreme red leaks arise from F218W and F225W observations of objects with $T_{eff}$ of ~4000 K or cooler, necessitating appropriate corrections.

Table 6.5: Fraction of flux longward of 4000 Å as a function of effective temperature.

| $T_{eff}$ (K) | F218W | F225W | F275W | F300X | F336W |
|---|---|---|---|---|---|
| 1000 | 1 | 1 | 1 | 1 | 1 |
| 2000 | 9.9E-01 | 9.9E-01 | 8.4E-01 | 5.5E-01 | 3.0E-02 |
| 3000 | 6.0E-01 | 2.7E-01 | 3.0E-02 | 8.9E-02 | 8.4E-04 |
| 4000 | 1.1E-01 | 1.8E-02 | 3.1E-03 | 3.3E-02 | 1.4E-04 |
| 5000 | 2.7E-02 | 3.2E-03 | 8.6E-04 | 1.7E-02 | 4.5E-05 |
| 6000 | 9.9E-03 | 1.0E-03 | 3.8E-04 | 1.0E-02 | 2.2E-05 |
| 7000 | 4.9E-03 | 4.6E-04 | 2.2E-04 | 7.3E-03 | 1.3E-05 |
| 8000 | 2.8E-03 | 2.5E-04 | 1.5E-04 | 5.5E-03 | 9.0E-06 |
| 9000 | 1.9E-03 | 1.6E-04 | 1.1E-04 | 4.4E-03 | 6.8E-06 |
| 10000 | 1.3E-03 | 1.1E-04 | 8.6E-05 | 3.7E-03 | 5.4E-06 |
| 11000 | 1.0E-03 | 8.6E-05 | 7.1E-05 | 3.2E-03 | 4.5E-06 |
| 12000 | 8.3E-04 | 6.9E-05 | 6.0E-05 | 2.8E-03 | 3.9E-06 |
| 13000 | 6.9E-04 | 5.7E-05 | 5.3E-05 | 2.6E-03 | 3.5E-06 |
| 14000 | 5.9E-04 | 4.8E-05 | 4.8E-05 | 2.3E-03 | 3.1E-06 |
| 15000 | 5.1E-04 | 4.2E-05 | 4.3E-05 | 2.2E-03 | 2.9E-06 |
| 20000 | 3.3E-04 | 2.6E-05 | 3.2E-05 | 1.7E-03 | 2.2E-06 |
| 30000 | 2.1E-04 | 1.7E-05 | 2.4E-05 | 1.3E-03 | 1.7E-06 |
| 40000 | 1.8E-04 | 1.4E-05 | 2.1E-05 | 1.2E-03 | 1.5E-06 |
| 50000 | 1.6E-04 | 1.3E-05 | 2.0E-05 | 1.1E-03 | 1.4E-06 |

### 6.5.3 Ghosts

The WFC3 UVIS channel exhibits three different types of optical ghosts: a) those due to reflections between the CCD front surface and the two detector package windows; b) those due to reflections between the window surfaces; and c) those due to reflections within the particular filter in use.

#### Window Ghosts

Window ghosts were predicted from early models of the UVIS detector (WFC3 ISR 2001-17) and were seen in ground testing using an optical stimulus (WFC3 ISR 2004-04).

When a point source is positioned in the lower right quadrant of the UVIS detector, out-of-focus reflections between the CCD and windows appear along a diagonal from the source towards the upper left, well removed from the source. These figure-eight shaped ghosts gradually move outside the field of view as the target moves out of the lower right corner. They contain a few percent of the flux of the target. Ghosts from a bright, saturated star are visible in the F606W exposure shown in Figure 6.13. Note that smaller window ghosts appear closer to the target; they are due to reflections between the window surfaces. In this case, the source from which the ghosts originate is so saturated that excessive charge has bloomed column-wise above and below the PSF (see Section 5.4.5 for a discussion of charge overflow due to saturation).

To prevent the worst effects of window ghosts, avoid placing very bright targets on the D quadrant. Also, pay attention to the location of key science targets if bright sources are in the lower right area of the field of view. The production of window ghosts has been modeled and an aid to observers has been produced to enable them to estimate the position of ghosts for a given field of view and ORIENT (WFC3 ISR 2011-16); this map is available as an XML overlay in APT (when viewing in Aladin, select "Window Ghosts" from the "Instrument Fields of Views (FoV)" menu). If ORIENTs are necessary, they must be requested in the Phase I proposal; the ORIENT special requirements can then be imposed within APT at the Phase II proposal preparation stage to control the positioning of bright sources on the detector. See Section 7.2.2 of the *Phase II Proposal Instruction*s, which gives detailed information on the relationship between detector coordinates, spacecraft coordinates, and ORIENT.

Figure 6.13: Figure-eight window ghosts in a UVIS F606W exposure from Program 14061 (ict201gzq_flt, display log stretched). Figure-8 ghosts are indicated by ovals, and are well-removed along a diagonal from the circled saturated stars in the lower right quadrant (amplifier quadrant D) that produced the ghosts. Colors indicate which ghosts were caused by which source.



ict201gzq_flt.fits
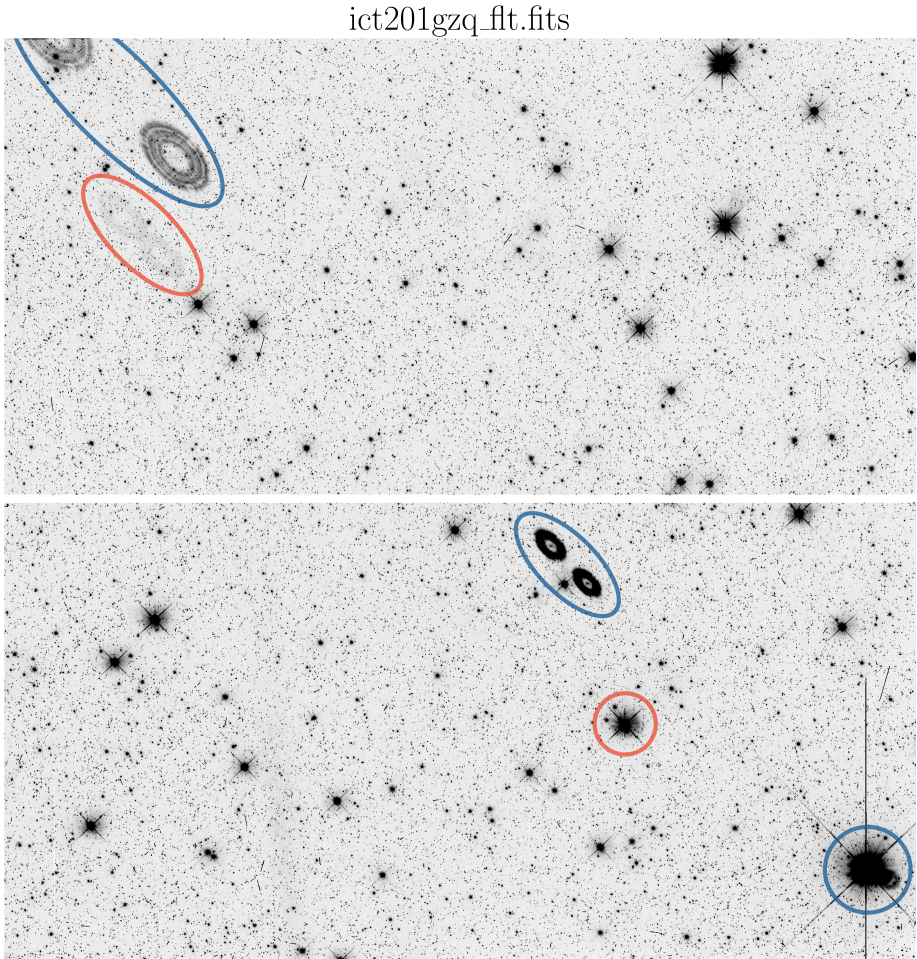
## Filter Ghosts

Filter ghosts for the WFC3 filters were specified to be less than 0.2%, and in most cases were measured during ground testing to be less than 0.1%. A few filters however, were found during testing to have ghosts that exceeded the specification. Some of these, the ones deemed highest priority, were remanufactured and installed in the SOFA (WFC3 ISR 2007-01). Consequently, there are a relatively small number of filters that exhibit filter ghosts at a level >0.2%. These are listed in Table 6.6. They have been retained in the flight instrument either because they were of lower scientific priority, or because the ghost level was deemed acceptable in light of the otherwise excellent performance characteristics of the filters (e.g., in- and out-of-band transmission, sharpness of bandpass edges). While some scientific programs (e.g., stellar photometry) may be unaffected by filter ghosts, others (e.g., observations of extended targets or faint objects adjacent to bright ones) could be adversely affected. In such cases, extra planning and/or data-analysis efforts may be needed, e.g., combining images taken at different dither positions and/or roll angles, or applying a deconvolution algorithm.

Table 6.6: Filters exceeding the filter ghost requirement, measured during ground testing of the integrated instrument (see WFC3 ISR 2007-09).

| Filter | Description | Ghost Level (% of total PSF flux) |
|--------|-------------|-----------------------------------|
| F200LP | Clear | 0.35[1] |
| F218W | ISM feature | 1.3 |
| F225W | UV wide | 0.4 |
| FQ232N | CII] 2326 | 7.0 |
| FQ243N | [Ne IV] 2425 | 5.0 |
| F280N | Mg II 2795/2802 | 0.6 |
| F300X | Extremely wide UV; grism reference | 0.3 |
| F656N | Hα 6562 | 0.4 |
| F658N | [N II] 6583 | 0.4 |
| F673N | [S II] 6717/6731 | 0.3 |
| F680N | $z$ (Hα + [NII]) | 0.3 |

[1] Laboratory measurement of stand-alone filter.

# 6.6 UVIS Optical Performance

Following the alignment of WFC3 to the OTA (WFC3 ISR 2009-45), a series of observations through a variety of filters were obtained to demonstrate the WFC3 optical performance (WFC3 ISR 2009-38). The WFC3 UVIS channel is meeting or exceeding all image quality specifications. Analysis of repeat observations in March 2010 and November 2011 has shown that the PSF has remained stable over time within a radius of 6 arcsec (WFC3 ISR 2013-13).

The following subsections summarize the measured flight optical performance for the UVIS channel, as described by its point-spread function (PSF), i.e., the spatial distribution of the flux in an image of a point source. The results shown are produced using an optical model which has been adjusted and correlated to the PSFs measured on-orbit and represent mean values averaged over the field. (See WFC3 ISR 2009-38.) This PSF model includes the pupil geometry, residual aberration, the mid-frequency wavefront error of the OTA, the effect of the detector charge diffusion, and first-order geometric distortion.

## 6.6.1 PSF Width and Sharpness

The PSFs over most of the UVIS wavelength range are well described by gaussian profiles (before pixelation). Two simple metrics of the size of the PSFs are the full width half maximum (FWHM) and the sharpness, defined as

$$S = \sum_{i,j}^{2} f_{i,j}$$

where $f_{ij}$ is the fraction of the flux from a point source in pixel $i, j$. Sharpness measures the reciprocal of the number of pixels that the PSF "occupies," and can be used to determine the number of pixels for optimal photometric extraction.

Table 6.7 lists the FWHM of the model PSF core (i.e., before pixelation) in units of pixel and arcsec and the sharpness parameter for 10 wavelengths. The sharpness range shown for each wavelength indicates the values for the PSF centered on the pixel corners and center. The degradation in image width and other performance measures in the near UV is due predominantly to the OTA mid-frequency, zonal polishing errors, which effectively move power from image core into progressively wider and stronger non-gaussian wings as wavelength decreases.

Table 6.7: WFC3/UVIS PSF FWHM (pre-pixelation, in units of pixels and arcseconds), and sharpness, vs. wavelength. Note that attempts to measure the FWHM by fitting functions to the pixelated PSF will generally give larger values.

| Wavelength (nm) | FWHM (pix) | FWHM (arcsec) | Sharpness |
|---|---|---|---|
| 200 | 2.069 | 0.083 | 0.040–0.041 |
| 300 | 1.870 | 0.075 | 0.051–0.056 |
| 400 | 1.738 | 0.070 | 0.055–0.061 |
| 500 | 1.675 | 0.067 | 0.055–0.061 |
| 600 | 1.681 | 0.067 | 0.053–0.058 |
| 700 | 1.746 | 0.070 | 0.050–0.053 |
| 800 | 1.844 | 0.074 | 0.047–0.048 |
| 900 | 1.960 | 0.078 | 0.042–0.043 |
| 1000 | 2.091 | 0.084 | 0.038–0.039 |
| 1100 | 2.236 | 0.089 | 0.034–0.035 |

Figure 6.14 plots the azimuthally-averaged model OTA+WFC3 PSF at four different UVIS wavelengths, indicating the fractional PSF flux per pixel at radii from 1 pixel to 4 arcsec.

**Figure 6.14:** Azimuthally averaged mean WFC3/UVIS PSF in F275W, F438W, F606W, and F814W.
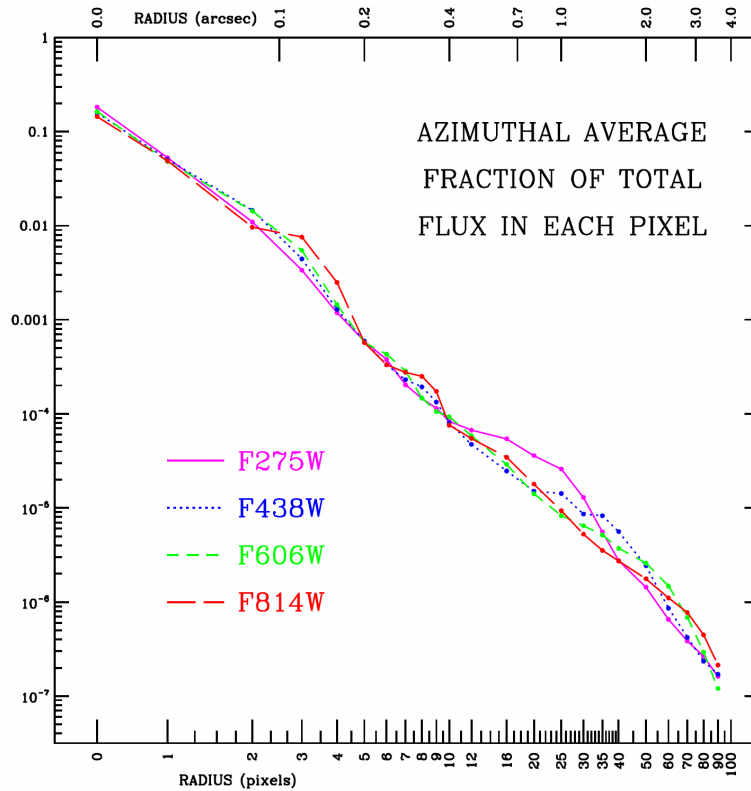


## 6.6.2 Encircled Energy

The **encircled energy** is the fraction of the total light from a point source that is contained within a circular aperture of a given radius. Figure 6.15 shows the model PSF encircled energy for 200, 400, and 800 nm. UVIS 1 empirical encircled energy fractions for 10 select aperture radii are given in Table 6.8 (see WFC3 ISR 2016-03 and WFC3 ISR 2022-02 for more details). The WFC3 UVIS Encircled Energy webpage provides the encircled energy curves for both CCDs at 51 total aperture radii as downloadable files.

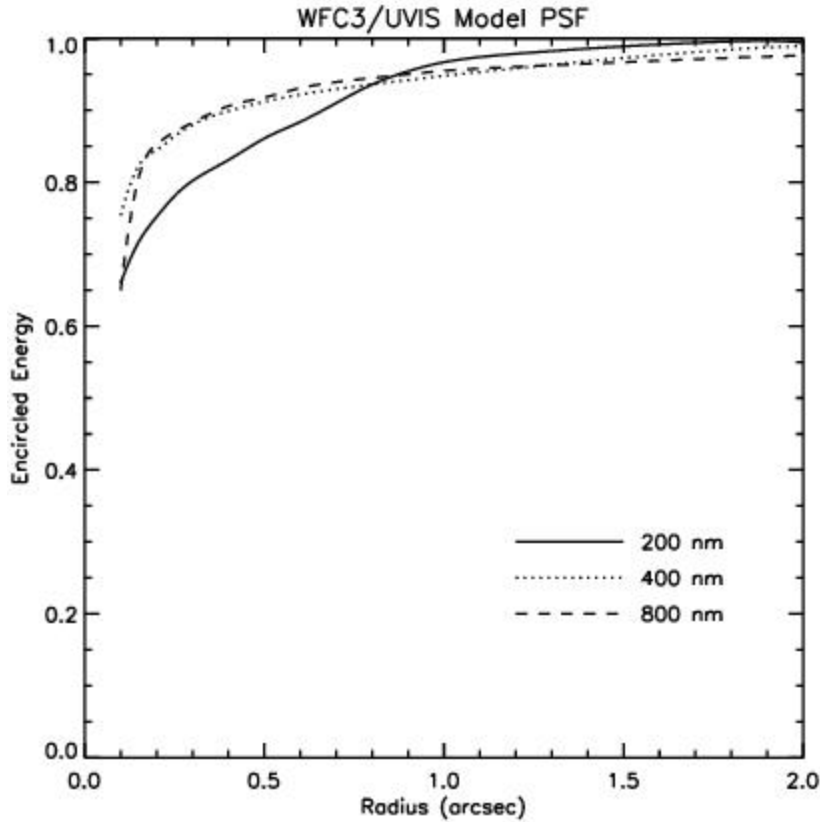Figure 6.15: Encircled energy for the WFC3/UVIS channel.



Table 6.8: WFC3/UVIS 1 encircled energy fractions by filter for selected aperture radii (arcsec). To access values for all 51 apertures, see the WFC3 UVIS Encircled Energy webpage.

| Filter | Wavelength (Å) | Aperture radius (arcsec) | | | | | | | | | |
|--------|----------------|-------|-------|-------|-------|-------|-------|-------|-------|-------|------|
| | | 0.04 | 0.12 | 0.20 | 0.28 | 0.40 | 0.59 | 0.79 | 0.99 | 1.98 | 6.00 |
| F218W | 2228.0 | 0.587 | 0.700 | 0.766 | 0.806 | 0.841 | 0.886 | 0.932 | 0.962 | 0.993 | 1 |
| F225W | 2372.1 | 0.603 | 0.716 | 0.780 | 0.818 | 0.851 | 0.891 | 0.931 | 0.958 | 0.993 | 1 |
| F275W | 2709.7 | 0.173 | 0.673 | 0.793 | 0.837 | 0.865 | 0.893 | 0.921 | 0.945 | 0.983 | 1 |
| F300X | 2820.5 | 0.250 | 0.713 | 0.813 | 0.850 | 0.874 | 0.900 | 0.926 | 0.951 | 0.992 | 1 |
| F280N | 2832.9 | 0.236 | 0.699 | 0.806 | 0.845 | 0.870 | 0.900 | 0.929 | 0.952 | 0.992 | 1 |
| F336W | 3354.5 | 0.203 | 0.666 | 0.816 | 0.863 | 0.890 | 0.911 | 0.929 | 0.946 | 0.991 | 1 |
| F343N | 3435.2 | 0.263 | 0.735 | 0.828 | 0.868 | 0.893 | 0.912 | 0.929 | 0.945 | 0.990 | 1 |
| F373N | 3730.2 | 0.286 | 0.751 | 0.836 | 0.876 | 0.900 | 0.919 | 0.932 | 0.946 | 0.989 | 1 |
| F390M | 3897.2 | 0.275 | 0.745 | 0.831 | 0.870 | 0.898 | 0.917 | 0.932 | 0.945 | 0.989 | 1 |
| F390W | 3923.7 | 0.265 | 0.740 | 0.833 | 0.873 | 0.900 | 0.919 | 0.933 | 0.946 | 0.989 | 1 |

| F395N | 3955.2 | 0.266 | 0.743 | 0.832 | 0.872 | 0.899 | 0.918 | 0.931 | 0.944 | 0.989 | 1 |
|-------|--------|-------|-------|-------|-------|-------|-------|-------|-------|-------|---|
| F410M | 4109.0 | 0.152 | 0.646 | 0.823 | 0.869 | 0.901 | 0.922 | 0.934 | 0.946 | 0.988 | 1 |
| F438W | 4326.2 | 0.265 | 0.746 | 0.838 | 0.878 | 0.906 | 0.926 | 0.937 | 0.948 | 0.987 | 1 |
| F467M | 4682.6 | 0.270 | 0.756 | 0.840 | 0.878 | 0.910 | 0.931 | 0.941 | 0.950 | 0.986 | 1 |
| F469N | 4688.1 | 0.267 | 0.747 | 0.835 | 0.874 | 0.906 | 0.928 | 0.939 | 0.949 | 0.986 | 1 |
| F475W | 4773.1 | 0.260 | 0.746 | 0.840 | 0.879 | 0.908 | 0.929 | 0.940 | 0.950 | 0.985 | 1 |
| F487N | 4871.4 | 0.158 | 0.650 | 0.831 | 0.876 | 0.908 | 0.930 | 0.942 | 0.950 | 0.985 | 1 |
| F475X | 4940.7 | 0.192 | 0.671 | 0.805 | 0.845 | 0.908 | 0.903 | 0.927 | 0.946 | 0.985 | 1 |
| F200LP | 4971.9 | 0.241 | 0.738 | 0.840 | 0.879 | 0.908 | 0.929 | 0.940 | 0.950 | 0.985 | 1 |
| F502N | 5009.6 | 0.278 | 0.760 | 0.845 | 0.882 | 0.912 | 0.933 | 0.944 | 0.951 | 0.984 | 1 |
| F555W | 5308.4 | 0.259 | 0.745 | 0.842 | 0.881 | 0.911 | 0.933 | 0.944 | 0.952 | 0.983 | 1 |
| F547M | 5447.5 | 0.248 | 0.745 | 0.842 | 0.880 | 0.911 | 0.934 | 0.946 | 0.953 | 0.982 | 1 |
| F350LP | 5873.9 | 0.237 | 0.725 | 0.834 | 0.873 | 0.904 | 0.926 | 0.939 | 0.949 | 0.980 | 1 |
| F606W | 5889.2 | 0.257 | 0.742 | 0.842 | 0.878 | 0.910 | 0.934 | 0.946 | 0.953 | 0.980 | 1 |
| F621M | 6218.9 | 0.266 | 0.747 | 0.845 | 0.881 | 0.910 | 0.936 | 0.948 | 0.955 | 0.979 | 1 |
| F625W | 6242.6 | 0.242 | 0.730 | 0.841 | 0.878 | 0.909 | 0.934 | 0.947 | 0.954 | 0.979 | 1 |
| F631N | 6304.3 | 0.271 | 0.743 | 0.842 | 0.877 | 0.906 | 0.933 | 0.946 | 0.954 | 0.979 | 1 |
| F645N | 6453.6 | 0.275 | 0.747 | 0.847 | 0.881 | 0.909 | 0.936 | 0.947 | 0.955 | 0.978 | 1 |
| F656N | 6561.4 | 0.271 | 0.740 | 0.844 | 0.877 | 0.908 | 0.935 | 0.948 | 0.957 | 0.978 | 1 |
| F657N | 6566.6 | 0.270 | 0.743 | 0.844 | 0.876 | 0.905 | 0.934 | 0.947 | 0.955 | 0.978 | 1 |
| F658N | 6584.0 | 0.271 | 0.734 | 0.839 | 0.873 | 0.903 | 0.930 | 0.945 | 0.954 | 0.978 | 1 |
| F665N | 6655.9 | 0.269 | 0.738 | 0.843 | 0.876 | 0.906 | 0.935 | 0.948 | 0.956 | 0.978 | 1 |
| F673N | 6765.9 | 0.150 | 0.634 | 0.825 | 0.870 | 0.903 | 0.931 | 0.943 | 0.953 | 0.977 | 1 |
| F689M | 6876.8 | 0.144 | 0.634 | 0.828 | 0.872 | 0.905 | 0.935 | 0.948 | 0.956 | 0.977 | 1 |
| F680N | 6877.6 | 0.260 | 0.729 | 0.843 | 0.874 | 0.905 | 0.933 | 0.947 | 0.954 | 0.977 | 1 |
| F600LP | 7468.1 | 0.238 | 0.716 | 0.842 | 0.874 | 0.906 | 0.933 | 0.947 | 0.955 | 0.976 | 1 |
| F763M | 7614.4 | 0.268 | 0.715 | 0.842 | 0.870 | 0.904 | 0.932 | 0.947 | 0.956 | 0.976 | 1 |
| F775W | 7651.4 | 0.261 | 0.708 | 0.842 | 0.870 | 0.904 | 0.932 | 0.945 | 0.954 | 0.976 | 1 |
| F814W | 8039.1 | 0.239 | 0.686 | 0.836 | 0.868 | 0.902 | 0.929 | 0.943 | 0.953 | 0.975 | 1 |
| F845M | 8439.1 | 0.239 | 0.686 | 0.836 | 0.868 | 0.902 | 0.929 | 0.943 | 0.953 | 0.975 | 1 |
| F850LP | 9176.1 | 0.239 | 0.686 | 0.836 | 0.868 | 0.902 | 0.929 | 0.943 | 0.953 | 0.975 | 1 |

| F953N | 9530.6 | 0.239 | 0.686 | 0.836 | 0.868 | 0.902 | 0.929 | 0.943 | 0.953 | 0.975 | 1 |

## 6.6.3 Other PSF Behavior and Characteristics

### Temporal Dependence of the PSF: *HST* Breathing

Short term variations in the focus of *HST* occur and affect all of the data obtained from all of the instruments on *HST*. A variety of terms, "OTA breathing", "*HST* breathing", "focus breathing", or simply "breathing" all refer to the same physical behavior. The focus changes are attributed to the contraction/expansion of the OTA due to thermal variations during an orbital period. Thermally-induced *HST* focus variations also depend on the thermal history of the telescope. For example, after a telescope slew, the telescope temperature variation exhibits the regular orbital component plus a component associated with the change in telescope attitude. The focus changes due to telescope attitude are complicated functions of Sun angle and telescope roll. More information and models can be found on the HST Focus and Pointing webpage.

For WFC3, breathing induces small temporal variations in the UVIS PSF (WFC3 ISR 2012-14). *The variations of the UVIS PSF FWHM due to breathing are expected to be as large as 8% at 200 nm, 3% at 400 nm and 0.3% at 800 nm, on typical time scales of one orbit.* Some variation over the field of the PSF response to breathing is also expected, since the detector surface is not perfectly matched to the focal surface, and the optical design includes some field-dependent aberration. This field dependence has been analyzed using observations of a globular cluster with filter F606W (WFC3 ISR 2013-11) and deep observations of an isolated star with filter F275W (WFC3 ISR 2013-13). PSFs near the A amplifier on UVIS1 are noticeably elongated by astigmatism. The variation in the asymmetry of PSFs as a function of focus near this amplifier is being explored as a means of measuring breathing and long term focus changes on the UVIS detector (WFC3 ISR 2015-08; WFC3 ISR 2018-14).

### Pixel Response Function

The point-spread function (PSF) is the distribution of light from a point source as spread over a number of pixels. Even with a very compact optical PSF, however, charge diffusion, or migration of charge from one pixel into adjacent neighbor pixels, can degrade the sharpness of a CCD PSF. The effect is usually described in terms of the pixel response function (PRF), which maps the response of the detector to light from a hypothetical very sharp PSF whose light all falls within an individual pixel. Observations using the integrated WFC3 instrument along with optical stimulus point-sources provided empirical PSFs for comparison with, and to provide constraints for, the models. Those models, which included an independent assessment of the low-order wavefront error, the pupil mask, and a reasonable estimate of the detector PRF, yield good agreement with the observed instrumental encircled-energy curves. The resulting best empirical fit to the pixel response convolution kernel is shown in Figure 6.16.

**Figure 6.16: CCD Pixel Response functions at 250 nm (left) and 800 nm (right).**

$$\begin{bmatrix} 0.023 & 0.105 & 0.023 \\ 0.105 & 0.488 & 0.105 \\ 0.023 & 0.105 & 0.023 \end{bmatrix} \begin{bmatrix} 0.007 & 0.071 & 0.007 \\ 0.071 & 0.688 & 0.071 \\ 0.007 & 0.071 & 0.007 \end{bmatrix}$$

## PSF Characteristics

The PSF of the UVIS channel was assessed during SMOV in 2009. As part of this assessment, exposures of a field containing unsaturated data (highlighting the bright PSF core) were combined with highly saturated data (emphasizing the faint PSF wings). The results are illustrated in Figure 6.17 , which shows the select portions of the composite image with a logarithmic stretch. No geometric distortion correction has been applied, so the images appear elongated along the diagonal, due to the 21 degree tilt of the detector to the chief ray. Although the target was chosen to be isolated, a number of field galaxies appear in the F625W image (right) but are absent in the F275W image; these galaxies are also seen in the IR channel images of the same target (Figure 7.6). Some detector artifacts, including warm pixels and imperfectly removed cosmic ray hits are evident.

**Figure 6.17:** High dynamic range composite UVIS star images through F275W (left) and F625W (right) subtending ~20 arcsec on each side at different locations in the field.
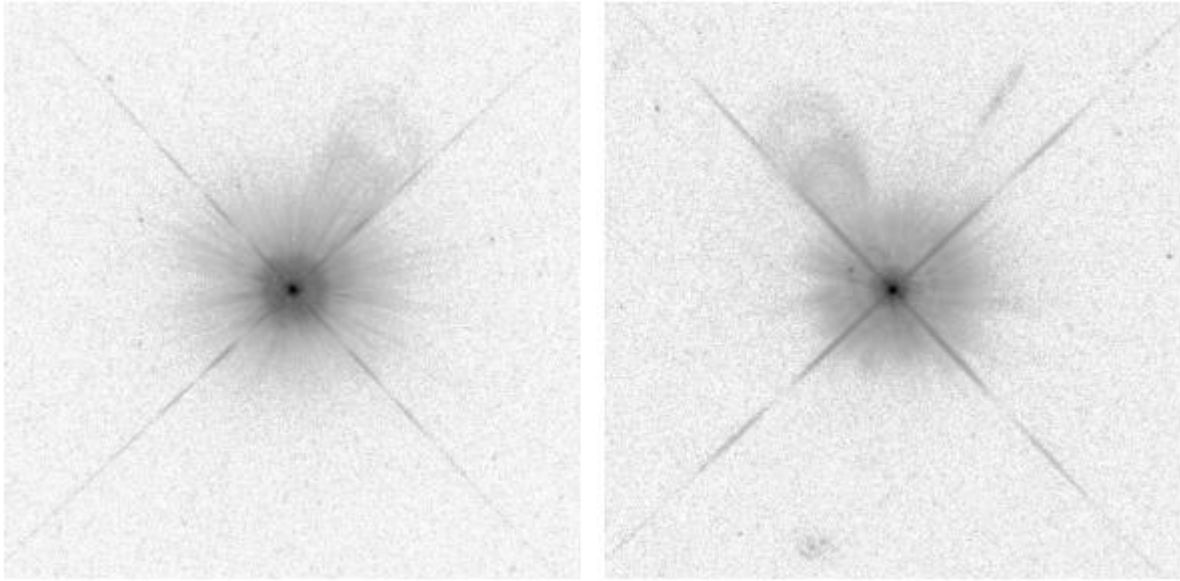


No distortion correction has been applied. Stretch is logarithmic from 1 to $10^6$ e⁻/pixel. (See text for description of "ghost" artifacts.)

Two different types of "ghost" artifacts are visible in the images. As expected from the UVIS channel design, there are low-level ghosts due to reflections between the four surfaces of the two anti-reflection-coated detector windows: these are the sets of relatively large diameter, ring-shaped ghosts seen extending out at PA ~330° (left panel) and PA ~30° (right panel) for N up and E to the right. Ghosts due to reflections from the CCD to the windows, as discussed in Section 6.5.3, fall further from the PSF, along the diagonal from lower right to upper left of the field of view, and are not visible in these frames which image only subsections of the WFC3 field of view.

Also evident is a filter ghost, due to reflections between the surfaces of the F625W filter (right). In multi-substrate filters (a stack of two or more substrates bonded or laminated together with a layer of optical adhesive) filter ghosts appear as faint, point-like features, such as the ghost at PA ~65 degrees, radius 1.6 arcsec, in the F625W image, which contains much less than 0.1% of the stellar flux. In single-substrate or air-gap filters (the latter consisting of two substrates joined via thin spacers), filter ghosts appear as small extended shapes (typically rings), closer to the PSF centers than the window ghosts. For the F275W image in Figure 6.13 the filter ghost level is <0.1% and is not obvious. A small number of filters exhibit brighter ghosts and are discussed in detail in Section 6.5.3 and are tabulated in Table 6.6.

A searchable database of over 30 million WFC3 PSFs is publicly available through MAST (WFC3 ISR 2021-12). For more details, see the WFC3 PSF Search webpage.

## 6.6.4 Super-sampled PSF Models

The PSF that we see exhibited in the image pixels is the combination of many factors: the telescope optics, the filter throughput, integration over the pixel-response function, etc. It is extremely hard to model all of these individual effects accurately, but fortunately that is not necessary. Anderson & King (2000 PASP 112 1360) showed that it is sufficient to model the net PSF, which they call the "effective" PSF. Their initial model was constructed for WFPC2, but since then accurate models have been constructed for a variety of *HST* instruments and filters.

Their model for the PSF is purely empirical and based on the fundamental question to answer: if a star is centered at location (x,y) on a detector, what fraction of its light will be recorded by pixel [i,j]? The "effective" PSF thus specifies what fraction of a star's light will land in a pixel that is offset by (delta x, delta y) from the center of the star. As such, the effective PSF is simply a two-dimensional function Psi (delta x, delta y) that returns a number between 0.0 and 1.0.

It makes sense that this "effective" PSF function must be smooth and continuous, since moving a star around the detector would result in a continuous variation of recorded flux in each pixel. That said, if the detector is under-sampled, then the "effective" PSF can have sharp variations.

The basis for the PSF model is a simple tabulation of the value of the effective PSF at an array of (delta x, delta y) offsets. This array is spaced by 0.25 flt image pixels, so that it can represent all the structure in WFC3's under-sampled pixels. The PSF model thus consists of an array of 101 x 101 grid points that describe the behavior of the PSF out to a radius of 12.5 pixels. Beyond this distance, unsaturated stars have no measurable flux. The PSFs are normalized to have a total flux of 1.0 within 10.0 pixels for WFC3/UVIS and within 5.5 pixels for WFC3/IR. Bi-cubic spline interpolation is adequate to interpolate the table to locations between the grid points.

The PSF also changes with location on the detector, so the models provide the PSF at an array of fiducial locations across the detectors. Simple bi-linear interpolation is adequate to provide a complete 101 x 101 PSF model at any given location on the detector. The PSF is thus a four-dimensional function: Psi (delta x, delta y; x, y).

Figure 6.18 shows the array of fiducial points where the WFC3/UVIS PSF is provided. On the left is a schematic of the detector and on the right the central value of the PSF, which represents the fraction of light from a point source that would land in a pixel if the star is exactly centered on that pixel. The fraction goes from about 16 percent in the upper left corner to over 22 percent in the region of strong fringing in red narrow-band filters (WFC3 ISR 2010-04) in the lower right-middle of the bottom chip.
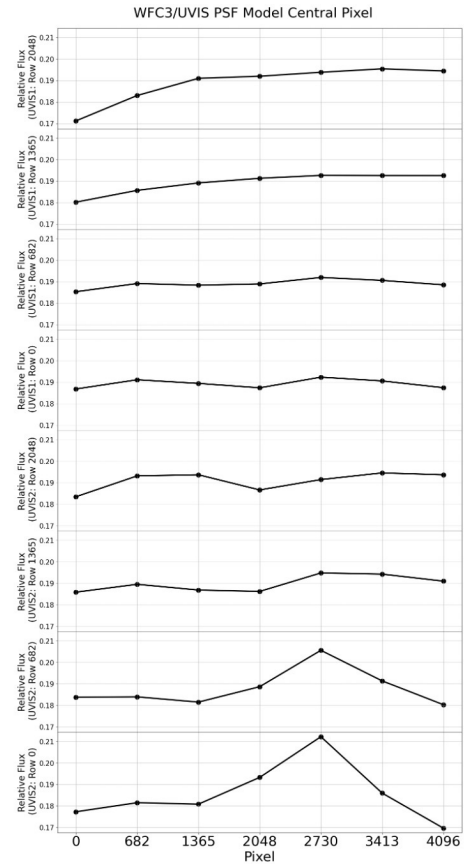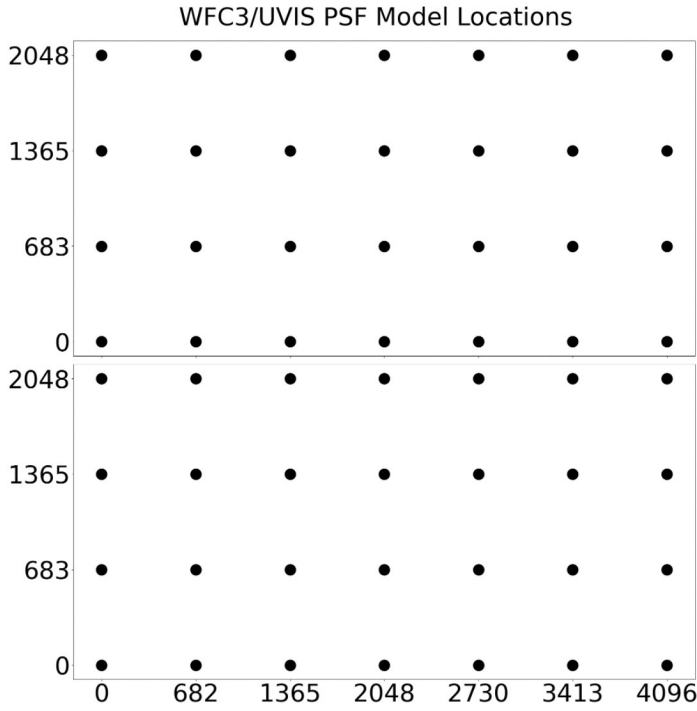
Figure 6.19 shows the full 2-dimensional spatial variation of the PSF. For each of the 7 × 8 fiducial PSFs, we show the difference between that super-sampled PSF and the average PSF, where black indicates more flux. It is clear that PSF varies across the detector in complicated ways.

**Figure 6.19:** Difference between the super-sampled PSF at the locations shown in Figure 6.14 and the average of these PSFs. Black indicates greater than average flux.
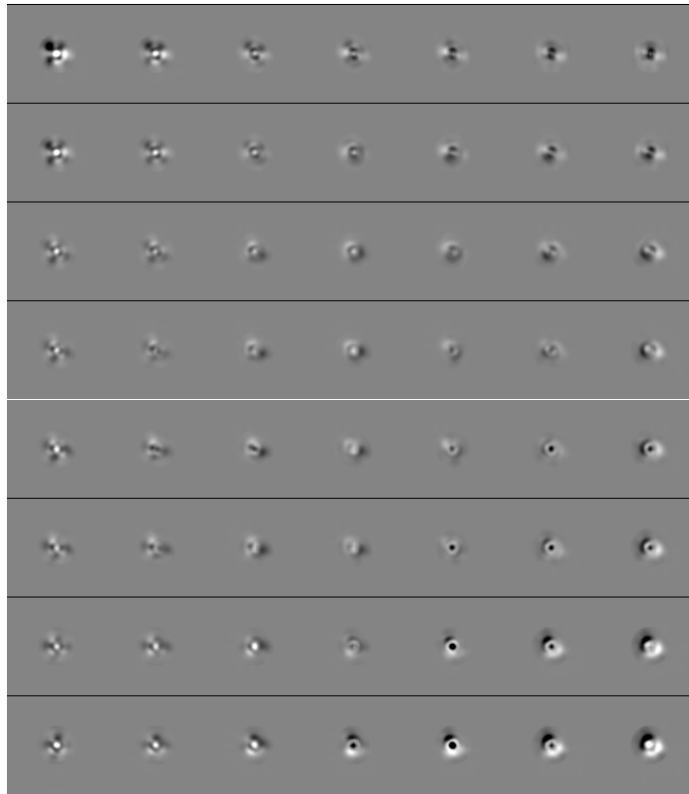


As discussed in the previous section (6.6.3), *HST*'s PSF is known to change with time due to "breathing", changes in the focal length caused by variations in the telescope's thermal environment (going into and out of the Earth's shadow, changes in orientation relative to the Sun, etc). The wealth of images in the archive provide samples of the PSF through various filters at a variety of focus levels. In WFC3 ISR 2018-14, Anderson cross-examined star images from the archival to trace out the focus locus for the PSF for the five of the most used filters (F275W, F336W, F438W, F606W, and F814W) and developed a set of "focus-diverse" PSF models. These models can be used to determine the focus of an image empirically, by determining which focus-level best matches the image of a star, and once the focus of an exposure is determined, the models can provide an accurate model of the PSF for that exposure.

Note that the above PSF discussion applies only for un-resampled "flt"-type images, since these are the images where each pixel can be a direct physical constraint on the scene. The "drz"-type images have been resampled, such that each pixel represents some combination of input pixels from one or multiple exposures. Such images are not well suited to high-precision PSF analysis. There are several challenges, however, in working in the "flt" frame. The first is that the images are generally under-sampled, such that each exposure is not a full representation of the astronomical scene. One generally must combine several dithered "flt"-type images to fully constrain the scene delivered to the telescope. The second challenge is that the "flt" images are severely distorted, and it is non-trivial to collect these constraints on the scene and analyze them together. For these reasons, even if a user does have access to a perfectly accurate PSF for a given exposure, it still requires considerable expertise to use it for analysis.

The instrument team, being aware of these challenges, has been working to provide PSF-related tools for users. Spatially variable, super-sampled models of the PSF can be found on the WFC3 PSF webpage, which contains additional resources relating to PSFs. Recently, a software routine that makes use of the PSFs to measure stars in HST images was released. This routine is named `hst1pass`, and WFC3 ISR 2022-05 describes how it can be downloaded and run. In 2024 the team added a Jupyter notebook for generating PSF models, also found on the PSF page.

In an effort to supplement these super-sampled model PSFs, the WFC3 team recently has built a searchable database of over 30 million WFC3 star images (PSFs extracted from science images) from 2009 to 2023. The PSF image library can also be searched using a team-developed Jupyter notebook (see WFC3 ISR 2021-12 and the WFC3 PSF Search webpage for more details). These images of PSFs can then be employed to generate PSFs that for users' observations and other science needs.

# 6.7 UVIS Exposure and Readout

## 6.7.1 Exposure Time

Exposure times in the UVIS channel are controlled by a rotating mechanical shutter blade (see Section 2.3.3). The time per UVIS exposure must be between 0.5 s and 3600 s, excluding 0.6 s, in steps of 0.1 s.[1] Early on-orbit observations revealed a slight, repeatable offset between the commanded and actual times for the two shortest exposures (0.5 s is 0.48 s and 0.7 s is 0.695 s); the data processing pipeline populates the EXPTIME header keyword with the actual exposure times. The repeatability of the shutter has been shown to be well within the contractual specifications of 10 ms r. m.s. (WFC3 ISR 2023-04). That analysis, based on short G280 exposures of a very bright star, allowed for substantially more precise measure of the repeatability than earlier measurements based on internal flat fields. In particular, the repeatablity of 0.5s, 0.7s, and > 0.99s exposures have been shown to be ~10x, ~2x, and ~4x better, respectively, than required by the specification. A Gaussian fit to the measured repeatability of 1, 2, and 4s exposures yields an r.m.s. of 2.43 ms +/-0.32 ms. Observers performing precise non-differential photometry using short exposures should note that although well within operational specifications, the shutter repeatability in 1-s exposures contributes ~0.24% photometric error (WFC3 ISR 2023-04). In addition, note that the point spread function can be affected by shutter-induced vibration in short (< 5s) exposures; see Section 6.10.4.

The shutter uniformity requirement specifies that any differences in exposure time across the field of view must be < 0.01 s. Comparisons of long (30 s) and short (0.5 s) exposures taken during instrument-level ground tests have shown that the shutter provides a uniform exposure time across the field of view to ~0.004 s, easily meeting the requirement. In on-orbit internal tungsten lamp exposures, the exposure time across the field was found to vary by less than 0.0009 sec (WFC3 ISR 2009-25). Based on tungsten lamp exposures and observations of a standard star made from Oct. 2014 to Aug. 2015, no noticeable change in on-orbit shutter performance since launch was detected ( WFC3 ISR 2015-12).

To allow for cosmic-ray removal during post-observation data processing, UVIS exposures can be split into multiple exposures. The preferred method of removing cosmic rays is to combine dithered exposures (see Section 6.11.1). As a result, the default value of CR-SPLIT in APT (to take undithered images) was changed from 2 to NO in 2010 (Cycle 18). In the rare case undithered observations are required, setting CR-SPLIT to a value will divide the specified exposure time by the requested number of subexposures, with the subexposure times rounded down to the nearest multiple of 0.1 s. At the end of this process, if the resulting subexposure times are not legal values, the APT proposal software adjusts them so that they are allowed and reports those changes to the observer.

## 6.7.2 ACCUM Mode

"**ACCUM**" is the only observing mode for the UVIS channel. In ACCUM mode, the shutter is opened and photons strike the CCDs and generate charge, which is accumulated until the shutter is closed at the end of the requested exposure time and the charge is read out. During the readout, the analog-to-digital (A-to-D) converter translates the charge into data numbers (DN) via the gain setting. There are four possible gain settings (1.0, 1.5, 2.0, and 4.0 e⁻/DN) in principle; however, the only setting offered to observers is the default value of 1.5 e⁻/DN, which provides an absolute gain of ~1.55 e⁻/DN (Table 5.1).

A full detector readout of both UVIS chips takes 96 s. The image contains all the exposed pixels from each CCD (2 times 2051 × 4096), as well as a variety of overscan pixels, described in more detail later in this section. Shorter readout times are possible by using smaller subarray readout sizes, as discussed in more detail in Section 6.4.4.

Each of the two CCD chips contains two on-chip amplifiers used for reading out. The fastest—and default—way to read out the entire detector, at full spatial resolution, is to use all four amplifiers simultaneously. Other full-detector readout modes are possible but take more time and involve more charge transfer shifts which will degrade the CTE. For example, two amplifier full frame readout takes more than twice as long as a four-amplifier readout (~193 s vs. 96 s). Non-default readout modes are not offered to General Observers.

Subarray frames, unlike full detector frames, are always read out by a single amplifier (the closest amplifier to the subarray center).

### Overscan Regions

The UVIS CCD detectors each have 4096 × 2051 pixels that are exposed to light. In addition, both chips have 25 extra columns at both ends that are not exposed to light; these 25 columns are *physical* overscan pixels. Moreover, during readout of the chips, extra pixels can be clocked in order to create *virtual* overscan pixels.

The location of the overscan regions in a raw image varies, depending upon the type of readout that is performed. The overscan regions are used to monitor the instrument, and are needed to measure the bias level. The bias level is subtracted from the raw image, normally through the BLEVCORR step in the WFC3 calibration pipeline (see the *WFC3 Data Handbook*).

Figure 6.20 shows the format of a raw image obtained with full-chip unbinned four-amplifier readout; dimensions are also tabulated in Table 6.9. The raw image has 25 columns of physical overscan pixels and two areas of virtual overscan: 60 columns of serial overscan in the center of each row and 38 rows (19 per chip) of parallel overscan next to the inter-chip gap. The serial physical overscan pixels are also known as the serial prescan, or leading-edge, overscan; the serial virtual overscan pixels are also called the trailing-edge pixels.

# Figure 6.20: Format of a Raw Full-Chip WFC3/UVIS image.
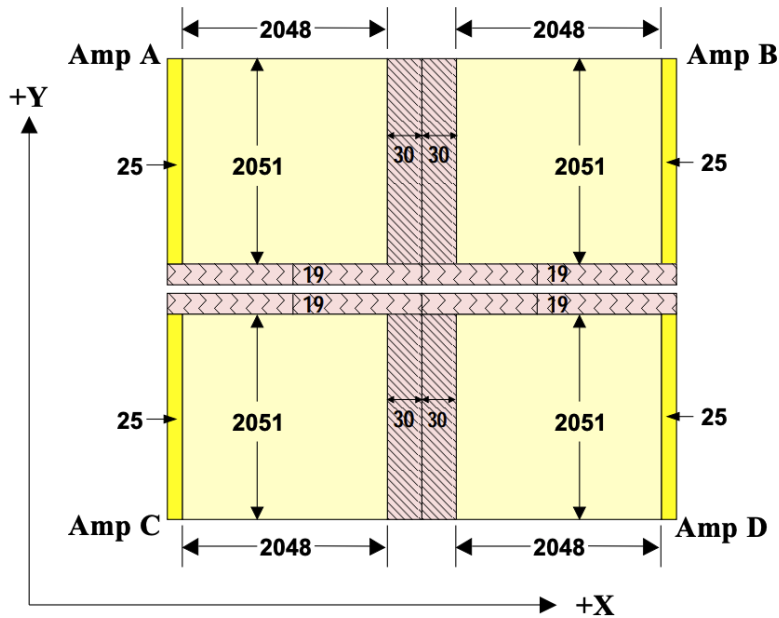


As Figure 6.20 illustrates, a raw image resulting from a default full-frame, four-amplifier readout of the UVIS channel contains 110 columns of serial overscan (25 × 2 physical and 30 × 2 virtual) plus 38 rows of parallel virtual overscan, which combined with the 4096 × 2051 science pixels, result in a raw image size of 4206 × 4140 pixels. Other types of readouts have differing amounts and/or locations of overscan. Subarrays contain no virtual overscan of either type (serial or parallel), although they can contain physical overscan if a subarray is chosen that overlaps the physical overscan region. Subarrays containing physical overscan data are listed in Table 6.1. In general, it is desirable to include some physical overscan in observations using subarrays for accurate bias level subtraction.

Exposures taken with on-chip binning are complicated by the need to truncate "odd" pixels and to treat each half of the chip's row separately. Also, due to the odd number of some overscan pixels, the boundary between the data and overscan pixels of a binned exposure can contain binned pixels resulting from a combination of both data and overscan pixels. A 2 × 2 binned frame readout, for example, contains 2102 columns × 2070 rows. That is, each binned chip readout contains 2102 columns (12 physical overscan + 1 combined data/overscan + 1023 columns of data + 1 combined data/virtual overscan column + 14 virtual overscan pixels for each of the two amps in a chip), and each binned chip readout has 1035 rows (9 binned virtual overscan + 1 combined data/virtual parallel overscan + 1025 data). A 3 × 3 binned image contains 1402 × 1380 pixels (8 overscan + 1 combined overscan/data + 682 data + 10 overscan columns in each amplifier of each chip and 6 overscan + 1 combined overscan/data + 683 data rows in each chip). These values, as well as the dimensions for unbinned full-frame exposures, are also presented in Table 6.9.

Table 6.9: Dimensions of unbinned (1 × 1) and binned (2 × 2 and 3 × 3) WFC3/UVIS exposures. Full readout size is given, and the number of columns and rows by type (science, overscan, etc.) are listed.

| | | Columns | | | | | Row |
|---|---|---|---|---|---|---|---|
| Binning | Readout Size | Science | Serial physical overscan | Mixed (data/serial physical overscan) | Serial virtual overscan | Mixed (data/serial virtual overscan) | Science | Parall virtua oversc |
| 1 × 1 | 4206 × 4140 | 4096 | 50 (25 per amp) | | 60 (30 per amp) | | 4102 (2051 per chip) | 38 (19 per chip |
| 2 × 2 | 2102 × 2070 | 2046 | 24 (12 per amp) | 2 (1 per amp) | 28 (14 per amp) | 2 (1 per amp) | 2050 (1025 per chip) | 18 (9 p chip) |
| 3 × 3 | 1402 × 1380 | 1364 | 16 (8 per amp) | 2 (1 per amp) | 20 (10 per amp) | | 1366 (683 per chip) | 12 (6 p chip) |

For completeness, we mention here that WFC3 can also be commanded to take EPER (extended pixel edge response) readouts. This capability is intended for calibration/engineering purposes only. The EPER images are a way to measure and monitor charge transfer inefficiency (CTI) effects using internal images, rather than external, pointed observations that would take *HST* observing time away from science observations. The EPER frame starts with an internal tungsten lamp flat field; any CTI present causes a fraction of charge from that flat field to be captured temporarily in traps. As the frame is read out, the trapped charge escapes and can appear in the overscan regions as an exponential tail of deferred charge. The EPER readout includes significantly larger areas of overscan so that the full extent of the exponential tail can be measured, ideally down to where it becomes indistinguishable from the nominal noise level of the detector. That is, the EPER image allows direct measurement of the charge losses during the readout since nearly all the lost electrons are expected to appear in the exponential tail. WFC3 ISR 2020-06 summarizes the EPER results based on 2009-2020 data.

[1] Under normal shutter operations, the 0.5 s exposure would not provide a sufficiently uniform exposure level. Thus, the shutter operation for 0.5 s has been implemented through a special "continuous sweep" operation, where the shutter disk moves smoothly through 180°, from one closed position to the next, thus meeting the uniformity requirement. All exposures longer than 0.5 s are obtained via pairs of closed-to-open and open-to-closed commands.

# 6.8 UVIS Sensitivity

## 6.8.1 Limiting Magnitudes

Table 6.10 presents the predicted limiting-magnitude performance of WFC3. The calculations are based on optimal extraction of a point source. The limiting ABMAG at an SNR of 10 was calculated for a 1-hour and a 10-hour exposure.

Table 6.10: Limiting-magnitude performance of WFC3 based on on-orbit sensitivity from SMOV4. The table provides limiting ABMAGs at an SNR of 10 for the indicated WFC3 filters.

| Band | Filter | Limiting magnitude in 1 hr | Limiting magnitude in 10 hrs |
|------|--------|----------------------------|------------------------------|
|      | WFC3   | WFC3                       | WFC3                         |
| NUV  | F225W  | 26.7                       | 28.1                         |
| U    | F336W  | 27.3                       | 28.7                         |
| B    | F438W  | 27.3                       | 28.7                         |
| V    | F606W  | 27.9                       | 29.2                         |
| I    | F814W  | 27.1                       | 28.4                         |

Chapter 9 gives further details on estimation of exposure times. Current estimates require use of the WFC3 Exposure Time Calculator (ETC), available online.

## 6.8.2 Sensitivity

The two WFC3/UVIS CCDs have very different quantum efficiencies in the UV, where UVIS2 is nearly 30% more sensitive at ~2200 Å. At wavelengths longer than ~4500 Å, the sensitivity of the two chips is within about ~1%, as shown in Figure 5.2. An independent photometric calibration is applied for the two UVIS CCDs, and temporal changes in the inverse sensitivity are accounted for in the latest UVIS photometric calibration (WFC3 ISR 2021-04; WFC3 ISR 2022-02). These new solutions correct the image header 'inverse sensitivity' keyword (PHOTFLAM) to account for changes of ~ 0.1 - 0.2% per year according to filter. Figure 6.21 shows an example of the time-dependent behavior of UVIS photometry over about 12 years, in this case for UVIS2 and the F814W filter. It also demonstrates the improved repeatability in observations acquired with spatial scans compared with that of staring mode observations.

The updated UVIS solutions improve the chip-sensitivity ratio (PHTRATIO) in FLT/FLC data by up to 1%, in agreement with early dithered star cluster and standard white dwarf observations. Accounting for the time-dependence also improves the encircled energy (EE) correction by ~ 1% in the ultraviolet filters and by ~ 0.5% at wavelengths larger than 7500 Å, in close agreement with the 2009 EE values. The updated calibration makes use of improvements in the HST CALSPEC models as well as an increase in the Vega reference flux.

For the latest information about the UVIS photometric calibration and the inverse sensitivity tables, users may visit the WFC3 Photometry webpage. The accuracy of the inverse sensitivity values is ~ 2% on average, with ~ 5-10% errors for narrowband filters. Additional discussion is provided in the Section 9.1 of the WFC3 Data Handbook.

**Figure 6.21: UVIS Photometry in F814W**
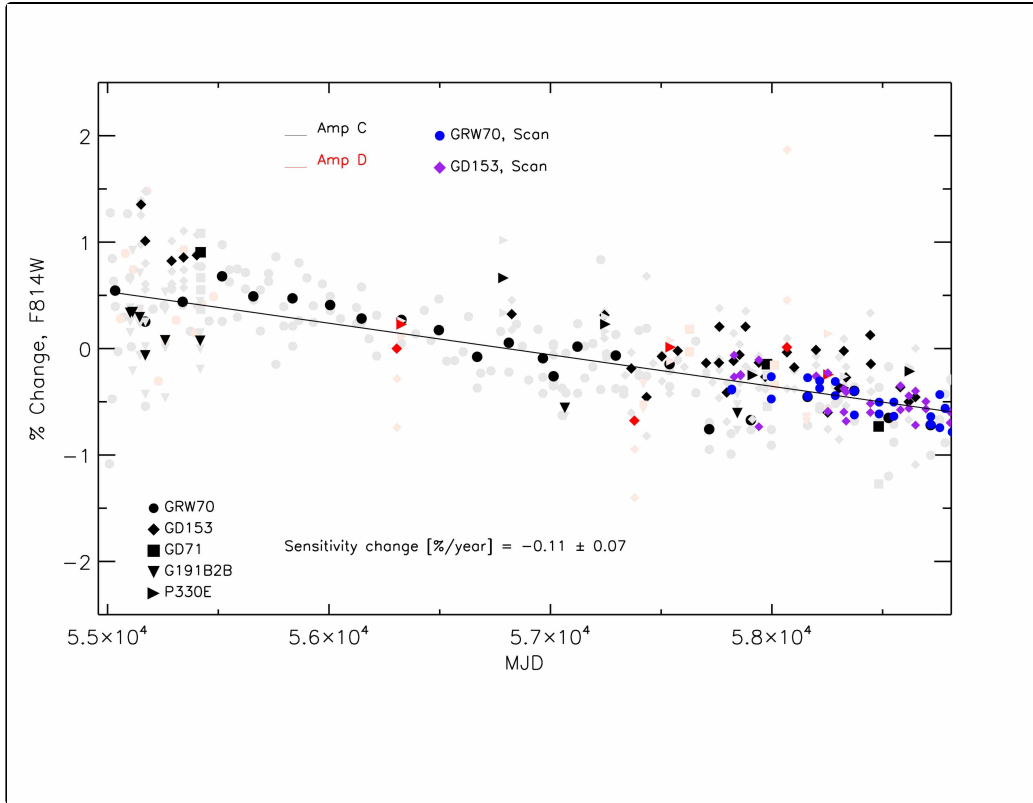


Percent change in the F814W observed count rates versus observation date (in MJD) for photometry of five CALSPEC standards measured in a 10-pixel radius aperture. Monitoring observations of four white dwarfs GRW+70d5824 (filled circle), GD153(diamond), GD71 (square), G191B2B (triangle), and the G-type star P330E (horizontal triangle) are shown for two UVIS2 subarrays, where black points indicate drizzled (drc) photometry for amp C and red points for amp D. For comparison, photometry in the corresponding single calibrated (flc) images is shown in grey. Photometry based on scanned data is overplotted for GRW+70d5824 (blue) and GD153 (purple). The solid line shows the fit to the photometry for all five standards, for both staring and scanned images, and indicates a loss in sensitivity of 0.11% per year +/- 0.07% in this filter.

# 6.9 Charge Transfer Efficiency

The charge transfer efficiency (CTE) of the UVIS detector has been steadily declining since its installation in 2009 on board HST. Faint sources in particular can suffer large flux losses or even be lost entirely if observations are not planned carefully. In this section, we describe the effect of CTE losses on data, observational strategies for minimizing losses, and data analysis techniques that can provide some correction for CTE losses.

> ✅ *For the latest information about CTE on the UVIS detector, see the WFC3 CTE webpage.*

## 6.9.1 Overview

The regular flux of energetic protons and electrons that *HST* encounters in its frequent passages through the South Atlantic Anomaly results in progressive damage to the silicon lattice of its CCD detectors. This damage manifests itself as an increase in the number of hot pixels, an increase in the overall dark current, and an increase in the population of charge traps.

The effect of hot pixels, about 1000 new/day/chip using a threshold of 54e⁻/hr/pix, is addressed with anneal procedures, dark calibration files, and dithering. The anneal procedures, which are performed monthly, warm the detectors to +20° C and restore some of the hot pixels to their nominal levels. Dark calibration files (running averages of daily dark images) can provide reasonable identification of hot pixels as well as a calibration for overall dark current (see Section 5.4.8). The calibration darks allow stable hot pixels and dark current to be subtracted from science images in the calibration pipeline. Since not all hot pixels are stable, the corrections are imperfect, but dithering can help reduce any residual impact of hot pixels in final image stacks.

The effect of charge traps is more difficult to address, as the damage to the detector is cumulative and appears irreversible. The traps prevent photo-electrons from moving perfectly from pixel to pixel during readout. This causes a loss in flux from sources, as well as a systematic shift in the source centroid as some of its charge is trapped and then slowly released during the readout process. The majority of the trapped charge is released within a half-dozen pixel shifts, as can be readily seen in the visible charge trails that follow hot pixels, cosmic rays, and bright stars. A low percentage of the initial signal can be seen extending out to ~50 pixels in length (see Figure 6.22).

## Figure 6.22: Residual Charge in Pixels Trailing Hot Pixels
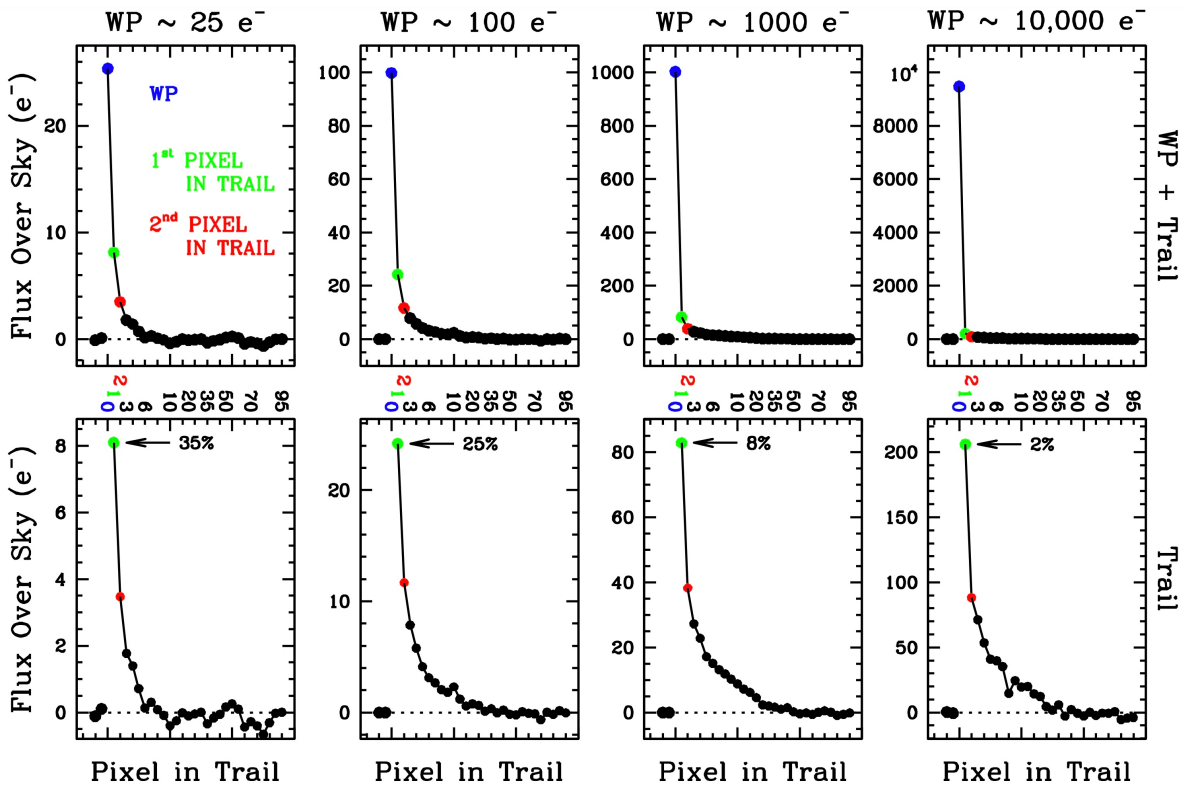


Observed charge trailing far from readout in WFC3/UVIS images with the recommended 20 e-background behind warm/hot pixels (WP) with observed intensities of 20, 100, 1000, and 10,000 electrons in January 2023. These plots give a sense of CTE losses for charge packets of various sizes. The top plot shows the entire range of WP+trail, and the bottom plot zooms in on the trail. The WP on the left started with around 40 e- and by the time of readout, the result is a 25 e- WP and 15 e- in the trail.

CTE flux losses at any given time depend on a variety of factors, including:

1. The number of rows between source and readout amplifier: sources farther from the amplifiers (i.e., those closer to the chip gaps) require more parallel transfers before they are read out and thus encounter more traps.
2. The intrinsic brightness of the source: fainter sources lose proportionally more charge than brighter sources. Very bright sources (those with $> 10^4$ electrons) suffer relatively small amounts of CTE loss (a few percent) (see Figure 6.20).
3. The image background: a higher background keeps many of the charge traps filled, thereby minimizing flux losses during readout of the source signal. WFC3/UVIS images can have very low intrinsic backgrounds due to the low detector readnoise and dark current as well as the small pixels of its CCDs, which intercept less sky. Furthermore, the WFC3 UV and narrowband filters have exceptionally low sky backgrounds. It is when backgrounds are low that CTE losses can become pathological.
4. Source size: because of the finite size of the telescope and its optics, point sources do not appear as delta functions on the detector, but rather as point-spread functions with a distribution of pixels above the background. The downstream pixels of a source can shield its upstream pixels from CTE loss by filling some of the charge traps. Resolved objects experience even more self-shielding.

For all these reasons, the impact of imperfect CTE for a particular object will depend on the location and morphology of the source and on the distribution of electrons in the field of view (from sources, background, cosmic rays, and hot pixels). The magnitude of the CTE loss increases continuously as new charge traps form over time. WFC3 ISR 2021-09 provides an overview of our overall current understanding of CTE in WFC3/UVIS, while WFC3 ISR 2024-04 presents updated coefficients for the empirical model for PSF photometry. The CTE website provides an up-to-date list of tools, tips, and insights.

The remainder of this section will discuss the available options for mitigating the impact of CTE losses and their associated costs. Broadly, the options fall into two categories: strategies to implement before data acquisition (i.e., optimizing the observations during the proposal and planning stage, including the use of post-flash if needed), and corrections applied during image analysis after the images have been acquired (i.e., formula- or table-based corrections or pixel-based image reconstruction).

## 6.9.2 CTE-Loss Mitigation Before Data Acquisition: Observation Planning

**1) Consider the placement of the target within the field of view**. When the target is small, it can be placed close to a readout amplifier. This reduces the number of parallel transfers during readout, thereby minimizing CTE losses for the target. This can be done by using a subarray aperture (see Figure 6.2); e.g., aperture UVIS2-C1K1C-SUB or UVIS2-C512C-SUB (see Table 6.1) which place the target 512 and 256 pixels, respectively, from the edges of the UVIS detector near amplifier C and read out 1025x1024 and 513x512 science pixels, respectively. (Apertures UVIS2-M1K1C-SUB and UVIS2-M512C-SUB, which place the target closer to the center of the detector, are not suitable for this purpose.) One advantage of subarrays is that many short exposures fit within a single orbit, since only a small portion of the full field of view of the detector is read out and stored.

Alternatively, one can place the target at the reference position of aperture UVIS2-C1K1C-SUB or UVIS2-C512C-SUB, *but read out the entire detector instead of only a subarray* (aperture names UVIS2-C1K1C-CTE and UVIS2-C512C-CTE, respectively). Full frames can be taken efficiently when the exposures are 348 sec or longer (see Section 10.3.1).  Even when a small target is placed near the readout at the bottom of the detector, a full-frame exposure provides more context and enriches the archival value of the exposure.  POS-TARGs can also be used to move the target to the lower part of the C quadrant (e.g., negative POS-TARG X and negative POS-TARG Y) to reduce CTE losses even further (See Section 6.4.4 for reasons to prefer quadrant C over the other quadrants).

Another approach, suitable for moderately populated fields involves obtaining observations at multiple spacecraft roll angles.  In this case, the different roll angles (ideally at or near 90 degrees) will result in sources having large variations in the number of pixels over which they must be transferred during readout. This permits a direct assessment of the reliability of the available CTE-correction calibrations that can be applied during post-processing (discussed in more detail below in Section 6.9.3).

If observations are being taken on a field larger than the instantaneous field of view of the cameras, then stepping in the Y direction (i.e., along the CCD columns) with some degree of overlap will place some sources at both small and large distances from the transfer register, thus permitting a direct assessment of the reliability of the CTE corrections applied during data processing (see section on formula/table-based corrections below in Section 6.9.3).

**2) Increase the image background.** This can be done by lengthening exposure times, using a broader filter, and/or applying an internal background (post-flash). Dividing observations into fewer, but longer, exposures has several benefits. It provides more natural sky background (thus requiring less post-flash and thereby less added noise), it increases the source signal relative to the readnoise and any added post-flash, and it saves on overheads (each full-frame requires ~90 sec to read out). Ensuring that images with faint sources contain a minimum of 20 e⁻/pix total background (dark+sky+post-flash, if needed) is a crucial CTE mitigation strategy for many WFC3/UVIS science proposals in 2020 and beyond (see WFC3 ISR 2020-08). It is worth noting that even higher backgrounds provide more CTE protection; however, more background also produces more noise, so a balance must be struck between preserved signal and added noise. The curves in WFC3 ISR 2021-13 can help with this determination.

On-orbit experimentation has shown that CTE losses are a non-linear function of both the source and image background signals. A faint source in a low-background image will lose a significantly larger proportion of its signal than a similar source in a high-background image. In some cases, faint sources can even disappear completely during the readout transfers, as illustrated in Figure 6.23 below. It is also clear from the curves that CTE affects astrometry as well as photometry: the profiles below are shifted to the right (i.e., away from the readout register), since a star's downstream electrons are more likely to be lost than its upstream electrons.

**Figure 6.23: Impact of background on source recovery (epoch late 2020).**
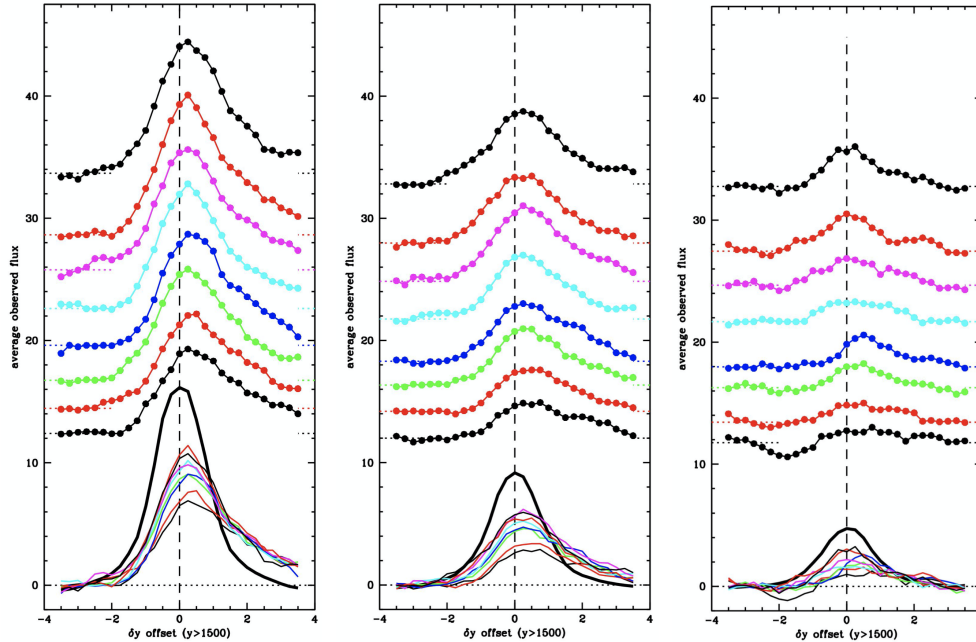


A reproduction of Figure 17 from WFC3 ISR 2021-09. The three panels show three "composite" point sources taken from actual images of real stars with total fluxes of 100 e⁻, 40 e⁻, and 16 e⁻, respectively. The sources were at the top of the detector (2000 pixels from the readout) on eight different image backgrounds ranging from 12 e⁻ to 34 e⁻. The connected dots show the profiles on top of the various backgrounds, while the curves at the bottom are background-subtracted. The heavy black line shows the true signal expected with no CTE loss. These curves provide a direct sense of the impact that imperfect CTE has on star images.

A more quantitative demonstration of how relatively low levels of background can significantly improve the CTE and increase the SNR of very faint sources is provided in Figure 6.24. The background level has a large impact on the photometry of faint sources, but does not have a large effect on bright sources. WFC3 ISR 2021-13 distills many such plots for both photometry and astrometry into tables so that users can anticipate or correct for losses.

**Figure 6.24: Quantitative CTE-related photometric losses.**
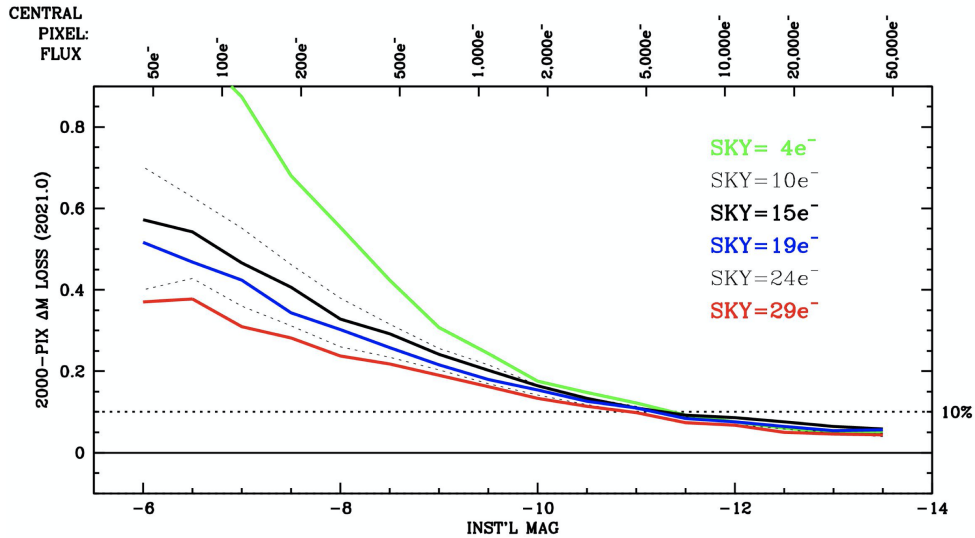


Reproduced from Figure 3 of WFC3 ISR 2021-13. Photometric losses for stars in late 2020 as a function of instrumental magnitude shown for six different backgrounds. Instrumental magnitude is defined as:    $m = -2.5 \log_{10}(\text{flux})$, where the flux is measured over a 5x5-pixel box and scaled according to a PSF model to correspond to the flux within a 10-pixel radius. The flux in the stars' central pixels are provided along the top of the plot as a reference.

The required increase in background necessary to provide effective CTE-loss mitigation can sometimes be obtained simply by lengthening exposure times or by using a broad filter. WFC3 ISR 2012-12 examines the background achieved in actual WFC3/UVIS observations with various exposure times through various filters. The plots in the appendix of that ISR show the distribution of backgrounds achieved as a function of exposure time for all the external observations in the archive through 2012.  Exposures longer than 1000s through wide-band filters with wavelengths F475W and longer have natural backgrounds greater than 20 e‾/pix. The UV and medium/narrow-band filters will have relatively low natural backgrounds, and some post-flash is recommended as a means of boosting the total background.  While it may seem counter-productive from an SNR perspective to use post-flash to increase the background in images, it will significantly increase the efficiency of the charge transfer for faint sources and, as a result, source signal can accumulate much faster than the noise increases.  Observers with faint sources in narrowband or UV filters or with science programs requiring the co-addition of multiple images to reach very faint limits should plan to achieve a total background level of ~20 e‾/pix per exposure.  Figure 6.23 represents this stacking situation.  Although 20 e‾/pix is our general recommendation (as of late 2023) to ensure a minimum of 50% flux preservation, concerned observers can themselves balance the level of post-flash used to mitigate CTE and the additional noise penalty incurred from adding extra background given their particular targets of interest. The tables and plots in WFC3 ISR 2021-09 can help with this.  Note that the location of the target on the detector also affects the calculation.

Once users determine the optimal background level for their observations, they need to estimate the natural background to determine how much post-flash to add. The Exposure Time Calculator provides such estimates, including contributions from sky, dark, zodiacal light, earthshine, airglow, and a selected level of post-flash. Alternatively, WFC3 ISR 2012-12 (described above) provides more empirical assessments.  In general, if the natural background of the exposure is expected to be higher than 20 e⁻/pix, then there is usually no need to add post-flash.  For images with very low background levels, enough post-flash should be applied to achieve the desired total background (natural + post-flash).

Observers invoke post-flash in APT by choosing the exposure optional parameter 'FLASH' and specifying the desired number of electrons per pixel to be added to the image using the LED post-flash lamp. (Section 12.2 in the *Phase II Proposal Instructions*.) The flash on WFC3 is performed after the shutter has closed at the end of the exposure: an LED is activated to illuminate the side of the shutter blade facing the CCD detector.

On-orbit experience with the LED, corroborated by the design analysis, has shown that although the illumination pattern varies by about +/-20% across the field of view, the pattern is stable and very repeatable (to much better than 1%). The two shutters produce similar though not identical flashes: those on shutter B are ~7% fainter than flashes on shutter A and the ratio of the shutter A/B flash pattern exhibits a smooth ~4% gradient along the diagonal from amplifier D to A (see the "Spatial Dependence of the Flash" section of the WFC3 CTE webpage). Regular monitoring of the post-flash has shown a long term ~0.2%/year decline in the measured counts in both shutter A and B along with apparent random brightness fluctuations from frame to frame of up to +/- 1% (WFC3 ISR 2023, in prep). The long term change is not attributed to the LED but is likely due to the UVIS detector given its consistency with the sensitivity decline measured via photometric monitoring of external targets (WFC3 ISR 2022-04; WFC3 ISR 2021-04).

The post-flash reference files are constructed from stacks of high signal-to-noise post-flash images as a function of shutter blade as well as LED current level setting, normalized to 1 e- per second of flash (WFC3 ISR 2013-12). Prior to 2023, the post-flash reference files were generated from data acquired over ~5 years (WFC3 ISR 2017-13). As of Dec 2022, the post-flash reference files are now time-dependent, generated from data acquired over 1 year time blocks as these provide a slight improvement in data quality (WFC3 ISR 2023-01). All archival data have been reprocessed with the annual post-flash reference files; observers with data retrieved prior to Dec 2022 can re-download their data from MAST to obtain the recent calibration. Note that the default calibration for flashed science images is to remove the flash signal. As a result, the background in the final calibrated pipeline products reflects the astronomical background. To have the pipeline skip the post-flash correction, set the header keyword FLASHCORR to 'OMIT' to turn off the flash subtraction and manually reprocess the data through `calwf3`.

The main disadvantage of post-flash is, of course, the increase in the background noise. In the worst case, a short exposure with low background and dark current would require the addition of about 20 e⁻/pix of post-flash. Thus the original readout noise of ~3.1 electrons is effectively increased to 5.4 e⁻ in un-binned exposures. (See Section 9.6 for SNR equations.) In most cases, however, the impact will be significantly less severe, as exposures will generally contain some natural background already and will not require a full 20 e⁻/pix post-flash. Also, observers can often take fewer exposures, which lessens both the need for and the impact of post-flash.

Finally, please note that even with moderate backgrounds of 20 electrons or more, larger charge packets from brighter stars, hotter pixels, or cosmic rays will still experience some loss/trailing of their initial distribution of electrons. Figure 6.24 shows that even stars near saturation can lose ~5% of their flux to CTE. Therefore, all measurements will require some correction for CTE losses.

**3) Use charge injection.** This option has been deprecated, but is described here for the sake of completeness. When CTE losses were first addressed, this mode was included as an observing strategy option for CTE-loss mitigation, since the noise penalty from charge injection was significantly lower than Poisson noise of post-flash. However, in practice it is no longer considered to be as useful as optimizing the placement of targets or optimizing the background with exposure times and post-flash. Use of charge-injection will be permitted only in exceptional cases where the science justifies it. Observers who wish to use this mode are advised to consult their Contact Scientist or contact the help desk at http://hsthelp.stsci.edu.

Charge injection is performed by electronically inserting charge as the chip is initialized for the exposure. Charge is injected either into all rows or spaced every 10, 17, or 25 rows. Only the 17-row spacing is supported as of mid-2012. The injected signal is ~15000 electrons (not adjustable) and it results in only about18 electrons of additional noise in the injected rows (Baggett et al. 2011). The rows above or below the charge-injected rows also have between 3 and 7 electrons of added noise due to charge-transfer effects. The charge-injection capability was supported through Cycle 19 (2012), but experience has demonstrated that it is useful for very few types of observations. The primary drawbacks are (1) the noise level in the injected and adjacent rows, (2) the uneven degree of protection from charge trapping in the rows between the injected charge rows, (3) a very difficult calibration challenge posed by the combination of sources in the field and the charge in injected rows, which give rise to different levels of CTE at different places within the image. Furthermore, the strong dependence of CTE losses on image background in the injected images makes it challenging to produce a suitable calibration, as typically there will be a mismatch in image backgrounds between the charge-injection-calibration frames and science frames (i.e., differing levels of CTE losses).

## 6.9.3 CTE-Loss Mitigation After Data Acquisition: Post-Observation Image Corrections

**1) Apply formula/table-based corrections for aperture photometry.** One way to correct CTE losses after the images have been acquired is to apply an empirical photometric correction to the measurement via either formulae or tables. The current formula-based results were constructed from stellar aperture photometry, and they provide corrections for CTE losses as a function of observation date, image background, source flux, and source distance from the amplifiers. Figure 6.25 summarizes some of the analysis from WFC3 ISR 2021-03. Plots such as these can be used either to anticipate losses or to correct for them.

As the plots show, larger corrections are required for fainter sources and/or sources observed on lower image backgrounds. The top left panel represents the worst-case scenario: for sources in exposures taken with a narrowband filter, with typically ~2 e⁻/pix background. Flux losses in early 2023 for sources far from the readout amplifier are ~1 magnitude for the faintest sources measured (a few hundred electrons within a 3-pixel radius aperture). The top right panel shows that a background of ~20-25 e⁻/pix (~2-12 e⁻ natural plus 10-18 e⁻ post-flash depending on the target) produces a noticeable improvement in CTE: the faintest sources experience about 0.3 mag of losses while moderately bright sources (with a few thousand electrons within a 3-pixel radius aperture) experience less than 0.2 mag of flux loss.

The lower panels in Figure 6.25 illustrate the efficacy of applying the pixel-based CTE correction (discussed in topic **2** below) to the data in the upper panels. Note that these results shown are for small apertures. Corrections for larger apertures will be smaller, as more of the trailed charge will end up getting released within the aperture.

The flux-loss information in these plots has been distilled into formulae, following previous treatments in WFC3 ISR 2015-03, WFC3 ISR 2016-17, and WFC3 ISR 2017-09. In brief, the flux loss is modeled as a function of source brightness, observation date, image-background level, and vertical distance from the readout amplifier and fit with a 2nd-degree polynomial whose coefficients are provided in WFC3 ISR 2021-03 for FLT data, and WFC3 ISR 2021-06 for FLC data, along with the analysis to allow observers to estimate flux corrections for their point-source photometry. The coefficients, as well as other CTE information, can also be found on the WFC3 CTE webpage.

**Figure 6.25: CTE Losses in FLT and FLC images as a function of star flux, observation date, and image background level.**
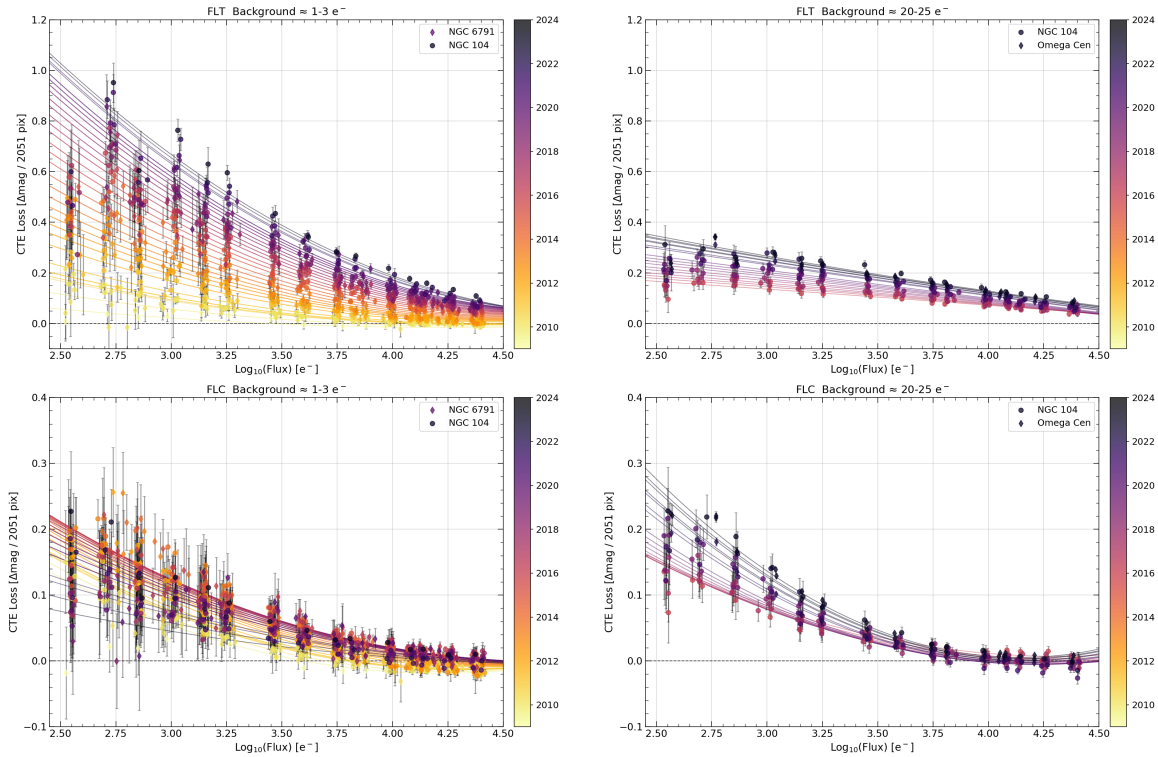


CTE flux losses in magnitudes per 2051 detector-row shifts as a function of star flux (within a 3-pixel radius) and year of observation (color-coded). The top panels show results for data without application of the pixel-based CTE correction (*flt.fits files), low background (~ 2e-/pix) at left and recommended background (~20-25 e-/pix total) at right. Data shown in the bottom row panels have also had the pixel-based CTE correction applied (*flc.fits files). Circular markers are based on NGC 104 (47 Tuc) and diamond markers denote either Omega Centauri or the sparse cluster NGC 6791; lines denote the best fits.

As a complement to the formulaic corrections discussed above, WFC3 ISR 2021-13 provides the photometric corrections in tabular form, along with providing corrections for astrometry as well. The two-dimensional tables specify the photometric losses and astrometric shifts for a source at row 2000 at epoch 2021.0 as a function of sky background and true source flux. The table values can be scaled up (or down) linearly to correspond to epochs after (or before) the reference epoch, or locations on the detector above (or below) the reference row. Since the tables are provided in terms of the true flux, one must use iteration to turn an observed flux into a true flux. The software routine `hst1pass`, described in WFC3 ISR 2022-05, takes an HST image and produces a list of stars measured in that image. One of the possible outputs of the routine is CTE-corrected photometry and astrometry based on these tables.

The formula- and table-based correction approaches can be effective for isolated point sources on flat backgrounds, but they are less suitable for extended sources or sources in crowded regions. However, one benefit of the formula/table-based corrections is that they are not impacted by the possibility of readnoise amplification, which can be a concern for faint sources in the pixel-based reconstruction described below. Photometric corrections are also useful for planning observations: they allow an estimate of the expected CTE losses for point-like sources in a planned observation for a given background and source flux.

**2) Apply the empirical pixel-based correction algorithm.** The ACS team developed and implemented a post-observation correction algorithm employing the Anderson and Bedin methodology (2010; PASP 122 1035). A similar capability was made available for WFC3, initially in the form of a FORTRAN routine. In Feb 2016, the pixel-based correction was incorporated into `calwf3` in the MAST pipeline, which now produces FLC and DRC data products as CTE-corrected versions of FLT and DRZ products. An updated v2.0 version of this correction was made available via the pipeline in 2021 (described in WFC3 ISR 2021-09, performance evaluated in WFC3 ISR 2021-06).

The charge-transfer model is calibrated by studying hot pixels, which serve as delta-function probes of the charge-transfer process. In the absence of CTE losses, the full charge of a hot pixel is entirely contained within a single pixel. If some of the hot pixel charge is trapped due to imperfect CTE, there will be fewer electrons in the hot pixel itself, and more in the trailing pixels (see Figure 6.22). The original charge-transfer model involved examining the trails to determine how many electrons were lost from each original delta-function hot pixel, a strategy that works well as long as the hot pixels suffer moderate fractional losses. To model CTE losses at background/source levels where losses are significant, we devised a strategy of pairing long and short darks to tease out the impact of CTE. The procedure for constraining the model is described in detail in WFC3 ISR 2021-09.

The pixel-based correction algorithm takes the charge-transfer model and uses an iterative forward-modeling procedure to determine from the observed distribution of pixel values what original pixel distribution could be pushed through the CTE-blurring readout simulation to yield the observed pixel distribution. The resulting correction essentially redistributes the counts in the image, "putting the electrons back where they belong" (Anderson et al. 2012).

While the pixel-based algorithm has been successful at removing trails behind stars, cosmic rays, and hot pixels, it has one serious and fundamental limitation: it cannot restore any lost SNR in the image. Faint sources and faint features of extended sources may be so strongly affected by CTE losses that they become undetectable and cannot be recovered (e.g., see Figure 6.23 and Figure 6.24).

Furthermore, the pixel-based reconstruction is essentially a deconvolution algorithm, and as such it can amplify noise or sometimes generate image artifacts. Over the years, CTE losses for faint sources on low backgrounds has become so severe that it is impossible to reconstruct the signal from the faint sources without incurring pathological readnoise amplification. As a general rule of thumb, *if CTE losses are greater than 10%, then the reconstruction becomes problematic. If the losses are greater than 25%, then it becomes impossible*. The v2.0 algorithm deliberately avoids readnoise amplification at the expense of leaving faint sources uncorrected. **As such, the FLC images should be used to measure only moderate-brightness sources (SNR>10)**. Kuhn et al. in WFC3 ISR 2021-06 provides a detailed comparison of FLT and FLC photometry against the known photometry.

The pixel-based correction algorithm also does not correct for sink pixels, which contain a number of charge traps (WFC3 ISR 2014-19). They comprise about 0.05% of the UVIS pixels, but can affect up to 1% of the pixels when the background is low. A calibration program to identify sink pixels and pixels impacted by them has been carried out. The strategy for flagging these pixels is presented in WFC3 ISR 2014-22. Since February 23, 2016, when `calwf3` version 3.3 was implemented in the pipeline, sink pixels and their trails have been identified in the DQI array with value 1024 (see Table E.3).

Serial CTE trailing - CTE along the X direction on the detector - can be seen in stars, warm pixels, and cosmic rays that are close to saturation. WFC3 ISR 2024-07 provides a comprehensive description of the impact of serial CTE on WFC3/UVIS images. Serial CTE has a much smaller impact than parallel CTE, but it can affect the positions of stars at the scale of 0.01-0.03 pixels. The serial CTE trails drop off much faster than similar parallel trails (the bulk of the trail is concentrated in the first few pixels), but there is an extended low-level tail over a thousand pixels. Serial CTE does not have a significant impact on most scientific measurements, but post-pipeline routines are available for users to correct images.

> ✅ *Note that `calwf3` automatically produces y-CTE-corrected image (FLC files), however the x-CTE correction must be performed manually using software available on the WFC3 CTE webpage.*

We end this CTE Mitigation section by noting that, depending on the science goals, a single mitigation method may not be sufficient for some programs. Observers, particularly those with faint sources, will want to consider applying both pre- and post-observation CTE-loss mitigation strategies, e.g., reduce CTE losses during the readout stage by taking fewer longer exposures to minimize the need for post-flash, but when needed adding post-flash to ensure a background of at least ~20 e⁻/pix and follow that with an application of either the formula/table-based or pixel-based corrections, depending on the nature of their sources. We note that the pixel-based correction algorithms are unable to operate on binned data, even aside from the fact that binning is an ineffective way of increasing the detectability of faint sources that may be impacted by CTE losses (see Section 6.4.4).

For the most current information on the WFC3 CTE and mitigation options, please refer to the WFC3 CTE webpage.

# 6.10 Other Considerations for UVIS Imaging

In this section, additional considerations users may have regarding WFC3/UVIS imaging are explored, including those that are determined to have little or no impact. We suggest that users pay particularly close attention to Section 6.10.1 (gain and full well saturation), Section 6.10.2 (cosmic rays and hot pixels), and Section 6.10.6 (optical anomalies).

## 6.10.1 Gain and Full-Well Saturation

When the default gain for the UVIS detector is used (1.5 e-/DN), photometric information well beyond saturation can be recovered for relatively isolated sources in unbinned exposures (where the CCD full well is the limiting factor), but not in binned exposures (where the ADC is the limiting factor). This is discussed in detail in Section 5.4.5 and Section 5.4.6.

## 6.10.2 Cosmic Rays and Hot Pixels

The cosmic-ray fluxes for WFC3 UVIS are comparable to the levels seen in ACS, STIS CCD, and WFPC2. As with these previous HST instruments, typical WFC3 imaging observations need to be dithered to obtain adequate cosmic-ray removal (see Section 5.4.10). Dithering will also mitigate bad pixel effects, and can be used to sample the point spread function; it is recommended for the vast majority of observations.

## 6.10.3 Image Persistence

No significant image-persistence effects following over-exposure were observed in instrument-level ground test or on-orbit data using the UVIS CCDs, as expected for back-illuminated devices.

## 6.10.4 Shutter Performance at Short Exposure Times

Shutter-induced vibration, or shutter jitter, affects only very short exposures. Shutter jitter causes slight blurring in image data and is not to be confused with exposure time deviation. Exposure time deviation is discussed further in Section 6.7.1, and the UVIS shutter mechanism is described in Section 2.3.3.

### Vibration Effects

The image quality analysis carried out during the third thermal-vacuum campaign revealed that vibration associated with the operation of the UVIS shutter caused systematic changes in the width and in the central pixel flux of point sources in a series of short exposures (WFC3 ISR 2008-44).

The shutter mechanism employs a rotary disc blade with 180 degree symmetry, including two cut-outs for the open (expose) positions. The blade is rotated 90 degrees from closed to open, for exposure, then another 90 degrees in the same direction from open to closed, etc., such that consecutive exposures use alternating cut-outs (sides) of the blade, designated A and B. A slight vibration occurs when the servo-control electronics are enabled to rotate the blade to side B. The observed PSF is thus alternately broader and narrower as sides B and A are used. The vibration lasts about 0.7 sec, and thus has diminishing effects on the PSF as longer time exposure times are executed and more time is spent in the quiescent state.

To test the on-orbit performance of the shutter, a series of images of the calibration standard star GD153 were made during SMOV (WFC3 ISR 2009-20), with exposure times from 0.5 sec to 20 sec. The widths of the PSFs in the consecutive 0.5 sec exposures are shown in Figure 6.26.

**Figure 6.26: FWHM of a star in a consecutive series of 0.5-second exposures; the shutter blade alternates from exposure to exposure.**
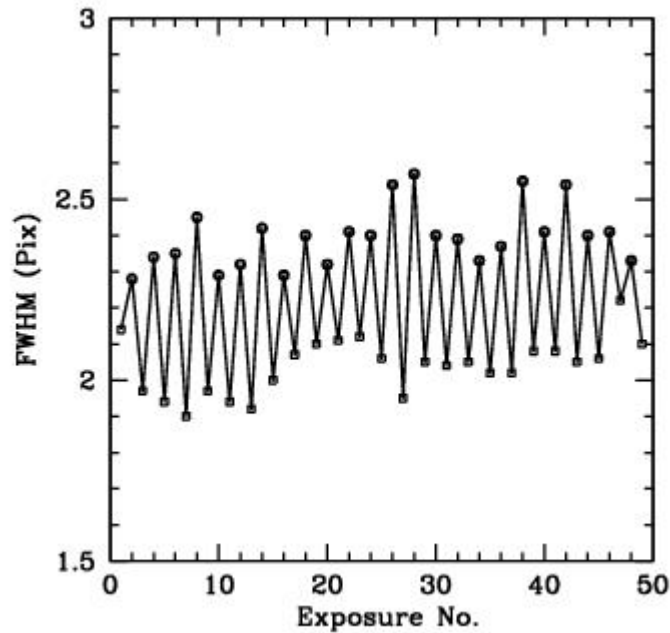


The shutter-dependent fluctuations in FWHM are superimposed on the gradual change in FWHM that is generally observed over the course of an HST orbit due to "breathing", a gradual periodic change in focus. In these SMOV observations from 2009, breathing is the primary determinant of FWHM for exposures of 3 sec (see Figure 2 in WFC3 ISR 2009-20).

Photometric consistency can be achieved in short exposures made with side A and side B by using a sufficiently large aperture (see WFC3 ISR 2009-20). Fluctuating PSF sizes pose a greater problem for science programs with very bright targets when the results depend on PSF stability or on the highest possible spatial resolution. Such programs may now be able to take short exposures with less vibration using the exposure-level option BLADE=A in APT (introduced in APT version 21.2.2). Testing of this mode is described in WFC3 ISR 2014-09. Since the BLADE option causes additional movement of the shutter mechanism, using only only blade A and bypassing B, its use will be allowed only as an available mode when sufficiently justified. The interested PI should send a scientific justification for using this mode for exposures with less than a specified exposure time to the Contact Scientist or the Program Coordinator, who will forward it to the appropriate instrument scientist for consideration.

### Exposure Time Repeatability

Early assessments of the shutter's exposure time repeatability yielded 4-6 ms r.m.s., easily satisfying the contract specification upper limit of 10 ms r.m.s. (WFC3 ISR 2009-25; WFC3 ISR 2015-12). Those studies, however, were based on extremely short internal flatfield exposures and thus may have been affected by shutter-induced vibrations in the calibration subsystem optics (WFC3 ISR 2018-11). To avoid this effect, a recent calibration program observed an external target with the G280 grism ( WFC3 ISR 2023-04). Use of the grism also provided data that allowed for an improved measurement precision since both +1 and -1 orders were captured simultaneously to provide a large dynamic range (the +1 order has ~3x higher throughput than the -1 order, see Section 8.2).

For 1-, 2-, and 4-s exposures, the exposure time repeatability was measured at 2.43 +/- 0.32 ms r.m.s repeatability (WFC3 ISR 2023-04), about 4 times better than required by the specification. The 0.7 sec exposures showed~5.5 ms r.m.s., still satisfying the requirement though worse performance than in the longer exposures, perhaps due to vibrations in the shutter operation (discussed above). The shortest possible UVIS exposures, 0.5 sec, showed ~0.24 ms r.m.s., or about 10 times smaller than the requirement. The improved performance compared to longer exposures could be due to shutter operation as well. For the 0.5 s exposure time (only), the shutter blade performs a continuous sweep across the field of view without stopping, which may help reduce any jitter effects experienced by exposures 0.7 sec or longer, where the shutter blade must rotate open, pause, then rotate shut. Accordingly, we recommend that observers consider substituting a 0.5-s exposure for any 0.7-s exposures that would otherwise be desired.

## 6.10.5 Droplets

The outer window was contaminated by a mineral residue introduced during acceptance testing of WFC3. These contamination features have been dubbed "droplets" due to their appearance at the time of discovery. In external flat-field images, these features have a strength of approximately ±0.5%. The droplets cause changes in PSF profile, such that flux in the core is redistributed to the near wings. In large-aperture (10 pixel radius) photometry of point sources stepped across a strong window feature, the feature does not significantly increase the photometric scatter. For small-aperture (3 pixel radius) photometry of point sources stepped across a strong window feature, the photometric scatter increases from ~0.5% to ~1%. Quadrant A has the lowest density of features. There are approximately 50, 129, 108, and 179 droplets in quadrants A, B, C, and D, respectively.

The best strategy for mitigating the flat-field features is an appropriate dither pattern. Although there are positions within a flat-field feature that cause systematic errors at the level of a few percent in point source photometry, other positions separated by 20 to 40 pixels show much smaller errors, suggesting that dithers on this scale would be sufficient for most photometric programs. To ensure a point source does not hit a particular feature twice requires larger dithers of approximately 100 pixels, which is the typical diameter of these features.

WFC3 ISR 2008-10 describes the characterization of the droplets and their photometric effects based on ground testing, and WFC3 ISR 2009-27 reports that about 30% of droplet positions have shifted by about 1 pixel after launch, but have been stable since then.

## 6.10.6 Optical Anomalies

In this section, we caution users to be aware of two well-known optical anomalies that may interfere with science objectives.

Additional detector anomalies, ghosts, and defects are detailed on the WFC3 Anomalies webpage for both the UVIS and IR detectors. Also available on the same webpage is a downloadable database of all known anomalies in all non-proprietary WFC3 data, as maintained by the daily monitoring of the WFC3 Quicklook Team (WFC3 ISR 2017-02, WFC3 ISR 2020-02).

### Dragon's Breath

In rare cases, the optical system causes stray light from sources outside the CCD FOV to be scattered into images. Analysis of this stray light, known as "dragon's breath", was first presented in WFC3 ISR 2017-02, and more recently explored in WFC3 ISR 2024-09.

The WFC3 team created an interactive plot showcasing the locations of known off-frame sources that caused dragon's breath to occur in previous observations. We share a static view of the tool in use in Figure 6.27; the actual interactive tool is linked under "UVIS Anomalies" on the WFC3 Anomalies webpage. This screenshot shows the interactive "dragon's breath" tool in use. When the user hovers over a source outside of the WFC3/UVIS footprint, an image of the observation pops up, in addition to other information (proposal, observation date, exposure time, V-band magnitude). In the example, the dragon's breath is the vertical shadow in the middle of the detector that crosses the chip gap. In addition, two sets of "figure-8" ghosts are also visible, caused by the bright source in quadrant D (bottom right).

Additionally, an XML overlay is available in APT to assist users planning their observations gauge the likelihood of an off-frame source causing dragon's breath. When viewing in Aladin, load the "Dragons Breath" overlay under "Instrument Fields of Views (FoV)".

**Figure 6.27: The dragon's breath interactive tool being used.**
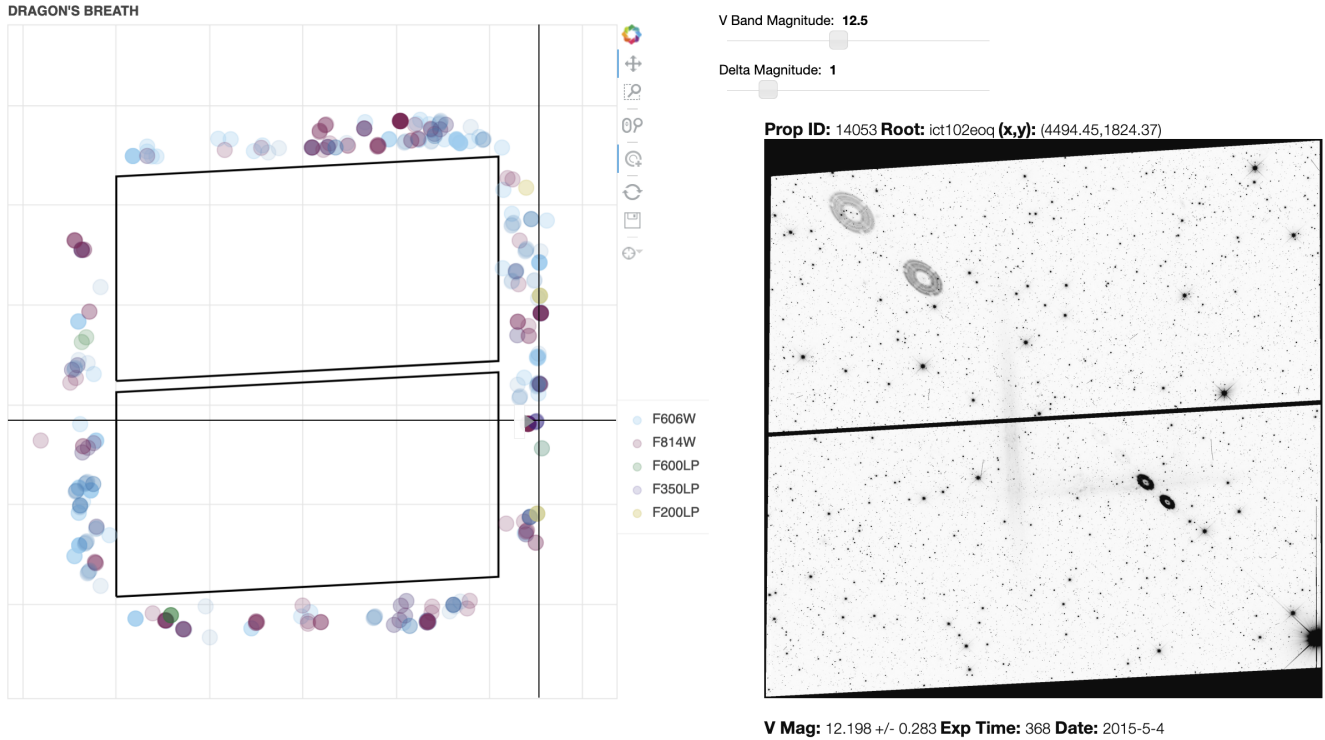


## Figure-8 Ghosts

Figure-8 ghosts are caused by reflections between the detector and the two windows of the CCD package. When a bright source is observed in UVIS quadrant D, these ghost reflections may contaminate sources which fall along a diagonal in quadrant A, as shown in Figure 6.28. Users may wish to set orientation restrictions to avoid having ghosts overlap the target of interest. Note: if ORIENTs are necessary, they must be requested in the Phase I proposal.

Additionally, an XML overlay of the projected map of figure-8 ghosts from bright sources in quadrant D is available in APT, for the benefit of users planning their observations. When viewing in Aladin, load the "Window Ghosts" overlay under "Instrument Fields of Views (FoV)".

**Figure 6.28: Full-frame observation with two "Figure-8" anomalies.**
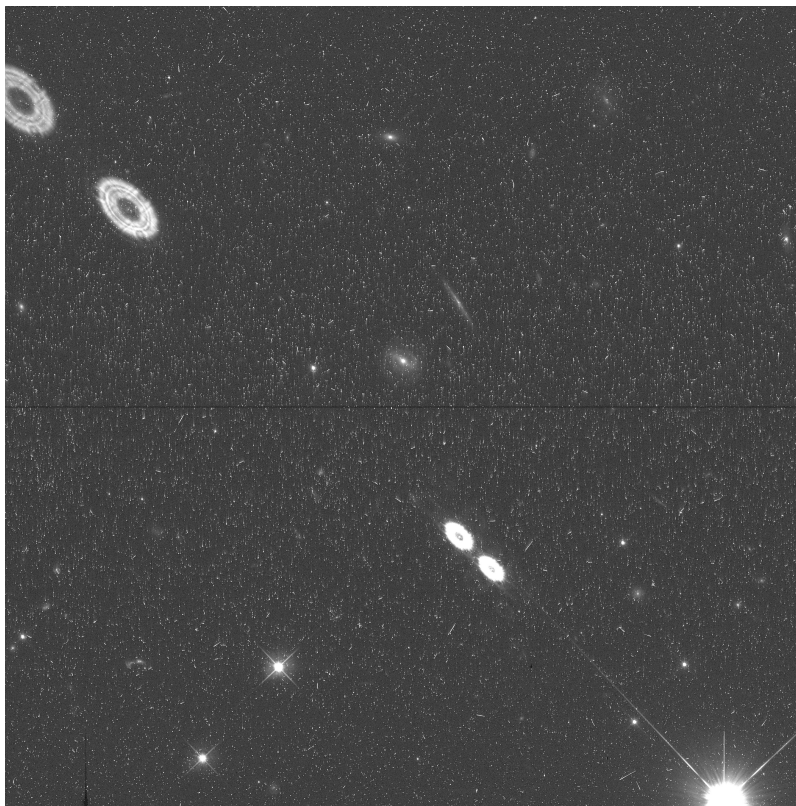


In this full-frame F814W observation (IDI121O8Q from GO Program 15166), the bright source in Quadrant D (bottom right corner) causes two Figure-8 anomalies projected across the diagonal from Quadrant D to Quadrant A.

> ✅ *Additional examples of stray light and other optical anomalies may be found on the* WFC3 *Anomalies website.*

# 6.11 UVIS Observing Strategies

## 6.11.1 Dithering Strategies

For imaging programs, STScI generally recommends that observers employ dithering patterns. Dithering refers to the procedure of moving the telescope by pre-determined amounts between individual exposures on a target. The resulting images are subsequently combined via post-observation processing techniques using software packages such as DrizzlePac.

Use of dithering can provide improved sampling of the point spread function (PSF) and better correction of undesirable artifacts in the images (e.g., hot pixels, cosmic rays, the UVIS channel's inter-chip gap, and the UVIS "droplets"). Cosmic ray removal is more effective if more than 2 images are obtained, especially for exposure times greater than 1000s. A sequence of offsets of a few pixels plus a fractional pixel in each coordinate is generally used to simultaneously remove hot pixels and cosmic rays and to sample the PSF. A larger offset along the image Y axis is needed to fill in the interchip gap in full-frame images (the WFC3-UVIS-MOS-DITH-LINE pattern uses a conservative step size of 2.4 arcsec). To ensure the best photometric accuracy,  consider dithering to compensate for droplets (Section 6.10.5).

Larger offsets, up to sizes approaching the detector's field of view, can also be used to create mosaics. However, as a result of geometric distortion (Appendix B), some objects shift by an integer number of rows (or columns), while others shift by an integer plus some fraction of a pixel. The PSF is not resampled in that dimension in the former case, but is resampled in the latter case. Where the exposures overlap, the PSF is thus better sampled for some objects than for others. If PSF sampling is important, a combination of mosaic steps and small dither steps should therefore be used. Note that, in practice, mosaic steps must be contained within a diameter ~130 arcsec or less (depending on the availability of guide stars in the region) to use the same guide stars for all exposures. The r.m.s. pointing repeatability is significantly less accurate if different guide stars are used for some exposures (see Appendix B of the DrizzlePac Handbook).

The set of Pattern Parameters in the observing proposal provides a convenient means for specifying the desired dither pattern of offsets. The pre-defined mosaic and dither patterns that have been implemented in APT to meet many of the needs outlined above are described in detail in the *Phase II Proposal Instructions*. The WFC3 patterns in effect in APT at the time of publication of this Handbook are summarized in Appendix C. Observers can also define their own custom patterns to tailor them to the amount of allocated observing time and the desired science goals of the program. Alternatively, they can use POS TARGs to implement dither steps (Section 6.4.3). Observers should note that thermally-driven drift of the image on the detector, typically 0.1 to 0.2 pixels per coordinate within one orbit (WFC3 ISR 2012-14), will limit the accuracy of execution of dither patterns. Dither strategies for WFC3 are further discussed in WFC3 ISR 2010-09, which provides a decision tree for selecting patterns and combining them with subpatterns. WFC3 ISR 2020-07 provides compact patterns with up to 9 steps (in the form of POS TARGs) designed to preserve sub-pixel sampling as much as possible over the face of the UVIS CCDs, given the scale changes introduced by geometric distortion.

WFC3 ISR 2023-05 presents new dithering patterns to optimize observations for programs using WFC3 and ACS simultaneously, i.e. for optimal pixel-phase coverage in the prime instrument and the best possible coverage in the parallel instrument. These dither patterns are not currently available as options in APT, so PIs are advised to input the desired POS-TARGs (see Tables 3, 4, 5, and 6 of WFC3 ISR 2023-05) into the "Special Requirements" tab for each individual exposure.

## 6.11.2 Parallel Observations

While the design of WFC3 prevents the simultaneous use of both the UVIS and IR channel, it is possible to use one or more of the other *HST* instruments in parallel with WFC3. Since each instrument covers a different location in the *HST* focal plane (see Figure 2.2), parallel observations typically sample an area of sky several arc minutes away from the WFC3 target. For extended targets such as nearby galaxies, parallel observations may be able to sample adjacent regions of the primary target. In other cases, the parallel observations may look at essentially random areas of sky.

For processing and scheduling purposes, *HST* parallel observations are divided into two groups: coordinated and pure.

A **coordinated parallel** is an observation directly related to (i.e., coordinated with) a specific primary observation, such as in the extended galaxy example above. A **pure parallel** is an observation typically unrelated to the primary observation, for example, parallel imaging scheduled during long spectroscopic observations. The primary restriction on parallel observations, both coordinated and pure, is that they must not interfere with the primary observations: they may not cause the primary observations to be shortened; and they must not cause the stored-command capacity and data-volume limits to be exceeded. The proposal software (APT) enforces these rules and notifies the observer when a specified parallel is not permitted.

In order to prolong the life of the *HST* transmitters, the number of parallels acquired during each proposal cycle is limited. Proposers must provide clear and strong justification in their Phase I proposal in order to be granted parallel observing time. Please refer to the *HST Call for Proposals* for current policies and procedures concerning parallels.

## 6.11.3 Spatial Scans

Spatial scanning of stellar images on the UVIS detector creates the potential for astrometry of unprecedented precision as well as improved relative photometry. Two representative scientific examples of the former are parallax measurement of Cepheid variable stars (program 12679, Riess et al. 2021 and references therein) and a high-precision trigonometric parallax to NGC 6397 (programs 13817, 14336, 14773; Brown et al., ApJ L 856, L6, 2018).

Results from non-proprietary data of program 12679 indicate that differential astrometry a few times less precise than that set by diffraction and Poisson statistics are attainable (Riess, priv. comm.). For *HST*, a 2.4-m telescope, operating at 600 nm, the diffraction limit is Θ ~ λ/D = 51 mas. In the theoretical limit, astrometry in one dimension is approximately equal to the FHWM Θ divided by the

signal to noise ratio, $\sqrt{N}$, where N is the number of photo-electrons recorded. If we adopt N equal to the full well of the UVIS CCD, ~64,000 e⁻, times a trail of length 4000 pixels, i.e., N = 128 million e⁻, then *the theoretical astrometric limit of scanned data is ~3 microarcsec per exposure*. A more conservative estimate of ~13 microarcsec can be derived as follows: the nominal, state-of-the-art astrometric precision of a staring-mode exposure is ~0.01 pixel, so the astrometric precision of a

1000-pixel-long scan could be ~ $\sqrt{1000}$ or ~30 times smaller, which, for the 40 mas WFC3 UVIS pixels, is 13 microarcsec. In 2012 the TAC recommended programs which anticipated a per-exposure precision of 30 to 40 microarcsec (13101 and 12909).

Some data analysis tools for spatial scans are currently being developed by the WFC3 team to aid users in reducing spatial scan data, but for the most part users should expect to develop their own analysis software to reduce images and obtain useful astrometric and photometric results (e.g. Riess et al. 2018; Riess et al. 2014).

Scans can be made at any angle, although users typically orient the scans approximately, but not exactly, parallel either to rows or to columns of the detector. For example, in order to sample pixel phase, program 12679 prescribed an angle of 90.05 degrees; the extra 0.05 degrees corresponds to a shift of ~1 pixel every 1000 pixels along the trail. In the interest of observing efficiency, this program performed forward and reverse scans alternately. Observers are cautioned that there will be a spatial offset between forward and reverse scans in the scan direction. Forward scans are centered in the frame as predicted in the APT display; reverse scans are offset by an amount that is greater for faster scan rates.

Boustrophedonic (from the Greek, literally, "as an ox turns in plowing") scans, are possible too. In boustrophedonic scans, a.k.a. serpentine scans, the user specifies a set of constant-speed scan lines separated by a specified angular distance, like rows in a farmer's field. An example is illustrated in Figure 6.27. The advantage is that more scan lines are possible per exposure, which can improve observing efficiency. The trajectory of such scans has been modeled (WFC3 ISR 2017-06).

**Figure 6.27:** A vertical boustrophedonic scan of a star field on the UVIS focal plane (from program 12679).
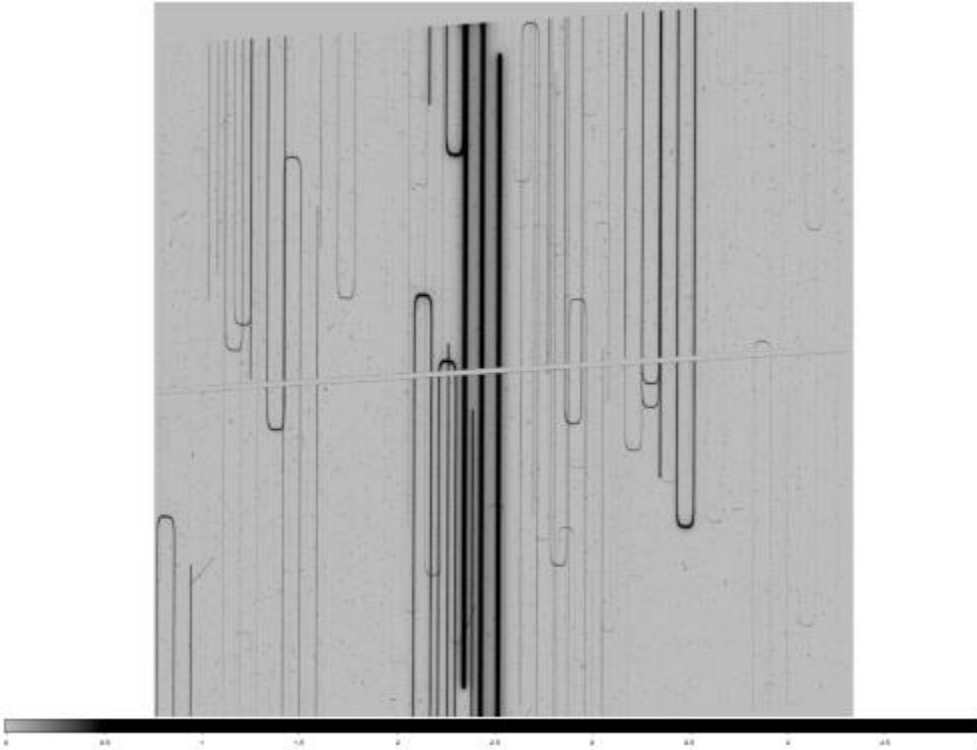


**The three thickest black lines in the center are the target star scanned upward, downward, and upward again in the same exposure. The U-shaped trails are from the turning points of nearby fainter stars.**

Spatial scanning generally permits more precise photometry than staring mode, by collecting more photons and averaging over more detector pixels. However, actual photometric precision may not achieve the theoretical limits due to at least two factors: 1) flat field errors (typically ~0.5%) and 2) shutter-timing non-repeatability (~0.004 s r.m.s. for the UVIS shutter). WFC3 ISR 2022-04 determined that photometric repeatability of spatial scan observations was ~2.5 times better than staring mode observations across multiple cycles (five years) of data; WFC3 ISR 2017-21 suggests that photometric repeatability may be ~3-5 times better than staring mode for observations within the same cycle.

Two examples of utilizing spatial scans for precision time-series photometry are program 14621 (P.I. Wang) and program 15129 (P.I. Burke). These programs take advantage of the orbit-to-orbit and visit-to-visit stability of the UVIS detector. Attempts to obtain precise photometric time-series within a single exposure, by using the trailed image of a star to record its flux versus time, have not been successful, because the positional feedback loop of the FGS control introduces lateral and longitudinal displacements from an idealized, constant-velocity scan, which results in photometric "flicker" of a few per cent (Figure 6.28). Although differential photometry of two or more stars would mitigate the FGS-induced "flicker", the two flat-field and shutter factors would remain.

For those preparing a phase II program description, we recommend WFC3 ISR 2012-08 and WFC3 ISR 2017-21. Also, IR imaging with spatial scanning is discussed in Section 7.10.4, and slitless spectroscopy with spatial scanning is discussed in Section 8.6. See Figure 8.12 for a diagram provided in APT to assist observers planning spatial scan observations. Note: starting in 2016 (Cycle 24), the Exposure Time Calculator (ETC) supports spatial scanning for UVIS and IR imaging and IR spectroscopy (WFC3 STAN issue 22).

**Figure 6.28: Photometric "flicker" appears in scans under FGS control.**
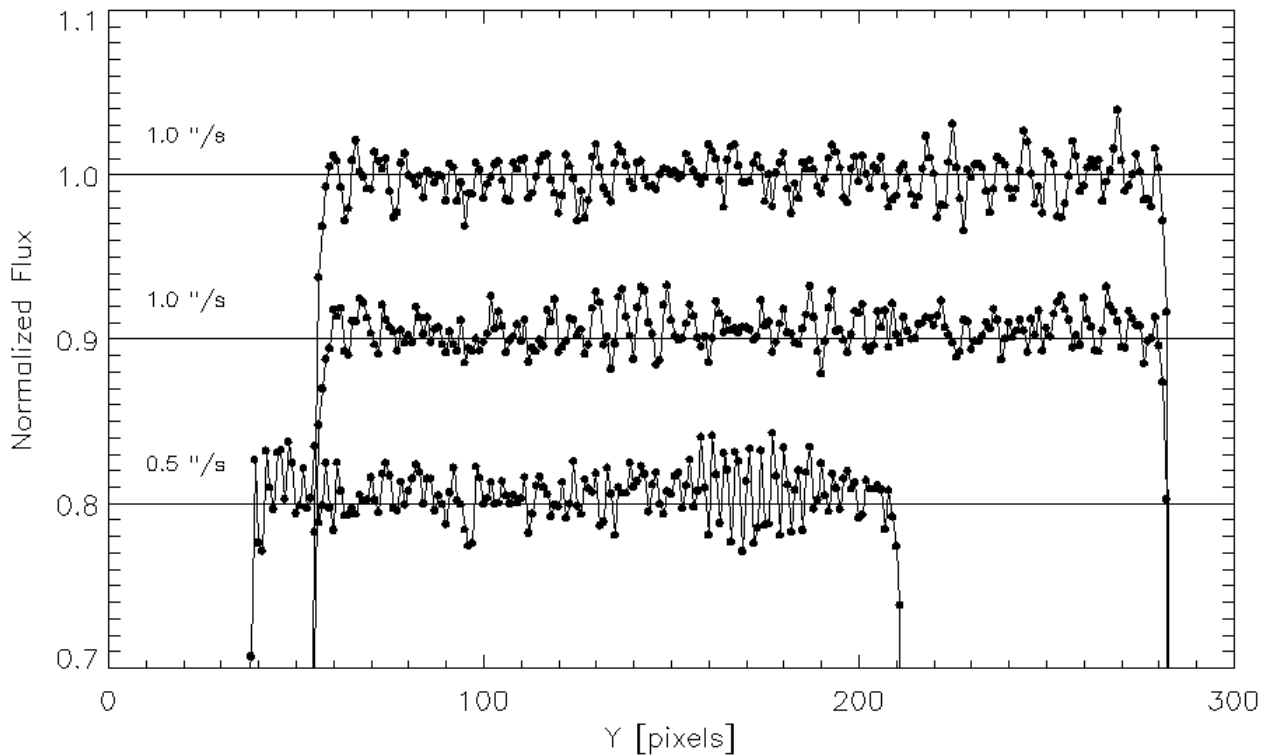


The same star was trailed across the WFC3 IR detector repeatedly, with rates of 1, 1, and 0.5 arcsec s$^{-1}$ respectively. Photometry integrated transverse to each of the three trails, show intermittent oscillations with ~3% amplitude at ~1.3 Hz, due to image motion or "jitter" during the scans. The 2nd and 3rd trails have been offset vertically by 0.1 and 0.2 for clarity.

## 6.11.4 PSF Subtraction

UVIS imaging has been shown to be highly effective in detecting faint point sources near bright point sources (WFC3 ISR 2011-03). For a variety of narrow, medium, and wide filters, when a high signal-to-noise drizzled image of a star was scaled down by 10 magnitudes and shifted and added to the original image, the simulated faint companion could usually be seen for separations greater than 1.0 arcsec. Based on the annular signal-to-noise of the deep stellar image, 5 sigma detections of companions fainter by two magnitudes could be made at a separation of 0.1 arcsec. Theoretically, companions several magnitudes fainter could be detected at that separation in deeper images, but, in practice, variations in the PSF (point spread function) due to telescope breathing limit the detectability within about 0.3 arcsec of a bright star.

If observers want to use stellar images to subtract the PSF from a target comprised of a point source and an extended source to detect or measure the extended source, they should keep several points in mind:

- UVIS pixels undersample the PSF (Section 6.6), so the stellar and target exposures must be dithered to produce good sampling of the PSF.

- Position drift and reacquisition errors can broaden the PSF (WFC3 ISR 2009-32, WFC3 ISR 2012-14).
- If a single guide star is used for a visit, roll angle drift causes a rotation of the target around that star, which in turn introduces a small translational drift of the target on the detector. In recent years, as gyroscopes have failed and been replaced, the typicalroll angle drift rate is 1-2 mas/sec, producing a translation at WFC3's location in the HST field of view of about 0.2 UVIS (0.05 IR) pixels in 1000 sec.
- The characteristics of the PSF depend on the focus, which generally changes measurably during an orbit; its range in a particular orbit will not be known in advance (WFC3 ISR 2012-14, WFC3 ISR 2013-11).
- The characteristics of the PSF vary with location on the detector (e.g., see WFC3 ISR 2013-11, ACS ISR 2003-06). PSFs near the A amplifier on UVIS1 are noticeably elongated by astigmatism (WFC3 ISR 2013-11, WFC3 ISR 2013-13).
- More than one exposure time may be needed to produce an image that is both unsaturated in the core and has good signal-to-noise to the desired radius.
- For exposures shorter than about 10 seconds, the UVIS PSF will be affected by vibration of the shutter (WFC3 ISR 2009-20). In some cases, use of the APT exposure-level option BLADE=A may be justified (Section 6.10.4).

**We do not recommend usage of the PSF modeling software** Tiny Tim. While STScI continues to host the software as a courtesy to the community, it is no longer maintained or supported. In addition, its applicability for WFC3/UVIS images is poor, as it was not optimized to reproduce observed PSFs and relies on outdated optical models (WFC3 ISR 2008-14). Sub-sampled empirical PSFs are available on the WFC3 PSF webpage, and Section 6.6.4 discusses in greater detail ongoing work to provide PSF models to observers.

## 6.11.5 The Drift and Shift (DASH) Observing Strategy

> ⓘ **Deprecated**
>
> As of the transition to Reduced Gyro Mode (RGM) in June 2024, **observing in DASH mode is no longer available**. The information in this section is provided for historical purposes. Additional details regarding HST guiding and considerations for DASH program design are similarly provided in Section 7.10.6.

The term DASH ("drift-and-shift", Momcheva et al., 2016) was originally adopted to describe the observing strategy of taking a series of WFC3/IR exposures of many targets within one orbit while the telescope is being guided under gyroscope control, thus avoiding the overhead cost of acquiring a new pair of guide stars for every slew between targets of greater than about 2 arcmin. A WFC3/IR sample sequence comprised of short exposure times was selected to avoid image smearing within each time step, and the differential samples in one exposure are later aligned and combined to compensate for the greater drift due to gyroscope control. The technique was designed to allow users to carry out shallow large-scale mosaic observations with the WFC3/IR camera, but was later adapted to efficiently observe a collection of bright targets within a field ~1 deg across with WFC3/IR subarray apertures (which have shorter time steps for a given sample sequence) and WFC3/UVIS subarray apertures.

Given that WFC3/UVIS is read-out as a traditional CCD, it was necessary to specify short exposure times when designing UVIS DASH observations in place of the non-destructive reads made in an IR sample sequence in a DASH program. Subarray apertures were used to increase the number of exposures that could fit into the on-board buffer before a time-consuming serial buffer dump must be made. Specifying small subarray apertures was considered risky, especially towards the end of an orbit, since the high drift rates could cause a target to fall outside the aperture. One mitigating strategy was to specify increasing subarray sizes as the orbit progressed, to allow for the uncertainty in predicting the drift. As discussed in Section 7.10.6, it was recommended that DASH visits be limited to one orbit, the exposures in an orbit grouped into a non-interruptible sequence container in APT, and the first exposure taken using guide stars to start the observations with accurate positioning.

# Chapter 7: IR Imaging with WFC3

**Chapter Contents**

# 7.1 WFC3 IR Imaging

As described in Chapter 2, the optical design of WFC3 features two independent channels, each with its own separate optics, filters and grisms, and detectors. The **UVIS channel** is sensitive to UV and optical wavelengths (200-1000 nm), and the **IR channel** is sensitive to near-infrared wavelengths (800-1700 nm).

Only a single channel, either UVIS or IR, can be used at any one time. In other words, they cannot be used in parallel but they can be used sequentially.

A schematic diagram showing the locations of the fields of view of the UVIS and IR detectors in the HST focal plane is given in Figure 2.2.

This chapter describes the capabilities of the IR channel. The previous chapter, Chapter 6, describes the UVIS channel. Detailed characteristics of the detectors used in both channels are given in Chapter 5 and summarized in Table 5.1.

# 7.2 Specifying an IR Observation

In the *HST* proposal system, the parameters for an IR observation available to General Observers are:

1. **Configuration**: always **WFC3/IR**.
2. **Mode**: always **MULTIACCUM**.
3. **Aperture**: must be specified. See Sections 7.4.4 and 7.4.5 for the dimensions, location, and reference point (target placement) of the full array and subarray apertures.
4. **Spectral Element**: must be specified for each exposure; see Section 7.5.
5. **Optional Parameters**: in the IR channel, **SAMPSEQ** specifies a predefined sequence of times at which the detector is read out, and NSAMP specifies the total number of readouts (and thus the total exposure time); see Section 7.7. **SAMPSEQ** and **NSAMP** are required for IR observations.
6. **Special Requirements**: see the *Phase II Proposal Instructions* for details of Special Requirements related to the timing of visits and for dithering and mosaicking. Also available is the exposure-level Special Requirement **POS TARG** for offsetting the target from the default reference point of the aperture (see Section 7.4.3 for a discussion of the IR channel coordinate system) and Appendix C for the POS TARGs associated with the WFC3/IR patterns.
7. **Number of Iterations and Time per Exposure**: in cases where two or more identical exposures are desired, the Number of Iterations may be set to 2 or more. In the IR channel, the Time per Exposure is fixed by the combination of **SAMPSEQ** and **NSAMP** (see item 5 above) and thus is not specified separately. Through various combinations of **SAMPSEQ** and **NSAMP,** it is possible to achieve exposure times ranging from 2.93 to 2756 s for readouts of the full detector array ( Table 7.8); considerably shorter exposures are possible using subarrays (Table 7.9).

# 7.3 IR Channel Characteristics

The WFC3 IR channel has been optimized for observing over the wavelength range 800-1700 nm. All the IR reflective optics (except for the WFC3 pick-off mirror) are coated with a silver layer for maximum IR throughput.

A schematic mechanical diagram showing both channels of WFC3 is given in Figure 2.1. Components of the IR channel include: the Channel Select Mechanism (CSM), which directs on-axis light from the *HST* OTA to the IR channel; a flat folding mirror; a two-mirror mechanism for providing focus and alignment adjustments; the Refractive Corrector Plate (RCP), which applies the spherical-aberration correction; the IR filter wheel (FSM or Filter Selection Mechanism); and finally the HgCdTe IR detector package.

The WFC3 IR detector is a HgCdTe 1024 × 1024 array, with 18 micron pixels, bonded to a silicon multiplexer, with 1014 × 1014 pixels sensitive to incoming light. It is a direct descendant of the NICMOS 256 × 256 and Hawaii-1 1024 × 1024 arrays (more details on the detector are given in Chapter 5).

# 7.4 IR Field Geometry

## 7.4.1 Field of View and Pixel Size

The inner 1014 × 1014 pixels of the IR detector are exposed to incoming light. There are no gaps in the field (such as the gap between the two CCDs in the UVIS channel), or mechanical occultations (such as the coronagraphic spots in NICMOS camera 2).

The IR focal plane is tilted by 24° with respect to the incoming beam. Thus the field of view as projected onto the sky is rectangular, with an aspect ratio of ~0.90. The pixels projected onto the sky are also rectangular, covering approximately 0.135 × 0.121 arcsec, with the shape varying slightly across the field. The field of view on the sky is 136 × 123 arcsec, or 4.65 arcmin$^2$.

## 7.4.2 Geometric Distortion

In addition to the rectangular field shape described above, the optical design of the IR channel also produces appreciable geometric distortion. Geometric distortions in both channels are discussed in more detail in Appendix B.
Distortion must be taken into account when exposures are flat-fielded, photometrically calibrated, used for astrometric measurements, or combined with other dithered exposures. The AstroDrizzle software appropriately carries out those operations; a combination of software packages in DrizzlePac can be used to optimize the combination of dithered exposures. (See the DrizzlePac documentation.)

## 7.4.3 Coordinate Systems

Like the CCD, the IR channel requires multiple coordinate reference frames, each relevant for a specific goal. Readers may also wish to refer to Section 6.4.3, which describes the coordinate systems for the UVIS channel. The coordinate systems used for the IR channel are illustrated in Figure 7.1 and are the following:

- **Data image-based system** (Axis1, Axis2; units of pixels)
- **Proposal POS TARG system** (X pos, Ypos; units of arcsec)
- *HST*-based system (V2, V3 or U2, U3; units of arcsec)

Figure 7.1: Diagram of IR apertures, illustrating the fiducial points of the full-detector apertures (IR and IR-FIX), and the outlines of the concentric subarray apertures (512 × 512, 256 × 256, 128 × 128, and 64 × 64). The regions imaged by the UVIS detector are shaded in blue, and regions imaged by the IR detector are shaded in red. The POSition TARGet coordinate system for the IR-FIX aperture is shown with its origin at that aperture's fiducial point. The POS TARG coordinate systems for other apertures are not shown in this diagram, but are orientated the same as the IR-FIX aperture, with each aperture's origin at the corresponding fiducial point. U2 = –V2 and U3 = –V3.



**WFC3/IR APERTURES**
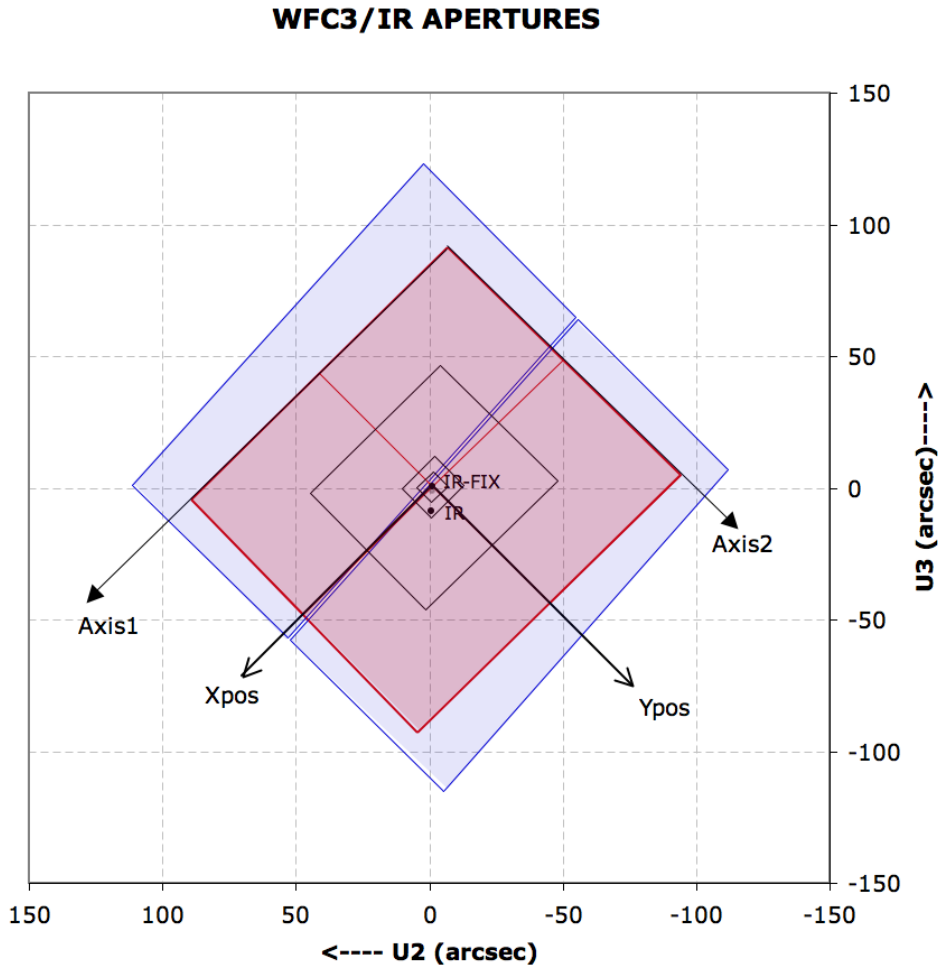
The **image-based coordinate system**, (Axis1, Axis2) in Figure 7.1, is a generic system used when an image is displayed on a computer screen. Coordinates are expressed in pixel units. This system is used primarily by the generic conversion pipeline software, which creates science FITS files from the data telemetry coming from the telescope.

The **POS TARG reference frame**, (Xpos, Ypos), is orthogonal on the sky, in units of arcseconds. It can be used to specify target placement at an offset location within the field of view, or for dithering or mosaicking purposes. In the IR channel, the POS TARG reference frame is designed to be virtually co-linear with the Axis reference frame, and it has its center located at the reference point (sometimes called the fiducial point) of the chosen IR aperture. The transformation between the undistorted POS TARG (arcsec) frame and Axis frame (pixels) contains non-linear distortion coefficients. For the IR detector, the POS TARG axes are almost exactly parallel to the detector edges. Note, however, that the IR POS TARG X,Y axes are not parallel to the UVIS POS TARG X,Y axes; the former are rotated a few degrees counterclockwise with respect to the latter.

The **HST-based**, or vehicle (V2, V3), system is an orthogonal reference frame tied to the telescope and is used operationally for alignment, pointing, and slewing purposes. The V1 axis lies along the optical axis while V2,V3 run parallel and perpendicular, respectively, to the solar-array rotation axis (see Figure 2.2). Note that the edges of the IR detector are rotated by approximately 45° with respect to the V2, V3 axes. Because WFC3 is on-axis, the origin of the V2,V3 system lies near the center of the WFC3 field of view. However, the V2,V3 (and U2, U3) coordinate axes have been shifted for clarity in Figure 7.1. *HST* observers may be more familiar with the U2,U3 coordinate system than V2,V3; for example, the specification of the ORIENT angle Special Requirement in APT uses the position angle of the U3 axis. The U2,U3 coordinates are defined as U2 = –V2 and U3 = –V3, and are marked in Figure 7.1. Observations of an astrometric field are made to locate the detector in the (V2, V3) system (WFC3 ISR 2009-36). Section 7.2.2 of the *Phase II Proposal Instructions* provides detailed information on the relationship between detector coordinates, spacecraft coordinates, and ORIENT.

## 7.4.4 Subarrays

In addition to obtaining standard full-field images, users can choose to read out smaller portions of the detector, called subarrays. Subarrays are useful to achieve reduced data volume, and/or to allow shorter exposure times. Shorter exposure times are especially important for the IR channel, because there is no physical shutter and the minimum integration time is limited by the time to read out the detector (2.9 s for full-frame readout). Very bright sources—including some of the primary "faint" IR photometric standards—may easily exceed the detector full-well of ~80,000 electrons in only a fraction of a second. Because the readout time is nearly proportional to the number of pixels read, subarrays can be used to reduce the effective integration time and make such observations feasible. Shorter integration times per readout have been implemented in the IR channel for several readout modes (Section 7.7.4)

All of the IR subarrays are centered on the detector field of view. Target placement on the subarray depends on the aperture selected (Section 7.4.5.). Four subarray sizes are supported, with pixel dimensions of 512 × 512, 256 × 256, 128 × 128, and 64 × 64. Note that the sizes of the subarrays refer to the actual active pixels, i.e., they do not include the reference pixels. (Of the 1024 × 1024 pixels of the WFC3 IR detector, only the inner 1014 × 1014 pixels are light-sensitive. The 5 rows and columns of pixels around the edge of the array use fixed capacitances to provide constant-voltage reference values.) The reference pixels, however, are still included in the output images, resulting in final datasets of 522 × 522, 266 × 266, 138 × 138, and 74 × 74 pixels. For subarray images, the reference pixels come from the same rows and columns of the subarray, with the 5 × 5 pixels at the subarray corners filled with the reference pixels at the corresponding corner of the detector (see Section 5.5 for details on reference pixels).

Beginning in Oct 2010 (Cycle 18), subarrays were provided for grism spectroscopy, in addition to imaging. The actual selection of a subarray is accomplished by requesting one of the IR channel's subarray apertures, as described in Section 7.4.5.

To avoid an IR image artifact known as banding, we recommend observers avoid mixing different IR aperture sizes in a single visit if possible. Should several different aperture sizes be necessary, the observations should be sequenced by aperture size from largest to smallest as this will prevent the banding. The phenomenon manifests as a rectangular region in which background pixel values are a few DN above or below the level in the rest of the image. The region of banding is centered vertically, and extends horizontally across the entire image and into the reference pixels. The structure of the vertical profile is more variable and irregular in full frame images than in subarray images. The height of the band is always either 64, 128, 256, or 512 pixels. A systematic study of banded data (see WFC3 ISR 2011-04) has revealed that the size of the band is always directly related to the size of prior subarray image(s). This coincidence accounts for the height of the bands, but the nature of the memory of prior subarray readout modes is not yet understood.

## 7.4.5 Apertures

The **APERTURE** parameter in the Phase II observing proposal defines two quantities: the active **region** of the detector to be read out (full frame or subarray), as well as the positioning of the target within the region (**reference point**). The default is to center the target at the reference point (also called the fiducial point), but a **POS TARG** Special Requirement may be added to offset the target from this position.

The available IR apertures are listed in Table 7.1. As with other HST instruments, there are two kinds of apertures with regard to their target reference point: "**fixed**" and "**optimum**." Apertures with their reference point at the geometric center of the array (or subarray) have "-FIX" appended of their name. These reference positions remain fixed during the HST mission. Apertures with their reference point at an "optimum" location (determined on the basis of best image quality, or detector cosmetics) have unadorned names and as the description implies, these aperture locations may be optimized from time to time by STScI as circumstances warrant. At present, the reference points of the optimum apertures are offset slightly from the mathematical center of the detector in order to avoid placing the target at the point where all amplifier boundaries meet.

> ⓘ For updates on subarray and aperture definitions, check the Science Instrument Aperture File (SIAF) page.

Table 7.1: WFC3 IR Apertures

| Aperture Name | Reference (fiducial) point |
|---|---|
| IR | Optimum point near center of IR detector |
| IR-FIX | Geometric center of IR detector |
| IRSUB64 | Optimum point near center of 64 × 64 subarray |
| IRSUB64-FIX | Geometric center of 64 × 64 subarray |
| IRSUB128 | Optimum point near center of 128 × 128 subarray |

| IRSUB128-FIX | Geometric center of 128 × 128 subarray |
|---|---|
| IRSUB256 | Optimum point near center of 256 × 256 subarray |
| IRSUB256-FIX | Geometric center of 256 × 256 subarray |
| IRSUB512 | Optimum point near center of 512 × 512 subarray |
| IRSUB512-FIX | Geometric center of 512 × 512 subarray |
| IR-UVIS | Pointing matched to UVIS aperture in Table 6.1 |
| IR-UVIS-CENTER | Pointing matched to UVIS-CENTER aperture in Table 6.1 |
| IR-UVIS-FIX | Pointing matched to UVIS-FIX aperture in Table 6.1 |
| GRISM64 | Optimum point in 64 × 64 subarray for grism spectrum or reference image |
| GRISM128 | Optimum point in 128 × 128 subarray for grism spectrum or reference image |
| GRISM256 | Optimum point in 256 × 256 subarray for grism spectrum or reference image |
| GRISM512 | Optimum point in 512 × 512 subarray for grism spectrum or reference image |
| GRISM1024 | Optimum point in full frame for grism spectrum or reference image |
| G102-REF | Unsupported after cycle 18. (Optimum point for reference image intended to accompany G102 grism image. Use GRISM apertures above instead.) |
| G141-REF | Unsupported after cycle 18. (Optimum point for reference image intended to accompany G141 grism image. Use GRISM apertures above instead.) |

# 7.5 IR Spectral Elements

## 7.5.1 Filter and Grism Summary

An overview of the IR spectral elements and of the process by which they were selected was given in Section 2.3. This section provides details of the IR filters and grisms. Table 7.2 lists the IR channel's filters, with a general description and fundamental parameters of each. Figures 7.2, 7.3, and 7.4 show the effective throughput curves of the WFC3/IR wide, medium, and narrow filters, respectively, including the filter transmission multiplied by the throughput of the OTA, WFC3 optics, and detector response.

More information on the integrated system throughput curves for all of the filters is given in Appendix A; in particular, Section A.2.1 describes how to generate tabular versions of the throughput curves using `synphot`. All measurements of the IR filters which involve wavelengths, as tabulated in Table 7.2 and plotted in Figures 7.2, 7.3, and 7.4, respectively, and in Appendix A, were done in helium rather than vacuum. In addition, the laboratory measurements were performed at a temperature of –30°C, whereas on-orbit operating temperature of the filters is –35°C; this may lead to wavelength shifts which are expected to be very small.

The IR channel is equipped with a single filter wheel with 18 slots, containing 15 passband filters, two grisms, and an opaque element (also referred to as the BLANK) for dark current measurements. The filter complement samples the spectral region between 800 and 1700 nm. All of the IR filter elements are full-sized, covering the entire field of view of the IR detector. Since all of the elements are mounted in a single wheel, only one element can be used at a given time.

The 900–1700 nm wavelength range is covered by a series of wide- and medium-band filters, with little wavelength overlap. Additional medium-band filters are centered on molecular bands and nearby continua, and several narrow-band filters are available for probing interstellar and nebular recombination lines.

The filter set is designed to include the most popular passbands used in extragalactic, stellar, and solar-system astronomy, as well as passbands similar to those already used in previous *HST* instruments.

Table 7.2: WFC3 IR Channel Filters and Grisms.

| Name [1] | Description | Pivot[2] $\lambda p$ (nm) | Width[3] (nm) | Peak System Throughput |
|---|---|---|---|---|
| IR Wide-Band (W) Filters | | | | |
| F105W | Wide *Y* | 1055.2 | 265.0 | 0.52 |
| F110W | Wide *YJ* | 1153.4 | 443.0 | 0.56 |

| F125W | Wide $J$ | 1248.6 | 284.5 | 0.56 |
|---|---|---|---|---|
| F140W | Wide $JH$ gap; red grism reference | 1392.3 | 384.0 | 0.56 |
| F160W | WFC3 $H$ | 1536.9 | 268.3 | 0.56 |
| IR Medium-Band (M) Filters | | | | |
| F098M | Blue grism reference | 986.4 | 157.0 | 0.47 |
| F127M | $H_2O/CH_4$ continuum | 1274.0 | 68.8 | 0.54 |
| F139M | $H_2O/CH_4$ line | 1383.8 | 64.3 | 0.54 |
| F153M | $H_2O$ and $NH_3$ | 1532.2 | 68.5 | 0.55 |
| IR Narrow-Band (N) Filters | | | | |
| F126N | [Fe II] | 1258.5 | 15.2 | 0.50 |
| F128N | Paschen β | 1283.2 | 15.9 | 0.52 |
| F130N | Paschen β continuum | 1300.6 | 15.6 | 0.54 |
| F132N | Paschen β (redshifted) | 1318.8 | 16.1 | 0.52 |
| F164N | [Fe II] | 1640.4 | 20.9 | 0.47 |
| F167N | [Fe II] continuum | 1664.2 | 21.0 | 0.46 |
| IR Grisms (G) | | | | |
| G102 | "Blue" high-resolution grism | Useful range: 800–1150 nm[4] | | 0.41 |
| G141 | "Red" low-resolution grism | Useful range: 1075–1700 nm[4] | | 0.48 |

1 See Footnote 1 of Table 6.2 for naming conventions.
2 "Pivot wavelength" is defined as in Table 6.2 and Section 9.3. Filter transmissions were measured in helium but have been converted to vacuum wavelengths for this table.
3 Passband rectangular width, defined as in Table 6.2.
4 See Chapter 8 for IR Grism details.

**Wide-Band Filters**

The IR channel's versions of the ground-based *J* and *H* filters are F125W and F160W, respectively. The F125W filter has a width somewhat wider than that of a typical *J* passband used in ground-based cameras. The F160W filter's bandpass has been modified relative to ground-based *H* in order to give a better fit to the QE curve of the IR detector. Specifically, the WFC3 *H* filter's bandpass has been narrowed to approximately 1400-1700 nm, in order to limit thermal background and to have the filter define the bandpass on the red side rather than the detector sensitivity cutoff. By contrast, NICMOS *H* filter (NICMOS F160W) covers about 1400-1800 nm. This narrowing for WFC3 reduces photometric errors due to spatial variations in the detector's QE cutoff.

The wide F140W filter covers the gap between the *J* and *H* bands that is inaccessible from the ground. F105W has a central wavelength similar to ground-based *Y*, but is considerably wider. The IR channel also includes a very wide filter, F110W, spanning the ground-based *Y* and *J* bands. This filter can be used for deep imaging, with a bandpass fairly similar to that of the corresponding wide-band filter in NICMOS (also called F110W).

**Figure 7.2:** Integrated system throughput of the WFC3 IR wide-band filters, presented in two panels for clarity. The throughput calculations include the *HST* OTA, WFC3 IR-channel internal throughput, filter transmittance, and the QE of the IR detector.
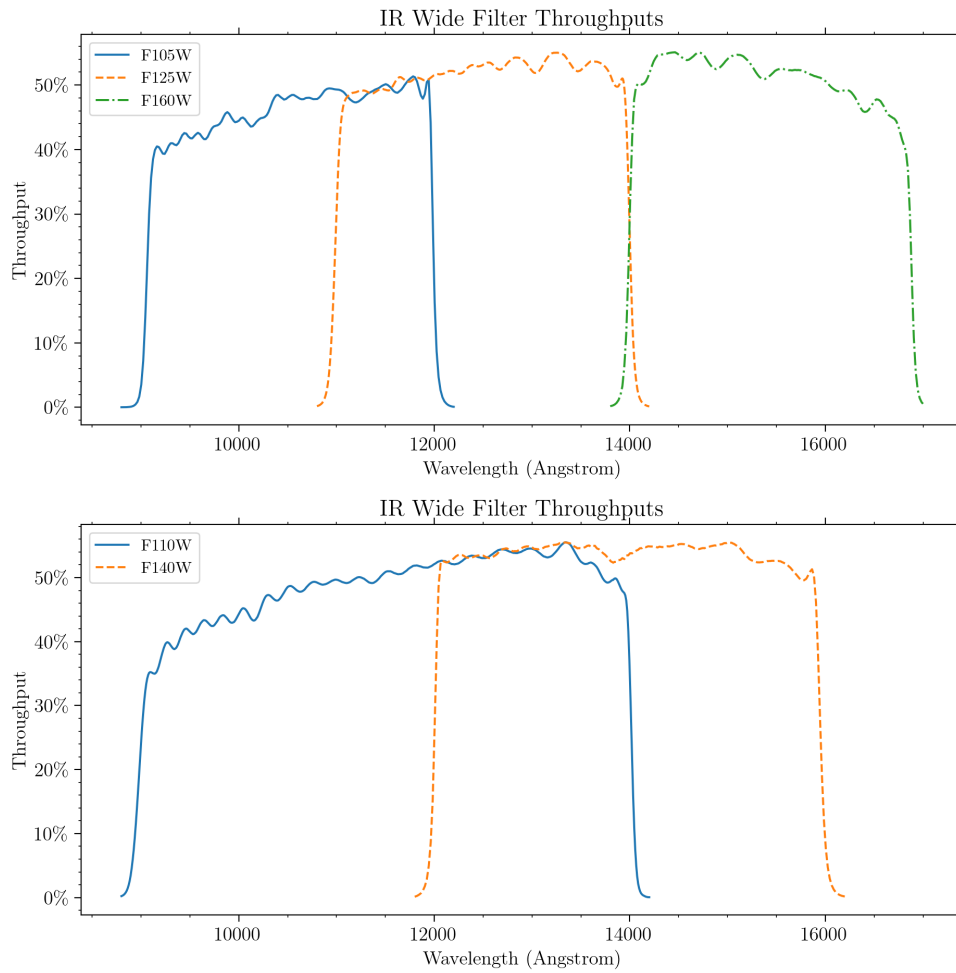


## Medium-Band filters

The F098M filter is useful as the G102 grism reference, allowing source selection and wavelength zero-point determination. It also complements the UVIS F845M filter, whose red 50% critical wavelength is ~900 nm. The overlap allows coverage over a continuous wavelength range across both WFC3 detectors.

The other medium filters span absorption bands of water and methane (F139M) and water and ammonia (F153M), with an adjacent continuum filter (F127M). These filters were intended for compositional studies of planets searching for water vapor (WFC3 ISR 2000-09). Solar system objects with visible inventories of these gas species are too bright to observe with the medium-band filters, and WFC3 lacks occulting hardware to access the high contrast ratios and small angular separations that would enable direct imaging of exoplanets. However, the high sensitivity of WFC3 enables compositional studies of the atmospheres of cool stars, brown dwarfs, and transiting exoplanets with the medium-band filters.

**Figure 7.3:** Integrated system throughput of the WFC3 IR medium-band filters. The throughput calculations include the *HST* OTA, WFC3 IR-channel internal throughput, filter transmittance, and the QE of the IR detector.
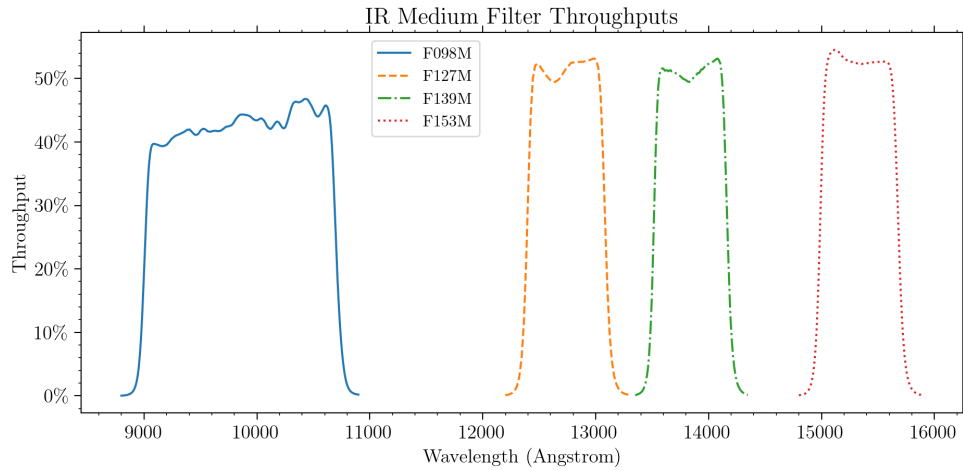


## Narrow-Band Filters

The IR channel includes six narrow-band filters which sample some of the most astrophysically-important planetary, stellar, and nebular spectral features in the near-IR (e.g., [Fe II] and Paschen-β).

Cosmological emission lines can be detected across a range of redshifts within the bandpasses of the narrow-band filters. Table 7.3 lists the redshifts that can be probed using the specified emission lines. These redshift ranges are offered as a guide; exact values depend on the wavelengths of the filter cutoffs. Filter cutoffs used in Table 7.3 were defined using the passband rectangular widths (defined in footnote 4 of Table 6.2). For consistency with Table 6.2, passband cutoffs were not centered on the filter pivot wavelengths $\lambda_p$ (defined in Section 9.3). Instead, a central wavelength for each filter was determined by maximizing the wavelength-integrated product of a rectangular passband of the specified width with the actual system throughput for the filter. For the IR narrow-band filters, these rectangular passband equivalent central wavelengths are within 0.3% of the pivot wavelengths.

**Figure 7.4:** Integrated system throughput of the WFC3 IR narrow-band filters. The throughput calculations include the HST OTA, WFC3 IR-channel internal throughput, filter transmittance, and the QE of the IR detector.
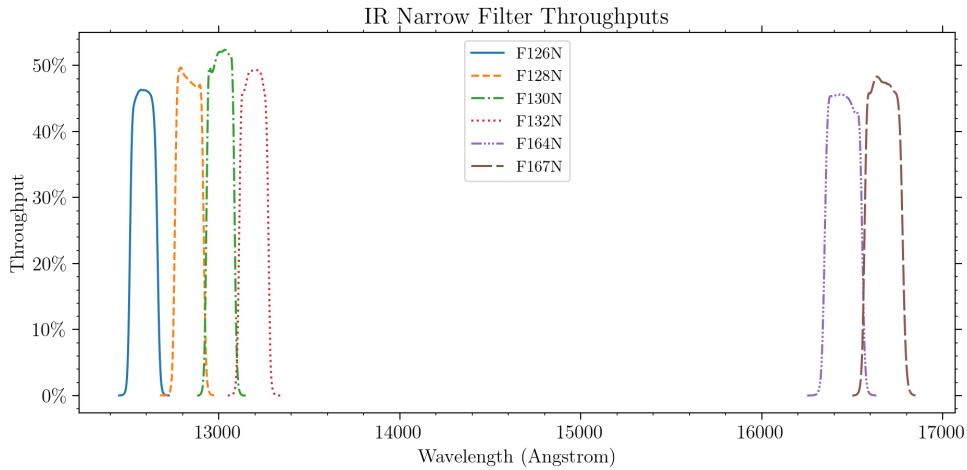


Table 7.3: Nominal redshift ranges for WFC3/IR narrow-band filters.

| Filter | Description | Filter $\lambda_p$ (nm) | Filter Width (nm) | Line Rest Wavelength (nm) | Minimum $cz$ (km/sec) | Maximum $cz$ (km/sec) |
|---|---|---|---|---|---|---|
| F126N | [Fe II] on | 1258.5 | 15.2 | 1256.7 | -1312 | 2314 |
| F128N | Pa β on or [Fe II] off | 1283.2 | 15.9 | 1281.8 | -1415 | 2304 |
| F130N | z (Pa β) or Pa β off | 1300.6 | 15.6 | 1281.8 | 2690 | 6338 |
| F132N | [Fe II] off or Pa β off | 1318.8 | 16.1 | | | |
| F164N | [Fe II] on | 1640.4 | 20.9 | 1643.6 | -1632 | 2180 |
| F167N | [Fe II] off | 1664.2 | 21.0 | 1643.6 | 2371 | 6202 |

## Grisms

The IR channel has two grisms that provide slitless spectra (see Chapter 8 for more details). The "blue" G102 grism provides a dispersion of 2.5 nm/pix (or a resolution of ~210) over the 800-1150 nm wavelength range. The "red" G141 grism has a dispersion of 4.7 nm/pix (resolution of ~130) over the 1100-1700 nm range. In most cases, a grism observation will be accompanied by a direct image, for source identification and wavelength calibration (see Section 8.3).

## 7.5.2 Filter Blue Leaks

All of the IR filters have been constructed using IR-transmitting colored glass with thin-film coatings to achieve the desired bandpasses. As with the UVIS filter designs, better in-band transmission generally means somewhat less suppression of out-of-band transmission. While the final IR filters have excellent in-band transmission (>90%), a few also have a small, narrow peak of transmission between 750-800 nm. After the filters were manufactured, a new IR detector was chosen which has appreciable sensitivity well down into the optical wavelength range (see Figure 5.25). Some of the IR filters thus have a small amount of blue leak (i.e., a small amount of short-wavelength out-of-band light is detected). None of the IR filters have significant red leaks.

Table 7.4 presents estimates of the blue-leak effect, listing the fraction of detected count rate expected from 710 to 830 nm for each filter. The throughput calculation includes transmission of the filter, the throughputs of the *HST* OTA and the IR optics, and the QE of the IR detector.

As can be seen from the table, blue leaks in all the wide-band and some of the narrow- and medium-band filters are minimal; however, several filters, notably F126N, F128N, and F153M, have some blue leak (e.g., ~1% for objects with effective temperatures of 5000 K.) In programs that may suffer adverse effects due to the blue leaks, it may be useful to obtain UVIS images in the F763M filter, which covers the problematic wavelength region (750-800 nm).

**Table 7.4: Fraction of detected count rate arising between wavelengths 710 to 830 nm as a function of effective temperature.**

| Filter | $T_{eff}$ (K) | | | | | | | | | | |
|--------|------|------|-------|-------|-------|-------|-------|-------|-------|-------|-------|
|        | 3500 | 5000 | 10000 | 15000 | 20000 | 25000 | 30000 | 35000 | 40000 | 45000 | 50000 |
| F098M | 3.8E-05 | 6.1E-05 | 8.4E-05 | 9.3E-05 | 9.8E-05 | 1.0E-04 | 1.0E-04 | 1.1E-04 | 1.1E-04 | 1.1E-04 | 1.1E-04 |
| F105W | 1.5E-05 | 2.2E-05 | 3.2E-05 | 3.5E-05 | 3.7E-05 | 3.9E-05 | 4.0E-05 | 4.1E-05 | 4.1E-05 | 4.1E-05 | 4.1E-05 |
| F110W | 8.8E-08 | 1.4E-07 | 2.4E-07 | 2.7E-07 | 2.9E-07 | 3.0E-07 | 3.1E-07 | 3.2E-07 | 3.2E-07 | 3.2E-07 | 3.2E-07 |
| F125W | 1.5E-07 | 2.4E-07 | 4.6E-07 | 5.3E-07 | 5.7E-07 | 6.1E-07 | 6.3E-07 | 6.5E-07 | 6.5E-07 | 6.5E-07 | 6.5E-07 |
| F126N | 6.4E-03 | 1.3E-02 | 2.6E-02 | 3.0E-02 | 3.3E-02 | 3.5E-02 | 3.6E-02 | 3.7E-02 | 3.8E-02 | 3.8E-02 | 3.8E-02 |
| F127M | 1.6E-03 | 3.2E-03 | 6.9E-03 | 8.0E-03 | 8.7E-03 | 9.2E-03 | 9.6E-03 | 9.8E-03 | 9.9E-03 | 1.0E-02 | 1.0E-02 |
| F128N | 5.7E-03 | 1.2E-02 | 2.7E-02 | 3.1E-02 | 3.3E-02 | 3.5E-02 | 3.6E-02 | 3.7E-02 | 3.7E-02 | 3.7E-02 | 3.7E-02 |
| F130N | 3.8E-04 | 6.7E-04 | 1.4E-03 | 1.6E-03 | 1.8E-03 | 1.9E-03 | 2.0E-03 | 2.0E-03 | 2.1E-03 | 2.1E-03 | 2.1E-03 |

| | | | | | | | | | | |
|---|---|---|---|---|---|---|---|---|---|---|
| F132N | 3.7E-04 | 6.6E-04 | 1.4E-03 | 1.7E-03 | 1.8E-03 | 1.9E-03 | 2.0E-03 | 2.1E-03 | 2.1E-03 | 2.1E-03 | 2.1E-03 |
| F139M | 2.2E-03 | 3.9E-03 | 9.0E-03 | 1.1E-02 | 1.2E-02 | 1.3E-02 | 1.3E-02 | 1.4E-02 | 1.4E-02 | 1.4E-02 | 1.4E-02 |
| F140W | 6.3E-05 | 1.0E-04 | 2.4E-04 | 2.9E-04 | 3.2E-04 | 3.4E-04 | 3.5E-04 | 3.7E-04 | 3.7E-04 | 3.7E-04 | 3.7E-04 |
| F153M | 5.6E-03 | 9.9E-03 | 2.8E-02 | 3.3E-02 | 3.6E-02 | 3.9E-02 | 4.1E-02 | 4.2E-02 | 4.3E-02 | 4.3E-02 | 4.3E-02 |
| F160W | 9.4E-05 | 1.7E-04 | 4.8E-04 | 5.7E-04 | 6.3E-04 | 6.8E-04 | 7.1E-04 | 7.4E-04 | 7.4E-04 | 7.5E-04 | 7.5E-04 |
| F164N | 3.8E-03 | 8.0E-03 | 2.6E-02 | 3.1E-02 | 3.4E-02 | 3.7E-02 | 3.9E-02 | 4.0E-02 | 4.0E-02 | 4.1E-02 | 4.1E-02 |
| F167N | 3.3E-03 | 7.0E-03 | 2.2E-02 | 2.7E-02 | 3.0E-02 | 3.2E-02 | 3.4E-02 | 3.6E-02 | 3.6E-02 | 3.6E-02 | 3.6E-02 |

## 7.5.3 Ghosts

No significant optical ghosts are present in the IR channel.

# 7.6 IR Optical Performance

Following WFC3's alignment to the OTA (WFC3 ISR 2009-46), a series of observations through a variety of filters were obtained to demonstrate the instrument's optical performance. The WFC3 IR channel meets or exceeds all image quality expectations. The following subsections summarize the measured flight optical performance for the IR channel, as described by its point-spread function (PSF), i.e., the spatial distribution of the flux in an image of a point source. The results shown are produced using an optical model which has been adjusted and correlated to the PSFs measured on-orbit and represent mean values averaged over the field (WFC3 ISR 2009-37). This PSF model includes the pupil geometry, including the cold stop, residual aberration, the mid-frequency wavefront error of the OTA, the effect of the detector inter-pixel capacitive cross-talk, and first-order geometric distortion.

## 7.6.1 PSF Width and Sharpness

The IR channel PSFs are well approximated by Gaussian profiles (before pixelation). As was discussed in more detail for the UVIS channel in Section 6.6.1, the PSFs can usefully be characterized by their FWHM or their sharpness, effectively the reciprocal of the number of pixels occupied by a point source (as defined in Section 6.6.1). Table 7.5 lists the FWHM of the model PSF core (before pixelation) in units of pixel and arcsec and the sharpness parameter for 10 wavelengths. The sharpness range shown for each wavelength indicates the values for the PSF centered on the pixel corners and center. The monotonic increase in FWHM and decrease in sharpness with wavelength is due to diffraction.

Table 7.5: WFC3/IR PSF FWHM (before pixelation, in units of pixels and arcseconds), and sharpness, vs. wavelength. (Note that attempts to measure the FWHM by fitting functions to the pixelated PSF will generally yield larger values.)

| Wavelength (nm) | FWHM (pix) | FWHM (arcsec) | Sharpness |
|---|---|---|---|
| 800 | 0.971 | 0.124 | 0.127–0.197 |
| 900 | 0.986 | 0.126 | 0.118–0.182 |
| 1000 | 1.001 | 0.128 | 0.109–0.169 |
| 1100 | 1.019 | 0.130 | 0.100–0.156 |
| 1200 | 1.040 | 0.133 | 0.093–0.144 |
| 1300 | 1.067 | 0.137 | 0.087–0.132 |
| 1400 | 1.100 | 0.141 | 0.083–0.121 |
| 1500 | 1.136 | 0.145 | 0.080–0.112 |

| 1600 | 1.176 | 0.151 | 0.077–0.102 |
| 1700 | 1.219 | 0.156 | 0.074–0.093 |

Figure 7.5 plots the azimuthally-averaged model OTA+WFC3 PSF at three different IR wavelengths., indicating the fractional PSF flux per pixel at radii from 1 pixel to 5 arcsec.

**Figure 7.5: Azimuthally averaged WFC3/IR PSF.**
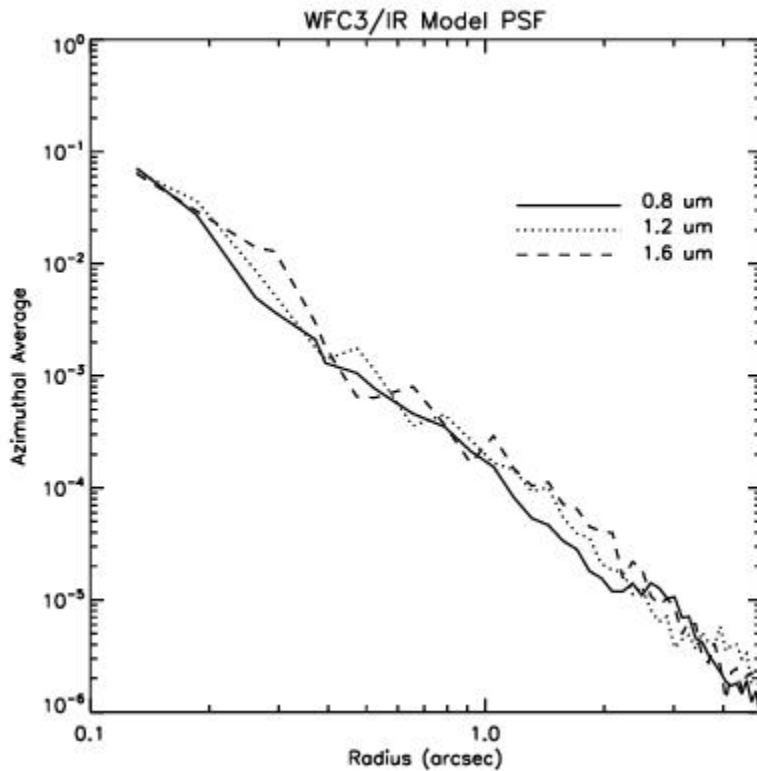


## 7.6.2 Encircled Energy

As described in more detail in Section 6.6.2 for the UVIS channel, encircled energy, the fraction of light contained in a circular aperture is one useful way of characterizing well-behaved profiles. Encircled energy profiles for the IR channel model PSF at three representative wavelengths are plotted in Figure 7.6. Empirical encircled energy values for 11 select aperture radii are presented in Table 7.6 (see WFC3 ISR 2009-37 for more details). The WFC3 IR Encircled Energy webpage provides the encircled energy curves for 19 total aperture radii as a downloadable file.

Figure 7.6: Encircled Energy for the WFC3/IR channel.
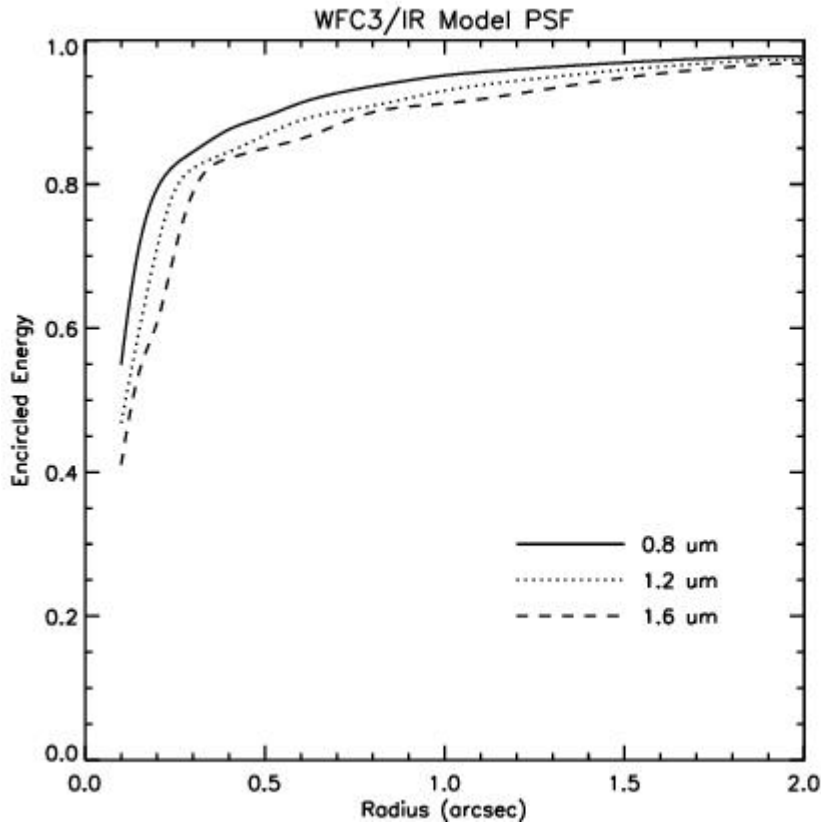


Table 7.6: WFC3/IR PSF Encircled Energy Fraction vs. Aperture Radius (arcsec).

| Filter | Wavelength (Å) | Aperture (arcsec) | | | | | | | | | | |
|---|---|---|---|---|---|---|---|---|---|---|---|---|
| | | 0.13 | 0.26 | 0.39 | 0.52 | 0.65 | 0.78 | 0.91 | 1.0 | 1.3 | 2.0 | 6.0 |
| F098M | 9865 | 0.596 | 0.818 | 0.857 | 0.887 | 0.905 | 0.922 | 0.934 | 0.943 | 0.956 | 0.974 | 1 |
| F105W | 10551 | 0.577 | 0.811 | 0.852 | 0.882 | 0.901 | 0.917 | 0.929 | 0.939 | 0.953 | 0.973 | 1 |
| F110W | 11534 | 0.553 | 0.797 | 0.845 | 0.873 | 0.895 | 0.909 | 0.922 | 0.933 | 0.948 | 0.97 | 1 |
| F125W | 12486 | 0.535 | 0.789 | 0.841 | 0.867 | 0.89 | 0.904 | 0.918 | 0.929 | 0.945 | 0.969 | 1 |
| F126N | 12585 | 0.534 | 0.789 | 0.84 | 0.867 | 0.89 | 0.904 | 0.917 | 0.929 | 0.944 | 0.969 | 1 |
| F127M | 12740 | 0.531 | 0.787 | 0.84 | 0.865 | 0.89 | 0.903 | 0.916 | 0.929 | 0.944 | 0.968 | 1 |
| F128N | 12832 | 0.529 | 0.786 | 0.839 | 0.865 | 0.889 | 0.902 | 0.916 | 0.928 | 0.943 | 0.968 | 1 |
| F130N | 13006 | 0.526 | 0.784 | 0.838 | 0.863 | 0.888 | 0.901 | 0.915 | 0.927 | 0.942 | 0.968 | 1 |
| F132N | 13188 | 0.523 | 0.78 | 0.838 | 0.862 | 0.887 | 0.9 | 0.914 | 0.926 | 0.942 | 0.967 | 1 |
| F139M | 13838 | 0.513 | 0.769 | 0.836 | 0.858 | 0.882 | 0.898 | 0.912 | 0.923 | 0.939 | 0.966 | 1 |
| F140W | 13923 | 0.512 | 0.764 | 0.837 | 0.86 | 0.882 | 0.9 | 0.912 | 0.923 | 0.94 | 0.967 | 1 |
| F153M | 15322 | 0.496 | 0.74 | 0.835 | 0.856 | 0.876 | 0.899 | 0.909 | 0.918 | 0.937 | 0.967 | 1 |

| F160W | 15369 | 0.494 | 0.736 | 0.833 | 0.855 | 0.875 | 0.897 | 0.908 | 0.918 | 0.935 | 0.966 | 1 |
|-------|-------|-------|-------|-------|-------|-------|-------|-------|-------|-------|-------|---|
| F164N | 16404 | 0.483 | 0.713 | 0.829 | 0.852 | 0.87 | 0.894 | 0.905 | 0.914 | 0.932 | 0.963 | 1 |
| F167N | 16642 | 0.48 | 0.706 | 0.828 | 0.851 | 0.869 | 0.893 | 0.904 | 0.913 | 0.931 | 0.962 | 1 |

During initial on-orbit tests in SMOV, high-dynamic-range isolated star images were obtained through several filters (WFC3 ISR 2009-37). These are shown with a logarithmic stretch in Figure 7.7. The images appear slightly elongated vertically, due to the 24 degree tilt of the detector to the chief ray and the fact that a distortion correction has not been applied. Although the target was chosen to be isolated, a number of field galaxies appear in both the F098M and the F160W filter images; these are also seen in long wavelength UVIS channel images of the same target (Figure 6.13). Some detector artifacts, including cold and warm pixels and imperfectly removed cosmic ray hits are evident.

Figure 7.7: High dynamic range WFC3/IR star images through F098M (left) and F160W (right) subtending ~20 arcsec on each side near field center. No distortion correction has been applied. Stretch is logarithmic from $10^{-3}$ to $10^3$ e$^-$ sec$^{-1}$ pixel$^{-1}$. Faint galaxies appear in the background.
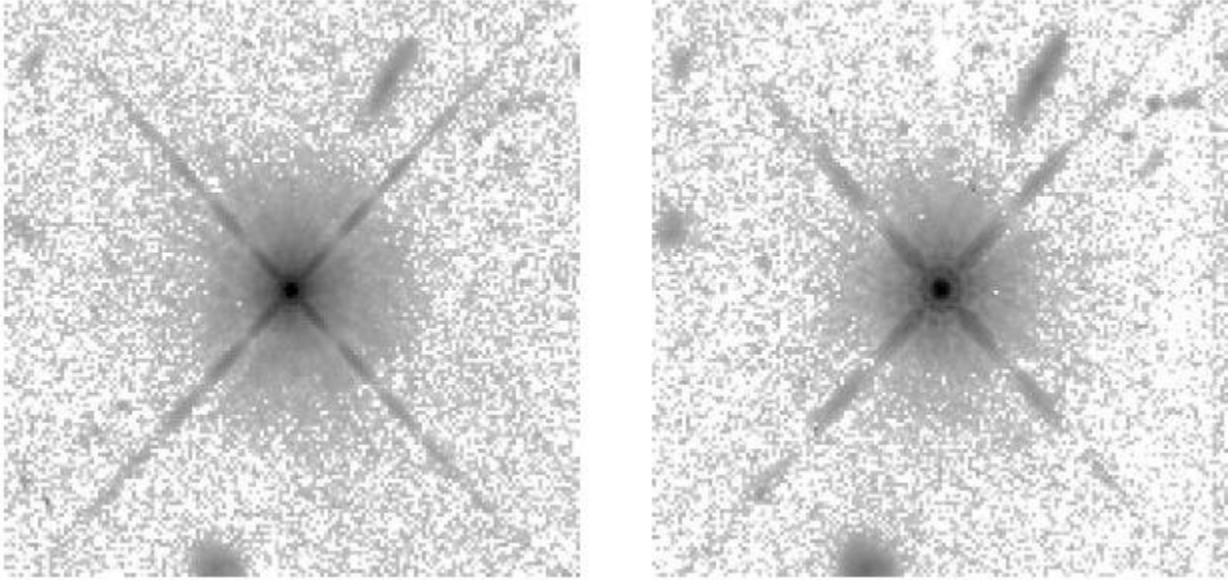


## 7.6.3 Other PSF Behavior and Characteristics

### Temporal Dependence of the PSF: *HST* Breathing

All *HST* observations are affected to some extent by short-term focus variations ("breathing"), which arise from the changing thermal environment of *HST* (See Section 6.6.3). For the IR channel, breathing is expected to produce variations of ~0.3% and less than 0.1% in the FWHM of the PSF of WFC3/IR at 700 nm and at wavelengths longer than 1100 nm, respectively, on typical time scales of one orbit.

### Intra-Pixel Response

The response of a pixel of an IR detector to light from an unresolved source varies with the positioning of the source within the pixel due to low sensitivity at the pixel's edges and dead zones between pixels. For the WFC3/IR flight detector, no measurable intra-pixel sensitivity variation was found during ground testing (WFC3 ISR 2008-19) or in-flight testing (WFC3 ISR 2011-19). For NICMOS, the intra-pixel sensitivity was found to be an important effect: it varied by as much as 40% (peak to valley). The WFC3 small pixel size (18 μm vs. NICMOS's 40 μm) and the much higher WFC3/IR detector temperature compared to NICMOS are probably responsible for this improvement.

**Inter-Pixel Capacitance**

The small pixel size, relative to that in NICMOS, increases the relevance of capacitive coupling between nearby pixels (Brown et. al., 2006, *PASP*, **118**, 1443; Moore et. al., 2006, Opt. Eng., 076402). It affects the gain measurements and the PSF. The easiest method of estimating the inter-pixel capacitance is to measure the ratio of DNs in pixels adjacent to a "hot" (high-dark-current) pixel to the DNs in the hot pixel. In the WFC3 IR detector, on the order of 5% of electrons may leak to the adjacent pixels. WFC3 ISR 2008-26 describes a method for correcting inter-pixel capacitance using Fourier deconvolution, and demonstrates its effectiveness on WFC3/IR ground-testing data. WFC3 ISR 2011-10 provides an improved deconvolution kernel with distinct values for each of the 8 pixels surrounding the central pixel.

## 7.6.4 Super-sampled PSF Models

The concept of empirical net ("effective") models of PSFs is introduced in Section 6.6.4. The WFC3/IR PSF has recently been modeled in WFC3 ISR 2016-12 for five commonly used filters (F105W, F110W, F125W, F140W, and F160W); these models are available to download on the WFC3 PSF webpage.

Figure 7.8 shows a log image of the F105W PSF in super-sampled (4x) pixels. The WFC3/IR PSF is extremely under-sampled by the detector pixels: over 40 percent of a star's flux will land in its central pixel if the star is centered on that pixel. Only 4 percent will fall in the directly adjacent pixels. Even with this extreme under-sampling, the 4x super-sampled grid-base model is easily able to represent the PSF.

**Figure 7.8: An image of the central WFC3/IR PSF for F105W where the PSF is super-sampled by a factor of 4 relative to the WFC3/IR image pixels.**
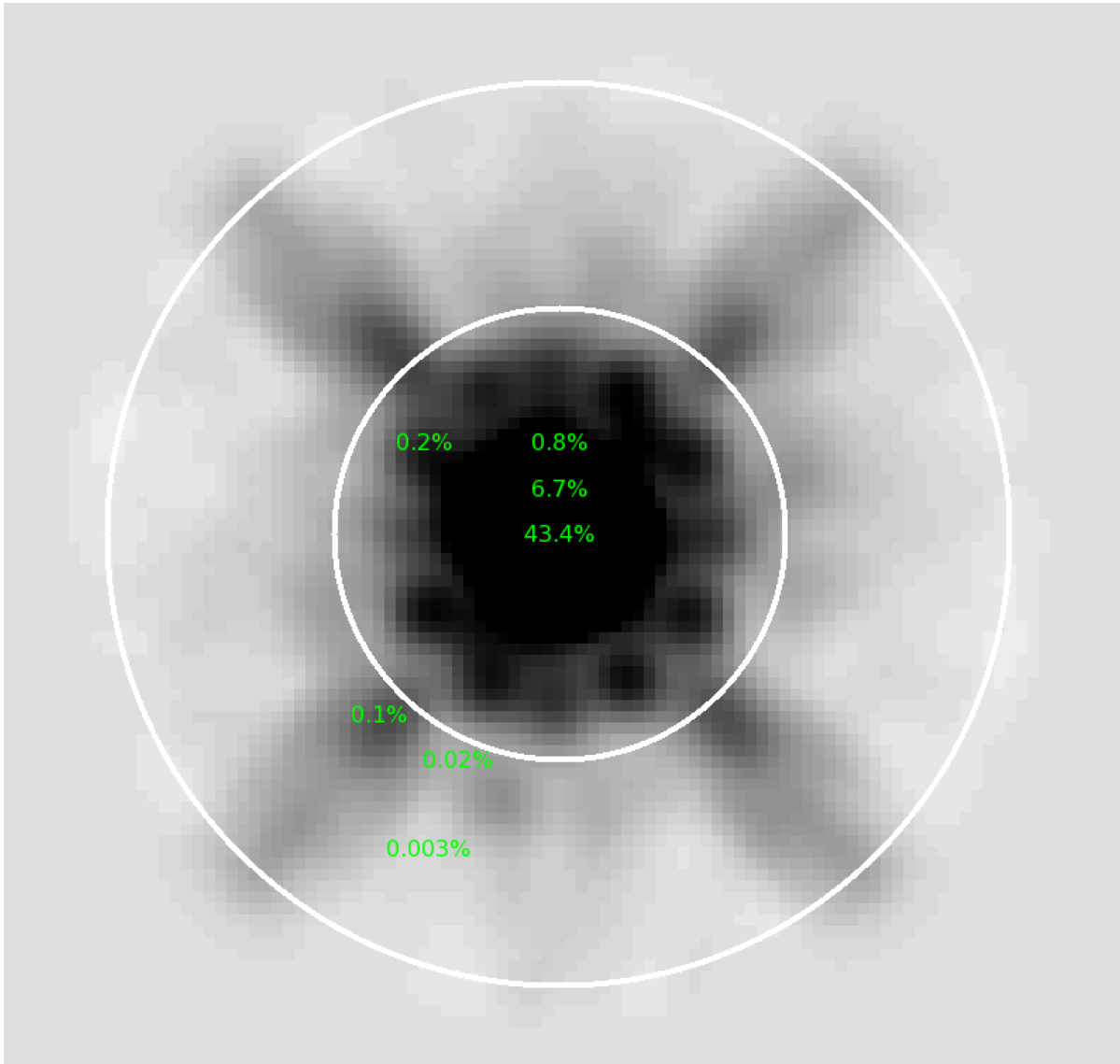


The white circles are drawn at r=5 and r=10 image pixels. The central label (43.4%) shows how much of the star's flux should be received by a pixel if the star happens to be centered on exactly that pixel. The label above it (6.7%) is the fraction of a star's flux which would land in a pixel that is exactly one image-pixel above the center of the star. The 0.8% label is the amount of light which would land in a pixel two up from the center of a star. The other labels show the fraction of light that lands in pixels at various other locations in the PSF: on inner-halo bumps (0.2%), on diffraction spikes at a distance of ~5 image pixels (0.1%), in the outer PSF halo at ~5 image pixels (0.02%) and in the outer halo at ~7.5 image pixels (0.003%).

Figure 7.9 illustrates how the WFC3/IR PSF varies across the face of the 1014 × 1014 pixel detector. A 3 × 3 array of models is adequate to represent the PSF across the detector.

Figure 7.9: For 9 locations on the detector in a 3 × 3 grid, a greyscale image shows the difference between each super-sampled PSF and the average of the PSFs. Dark represents more flux, and light less flux. The largest variation is about 0.04, which is about 10% of the central value of the PSF.
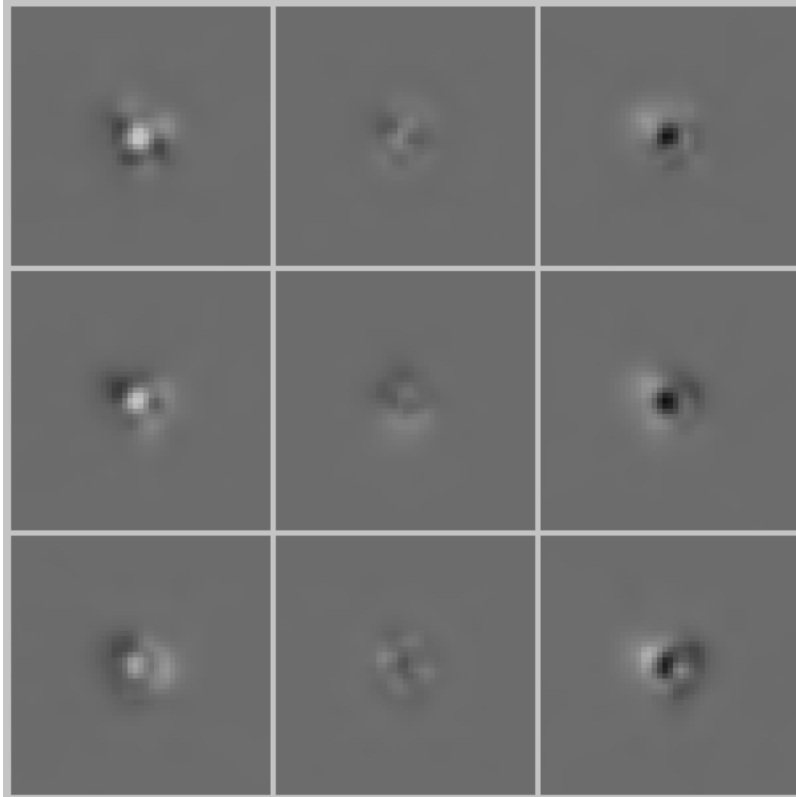


As mentioned in Section 6.6.4, the flt-frames provide the only clean constraints on the scene. Our high-precision PSF models are designed to be used in this frame, even though dithering and distortion make such analysis complicated. The WFC3 instrument team has produced some tools that can help users make use of these PSFs. WFC3 ISR 2016-12 contains some FORTRAN routines that show how to use the WFC3/IR PSFs, and the resulting spatially variable, super-sampled models of the IR PSF can be found on the WFC3 PSF webpage, which contains additional resources relating to PSFs. Additionally, a software routine that makes use of the PSFs to measure stars in HST images was recently released. This routine is named `hst1pass`, and WFC3 ISR 2022-05 describes how it can be downloaded and run.

In an effort to supplement these super-sampled model PSFs, the WFC3 team recently has built a searchable database of over 5 million WFC3/IR extracted star images (PSFs) from 2009 to 2023 (see WFC3 ISR 2021-12 and the WFC3 PSF Search webpage for more details). These images of PSFs can then be employed to generate PSFs that for users' observations and other science needs.

# 7.7 IR Exposure and Readout

The general operating modes of IR detectors have been described in Chapter 5. In this section we will detail the readout modes implemented in WFC3.

## 7.7.1 Exposure Time

Unlike the UVIS channel, the IR channel does not have a mechanical shutter. Integration times are thus determined purely electronically, by resetting the charge on the detector, and then accumulating signal until the exposure is completed. A second major difference from the UVIS channel is that the IR detector is read out non-destructively as the exposure accumulates, as opposed to the single destructive readout at the end of a CCD exposure.

There are pre-defined accumulation and readout sequences available to IR observers, which are used to set the total exposure time as described in the next subsection.

## 7.7.2 MULTIACCUM Mode

In IR observing it is possible, and desirable, to sample the signal multiple times as an exposure accumulates, and the MULTIACCUM mode accomplishes this. MULTIACCUM is the only observing mode available for the IR channel.

Multiple readouts offer three major advantages. First, the multiple reads provide a way to record a signal in a pixel before it saturates, thus effectively increasing the dynamic range of the final image. Second, the multiple reads can be analyzed to isolate and remove cosmic-ray events. Third, fitting to multiple reads provides a means for reducing the net effective read noise, which is relatively high for the IR detector.

The disadvantage of multiple readouts is that they are data-intensive. The HgCdTe detector array is 1024 × 1024 pixels, which is only about 1/16 by pixel number of the 4096 × 4102 UVIS array. However, since up to 16 IR readouts are used, the total data volume of a single IR exposure approaches that of a single UVIS frame. A maximum of 32 IR full array readouts can be stored in the instrument buffer, after which the content of the buffer must be dumped to the *HST* Solid State Recorder (SSR). A buffer dump of 16 full array reads takes about 5.8 minutes.

MULTIACCUM readout consists of the following sequence of events:

1. **Array reset**: After a fast calibration of the analog-to-digital converters, all pixels are set to the detector bias level via two rapid reset cycles of the entire chip.
2. **Array read**: The charge in each pixel is measured and stored in the on-board computer's memory. This is done as soon as practical after the second array reset in step 1. In effect, given the short delay and the time needed to read the array, a very short-exposure image is stored in memory. This is known as the zero read.
3. **Multiple integration-read cycles**: The detector integrates for a certain amount of time and then the charge in each pixel is read out. This step can be repeated up to a total of 15 times

following the zero read during the exposure. All frames are individually stored in the on-board computer memory. Note that it takes a finite time (2.93 sec) to read the full array, so there is a time delay between reading the first and last pixel. Because this delay is constant for each read, it cancels out in difference images.

4. **Return to idle mode**: The detector returns to idle mode, where it is continuously flushed in order to prevent charge build-up and to limit the formation of residual images.

All sequences start with the same "reset, reset, read, read" sequence, where the two reads are done as quickly as possible. This "double reset read" was originally implemented because the very first read after the reset may show an offset that does not reproduce in the following reads.

## 7.7.3 MULTIACCUM Timing Sequences: Full Array Apertures

There are 12 pre-defined sample sequences, optimized to cover a wide range of observing situations, available for the full-frame IR apertures. *(See Section 7.7.4 for a discussion of the sample sequences available for the IR subarray apertures. The same names are used for the sample sequences, but the times are different.)* The maximum number of reads (following the zero read) during an exposure is 15, which are collected as the signal ramps up. It is possible to select less than 15 reads, thus cutting the ramp short and reducing the total exposure time. However, the timing of the individual reads within any of the 12 sequences cannot be adjusted by the user. This approach has been adopted as  the optimal calibration of IR detectors requires a dedicated set of reference files (e.g., dark frames) for each timing pattern.

In summary, a WFC3/IR exposure is fully specified by choosing:

- one of the 12 available pre-defined timing sequences, and
- the total number of samples (NSAMP, which must be no more than 15), which determines the total exposure time

The 11 timing sequences for the IR channel are:

- One **RAPID** sequence: the detector is sampled with the shortest possible time interval between reads.

- Six linear (**SPARS**) sequences: the detector is sampled with uniform time intervals between reads, a so-called "linear sample up the ramp." ("SPARS" is a contraction of the word "sparse.")
- Five rapid-log-linear (**STEP**) sequences: the detector is initially sampled with the shortest possible time interval between reads, then uses logarithmically spaced reads to transition to a sequence of uniform samples.

All 12 of the sequences above refer to readouts of the full 1024 × 1024 detector array. See Section 7.7.4 below for the timing sequences available for subarrays. Details of the sequences are in the following paragraphs. The timings of the individual reads are given in Table 7.8.

### RAPID Sequence

The RAPID sequence provides linear sampling at the fastest possible speed. For the full array, this equates to one frame every 2.9 s, and the entire set of 16 reads completed in less than 44 s. The RAPID mode is mainly intended for the brightest targets. Due to the overheads imposed by buffer dumps (see Chapter 10), observations in this mode done continuously would have low observing efficiency.

**SPARS Sequences**

The SPARS sequences use evenly spaced time intervals between reads. The six available SPARS sequences are designated SPARS5, SPARS10, SPARS25, SPARS50, SPARS100 and SPARS200, corresponding to sampling intervals of approximately 5, 10, 25, 50, 100, and 200 s, respectively.

The SPARS modes can be regarded as the most basic readout modes, and they are applicable to a wide range of target fluxes. They provide flexibility in integration time and are well-suited to fill an orbital visibility period with several exposures.

SPARS5, introduced during cycle 23, has time steps intermediate between those of RAPID and SPARS10. It is especially useful for spatially scanned grism observations of bright stars (see Section 8.6) with subarray apertures (see Section 7.7.4).

**STEP Sequences**

The five available rapid-logarithmic-linear sequences are STEP25, STEP50, STEP100, STEP200, and STEP400. They begin with linear spacing (the same as the RAPID sequence), continue with logarithmic spacing up to the given number of seconds (e.g., 50 s for STEP50), and then conclude with linear spacing in increments of the given number of seconds for the remainder of the sequence. See Figure 7.10 for an illustration of a STEP sequence.

The STEP mode is intended to provide a more uniform sampling across a wide range of stellar magnitudes, which is especially important for imaging fields containing both faint and bright targets. The faint targets require a long, linearly sampled integration, while the bright targets need to be sampled several times early in the exposure, before they saturate. Thus, the dynamic range of the final image is increased.

Figure 7.10: Example of STEP sequence with NSAMP=4. NSAMP+1 images are stored in the observer's FITS image
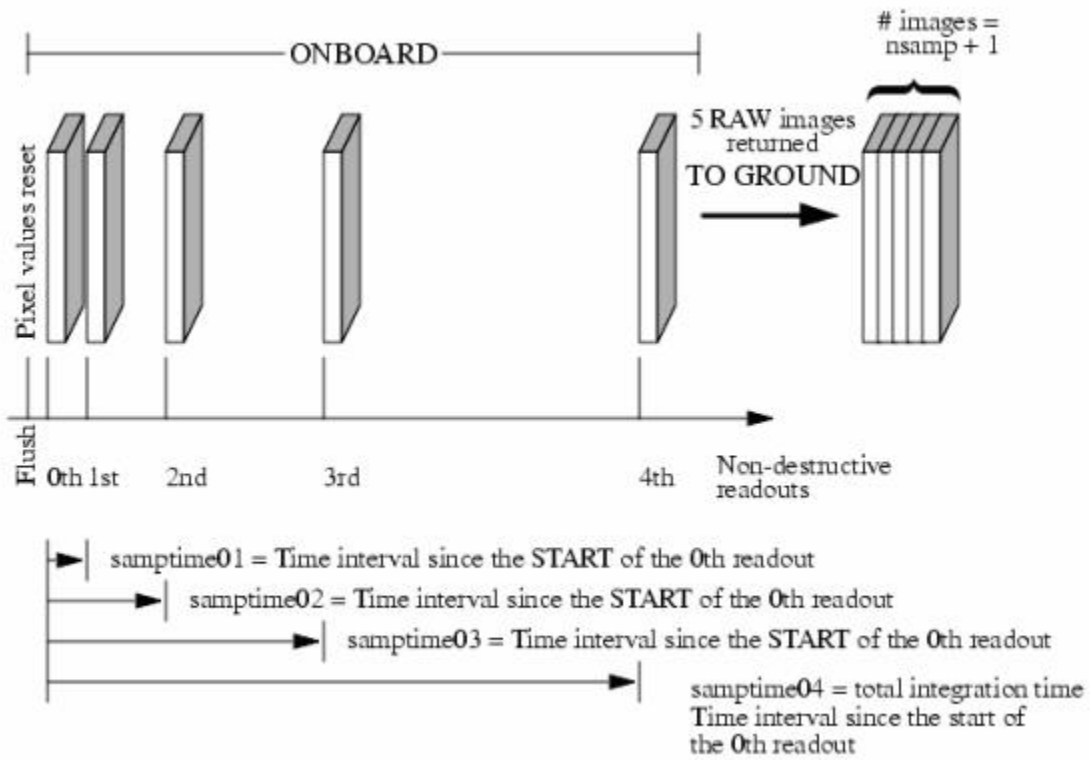


Table 7.8: Sample times of 1024 × 1024 MULTIACCUM readouts in seconds (this information is also in Table 13.4 of the *Phase II Proposal Instructions).*

| NSAMP | RAPID (sec) | SPARS (sec) | | | | | |
|---|---|---|---|---|---|---|---|
| | | SPARS5 | SPARS10 | SPARS25 | SPARS50 | SPARS100 | SPARS200 |
| 1 | 2.932 | 2.932 | 2.932 | 2.932 | 2.932 | 2.932 | 2.932 |
| 2 | 5.865 | 7.933 | 12.933 | 27.933 | 52.933 | 102.933 | 202.932 |
| 3 | 8.797 | 12.934 | 22.934 | 52.933 | 102.933 | 202.933 | 402.932 |
| 4 | 11.729 | 17.935 | 32.935 | 77.934 | 152.934 | 302.933 | 602.932 |
| 5 | 14.661 | 22.935 | 42.936 | 102.934 | 202.934 | 402.934 | 802.933 |
| 6 | 17.594 | 27.936 | 52.937 | 127.935 | 252.935 | 502.934 | 1002.933 |
| 7 | 20.526 | 32.937 | 62.938 | 152.935 | 302.935 | 602.934 | 1202.933 |
| 8 | 23.458 | 37.938 | 72.939 | 177.936 | 352.935 | 702.935 | 1402.933 |

| 9 | 26.391 | 42.938 | 82.940 | 202.936 | 402.936 | 802.935 | 1602.933 |
|---|---|---|---|---|---|---|---|
| 10 | 29.323 | 47.939 | 92.941 | 227.937 | 452.936 | 902.935 | 1802.933 |
| 11 | 32.255 | 52.940 | 102.942 | 252.937 | 502.937 | 1002.936 | 2002.933 |
| 12 | 35.187 | 57.941 | 112.943 | 277.938 | 552.937 | 1102.936 | 2202.933 |
| 13 | 38.120 | 62.942 | 122.944 | 302.938 | 602.938 | 1202.936 | 2402.933 |
| 14 | 41.052 | 67.942 | 132.945 | 327.939 | 652.938 | 1302.936 | 2602.933 |
| 15 | 43.984 | 72.943 | 142.946 | 352.940 | 702.939 | 1402.937 | 2802.933 |
|  |  |  |  |  |  |  |  |

| NSAMP | RAPID (sec) | STEP (sec) | | | | | |
|---|---|---|---|---|---|---|---|
|  |  | STEP25 | STEP50 | STEP100 | STEP200 | STEP400 | |
| 1 | 2.932 | 2.932 | 2.932 | 2.932 | 2.932 | 2.932 | |
| 2 | 5.865 | 5.865 | 5.865 | 5.865 | 5.865 | 5.865 | |
| 3 | 8.797 | 8.797 | 8.797 | 8.797 | 8.797 | 8.797 | |
| 4 | 11.729 | 11.729 | 11.729 | 11.729 | 11.729 | 11.729 | |
| 5 | 14.661 | 24.230 | 24.230 | 24.230 | 24.230 | 24.230 | |
| 6 | 17.594 | 49.230 | 49.230 | 49.230 | 49.230 | 49.230 | |
| 7 | 20.526 | 74.231 | 99.231 | 99.231 | 99.231 | 99.231 | |
| 8 | 23.458 | 99.231 | 149.231 | 199.231 | 199.231 | 199.231 | |
| 9 | 26.391 | 124.232 | 199.232 | 299.231 | 399.231 | 399.231 | |
| 10 | 29.323 | 149.232 | 249.232 | 399.232 | 599.231 | 799.232 | |
| 11 | 32.255 | 174.233 | 299.232 | 499.232 | 799.231 | 1199.232 | |
| 12 | 35.187 | 199.233 | 349.233 | 599.232 | 999.231 | 1599.233 | |
| 13 | 38.120 | 224.234 | 399.233 | 699.233 | 1199.231 | 1999.233 | |
| 14 | 41.052 | 249.234 | 449.234 | 799.233 | 1399.231 | 2399.234 | |
| 15 | 43.984 | 274.235 | 499.234 | 899.233 | 1599.231 | 2799.235 | |

## 7.7.4 MULTIACCUM Timing Sequences: Subarray Apertures

As described in Section 7.4.4, subarrays are available in order to reduce data volume and enable short exposure times, defined in sample sequences. *For a given sample sequence name, the sample times are shorter for smaller subarrays.* Note that only certain combinations of subarrays and sample sequences are supported by STScI. Other MULTIACCUM sequences can be used in principle but are not supported, and additional calibration observations would have to be made by the observer. The supported combinations are presented in Table 7.9. The exposure times may be found in the *Phase II Proposal Instructions*, Chapter 12 (Wide Field Camera 3).

SPARS5, introduced during Oct 2015 (cycle 23), is especially useful for spatially scanned grism observations of bright stars (see Section 8.6).

Certain combinations of IR subarrays and sample sequences give rise to images containing a sudden low-level jump in the overall background level of the image. Observers can avoid this effect by ordering image sizes within a visit from large to small (see Section 7.4.4).

Table 7.9: Supported subarray sample sequences.

| Aperture | Sample Sequence | | | | |
|---|---|---|---|---|---|
| | RAPID | SPARS5 | SPARS10 | SPARS25 | STEP25 |
| IRSUB64 | yes | no | no | no | no |
| IRSUB64-FIX | yes | no | no | no | no |
| IRSUB128 | yes | no | yes | no | no |
| IRSUB128-FIX | yes | no | yes | no | no |
| IRSUB256 | yes | yes | yes | yes | no |
| IRSUB256-FIX | yes | yes | yes | yes | no |
| IRSUB512 | yes | yes | no | yes | yes |
| IRSUB512-FIX | yes | yes | no | yes | yes |

✓ See Section 12.3.1 of the *Phase II Proposal Instructions*, Tables 12.6 to 12.7, for the sample times associated with each combination of sample sequence and subarray size. Note that the sample times for a given sample sequence name are shorter for smaller subarrays.

# 7.8 IR Sensitivity

## 7.8.1 Limiting Magnitudes

Table 7.10 presents the predicted limiting-magnitude performance of the WFC3 IR channel and compares it with that of the camera 3 on NICMOS (NIC3). The calculations are based on an optimal extraction of a point source. The limiting ABMAG at an SNR of 10 was calculated for a 1-hour and a 10-hour exposure. The throughput curves for the WFC3 filters listed in column 2 were used; for NIC3, the most similar wide-band filter was used, and its name is given in column 3.

An online Exposure Time Calculator (ETC) is available (see Section 9.2).

Table 7.10: Limiting-magnitude performance of WFC3 compared with that of the NICMOS NIC3, based on on-orbit sensitivity from SMOV.

| Band | Filter | | | Limiting magnitude in 1 hr | | | Limiting magnitude in 10 hrs | |
|------|--------|------|---|------|------|---|------|------|
| | WFC3 | NIC3 | | WFC3 | NIC3 | | WFC3 | NIC3 |
| J | F110W | F110W | | 27.3 | 26.1 | | 28.6 | 27.4 |
| H | F160W | F160W | | 26.6 | 25.9 | | 27.9 | 27.1 |

## 7.8.2 Sensitivity

⚠ Note: new reference files and calibration pipeline updates discussed in this section were not "live" at the original date of publication. This banner will be removed when these are available.

The WFC3/IR detector exhibits a low level sensitivity loss at rates of ~0.1% per year, with greater losses at shorter wavelengths (WFC3 ISR 2024-06). The total sensitivity loss since WFC3 installation in 2009 is ~ 1-2%, comparable to the IR detector repeatability (WFC3 ISR 2024-01; WFC3 ISR 2021-05 ; WFC3 ISR 2020-10; WFC3 ISR 2019-07).

To account for the time-dependent sensitivity of the IR detector, inverse sensitivities for all 15 WFC3 /IR filters were updated in December 2024 (Calamida et al., in prep). These new time-dependent inverse sensitivities were derived by using ~ 14 years of observations of five CALSPEC standards, corrected for the recommended loss rates from WFC3 ISR 2024-06 (see Table 7.11). In addition, a new version of the calibration pipeline, `calwf3` v3.7.2, implements the time-dependent flux calibration and populates the image file header with time-dependent photometric keywords. The new inverse sensitivities provide an internal photometric precision better than 0.5% for all wide--, medium--, and narrow-band filters.

The new inverse sensitivities can now be computed for specific observation dates by using the Python package `stsynphot` (Calamida et al., in prep).

Table 7.11: Sensitivity loss rates and pivot wavelengths for F098M and all five wide-band filters. Remaining medium-band and all narrow-band filters should use the nearest wavelength solution.

| Filter | Pivot λ (nm) | Sensitivity Loss Rate (% / year) |
|--------|--------------|----------------------------------|
| F098M  | 986.4        | - 0.120 +/- 0.003                |
| F105W  | 1055.5       |                                  |
| F110W  | 1153.4       |                                  |
| F125W  | 1248.6       | - 0.075 +/- 0.006                |
| F140W  | 1392.3       | - 0.060 +/- 0.005                |
| F160W  | 1536.9       |                                  |

Monitoring of the IR channel sensitivity is carried out via several ongoing calibration programs. Staring mode observations of stellar clusters over a ~14-year baseline suggests small sensitivity loss rates of ~0.1% per year (WFC3 ISR 2024-06; WFC3 ISR 2022-07). Studies of WFC3/IR grism observations of CALSPEC standards also show small declines in sensitivity, about 0.1-0.3% per year, depending on the length of the observation baseline and the extraction wavelength range (WFC3 ISR 2024-06; WFC3 ISR 2024-01; Bohlin and Deustua, 2019). WFC3/IR scan observations of stars in the open cluster M35 over ~ 7 years suggest losses of about 0.16% per year in F098M and 0.06% per year in F140W. Recent analysis of 13 cycles of WFC3/IR internal flat field calibration programs indicated greater count rate losses at bluer wavelengths, with an average of ~0.3% per year averaged across all filters, suggesting a combination of effects from both the changing overall sensitivity as well as previously observed lamp reddening (WFC3 ISR 2024-10).

In contrast to the UVIS detector, staring mode monitoring of CALSPEC standards in the IR filters have large systematic uncertainties which limit their 1-sigma photometric repeatability to +/- 1.0% (WFC3 ISR 2024-06), and therefore cannot be used for accurately measuring the sensitivity loss rates, despite their significant time baseline (~14 years). However, these data can be (and were) used to test the appropriateness of calculated sensitivity loss rates, such as those previously listed; this approach was leveraged in WFC3 ISR 2024-06 in order to optimize sensitivity loss rates for each WFC3 /IR filter.

For a more detailed discussion of WFC3/IR sources of errors, see Section 7.11 and Section 9.1 of the WFC3 Data Handbook.

# 7.9 Other Considerations for IR Imaging

In this section, additional considerations users may have regarding WFC3/IR imaging are explored, including those that are determined to have little or no impact. We suggest that users pay particularly close attention to Section 7.9.1 (gain and full well saturation), Section 7.9.4 (image persistence), and Section 7.9.7 (optical anomalies).

## 7.9.1 Gain and Full-Well Saturation

Like the UVIS channel, the IR channel uses 16-bit analog-to-digital converters (ADCs), providing a digital output signal in the range between 0 and 65,535 data numbers (DNs). The default gain setting for the IR channel is 2.5 electrons/DN and is the only one offered to observers. In ground-based testing, the measured gain for this setting was 2.3 to 2.4 e¯/DN, depending on quadrant (WFC3 ISR 2008-50). Values of 2.2 to 2.3 e¯/DN were measured using internal flat field exposures taken from 2010 to 2015 (WFC3 ISR 2015-14) and from 2016 to 2023 (WFC3 Technical Instrument Report 2024-01, available upon request).

The default gain is chosen based on the full-well saturation level of the IR channel, which is about 78,000 electrons (~34,000 DN at the default gain), and on the detector readout noise, of order 20-22 electrons per correlated double sampling.

## 7.9.2 Cosmic Rays and Snowballs

Cosmic rays degrade the image quality. On-orbit measurements indicate that cosmic ray events occur at a rate of 11 ± 1.5 CR/s for WFC3/IR. The IR channel's MULTIACCUM mode, a series of intermediate non-destructive reads, makes it possible to filter out cosmic rays. The intermediate reads are used by the WFC3 data pipeline to identify cosmic ray hits, similar to the use of CR-SPLITs in CCD observations. AstroDrizzle also checks for and attempts to remove any residual cosmic rays from the "drizzled" images when there are multiple (usually dithered) exposures of the same field (see the DrizzlePac documentation).

Passages through the South Atlantic Anomaly (SAA) cause the highest number of cosmic ray hits. When the HST is within the predefined SAA exclusion zone, IR observations are not normally taken and the detector is set to auto-flush mode to minimize the effects of SAA passage on instrument performance. Unlike NICMOS, where it was necessary to switch off the detector electronics during SAA passage, it is possible to perform time-critical observations in the SAA with WFC3/IR although the cosmic ray rate will be high (about 12% of the pixels per minute (WFC3 ISR 2009-40).

Snowballs (named for their fuzzy appearance) are transient, extended sources that appear in IR exposures at the rate of about one per hour. They were characterized during ground-based testing ( WFC3 ISR 2009-43) and were hypothesized to be caused by the emission of alpha particles by radioactive isotopes in the detector (WFC3 ISR 2009-44). The rate of appearance of snowballs has remained constant over 11 years of on-orbit observations, consistent with the hypothesis that the uranium-238 decay chain is the source (WFC3 ISR 2015-01, WFC3 ISR 2020-03). Typical snowballs affect about 8 to 25 pixels, saturate 2-5 of those, and deposit about 200,000 to 500,000 electrons on the detector. The energy is deposited in the pixels instantaneously, so snowballs can be removed like cosmic rays, via up-the-ramp fitting.

## 7.9.3 On-Orbit Degradation

Unlike the CCDs, minimal cosmic-ray damage to the IR detectors was anticipated, and essentially none has been observed. During ground testing using a particle accelerator, the WFC3/IR arrays were subjected to radiation doses much higher than expected in their entire orbital lifetime, without sustaining significant long-term damage or measurable degradation in QE. Searches for the development of new bad pixels are conducted as part of the regular calibration program; the number is growing slowly if at all (WFC3 ISR 2010-13, WFC3 ISR 2012-10, WFC3 ISR 2024-02). The median dark current shows no evolution over time (WFC3 ISR 2017-04, WFC3 ISR 2012-11) although the level can vary from ramp to ramp by about 0.03 e-/s (Section 5.7.2).

In-flight dark reference files made from SMOV and cycle 17 data were delivered in March 2010 (full array) and October 2010 (subarrays) to replace the ground-based reference files. Subarray darks made from non-banded data were delivered in February 2011 (WFC3 ISR 2010-16 and Section 7.4.4). Full array darks with improved signal-to-noise, generated from data taken 2009-2013, were delivered in October 2013. Descriptions of the WFC3 reference files are available at: http://newcdbs.stsci.edu /doc/ICD47/Section11.html.

## 7.9.4 Image Persistence

As discussed in Section 5.7.9, the WFC3/IR detector exhibits image persistence, particularly during and following observations of targets that saturate the detector by more than the pixel full well depth. The amount of image persistence depends primarily on the brightness of the amount of charge accumulated by a pixel in an exposure, and secondarily on the length of time in an exposure. There is also some dependence on the location on the detector. The underlying cause of this behavior is that the traps involved in persistence have finite trapping and release times.

Image persistence has been observed within exposures in a single orbit as well as in observations where the target observed in a previous orbit was particularly bright, manifesting in the same pixels where the causing source previously landed.  Two examples of persistence are shown in Figure 7.11. The left panel shows an image obtained with WFC3/IR in parallel to a COS exposure (program 11519, Visit 0V). The bright diffuse object in the center of the field is the persistence after-image of the nearby Sb galaxy NGC 2841 observed two hours earlier (program 11360 visit R1). The right panel shows an image obtained of the gamma ray burst GRB090423 (program 11189 visit H2) which followed observations of globular cluster 47 Tuc (program 11677 visit 19) and a stellar field in Orion (program 11548 visit AJ). The patterns seen stepping diagonally across the image are the result of the dither pattern used in the previous observations. Persistence caused by sources observed within the same visit is known as self-persistence and often contributes the strongest persistence signals due to temporal proximity.

**Figure 7.11:** Persistence evident in WFC3/IR exposures following exposures of a bright nearby galaxy (left) and following dithered exposures of two fields of bright stars (right).
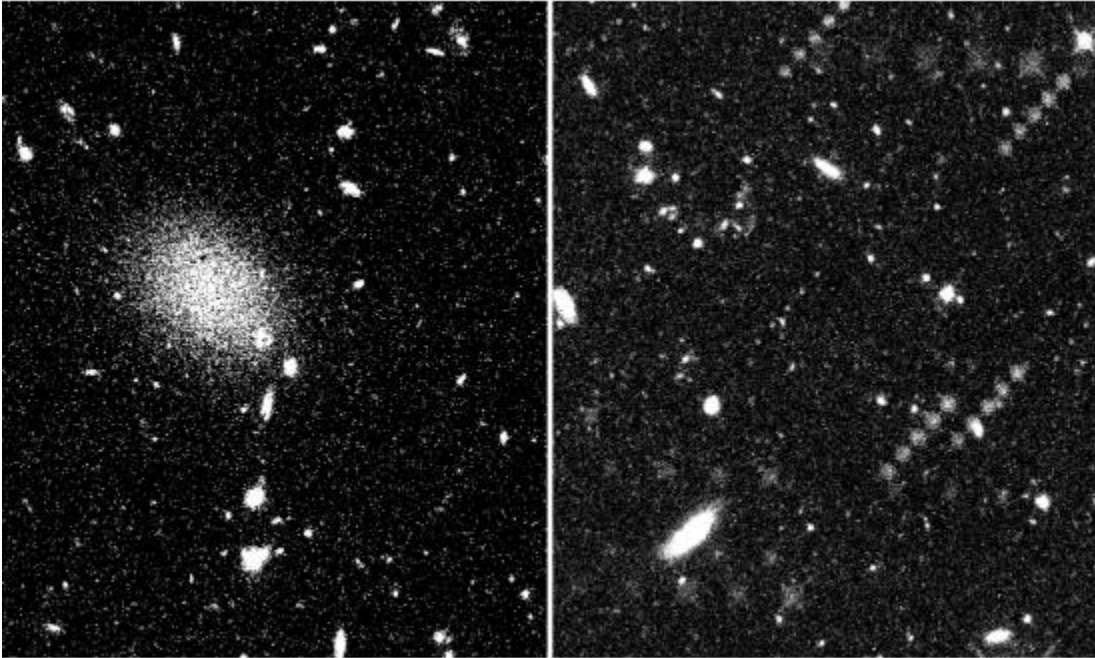


Obvious examples of persistence such as that shown in Figure 7.11 are fairly rare in the *HST* data. As part of the process of finalizing proposals for execution on-orbit, the WFC3 Contact Scientists (CS) perform detailed reviews of all submitted Phase II programs. For IR programs, the CS's flag visits that are likely to cause this much persistence so that the schedulers can inhibit WFC3/IR observations for several orbits after these "bad actors", long enough for the afterglow images to fade. *Observers can help in preventing persistence from affecting future observations with appropriate observing strategies, and, in cases where persistence cannot be avoided, by flagging possible bad actors with written comments in the phase II proposal and notifying the Contact Scientist or Program Coordinator.*

While the screening process generally eliminates the worst cases of persistence, such as those in Figure 7.11, since the process is manual it is not perfect and so observers need to be aware of the possibility of persistence in their images. Indeed, in light of the fact that WFC3/IR exposures constitute a significant fraction of the overall *HST* observing program and in order to maintain *HST* scheduling efficiency, only a small fraction of the visits can be declared to be "bad actors". This means that many IR images have some pixels that are affected by persistence. In the vast majority of cases, the number of pixels that are affected by persistence due to exposures from earlier visits is small compared to the number of pixels that should be flagged for other reasons. The tools and procedures needed to identify pixels affected by persistence and to mitigate its affect are described in the *WFC3 Data Handbook*. Observers are advised to take advantage of these tools to check whether the ability to extract science from their data has been adversely affected by persistence. *It is the responsibility of observers to check their data and request a repeat of a visit that has been compromised by persistence by filing a HOPR within the prescribed period.*

While avoiding persistence created by other programs is outside of the control of an individual investigator, evaluating whether persistence within a visit will affect the quality of their data is the responsibility of the observer. Specifically, observers need to consider whether persistence within a single visit will affect their ability to extract science from their data. In carrying out this evaluation, note that fairly short exposures (100 sec) of relatively bright (18th mag) stars observed through the broad-band filters saturate pixels in the IR array and thus will generate self-persistence within visits. Furthermore, the amount of persistence decays inversely with time such that a pixel that has been saturated to an effective fluence of ~100,000 electrons will show an afterglow of about 0.3 electrons per sec at 1000 seconds, but ~2 electrons per sec at 200 seconds (Figure 5.31 in Section 5.7.7). Persistence at very short time scales is not as well characterized, although there are indications that persistence decays more slowly at first (WFC3 ISR 2019-02).

In most cases, persistence will not turn out to be a serious problem, particularly if the objects that have the potential to cause persistence are spatially separated from the area of the image from which science is obtained, and/or if the number of affected pixels is small, and/or if dither patterns are small. In these cases, the procedures described in the *WFC3 Data Handbook* should be sufficient to address any issues associated with internal persistence in the images.

However, in some cases, persistence will be an issue, for example if the science target is faint and the field is filled with considerably brighter objects. In these cases, one should avoid the tendency to set the exposure time for the faint science target thereby ignoring the problem that will be caused by the rest of the field. *Observers should take care that bright or saturated sources within a field are not dithered across the same parts of the detector that record the highest science priority areas of the field.*

*O*bservations of dense fields, globular clusters, or very bright star formation regions may also be problematic e.g. in instances where precise photometry or very large dynamic range are required. On-orbit measurements of *undithered* exposures have shown that the flux rises across a sequence of exposures, affecting photometry at the level of 0.02-0.04 mag (WFC3 ISR 2016-11). This phenomenon, likely associated with persistence, is related to the slow rise in measured flux seen in grism observations of planetary transits (e.g. Wakeford et al., 2016, ApJ 819,10). Even in cases where data is dithered, persistence can affect photometric results if the steps are too small to avoid pixels previously illuminated; **for this reason, step sizes of at least 10 pixels should be used when possible** ( WFC3 ISR 2019-07).

There are a variety of strategies one can adopt to minimize the effects of persistence. In many cases, the best approach is to take more shorter exposures to limit the numbers of pixels affected. In addition, executing dithers greater than 10 pixels, always to unique positions, substantially aids in persistence mitigation (WFC3 ISR 2019-07). This approach does, however, incur a greater cost in overheads, and becomes less effective as crowding increases. Taking shorter exposures or narrow band exposures before long or wide band exposures yields less fluence in previous exposures, thus leading to less persistence.

Various tools to estimate which regions of an image are likely to cause persistence and additional strategies to mitigate its effects are described in Appendix D.

> ✅ *Updates on persistence characterization and tools for persistence artifact removal will be posted on the WFC3 persistence page.*

## 7.9.5 The IR Background

In space, the dominant sources of background radiation are zodiacal light and earthshine at shorter IR wavelengths, and the telescope thermal emission at longer wavelengths. For *HST*, the sum of these two background components has a minimum at about 1600 nm (e.g., section 4.7 in the NICMOS Instrument Handbook). This wavelength lies near the red end of the reddest WFC3/IR filter, F160W (WFC3 H). A variable airglow line of He I at 10830 Å can be a significant, even dominant, component of the sky background in the F105W and F110W filters as well as the G102 and G141 grisms (WFC3 ISR 2014-03).

Figure 7.12 shows the observed background levels in the first few months of WFC3's operation (green points and error bars), compared with values predicted from known instrument sensitivities and three levels of zodiacal light selectable in the Exposure Time Calculator (ETC). Even allowing for small sample sizes and possible systematics in the observations, it is apparent that a rough estimate of the zodiacal light level may not adequately predict the observed background level of an exposure. The WFC3 team has performed extensive studies of zodiacal light and earth-shine in WFC3/IR exposures as well as the He I airglow line to improve our understanding of the sky background, described in more detail below.

**Figure 7.12: Infrared background levels for WFC3.**
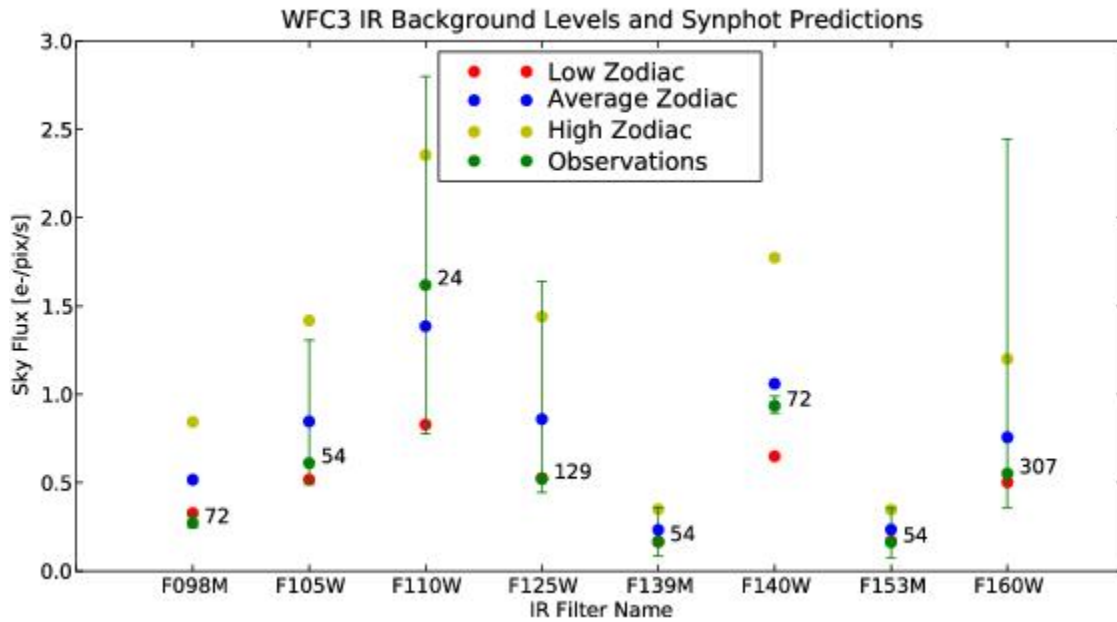


The average, low and high zodiac points show the `synphot` predictions for three levels of zodiacal light and no earth-shine. The observations selected include calibration and GO images of empty or sparsely populated fields, giving an accurate representation of early WFC3 observations but not covering all background conditions. Observational means (green points), ranges (error bars), and exposure counts are plotted.

The zodiacal background level observed in WFC3/IR exposures has been modeled as a function of ecliptic latitude and angular distance of the target from the sun (WFC3 ISR 2014-11). The dependence can be formulated as a function of ecliptic latitude and angular separation of the target from the sun in ecliptic longitude, or ecliptic latitude and the angle between the target and the sun as viewed by *HST*. The latter coordinate system has been adopted because it has practical advantages for planning and analyzing *HST* observations. The model derived for filter F160W is shown in Figure 7.13. The Sun Angle in the figure corresponds to the keyword SUNANGLE in the *HST* science image header. WFC3 ISR 2014-11 provides scaling factors to apply this model to other IR filters and the G141 grism, and shows that *the model provides significantly better estimates of the zodiacal light than the model used by the ETC*.

**Figure 7.13: Zodiacal background level for filter F160W as a function of the target's ecliptic latitude and angular distance from the sun.**
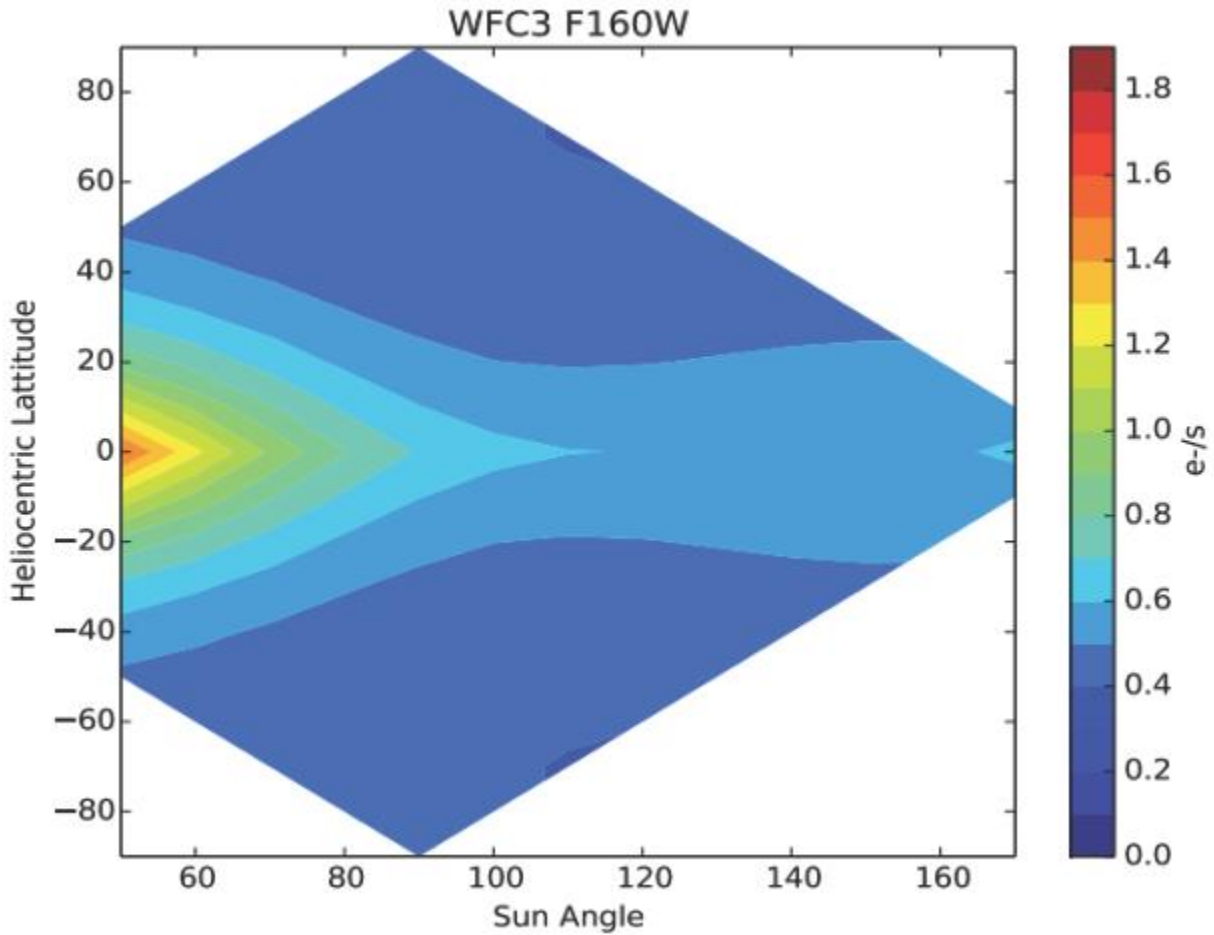


The highest levels of zodiacal light are avoided automatically by the *HST* observatory requirement that the Sun Angle be greater than 55°. For programs where a low background level is critical to the science goals, observers with a target at low ecliptic latitude may want to increase the solar avoidance angle from the default minimum of 55° to 60° or greater by excluding the range of dates when the target would be at the undesired angles, using Figure 7.13 as a guide. This can be implemented by applying BETWEEN statements to visits in the phase II proposal. The range of dates corresponding to the 55° exclusion rule can be displayed in the Visit Planner window in APT by clicking on the arrowhead that expands the schedulability plot for a visit into its components; Sun is the Sun Angle component. (Hold the cursor on a date range band to read the dates.) At low ecliptic latitudes, the Sun Angle of a target changes about 1° per day, so trimming 5 days from each end of the Sun schedulability date range increases the minimum Sun Angle to 60°. This approach provides many more opportunities for scheduling than the use of the LOW-SKY option (Section 9.7.1).

For pointings very close to the bright Earth limb, the zodiacal background may be exceeded by earth-shine. The brightness of the earth-shine falls very rapidly with increasing angle from the Earth's limb thanks to the effectiveness of the *HST* baffles, and for most observations only a few minutes at the beginning and end of the target visibility period are significantly affected. Selective data reduction, i.e. excluding some readouts of the sample sequence in the affected exposures and recalibrating, can be a better option than accepting the shorter visibility period required by LOW-SKY (WFC3 ISR 2014-03 and Section 9.7.1). Targets observed in the continuous viewing zone (CVZ) will always be rather close to the Earth's limb, and so can sometimes contain an elevated background for a larger part of the orbit, even at shorter wavelengths where zodiacal emission ordinarily dominates. Observers have the possibility of specifying a non-standard Bright Earth Avoidance (BEA) angle, which increases the angle from the Earth's limb from 20° to 25°, but this comes at the cost of observing time and would not significantly improve most programs. Note that this is an special mode and must be requested through a Contact Scientist.

Investigation of unexpectedly high background levels in some early WFC3/IR imaging and spectroscopic exposures led to the identification of a He I airglow line at 10,830 Angstroms as the source (WFC3 ISR 2014-03). This line falls within the passbands of the F105W and F110W filters and both IR grisms. It is negligible in the Earth's shadow, generally strongest at low Earth limb angles outside the shadow, but sometimes strong even 40° above the Earth limb. In the worst cases, the airglow line is the dominant background emission. Examples of strongly affected exposures (with F105W, G102, G141) and unaffected exposures (with F125W, F160W) are illustrated in Figure 7.14.

**Figure 7.14:** Earth limb angle and background count rate for some of the spectral elements affected by He I airglow (F105W, G102, G141) and unaffected (F125W, F160W).
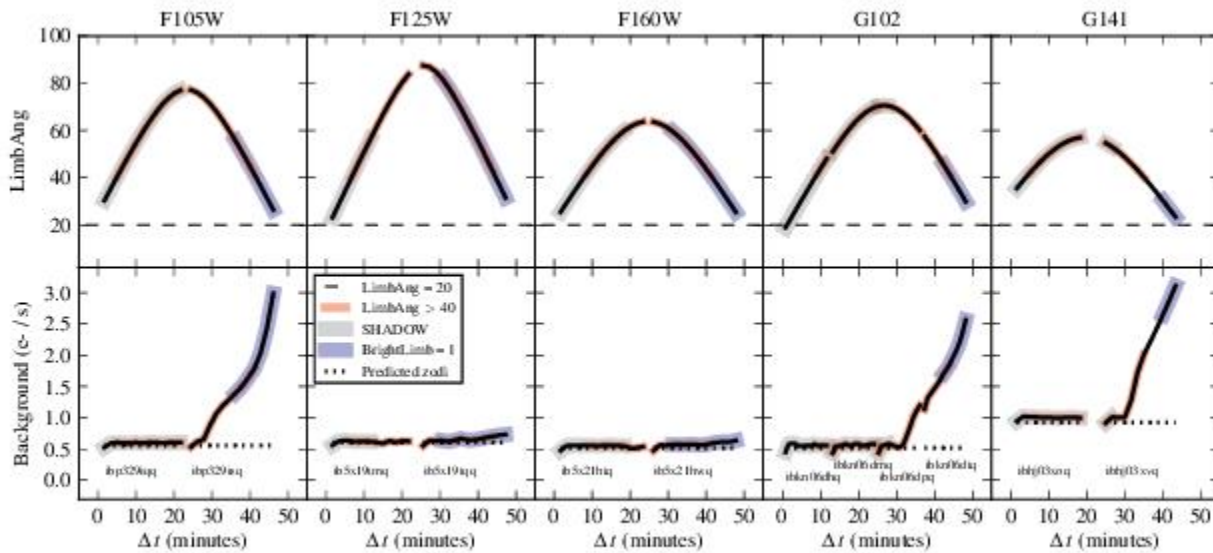


Top panels: Variation of Earth limb angle over the course of an orbit. The curves are colored following the labels in the legend.
Bottom panels: Variation of the background count rate throughout an orbit for specific filters and grisms. The predicted background level from the `synphot`/ETC zodiacal model is shown in the dotted line.

Where possible, observers should consider selecting alternative filters to F105W and F110W to avoid elevated background due to the He I airglow line. If other filters are used in the proposal, the observer should consider placing exposures unaffected by the airglow line at the beginning and end of an orbit and the exposures in that orbit should be placed in a non-interruptible exposure sequence, as described in the APT Training Materials. Use of the APT special requirement SHADOW to exclude the airglow line is not generally recommended due to the severe restrictions that it places on observing opportunities and orbit length (Section 9.7.2). The APT special requirement LOW-SKY may be helpful, but it also limits scheduling opportunities and orbit length (Section 9.7.1) and will not always exclude the airglow line, which can be bright at the permitted limb angles (>40°).

Strategies for processing exposures with frames affected by strongly variable airglow are described in the WFC3 Data Handbook (as well as WFC3 ISR 2014-03 and WFC3 ISR 2016-16). If an `flt` image has an unexpectedly high background or excessive cosmic ray flagging, the observer should check the `ima` files for evidence of a variable background. The standard up-the-ramp fitting of the non-destructive reads in a WFC3/IR exposure does not work properly on images with a variable background since the variations are treated as cosmic rays. An improved `flt` image (at least for unsaturated sources) can be obtained by rerunning **calwf3** with **CRCORR=OMIT** to turn off the ramp fitting and cosmic ray rejection. Cosmic rays can then be removed by using AstroDrizzle to combine sets of exposures. Alternatively, after running `calwf3` without cosmic ray rejection, one can "flatten" the nonlinear ramps by subtracting the variable background of each read averaged over many pixels and adding back a constant for the overall average background count rate, then feed the flattened `ima` files back to `calwf3` for the final step of identifying the cosmic rays. Scripts and examples are provided in the WFC3 Data Handbook and the HST Software Library.

There is noticeable diversity in the background of G102 and G141 exposures due to the varying contributions of zodiacal light and the He I airglow line. Because these contributions are spectrally distinct, the background can best be modeled using a combination of these components (WFC3 ISR 2020-04, WFC3 ISR 2015-17). See Section 8.5 for a discussion of this technique in the processing of WFC3/IR grism spectra.

## 7.9.6 Blobs

Image blemishes peculiar to the WFC3-IR detector have been described in Section 5.7.7. Other spots of reduced sensitivity in IR images, dubbed "blobs", are caused by reduced reflectivity of the Channel Select Mechanism mirror. The blobs typically have a measured half-light radius of 10-15 pixels and absorb up to 15% of the incoming light at their centers.

Blobs were first noticed in IR images shortly after WFC3 was installed on *HST*. Their characteristics and the history of their occurrence are described in detail (WFC3 ISR 2010-06, WFC3 ISR 2012-15, WFC3 ISR 2014-21, and WFC3 ISR 2018-06). Pixels affected by blobs were initially identified in a single bad pixel table (BPIXTAB) that was designed to be applied to data taken after June 13, 2010 (WFC3 ISR 2012-10). This table has been superseded by a series of date-dependent bad pixel tables that track the appearance of "strong" and "medium" blobs (WFC3 ISR 2014-21, WFC3 ISR 2018-06). Figure 7.15 shows the location of blobs on the detector as of May 2024.

Corrections as large as 0.1 mag have been found for blob-impacted stars in Omega Centauri, and the accuracy of the corrected photometry is comparable to the photometric accuracy for stars in blob-free regions (WFC3 ISR 2015-06). Nevertheless, most observations will not be significantly affected by blobs, since blobs occupy only 2.25% of the detector area and their effects can be mitigated by dithering and drizzling. Appropriate dither strategies to mitigate the effects of blobs and other artifacts in IR images are described in WFC3 ISR 2010-09. See Section C.2 for the specifications of the WFC3-IR-DITHER-BLOB pattern implemented in APT.

Recent delta flat field reference files now include epoch-dependent corrections for blobs for six filters (F098M, F105W, F110W, F125W, F140W, and F160W; WFC3 ISR 2021-01; Section 5.7.4). Early versions of "blob flat fields", to improve stellar photometry in crowded fields, were made in 2015 (described in WFC3 ISR 2014-21, available via the WFC3 IR flats webpage).

**Figure 7.15:** As of May 2024, there are 153 blobs on the WFC3/IR detector, which are identified by circles in the image below. They are color-coded according to their strength: very weak (cyan), weak (blue), moderate (green), and strong (red). Strong and moderate blobs (red and green respectively) are flagged in the BPIXTAB reference file.
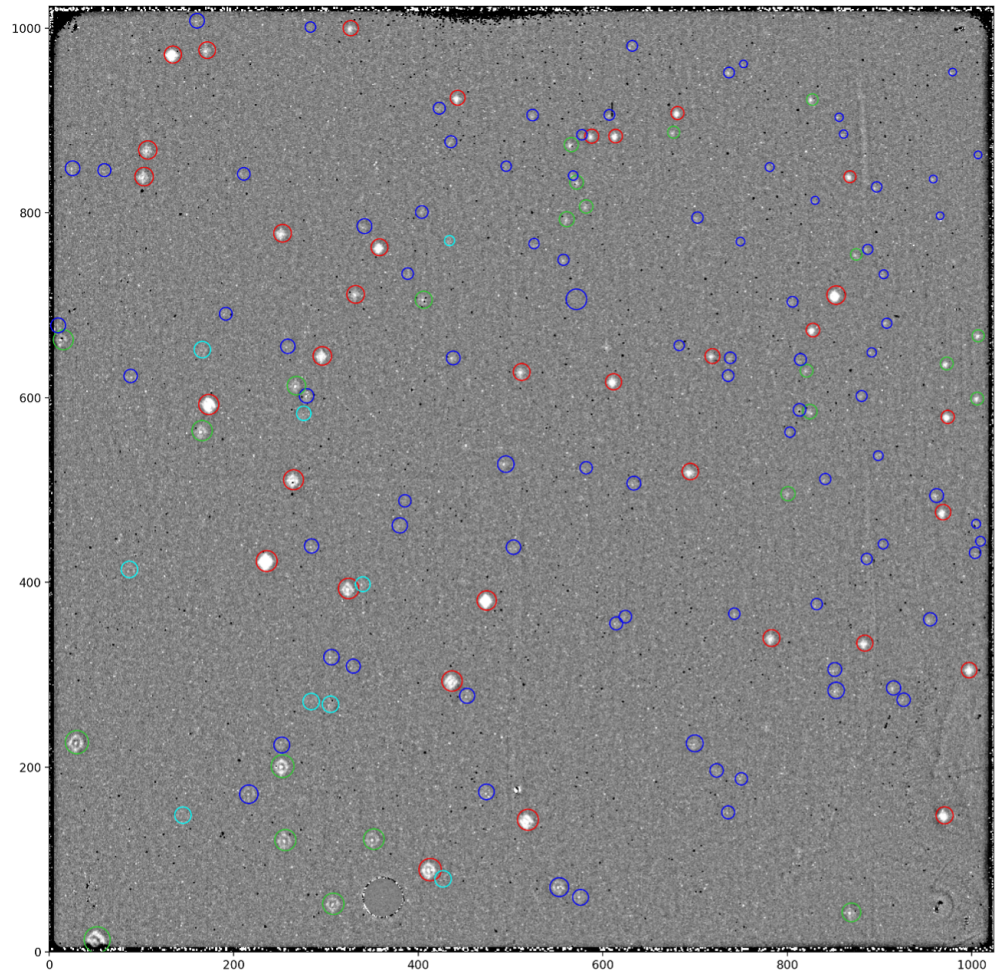


## 7.9.7 Optical Anomalies

Anomalous features can be found in some WFC3/IR detector images due to a number of causes. For example, the optical system may cause stray light from sources outside the detector FOV to be scattered into images. Scattered earthlight can greatly increase the background on part of the detector when *HST* is pointing near the bright earth limb (see the WFC3 Data Handbook). Additional detector anomalies, ghosts, and defects are detailed on the WFC3 Anomalies webpage for both the UVIS and IR detectors. Also available on the same webpage is a downloadable database of all known anomalies in all non-proprietary WFC3 data, as maintained by the daily monitoring of the WFC3 Quicklook Team (WFC3 ISR 2017-02, WFC3 ISR 2020-02).

# 7.10 IR Observing Strategies

## 7.10.1 Dithering Strategies

For imaging programs, STScI generally recommends that observers employ dithering patterns. Dithering refers to the procedure of moving the telescope by small angle offsets between individual exposures on a target. The resulting images are subsequently combined in the pipeline or by the observer using software such as AstroDrizzle.

Dithering is used to improve both image quality and resolution. By combining multiple images of a target at slightly different positions on the detector, one can compensate for detector artifacts (blemishes, dead pixels, hot pixels, transient bad pixels, flatfielding errors, and plate-scale irregularities) that may not be completely corrected by application of the calibration reference files. Combining images, whether dithered or not, can also remove any residual cosmic ray flux that has not been well removed by the up-the-ramp fitting procedure used to produce flt images (see Section 7.7.2 and Appendix E). Effective resolution can be improved by combining images made with sub-pixel offsets designed to better sample the PSF which is particularly important for WFC3/IR because the PSF is undersampled by about a factor of 2 (Table 7.5).

Larger offsets are used to mosaic a region of sky larger than the detector field of view and can also be used for "chopping" to sample the thermal background. While "chopping" was recommended for NICMOS exposures at wavelengths longer than 1.7 microns, where the telescope thermal background becomes dominant, the thermal background is not a problem for WFC3/IR. In WFC3, all offsets must be accomplished by moving the telescope (in NICMOS it was also possible to move the Field Offset Mirror).

Dithers must be contained within a diameter ~130 arcsec or less (depending on the availability of guide stars in the region) to use the same guide stars for all exposures. The rms pointing repeatability is significantly less accurate if different guide stars are used for some exposures (see Appendix B of the *DrizzlePac Handbook*). Mosaic steps and small dither steps are often combined to increase the sky coverage while also increasing resolution and removing artifacts. Section 6.11.1 provides a discussion of the effect of geometric distortion on PSF sampling for mosaic steps.

The set of Pattern Parameters in the observing proposal provides a convenient means for specifying the desired pattern of offsets. The pre-defined mosaic and dither patterns that have been implemented in APT to meet many of the needs outlined above are described in detail in the *Phase II Proposal Instructions*. The WFC3 patterns in effect in APT at the time of publication of this Handbook are summarized in Appendix C. Observers can define their own APT patterns to tailor them to the amount of allocated observing time and the desired science goals of the program. Alternatively, they can use POS TARGs to implement dither steps (Section 7.4.3). WFC3 ISR 2016-14 provides compact patterns with up to 9 steps (in the form of POS TARGs) designed to preserve sub-pixel sampling as much as possible over the face of the detector, given the scale changes introduced by geometric distortion. Observers should note that thermally-driven drift of the image on the detector, occasionally larger than 0.15 pixels in two orbits, will limit the accuracy of execution of dither patterns (WFC3 ISR 2009-32). Additional information on dither strategies can be found in WFC3 ISR 2010-09, which provides a decision tree for selecting patterns and combining them with sub-patterns.

## 7.10.2 Parallel Observations

Parallel observations, i.e., the simultaneous use of WFC3 with one or more other *HST* instruments, are the same for the IR channel as for the UVIS channel, previously described in Section 6.11.2. Note that there are new patterns available to optimize dither patterns for proposals using WFC3 and ACS simultaneously (WFC3 ISR 2023-05).

## 7.10.3 Exposure Strategies

Given the variety of requirements of the scientific programs that are being executed with WFC3/IR, it is impossible to establish a single optimum observing strategy. In this section we therefore provide a few examples after guiding the reader through the main constraints that should be taken into account when designing an observation:

- Integrate long enough to be limited by background emission and not read noise. Dark current (~0.05 e⁻/s/pixel) is rarely the limiting factor.
- Dither enough so that resolution can be restored to the diffraction limit and bad pixels and cosmic-ray impacts can be removed, while maintaining a homogeneous SNR across the field.
- Dither in large enough steps (> 10 pixels, WFC3 ISR 2019-07) and sequence exposures from low to high S/N when possible to avoid self-persistence.
- Use MULTIACCUM ramps with as many reads as possible for readout noise suppression.

In this regard, it is useful to consider Table 7.12, which summarizes the total background seen by a pixel, including sky, telescope, and nominal dark current, and the time needed to reach 400 e⁻/pixel of accumulated signal, corresponding to 20 e⁻/pixel of Poisson-distributed background noise. The latter, higher than the expected readout noise of ~12 electrons after 16 reads, is used here to set the threshold for background-limited performance. *The passage from readout-limited performance to background-limited performance can be regarded as the optimal exposure time for that given filter, in the sense that it allows for the largest number of dithered images without significant loss of SNR* (for a given total exposure time, i.e., neglecting overheads). For faint sources, the optimal integration time strongly depends on the background (zodiacal, Earth-shine thermal, and dark current) in each filter, ranging from just 220 s for the F110W filter to 2700 s for some of the narrow-band filters.

These constraints put contradictory requirements on the ideal observing strategy. It is clear that given a certain amount of total observing time, the requirement of long integrations for background limited performance is incompatible with a large number of dithering positions. Also, to increase the number of reads within a ramp for readout noise suppression decreases the observing efficiency, with a negative impact on the signal to noise ratio. Because the background seen by each pixel depends on the filter (Section 7.9.5), the optimal compromise must be determined on a case-by-case basis.

The optimal integration time needed to reach background-limited performance (Table 7.12) can be compared with the integration times of the sampling sequences from Table 7.8. Table 7.13 synthesizes the results, showing for each filter which sample sequence most closely matches the optimal integration times for NSAMP=15.

Table 7.12: Background levels  (e–/pix/s) at the WFC3/IR detector. The columns show, from left to right: a) filter name; b) thermal background from the telescope and instrument; c) zodiacal background; d) earth-shine background; e) dark current; f) total background; g) integration time needed to reach background-limited performance, assuming an equivalent readout noise of 20 electrons.

| Filter | Thermal | Zodiacal | Earth-shine | Dark Current | Total | Optimal Integration Time (sec) |
|---|---|---|---|---|---|---|
| F105W | 0.051 | 0.774 | 0.238 | 0.048 | 1.111 | 360 |
| F110W | 0.052 | 1.313 | 0.391 | 0.048 | 1.804 | 222 |
| F125W | 0.052 | 0.786 | 0.226 | 0.048 | 1.112 | 360 |
| F140W | 0.070 | 0.968 | 0.267 | 0.048 | 1.353 | 296 |
| F160W | 0.134 | 0.601 | 0.159 | 0.048 | 0.942 | 425 |
| F098M | 0.051 | 0.444 | 0.140 | 0.048 | 0.683 | 586 |
| F127M | 0.051 | 0.183 | 0.052 | 0.048 | 0.334 | 1198 |
| F139M | 0.052 | 0.159 | 0.044 | 0.048 | 0.303 | 1320 |
| F153M | 0.060 | 0.153 | 0.041 | 0.048 | 0.302 | 1325 |
| F126N | 0.051 | 0.037 | 0.011 | 0.048 | 0.147 | 2721 |
| F128N | 0.051 | 0.040 | 0.011 | 0.048 | 0.150 | 2667 |
| F130N | 0.051 | 0.041 | 0.011 | 0.048 | 0.151 | 2649 |
| F132N | 0.051 | 0.039 | 0.011 | 0.048 | 0.149 | 2685 |
| F164N | 0.065 | 0.036 | 0.009 | 0.048 | 0.158 | 2532 |
| F167N | 0.071 | 0.035 | 0.009 | 0.048 | 0.163 | 2454 |

The selection of sample sequence type (RAPID, SPARS, STEP; Section 7.7.3) must take into account the science goals and the restrictions placed on their use. Most observers have found that the SPARS ramps best meet the needs of their programs. Here are some factors to consider when selecting a sample sequence:

- The RAPID ramp is a uniform sequence of short exposures. With its relatively short maximum exposure time, RAPID is suitable for a target consisting of bright objects that would saturate after a few reads in the other sequences. It is not appropriate for background-limited performance.
- SPARS ramps, with their uniform sampling, provide the most robust rejection of cosmic-ray events, and can be trimmed by removing a few of the final reads to fine-tune the integration time with little degradation of the achieved readout noise. Thus they are considered the standard sampling mode.
- STEP ramps are preferable where large dynamic range is needed; e.g., for photometry of stellar clusters. These ramps begin with a sequence of four uniform (RAPID) reads and end with a sequence of much longer uniform reads. The transition between the two uniform read rates is provided by a short sequence of logarithmically increasing read times. This design provides for correction of any non-linearities early in the exposure and allows for increased dynamic range for both bright and faint targets.

Finally, the selection of a given sample sequence type should also be made in conjunction with the number of samples (nsamp) that will be used to achieve the desired total exposure time for the observation. Long exposures should in general use a minimum of 5-6 samples in order to allow for reliable CR rejection and to allow for at least a few unsaturated samples of bright targets in the field. For very faint targets in read-noise limited exposures, a larger number of samples will result in greater reduction of the net read noise and a more reliable fit to sources with low signal. Short exposures of bright targets, on the other hand, can get by with fewer samples. This is especially true, for example, for the direct images that accompany grism observations. Since the purpose of the direct image is to simply measure the location of sources - as opposed to accurate photometry - an NSAMP of only 2 or 3 suffices for direct images required with grism observations.

Table 7.13: Optimal exposure time needed to reach background-limited performance (see Table 7.12) for each WFC3/IR filter, along with the NSAMP=15 sequences that provide the closest match. The benefits and disadvantages of each sequence type are discussed in the accompanying text.

| Filter | Optimal exposure time (sec) | SPARS | STEP |
|--------|------------------------------|----------|---------|
| F105W | 360 | SPARS25 | STEP50 |
| F110W | 222 | SPARS25 | STEP25 |
| F125W | 360 | SPARS25 | STEP50 |
| F140W | 296 | SPARS25 | STEP25 |
| F160W | 425 | SPARS25 | STEP50 |
| F098M | 586 | SPARS50 | STEP50 |
| F127M | 1198 | SPARS100 | STEP200 |

| | | | |
|---|---|---|---|
| F139M | 1320 | SPARS100 | STEP200 |
| F153M | 1325 | SPARS100 | STEP200 |
| F126N | 2721 | SPARS200 | STEP400 |
| F128N | 2667 | SPARS200 | STEP400 |
| F130N | 2649 | SPARS200 | STEP400 |
| F132N | 2685 | SPARS200 | STEP400 |
| F164N | 2532 | SPARS200 | STEP400 |
| F167N | 2454 | SPARS200 | STEP400 |

## 7.10.4 Spatial Scans

Spatial scanning is available with either WFC3 detector, UVIS or IR i.e. producing star trails on the IR detector is the same as producing star trails on the UVIS detector, with a few differences discussed in WFC3 ISR 2012-08. This document is recommended to anyone preparing a phase II proposal that uses spatial scans for any purpose. Spatial scans are discussed more extensively in Section 6.11.5 (UVIS imaging) and Section 8.6 (IR slitless spectroscopy). The former section describes star trails and the latter section describes spectra trailed perpendicular to the dispersion direction.

## 7.10.5 PSF Subtraction

IR imaging has been shown to be highly effective in detecting faint point sources near bright point sources (WFC3 ISR 2011-07). In that study, deep dithered exposures of a star were made at a variety of roll angles. Unsaturated exposures of a star, scaled down in flux to simulate faint companions of various magnitudes, were added to the deep exposures. The faintness of the companion that can be detected at a certain separation from the bright star depends on the degree of sophistication used to generate a reference image of the PSF to subtract from each set of dithered exposures. For a separation of 1.0 arcsec, five sigma detections could be made fairly easily for companions 8 or 9 magnitudes fainter than the bright star, and companions more than 12 magnitudes fainter than the bright star could be detected at separations of a few arcsec. Substantial improvements in detectability at separations less than about 2 arcsec could be made using the methodology described in the ISR to generate the reference PSF.

If observers want to use stellar images to subtract the PSF from a target comprised of a point source and an extended source to detect or measure the extended source, they should keep several points in mind:

- IR pixels under-sample the PSF (Section 7.6), so the stellar and target exposures should be dithered to produce good sampling of the PSF.
- Position drift and reacquisition errors can broaden the PSF (WFC3 ISR 2009-32, WFC3 ISR 2012-14).
- If a single guide star is used for a visit, roll angle drift causes a rotation of the target around that star, which in turn introduces a small translational drift of the target on the detector. In recent years, as gyroscopes have failed and been replaced, the typical roll angle drift rate is 12 mas/sec, producing a translation at WFC3's location in the HST field of view of about 0.05 IR (0.2 UVIS) pixels in 1000 sec.
- The characteristics of the PSF depend on the focus, which generally changes measurably during an orbit; its range in a particular orbit will not be known in advance (WFC3 ISR 2012-14).

- The characteristics of the PSF vary with location on the detector (e.g. WFC3 ISR 2018-14).
- If exposures long enough to have good signal-to-noise to the desired radius will saturate the central pixels, one should consider making shorter exposures to avoid the effects of self-persistence. (Section 7.9.4, Appendix D.)

**We do not recommend usage of the PSF modeling software Tiny Tim.** While STScI continues to host the software as a courtesy to the community, it is no longer maintained or supported. Short-comings of WFC3/IR modeling in Tiny Tim version 7.4 are documented in WFC3 ISR 2012-13 and WFC3 ISR 2014-10. See Section 7.6.4 for discussion of ongoing work to provide PSF models to observers.

## 7.10.6 The Drift and Shift (DASH) Observing Strategy

> ⓘ **Deprecated**
>
> As of the transition to Reduced Gyro Mode (RGM) in June 2024, **observing in DASH mode is no longer available**. The information in this section is provided for historical purposes. See Section 6.11.5 for a brief discussion regarding DASH mode with WFC3/UVIS.

The term DASH ("drift-and-shift", Momcheva et al., 2016) was adopted to describe the observing strategy of taking a series of WFC3/IR exposures of many targets within one orbit while the telescope is being guided under gyroscope control, thus avoiding the overhead cost of acquiring a new pair of guide stars for every slew between targets of greater than about 2 arcmin. A WFC3/IR sample sequence comprised of short exposure times was selected to limit image smearing within each time step, and the differential samples in one exposure were later aligned and combined to compensate for the greater drift due to gyroscope control (Figure 7.16).

The DASH technique was originally designed to allow users to carry out shallow large-scale mosaic observations with the WFC3/IR camera but was later adapted to efficiently observe a collection of bright targets within a field ~1 deg across with WFC3/IR subarray apertures (which have shorter time steps for a given sample sequence) and with WFC3/UVIS subarray apertures. Section 6.11.5 provides discussion of using the DASH mode with WFC3/UVIS observations. Below, we provide a detailed discussion regarding *HST* guiding and previous considerations for program design.

A DASH orbit must begin with a guide star acquisition followed by at least one exposure using fine guiding to ensure adequate pointing at the beginning of the orbit. Gyroscope performance in later cycles made it necessary to limit each DASH visit to one orbit and to institute a required minimum amount of time using fine guiding. When DASH was supported, the Orbit Planner in APT would show FGS Pause after the exposure(s) taken with fine guiding. The time between the end of the guide star acquisition (GS Acq) and the FGS Pause was required to be at least 5 minutes in order to provide time to update the gyroscope bias before proceeding with a slew or dropping to gyroscope mode. Therefore, in later cycles the orbit must have begun with more or longer guided exposures than in earlier cycles. Previously, Program Coordinators would work with the Principal Investigator (PI) to see if it was possible to plan orbits to achieve the proposed science that fit the scheduling windows.

In APT, all of the exposures must have been grouped together into a non-interruptible sequence container to confine them to one uninterrupted orbit. When placed in this container, the exposures would be observed without gaps due to Earth occultation or SAA passages. As a further precaution, if subarrays were used, it was recommended that PIs carefully choose the minimum size, and use a series of increasingly large subarrays over the course of the orbit as needed to allow for the accumulating telescope pointing drift. PIs were also advised to consider using the offset pattern that minimizes the length of moves during an orbit; offsets are made with a small angle maneuver (SAM), and the repositioning overheads increase with the offset size of the SAM. Overheads for SAMs of different sizes are shown in Table 10.1. More details on planning DASH observations in APT are presented in WFC3 STAN Issue 23.

Some of the earliest IR DASH observations were made under very stable gyro guiding, e.g. Program 14114 (PI: van Dokkum, Momcheva et al., 2016). The exposures were taken with the full array using the SAMP-SEQ=SPARS25 with NSAMP=10, 11, or 12, with 8 sample sequences per orbit. Each sample sequence had 9 to 11 differential exposures of 25 sec, and after dropping to gyro mode the drift in each 25 second interval was on average less than half of a WFC3/IR pixel. The pattern of SAMs resulted in overheads ~1 minute. Suitable step sizes in the WFC3/IR sample sequence depended on the expected accuracy of gyroscope guiding, which has changed with time. When preparing the phase II proposal for a program using DASH mode, it was advised that PIs consult with their Contact Scientist to determine short enough step sizes to mitigate smearing.

The WFC3 team released a set of tools in a DASH pipeline (WFC3 ISR 2021-02; STAN issue 34). Although they are no longer actively maintained, these tools, along with a Jupyter notebook tutorial, remain available through GitHub to assist users with calibrating and reducing WFC3/IR DASH observations.

Figure 7.16: Illustration of the deprecated "drift and shift" (DASH) method of restoring unguided WFC3/IR images. (a) The standard data product (the FLT file) of an unguided, gyro-controlled exposure. Objects are smeared due to the lack of fine guidance sensor corrections. (b) Individual samples that comprise the final exposure. The smearing is small in each individual sample. (c) The reconstructed image after shifting the samples to a common frame and adding them.
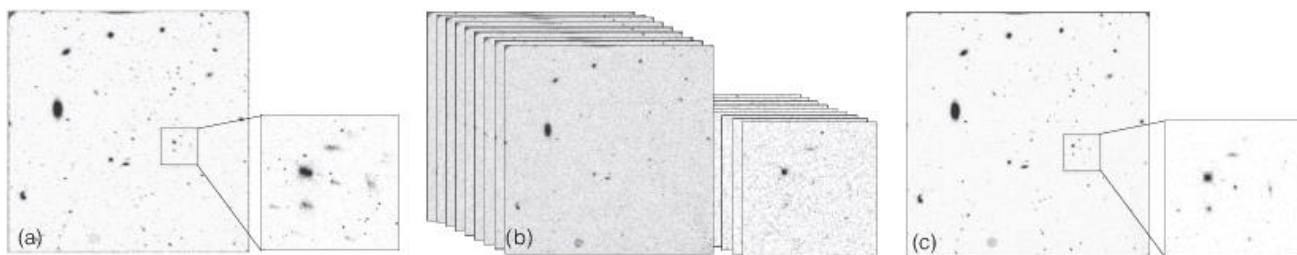
# Chapter 8: Slitless Spectroscopy with WFC3

**Chapter Contents**

# 8.1 Grism Overview

WFC3 provides a slitless spectroscopy mode in both of its channels. The UVIS channel has a single grism and the IR channel two grisms, enabling low-resolution slitless spectroscopy over the entire field of view of both detectors.

In the UVIS channel, the G280 grism provides spectroscopy over a useful wavelength range of 190–800 nm (WFC3 ISR 2020-09), at an average dispersion of about 1.3 nm per pixel in the first order. Note, however, that beyond ~450 nm, reduced sensitivity and overlapping orders interfere with grism observations.

The two grisms for the IR channel cover the wavelength ranges 800–1150 nm (G102), and 1075 nm to 1700 nm (G141). The dispersions are 2.45 and 4.65 nm per pixel, respectively.

The observing technique of spatial scanning can be used for WFC3 spectroscopic observations. See Section 8.6.

Table 8.1 summarizes the capabilities of the three WFC3 grisms in first-order mode. The resolving power is listed for each grism at a wavelength near the center of its range of coverage. The dispersion differs slightly between the two chips of the UVIS channel, and the mean value is listed. The tilt of the dispersion direction relative to the detector *x*-axis is also listed.

Table 8.1: WFC3 UVIS and IR Grisms.

| Grism | Channel | Wavelength range (nm) | Resolving power[1] | Dispersion (nm/pixel) | Tilt (deg)[2] |
|-------|---------|----------------------|-------------------|----------------------|---------------|
| G280 | UVIS | 190 – 800 | 70 @ 300 nm | 1.30 | −3.0 |
| G102 | IR | 800 – 1150 | 210 @ 1000 nm | 2.45[3] | +0.7 |
| G141 | IR | 1075 – 1700 | 130 @ 1400 nm | 4.65 | +0.5 |

1 Resolving power is based on the FWHM of the Gaussian image core measured in direction perpendicular to the dispersion.
2 Tilt of dispersion direction with respect to the positive x-axis of the image frame.
3 The dispersion varies over the field by ±4%; the tabulated value refers to the field center.

✔ *For the latest information on WFC3 spectroscopy, see the WFC3 Spectroscopy Resource page.*

## 8.2 Slitless Spectroscopy with the UVIS G280 Grism

The G280 grism is a WF/PC1 spare. Figure 8.1 shows a spectrum of the wavelength calibration star WR14 observed as part of the Cycle 17 calibration program 11935. The circled spot shows the location of a direct image of the source obtained with a separate (undispersed) F300X filter exposure, but superposed on the grism image for illustrative purposes only. The prominent star-like feature near the center of the picture is the zeroth-order grism image, and the positive and negative higher orders extend towards the left and right of the zeroth order, respectively. The +1st order is defined to be the order with the higher throughput (due to the grating blaze), even though it falls at lower $x$-pixels than the position of the zeroth order. The +1st order extends to the left of the zeroth order a distance of about 1/4 of the image size. Further left there is heavy overlap with higher orders. Some prominent emission lines can be seen along the spectral trace.

**Figure 8.1:** Appearance of the G280 spectral orders on the detector. The circled source is the position of the direct image formed by summing an F300X image with the grism image. The stronger 1st order is to the left and the 0th order is in the center. Above the 1st orders, much weaker 2nd and 3rd orders are barely visible. The image shows the full extent of the detector in the x-axis (4096 pixels) and about 500 pixels in the y-axis.
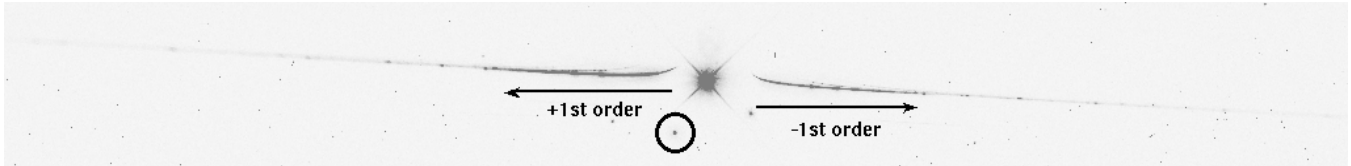


There are several features of this grism that differ, for example, from the G800L grism on ACS. There is an offset of about 175 pixels in the *y*-direction between the direct image and the spectra, the zeroth-order is relatively bright due to a lower grating efficiency and clear substrate, and there is curvature of the spectra at the blue ends of the first orders (nearest the zeroth order). The amplitude of the curvature is about 30 pixels in the detector y-direction. Figure 8.2 shows a close up view of the first few positive orders of the WR14 spectrum, which illustrates the curvature at the short-wavelength end of each order.

**Figure 8.2: Close up view of the first few positive orders of the WR14 spectrum**
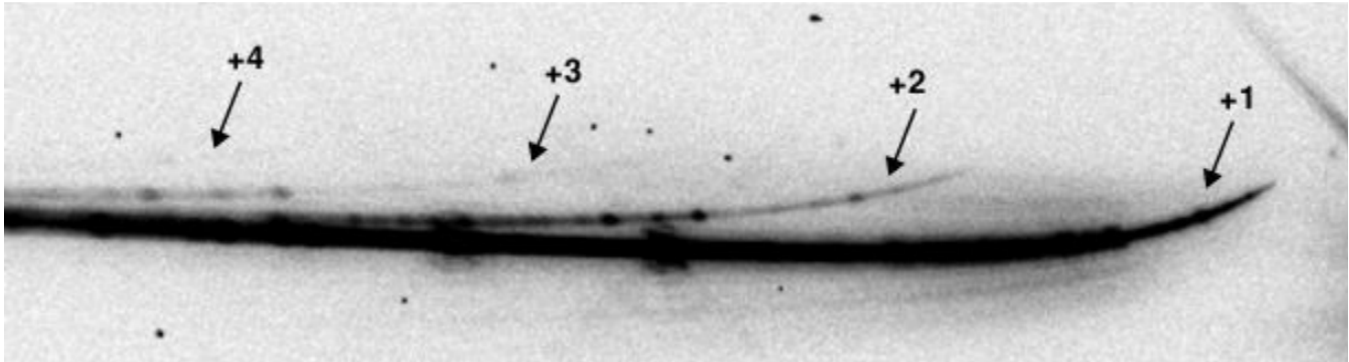


The spectral trace and dispersion have been measured both during ground calibration and on-orbit using the wavelength calibration star WR14. The mean dispersion in the 1st order at 2200 Å is 12.2 Å /pixel, varying from 10.8 Å/pixel at 1850 Å to 14.4 Å/pixel at 4000 Å. The dispersion per pixel in the higher orders is higher by the approximate ratio of the orders; for example, in +3rd order it is 48 Å /pixel.

The flux calibration of G280 spectra is best at the center of chip 2, and next best at the center of chip 1. Observers having a single target of interest are encouraged to place the target near the center of chip 2, due to the higher QE of chip 2 at very short wavelengths.

Field-dependent calibrations of the trace and dispersion for the -1 and +1 orders over the entire UVIS field of view are presented in WFC3 ISR 2017-20. The best fit to the shape of the G280 curved spectra on multiple locations on the detector was achieved using a 6th order trace polynomial with a linear 2D field dependence. The model reproduces the location of the curved traces of the +1 and -1 order spectra to within a fraction of a pixel. It fits a longer portion of the red part of each spectrum than the earlier ground calibration, and overall is a significant improvement over that calibration. The accuracy of the wavelength calibration is estimated to be ±7 Å, or about half of a UVIS resolution element.

A full calibration of the WFC3 UVIS G280 slitless spectroscopic mode was performed in 2020 (see WFC3 ISR 2020-09). We combined all G280 calibration data through 2020 (nearly 600 datasets) to determine the traces, wavelength calibration, and flux calibration across the entire field of view of both UVIS detectors, modeling the large amount of field dependence of the G280 grism. This was done for the ±1, ±2, ±3, and ± 4 orders, and we have calibrated the position of the 0th order as well. Figure 8.3 shows the updated total 1st-order transmission for the WFC3 G280 mode.

The current absolute flux calibration of the G280 is estimated to be accurate to better than 10%. On deep exposures, orders out to at least -8 and +8 have been detected. Due to the relatively high throughput of the 2nd order, 1st order spectra longward of 400 nm are likely to be overlapped by 2nd order light longward of 200 nm, at least for sufficiently hot sources.

In 2023, the first background sky images for G280 were released (WFC3 ISR 2023-06). One set (two files, one for each CCD) were derived from individual flat-fielded (FLT) science exposures, while a second set were derived from their corresponding CTE-corrected (FLC) frames. Multiple parameters, such as the Earth limb angle, higher sun altitude, smaller sun angle, and the presence of zodiacal light, can increase the sky background for any given observation. However, it was found that all stray light scatters onto the CCD in a similar manner, so the background is well-modeled by a single component. While He I emission was detected in the WFC3/IR grisms (WFC3 ISR 2014-03), no emission line features have been detected in G280.

> ✅ The *Grism Resource page* provides a landing page for new and updated WFC3 grism information.

**Figure 8.3: The throughput of the G280 grism as a function of wavelength for the positive and negative first order, using the most updated calibration reference files generated by the calibration presented in WFC3 ISR 2020-09.**
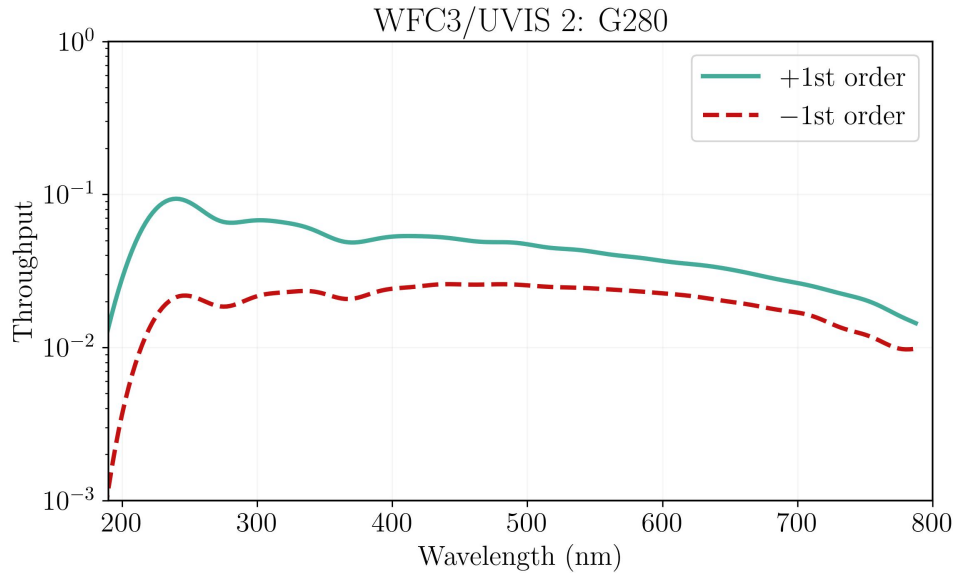


Grism exposures of a given target field should always be accompanied by a direct image. The direct image provides source sizes and identifications, from which the corresponding locations of spectra in the grism images are determined. Knowledge of the direct-to-grism exposure source offsets is necessary to set the wavelength zero-point for each extracted spectrum and the source size measurements enable the software extraction slit to be tuned to each object (see Section 8.5). The 0th-order trace in G280 images is slightly dispersed (making it difficult to centroid) and often saturated (making it impossible to centroid), therefore it cannot be used in place of a direct image.

The natural choice of a direct-imaging filter to provide the reference image for G280 exposures is the F300X, because its response matches most closely the +1st-order grism response. The broader F200LP filter may be preferable for fainter objects. The shape of the spectra in G280 exposures varies significantly across the field of view but has been calibrated (WFC3 ISR 2020-09). The sensitivity of the +1 order also varies, but its field variation could not be handled by the **aXe** package and is only calibrated at the center of chip 2. The separate software package **hstaxe**, a Python follow-up to aXe, can now be used to extract and calibrate one-dimensional spectra from WFC3 grism exposures. Jupyter cookbooks illustrating the procedures for full- and subarray-frames of G280 data are available in the WFC3 section of the hstaxe Github repository. Small dithers of G280 exposures and accompanying direct image exposures are recommended to remove the effects of bad pixels. In addition, it is recommended that CR_SPLIT be used in both the direct and dispersed exposures to allow for cosmic-ray identification and removal.

G280 exposures can only be obtained using the "UVIS" aperture selection, which places the target at the reference point of the UVIS field of view, about 10" above the inter-chip gap, i.e. on chip 1. Accompanying direct images should use the G280-REF aperture selection, which places the target at the same location as in the dispersed exposures. If your observations are of a single primary target, it is best to specify a POS TARG Y of -50", for *both* the dispersed and direct exposures, to place the target at the center of chip 2, where the spectral calibrations are best determined and the near-UV sensitivity is somewhat higher than on chip 1.

For sufficiently bright objects, the multiple spectral orders may extend across the full field of view of the camera. This leads to overlapping of fainter spectra in the vicinity of the bright-object spectrum. Therefore, a careful determination of the optimum telescope roll angle is required to obtain non-overlapped spectra of faint objects in the vicinity of much brighter objects. i.e., the observer needs to set the orientation of the detector on the sky by using the Visit Orientation Requirements parameter "ORIENT" in the phase II proposal; e.g. ORIENT = 135.17 degrees aligns the Y axis of the UVIS detector with North for the G280 and G280-REF apertures. See Section 6.2. of the Phase II Proposal Instructions, which gives detailed information on the relationship between detector coordinates, spacecraft coordinates, and ORIENT. **Note: if ORIENTs are necessary, they must be requested in the Phase I proposal.**

CTE losses can be large for faint spectra on faint backgrounds. They should be taken into account when planning UVIS exposures. See Sections 5.4.11 and 6.9 for information on CTE and observing strategies.

# 8.3 Slitless Spectroscopy with the IR G102 and G141 Grisms

8.3.1 IR G102
8.3.2 IR G141

IR grism observations can be obtained using either full-frame or subarray apertures. Subarrays are useful for reducing exposure times for bright objects and for reducing data volume to avoid time lost to serial buffer dumps. First-order spectra for both the G102 and G141 grisms comfortably fit within 512 × 512 and 256 × 256 pixel subarrays.

**Grism observations of a given target field should always be accompanied by a direct image**, which is used to locate sources and determine source sizes. The locations of sources in the direct image are then used to guide the placement of extraction apertures in dispersed images, and to tune the size of the extraction apertures to the source size. The location of sources in direct images is also used to establish the wavelength zero-point for extracted spectra by using offsets from the direct image. Appropriate filters to use for direct images are discussed in the following sections for each IR grism. As with normal imaging observations, grism observations should be dithered to aid in the removal of bad pixels. Accompanying direct images can be obtained at each of the same grism dither positions, but this is not strictly necessary. It is usually sufficient to obtain a direct image at just 1 or 2 of the dither positions. Direct imaging is best taken at the beginning and/or end of a visit so that the grism observations are less likely to be impacted by temporal variations in the background from the bright Earth limb and scattered light.

While a direct image is required for identifying the full complex of overlapping orders in spectral images, wavelength assignments for sources with known coordinates can be derived using the offsets from the zero order grism images (see WFC3 ISR 2015-10). The inaccuracy caused by any non-linearity in the dispersion is estimated at ~0.1 pixel or ~2.5 Å for G102 and ~5 Å for G141. The rms precision of the assigned wavelengths for individual spectra is better than 0.2 pixel. For the same or very similar POSTARGs, the separation from direct image to zero order varies by up to 0.5 pixels in both x and y directions, corresponding to an uncertainty of about ~12Å (G102) and ~23Å (G141).

The GRISM apertures (given at the bottom of Table 7.1) are designed to be used for both the grism exposure and the associated direct image. At a given telescope pointing, the first order spectrum and the location of the target in the direct image are roughly aligned in the x direction. The G102 spectrum starts at about 55 pixels to the right of the target image location and extends about 155 pixels; the G141 spectrum starts at about 35 pixels to the right of the target image location and extends about 135 pixels. For either grism, the same pointing can thus be used to place the target image and the first order spectrum on an array with dimensions greater than about 210 pixels. The apertures GRISM1024, GRISM512, and GRISM256 have been designed to take advantage of this, with the placement of the target optimized for the dimensions of the array, which is indicated by the number in the aperture name. For the smaller apertures, GRISM128 and GRISM64, different pointings are automatically used for the direct image and the grism exposure so that the target is within the aperture in the direct image and the target's spectrum is also inside the aperture in the grism image. See WFC3 Grism Resources webpage for details on selecting GRISM apertures and using combinations of these apertures.

Objects that are off the edges of the detector will still produce dispersed spectra since the detector field of view is smaller than the rest of the WFC3 optics. Any object that is within -183 pixels (-22 arcsec) of the left edge, or +85 pixels (+10 arcsec) of the right edge of the detector will result in positive or negative orders spectra, respectively. This is described in WFC3 ISR 2016-15.

**Figure 8.4:** Overview of total transmission for the G102 and G141 grisms (from WFC3 ISR 2011-05 ). The spectral ranges with more than 10% throughput are indicated.
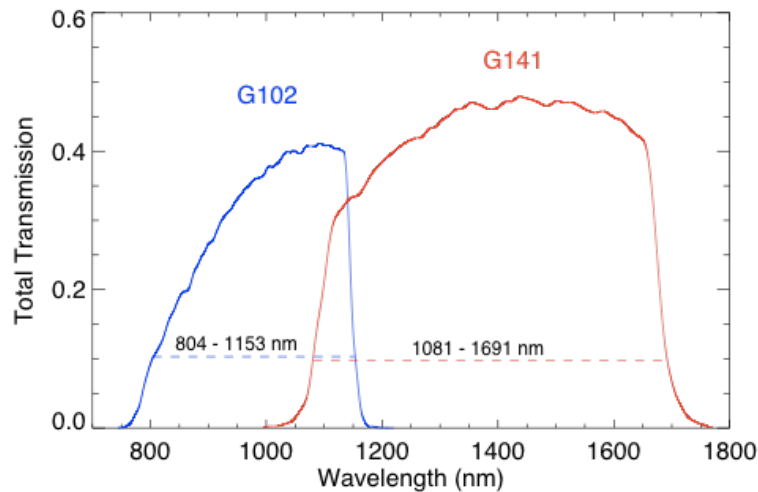


The performance of the IR grisms was analyzed during SMOV (WFC3 ISR 2009-17, WFC3 ISR 2009-18 ). The flux calibration was revised based on calibration observations made in cycle 17 (WFC3 ISR 2011-05). Figure 8.4 shows the total transmission for both grisms as a function of wavelength; indicated are the spectral ranges with total throughput greater than 10%. Analysis of monitoring observations made from SMOV through cycle 20 has shown that the flux calibrations of the +1st order spectra have excellent temporal stability, varying by less than 1%, and that the calibration of the large-scale throughput variations over the detector are good to 4% (WFC3 ISR 2012-06 and WFC3 ISR 2014-01). Point source aperture corrections measured in cycle 20 (WFC3 ISR 2014-01) are generally consistent with those derived in cycle 17 (WFC3 ISR 2011-05) to 1%. Sky images for the IR grisms have been constructed using publicly available data; the average sky brightness measured in the G102 and G141 images is 0.8 e-/s and 1.3 e-/s, respectively (WFC3 ISR 2011-01). Multiple components of the sky backgrounds have been modeled and include three components: Zodiacal light, He I glow, and scattered light, providing a significantly improved background subtraction (WFC3 ISR 2020-04). A separate software package called `hstaxe` can be used to extract and calibrate one-dimensional spectra from WFC3 grism exposures (see specifically the WFC3 Jupyter notebooks in the `hstaxe` Github repository, and WFC3 ISR 2023-07). In 2023, a different Python package to extract wide-field slitless spectroscopy for the IR grisms, `slitlessutils`, was released (see Section 8.5).

The wavelength calibration of the +1, -1, and +2 G102 and G141 orders were re-derived using all of the available multi-cycle calibration data (WFC3 ISR 2016-15). The accuracy of this new calibration is estimated to be better than 0.1 pixel for the trace description and better than 0.5 pixel (~10A and 20A for the G102 and G141 grisms, respectively) for the wavelength calibration. Previous calibration assumed that grism observations would be paired with F098M and F140W direct images for the G102 and G141 grisms, respectively. Calibration solutions that include the effect of the filter wedge offset ( WFC3 ISR 2010-12) are now also available.

> ✅ *Please see the G102 Calibrations and G141 Calibrations webpages for the most updated calibration and reference files, as well as a full calibration history.*

# 8.3.1 IR G102

The G102 grism provides first-order spectra over the wavelength range from the grism short-wavelength cutoff at about 800 nm up to 1150 nm. The dispersion is high enough that only the positive first and second-order spectra, as well as the zeroth-order image, are visible on the detector when the positive first-order spectrum is centered in the field of view.

Figure 8.5 shows the position of the zeroth-order image and +1st-order spectrum (which has much higher sensitivity than the –1st order due to the grating blaze) for the G102 grism. The location of the direct image (superposed from an F098M undispersed exposure) is indicated in the figure.

Figure 8.5: G102 grism observation of the flux standard star GD153 (program 11552) with a F098M direct image (circled) superimposed to illustrate the relative positions. Spectral orders 0, +1, and +2 can be seen on the image. The image shows the full extent of the detector in the *x*-axis (1024 pixels) and about 200 pixels in the *y*-axis.
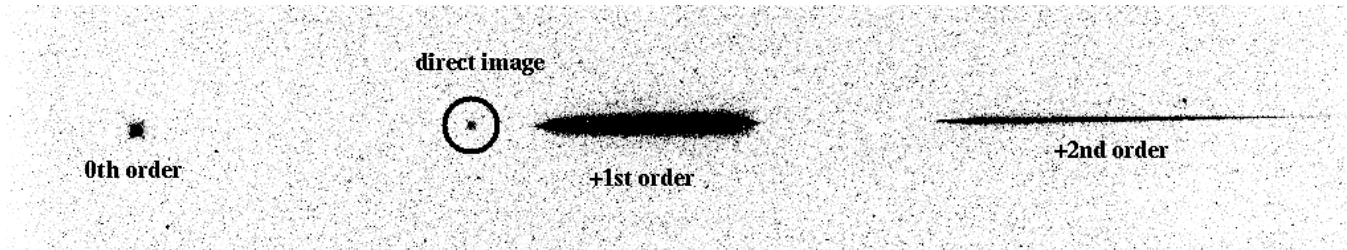


The trace of the first-order spectrum is well described by a first-order polynomial, however the offset and slope are a function of source position in the field. The tilt of the spectrum is 0.7° with respect to the detector x-axis. The total throughput (including *HST* optics) of the G102 grism has a maximum of 41% at 1100 nm in the positive first order and is above 10% between 805 and 1150 nm. The zeroth order and other negative and positive orders show much lower throughput (see Figure 8.6). The dispersion in the +1st order varies over the field from 2.36 to 2.51 nm/pixel; this variation was calibrated from both ground and on-orbit data to allow absolute wavelength calibration to better than one pixel. The absolute throughput of the G102 orders –1 to +3, including the instrument and the detector, is shown in Figure 8.6. Suitable filters for the accompanying direct images for source selection and wavelength zero-point determination are F098M (preferred) or F105W (see Section 7.9.5 for discussion of the IR background), but any of the narrower filters can also be used to prevent bright sources from saturating.

**Figure 8.6:** The absolute throughput (log-scaled) of the G102 grism as a function of wavelength for the +1st, +2nd, +3rd, and -1st orders (from WFC3 ISR 2011-15).
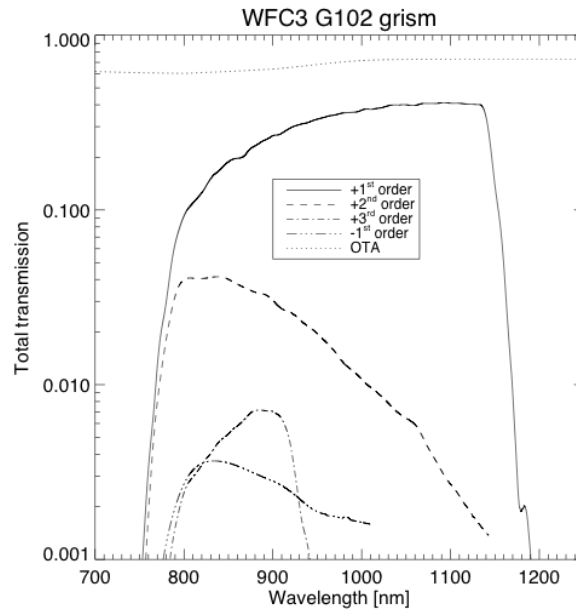


## 8.3.2 IR G141

For the lower-dispersion G141 grism, the 0th-, 1st-, 2nd-, and 3rd-order spectra all lie within the field of view when the positive first-order is roughly centered. Figure 8.7 shows the appearance of the spectra on the detector, with the superposed direct image, for the G141 grism. The useful spectral range is from 1075 nm to about 1700 nm, limited in the red by the grism bandpass. Over most of the spectral range, more than 80% of the throughput is in the +1st-order spectrum. The trace of the first-order spectrum is well described by a first-order polynomial. The average tilt of the spectrum is 0.5 degrees with respect to the detector x-axis. The dispersion in the +1st-order varies over the field from 4.47 to 4.78 nm/pixel; this variation has been measured from both ground and on-orbit data to allow absolute wavelength calibration to better than one pixel. The total throughput (including *HST* optics) of the G141 grism reaches a maximum of 48% at ~1450 nm in the positive first order and is above 10% between 1080 and 1690 nm (see Figure 8.8).

256
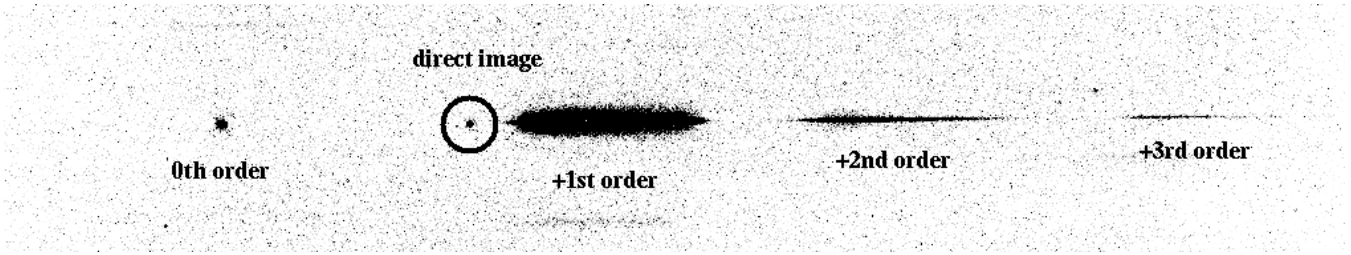
**Figure 8.8:** The absolute throughput (log-scaled) of the G141 grism as a function of wavelength for the +1st, +2nd, +3rd, and -1st orders (from WFC3 ISR 2011-15).
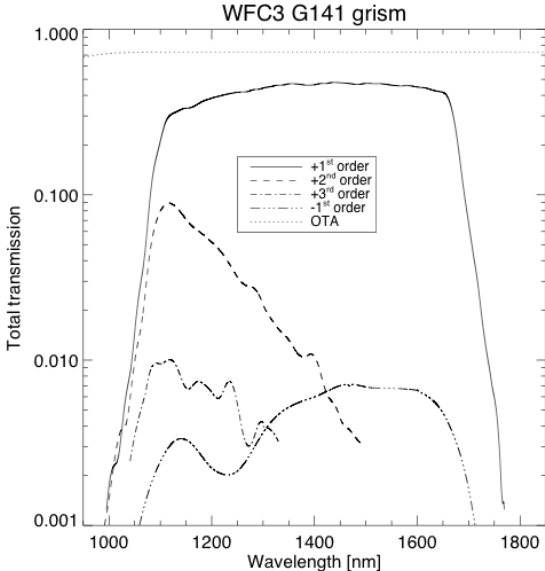


WFC3 G141 grism

Suitable filters for the accompanying direct images for source selection and wavelength zero-point determination are F140W (preferred) or F160W in the case of extremely red sources. Any of the narrower IR filters can also be used in order to avoid saturation of bright targets.

# 8.4 Sensitivities and Exposure-Time Estimation

Table 8.2 lists current estimates of the detection limits for slitless spectroscopy with the UVIS and IR modes. The numbers in the table are the *V* magnitudes of point sources for which a 1-hour exposure yields a spectrum with a S/N of 5 per resolution element, with extraction boxes of 1 × 5 and 1 × 3 pixels for the UVIS and IR, respectively. V magnitudes are given for three different assumed source spectral types.

Table 8.2: *V*-band detection limits for the WFC3 grism modes for 1-hour exposure and 5σ detection.

| Mode | Spectral Type | | | Wavelength (nm) |
| --- | --- | --- | --- | --- |
| | O3 V | A0 V (Vega) | G2 V | |
| UVIS2/G280 | 25.0 | 21.9 | 18.2 | 250 |
| IR/G102 | 21.3 | 22.0 | 22.9 | 1050 |
| IR/G141 | 20.5 | 21.3 | 22.8 | 1550 |

For more accurate estimations of exposure times, observers should use the WFC3 Exposure Time Calculator (ETC). The ETC supports all three spectroscopic modes.

# 8.5 Extraction and Calibration of Spectra

Because there is no slit in the WFC3 grism mode, the PSF of the target determines the spectral resolution. In the case of non-stellar sources, it is the extent of the target in the direction of dispersion that limits the spectral resolution. The height of the software extraction slit is based on the object extent in the cross-dispersion direction of the direct image.

The dispersion of the grisms is well characterized, but in order to set the wavelength zero-point, it is necessary to know the position of the target in the direct image. The zeroth-order is generally too weak and is also slightly extended in a dispersed image to allow the wavelength zero-point to be set reliably. Given the typical spacecraft jitter, wavelength zero-points to ±0.5 pixels should be routinely achievable using a direct image taken just before or after the grism image.

Initially, a spectral extraction software package, called `aXe`, was made available to extract, flat-field, wavelength- and flux-calibrate WFC3 grism spectra. A separate software package, **hstaxe**, which is a follow-up to `aXe`, can now be used to extract and calibrate one-dimensional spectra from WFC3 grism exposures. Python Jupyter notebooks illustrating the extraction and calibration workflow for both UVIS and IR grisms are available in the WFC3 section of the `hstaxe` Github repository. Additionally, at the end of 2023, STScI released a preliminary version of **slitlessutils**, a new Python package for extracting and simulating wide-field slitless spectroscopy for WFC3 and ACS. An implementation of the LINEAR algorithm developed for fields of multiple orients (WFC3 ISR 2018-13), `slitlessutils` also includes a modified version of the `aXe` extraction for fields with a single orient. Several accompanying utility functions can be used to preprocess grism data (e.g. astrometric updates, background subtraction, and cosmic ray rejections) and thereby improve the final calibrated extractions.

The spectral trace and dispersion solutions are a function of source position within the field of view. These 2-dimensional variations were determined during the ground calibration campaigns and from on-orbit data. The resulting reference and calibration files are available on the WFC3 Grism Resources webpage. For bright sources, the multiple spectral orders of the G280, G102, and G141 grisms may extend across the full detector extent. Therefore, a careful selection of the optimum telescope roll angle is required to obtain non-overlapping spectra of faint sources in the vicinity of brighter objects. i.e., the observer needs to set the orientation of the detector on the sky by using the Visit Orientation Requirements parameter "ORIENT" in the Phase II; e.g. ORIENT ~135 degrees aligns the Y axis of the IR detector with North. See Section 6.2.2 of the Phase II Proposal Instructions, which gives detailed information on the relationship between detector coordinates, spacecraft coordinates, and ORIENT, and works out this example for aperture GRISM1024 (ORIENT = 135.3). Using the information in that section, one finds ORIENT ranging from 135.12 to 135.32 for the IR GRISM apertures (used for the grism exposures and matching reference images) and ORIENT = 135.17 for the G280 and G280-REF apertures). **Note that any ORIENT requirement must be specified in the proposal Phase I** in the *"Special Requirements"* section (see also the news section in the Phase I proposal instructions).

The quality of extracted spectra from single grism exposures can be degraded by bad pixels (e.g., dead, hot, strong cosmic ray hit). We recommend a dithering strategy for grism exposures. The `hstaxe` software automatically takes dither steps into account by using the information in the image headers to produce a combined spectrum with cosmic rays and bad pixels removed, while the new `slitlessutils` package provides cosmic ray mitigation via a preprocessing step

# UVIS Grism Extraction

The `hstaxe` packaage can be used to locate and extract slitless spectra of individual sources from calibrated G280 images, and perform wavelength calibration, background subtraction, flat fielding, and absolute flux calibration for the extracted spectra.

Characterizing and minimizing the background light is necessary to optimize spectral extraction. WFC3 ISR 2023-06 presented the first background sky images for G280 (Figure 8.8), now available to download from the UVIS Grism Sky Images webpage. A single component was determined to be sufficient to model the scattered light, primarily originating from zodiacal light. While Earth limb angle, sun altitude, and sun angle were found to impact the background level, no additional spectral components attributable to OII emission in Earth's atmosphere were detected. Additionally, it was found that stray light scatters similarly regardless of component source.

These background sky calibration frames can be used as input in the `hstaxe` spectral extraction software by setting background subtraction to `True` using the `backgr` keyword and defining the path to the G280 sky frames using the `backims` keyword (see the G280 extraction cookbook for an in-depth tutorial on using `hstaxe` to extract spectra from G280 exposures).

**Figure 8.8: G280 background sky for UVIS 1 and UVIS 2 derived from individual flat-fielded, CTE-corrected science exposures (from WFC3 ISR 2023-06).**
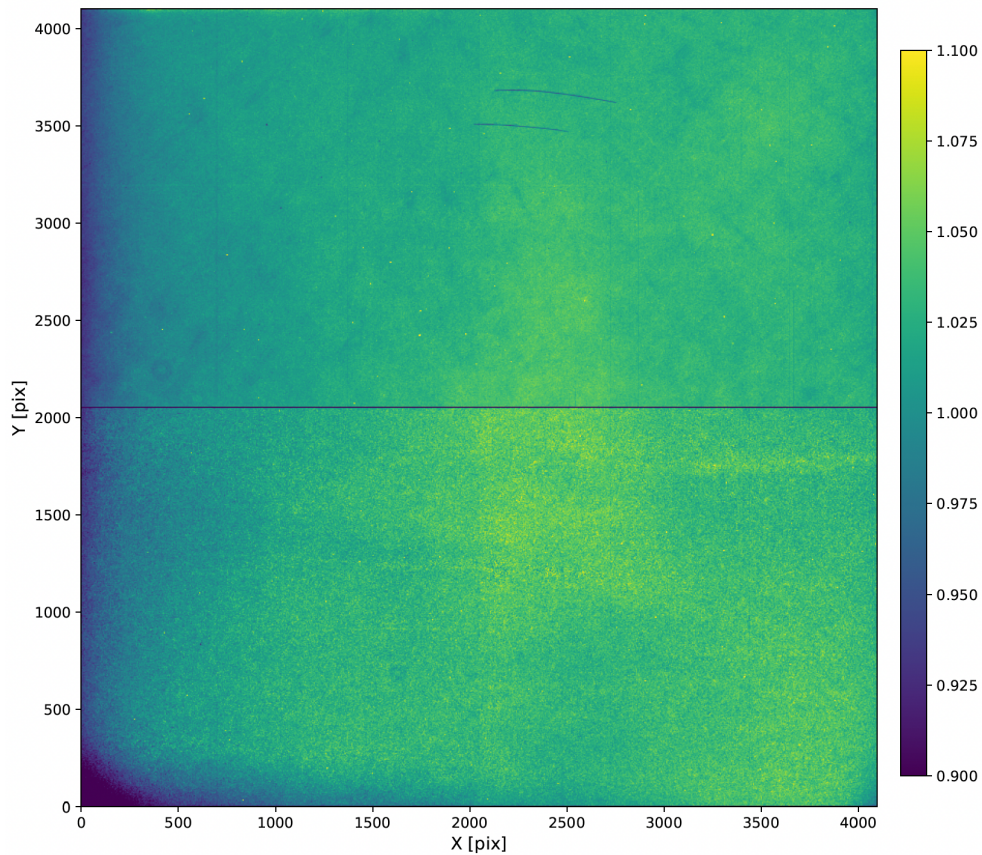


## IR Grism Extraction

Extraction of WFC3/IR slitless spectra depends on an accurate determination of the diffuse background light that is observed in all grism exposures. The two-dimensional structure in the background of WFC3/IR grism exposures is caused primarily by overlapping grism spectral orders that are vignetted at different locations within the detector field of view and by the spectrum of the diffuse background. Both `hstaxe` and `slitlessutils` can be used to locate and extract spectra of individual sources from calibrated images and perform wavelength calibration, background subtraction, flat fielding, and absolute flux calibration for the extracted spectra. For examples of how to preprocess WFC3/IR data and extract 1D spectra, see the `hstaxe` Jupyter notebooks.

A more accurate background subtraction can be achieved by using separate images for each of these background components: zodiacal light, He I emission, and scattered light. These components are shown for G102 and G141 in Figure 8.9 and Figure 8.10, respectively. The He I component is due to a 1.083 µm emission line in the Earth's upper atmosphere and often appears in exposures obtained while the spacecraft is outside of the earth's shadow (see Section 7.9.5). The intensity of this airglow line varies on timescales of an orbit or even a single sample sequence. Scattered light produces a different structure, having bypassed the grism to reach the detector. WFC3 ISR 2015-17 presented a file containing all three component images for G141 and two of the component images for G102 (zodiacal light and He I emission) and an algorithm for applying them to observed WFC3/IR grism data. Images of all three background components for both IR grisms and software to background-subtract grism datasets are now available on the WFC3 Grism Resources webpage. Further discussion of the modeling and removal of background components are given in WFC3 ISR 2017-01 and WFC3 ISR 2020-04. See WFC3 ISR 2023-07 for more details regarding background subtraction with `hstaxe`.

**Figure 8.9: Background components for G102.**
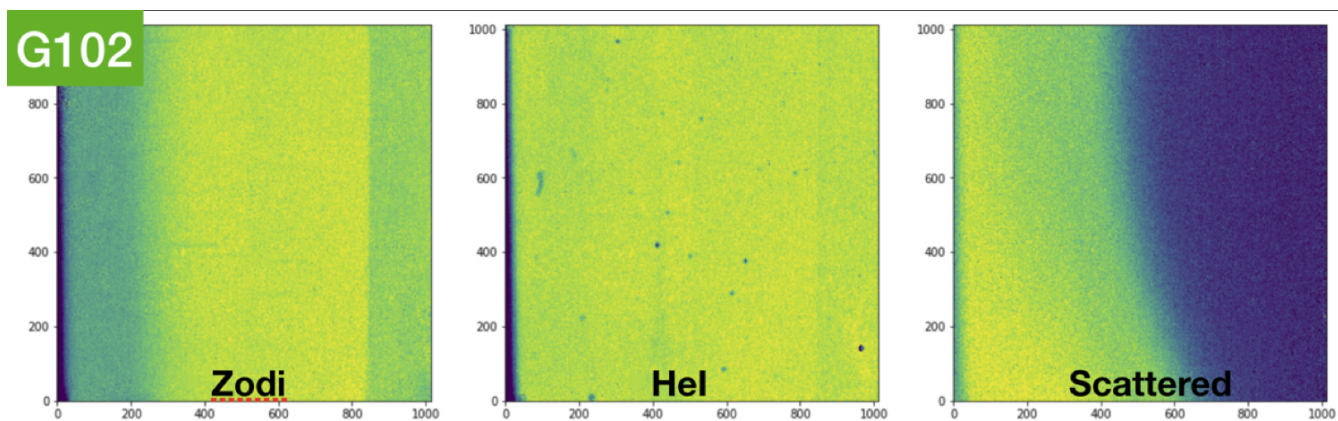
**Figure 8.10: Background components for G141.**
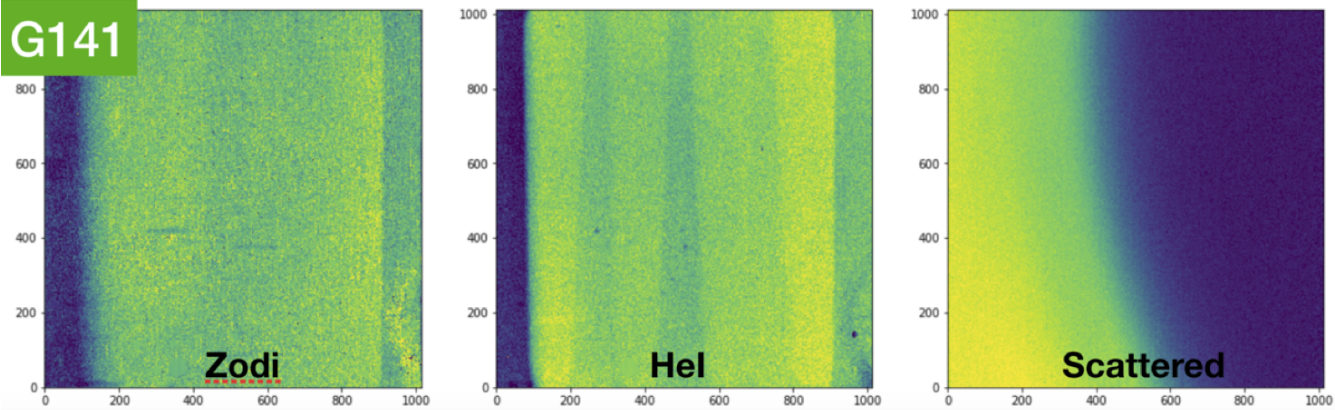
# 8.6 Slitless Spectroscopy with Spatial Scanning

Spatial scanning of stellar spectra using the IR detector creates the potential for spectrophotometry of higher precision than possible via staring mode. By spreading a stellar spectrum perpendicular to its dispersion (Figure 8.11), more photons can be collected per exposure, and the exposure times can be longer without saturating the detector. This strategy results in higher signal-to-noise observations and an increased duty cycle. The most prevalent scientific application is transit spectroscopy, in which a time series of stellar spectra are obtained before, during, and after an exoplanet transit or eclipse; observations of this type with one-sigma precision of ~20 ppm in ~20 nm spectral bins from two transits have been reported (Knutson et al. 2014). Results for exoplanet transit spectroscopy have been published by numerous investigators; recent examples using WFC3 spatial scanning include Alam et al. 2022, Alderson et al. 2022, Barat et al. 2023, and Barclay et al. 2023.

The WFC3 team has introduced and will continue to update the Transiting Exoplanets List of Space Telescope Spectroscopy (TrExoLiSTS, formerly called ExoCat; see WFC3 ISR 2022-09) that summarizes the existing WFC3/IR spatial scanning observations of time series observations acquired during primary transits, secondary eclipses, and phase curves. Information presented includes the observational parameters along with the direct image, white light curve, and the measured drift of the spectrum in the field of view. The goal of presenting this catalog is to facilitate the preparation of WFC3 exoplanet programs by providing observers with information that they can use to optimize their target selection and to prevent target duplications.

In the time series, the integrated flux of a WFC3/IR spectrum exhibits a hook-shaped rise in each *HST* orbit due to charge trapping within the detector pixels. Mitigation of the "hook" has been attempted in observational techniques (WFC3 ISR 2014-14) and in post-observation modeling (e.g., Zhou et al. 2017).

**Figure 8.11:** A spatially-scanned IR spectrum, labeled with its 0th and +1st order light, compared to a nominal staring-mode slitless spectrum of the same field (red outlined inset, WFC3 ISR 2012-08). The images are 512 columns wide, centered in the detector's 1024 columns. The scan was 40 pixels high (4.8 arcsec).
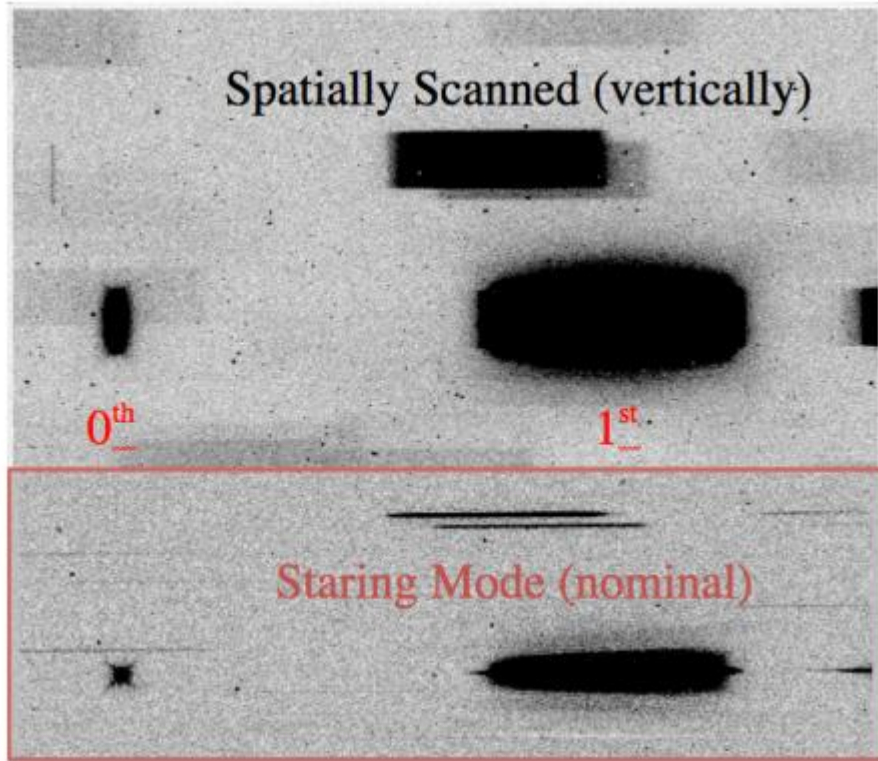


Spatial scanning is available with either WFC3 detector, UVIS or IR. However, overlap of spectral orders and curved spectral traces will compromise scanning's utility for the UVIS grism. In this section, we assume that for IR spectroscopy, the observer desires the +1st order spectrum. Spatial scans are discussed elsewhere in this handbook (for UVIS imaging in Section 6.11.3, for IR imaging in Section 7.10.4) and in WFC3 ISR 2012-08. The latter is particularly relevant for anyone preparing a Phase II proposal.

Potential benefits of spatial scanning are 1) reducing overhead for time-series of short exposures due to detector operations required before and after each exposure, 2) avoiding saturation for very bright stars, 3) improved spectrophotometry, as collecting more photons per *HST* orbit improves the signal-to-noise ratio. We note that the main disadvantages are 1) STScI pipelines do not work on spatially-scanned IR data so the observer will need to reduce IR data themselves even to produce simple images, and 2) astronomical sources will overlap more often than with staring-mode observations, especially for spectra.

As of June 2024, allowable single-line scan rates under FGS control can be any value between 0.0 and 4.9 arcsec s$^{-1}$; serpentine (boustrophedonic) scan rates can be 0.0 and 0.99 arcsec s$^{-1}$. Scan rates higher than these (as well as gyro pointing control) are no longer possible as HST operation has transitioned to Reduced Gyro Mode. WFC3 ISR 2012-08 provides recommended scan rates for WFC3 IR spectroscopy of bright stars as well as formulae to predict appropriate scan rates.

Python code and web tools are available to assist observers in designing spatial scanning observations for exoplanet transits. The PandExo code (Batalha et al. 2017) was extensively tested using WFC3 observations, and provides realistic noise estimates for simulated time-series observations based on system parameters, an input planetary model, and various observation parameters (e.g., number of transits/eclipses, number of spectrophotometric channels, size of the observation start window) and various WFC3 parameters (e.g., disperser, subarray size, N_SAMP, SAMP_SEQ, scan direction). The simulations can also account for the WFC3 ramp effects described above. The GUI for PandExo is integrated into ExoCTK (Exoplanet Characterization Toolkit) and can be used to make one-off calculations in a web form. PandExo_HST can be locally installed to perform more detailed calculations on one's own computer.

The sample sequence SPARS5, introduced during Cycle 23, has time steps intermediate between those of RAPID and SPARS10. As for all WFC3/IR sample sequences, the time intervals depend on the size of the aperture (see Sections 7.7.3 and 7.7.4). SPARS5 was designed to allow the efficiency and uninterrupted time series of SPARS10 and yet be short enough in cadence to better isolate a target exoplanet-host star from a nearby stellar companion in spatially-scanned observations using an IR grism. Better isolation may enable the observer to specify wider orient ranges, which may increase scheduling opportunities, which are often rare for these time-constrained observations. We expect that SPARS5 will be advantageous especially for G141 or G102 grism observations of stars brighter than approximately 7th magnitude in H band, scanned at approximately 1 arcsec per second or faster. The subarray apertures are especially useful for IR grism observations of bright stars with the sample sequences RAPID, SPARS5, and SPARS10 because of their short time steps and efficient orbit packing. The combination of SPARS10 with a 512 × 512 aperture is not currently supported (and therefore has a lower quality dark reference file), but spectroscopic spatial scan observers who need it for improved observing efficiency and consequent increases in signal-to-noise may send a justification for available mode use to the Contact Scientist or the Program Coordinator.

APT provides a diagram to assist observers planning spatial scan observations as shown in Figure 8.12. The line connecting the green and red arrows corresponds to where the target's direct image would appear. In grism observations, the first order spectrum appears at larger X coordinate values than the direct image (see Figures 8.5 and 8.7). By design of the GRISM128, GRISM256 and GRISM512 subarrays, a POSTARGX = 0 centers the first order spectrum in each subarray in the X coordinate. Because the diagram is only approximate and because of on-going developments in APT and spacecraft operations, users of fast spatial scans (~1 arcsec/sec or faster) should consult with their contact scientist to optimize the POSTARGY value.

**Figure 8.12: Diagram provided in APT to assist planning of spatial scan observations.**



Approximate target trajectory on detector
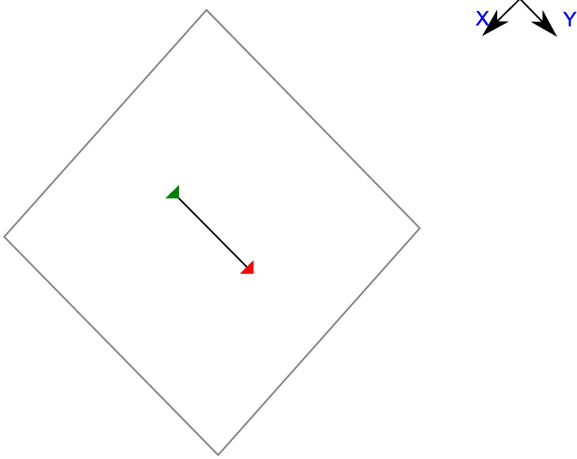
▶ Scan start
▶ Scan end
*These scan positions are shown in the same colors in Aladin.*

# Chapter 9: WFC3 Exposure-Time Calculation

## Chapter Contents

# 9.1 Overview

Chapter 4 of this Handbook describes the procedures for designing a Phase I WFC3 observing proposal. Two of the steps involved in this process are estimating the exposure times needed to achieve your scientific goals, and then combining these individual exposures with their associated overheads to derive the number of spacecraft orbits that you will request in your Phase I proposal.

This chapter provides guidance on estimating exposure times. The following chapter, Chapter 10, then describes how to include the various overheads so as to determine the total number of spacecraft orbits needed for your program.

You should also refer to the *HST Call for Proposals*, which includes information on policies and practices with respect to orbit-time requests. The *HST Primer* provides specific advice on orbit determination. In particular, please be sure to check the What's New section in the Primer for any late-breaking news. In this chapter, we provide a summary of the WFC3 sensitivities and give several examples that illustrate how to calculate your exposure times for Phase I Proposals.

# 9.2 The WFC3 Exposure Time Calculator - ETC

In most cases, you will find it convenient to use the online WFC3 Exposure Time Calculator (ETC) to make estimates of the required exposure times for your project.

The ETC calculates counts (e⁻) and count rates (e⁻/s) for input source and background parameters and assumed characteristics of the detectors. Once these are entered, the ETC then outputs signal-to-noise ratios (SNRs) achieved for a given exposure time, or the exposure times required to achieve a given SNR The ETC supports both direct-imaging and spectroscopic (grism) observations. Starting in 2016 (Cycle 24), the ETC supports spatial scanning for UVIS and IR imaging and IR spectroscopy (WFC3 STAN issue 22). A variety of circular and square extraction apertures are available in the ETC, allowing the user to select either a radius in arcseconds or a size in pixels. It is also possible to input a calibrated spectral-energy distribution (SED) of your source directly into the ETC. The ETC also outputs peak per-pixel count rates and total count rates, to aid in feasibility assessment. Warnings will appear if the source will saturate the detector, which would not only compromise CCD and IR observations, but might even affect subsequent exposures with the IR channel (Appendix D). The ETC has online help for its execution and interpretation of results.

There are some items worth noting:

- For the UVIS channel, the ETC uses a CCD full-well value of 63,000 e⁻, the minimum value for either CCD chip, to determine saturation; users wishing to strictly avoid this occurrence should allow a buffer of at least 10% below this. (Section 5.4.5 presents a discussion of saturation.)
- For the UVIS channel, to the extent possible, one should select Detector chip 2 for UV filter exposures and place the target on chip 2 (e.g., aperture UVIS2 in Figure 6.1 or the subarray apertures in the lower left quadrant of Figure 6.2) since chip 2 has better quantum efficiency than chip 1 (Figure 5.2). Note, however, that the quad filters have quadrant-dependent passbands as specified in Table 13.5 in Section 13.4.1 of the *Phase II Proposal Instructions*. The user should be careful to select the Detector chip corresponding to the relevant quadrant for a given filter name, since the ETC will incorrectly allow either chip to be selected. (Quads A and B are on chip 1; quads C and D are on chip 2.)
- To mitigate CTE losses, observers can add background to UVIS exposures by using the post-flash option (Section 6.9.2). See Section 9.6 for equations that show how the post-flash background affects the calculation of SNR and exposure time.
- For the IR channel, when the # of Frames = 1, the ETC assumes a complete timing sequence (NSAMP = 15). For smaller NSAMP, the read noise is greater (Section 5.7.3). For most programs, NSAMP should be greater than 5, and ideally more if possible, to achieve the best readnoise and cosmic ray correction (Section 7.10.3).
- The He I airglow line at 10,830 Angstroms is being added as a component of the IR sky background for Cycle 24 and beyond (Section 7.9.5). It only contributes to the background observed in the F105W and F110W filters and the G102 and G141 grisms. The default ETC value of "None" will provide ETC estimates unchanged from those of previous cycles. The other available options---Average, High, Very High---are the 50%, 75% and 95% percentile values of the excess background, per exposure, observed over the value estimated for the zodiacal light alone (e.g., Figure 7.12). Determined from an analysis of archival exposures, these percentiles correspond to an additional 0.1, 0.5, and 1.5 e-/s, respectively, normalized in the F105W filter. Note that the "Average" value of 0.5 e-/s is comparable to the flux predicted for the zodiacal background (Figure 7.12). Furthermore, achieving the He I value of "None" is essentially only possible if the SHADOW special requirement is used, though this is not recommended as the available usable orbit duration is then dramatically reduced; it is almost always preferable to keep observing even in the presence of elevated backgrounds for part of the orbit (WFC3 ISR 2014-03).

It is also possible to use `stsynphot` to calculate count rates and the wavelength distribution of detected counts.

The remaining sections of this chapter give detailed information on the sensitivities of the UVIS and IR channels when combined with the various spectral elements, and the use of this information in the determination of count rates, for those who wish to understand the subject in depth.

# 9.3 Calculating Sensitivities from Tabulated Data

> ⚠️ Note: the updated (2024) WFC3/IR photometric calibration discussed in this section was not "live" at the original date of publication. This banner will be removed when the relevant reference files and calibration pipeline changes are available.

Most observers will use the ETC or `stsynphot` to determine count rates and sensitivities for WFC3 observations. However, it is also possible to calculate count rates and signal-to-noise ratios (SNRs) manually, and this exercise will give the observer better insight into the sensitivity calculations. The formulae and tabular values required to calculate sensitivities for the WFC3 imaging and spectroscopic modes are provided in this section. Using them, one can calculate the expected count rates and the SNR achieved in a given exposure time, based on the spectral energy distribution of a source. The formulae are given in terms of sensitivities, but we also provide transformation equations between throughput ($QT$) and sensitivity ($S$) for imaging and spectroscopic modes.

The tabular data presented here were derived using on-orbit data acquired over ~10 years (see WFC3 ISR 2021-04 and WFC3 ISR 2024-06 for the latest UVIS and IR photometric calibration). Monitoring of the photometric performance shows that the WFC3/UVIS detector sensitivity changes by ~0.1 - 0.2 % per year, depending on the filter; WFC3/IR sensitivity losses are ~0.1% per year, also filter-dependent. The values listed in Table 9.1 (UVIS) and Table 9.2 (IR) are calculated for a 'reference epoch' defined at MJD = 55008 (June 26, 2009). A Jupyter notebook shows how to use `stsynphot` to compute sensitivity values for any WFC3 observing mode, 'obsmode', i.e. a combination of the desired 'instrument, detector, filter, date, and aperture'. This may be used to determine the UVIS tabular values for any observation date. The new time-dependent inverse sensitivities provide a photometric internal precision of < 0.5% for wide-, medium-, and narrow-band filters. As of early 2024, the WFC3/IR inverse sensitivities do not include any time-dependence, and the values listed in Table 9.2 are valid for all observation dates. Current estimates of the IR photometric uncertainties are ~2% for broad-band filters and 5-10% for narrow-band filters. For a more detailed discussion about WFC3 photometric calibration, see Section 9.1 of the Data Handbook.

Sensitivity data for the G280 grism listed in Table 9.1 is derived from ground-based calibration during Thermal Vacuum testing, as described in WFC3 ISR 2009-01. Sensitivity data for the G102 and G141 grisms provided in Table 9.2 were established by observing the white dwarf spectrophotometric standard stars GD153 and GD71 at several positions across the field (WFC3 ISRs 2009-17, 2009-18, and 2011-05).  For more detail on the calibration of the WFC3 grisms, see Section 9.3 of the Data Handbook.

> ✅ *For the latest set of photometric inverse sensitivities (zeropoints), see the WFC3 Photometric Calibration website.*

Filter throughputs are presented in graphical form as a function of wavelength for both chips, UVIS1 and UVIS2, and all the imaging filters and grisms in Appendix A. Given the source characteristics and the sensitivity of the WFC3 configuration, calculating the expected count rate over a given number of pixels is straightforward. The additional information required is the encircled energy fraction ($\varepsilon_f$) in the peak pixel, the plate scale, and (for the spectroscopic modes) the dispersions of the grisms.

The sensitivity information is summarized in Tables 9.1 and 9.2. Here and in the following discussion, the filter transmission functions are denoted $T_\lambda$ , and the overall system response function (apart from the filter transmission) is denoted $Q_\lambda$. The terms 'counts' and 'count rates' always refer to the number of detected electrons, which is converted to data numbers, or DNs, upon readout according to the gain factors for the detectors. The measured gain is 1.55 e¯/DN for the UVIS channel and ~2. 4 e¯/DN for the IR channel (see Table 5.1).

In Tables 9.1 and 9.2, the following quantities are listed:

1. The filter or grism designation.
2. The 'pivot wavelength' for that filter or grism, $\lambda_p$. Pivot wavelength is a source-independent measure of the characteristic wavelength of a bandpass, defined such that it is the same if the input spectrum is given in units of $F_\lambda$ or $F_\nu$ (see Tokunaga & Vacca 2005, *PASP*, **117**, 421). For further discussion on `synphot` formulae, see the `synphot` documentation on photometric properties.

$$\lambda_p = \sqrt{\frac{\int Q_\lambda T_\lambda \lambda d\lambda}{\int Q_\lambda T_\lambda \lambda^{-1} d\lambda}}$$

3. The bandpass 'efficiency', defined as the integral $\int Q_\lambda T_\lambda \lambda^{-1} d\lambda$, is used to determine the count rate when given the astronomical magnitude of the source. In the latest python-based `stsynphot` software (Lim et al. 2016), this dimensionless quantity 'efficiency' is equivalent to the result for 'qtlam' in the older IRAF STSDAS `synphot` task 'bandpar'.
4. The ABmag zero-point, defined as the AB magnitude of a source with a flat $F_\nu$ that yields 1 $e^-$ $s^{-1}$ with the specified configuration.
5. The sensitivity integral, $\int S_\lambda \, d\lambda$, defined as the count rate that would be detected from a flat $F_\lambda$ source with a flux of 1 $erg \, cm^{-2} \, s^{-1} \, Å^{-1}$ (see Section 9.4). The sensitivity integral is equivalent to PHOTFLAM$^{-1}$, where PHOTFLAM is a header keyword defined as the 'inverse sensitivity', representing the flux density ($erg \, cm^{-2} \, s^{-1} \, Å^{-1}$) of a source that produces a count rate of $1 \, e^- \, s^{-1}$.
6. The ensquared energy, defined as the fraction of PSF flux enclosed in the default photometry aperture (5 × 5 pixels for the UVIS and 3 × 3 pixels for the IR).
7. The fraction of the total PSF flux in the central pixel for a centered stellar source, useful for determining the peak count rate to check for saturation (see also Appendix D).
8. The sky background count rate (in $e^- \, s^{-1}$), which is the count rate that would be measured with average zodiacal background and average earth-shine. For the IR channel, this quantity also includes the thermal background from HST and the instrument. It does not include the contribution from the detectors themselves (i.e., dark current and read noise).

The next two sections describe how to calculate two quantities:

- $C$, the count rate of the source in $e^- \, s^{-1}$ over some selected area on the detector containing $N_{pix}$ -pixels.

- $P_{cr}$, the peak count rate of the source in $e^- \, s^{-1} \, pixel^{-1}$, which is useful for avoiding saturated exposures.

We consider the cases of point sources and diffuse sources separately in each of the following imaging and spectroscopy sections.

Table 9.1: Sensitivity data for the WFC3/UVIS Channel, provided for both UVIS1 and UVIS2. Values for the quad filters are listed in the UVIS1 column, but are specific to the spectral element associated with each detector amplifier. For more discussion, see Section 6.5.

| Spectral Element | UVIS1 Pivot λ (Å) | UVIS2 Pivot λ (Å) | UVIS1 Efficiency $\int Q_\lambda T_\lambda \lambda^{-1} d\lambda$ | UVIS2 Efficiency $\int Q_\lambda T_\lambda \lambda^{-1} d\lambda$ | UVIS1 AB zeropoint | UVIS2 AB zeropoint | UVIS1 Sensitivity $\int S_\lambda \, d\lambda$ | UVIS2 Sensitivity $\int S_\lambda \, d\lambda$ | Ensq en |
|---|---|---|---|---|---|---|---|---|---|
| F200LP | 4971.9 | 4875.1 | 0.3614 | 0.3770 | 27.336 | 27.380 | 1.9518 E+19 | 1.9556 E+19 | 0 |
| F218W | 2228.0 | 2223.7 | 0.0061 | 0.0078 | 22.937 | 23.212 | 6.8194 E+16 | 8.7489 E+16 | 0 |
| F225W | 2372.1 | 2358.4 | 0.0171 | 0.0209 | 24.063 | 24.279 | 2.1811 E+17 | 2.6305 E+17 | 0 |
| F275W | 2709.7 | 2703.3 | 0.0186 | 0.0197 | 24.157 | 24.222 | 3.1030 E+17 | 3.2800 E+17 | 0 |
| F280N | 2832.9 | 2830.0 | 0.0010 | 0.0010 | 20.918 | 20.930 | 1.7173 E+16 | 1.7333 E+16 | 0 |
| F300X | 2820.5 | 2805.8 | 0.0392 | 0.0425 | 24.964 | 25.051 | 7.0686 E+17 | 7.5838 E+17 | 0 |
| F336W | 3354.5 | 3354.7 | 0.0304 | 0.0313 | 24.691 | 24.719 | 7.7760 E+17 | 7.9777 E+17 | 0 |
| F343N | 3435.2 | 3435.2 | 0.0145 | 0.0150 | 23.887 | 23.924 | 3.8886 E+17 | 4.0228 E+17 | 0 |
| F350LP | 5873.9 | 5851.2 | 0.2465 | 0.2399 | 26.965 | 26.936 | 1.9360 E+19 | 1.8702 E+19 | 0 |
| F373N | 3730.2 | 3730.2 | 0.0023 | 0.0024 | 21.908 | 21.935 | 7.4080 E+16 | 7.5971 E+16 | 0 |
| F390M | 3897.2 | 3897.0 | 0.0113 | 0.0115 | 23.622 | 23.638 | 3.9206 E+17 | 3.9780 E+17 | 0 |
| F390W | 3923.7 | 3920.7 | 0.0569 | 0.0575 | 25.372 | 25.381 | 1.9932 E+18 | 2.0061 E+18 | 0 |

| F395N | 3955.2 | 3955.2 | 0.0047 | 0.0047 | 22.668 | 22.670 | 1.6774 E+17 | 1.6808 E+17 | 0 |
|---|---|---|---|---|---|---|---|---|---|
| F410M | 4109.0 | 4108.9 | 0.0111 | 0.0111 | 23.596 | 23.594 | 4.2562 E+17 | 4.2499 E+17 | 0 |
| F438W | 4326.2 | 4325.1 | 0.0348 | 0.0347 | 24.837 | 24.834 | 1.4794 E+18 | 1.4754 E+18 | 0 |
| F467M | 4682.6 | 4682.6 | 0.0121 | 0.0122 | 23.694 | 23.698 | 6.0474 E+17 | 6.0750 E+17 | 0 |
| F469N | 4688.1 | 4688.1 | 0.0021 | 0.0022 | 21.816 | 21.820 | 1.0754 E+17 | 1.0793 E+17 | 0 |
| F475W | 4773.1 | 4772.2 | 0.0772 | 0.0767 | 25.704 | 25.696 | 4.0026 E+18 | 3.9727 E+18 | 0 |
| F475X | 4940.7 | 4937.4 | 0.1172 | 0.1166 | 26.156 | 26.152 | 6.5024 E+18 | 6.4704 E+18 | 0 |
| F487N | 4871.4 | 4871.4 | 0.0031 | 0.0032 | 22.227 | 22.241 | 1.6953 E+17 | 1.7182 E+17 | 0 |
| F502N | 5009.6 | 5009.6 | 0.0034 | 0.0034 | 22.326 | 22.322 | 1.9647 E+17 | 1.9562 E+17 | 0 |
| F547M | 5447.5 | 5447.2 | 0.0323 | 0.0324 | 24.755 | 24.759 | 2.1759 E+18 | 2.1838 E+18 | 0 |
| F555W | 5308.4 | 5307.9 | 0.0853 | 0.0843 | 25.810 | 25.796 | 5.4573 E+18 | 5.3891 E+18 | 0 |
| F600LP | 7468.1 | 7453.7 | 0.0913 | 0.0894 | 25.882 | 25.857 | 1.1546 E+19 | 1.1242 E+19 | 0 |
| F606W | 5889.2 | 5887.7 | 0.1100 | 0.1093 | 26.087 | 26.079 | 8.6738 E+18 | 8.5992 E+18 | 0 |
| F621M | 6218.9 | 6219.2 | 0.0283 | 0.0281 | 24.612 | 24.607 | 2.4865 E+18 | 2.4732 E+18 | 0 |
| F625W | 6242.6 | 6242.0 | 0.0657 | 0.0656 | 25.525 | 25.525 | 5.8055 E+18 | 5.8035 E+18 | 0 |
| F631N | 6304.3 | 6304.3 | 0.0023 | 0.0023 | 21.885 | 21.890 | 2.0722 E+17 | 2.0819 E+17 | 0 |
| F645N | 6453.6 | 6453.6 | 0.0032 | 0.0032 | 22.243 | 22.238 | 3.0211 E+17 | 3.0063 E+17 | 0 |
| F656N | 6561.4 | 6561.4 | 0.0006 | 0.0006 | 20.422 | 20.457 | 5.8353 E+16 | 6.0241 E+16 | 0 |
| F657N | 6566.6 | 6566.6 | 0.0047 | 0.0047 | 22.659 | 22.658 | 4.5840 E+17 | 4.5821 E+17 | 0 |
| F658N | 6584.0 | 6583.9 | 0.0010 | 0.0010 | 21.027 | 21.038 | 1.0260 E+17 | 1.0356 E+17 | 0 |

| | | | | | | | | |
|---|---|---|---|---|---|---|---|---|---|
| F665N | 6655.9 | 6655.8 | 0.0050 | 0.0050 | 22.734 | 22.721 | 5.0485 E+17 | 4.9898 E+17 | 0 |
| F673N | 6765.9 | 6765.9 | 0.0044 | 0.0043 | 22.588 | 22.562 | 4.5598 E+17 | 4.4549 E+17 | 0 |
| F680N | 6877.6 | 6877.4 | 0.0136 | 0.0133 | 23.818 | 23.797 | 1.4634 E+18 | 1.4355 E+18 | 0 |
| F689M | 6876.8 | 6876.5 | 0.0250 | 0.0248 | 24.478 | 24.468 | 2.6854 E+18 | 2.6620 E+18 | 0 |
| F763M | 7614.4 | 7612.7 | 0.0198 | 0.0194 | 24.226 | 24.205 | 2.6112 E+18 | 2.5606 E+18 | 0 |
| F775W | 7651.4 | 7648.3 | 0.0359 | 0.0355 | 24.871 | 24.861 | 4.7778 E+18 | 4.7284 E+18 | 0 |
| F814W | 8039.1 | 8029.3 | 0.0453 | 0.0446 | 25.127 | 25.112 | 6.6756 E+18 | 6.5651 E+18 | 0 |
| F845M | 8439.1 | 8437.3 | 0.0136 | 0.0135 | 23.822 | 23.812 | 2.2101 E+18 | 2.1910 E+18 | 0 |
| F850LP | 9176.1 | 9169.9 | 0.0141 | 0.0135 | 23.856 | 23.810 | 2.6964 E+18 | 2.5816 E+18 | 0 |
| F953N | 9530.6 | 9530.5 | 0.0006 | 0.0006 | 20.425 | 20.383 | 1.2343 E+17 | 1.1878 E+17 | 0 |
| FQ232N | 2432.2 | - | 0.0006 | - | 20.412 | - | 7.9447 E+15 | - | 0 |
| FQ243N | 2476.3 | - | 0.0008 | - | 20.738 | - | 1.1074 E+16 | - | 0 |
| FQ378N | 3792.4 | - | 0.0049 | - | 22.751 | - | 1.6584 E+17 | - | 0 |
| FQ387N | 3873.7 | - | 0.0014 | - | 21.340 | - | 4.7783 E+16 | - | 0 |
| FQ422M | 4219.2 | - | 0.0047 | - | 22.673 | - | 1.9275 E+17 | - | 0 |
| FQ436N | 4367.2 | - | 0.0018 | - | 21.630 | - | 7.8839 E+16 | - | 0 |
| FQ437N | 4371.0 | - | 0.0013 | - | 21.268 | - | 5.7864 E+16 | - | 0 |
| FQ492N | 4933.4 | - | 0.0056 | - | 22.868 | - | 3.1361 E+17 | - | 0 |
| FQ508N | 5091.1 | - | 0.0058 | - | 22.881 | - | 3.3360 E+17 | - | 0 |
| FQ575N | 5757.7 | - | 0.0007 | - | 20.530 | - | 4.9392 E+16 | - | 0 |

| FQ619N | 6198.5 | - | 0.0024 | - | 21.940 | - | 2.1192 E+17 | - | 0 |
| FQ634N | 6349.2 | - | 0.0024 | - | 21.958 | - | 2.2567 E+17 | - | 0 |
| FQ672N | 6716.4 | - | 0.0006 | - | 20.395 | - | 6.5820 E+16 | - | 0 |
| FQ674N | 6730.7 | - | 0.0006 | - | 20.692 | - | 6.0035 E+16 | - | 0 |
| FQ727N | 7275.2 | - | 0.0017 | - | 21.581 | - | 2.1112 E+17 | - | 0 |
| FQ750N | 7502.5 | - | 0.0017 | - | 21.502 | - | 2.1647 E+17 | - | 0 |
| FQ889N | 8892.2 | - | 0.0011 | - | 21.057 | - | 1.9722 E+17 | - | 0 |
| FQ906N | 9057.8 | - | 0.0010 | - | 20.951 | - | 1.8748 E+17 | - | 0 |
| FQ924N | 9247.6 | - | 0.0008 | - | 20.753 | - | 1.5735 E+17 | - | 0 |
| FQ937N | 9372.4 | - | 0.0007 | - | 20.648 | - | 1.3818 E+17 | - | 0 |
| G280 | 5047.0 | - | 0.3172 | - | 25.87 | - | 2.89E+18 | - | 0 |

Table 9.2: Sensitivity Data for the WFC3/IR Channel.

| Spectral Element | Pivot λ (Å) | Efficiency $\int Q_\lambda T_\lambda \lambda^{-1} d\lambda$ | AB zeropoint | Sensitivity $\int S_\lambda d\lambda$ | Ensquared energy | Energy in central pixel | Background (sky + thermal) rate |
|---|---|---|---|---|---|---|---|
| F098M | 9864.7 | 0.0745 | 25.666 | 1.6487 E+19 | 0.79 | 0.38 | 0.6106 |
| F105W | 10551.1 | 0.1293 | 26.264 | 3.2779 E+19 | 0.78 | 0.37 | 1.0150 |
| F110W | 11534.5 | 0.2149 | 26.819 | 6.5283 E+19 | 0.76 | 0.36 | 1.6611 |
| F125W | 12486.1 | 0.1257 | 26.232 | 4.4551 E+19 | 0.74 | 0.34 | 0.9986 |
| F126N | 12584.9 | 0.0056 | 22.849 | 2.0132 E+18 | 0.74 | 0.34 | 0.0957 |
| F127M | 12740.3 | 0.0287 | 24.625 | 1.0579 E+19 | 0.74 | 0.34 | 0.2697 |
| F128N | 12831.8 | 0.0062 | 22.956 |  | 0.74 | 0.33 | 0.0984 |

|  |  |  |  | 2.2999 E+18 |  |  |  |
|---|---|---|---|---|---|---|---|
| F130N | 13005.7 | 0.0063 | 22.981 | 2.4145 E+18 | 0.73 | 0.33 | 0.0993 |
| F132N | 13187.7 | 0.0060 | 22.933 | 2.3755 E+18 | 0.73 | 0.33 | 0.0976 |
| F139M | 13837.6 | 0.0247 | 24.466 | 1.0737 E+19 | 0.71 | 0.32 | 0.2391 |
| F140W | 13922.9 | 0.1536 | 26.450 | 6.7755 E+19 | 0.71 | 0.32 | 1.1694 |
| F153M | 15322.1 | 0.0244 | 24.447 | 1.2960 E+19 | 0.67 | 0.29 | 0.2361 |
| F160W | 15369.2 | 0.0963 | 25.936 | 5.1469 E+19 | 0.67 | 0.29 | 0.8002 |
| F164N | 16403.5 | 0.0058 | 22.892 | 3.5389 E+18 | 0.65 | 0.28 | 0.1050 |
| F167N | 16641.6 | 0.0061 | 22.937 | 3.8146 E+18 | 0.64 | 0.27 | 0.1092 |
| G102 | 9970.4 | 0.1110 | 26.10 | 2.51E+19 | 0.79 | 0.42 | 1.2040 |
| G141 | 13860.0 | 0.1796 | 26.62 | 7.86E+19 | 0.73 | 0.34 | 1.8619 |

# 9.4 Count Rates: Imaging

## 9.4.1 Point Source

For a point source, the count rate, $C$ ($e^-$ $s^{-1}$), can be expressed as the following integral over the bandpass of the filter:

$$C = A \int F_\lambda \frac{\lambda}{hc} Q_\lambda T_\lambda \epsilon_f \, d\lambda = \int F_\lambda S\lambda \epsilon_f \, dh$$

where

- $A$ is the area of an unobstructed 2.4-m telescope (i.e., 45,239 cm$^2$).
- $F_\lambda$ is the flux from the astronomical source in erg cm$^{-2}$ s$^{-1}$ Å$^{-1}$.
- The factor $\lambda/hc$ (where $h$ is Planck's constant and $c$ is the speed of light) converts ergs to photons.
- $Q_\lambda T_\lambda$ is the system fractional throughput, i.e., the probability of detecting an electron per incident photon, including losses due to obstructions of the full 2.4-m OTA aperture. It is specified this way to separate out the instrument sensitivity $Q_\lambda$ and the filter transmission $T_\lambda$.
- $\epsilon_f$ is the fraction of the point-source energy encircled within $N_{pix}$ pixels.
- $S_\lambda$ is the total imaging point-source sensitivity in units of $e^-$ s$^{-1}$ Å$^{-1}$
  per incident erg cm$^{-2}$ s$^{-1}$ Å$^{-1}$.

The peak $e^-$ s$^{-1}$ pixel$^{-1}$ from the point source, $C_{peak}$, is given by the following integral over the bandpass:

$$C_{peak} = \int F_\lambda S_\lambda \epsilon_f(1) \, d\lambda$$

where

- $F_\lambda$, and $S_\lambda$ are as above.
- $\epsilon_f(1)$ is the fraction of energy contained within the peak pixel.

If the flux from the source can be approximated by a flat continuum ($F_\lambda$ = constant) and $\epsilon_f$ is roughly constant over the bandpass, then:

$$C = F_\lambda \epsilon_f \int S_\lambda d\lambda$$

We can now define an equivalent bandpass of the filter, $B_\lambda$, such that

$$\int S_\lambda d\lambda = S_{peak} B_\lambda$$

where

- $S_{peak}$ is the peak sensitivity.
- $B_\lambda$ is the effective bandpass of the filter.

The count rate from the source can now be written as:

$$C = F_\lambda \epsilon_f S_{peak} B_\lambda$$

In Tables 9.1 and 9.2 above, we give the value of

$$\int S_\lambda d\lambda$$

for each of the filters.

Alternatively, we can write the count-rate equation in terms of $V$ magnitudes:

$$C = 2.5 \times 10^{11} \epsilon_f \left( \int QT d\lambda/\lambda \right) \times 10^{-0.4(V+AB_\nu)}$$

where $V$ is the visual magnitude of the source, the quantity under the integral is the mean sensitivity of the detector+filter combination (also tabulated in Tables 9.1 and 9.2), and $AB_\nu$ is the filter-dependent correction for the deviation of the source spectrum from a constant $F_\nu$ spectrum. This latter quantity is tabulated for some representative astronomical spectra in Appendix A.

## 9.4.2 Diffuse Sources

For a diffuse source, the count rate, $C$ ($e^- \; s^{-1} \; pixel^{-1}$), which is now per pixel, due to the astronomical source can be expressed as

$$C = \int I_\lambda S_\lambda m_x m_y d\lambda$$

where

- $I_\lambda$ is the surface brightness of the astronomical source, in erg cm$^{-2}$ s$^{-1}$ Å$^{-1}$ arcsec$^{-2}$.

- $S_\lambda$ is as above.

- $m_x$ and $m_y$ are the plate scales in arcsec pixel$^{-1}$ along orthogonal axes.

### 9.4.3 Emission-Line Sources

For a source where the flux is dominated by a single emission line, the count rate can be calculated from

$$C = 2.28 \times 10^{12} \times (QT)_\lambda \times F(\lambda) \times \lambda$$

where $C$ is the observed count rate in e$^-$ s$^{-1}$, $(QT)_\lambda$ is the system throughput at the wavelength of the emission line, $F(\lambda)$ is the emission-line flux in units of erg cm$^{-2}$ s$^{-1}$, and $\lambda$ is the wavelength of the emission line in angstroms. $(QT)_\lambda$ can be determined by inspection of the plots in Appendix A. See Section 9.9.4 for an example of count-rate estimation for an emission-line source.

# 9.5 Count Rates: Slitless Spectroscopy

We now turn to estimation of count rates for slitless spectroscopy using the WFC3 grisms. In this case we are dealing with a dispersed image of the source.

For a point source with a continuous spectrum, the count rate, $C$, is calculated per pixel along the dispersed spectral trace, and is integrated over a fixed extraction height $N_{spix}$ in the spatial direction perpendicular to the dispersion. The count rate is:

$$C = F_\lambda S'_\lambda \epsilon'_{N_{spix}} = F_\lambda A \frac{\lambda}{hc} Q_\lambda T_\lambda \epsilon'_{N_{spix}} d$$

where:

- $S_\lambda$ is the total point source sensitivity in units of $e^- s^{-1}$ per incident erg $cm^{-2}$ $s^{-1}$ $Å^{-1}$; and

$$S'_\lambda = S_\lambda \times d.$$

- $d$ is the spectral dispersion in Å $pixel^{-1}$.

- $\epsilon'_{N_{spix}}$ is the fraction of the point-source energy within $N_{spix}$ in the spatial direction.
- the other quantities are as defined in the previous section.

For a source with an unresolved emission line with a flux of $F$ in units of erg $cm^{-2}$ $s^{-1}$, the total count rate recorded over the $N_{spix}$ extraction height is:

$$C = F S_\lambda \epsilon'_{N_{spix}}$$

These counts will be distributed over pixels in the dispersion direction according to the instrumental line-spread function.

The spectroscopic point source sensitivity calibration $\left( S'_\lambda \times \epsilon'_{N_{spix}} \right)$ for a default extraction height of $N_{spix}$ was measured directly from observations of stellar flux standards during SMOV and Cycle 17 (programs 11934, 11936, and 11552). Therefore, the accuracy in laboratory determinations of $T_\lambda$ for the WFC3 grisms are not crucial to the final accuracy of their sensitivity calibrations.

The peak $e^- s^{-1}$ $pixel^{-1}$ from the point source is given by:

$$P_{cr} = \epsilon'_f(1) F_\lambda S'_\lambda$$

where:

- $\epsilon'_f(1)$ is the fraction of energy contained within the peak pixel.
- the other quantities are as above.

# 9.6 Estimating Exposure Times

## 9.6.1 SNR Reached in a Given Exposure Time

To derive the exposure time to achieve a given SNR ratio, or to derive the SNR ratio achieved in a given exposure time, there are four principal ingredients:

- Expected count rate $C$ (e¯ s$^{-1}$) from your source over some area.

- The area (in pixels) over which those e¯ are received ($N_{pix}$).

- Sky background ($B_{sky}$) in e¯ s$^{-1}$ pixel$^{-1}$.

- The detector background, or dark, ($B_{det}$) in e¯ s$^{-1}$ pixel$^{-1}$ and the read noise ($R$) in e¯. (Section 9.7 provides information for determining the sky-plus-detector background.)

The SNR ratio $\Sigma$ achieved in exposure time $t$ seconds, is given by

$$\Sigma = \frac{Ct}{\sqrt{Ct + N_{pix}\left(B_{sky} + B_{det}\right)t + N_{pix}\,N_{read}\,P + \frac{N_{pix}}{N_{bin}}\,N_{read}\,R^2}}$$

where:

- $C$ = the signal from the astronomical source in e¯ s$^{-1}$. (Note that the raw output image uses DN, which will be equal to $C/G$, where $G$ is the gain.)
- $N_{pix}$ = the total number of detector pixels integrated over to achieve $C$.
- $N_{bin}$ = the number of detector pixels binned to one read-out pixel when on-chip binning is used.

- $B_{sky}$ = the sky background in e¯ s$^{-1}$ pixel$^{-1}$.

- $B_{det}$ = the detector dark current in e¯ s$^{-1}$ pixel$^{-1}$.

- $R$ = the read noise in electrons; 3.1 e¯ for the UVIS channel and 12. e¯ for the IR channel (this is the effective read noise achieved by fitting the ramp of IR readouts, if close to the full sequence of 16 readouts is used).
- $N_{read}$ = the number of detector readouts.

- $P$ = the background added using the post-flash option (Section 6.9.2) in e¯ pixel$^{-1}$

The above equation assumes the optimistic (but often realistic) condition that the background zero-point level under the object that is subtracted could be well known (from integrating over many pixels) but is still noisy in $N_{pix}$ and does not significantly contribute to the error budget; in crowded fields this may not be true. In general, $C$ in the numerator should be the signal in $N_{pix}$ from the component to be measured (e.g., the point source in an image or the line emission in a spectrum), while $C$ in the denominator is the total astronomical signal in $N_{pix}$ (e.g., including light from the underlying galaxy in the image or from the continuum in the spectrum).

## 9.6.2 Exposure Time to Reach a Given SNR

Observers normally take sufficiently long integrations that the read noise is not important. This condition is met when:

$$ Ct + N_{pix}\left(B_{sky} + B_{det}\right)t + N_{pix}\,N_{read}\,P > 2\,\frac{N_{pix}}{N_{bin}}\,N_{read}\,R^2 $$

In the regime where read noise is unimportant, and virtually all of the astronomical signal in $N_{pix}$ comes from the component being measured, the integration time to reach a given signal-to-noise ratio $\Sigma$ is:

$$ t = \frac{\Sigma^2\left[C + N_{pix}\left(B_{sky} + B_{det}\right) + N_{pix}\,N_{read}\,P\right]}{C^2} $$

If the source count rate is much higher than that of the sky plus detector backgrounds, then this expression reduces further to:

$$ t = \frac{\Sigma^2}{C} $$

i.e., the usual result for Poisson statistics of $\Sigma = \sqrt{\text{total counts}}$.

More generally, the required integration time to reach a given SNR ratio is:

$$ t = \frac{\Sigma^2[C + N_{pix}(B_{sky} + B_{det})] + \sqrt{\Sigma^4[C + N_{pix}(B_{sky} + B_{det})]^2 + 4\Sigma^2 C^2\left[N_{pix}\,N_{read}\,P + \frac{N_{pix}}{N_{bin}}\,N_{read}\,R^2\right]}}{2C^2} $$

## 9.6.3 Exposure Time Estimates for Red Targets in F850LP

At long wavelengths, ACS CCD observations are affected by a red halo due to light scattered off the CCD substrate; i.e. an increasing fraction of the light as a function of wavelength is scattered from the center of the PSF into the wings. This problem affects particularly the very broad z-band F850LP filter in ACS, for which the encircled energy depends on the underlying spectral energy distribution the most. **This problem has not been seen in WFC3/UVIS observations, and so should not be a concern for those planning WFC3 observations.**

# 9.7 Sky Background

As noted in the previous section, the backgrounds from the sky and from the detector must be taken into account when calculating expected signal-to-noise ratios (SNRs) or exposure times.

Detector backgrounds (as well as read-out noise) for the CCDs and IR detector are discussed in Chapter 5. Background added to CCD exposures using the post-flash option is discussed in Section 6.9.2. This section deals with the sky backgrounds that can affect WFC3 observations.

The most important sources of sky background are:

- Earthshine (ES).
- Zodiacal light (ZL).
- Geocoronal emission (GC).

The background in counts $e^-$ $s^{-1}$ $pixel^{-1}$ for imaging observations can be computed as:

$$B_{sky} = \int I_\lambda S_\lambda m_x m_y d\lambda$$

where:

- $I_\lambda$ is the surface brightness of the sky background, in erg $cm^{-2}$ $s^{-1}$ $Å^{-1}$ $arcsec^{-2}$.

- $S_\lambda$ is the point-source sensitivity for the imaging mode.

- $m_x$ and $m_y$ are the plate scales in arcsec $pixel^{-1}$ along orthogonal axes.

In the case of slitless spectroscopy, the image of the sky through a disperser is not uniform, because some wavelengths fall off the detector for regions of sky near the edge of the field of view. The regions of lower sky background will be strips at the long- and short-wavelength edges of the field of view; a UVIS grism spectrum is roughly 270 pixels long, while an IR grism spectrum is roughly 170 pixels long. The maximum width of the strips from where the signal starts to decline to the edge, where the signal is down by roughly a factor of 2, will be about half the total length of a spectrum of a point source, i.e., roughly 135 pixels (UVIS) or 85 pixels (IR), in the case of a sky background with a continuum of wavelengths. These small strips of lower sky background are ignored in the following formulae. Furthermore, since the spectra do not lie along the direction of the anamorphic distortion, the plate scales of $m_x$ and $m_y$ above must be replaced by the plate scales $m_s$ and $m_y$ in the orthogonal spatial and dispersion directions, respectively. Interior to the strips, a point on the detector sees a region of sky over the full wavelength coverage of the disperser. Thus, for **spectroscopic observations**:

$$B^\lambda_{sky} = \int I_\lambda S'_\lambda m_s m_\lambda d\lambda$$

For a **monochromatic** sky emission line at $\lambda = L$ like [O II] 2471, which will dominate the background through the UVIS/G280 grism:

$$B^{L}_{sky} = I_L \, S'_\lambda \, m_s \, \frac{m_\lambda}{d}$$

where

- $I_L$ is the monochromatic intensity of a line at wavelength $L$ in erg cm$^{-2}$ s$^{-1}$ arcsec$^{-2}$.

The total sky background is:

$$B_{sky} = B^{\lambda}_{sky} + B^{L}_{sky}$$

Figure 9.1 and Table 9.3 show "high" sky background intensity as a function of wavelength, identifying the separate components which contribute to the background. The "shadow" and "average" values of the earth-shine contribution in the WFC3 Exposure Time Calculator (ETC) correspond, respectively, to 0% and 50% of the "high" values in Figure 9.1 and Table 9.3. For the zodiacal sky background, the values in Figure 9.1 and Table 9.3 correspond to the high value of $V$-band surface brightness of 22.1 mag arcsec$^{-2}$ from Table 9.4, while the "low" and "average" zodiacal light is scaled to $V$ surface brightnesses of 23.3 and 22.7 mag arcsec$^{-2}$, respectively.

In Table 9.3 we present the "high" sky-background numbers, which are plotted in Figure 9.1. See the text and the caption of Figure 9.1 for more details. These high sky values are defined as the earth-shine at 38° from the limb and the high zodiacal light of $V = 22.1$ mag arcsec$^{-2}$.

Table 9.3: High Sky Backgrounds.

| Wavelength (Å) | Earth-shine (erg cm² s¹ Å¹arcsec$^{-2}$) | Zodiacal light (ergcm² s¹ Å¹ arcsec$^{-2}$) | Total sky background (erg cm² s¹ Å¹ arcsec$^{-2}$) |
|---|---|---|---|
| 2000 | 7.69E-22 | 7.94E-20 | 8.02E-20 |
| 2500 | 1.53E-21 | 3.83E-19 | 3.84E-19 |
| 3000 | 1.43E-19 | 1.63E-18 | 1.77E-18 |
| 3500 | 8.33E-19 | 2.72E-18 | 3.55E-18 |
| 4000 | 1.66E-18 | 3.12E-18 | 4.78E-18 |
| 4500 | 2.59E-18 | 4.97E-18 | 7.57E-18 |
| 5000 | 2.63E-18 | 5.07E-18 | 7.70E-18 |
| 5500 | 2.55E-18 | 5.17E-18 | 7.72E-18 |
| 6000 | 2.42E-18 | 5.14E-18 | 7.56E-18 |
| 7000 | 1.95E-18 | 4.48E-18 | 6.42E-18 |

| | | | |
|---|---|---|---|
| 8000 | 1.56E-18 | 3.82E-18 | 5.38E-18 |
| 9000 | 1.23E-18 | 3.18E-18 | 4.40E-18 |
| 10000 | 9.97E-19 | 2.70E-18 | 3.70E-18 |
| 11000 | 8.02E-19 | 2.26E-18 | 3.06E-18 |
| 12000 | 6.65E-19 | 1.94E-18 | 2.61E-18 |
| 13000 | 5.58E-19 | 1.68E-18 | 2.24E-18 |
| 14000 | 4.70E-19 | 1.46E-18 | 1.93E-18 |
| 15000 | 3.97E-19 | 1.26E-18 | 1.66E-18 |
| 16000 | 3.35E-19 | 1.09E-18 | 1.43E-18 |
| 17000 | 2.79E-19 | 9.27E-19 | 1.21E-18 |

**Figure 9.1: Sky background intensity as a function of wavelength.**
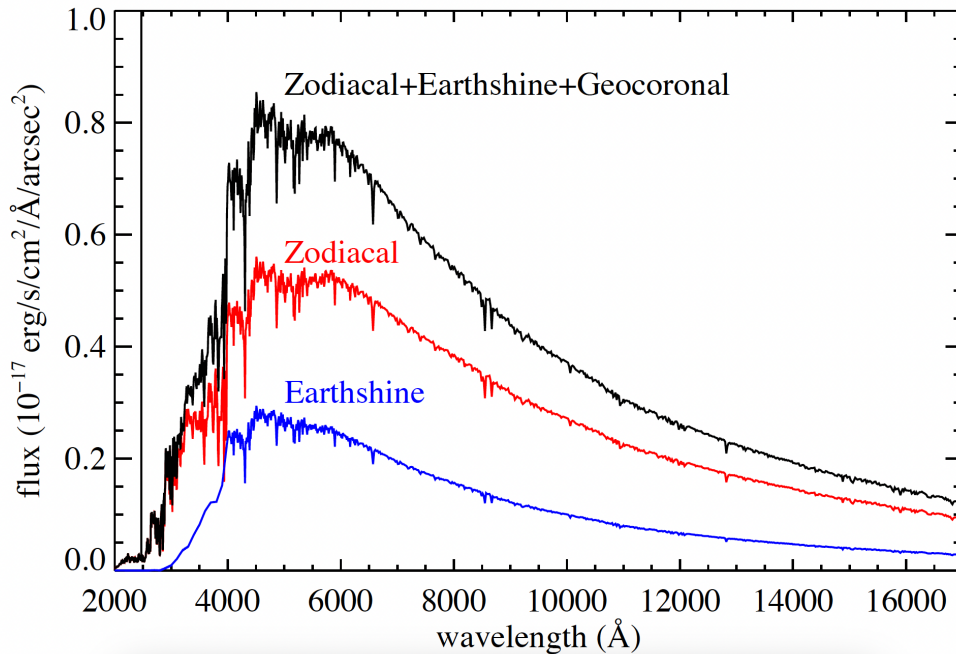


The total sky spectrum (black) for the "high-background" case adopted in the WFC3 ETC, along with the individual contributions from zodiacal light and earth-shine. These data correspond to a *V*-band surface brightness of 22.1 mag arcsec$^{-2}$. The geocoronal emission line [O II] 2471 Å has a flux of $1.5 \times 10^{-15}$ erg cm$^{-2}$ s$^{-1}$ arcsec$^{-2}$, extending beyond the upper limit of the plot. See Section 7.9.5 for discussion of the He I emission line at 10830 Å, not plotted here.

## 9.7.1 Zodiacal Light, Earth Shine, and LOW-SKY

Zodiacal light varies as a function of angular distance of the target from the Sun and from the ecliptic. Table 9.4 gives the variation of the zodiacal background as a function of heliocentric ecliptic longitude and ecliptic latitude in V-mag per arcsec$^2$. The entries in the table are derived from data in Leinert et al. (1998). As shown by this table, over most of the sky the zodiacal background is within 1 magnitude of the minimum value of 23.4 V-mag per arcsec$^2$. It is greater than that at low ecliptic latitudes and at angles from the sun approaching the minimum permitted observing angle of 55°. At the lower ecliptic latitudes, it rises rapidly as this 55° limit is approached. For a target near heliocentric ecliptic coordinates (50,0) or (−50,0), not shown in the table, the zodiacal light level is 20.9 V-mag per arcsec$^2$, i.e., about 10 times the faintest value. For an empirical determination of the dependence of zodiacal light on the ecliptic latitude and the angle between the target and the sun for WFC3/IR observations, see Section 7.9.5. Figure 7.12 illustrates this dependence.

**Table 9.4: Approximate zodiacal sky background as a function of heliocentric ecliptic longitude and ecliptic latitude (in *V*-mag per arcsec$^2$). SA stands for Solar Avoidance zone (*HST* pointing within 55 deg of the sun), where observations may not be made.**

| Ecliptic longitude (degrees) | Ecliptic latitude (degrees) | | | | | | |
|---|---|---|---|---|---|---|---|
| | 0 | 15 | 30 | 45 | 60 | 75 | 90 |
| 0 | SA | SA | SA | SA | 22.6 | 23.0 | 23.3 |
| 15 | SA | SA | SA | SA | 22.6 | 23.1 | 23.3 |
| 30 | SA | SA | SA | 22.3 | 22.7 | 23.1 | 23.3 |
| 45 | SA | SA | 22.1 | 22.5 | 22.9 | 23.1 | 23.3 |
| 60 | 21.3 | 21.9 | 22.4 | 22.7 | 23.0 | 23.2 | 23.3 |
| 75 | 21.7 | 22.2 | 22.6 | 22.9 | 23.1 | 23.2 | 23.3 |
| 90 | 22.0 | 22.3 | 22.7 | 23.0 | 23.2 | 23.3 | 23.3 |
| 105 | 22.2 | 22.5 | 22.9 | 23.1 | 23.3 | 23.3 | 23.3 |
| 120 | 22.4 | 22.6 | 22.9 | 23.2 | 23.3 | 23.3 | 23.3 |
| 135 | 22.4 | 22.6 | 22.9 | 23.2 | 23.3 | 23.4 | 23.3 |
| 150 | 22.4 | 22.6 | 22.9 | 23.1 | 23.3 | 23.4 | 23.3 |
| 165 | 22.3 | 22.5 | 22.8 | 23.0 | 23.2 | 23.4 | 23.3 |
| 180 | 22.1 | 22.4 | 22.7 | 23.0 | 23.2 | 23.4 | 23.3 |

Earth-shine varies strongly depending on the angle between the target and the bright Earth limb. The variation of the earth-shine as a function of limb angle from the sunlit Earth is shown in Figure 9.2. The figure also shows the contribution of the moon, which is typically much smaller than the zodiacal contribution, for which the upper and lower limits are shown. For reference, the limb angle is approximately 24° when the *HST* is aligned toward its orbit pole (i.e., the center of the CVZ). The earth-shine contribution shown in Figure 9.1 and Table 9.3 corresponds to this position.

**Figure 9.2:** Background contributions in V magnitude per arcsec$^2$ due to the zodiacal light, Moon, and sunlit Earth, as a function of angle between the target and the limb of the Earth or Moon. The two zodiacal light lines show the extremes of possible values.
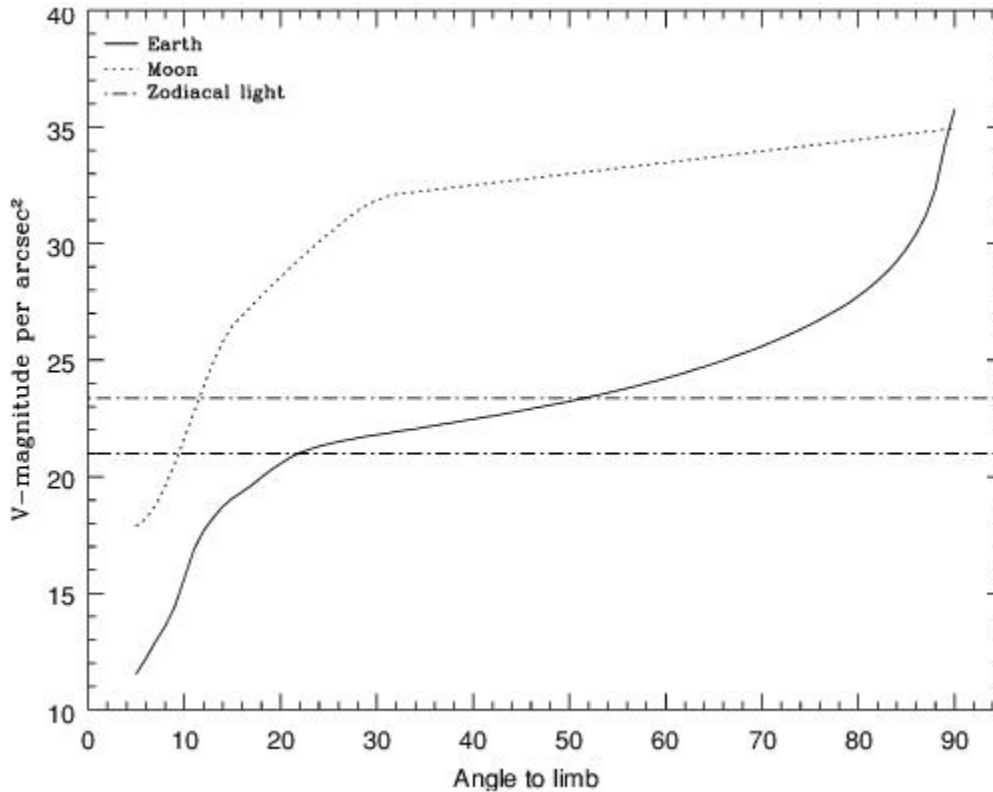


For observations taken longward of 3500 Å, earth-shine dominates the background at small (<22°) limb angles. In fact, the background increases exponentially for limb angles <22°. The background near the bright limb can also vary by a factor of ~2 on timescales as short as two minutes, which suggests that the background from earth-shine also depends upon the reflectivity of the terrain and the amount of cloud cover over which *HST* passes during the course of an exposure.

Observations of the faintest objects may benefit from the use of the Phase II Special Requirement LOW–SKY, which must be requested and justified in the Phase I proposal. LOW–SKY observations are scheduled during the part of the year when the zodiacal background light is no more than 30% greater than the minimum possible zodiacal light for the given target position. LOW–SKY also invokes the restriction that exposures will be taken only at angles greater than 40° from the bright Earth limb to minimize earth-shine and the airglow lines (but also see Section 9.7.2). However it is not always effective in suppressing the He I 10830 Å airglow line (Section 7.9.5).

One disadvantage of using the LOW–SKY requirement is that it greatly reduces scheduling opportunities due to the restriction on zodiacal light. That restriction may be stricter than scientifically necessary, especially for targets at high ecliptic latitudes where even the maximum attainable zodiacal background is quite low, and for filters where other background components dominate the noise.

For targets and filters where high zodiacal background could be a problem, observers may want to limit that background by placing their own less stringent restrictions on scheduling dates to avoid observing the target when it is too near the sun. *HST* is already constrained to point at least 55° from the sun. For targets at low ecliptic latitude, that limit can be extended to ~60° by excluding 5 days from the ends of the default solar exclusion window, as described in Section 7.9.5.

Another disadvantage of using the `LOW-SKY` requirement is that it limits visibility to about 48 minutes per orbit. Rather than accept an automatic reduction in observing time by using `LOW-SKY`, the observer may be able to structure an orbit so that the exposures that would be most significantly affected by earth-shine do not occur at the beginning or end of the orbit, where the earth-shine is likely to be highest. The exposures in that orbit should be placed in a non-interruptible exposure sequence, as described in the APT Training Materials. For WFC3/IR exposures, frames in the non-destructive readouts that are badly affected by earth-shine can be excluded from the data reduction (see Section 7.9.5).

WFC3/UVIS observers should keep in mind that the total background (dark + sky + post-flash if needed) must be at least 20 electrons/pix/s to minimize CTE losses, so for some targets and filters it may be advisable to increase the background using post-flash rather than to attempt to minimize it (Section 6.9).

The ETC provides the user with the flexibility to separately adjust the zodiacal and earth-shine sky background component levels to help observers decide where special care is needed to avoid background levels that could be detrimental to their science. The RA, Dec and date option can be used to compute the zodiacal light for specific targets, which is especially useful for targets at low ecliptic latitudes where the zodiacal background increases rapidly as the angle between the target and the sun approaches the *HST* observable limit of 55°. Note that the standard normalizations for zodiacal light and earth-shine (from none to high or extremely high) provide approximations that may not accurately predict the levels in individual exposures. For WFC3/IR exposures, one can check the empirically determined zodiacal light model discussed in Section 7.9.5.

## 9.7.2 Geocoronal Emission, Airglow, and SHADOW

Background due to geocoronal emission originates mainly from hydrogen and oxygen atoms in the exosphere of the Earth. In the far-UV spectral region, the strongest geocoronal emission lines are Lyman$-\alpha$ at 1216 Å, O I at 1304 Å, and O I] at 1356 Å, but WFC3 is of course not sensitive at these wavelengths. The only significant UV geocoronal emission line to which WFC3 is sensitive is [O II] 2471 Å, shown in Figure 9.1. This line varies in intensity from day to night and as a function of *HST* orbital position. It can be the dominant sky contribution in the UV both for imaging and spectroscopic observations. In sunlight it can be as bright as ~$1.5 \times 10^{-15}$ erg cm$^{-2}$ s$^{-1}$ arcsec$^{-2}$, while in Earth shadow it is much fainter, typically ~$7.5 \times 10^{-18}$ erg cm$^{-2}$ s$^{-1}$ arcsec$^{-2}$. However, note that WFC3 ISR 2023-06 did not find any contribution attributable to [O II] to the G280 grism sky background.

To minimize geocoronal emission, the Special Requirement SHADOW can be used if requested and justified in the Phase I proposal. Exposures using this special requirement are limited to roughly 25 minutes per orbit, exclusive of the guide-star acquisition (or re-acquisition), and can be scheduled only during a small percentage of the year. SHADOW therefore restricts scheduling opportunities and orbit duration much more severely than LOW–SKY (see Section 7.9.1). SHADOW reduces the contribution from the geocoronal emission lines by roughly a factor of ten while the continuum earth-shine is set to zero. SHADOW requirements must be included and justified in your Phase I proposal (see the Call for Proposals). Observers should keep in mind that the total background should be at least 20 electrons /pix/s to minimize CTE losses in WFC3/UVIS images, so it may be advisable to increase the background using post-flash rather than to attempt to minimize it. (See Section 6.9)

Analysis of archival WFC3/IR grism and broad-band filter observations has shown that a variable airglow line of He I at 10830 Å can be a significant component of the sky background for the F105W and F110W filters and the G102 and G141 grisms. See Section 7.9.5 for discussion of the WFC3/IR sky background and observing strategies. The use of SHADOW is generally not recommended for WFC3/IR exposures.

# 9.8 Interstellar Extinction

Interstellar extinction can dramatically reduce the count rate detected from your source, particularly if you are working in the ultraviolet range but are inferring source brightnesses from optical data. Conversely, optically obscured objects may be much brighter in the IR than in the optical.

The Exposure Time Calculator includes the ability to correct exposure-time estimates for interstellar extinction based on the color excess $E(B-V)$. It may also be useful to refer to the standard references on interstellar extinction and its variations with location and metallicity, e.g., Fitzpatrick (1999) and references therein. Some common IR extinction laws are found in e.g. Weingartner & Draine (2001) and Chapman et al. 2009.

# 9.9 Exposure-Time Calculation Examples

In the following sections you will find a set of examples for the two different channels and for different types of sources. The examples were chosen in order to present typical objects for the two channels as well as interesting cases as they may arise with the use of WFC3.

## 9.9.1 Example 1: UVIS Imaging of a Faint Point Source

What is the exposure time needed to obtain a signal-to-noise ratio (SNR) of 10 for a point source of spectral type F0 V (Castelli and Kurucz Model, T=7250 K), normalized to V = 27.5, when using the UVIS F555W filter? Assume a photometry box size of 5 × 5 pixels, detector chip 2 (generally the preferred chip; see Section 6.4.4), average standard zodiacal light and earth shine, and, to start with, 1 frame.

The WFC3 Exposure Time Calculator (ETC) gives an exposure time of 4676 sec or about 78 min. A single long exposure ~48 min will fit the typical *HST* orbit, so this observation will require more than 1 orbit. One long exposure per orbit would be a poor choice because many pixels would have bad fluxes in both of the exposures due to cosmic rays (Section 5.4.10). For multi-orbit observations, taking two dithered exposures per orbit (to move bad pixels as well as to allow for cosmic ray removal) is generally sufficient. Recalculating the needed exposure time using 4 frames (more read noise, higher fluxes and flux-dependent noise components to preserve SNR=10) gives 5175 sec, or 1294 sec or about 22 min per frame. In a typical *HST* orbit, there is time for two 23 min exposures, so a box pattern (for optimal sampling of the PSF: see Appendix C) will nicely fit two orbits. The natural sky background in this filter in 22 min far exceeds the level where CTE losses become a concern (see Section 6.9), so post-flash is not needed and the ETC does not post an advisory.

Using the pencil-and-paper method, for filter F555W Table 9.1 gives the integral ∫QTdλ/λ as 0.0843 and indicates that the fraction of the star's light included in the 5 × 5 pixel square aperture is 0.78. Table A.1 shows an $AB_v$ correction term of 0.03 for filter F555W for a star with an effective temperature of 7,500 K (the closest value to our star's effective temperature 7250 K). The count rate for our V = 25 mag star can then be calculated from the equation

$$C = 2.5 \times 10^{11} \epsilon_f \left( \int QT \frac{d\lambda}{\lambda} \right) \times 10^{-0.4(V+AB_v)}$$

or

C= 2.5×10$^{11}$*0.0843*0.78*10$^{-0.4(27.5+0.03)}$ = 0.1599 e$^-$ s$^{-1}$,

which agrees with the ETC-returned value of 0.159 e$^-$ s$^{-1}$. The exposure time can then be found by using the equation

$$t = \frac{\Sigma^2[C + N_{pix}(B_{sky} + B_{det})] + \sqrt{\Sigma^4[C + N_{pix}(B_{sky} + B_{det})]^2 + 4\Sigma^2 C^2\left[\frac{N_{pix}}{N_{bin}} N_{read} R^2\right]}}{2C^2}$$

where we use:

- signal-to-noise ratio (SNR; $\Sigma$) = 10
- $N_{pix}$ = 25
- $B_{sky}$ = 0.0377 e-/s/pix from Table 9.1
- $B_{det}$ = 0.0027 e-/s/pix from Table 5.1
- $R$ = read noise = 3.1 e- from Table 5.1
- $N_{read}$ = 4
- $N_{bin}$ = 1
- $P$ = 0 (no post-flash, so the post-flash noise term is not included)

This gives t = 5287 sec, within ~2% of the ETC-derived value (5175 sec).

## 9.9.2 Example 2: UVIS Imaging of a Faint Source with a Faint Sky Background

Calculate the SNR obtained in 1200 seconds for a point source of spectral type F0 V (Kurucz & Castelli Model, T=7250 K)), normalized to Johnson V = 23.5 mag, using the UVIS F225W filter, a photometry box size of 5 × 5 pixels, 1 frame, detector chip 2, and with average standard zodiacal light, average standard earth shine and average Air Glow values.

The ETC returns SNR=4.8, as well as a warning message indicating that the background electrons per pixel (6.1) is less than the recommended threshold of 20 electrons per pixel to avoid charge transfer efficiency effects. For a discussion on CTE effects please refer the CTE webpage.

Recalculate the SNR as before, but this time adding 14 post-flash electrons. Now the ETC returns SNR=3.7, and no warning messages. This SNR value is lower than the case without post-flash because the post-flash electrons increase the noise.

To calculate the SNR by hand, we must first calculate the count rate for the object using the first equation in Example 9.9.1 above and values of:

- $AB_\nu$ = 2.84 (from Table A.1)
- $V$ = 23.5 mag
- $\int QTd\lambda/\lambda$ = 0.0209  (from Table 9.1)
- $\varepsilon_f$ = 0.71 (from Table 9.1)

This yields $C$ = 0.1080 e⁻/sec.

Now we can calculate the SNR using the equation given in Section 9.6.1 and values of:

- $N_{pix}$ = 25
- $B_{sky}$ = 0.0066 e⁻/s/pix *from Table 9.1)

- $B_{det}$ = 0.0015 e⁻/s/pix (from Table 5.1)

- $R$ = read noise = 3.1 e⁻ per read (from Table 5.1)
- $N_{read}$ = 1

- $N_{bin}$ = 1

- $P$ = 9 post flash electrons

This yields an estimated signal-to-noise ratio of 3.9. Note that the results computed manually are approximations. The ETC utilizes the chosen model spectrum to determine the object count rate in a given filter while the equations calculate an estimated count rate based on approximations to the true color of a star.

## 9.9.3 Example 3: IR Imaging of a Faint Extended Source

What is the exposure time needed to obtain an SNR of 10 for an E0 elliptical galaxy that subtends an area of 1 arcsec$^2$ with an integrated *V*-magnitude of 26.7, when using the IR F140W filter? Assume a photometry box size of 9 × 9 pixels, and average sky values. The galaxy has a diameter of 1.13 arcsec, a surface brightness of 26.7 mag/arcsec$^2$, and fits within the 9 × 9 pixel box. For simplicity we will assume a redshift of 0.

The WFC3 Exposure Time Calculator (ETC) gives a total exposure time of 1241 sec to obtain this SNR in a single exposure. Although the non-destructive MULTIACCUM sequences on the IR channel can mitigate cosmic rays in a single read sequence, users are encouraged to dither their observations so that there are least 2 read sequences per field, to mitigate hot pixels and resample the point spread function. Re-running the calculation with 2 exposures gives an exposure time of 1355 sec. If we assume (as in Example 1) that we can fit two 1200-second exposures in an orbit, this program fits within a single orbit. Two SPARS50 sequences, with 15 samples (703 sec) per sequence should work well for this program.

Using the pencil-and-paper method, Table 9.2 gives the integral $\int QTd\lambda/\lambda$ as 0.1536. We will assume that the elliptical galaxy resembles an old (10 Gyr) burst of star formation; looking in Table A.2, the $AB_\nu$ correction term is −1.41. We will assume that the 9 × 9 pixel box encloses all of the light for this object. The count rate can then be calculated using the first equation from Example 1 above, yielding $2.5 \times 10^{11}$*0.1536*1.0*10$^{-0.4(26.7-1.41)}$) = 2.94 e-/sec, which is close to the ETC-returned value of 3.18 e-/sec. The exposure time can then be found by using the second equation from Example 1 above, to give $t$ = 1388 sec, which is close to the ETC-derived value of 1355 sec. We have used background rates of $B_{sky}$ = 1.1694 (Table 9.2), $B_{det}$ = 0.05 (Table 5.1), an effective read noise of 12.5 e⁻ per read (Section 5.7.3, assuming we are fitting the MULTIACCUM sequence), and 2 reads.

## 9.9.4 Example 4: Imaging an H ɪɪ region in M83 in H-alpha

What is the exposure time needed to obtain an SNR of 10 for Hα emission in an HII region which has a diameter of 2" and a flux Fλ in Hα of $5 \times 10^{-16}$ ergs/cm$^2$/sec? Suppose that the H ɪɪ region is in the outskirts of M83 (i.e., insignificant continuum radiation in a narrowband filter). It has a redshift of 0.0017, so Hα appears at approximately 6574 Å. From an inspection of the throughput curves in Appendix A, we find the Hα (F656N) filter cuts off at too short a wavelength, so we elect to use the Wide Hα + [N ɪɪ] (F657N) filter, which has a system throughput $(QT)_\lambda$ of 25% at 6574 Å.

We use the equation in Section 9.4.3 to estimate the total count rate $C$ for the emission line to be $2.28 \times 10^{12} * 0.25 * 5 \times 10^{-16} * 6574 = 1.87$ e⁻/sec; the ETC predicts 1.82 e-/sec. The source covers approximately 2012 pixels, and the sky for this filter contributes 0.0029 e⁻/sec/pixel (Table 9.1) while the dark rate is 0.0027 e⁻/sec/pixel (Table 5.1) for a total background rate of 0.0056 e-/sec. Assuming 2 reads, no binning and a read noise of 3.1 e⁻ per read (Table 5.1), we find using the same formula as in Section 9.9.1 that the time to reach SNR of 10 is 1217 sec.

For comparison, using the ETC, specify the source size as 2 arcsec in diameter, use a circular 1 arcsec radius extraction region, enter the emission line flux in ergs/cm²/s/arcsec² as $1.6 \times 10^{-16}$ at 6574 Å. Assume a FWHM of 1 Å. The linewidth is not critical since the system throughput of this filter varies slowly with wavelength at 6574 Å, as can be seen in the throughput plot provided by the ETC. Assume average zodiacal light and average earthshine. The ecliptic latitude of the target is 18.4 deg; Figure 9.2 shows that this precludes very high levels of zodiacal light. To start with, assume that post-flash will not be used (0 electrons). The ETC computes that the exposure time for the two frames must sum to 1255 sec to achieve SNR = 10. However, it gives a warning that the electrons per pixel due to background (3.4) is less than the recommended threshold of 20 e⁻/pix to avoid poor charge transfer efficiency (see Section 6.9). A post-flash level ~17 e⁻, to be added to each of the two frames, will be needed to bring the background up to the recommended level. Repeating the ETC calculation with Post Flash = 17 e⁻, you find that you need a total of 1979 sec to take exposures with optimal CTE mitigation over the entire field of view.

# Chapter 10: Overheads and Orbit Time Determinations

## Chapter Contents

# 10.1 Overview

This chapter provides information for Phase I proposers who plan to use WFC3 for some or all of their planned *HST* observations. Because your Phase I proposal must state a specific integer number of *HST* orbits that are requested for your program, it is important that this number be as accurate as possible.

After you establish a set of scientific exposures required for your program (and if using an unsupported mode, additional calibration exposures), you are ready to determine the total number of orbits to request in your Phase I proposal. The time requested should include not only the total exposure time, but also the additional time for the observatory and instrument operations needed to support those exposures. Those operations usually include acquiring (and possibly re-acquiring) guide stars, configuring WFC3 in preparation for an exposure, transferring data, and possibly repositioning the target in the focal plane between exposures.

It will often be necessary or desirable to achieve the total exposure time through a sequence of shorter exposures. For example, an exposure totaling several hours will be interrupted by target occultations. Moreover, UVIS exposures will almost always be obtained as a sequence of shorter exposures, in order to allow for cosmic ray removal. For your Phase I proposal, you should plan the sequences of exposures and overhead activities for each of the requested orbits. An overview of observation planning is given in Chapter 4.

Generally, you will need to compile the overheads for your individual exposures, having packed an integer number of exposures and their supporting activities into individual orbits. Some activities may be executed while the target is occulted by the Earth, allowing more efficient utilization of an orbit. Finally, you will tally the exposure times and resulting overhead times required during visibility of the target in order to determine the total number of orbits needed. This may be an iterative process as you refine your exposures to better use the targets' orbit visibility.

**The Phase I *Call for Proposals* includes instructions on observatory policies and practices regarding orbit time requests. The *HST Primer* provides additional specific advice on how to determine the number of required orbits for your scientific program**. See HST Proposal Opportunities and Science Policies for these documents.

In the following sections, we provide a summary of the WFC3-specific overheads and give several examples that illustrate how to calculate your orbit request for a Phase I proposal. **If you are already familiar with the APT scheduling software used to prepare the Phase II, you may wish to use it to estimate the number of orbits required for your Phase I request.**

The overheads presented in this chapter are approximate. These overhead times are to be used, in conjunction with the exposure times you determine and the instructions in the *HST Primer*, in order to estimate the total number of orbits for your Phase I proposal. If your *HST* proposal is accepted, you will then develop and submit a Phase II proposal to support the actual scheduling of your approved observations. At that time you will use the APT scheduling software (which employs more precise values for the various overheads) to craft exposure sequences that match orbital target visibility intervals and your allocation of orbits. Therefore, requesting sufficient time in your Phase I proposal for overhead operations is important; additional time to cover unplanned overhead will not be granted later.

# 10.2 Observatory Overheads

This section discusses the overheads involved in preparing the telescope for observations of a target. The next section describes the additional instrument-specific overheads involved in obtaining and storing the actual individual WFC3 exposures.

At the beginning of a sequence of WFC3 exposures, the telescope must acquire guide stars. The time required for this initial guide-star acquisition is 6.5 minutes. If the observations extend into the following orbit(s) following Earth occultation, you must also include the overhead for guide-star re-acquisition (another 6.5 minutes at the beginning of each new orbit).

Following guide-star acquisition (or re-acquisition) and the first exposure during the orbit, it is likely that you will want to make a series of small telescope motions for the purpose of obtaining dithered observations. Each commanded movement of the telescope requires an amount of time ranging from 0.3 to 1.3 minutes, depending on the size of the motion. Furthermore, each time the telescope is moved more than 2 arcmin (e.g., for the purpose of constructing a mosaicked image), an additional guide-star acquisition will be necessary, requiring another 6 minutes.

When using WFC3's UVIS quad filters, it will often be necessary to repoint the telescope to place the target in the desired quadrant. This repositioning will require 1 minute. Due to the large field of view of WFC3/UVIS, offsets to different quadrants may require new guide stars to be acquired. Offsets between adjacent quadrants (e.g., A to B, or A to C) are small enough to maintain the same guide stars in many cases. However, offsets between diagonal quadrants (i.e., A to D, or B to C) are larger than 2 arcmin when using the "optimum" apertures, so the same guide stars cannot be used for diagonal quadrant offsets. For the "fixed" apertures, diagonal quadrant offsets are very close to 2 arcmin, so it is possible that the same guide stars may be used, depending on the placement of the particular guide stars. To determine whether quad filter observing sequences may require new guide star acquisitions, refer to Table 6.4 for quad filter positions, to Table 6.1 for aperture descriptions, and to the SIAF for aperture reference point definitions.

Table 10.1 summarizes the observatory-level overheads involved in WFC3 observing.

Table 10.1: Observatory Overhead Times.

| Action | Overhead Time (minutes) |
| --- | --- |
| Guide-star acquisition, first orbit | 6.5 |
| Guide-star re-acquisitions, at beginning of each new orbit for non-CVZ observing | 6.5 |
| Guide-star re-acquisitions for CVZ observing | 0 |
| New guide-star acquisition following dither of >2 arcmin | 6 |
| Spacecraft maneuvers      0" < step-size < 1.25" | 0.3 |
| 1.25" < step-size < 10" | 0.5 |
| 10" < step-size < 28" | 0.6 |

| | |
|---|---|
| 28" < step-size <60" | 0.8 |
| 60" < step-size < 2' | 1.0 |
| 3' | 1.1 |
| 6' | 1.4 |
| 12' | 2.2 |
| 18' | 2.9 |
| 24' | 3.7 |
| 30' | 4.5 |
| 60' | 8.3 |
| Offset between adjacent quad filters for any QUAD aperture | 1.0 |
| Offset between diagonal quad filters for UVIS-QUAD-FIX aperture | 1.0 |

# 10.3 Instrument Overheads

## 10.3.1 Exposure Overheads

The instrument-specific overhead times for WFC3 exposures are dominated by the time to move the filter wheels, to read out the detector, and especially to transfer and store the data. Although in a Phase II proposal the overheads computed with APT may prove to be smaller than the values given in this section, it is nevertheless important to plan your Phase I proposal using the conservative values given here in order to ensure the award of time is adequate to attain your scientific goals.

Several kinds of overhead activities are associated with each exposure, and the specific activities depend on whether the exposure is a new one, or part of a series of associated ones. Associated exposures are defined as exposures of the same target, using the same filter and aperture, executed with or without dithering. Identical exposures are undithered associated exposures. Dithering is the preferred method of acquiring more than one exposure in a given observing mode as it improves the PSF sampling as well as the photometry (averages over flatfield errors as well as UVIS or IR channel image artifacts).

For UVIS (i.e. CCD) exposures, dithered associated readouts are generated when the observer creates images within an APT Pattern container or when applying appropriate POS TARGs to individual exposure specifications. Nearly all observers use dithering as it improves the removal of hot and bad pixels, improves PSF sampling, and improves photometry (averages over flat-fielding errors). In rare situations, identical exposures can be generated if the observer specifies a CR-SPLIT number greater than 1 or specifies a Number of Iterations greater than 1.

For IR MULTIACCUM exposures, CR-splitting is not used, although identical exposures can still be generated with Number of Iterations greater than 1. Dithered associated exposures can be generated as well.  The full set of readouts generated by a Sample Sequence is considered to be one exposure.

At the end of each UVIS or IR exposure, images are read into WFC3's internal buffer memory, where they are stored until they are transferred to *HST*'s solid-state data recorder. The time needed to read a UVIS CCD image is 98 seconds. The time needed for a single read of an IR image is 3 seconds, leading to a total of 48 seconds for a full 16-read exposure. These times are included in the overhead times for the first and subsequent exposures presented in Table 10.2 below.

## Dumping of the WFC3 Buffer

The WFC3 buffer provides temporary storage of images read from the WFC3 detectors before they are dumped through the *HST* science data formatter (SDF) to the solid state recorder (SSR). The buffer can be dumped either between exposures (a "serial" dump), or during an exposure (a "parallel" dump), but cannot overlap any commands executed in WFC3, including the commands at the beginning or at the end of an exposure. The buffer may be dumped during pointing maneuvers, but not during acquisition of guide stars. The buffer may be dumped during target occultation, which does not deduct from the target visibility time. Switching channels from IR to UVIS and vice-versa does not require dumping the buffer (but will require 1 min of overhead time as noted below). Observers will generally prefer to use parallel dumps, in order to more fully utilize the time when a target is visible for science exposures. Although buffer dumps are typically forced by science data volume, a buffer dump will also be forced whenever the buffer holds 304 image headers, regardless of the size of the images themselves. The 304-file limit is unlikely to be reached under typical conditions.

The rules for dumping the buffer in parallel with UVIS exposures differ in some respects from those for dumping in parallel with IR exposures. The two channels are considered separately in the following paragraphs.

## UVIS Parallel Buffer Dumps

The buffer can hold up to two full-frame UVIS images. A single full-frame image can be dumped in parallel with a UVIS exposure greater than 347 seconds, and two full-frame images can be dumped in parallel with a UVIS exposure greater than 663 seconds. When the buffer is dumped, all stored images must be dumped. Consequently, a sequence of 348-second (or longer) exposures can effectively "hide" a buffer dump overhead within the exposure time of the following image, thereby maximizing exposure time during the orbit. Whether a sequence comprised of short exposures (less than 348 seconds) and long exposures (greater than 347 seconds) will require serial buffer dumps will depend upon the order of the long and short exposures and the duration of the long exposures. Dumping the buffer during a sequence of short and long exposures will be more efficient if the long exposures are 664 seconds (or longer). For example, an orbit with exposures with exposure times in the sequence 10-348-10-664-10-664-10 will incur no serial dump overhead penalty. The observer will plan such sequences with APT in Phase II. Sequences of full-frame, un-binned exposures less than 348 seconds will require the overhead of serial buffer dumps. For short exposures, using subarrays or binning can help reduce the overhead of serial buffer dumps. The time to dump small subarrays or a binned exposure scales approximately with the number of pixels stored in the buffer.

## IR Parallel Buffer Dumps

The buffer can hold up to two full-frame, 15-sample IR images (which, along with the zeroth read, result in FITS files containing 16 reads). To dump one such image in parallel with an IR exposure requires that exposure to be longer than 348 seconds. To dump two such images requires an exposure longer than 646 seconds. The rules for dumping IR exposures are somewhat more efficient than those for dumping UVIS exposures as each readout sample is treated individually.  That is, all samples in the buffer are not required to be dumped together and samples can be dumped during the non-destructive read of the IR detector. Sequences of full-frame, 15-sample exposures shorter than 349 seconds will require serial dumps after the second and subsequent exposures. Sequences of longer-exposure (i.e., greater than 348 seconds), full-frame, 15-sample exposures will incur no overhead for dumping the buffer. Sequences comprised of short (less than 349 seconds) full-frame, 15-sample exposures and long exposures (greater than 348 seconds) may incur overhead for serial dumps, depending upon the sequence of exposures and the duration of the long exposures. The observer will plan such sequences with APT in Phase II. The time to dump an $n$-sample, full-frame exposure is approximately $39 + 19 \times (n + 1)$ seconds. Subarrays may also be used to reduce the overhead of serial buffer dumps.

## Filter and Channel Select Overheads

Both the UVIS and IR channels may be used during a single orbit, although not simultaneously. Only one channel switch (from UVIS to IR, or IR to UVIS) is permitted per orbit, and the time required to reconfigure between the two channels is 1 minute. If the buffer is full when switching channels, then time must also be taken to dump it before the exposure can begin with the other channel. Because the centers of the fields of view of the UVIS and IR channels are the same, acquisition of new guide stars is not required when changing channels to observe the same target.

The overhead for each exposure includes an allowance for the time required to position the filter or grism; however, selecting a UVIS quad filter requires an additional 1 minute of overhead to re-position the telescope, as indicated in Table 10.1.

Table 10.2 summarizes all of the instrument overheads described in this subsection.

## Table 10.2: WFC3 Instrument Overhead Times.

| Action | Overhead Time (minutes) |
|---|---|
| Reconfiguration between UVIS & IR channels during a single orbit | 1.0 |
| UVIS ACCUM Mode | |
| Single exposure or first exposure in a set of associated exposures (e.g., the first sub-exposure of a Pattern or CR-SPLIT set) | 2.6 |
| Subsequent exposures in set of associated exposures (e.g., subsequent exposures in a Pattern or CR-SPLIT set), per exposure | 2.1 |
| Buffer dump if exposure is not last one in an orbit, or if next exposure is less than 348 seconds | 5.8 |

| | |
|---|---|
| Post-flash - overhead depends on flash level required to reach the recommended background value | 0.1-0.2 |
| **IR MULTIACCUM Mode** | |
| Each exposure | 1.0 |
| Buffer dump if 16-read exposure is not last one in an orbit, or if next exposure is less than 346 seconds | 5.8 |

## 10.3.2 Reducing Overheads with Subarrays and Binning

If your science program is such that a field of view smaller than the full detector size is adequate and you require many short exposures, then one way to reduce the frequency of buffer dumps, and hence their associated overheads, is to use a WFC3 subarray. Subarrays are described for the UVIS channel in Section 6.4.4, and for the IR channel in Section 7.4.4.

When subarrays are used, only a small region of the detector is read out and stored in WFC3's buffer. The reduced data volume permits a larger number of exposures to be stored in the buffer before the memory fills and it becomes necessary to transfer them to the telescope's solid-state recorder. Use of subarrays reduces the amount of time spent dumping the buffer, and also usually reduces detector readout time. An additional bonus of using subarrays is the ability to place the target close to the readout amp, thereby providing some CTE loss mitigation (see Section 6.9).  Note, however, that the full-quadrant UVIS 2K2 and UVIS-QUAD-SUB apertures have somewhat longer readout times than the full- detector apertures because of the way that the readout is performed. A dump is still required if the 304-file limit is reached before buffer memory is filled.

Table 10.3 illustrates the advantage in orbit packing to be gained by using UVIS subarray apertures. We consider the case of a sequence of 5-second exposures without FLASH that fill a 3200 sec orbit as fully as possible. The table lists three subarray apertures of different sizes and a full detector aperture. The subarray apertures have been defined such that they can be read out by one amplifier. The quadrants of the full detector aperture are read out by the four amplifiers simultaneously.

Table 10.3: Orbit structure for an orbit filled with 5-second exposures

| Aperture | size (pixels | #exp | Location of Buffer Dumps |
|---|---|---|---|
| UVIS2-C512C-SUB | 513 × 512 | 44 | In occultation |
| UVIS2-M1K1C-SUB | 1024 × 1024 | 28 | In occultation |
| UVIS2-2K2C-SUB | 2047 × 2050 | 12 | After 8 exposures & in occultation |
| UVIS-CENTER | 4 × 2048 × 2051 | 7 | After pairs of exposures & in occultation |

The areas ($A_{SA}$) of the supported UVIS subarrays are 1/4, 1/16, or 1/64 of the area ($A_{FF}$) of a full-frame image. The areas of the IR subarrays are 1/4, 1/16, 1/64, or 1/256 of the area of a full-frame image. The number of subarray exposures that may be stored in the buffer, limited by image data volume, is $n = 2$ ($A_{FF}/A_{SA}$). For example, eight 1/4-area exposures may be stored in the buffer, which would allow eight 4-minute exposures to be taken and stored before having to dump the buffer. If the exposures were full-frame, the buffer would have to be dumped after each pair of observations, thus leading to very low observing efficiency.

The 304-file limit must also be considered in optimizing buffer dumps. For UVIS exposures, the limit will almost never be encountered. For IR exposures, each read (not each exposure) counts against the limit. The number of IR exposures that can be stored before a buffer dump is forced is therefore n = 304/(NSAMP +1), or 19 exposures for NSAMP = 15.

In the IR channel, certain combinations of subarrays and sample sequences give rise to images containing a sudden low-level jump in the overall background level of the image. This jump artifact can be prevented by sequencing the IR images within an orbit from large to small (see Section 7.4.4).

Data volume and overhead time can also be reduced for UVIS images by using on-chip binning of adjacent pixels, as described in Section 6.4.4. By using 2 × 2 pixel binning, the data volume is reduced by a factor of 4, although the readout time is only reduced by about 2 to 50 sec. For 3 × 3 pixel binning, the data volume is reduced by a factor of 9, and the readout time by 4 to 23 s. Note, however, that post-flash diminishes the data volume gains of binned mode as the post-flash level required to mitigate CTE losses (see Section 6.9) is the same level as that required for unbinned images. Thus, for example, an image requiring 20 e- post-flash for CTE mitigation will result in 80 e- or 180 e- in a 2x2 or 3x3 binned pixel, respectively, along with the concomitant reduction in signal to noise. IR readouts cannot be binned, but data volume may be reduced by taking less than the default 15 samples during an exposure.

# 10.4 Orbit Use Examples

One way to learn to estimate total orbit time requests is to work through a few examples. Below we provide five different cases:

1. A simple pair of UVIS images using one filter.
2. A set of short UVIS exposures that require large overheads associated with buffer dumps.
3. A one-orbit IR observation using two different filters.
4. A two-orbit UVIS observation using dithering.
5. A one orbit IR grism spectroscopic observation.

Note that some of the examples use un-dithered images; however, observers are advised to use dithering whenever possible (see Appendix C). In addition, although observers can request the use of shadow or low-sky target visibility restrictions, the examples below are all for the standard (i.e., unrestricted) target visibility (see the *HST Primer*, Section 6.3, for further discussion).

## 10.4.1 Example 1: UVIS, 1 Orbit, 1 Filter

Consider a target to be imaged with UVIS in a given filter in one orbit. Let us suppose that, by using the Exposure Time Calculator (ETC) (see Chapter 9), we find that we need a total exposure time of 2400 s to reach the desired signal-to-noise ratio (SNR). Given that we desire the observation to be divided into two exposures for cosmic-ray removal (with a small dither step between them), we map the overheads and the science exposure times onto the orbit as follows.

**Table 10.4: Orbit Calculation for Example 1**

| Action | Time (minutes) | Explanation |
|---|---|---|
| Guide-star acquisition | 6.5 | Needed at start of observation of new target |
| UVIS overhead for first exposure | 2.6 | Includes filter selection, camera set-up, and readout |
| First science exposure | <u>20.0</u> | |
| Small dither maneuver (< 1.25") | 0.3 | |
| UVIS overhead for second exposure | 2.1 | Includes readout |
| Second science exposure | <u>20.0</u> | Total exposure time is 40 min |
| Total time used | 51.5 | |

Thus, with a total time of nearly 52 minutes, this set of observations would fit into all unrestricted *HST* orbits. The exposure time could, if needed, be adjusted so as to fill the actual target visibility interval (which depends on several factors, including the date and target location in the sky, as described in Chapter 6 of the *HST Primer*). The time needed to dump the buffer following the second sub-exposure incurs no overhead in this example, because it can be performed during target occultation.

Note that this simple sequence of two fairly long exposures would, with an appropriately-oriented dither step, just cover the 1.2" gap between the two CCD chips (see Section 6.3).

## 10.4.2 Example 2: UVIS, 1 Orbit, Short Exposures

This example illustrates the impact of short exposures on the useful time in the orbit. Suppose we intend to use one orbit to observe a target with UVIS in two filters, F606W and F814W. The observation consists of two sequences, each one with two identical CR-SPLIT exposures, for a total of four individual sub-exposures. Suppose that the ETC shows that the exposure time must be 540 seconds for each of the filters, so each of the CR-SPLIT sub-exposures must be at least 270 seconds long. For the target declination, which in this example is −35°, we find that the unrestricted visibility time is 55 minutes. The time budget for the orbit (under-filling it) is as follows.

Table 10.5: Orbit Calculation for Example 2

| Action | Time (minutes) | Explanation |
|---|---|---|
| Guide-star acquisition | 6.5 | Needed at start of observation of new target |
| UVIS overheads for first sub-exposures in both series | 2 × 2.6 = 5.2 | Includes filter change, camera set-up, and readouts |
| UVIS overheads for subsequent sub-exposures in both series | 2 × 2.1 = 4.2 | Includes readouts |
| Buffer dump after 2nd sub-exposure | 2 × 5.8 = 11.6 | Full buffer must be dumped in target visibility in order to obtain the last two exposures, which are too short to accommodate dump (270 sec < 348 sec). |
| Science exposures | 4 × 4.5 = 18.0 | |
| Total time used | 45.5 | |

Compared with Example 1, we see that the observing efficiency is very low due to the large overheads associated with buffer dumps. We have achieved only 18 minutes of exposure time during 45 minutes of total time used, whereas in Example 1 we obtained 40 minutes of exposure time during 51.5 minutes of total time used. Of course, this is caused by the short exposures versus the long exposures of Example 1, where "short" and "long" are relative to the time to dump the buffer, 348 seconds.

The time that is "lost" to dumping the buffer in this example can be recovered by sufficiently increasing the exposure time (as discussed in Section 10.3) to enable dumping while an exposure is being made. For example, if the 540-second exposure time per filter is required to obtain a minimum SNR (and not to avoid saturation), then increasing the exposure times to 720 s (2 x 360 s) per filter will improve the SNR and bring the total time used to 40 minutes.

Alternatively, if compatible with the scientific goals, a subarray could have been used to read out only a fraction of the detector area, allowing more frames to be stored in the buffer before requiring a dump. In this example, using UVIS 2k × 2k subarrays for 4 short (<348 seconds) exposures would save about 8 minutes of readout time and 12 minutes of dump time.

## 10.4.3 Example 3: IR, 1 Orbit, 2 Filters

The third example demonstrates the orbit calculation for a simple IR observation. We want to obtain full-frame images of a target in two filters, F110W and F160W. Suppose that the ETC has shown that the exposure times adequate for our scientific goals are 10 minutes in F110W and 20 minutes in F160W. These times can be achieved with the up-the-ramp MULTIACCUM sequences SPARS50, NSAMP=15 (11.7 min) and SPARS100, NSAMP=15 (23.4 min), respectively. From the orbit visibility table (see Chapter 6 of the *HST Primer*), suppose that we find that at the target declination (here assumed to be 0°) the unrestricted target visibility time is 54 minutes. The resulting orbit calculation is as follows.

**Table 10.6: Orbit Calculation for Example 3**

| Action | Time (minutes) | Explanation |
|---|---|---|
| Guide-star acquisition | 6.5 | Needed at start of observation of new target |
| IR overheads for 2 exposures | 2 × 1.0 = 2.0 | Includes filter changes, camera set-ups, and readouts |
| Science exposure in F110W | <u>11.7</u> | |
| Science exposure in F160W | <u>23.4</u> | |
| Total time used | 43.6 | |

The total time used in the orbit shows that our target can indeed be imaged in the selected filters within one orbit. Furthermore, the first exposure can be dumped from the buffer during the second exposure. The ~9 minutes of unused time could be used for an additional exposure, during which the second exposure would be dumped.

# 10.4.4 Example 4: UVIS, Dithering, 2 Orbits, 1 Filter

This example illustrates the orbit calculation for a UVIS observation with a WFC3 UVIS box dithering pattern, which implements imaging at four pointings. The goal of the observation is to obtain a dithered image of a field in such a way that would allow us to bridge the ~1.2 arcsec inter-chip gap between the UVIS CCDs in the combined image. As indicated in Table 10.1, for a 2-arcsec offset maneuver, the three dithers will take 0.5 minutes each. Suppose we have determined that the exposure time necessary to reach the desired SNR is 80 minutes, and that the visibility time at our target declination, assumed to be +53°, is 58 minutes. Furthermore, we will use the cosmic-ray removal provided by the dither data-reduction package. As a result, the orbit calculation will involve a sequence of four exposures of 20-minutes duration (i.e., one exposure at each of the four dither pointings). These observations will be distributed across two *HST* orbits, as shown in the following Table 10.7.

Table 10.7: Orbit Calculation for Example 4

| Action | Time (minutes) | Explanation |
|---|---|---|
| Orbit 1 | | |
| Guide-star acquisition | 6.5 | Needed at start of observation of new target |
| UVIS overhead for first exposure | 2.6 | Includes filter change, camera set-up, and readout |
| UVIS overhead for second exposure | 2.1 | Includes readout |
| Spacecraft maneuver | 0.5 | To offset from first to second dither pointing |
| Two science exposures | 2 × 20 = 40.0 | Exposures at the first two pointings in the dither pattern |
| Total time used in orbit 1 | 51.7 | |
| Orbit 2 | | |
| Guide-star re-acquisition | 6.5 | Needed at start of new orbit to observe same target |
| UVIS overheads for 3rd and 4th exposures | 2 × 2.1 = 4.2 | Includes readouts |
| Spacecraft maneuvers | 2 × 0.5 = 1.0 | To offset to the 3rd and 4th dither pointings |
| Two science exposures | 2 × 20 = 40.0 | Exposures at the final two pointings in the dither pattern |
| Total time used in orbit 2 | 51.7 | |

No overhead is incurred to dump the exposures, because they are all longer than 348 seconds. Thus the desired exposures can be accomplished within the two orbits, and in fact there are ~7–8 minutes of unused visibility time per orbit that could be used to increase the exposure times.

## 10.4.5 Example 5: IR, 1 Orbit, Grism

This example illustrates the orbit calculation for an IR G102 grism spectroscopic observation. We will use the full-frame, up-the-ramp MULTIACCUM sequence SPARS200 with NSAMP=13, requiring 40 minutes to expose. We will also obtain undispersed (direct) images to calibrate target positions and wavelengths, using a SPARS10, NSAMP=15 (2.4-minute) exposure before and after the grism exposure. The overhead calculations are presented in Table 10.8.

Table 10.8: Orbit Calculation for Example 5

| Action | Time (minutes) | Explanation |
|---|---|---|
| Guide-star acquisition | 6.5 | Needed at start of observation of new target |
| IR overheads for 3 exposures | 3 × 1.0 = 3.0 | Includes filter changes, camera set-ups, and readouts |
| Science exposure (undispersed) | 2 × 2.4 = 4.8 | SPARS10, NSAMP=15 |
| Science exposure (grism) | 40.0 | SPARS200, NSAMP=13 |
| Total time used | 54.3 | |

The buffer dumps incur no overhead because the first undispersed exposure can be dumped during the long grism exposures, and the last two can be dumped during the subsequent target occultation. Thus, since at least 54 minutes of target visibility are available at any target's declination, this set of observations can be obtained in one orbit.

# Appendix A: WFC3 Filter Throughputs

## Appendix Contents

- UVIS FQ422M
- UVIS FQ436N
- UVIS FQ437N
- UVIS FQ492N
- UVIS FQ508N
- UVIS FQ575N
- UVIS FQ619N
- UVIS FQ634N
- UVIS FQ672N
- UVIS FQ674N
- UVIS FQ727N
- UVIS FQ750N
- UVIS FQ889N
- UVIS FQ906N
- UVIS FQ924N
- UVIS FQ937N
- IR F098M
- IR F105W
- IR F110W
- IR F125W
- IR F126N
- IR F127M
- IR F128N
- IR F130N
- IR F132N
- IR F139M
- IR F140W
- IR F153M
- IR F160W
- IR F164N
- IR F167N

# A.1 Introduction

This appendix, organized by channel and filter, contains the system throughputs and sensitivities of each filter. For each imaging mode the following are provided:

- Plots of integrated system throughput for each filter as a function of wavelength.
- Plots of the time needed to achieve a desired signal-to-noise ratio vs. magnitude for each filter for a point-source and for a 1"× 1" extended source.
- Tables of color corrections $AB_\nu$ to go from Johnson $V$ magnitude to $AB$ magnitude for stellar spectra (as a function of effective temperature) and composite populations (as a function of age). The stellar spectra come from the Lejeune et al. (1997, *A&AS*, **125**, 229) grid, and assume a surface gravity of log $g$ = 5 and solar metallicity. The composite populations come from the "instantaneous burst" and "continuous star formation" models of Bruzual & Charlot (1993, *ApJ*, **405**, 539), updated in 1995, assuming a Salpeter IMF spanning 0.1 to 125 solar masses.

The filter throughput values presented here were derived with `stsynphot` by using the latest WFC3 photometric calibration released on October 2020 for both the UVIS (WFC3 ISR 2020-10) and the IR ( WFC3 ISR 2021-04) detectors. The throughput values for WFC3/UVIS are calculated at a reference time, June 26, 2009, i.e. approximately when WFC3 was installed on HST. For more information on the latest calibration please see the photometric calibration webpage.

To derive photometric transformation coefficients for converting magnitudes from the native WFC3 /UVIS passbands to Johnson/Cousins UBVRI passbands in the ABMAG, STMAG, and VEGAMAG systems, a Jupyter notebook is provided. This notebook uses the latest WFC3 filter throughput tables and replaces the functionality provided in the "WFC3 Photometric Conversion Tool", which is no longer supported. For more details on photometric transformations to other systems, please see WFC3 ISR 2014-16.

> ✅ *For more information on system throughputs and tabular files to download, see the HST System Throughputs website.*

# A.2 Throughputs and Signal-to-Noise Ratio Data

A.2.1 Sensitivity Units and Conversions
A.2.2 Signal-to-Noise Ratio

## A.2.1 Sensitivity Units and Conversions

This appendix contains plots of throughputs for each WFC3 filter. Section 9.3 explains how to use these throughputs to calculate expected count rates from your source.

The first figure for each filter gives the integrated system throughput based on on-orbit observations of spectrophotometric standards. This is the combination of the efficiencies of the detector and of the optical elements in the light path. The throughput is defined as the number of detected *counts/second* /*cm²* of telescope area relative to the incident flux in *photons/cm²/s*. For both the UVIS and IR channels, "*counts*" is the number of electrons detected. In both channels the detected counts obey Poisson statistics, except that at short wavelengths in the UVIS channel, a single incoming photon has a finite chance of producing multiple electrons in the CCD. Section 5.4.2 describes this phenomenon, which was measured to have a much smaller effect in the UVIS detectors compared to theoretical predictions. The signal-to-noise plots in this appendix have been corrected to remove multiple electrons generated by UV photons, using a correction that is intermediate between the theoretical and measured UVIS "quantum yields." The throughput includes all obscuration effects in the optical train (e.g., due to the *HST* secondary).

All wavelength measurements for the UVIS and IR channel filters were done in a gaseous medium: air for UVIS measurements and helium for IR measurements. The results have been converted to vacuum wavelengths using the indices of refraction of the gaseous media. The UVIS laboratory measurements were done at a temperature of 20°C, whereas the filters are operated on orbit at 0°C; this may lead to wavelength shifts which are expected to be small. The IR laboratory measurements were done at a temperature of –30°C, whereas the filters are operated on orbit at –35°C; this may lead to wavelength shifts which are expected to be very small.

Note that the tables in the **stsynphot** package and the WFC3 Exposure Time Calculator all assume vacuum wavelengths for both the UVIS and IR filter transmission data.

Because we have applied a correction to the throughputs for quantum yield in order to derive appropriate counting statistics for the source, the sensitivity calculations shown here are conservative in background- or read-noise-dominated regimes; the additional signal electrons from the enhanced UV quantum yield will increase the detection of faint sources in the 200–300 nm range somewhat vs. these sample calculations.

To recalculate the throughputs with the most recent detector QE tables in stsynphot, you can create total-system-throughput tables (instrument plus OTA) using the stsynphot **band** function, which takes any valid **obsmode** as input and produces a table with two columns of data called "*wavelength*" and "*throughput*" as its output.

For example, to evaluate the UVIS1 throughput for the F475W filter in an infinite aperture at the time of WFC3's installation, you would use the following commands:

```
import stsynphot as stsyn
bp = stsyn.band('wfc3,uvis1,f475w')
```

Whereas to evaluate the UVIS1 F475W throughput on MJD 58000 for a 10-pixel radius aperture, you would use the following commands:

```
import stsynphot as stsyn
bp = stsyn.band('wfc3,uvis1,f475w,mjd#58000,aper#0.40')
```

A Jupyter notebook tutorial is provided to calculate filter throughputs and inverse sensitivities for the WFC3 UVIS and IR detectors.

## A.2.2 Signal-to-Noise Ratio

For each imaging mode, plots are provided to estimate the signal-to-noise ratio (S/N) for a representative source. The first figure shows S/N for point sources. The second figure shows S/N for uniform extended sources of area 1 arcsec$^2$.

The different line styles in the S/N figures delineate regions where different sources of noise dominate. If the total noise from backgrounds (read noise, sky, thermal, dark) is larger than the noise from the source, the observation is considered to be background-dominated, and the line style reflects which background source is largest. Note that for the WFC3 detectors, the dark current can never be the largest source of noise when a source is background-dominated, because the read noise is always larger than the dark count noise when exposures are 1000 s or less. The point- and extended-source S/N figures assume average sky levels. These plots also indicate where an observation will saturate the full well of the detector.

For point sources, an aperture size of 5 × 5 pixels has been used for the UVIS channel, while an aperture size of 3 × 3 pixels has been used for the IR channel. For extended sources, a 1 arcsec$^2$ aperture was used. The read noise has been computed assuming a number of readouts NREAD= integer ($t$/1000 s), where $t$ is the exposure time, with a minimum NREAD=2.

In situations requiring more detailed calculations (non-stellar spectra, extended sources, other sky background levels, unknown target $V$ magnitude, etc.), the WFC3 Exposure Time Calculator should be used.

Follow these steps to use the signal-to-noise plots:

1. Determine the *AB* magnitude of your source at the wavelength of interest. There are several ways to do this.
   - Examine Tables A.1, A.2, or A.3 and find $AB_\nu$ for the desired spectral type and filter. Sum the $V$ magnitude of the target and $AB_\nu$ derived from the table.
   - Alternatively, compute *ABMAG* ($= V{+}AB_\nu$) from the source flux, using the relation.

$$ABMAG = -2.5 \log f_\nu - 48.60 \ ,$$

   or

$$ABMAG = -2.5 \log f_\lambda - 5 \log \lambda - 2.406 \ .$$

2. Find the appropriate plot for the filter in question, and locate $V+AB_v$ on the horizontal axis. Then read off the signal-to-noise ratio for the desired exposure time, or vice-versa.

Note that the plots show the S/N as a function of source magnitude for exposure times as short as 0.1 s, although the minimum exposure time for the UVIS channel is actually 0.5 s.

**Table A.1: Color corrections $AB_v$ to go from Johnson *V* magnitude to AB magnitude for WFC3 as a function of stellar effective temperature.**

| | | | | $T_{eff}$ | | | | |
|---|---|---|---|---|---|---|---|---|
| **Mode** | **2500K** | **5000K** | **7500K** | **10000K** | **15000K** | **20000K** | **30000K** | **50000K** |
| UVIS/F200LP | –2.22 | 0.45 | 0.48 | 0.40 | 0.08 | –0.12 | –0.40 | –0.57 |
| UVIS/F218W | 7.21 | 7.82 | 2.95 | 1.51 | 0.09 | –0.53 | –1.22 | –1.55 |
| UVIS/F225W | 6.07 | 7.22 | 2.84 | 1.51 | 0.12 | –0.49 | –1.15 | –1.46 |
| UVIS/F275W | 7.30 | 5.30 | 2.27 | 1.35 | 0.10 | –0.42 | –0.96 | –1.24 |
| UVIS/F280N | 3.29 | 4.49 | 2.50 | 1.44 | 0.13 | –0.40 | –0.90 | –1.17 |
| UVIS/F300X | 5.96 | 4.05 | 1.98 | 1.26 | 0.10 | –0.39 | –0.91 | –1.19 |
| UVIS/F336W | 4.98 | 2.71 | 1.31 | 1.00 | 0.10 | –0.26 | –0.64 | –0.86 |
| UVIS/F343N | 4.74 | 2.62 | 1.24 | 0.97 | 0.11 | –0.24 | –0.60 | –0.82 |
| UVIS/F350LP | –2.64 | 0.07 | 0.18 | 0.18 | 0.09 | 0.04 | –0.02 | –0.07 |
| UVIS/F373N | 7.03 | 2.53 | 1.10 | 0.94 | 0.21 | –0.09 | –0.43 | –0.65 |
| UVIS/F390M | 4.25 | 2.08 | 0.67 | 0.25 | –0.20 | –0.33 | –0.48 | –0.60 |
| UVIS/F390W | 3.80 | 1.63 | 0.59 | 0.26 | –0.14 | –0.29 | –0.47 | –0.60 |
| UVIS/F395N | 3.91 | 1.92 | 0.67 | 0.15 | –0.27 | –0.37 | –0.49 | –0.58 |
| UVIS/F410M | 2.96 | 1.16 | 0.29 | –0.10 | –0.32 | –0.39 | –0.46 | –0.52 |
| UVIS/F438W | 2.28 | 0.86 | 0.18 | –0.12 | –0.28 | –0.33 | –0.39 | –0.43 |
| UVIS/F467M | 1.74 | 0.34 | 0.02 | –0.15 | –0.22 | –0.24 | –0.26 | –0.27 |
| UVIS/F469N | 1.64 | 0.33 | 0.03 | –0.14 | –0.21 | –0.24 | –0.26 | –0.26 |
| UVIS/F475W | 1.23 | 0.44 | 0.09 | –0.07 | –0.17 | –0.20 | –0.24 | –0.26 |
| UVIS/F475X | 0.61 | 0.35 | 0.12 | –0.01 | –0.12 | –0.15 | –0.19 | –0.23 |
| UVIS/F487N | 1.47 | 0.29 | 0.20 | 0.28 | 0.06 | –0.02 | –0.11 | –0.17 |
| UVIS/F502N | 2.32 | 0.32 | 0.02 | –0.07 | –0.11 | –0.12 | –0.14 | –0.15 |
| UVIS/FQ508N | 1.07 | 0.32 | 0.01 | –0.06 | –0.08 | –0.10 | –0.11 | –0.12 |
| UVIS/F547M | 0.08 | 0.03 | 0.02 | 0.01 | 0.01 | 0.01 | 0.01 | 0.02 |

| | | | | | | | | |
|---|---|---|---|---|---|---|---|---|
| UVIS/F555W | 0.15 | 0.09 | 0.03 | −0.01 | −0.03 | −0.04 | −0.05 | −0.06 |
| UVIS/F600LP | −3.71 | −0.42 | 0.09 | 0.34 | 0.47 | 0.52 | 0.57 | 0.60 |
| UVIS/F606W | −0.83 | −0.11 | 0.04 | 0.10 | 0.12 | 0.12 | 0.13 | 0.13 |
| UVIS/F621M | −1.23 | −0.26 | 0.03 | 0.16 | 0.22 | 0.25 | 0.27 | 0.28 |
| UVIS/F625W | −1.17 | −0.25 | 0.04 | 0.16 | 0.22 | 0.24 | 0.26 | 0.27 |
| UVIS/F631N | −0.33 | −0.28 | 0.03 | 0.17 | 0.24 | 0.27 | 0.30 | 0.31 |
| UVIS/F645N | −2.20 | −0.29 | 0.04 | 0.20 | 0.28 | 0.31 | 0.35 | 0.35 |
| UVIS/F656N | −1.99 | −0.26 | 0.36 | 0.63 | 0.56 | 0.54 | 0.52 | 0.45 |
| UVIS/F657N | −2.31 | −0.31 | 0.14 | 0.37 | 0.39 | 0.41 | 0.42 | 0.41 |
| UVIS/F658N | −2.04 | −0.31 | 0.18 | 0.42 | 0.42 | 0.43 | 0.44 | 0.41 |
| UVIS/F665N | −1.30 | −0.35 | 0.06 | 0.26 | 0.34 | 0.38 | 0.42 | 0.42 |
| UVIS/F673N | −0.69 | −0.37 | 0.04 | 0.24 | 0.35 | 0.39 | 0.44 | 0.45 |
| UVIS/F680N | −1.61 | −0.38 | 0.05 | 0.26 | 0.38 | 0.42 | 0.47 | 0.48 |
| UVIS/F689M | −1.69 | −0.37 | 0.06 | 0.28 | 0.39 | 0.43 | 0.47 | 0.48 |
| UVIS/F763M | −3.09 | −0.45 | 0.09 | 0.37 | 0.53 | 0.59 | 0.65 | 0.69 |
| UVIS/F775W | −3.60 | −0.45 | 0.09 | 0.38 | 0.54 | 0.59 | 0.65 | 0.70 |
| UVIS/F814W | −4.14 | −0.48 | 0.12 | 0.43 | 0.60 | 0.67 | 0.74 | 0.79 |
| UVIS/F845M | −4.56 | −0.51 | 0.16 | 0.51 | 0.70 | 0.77 | 0.84 | 0.91 |
| UVIS/F850LP | −5.03 | −0.56 | 0.21 | 0.56 | 0.79 | 0.89 | 0.98 | 1.06 |
| UVIS/F953N | −5.52 | −0.59 | 0.27 | 0.68 | 0.91 | 1.00 | 1.10 | 1.16 |
| UVIS/FQ232N | 2.15 | 4.54 | 2.68 | 1.53 | 0.20 | −0.43 | −1.12 | −1.46 |
| UVIS/FQ243N | 2.84 | 5.10 | 2.76 | 1.52 | 0.18 | −0.44 | −1.11 | −1.40 |
| UVIS/FQ378N | 4.90 | 2.32 | 0.86 | 0.61 | 0.01 | −0.20 | −0.44 | −0.62 |
| UVIS/FQ387N | 6.34 | 2.42 | 0.61 | 0.25 | −0.21 | −0.34 | −0.49 | −0.61 |
| UVIS/FQ422M | 5.05 | 1.17 | 0.18 | −0.22 | −0.36 | −0.41 | −0.46 | −0.48 |
| UVIS/FQ436N | 2.64 | 0.84 | 0.23 | 0.08 | −0.16 | −0.24 | −0.31 | −0.39 |
| UVIS/FQ437N | 2.59 | 0.83 | 0.18 | 0.00 | −0.21 | −0.28 | −0.34 | −0.40 |
| UVIS/FQ492N | 0.91 | 0.27 | 0.04 | −0.02 | −0.10 | −0.13 | −0.16 | −0.17 |
| UVIS/FQ575N | −0.58 | −0.18 | 0.01 | 0.07 | 0.10 | 0.11 | 0.13 | 0.13 |
| UVIS/FQ619N | 0.72 | −0.25 | 0.03 | 0.15 | 0.22 | 0.24 | 0.27 | 0.27 |
| UVIS/FQ634N | −0.96 | −0.28 | 0.03 | 0.18 | 0.26 | 0.29 | 0.32 | 0.32 |

| | | | | | | | |
|---|---|---|---|---|---|---|---|
| UVIS/FQ672N | −0.77 | −0.35 | 0.04 | 0.23 | 0.34 | 0.38 | 0.42 | 0.44 |
| UVIS/FQ674N | −0.39 | −0.37 | 0.04 | 0.24 | 0.35 | 0.39 | 0.43 | 0.44 |
| UVIS/FQ727N | −2.81 | −0.41 | 0.07 | 0.32 | 0.46 | 0.52 | 0.57 | 0.60 |
| UVIS/FQ750N | −3.06 | −0.44 | 0.08 | 0.36 | 0.51 | 0.57 | 0.63 | 0.66 |
| UVIS/FQ889N | −4.98 | −0.55 | 0.20 | 0.57 | 0.78 | 0.86 | 0.95 | 1.01 |
| UVIS/FQ906N | −5.15 | −0.56 | 0.21 | 0.57 | 0.79 | 0.88 | 0.98 | 1.05 |
| UVIS/FQ924N | −4.89 | −0.57 | 0.26 | 0.66 | 0.87 | 0.95 | 1.04 | 1.10 |
| UVIS/FQ937N | −5.19 | −0.58 | 0.19 | 0.48 | 0.77 | 0.89 | 1.01 | 1.11 |
| IR/F098M | −5.40 | −0.60 | 0.25 | 0.60 | 0.88 | 1.00 | 1.12 | 1.21 |
| IR/F105W | −5.68 | −0.62 | 0.31 | 0.69 | 0.98 | 1.11 | 1.24 | 1.34 |
| IR/F110W | −5.77 | −0.64 | 0.39 | 0.80 | 1.12 | 1.25 | 1.39 | 1.49 |
| IR/F125W | −5.91 | −0.67 | 0.48 | 0.94 | 1.28 | 1.43 | 1.58 | 1.69 |
| IR/F126N | −5.99 | −0.67 | 0.49 | 0.96 | 1.31 | 1.46 | 1.61 | 1.72 |
| IR/F127M | −6.04 | −0.67 | 0.52 | 1.01 | 1.35 | 1.49 | 1.65 | 1.75 |
| IR/F128N | −6.08 | −0.67 | 0.59 | 1.11 | 1.41 | 1.55 | 1.69 | 1.78 |
| IR/F130N | −6.13 | −0.68 | 0.53 | 1.02 | 1.37 | 1.52 | 1.68 | 1.79 |
| IR/F132N | −6.04 | −0.67 | 0.54 | 1.03 | 1.39 | 1.55 | 1.71 | 1.82 |
| IR/F139M | −5.64 | −0.69 | 0.60 | 1.11 | 1.49 | 1.64 | 1.81 | 1.92 |
| IR/F140W | −5.89 | −0.69 | 0.61 | 1.12 | 1.49 | 1.64 | 1.80 | 1.92 |
| IR/F153M | −6.03 | −0.71 | 0.73 | 1.29 | 1.69 | 1.85 | 2.02 | 2.14 |
| IR/F160W | −6.05 | −0.70 | 0.74 | 1.30 | 1.69 | 1.85 | 2.02 | 2.15 |
| IR/F164N | −6.39 | −0.70 | 0.84 | 1.42 | 1.82 | 1.99 | 2.16 | 2.28 |
| IR/F167N | −6.32 | −0.69 | 0.84 | 1.41 | 1.83 | 2.00 | 2.18 | 2.31 |

Table A.2: Color corrections $AB_v$ to go from Johnson $V$ magnitude to AB magnitude for WFC3 as a function of age in an instantaneous burst population.

| | | | Age | | |
|---|---|---|---|---|---|
| Mode | 10 Gyr | 1 Gyr | 100 Myr | 10 Myr | 1 Myr |
| UVIS/F200LP | 0.38 | 0.48 | 0.29 | 0.02 | −0.48 |
| UVIS/F218W | 6.11 | 3.89 | 1.06 | 0.15 | −1.22 |
| UVIS/F225W | 5.83 | 3.76 | 1.03 | 0.16 | −1.15 |

| | | | | | |
|---|---|---|---|---|---|
| UVIS/F275W | 4.75 | 3.14 | 0.93 | 0.19 | –0.97 |
| UVIS/F280N | 4.32 | 3.03 | 0.89 | 0.21 | –0.92 |
| UVIS/F300X | 3.95 | 2.80 | 0.89 | 0.20 | –0.94 |
| UVIS/F336W | 2.69 | 1.98 | 0.77 | 0.27 | –0.67 |
| UVIS/F343N | 2.55 | 1.89 | 0.76 | 0.28 | –0.63 |
| UVIS/F350LP | –0.09 | 0.04 | 0.06 | –0.06 | –0.04 |
| UVIS/F373N | 2.28 | 1.57 | 0.66 | 0.34 | –0.49 |
| UVIS/F390M | 2.03 | 1.12 | 0.22 | 0.14 | –0.50 |
| UVIS/F390W | 1.63 | 1.00 | 0.27 | 0.15 | –0.50 |
| UVIS/F395N | 1.88 | 1.03 | 0.14 | 0.11 | –0.49 |
| UVIS/F410M | 1.23 | 0.64 | 0.02 | 0.02 | –0.47 |
| UVIS/F438W | 0.90 | 0.48 | 0.01 | 0.02 | –0.39 |
| UVIS/F467M | 0.44 | 0.22 | –0.03 | –0.01 | –0.26 |
| UVIS/F469N | 0.46 | 0.23 | –0.02 | –0.01 | –0.25 |
| UVIS/F475W | 0.48 | 0.27 | 0.02 | 0.04 | –0.23 |
| UVIS/F475X | 0.38 | 0.24 | 0.03 | 0.03 | –0.20 |
| UVIS/F487N | 0.36 | 0.27 | 0.12 | 0.10 | –0.14 |
| UVIS/F502N | 0.33 | 0.17 | 0.02 | 0.08 | –0.12 |
| UVIS/F547M | 0.04 | 0.03 | 0.03 | 0.03 | 0.02 |
| UVIS/F555W | 0.11 | 0.07 | 0.02 | 0.01 | –0.05 |
| UVIS/F600LP | –0.72 | –0.38 | –0.04 | –0.27 | 0.54 |
| UVIS/F606W | –0.17 | –0.08 | 0.01 | –0.04 | 0.13 |
| UVIS/F621M | –0.33 | –0.18 | 0.00 | –0.10 | 0.26 |
| UVIS/F625W | –0.33 | –0.18 | –0.00 | –0.10 | 0.26 |
| UVIS/F631N | –0.34 | –0.19 | 0.00 | –0.10 | 0.29 |
| UVIS/F645N | –0.43 | –0.23 | –0.02 | –0.15 | 0.33 |
| UVIS/F656N | –0.45 | –0.18 | 0.06 | –0.16 | 0.37 |
| UVIS/F657N | –0.47 | –0.22 | 0.00 | –0.18 | 0.37 |
| UVIS/F658N | –0.47 | –0.22 | 0.00 | –0.18 | 0.37 |
| UVIS/F665N | –0.48 | –0.26 | –0.03 | –0.18 | 0.39 |

| | | | | | |
|---|---|---|---|---|---|
| UVIS/F673N | –0.49 | –0.28 | –0.02 | –0.15 | 0.42 |
| UVIS/F680N | –0.54 | –0.30 | –0.02 | –0.17 | 0.45 |
| UVIS/F689M | –0.53 | –0.29 | –0.02 | –0.18 | 0.45 |
| UVIS/F763M | –0.77 | –0.40 | –0.05 | –0.32 | 0.64 |
| UVIS/F775W | –0.78 | –0.41 | –0.05 | –0.31 | 0.64 |
| UVIS/F814W | –0.89 | –0.47 | –0.07 | –0.36 | 0.71 |
| UVIS/F845M | –1.00 | –0.53 | –0.09 | –0.41 | 0.82 |
| UVIS/F850LP | –1.18 | –0.65 | –0.13 | –0.47 | 0.96 |
| UVIS/F953N | –1.27 | –0.71 | –0.12 | –0.50 | 1.06 |
| UVIS/FQ232N | 4.48 | 3.43 | 1.03 | 0.17 | –1.14 |
| UVIS/FQ243N | 4.88 | 3.62 | 0.98 | 0.14 | –1.10 |
| UVIS/FQ378N | 2.24 | 1.37 | 0.42 | 0.22 | –0.51 |
| UVIS/FQ387N | 2.27 | 1.16 | 0.23 | 0.14 | –0.51 |
| UVIS/FQ422M | 1.16 | 0.55 | –0.03 | 0.01 | –0.44 |
| UVIS/FQ436N | 0.86 | 0.49 | 0.04 | 0.05 | –0.36 |
| UVIS/FQ437N | 0.86 | 0.46 | 0.00 | 0.03 | –0.37 |
| UVIS/FQ492N | 0.31 | 0.17 | 0.01 | 0.05 | –0.15 |
| UVIS/FQ508N | 0.31 | 0.17 | 0.04 | 0.12 | –0.09 |
| UVIS/FQ575N | –0.18 | –0.08 | 0.00 | –0.06 | 0.12 |
| UVIS/FQ619N | –0.28 | –0.16 | 0.02 | –0.06 | 0.26 |
| UVIS/FQ634N | –0.37 | –0.21 | –0.01 | –0.12 | 0.30 |
| UVIS/FQ672N | –0.47 | –0.27 | –0.02 | –0.16 | 0.40 |
| UVIS/FQ674N | –0.48 | –0.27 | –0.02 | –0.16 | 0.41 |
| UVIS/FQ727N | –0.65 | –0.34 | –0.01 | –0.26 | 0.56 |
| UVIS/FQ750N | –0.81 | –0.43 | –0.07 | –0.33 | 0.61 |
| UVIS/FQ889N | –1.12 | –0.61 | –0.14 | –0.46 | 0.91 |
| UVIS/FQ906N | –1.22 | –0.68 | –0.15 | –0.49 | 0.94 |
| UVIS/FQ924N | –1.21 | –0.65 | –0.12 | –0.48 | 1.00 |
| UVIS/FQ937N | –1.16 | –0.65 | –0.11 | –0.47 | 1.00 |
| IR/F098M | –1.35 | –0.74 | –0.15 | –0.51 | 1.10 |

| | | | | |
|---|---|---|---|---|
| IR/F105W | –1.39 | –0.74 | –0.14 | –0.54 | 1.22 |
| IR/F110W | –1.38 | –0.70 | –0.11 | –0.57 | 1.36 |
| IR/F125W | –1.39 | –0.67 | –0.08 | –0.60 | 1.57 |
| IR/F126N | –1.37 | –0.64 | –0.07 | –0.62 | 1.60 |
| IR/F127M | –1.38 | –0.64 | –0.07 | –0.62 | 1.62 |
| IR/F128N | –1.39 | –0.64 | –0.07 | –0.63 | 1.64 |
| IR/F130N | –1.40 | –0.65 | –0.07 | –0.63 | 1.66 |
| IR/F132N | –1.40 | –0.64 | –0.07 | –0.62 | 1.69 |
| IR/F139M | –1.37 | –0.62 | –0.05 | –0.60 | 1.78 |
| IR/F140W | –1.41 | –0.65 | –0.06 | –0.64 | 1.77 |
| IR/F153M | –1.49 | –0.69 | –0.07 | –0.70 | 1.98 |
| IR/F160W | –1.49 | –0.68 | –0.07 | –0.70 | 1.97 |
| IR/F164N | –1.59 | –0.75 | –0.11 | –0.79 | 2.10 |
| IR/F167N | –1.58 | –0.74 | –0.10 | –0.78 | 2.13 |

Table A.3: Color corrections $AB_v$ to go from Johnson $V$ magnitude to AB magnitude for WFC3 as a function of age in a population with constant star formation.

| | | | Age | | |
|---|---|---|---|---|---|
| Mode | 10 Gyr | 1 Gyr | 100 Myr | 10 Myr | 1 Myr |
| UVIS/F200LP | 0.31 | 0.24 | 0.03 | –0.15 | –0.48 |
| UVIS/F218W | 1.39 | 0.79 | 0.08 | –0.48 | –1.22 |
| UVIS/F225W | 1.39 | 0.79 | 0.09 | –0.44 | –1.15 |
| UVIS/F275W | 1.35 | 0.78 | 0.12 | –0.36 | –0.97 |
| UVIS/F280N | 1.34 | 0.77 | 0.14 | –0.33 | –0.92 |
| UVIS/F300X | 1.31 | 0.76 | 0.13 | –0.34 | –0.93 |
| UVIS/F336W | 1.15 | 0.71 | 0.19 | –0.21 | –0.66 |
| UVIS/F343N | 1.13 | 0.71 | 0.20 | –0.18 | –0.62 |
| UVIS/F350LP | 0.00 | 0.03 | –0.01 | –0.01 | –0.04 |
| UVIS/F373N | 1.04 | 0.66 | 0.24 | –0.11 | –0.49 |
| UVIS/F390M | 0.67 | 0.28 | –0.00 | –0.25 | –0.50 |

| | | | | | |
|---|---|---|---|---|---|
| UVIS/F390W | 0.64 | 0.30 | 0.03 | –0.23 | –0.49 |
| UVIS/F395N | 0.60 | 0.21 | –0.04 | –0.27 | –0.49 |
| UVIS/F410M | 0.37 | 0.07 | –0.11 | –0.30 | –0.47 |
| UVIS/F438W | 0.29 | 0.05 | –0.09 | –0.25 | –0.39 |
| UVIS/F467M | 0.14 | –0.00 | –0.08 | –0.18 | –0.26 |
| UVIS/F469N | 0.15 | 0.00 | –0.07 | –0.17 | –0.25 |
| UVIS/F475W | 0.18 | 0.04 | –0.03 | –0.14 | –0.23 |
| UVIS/F475X | 0.16 | 0.05 | –0.02 | –0.11 | –0.20 |
| UVIS/F487N | 0.21 | 0.14 | 0.05 | –0.05 | –0.14 |
| UVIS/F502N | 0.13 | 0.04 | 0.01 | –0.06 | –0.13 |
| UVIS/F547M | 0.03 | 0.03 | 0.03 | 0.03 | 0.02 |
| UVIS/F555W | 0.05 | 0.02 | –0.00 | –0.03 | –0.05 |
| UVIS/F600LP | –0.36 | –0.13 | –0.05 | 0.22 | 0.54 |
| UVIS/F606W | –0.06 | –0.00 | 0.01 | 0.07 | 0.13 |
| UVIS/F621M | –0.14 | –0.03 | 0.01 | 0.13 | 0.26 |
| UVIS/F625W | –0.14 | –0.03 | 0.01 | 0.12 | 0.26 |
| UVIS/F631N | –0.15 | –0.03 | 0.02 | 0.14 | 0.29 |
| UVIS/F645N | –0.19 | –0.05 | –0.01 | 0.15 | 0.33 |
| UVIS/F656N | –0.16 | 0.01 | 0.02 | 0.19 | 0.37 |
| UVIS/F657N | –0.20 | –0.04 | –0.01 | 0.16 | 0.37 |
| UVIS/F658N | –0.20 | –0.04 | –0.02 | 0.16 | 0.37 |
| UVIS/F665N | –0.23 | –0.07 | –0.02 | 0.16 | 0.39 |
| UVIS/F673N | –0.23 | –0.06 | 0.01 | 0.19 | 0.42 |
| UVIS/F680N | –0.26 | –0.07 | 0.00 | 0.20 | 0.45 |
| UVIS/F689M | –0.25 | –0.07 | –0.01 | 0.20 | 0.45 |
| UVIS/F763M | –0.39 | –0.13 | –0.06 | 0.25 | 0.64 |
| UVIS/F775W | –0.39 | –0.14 | –0.06 | 0.25 | 0.64 |
| UVIS/F814W | –0.46 | –0.18 | –0.08 | 0.26 | 0.71 |
| UVIS/F845M | –0.53 | –0.22 | –0.12 | 0.28 | 0.82 |
| UVIS/F850LP | –0.66 | –0.31 | –0.14 | 0.30 | 0.96 |

| | | | | | |
|---|---|---|---|---|---|
| UVIS/F953N | –0.72 | –0.34 | –0.15 | 0.32 | 1.06 |
| UVIS/FQ232N | 1.37 | 0.79 | 0.10 | -0.43 | -1.14 |
| UVIS/FQ243N | 1.37 | 0.78 | 0.08 | -0.43 | -1.10 |
| UVIS/FQ378N | 0.85 | 0.46 | 0.10 | -0.20 | -0.50 |
| UVIS/FQ387N | 0.70 | 0.29 | 0.01 | -0.25 | -0.51 |
| UVIS/FQ422M | 0.32 | 0.02 | -0.12 | -0.30 | -0.44 |
| UVIS/FQ436N | 0.31 | 0.08 | -0.06 | -0.22 | -0.37 |
| UVIS/FQ437N | 0.28 | 0.05 | -0.09 | -0.24 | -0.38 |
| UVIS/FQ492N | 0.12 | 0.03 | -0.01 | -0.09 | -0.15 |
| UVIS/FQ508N | 0.14 | 0.06 | 0.04 | -0.03 | -0.09 |
| UVIS/FQ575N | –0.07 | –0.01 | –0.00 | 0.06 | 0.13 |
| UVIS/FQ619N | –0.12 | –0.01 | 0.03 | 0.14 | 0.26 |
| UVIS/FQ634N | –0.17 | –0.04 | 0.00 | 0.14 | 0.30 |
| UVIS/FQ672N | –0.22 | –0.06 | –0.00 | 0.18 | 0.40 |
| UVIS/FQ674N | –0.22 | –0.06 | 0.00 | 0.19 | 0.41 |
| UVIS/FQ727N | –0.31 | –0.09 | –0.03 | 0.23 | 0.56 |
| UVIS/FQ750N | –0.42 | –0.16 | –0.08 | 0.23 | 0.61 |
| UVIS/FQ889N | –0.62 | –0.28 | –0.15 | 0.28 | 0.91 |
| UVIS/FQ906N | –0.69 | –0.34 | –0.17 | 0.27 | 0.94 |
| UVIS/FQ924N | –0.67 | –0.30 | –0.14 | 0.31 | 1.00 |
| UVIS/FQ937N | –0.65 | –0.30 | –0.14 | 0.31 | 0.99 |
| IR/F098M | –0.76 | –0.37 | –0.16 | 0.33 | 1.10 |
| IR/F105W | –0.78 | –0.37 | –0.17 | 0.36 | 1.22 |
| IR/F110W | –0.76 | –0.33 | –0.17 | 0.39 | 1.36 |
| IR/F125W | –0.74 | –0.30 | –0.17 | 0.44 | 1.57 |
| IR/F126N | –0.73 | –0.29 | –0.18 | 0.45 | 1.60 |
| IR/F127M | –0.73 | –0.29 | –0.18 | 0.45 | 1.62 |
| IR/F128N | –0.74 | –0.29 | –0.18 | 0.45 | 1.64 |
| IR/F130N | –0.74 | –0.29 | –0.18 | 0.46 | 1.66 |
| IR/F132N | –0.74 | –0.28 | –0.17 | 0.47 | 1.69 |

| | | | | | |
|---|---|---|---|---|---|
| IR/F139M | –0.71 | –0.25 | –0.14 | 0.49 | 1.78 |
| IR/F140W | –0.75 | –0.28 | –0.17 | 0.47 | 1.77 |
| IR/F153M | –0.81 | –0.32 | –0.20 | 0.47 | 1.97 |
| IR/F160W | –0.80 | –0.32 | –0.21 | 0.46 | 1.97 |
| IR/F164N | –0.88 | –0.39 | –0.27 | 0.43 | 2.10 |
| IR/F167N | –0.88 | –0.38 | –0.26 | 0.44 | 2.13 |

# UVIS F200LP

**Description**
Clear.

**Figure A.1: Integrated system throughput for F200LP.**
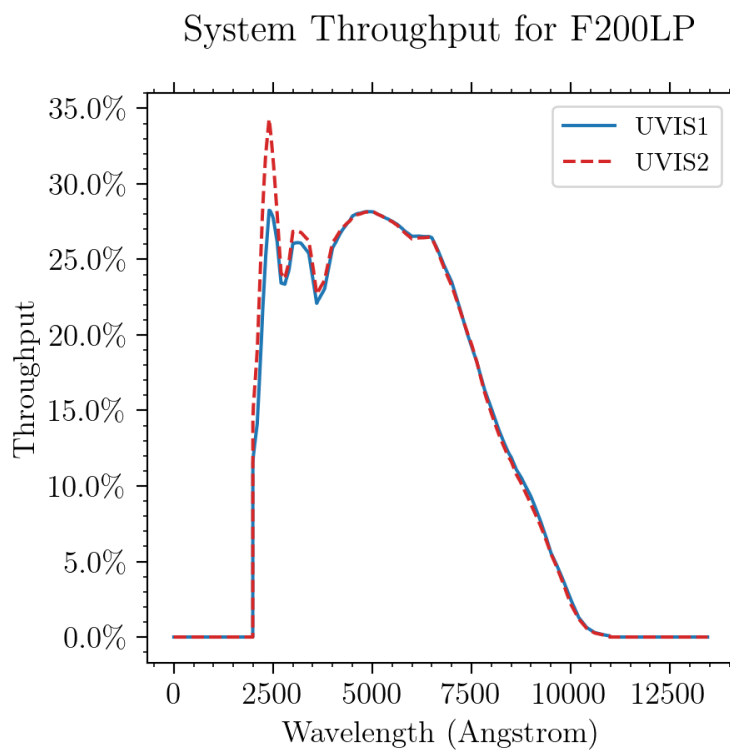
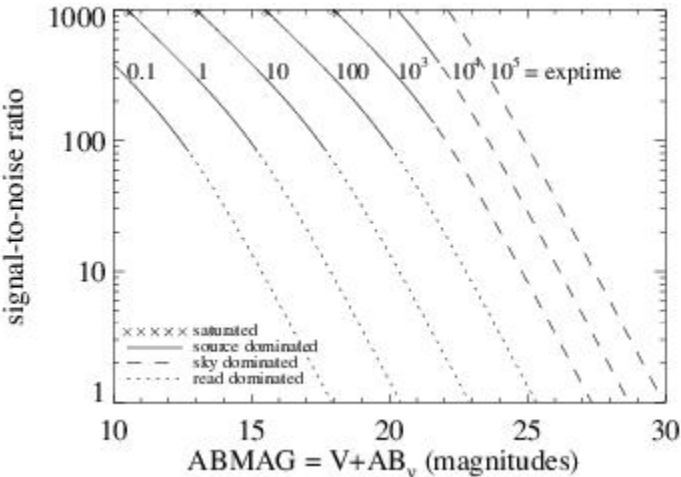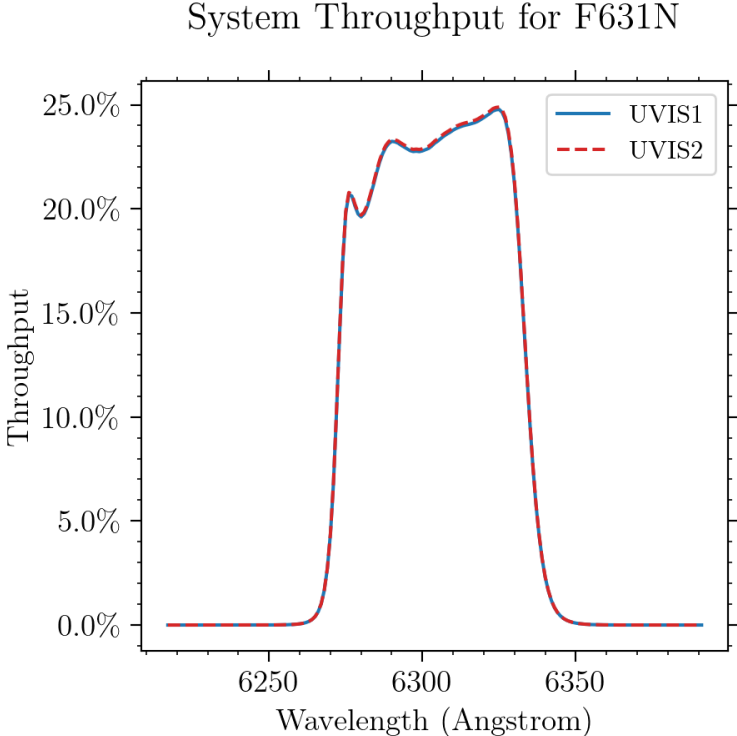Figure A.2: Point source S/N vs. V+AB$_\nu$ for the F200LP filter, assuming high sky backgrounds and a 5 × 5 pixel aperture.
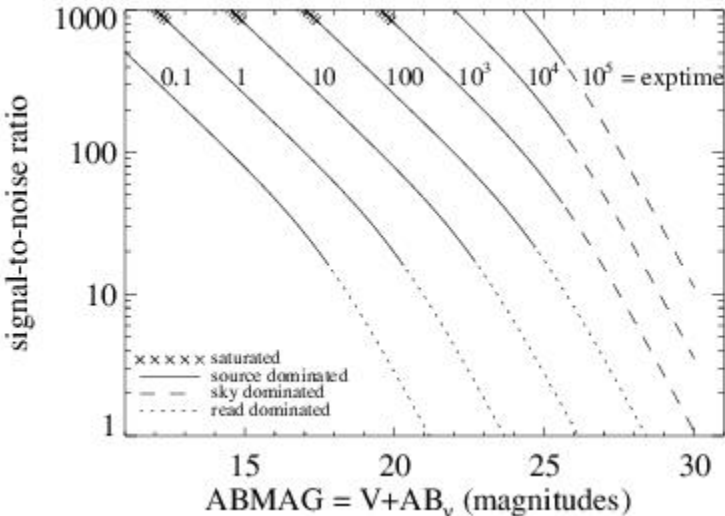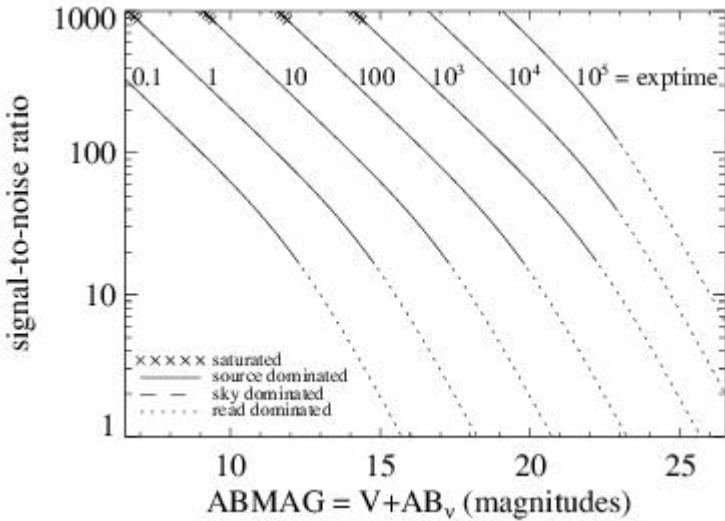
Figure A.3: Extended source S/N vs. V+AB$_\nu$ for the F200LP filter, assuming high sky backgrounds and a source uniformly filling a 1 arcsec$^2$ aperture.
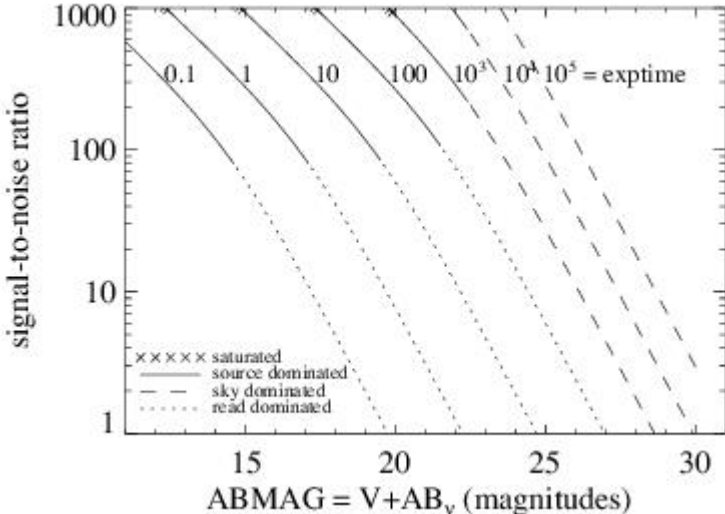
# UVIS F218W

**Description**
ISM feature filter.

**Figure A.4: Integrated system throughput for F218W.**



System Throughput for F218W
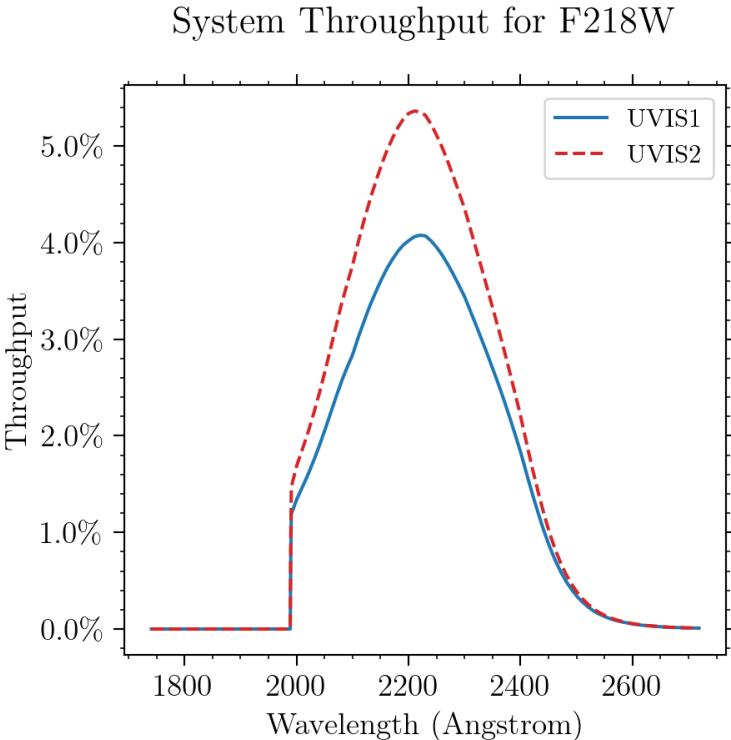
Figure A.5: Point source S/N vs. V+AB$_\nu$ for the F218W filter, assuming high sky backgrounds and a 5 × 5 pixel aperture.
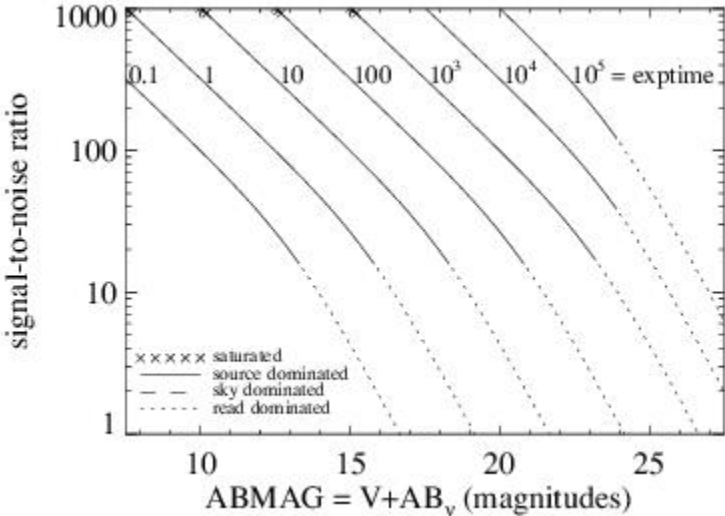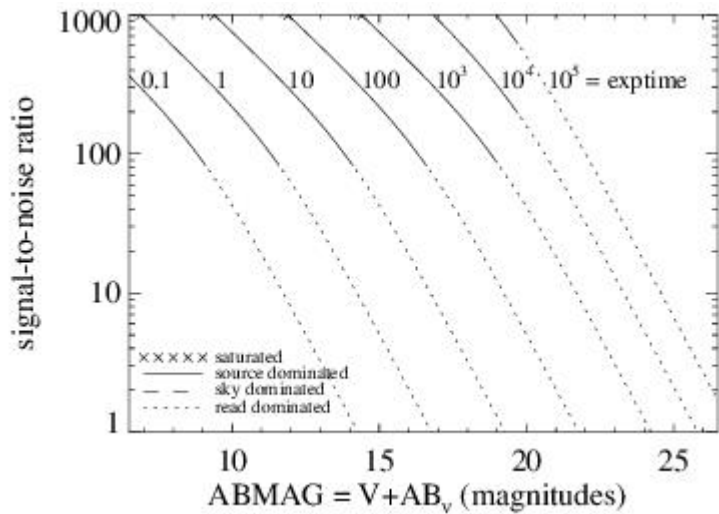
Figure A.6: Extended source S/N vs. $V+AB_\nu$ for the F218W filter, assuming high sky backgrounds and a source uniformly filling a 1 arcsec$^2$ aperture.
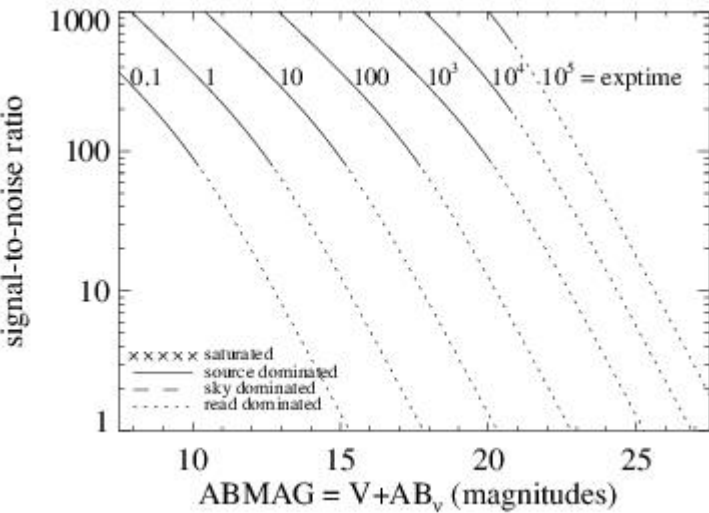
# UVIS F225W

**Description**
UV wide filter.
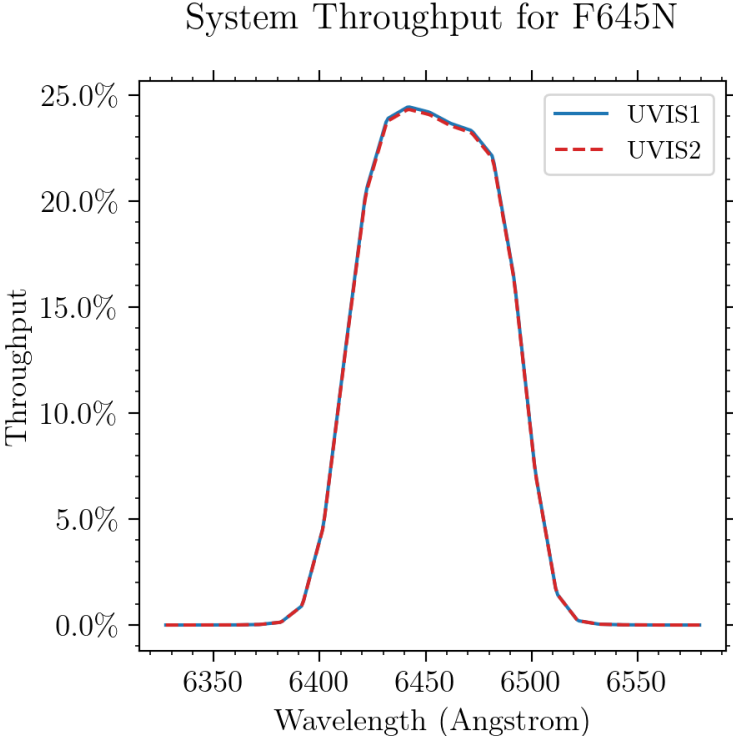
**Figure A.7: Integrated system throughput for F225W.**
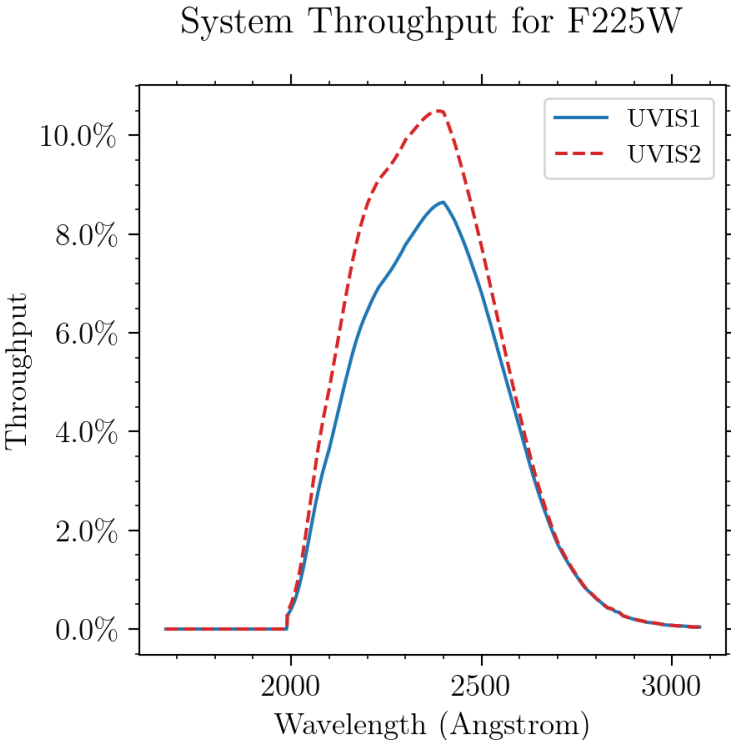
Figure A.8: Point source S/N vs. V+AB$_\nu$ for the F225W filter, assuming high sky backgrounds and a 5 × 5 pixel aperture.
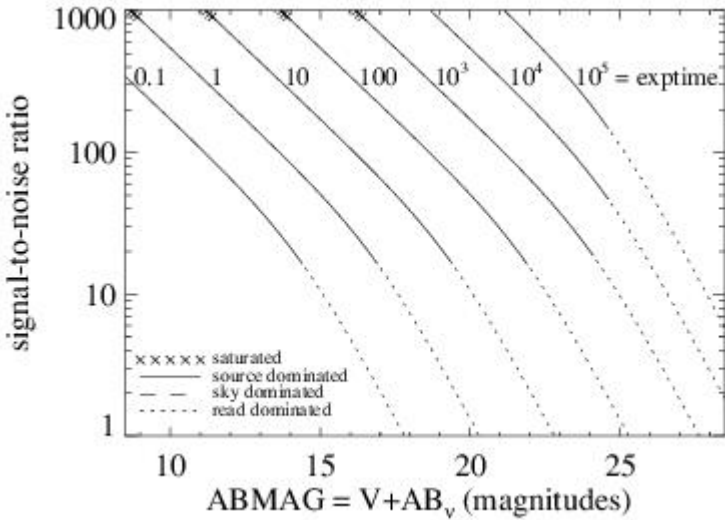
Figure A.9: Extended source S/N vs. $V+AB_\nu$ for the F225W filter assuming high sky backgrounds and a source uniformly filling a 1 arcsec$^2$ aperture.
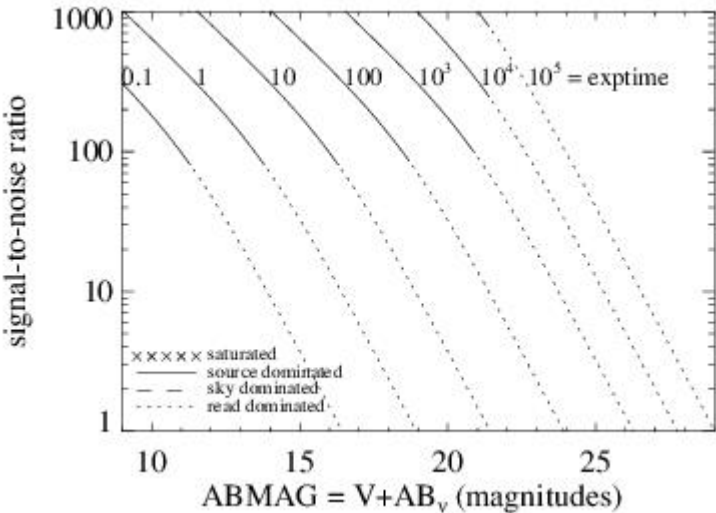
# UVIS F275W

**Description**
UV wide filter.

**Figure A.10: Integrated system throughput for F275W.**



System Throughput for F275W
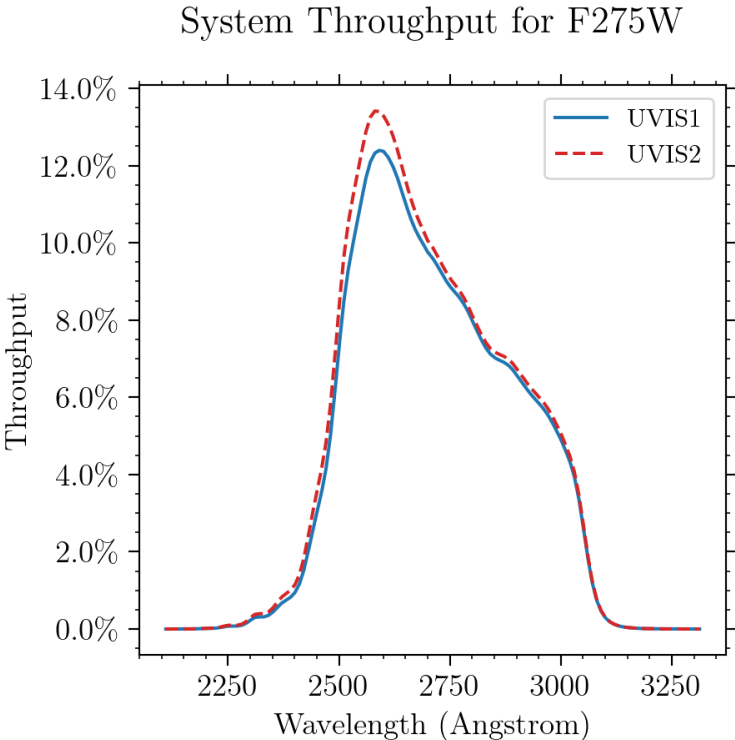
**Figure A.11:** Point source S/N vs. V+AB$_\nu$ for the F275W filter, assuming high sky backgrounds and a 5 × 5 pixel aperture.
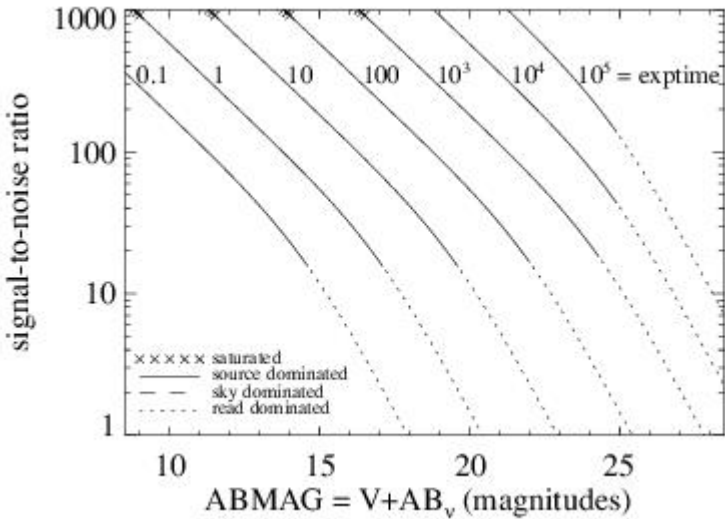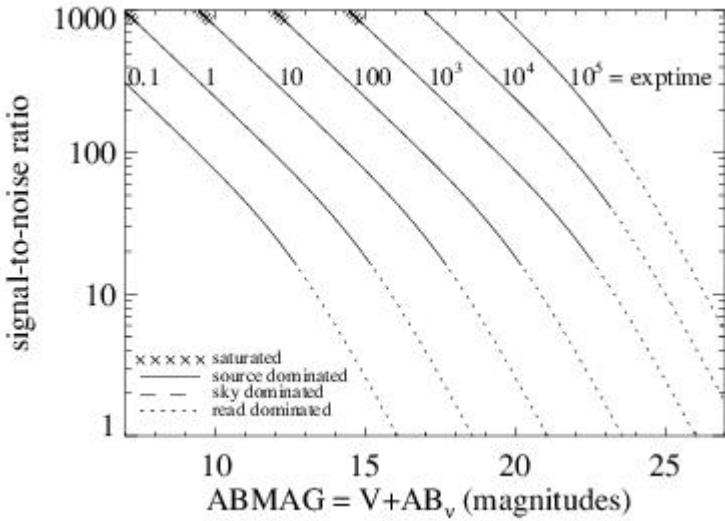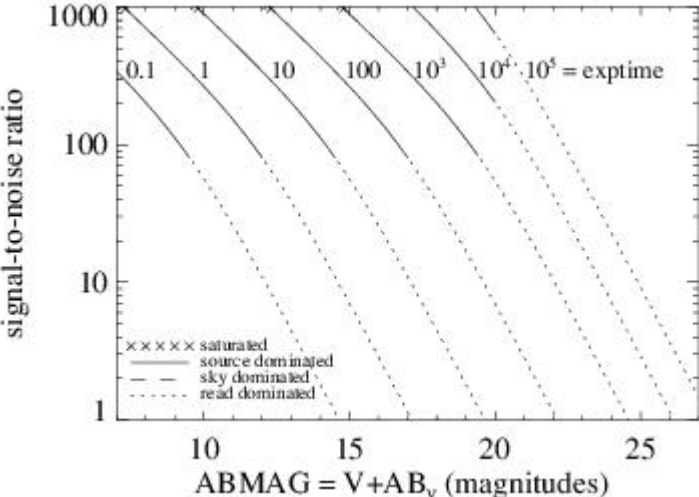
Figure A.12: Extended source S/N vs. V+AB$_\nu$ for the F275W filter, assuming high sky backgrounds and a source uniformly filling a 1 arcsec$^2$ aperture.
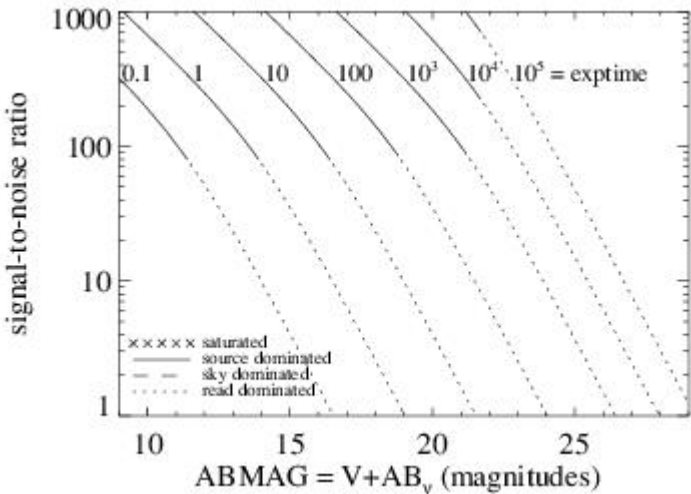
# UVIS F280N

**Description**
Mg II 2795/2802 filter.
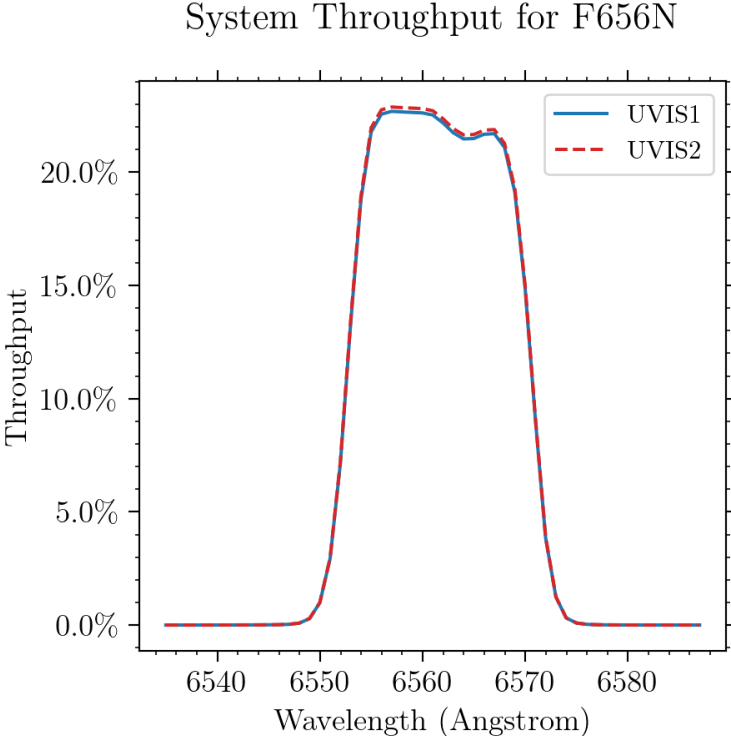
**Figure A.13: Integrated system throughput for F280N.**
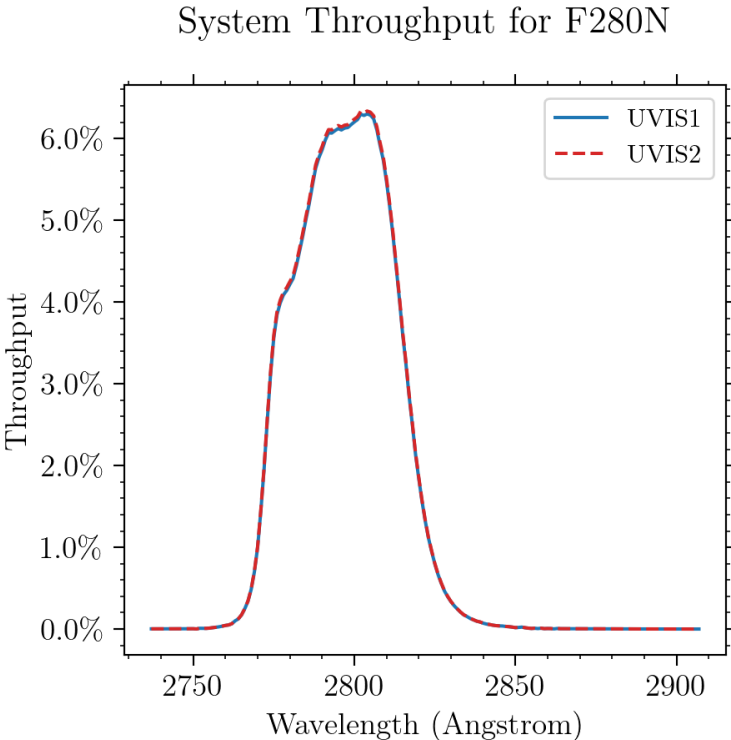
Figure A.14: Point source S/N vs. V+AB$_\nu$ for the F280N filter, assuming high sky backgrounds and a 5 × 5 pixel aperture.
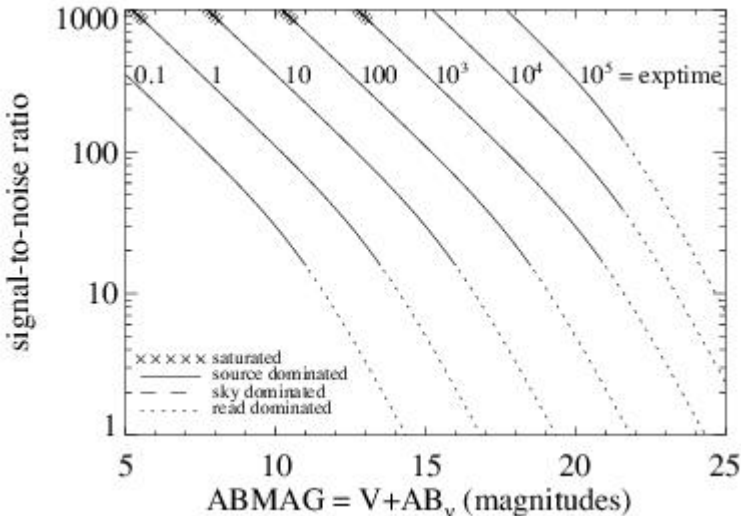
**Figure A.15:** Extended source S/N vs. V+AB$_v$ for the F280N filter, assuming high sky backgrounds and a source uniformly filling a 1 arcsec$^2$ aperture.
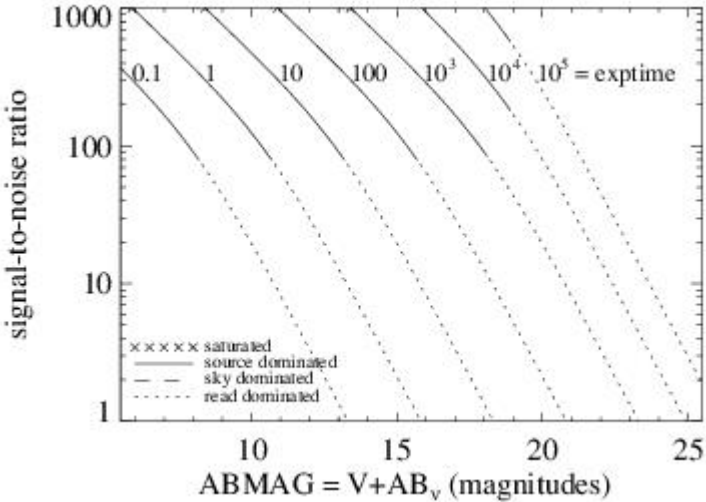
# UVIS F300X

**Description**
Extremely wide UV filter; grism reference.

**Figure A.16: Integrated system throughput for F300X.**
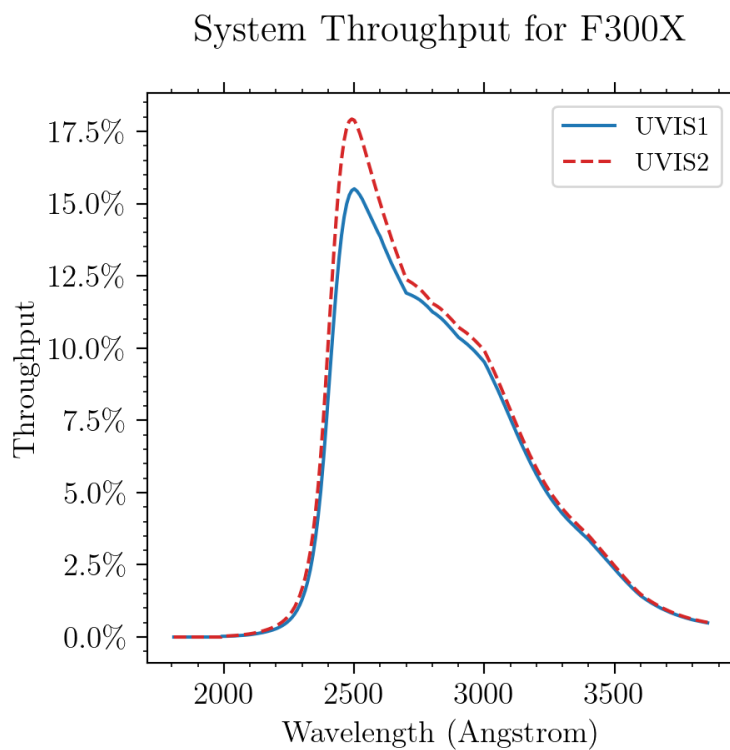
Figure A.17: Point source S/N vs. V+AB$_\nu$ for the F300X filter, assuming high sky backgrounds and a 5 × 5 pixel aperture.
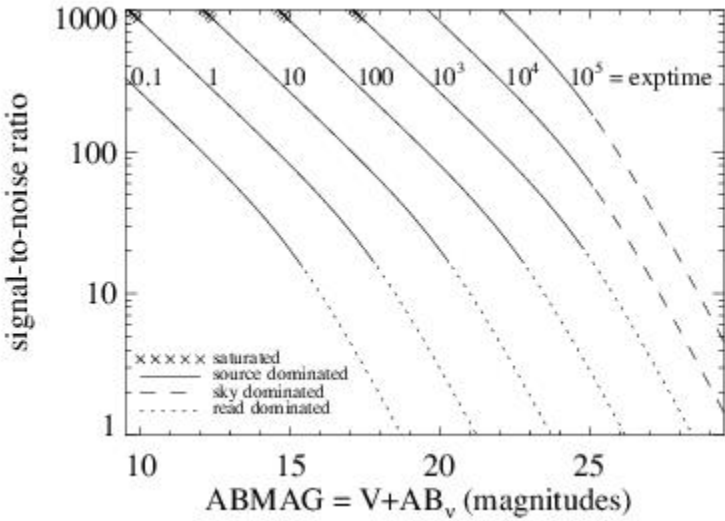
**Figure A.18:** Extended source S/N vs. V+AB$_\nu$ for the F300X, assuming high sky backgrounds and a source uniformly filling a 1 arcsec$^2$ aperture.
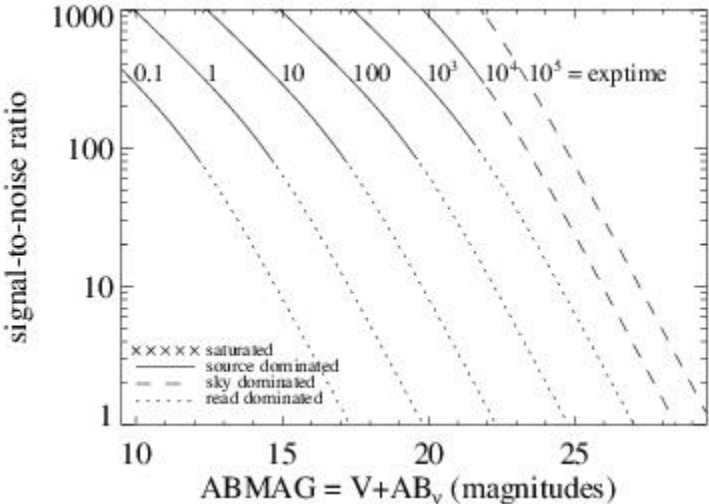
# UVIS F336W

**Description**
*U*, Strömgren *u* filter.

**Figure A.19: Integrated system throughput for F336W.**
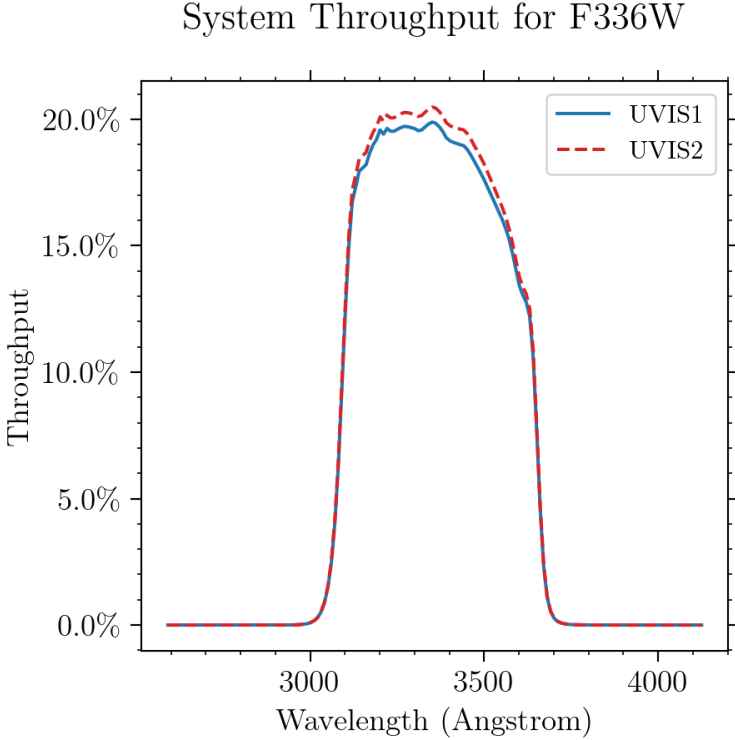
Figure A.20: Point source S/N vs. V+AB$_\nu$ for the F336W filter, assuming high sky backgrounds and a 5 × 5 pixel aperture.
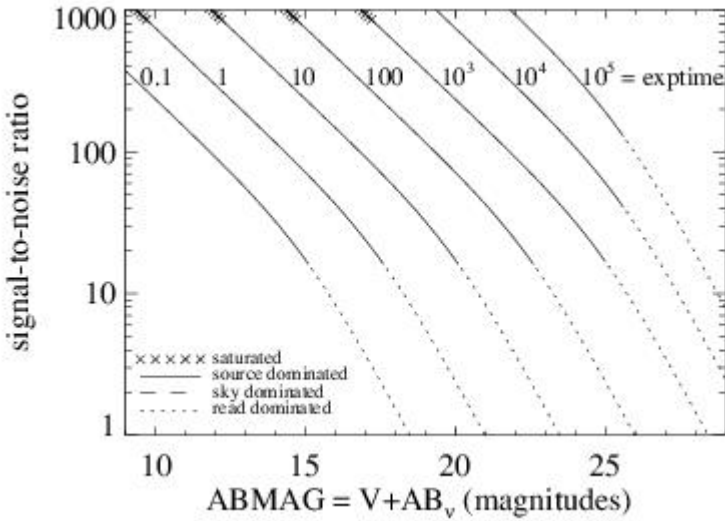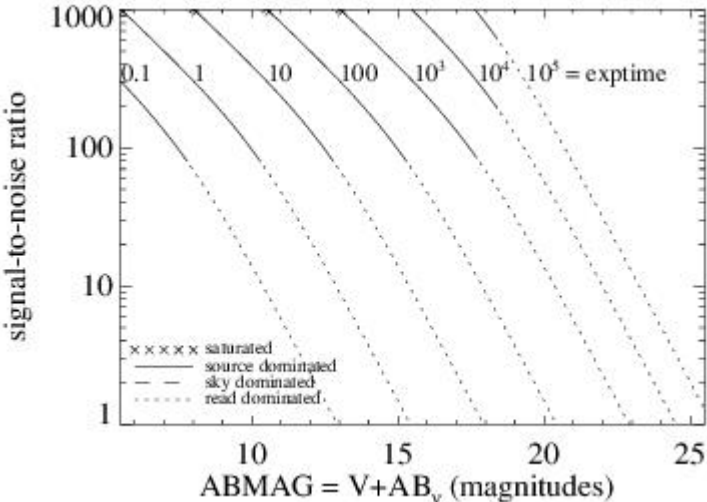
Figure A.21: Extended source S/N vs. V+AB$_{\nu}$ for the F336W filter, assuming high sky backgrounds and a source uniformly filling a 1 arcsec$^2$ aperture.
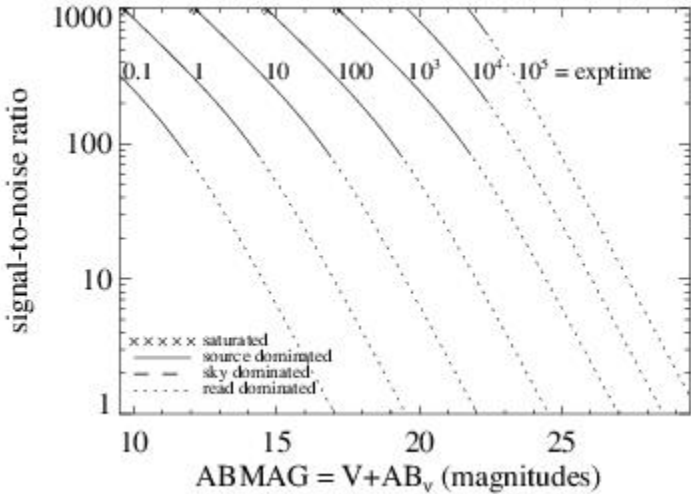
# UVIS F343N

**Description**
[Ne v] 3426 filter.

**Figure A.22: Integrated system throughput for F343N.**
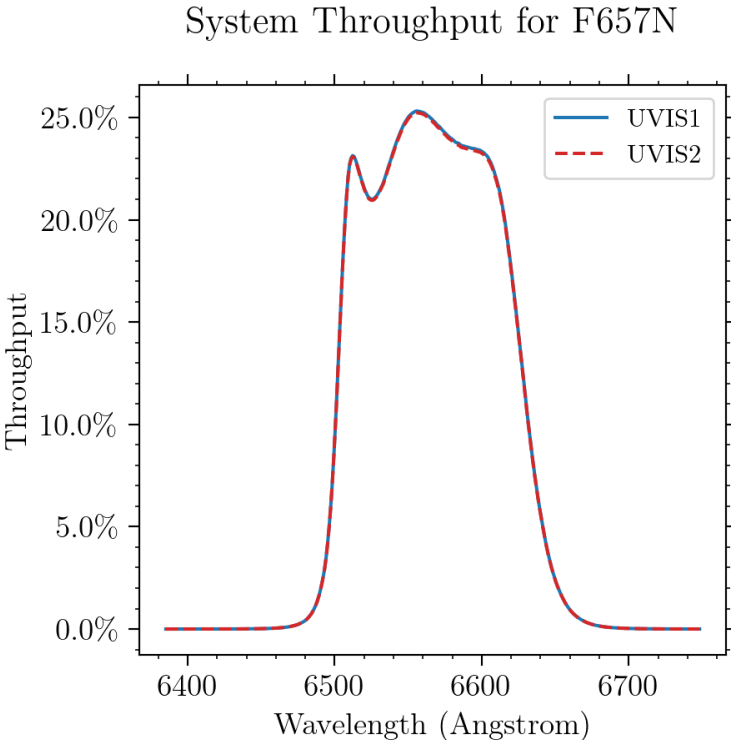


System Throughput for F343N
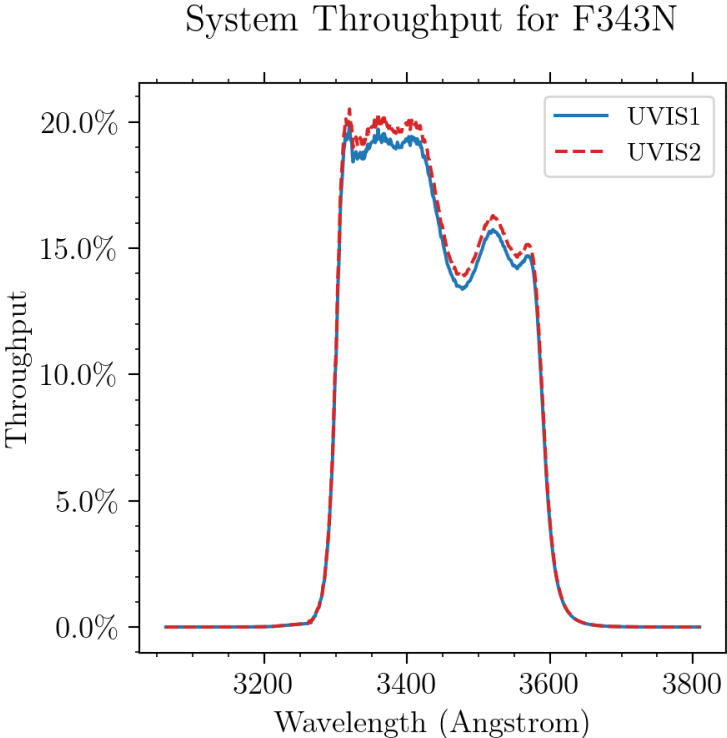
**Figure A.23:** Point source S/N vs. V+AB$_\nu$ for the F343N filter, assuming high sky backgrounds and a 5 × 5 pixel aperture.
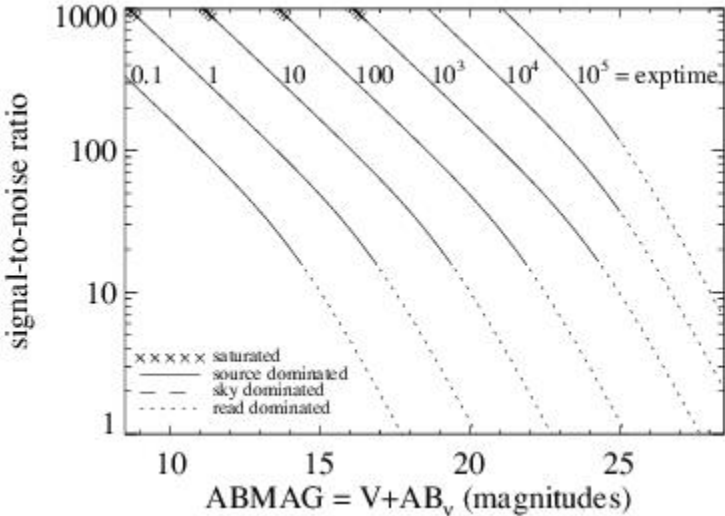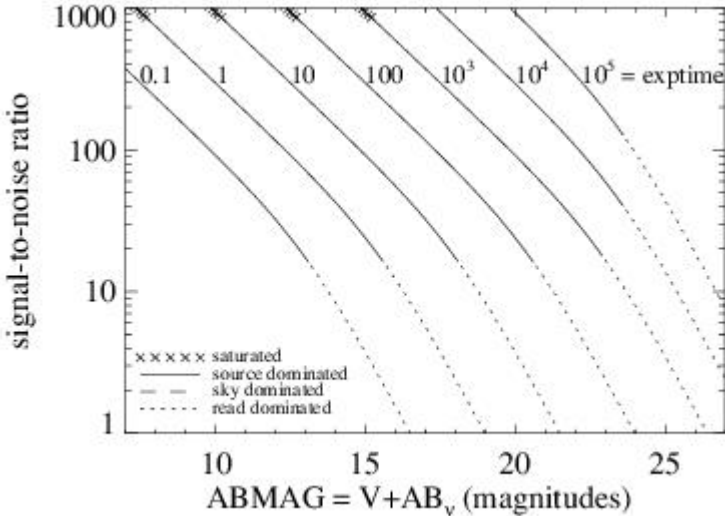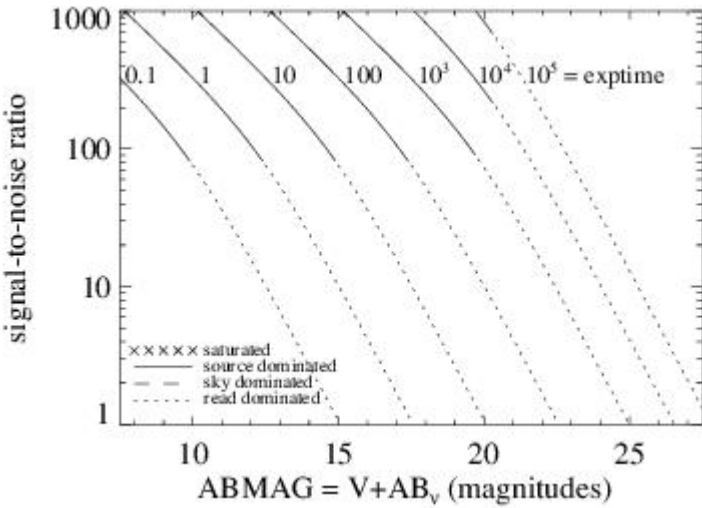
Figure A.24: Extended source S/N vs. V+AB$_\nu$ for the F343N filter, assuming high sky backgrounds and a source uniformly filling a 1 arcsec$^2$ aperture.
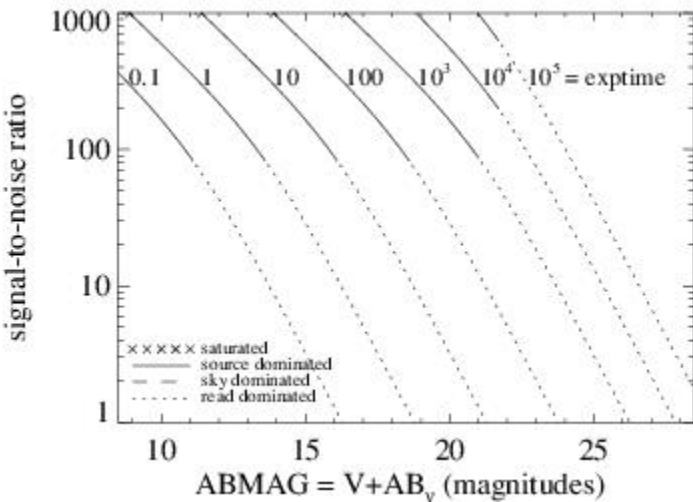
# UVIS F350LP

**Description**
Long pass filter.

**Figure A.25: Integrated system throughput for F350LP.**



System Throughput for F350LP
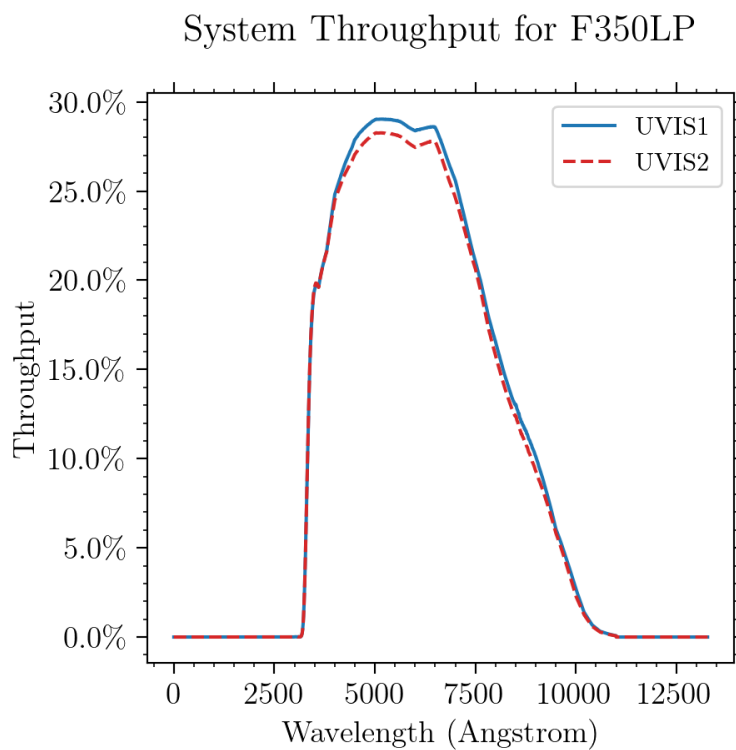
**Figure A.26:** Point source S/N vs. V+AB$_\nu$ for the F350LP filter, assuming high sky backgrounds and a 5 × 5 pixel aperture.
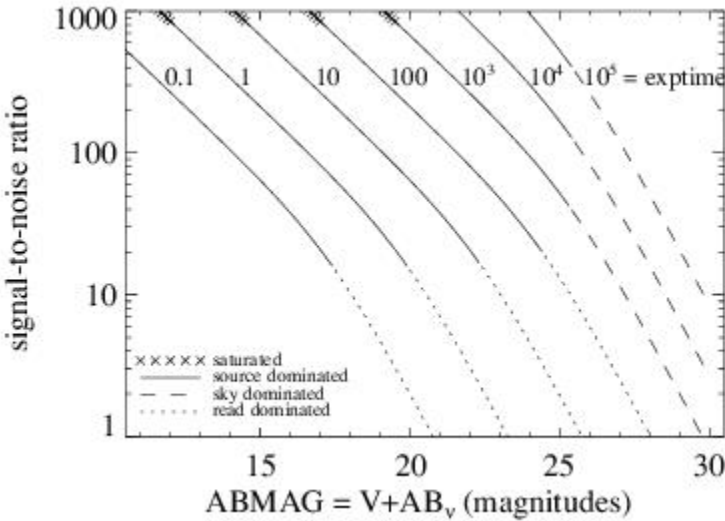
Figure A.27: Extended source S/N vs. V+AB$_\nu$ for the F350LP filter, assuming high sky backgrounds and a source uniformly filling a 1 arcsec$^2$ aperture.
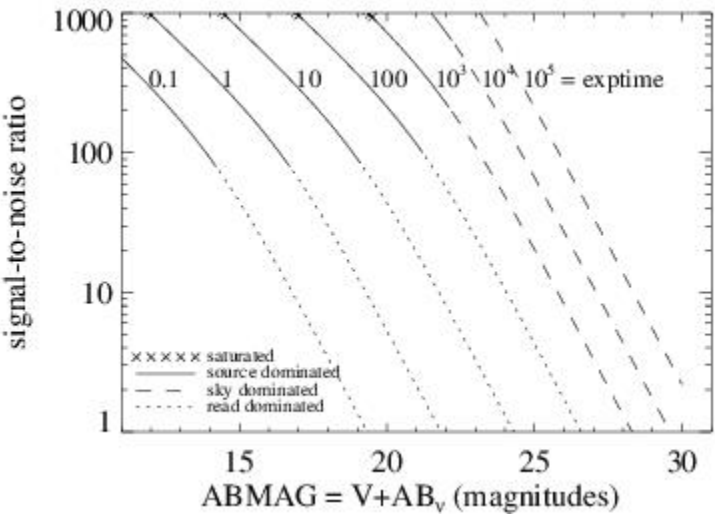
# UVIS F373N

**Description**
[O II] 3726/3728 filter.
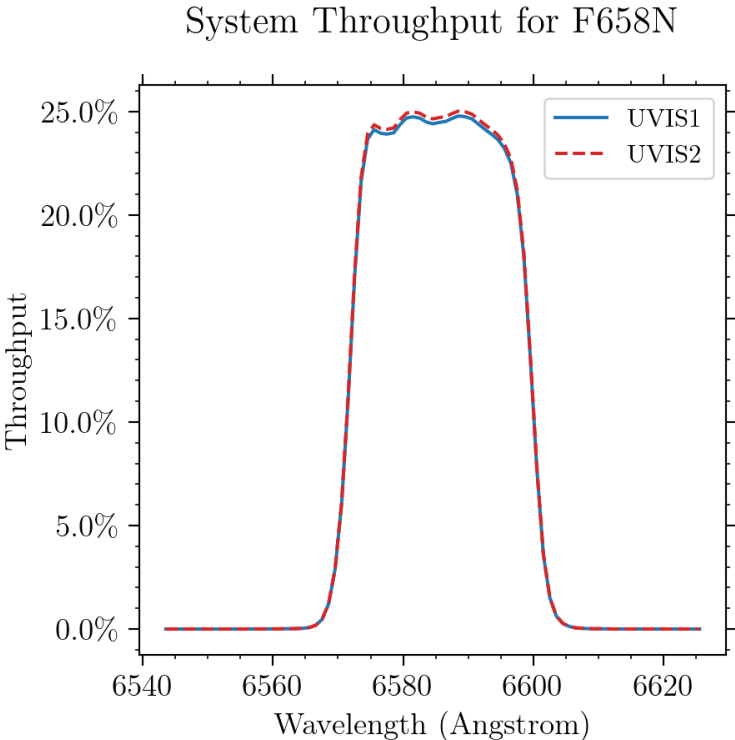
**Figure A.28: Integrated system throughput for F373N.**
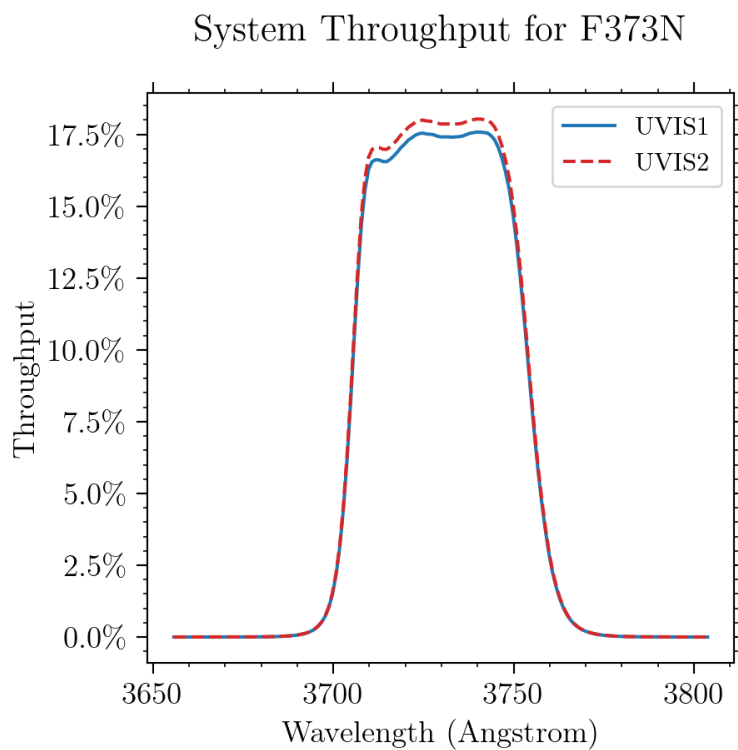
Figure A.29: Point source S/N vs. V+AB$_\nu$ for the F373N. filter, assuming high sky backgrounds and a 5 × 5 pixel aperture.
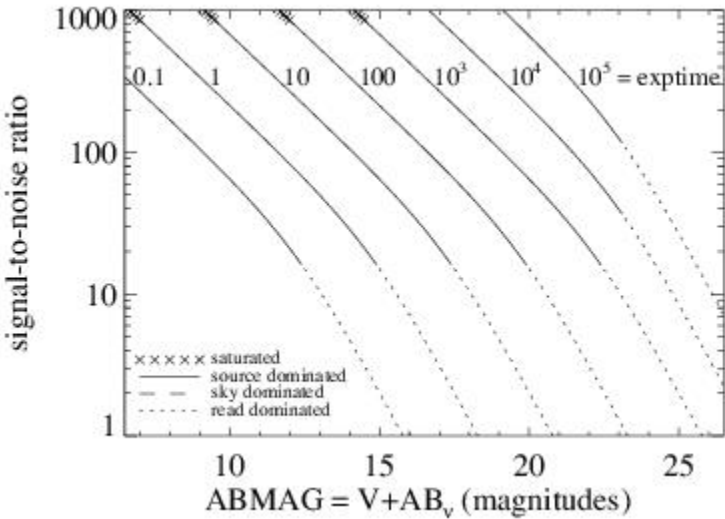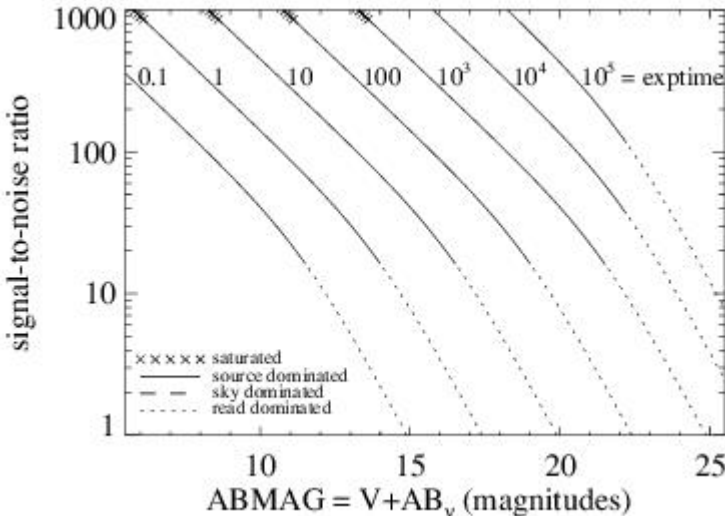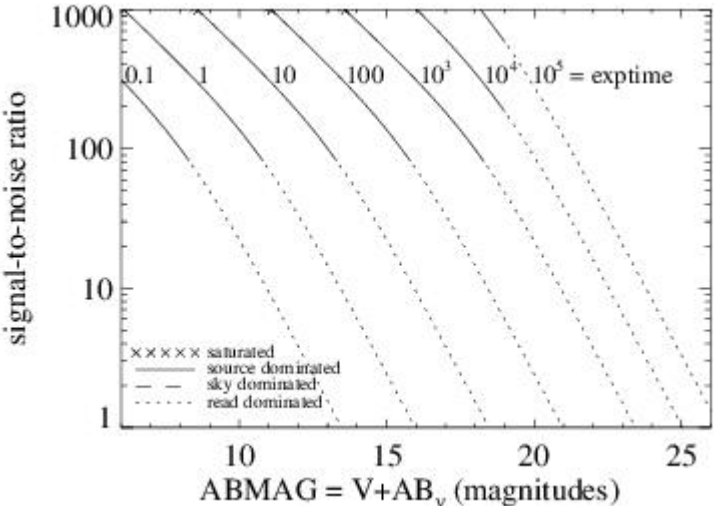
Figure A.30: Extended source S/N vs. V+AB$_\nu$ for the F373N. filter, assuming high sky backgrounds and a source uniformly filling a 1 arcsec$^2$ aperture.
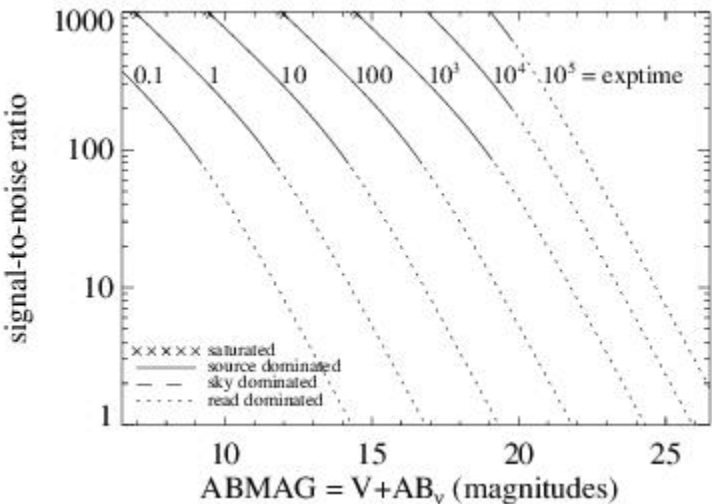
# UVIS F390M

**Description**
Ca II continuum filter.

**Figure A.31: Integrated system throughput for F390M.**



System Throughput for F390M
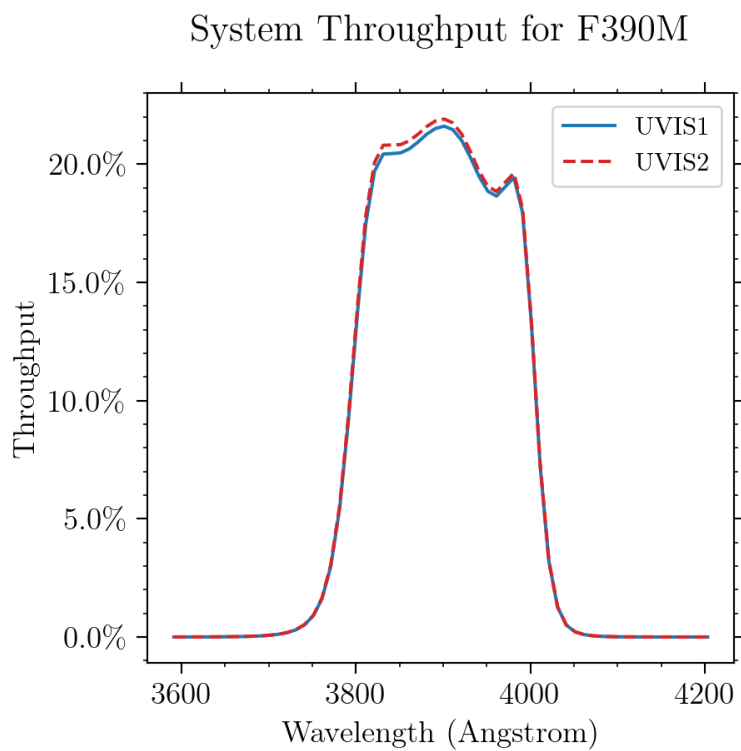
Figure A.32: Point source S/N vs. V+AB$_\nu$ for the F390M filter, assuming high sky backgrounds and a 5 × 5 pixel aperture.
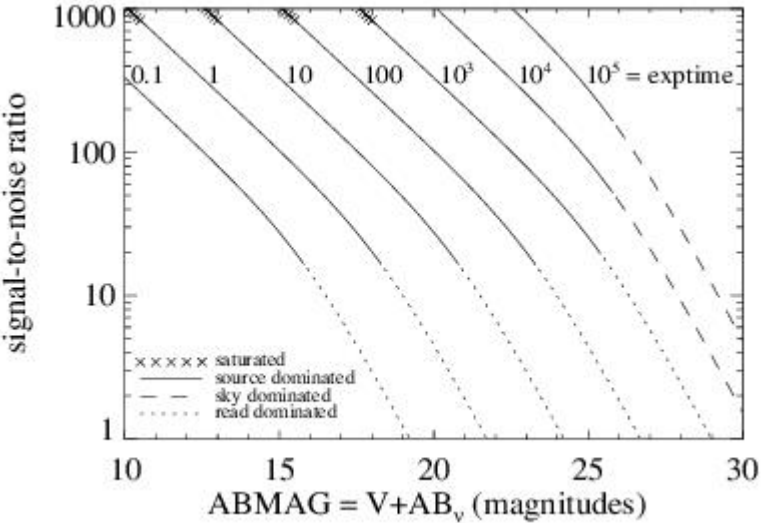
Figure A.33: Extended source S/N vs. V+AB$_\nu$ for the F390M filter, assuming high sky backgrounds and a source uniformly filling a 1 arcsec$^2$ aperture.
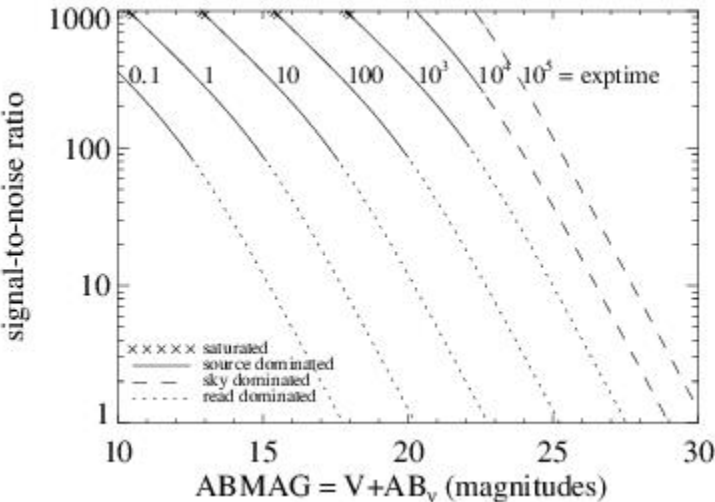
# UVIS F390W

**Description**
Washington *C* filter.

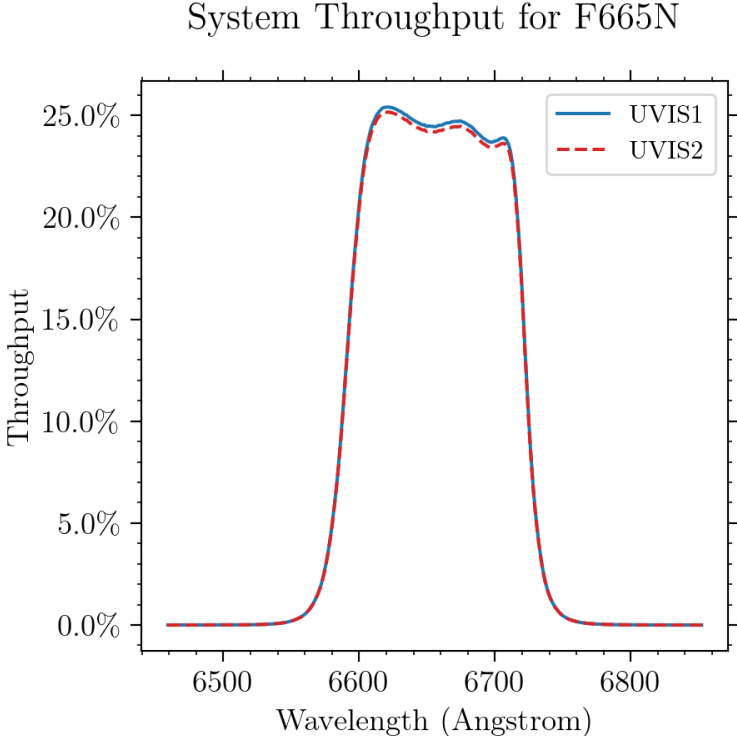**Figure A.34:** Integrated system throughput for F390W.



System Throughput for F390W
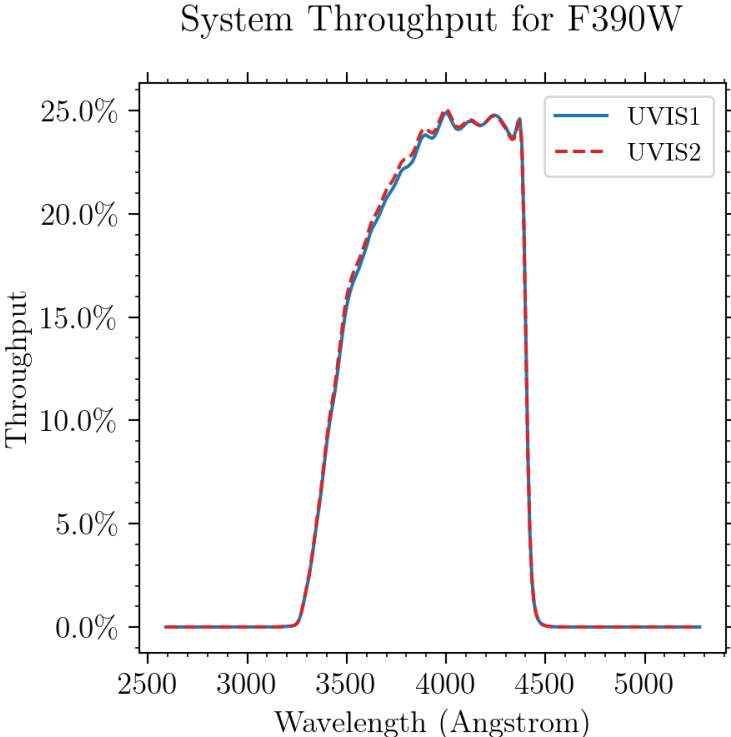
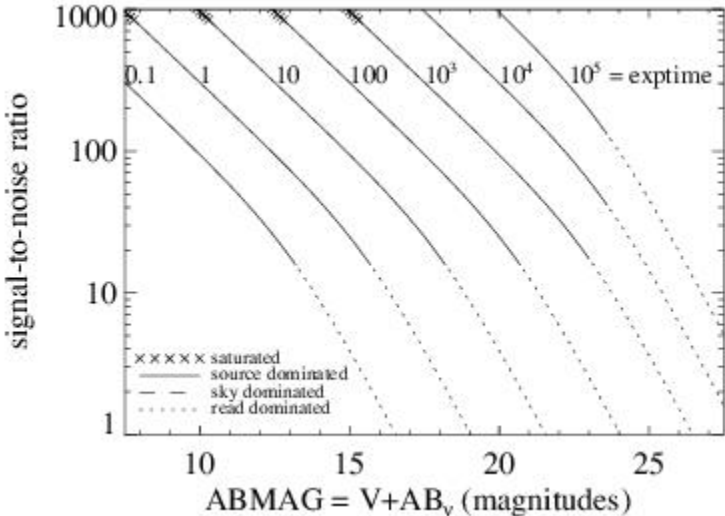Figure A.35: Point source S/N vs. V+AB$_\nu$ for the F390W filter, assuming high sky backgrounds and a 5 × 5 pixel aperture.
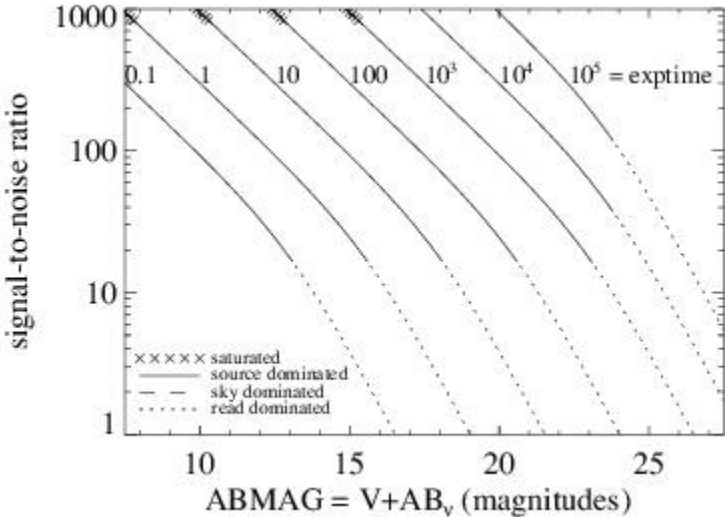
Figure A.36: Extended source S/N vs. V+AB$_\nu$ for the F390W filter, assuming high sky backgrounds and a source uniformly filling a 1 arcsec$^2$ aperture.
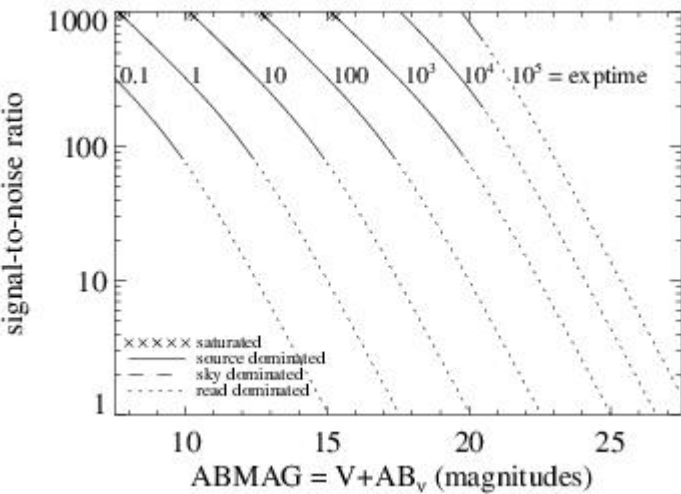
# UVIS F395N

**Description**
Ca II 3933/3968 filter.

**Figure A.37: Integrated system throughput for F395N.**



System Throughput for F395N
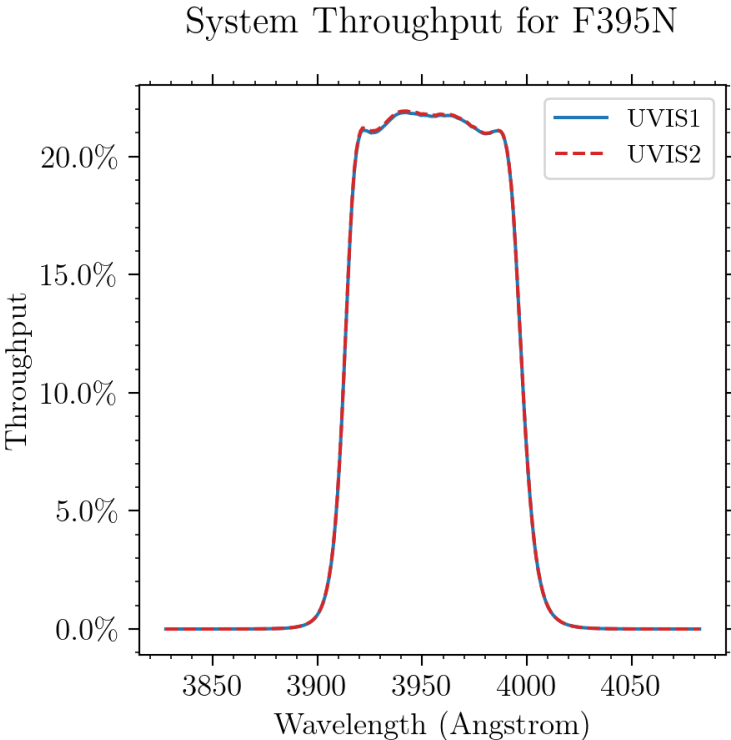
Figure A.38: Point source S/N vs. V+AB$_\nu$ for the F395N filter, assuming high sky backgrounds and a 5 × 5 pixel aperture.
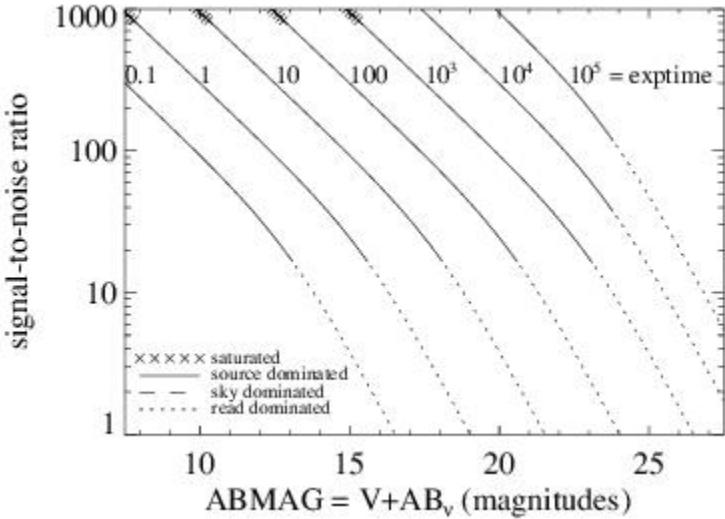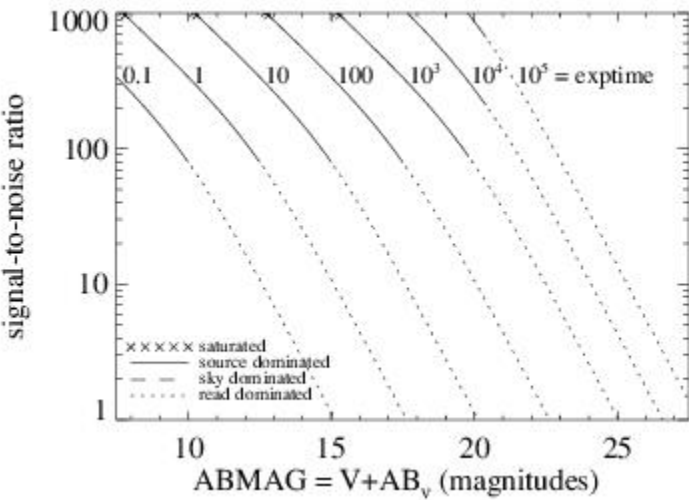
Figure A.39: Extended source S/N vs. V+AB$_\nu$ for the F395N filter, assuming high sky backgrounds and a source uniformly filling a 1 arcsec$^2$ aperture.
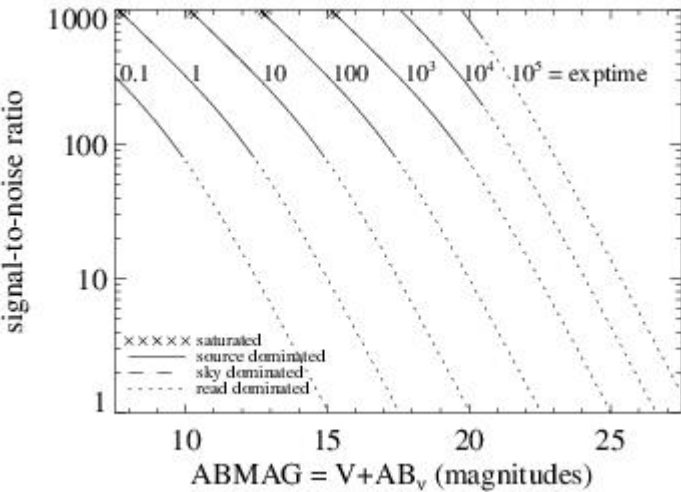
# UVIS F410M

**Description**
Strömgren *v* filter.

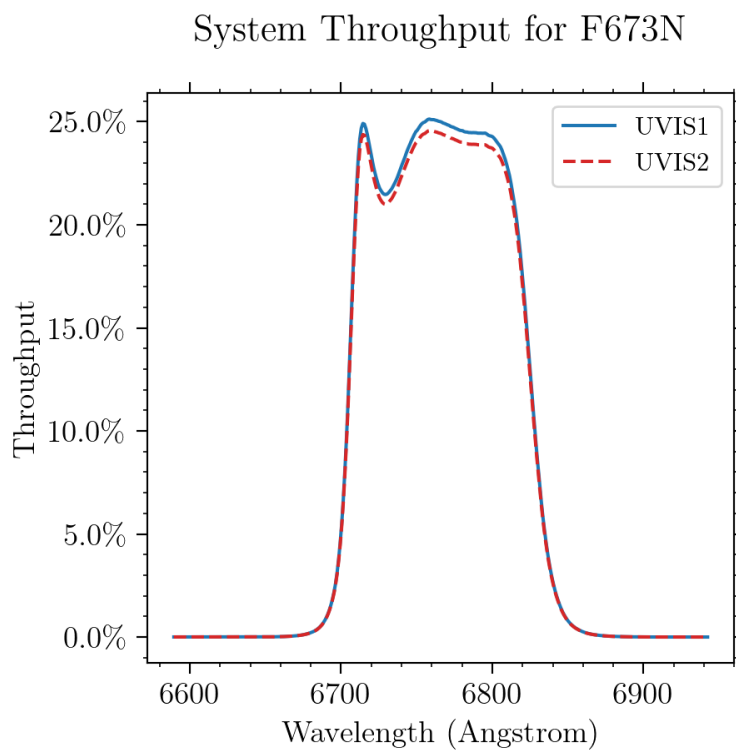**Figure A.40: Integrated system throughput for F410M.**



System Throughput for F410M
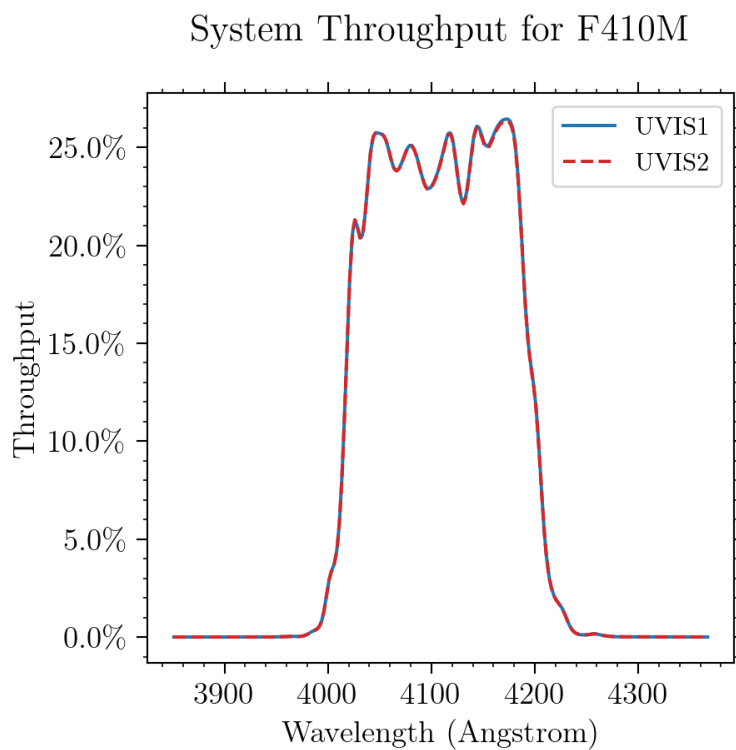
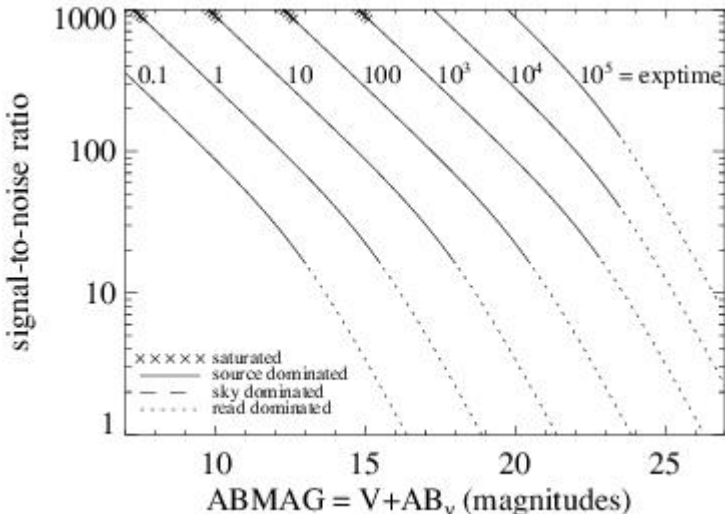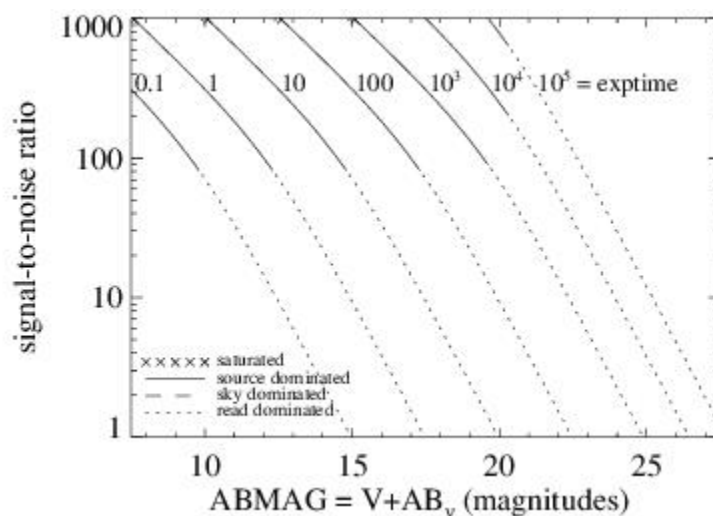Figure A.41: Point source S/N vs. V+AB$_\nu$ for the F410M filter, assuming high sky backgrounds and a 5 × 5 pixel aperture.
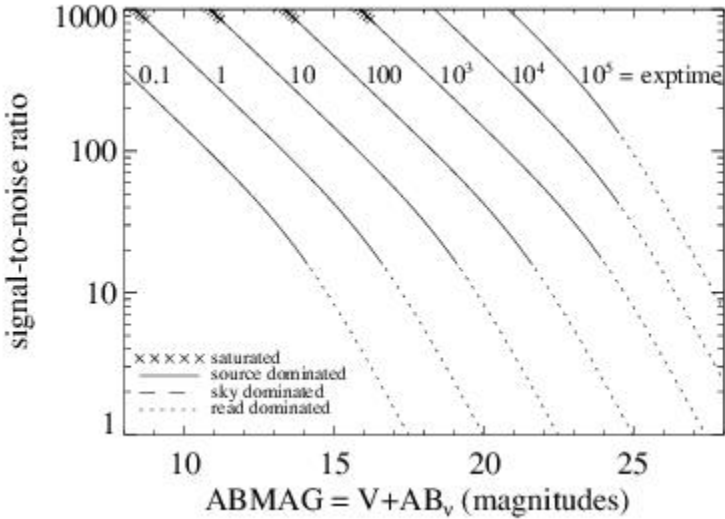
Figure A.42: Extended source S/N vs. V+AB$_\nu$ for the F410M filter, assuming high sky backgrounds and a source uniformly filling a 1 arcsec$^2$ aperture.
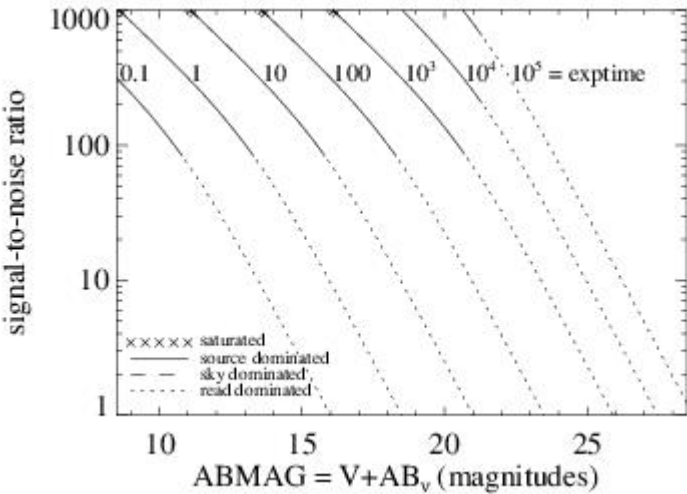
# UVIS F438W

**Description**
WFPC2 *B* filter.

**Figure A.43: Integrated system throughput for F438W.**



System Throughput for F438W
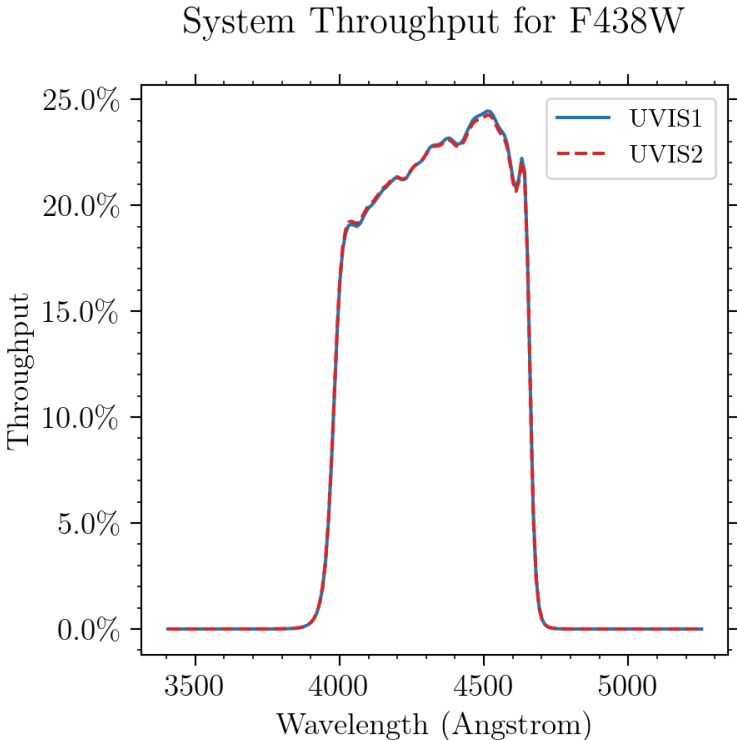
**Figure A.44:** Point source S/N vs. V+AB$_\nu$ for the F438W filter, assuming high sky backgrounds and a 5 × 5 pixel aperture.
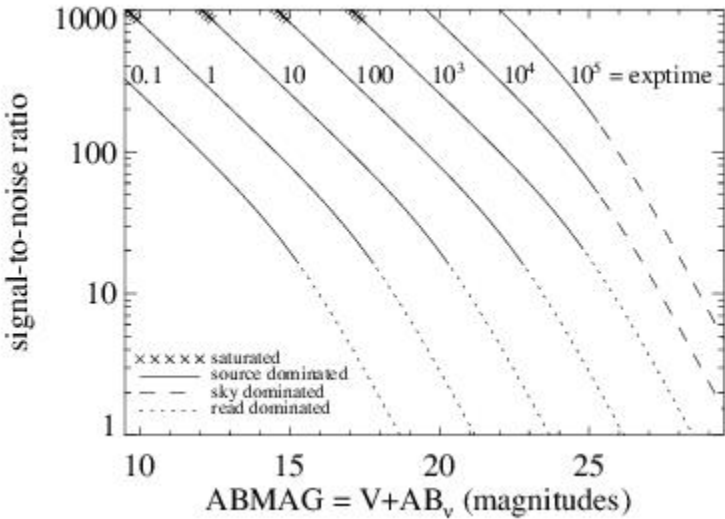
**Figure A.45:** Extended source S/N vs. V+AB$_\nu$ for the F438W filter, assuming high sky backgrounds and a source uniformly filling a 1 arcsec$^2$ aperture.
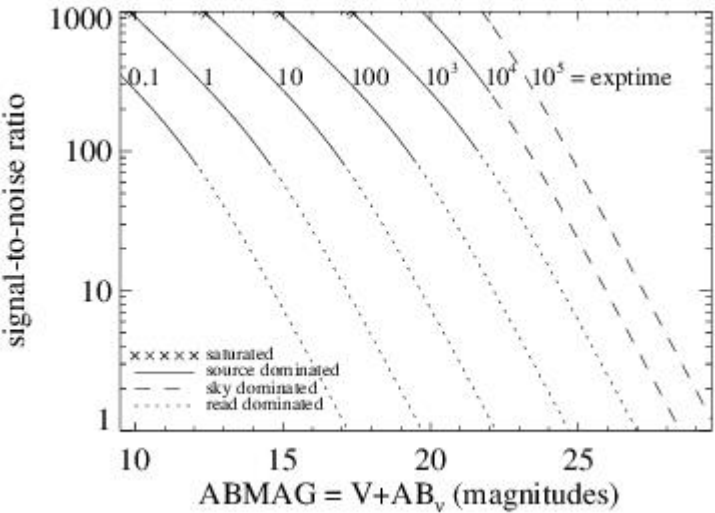
# UVIS F467M

**Description**
Strömgren *b* filter.

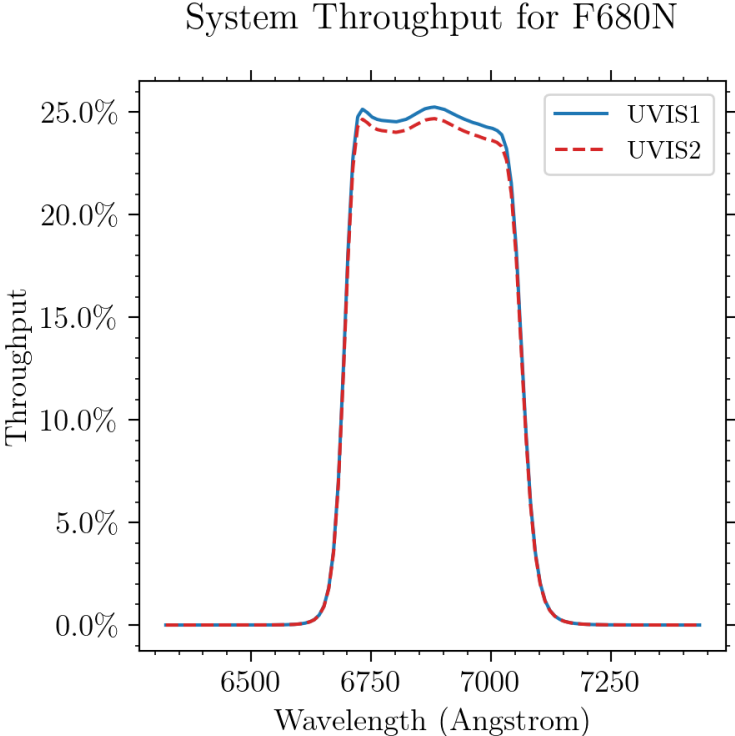**Figure A.46:** Integrated system throughput for F467M.



System Throughput for F467M
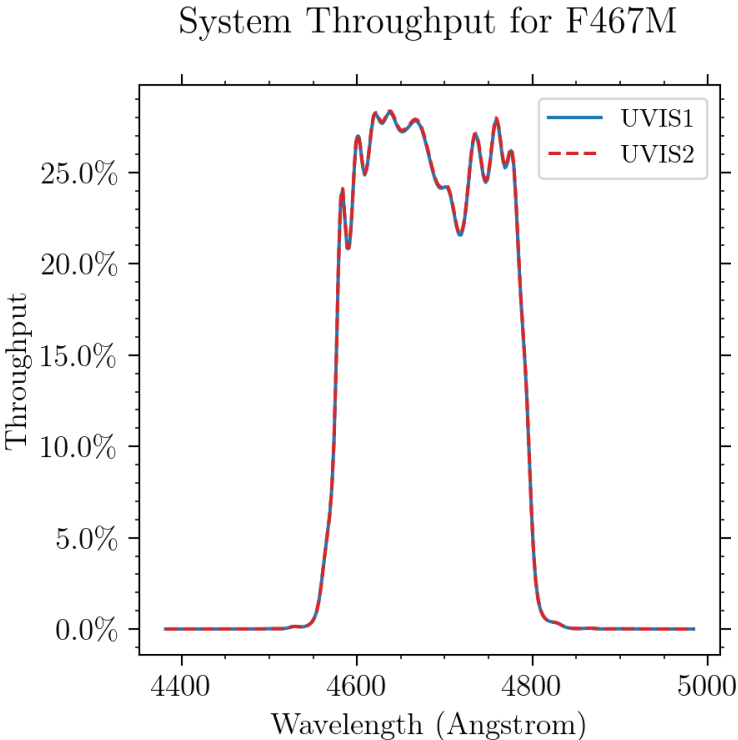
**Figure A.47:** Point Source S/N vs. V+AB$_\nu$ for the F467M filter, assuming high sky backgrounds and a 5 × 5 pixel aperture.
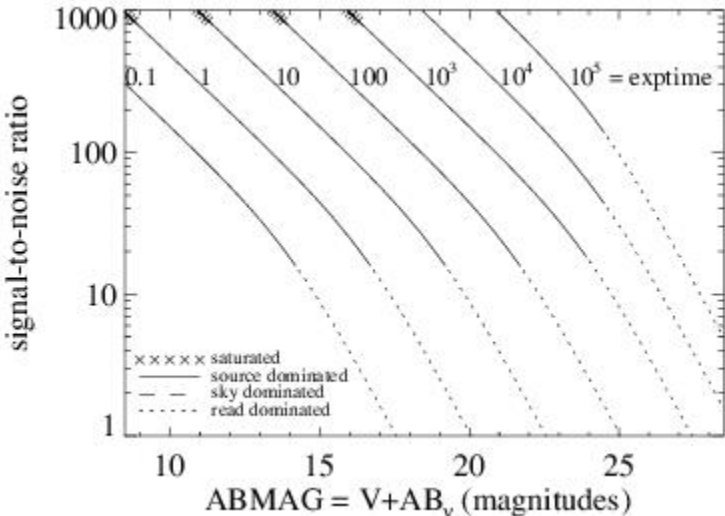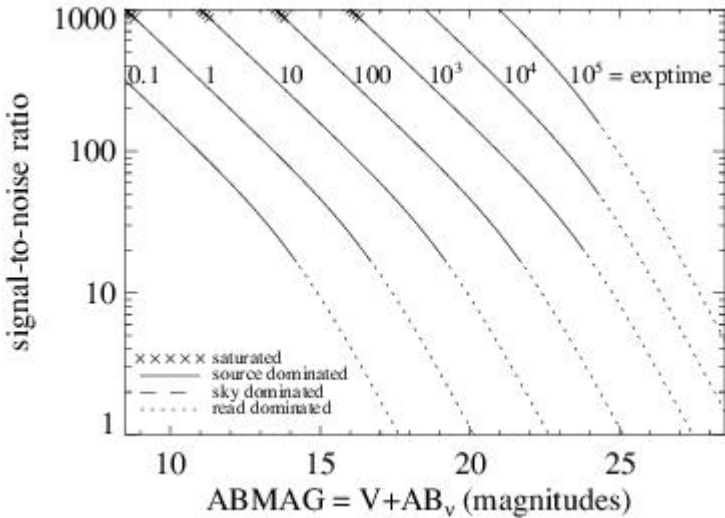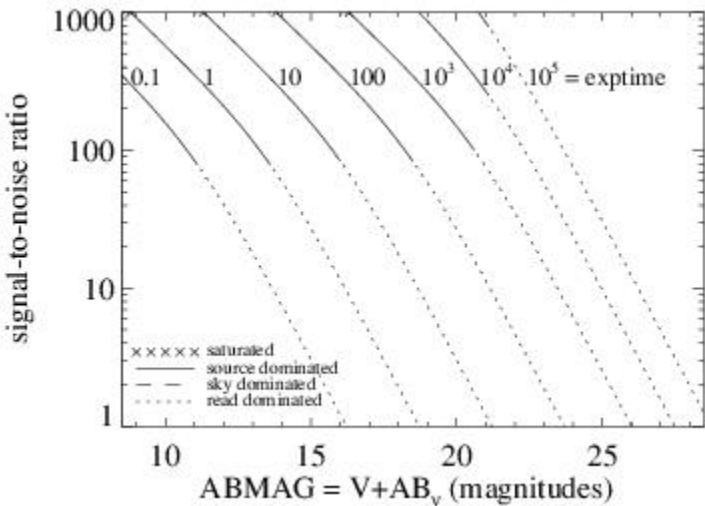
Figure A.48: Extended Source S/N vs. V+AB$_\nu$ for the F467M filter, assuming high sky backgrounds and a source uniformly filling a 1 arcsec$^2$ aperture.
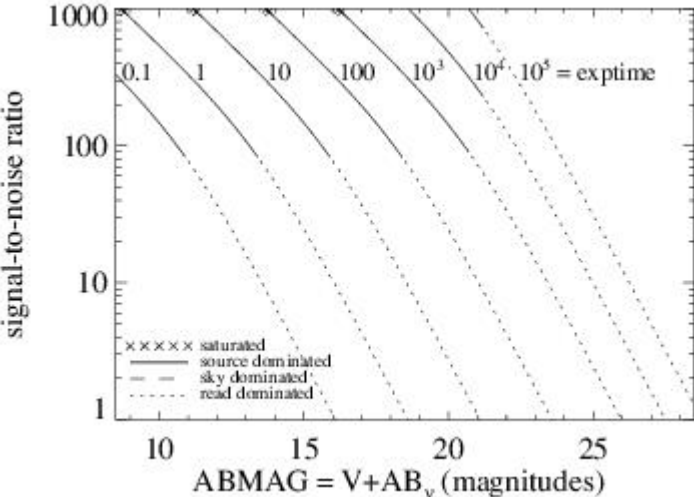
# UVIS F469N

**Description**
He II 4686 filter.

**Figure A.49: Integrated system throughput for F469N.**



System Throughput for F469N
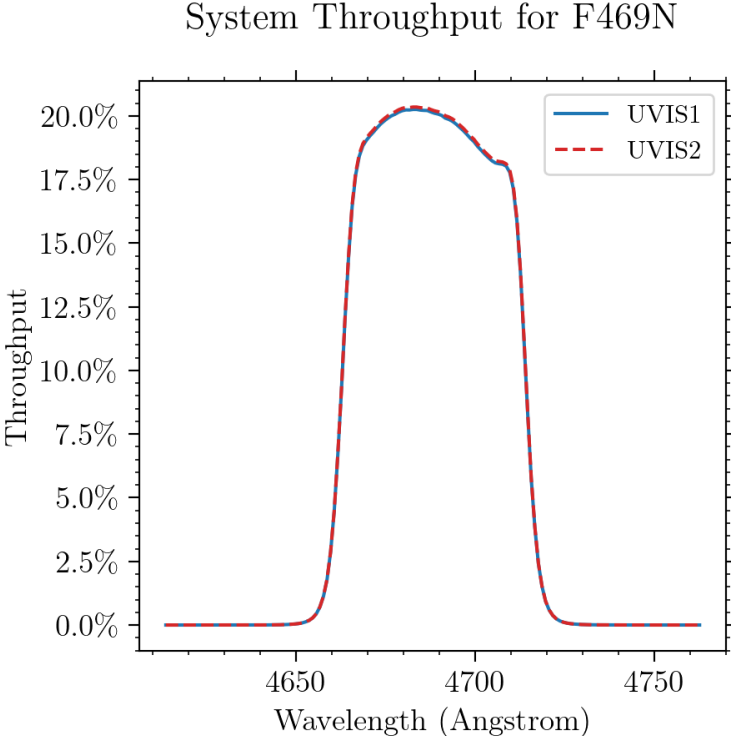
**Figure A.50: Point source S/N vs. V+AB$_\nu$ for the F469N filter, assuming high sky backgrounds and a 5 × 5 pixel aperture.**
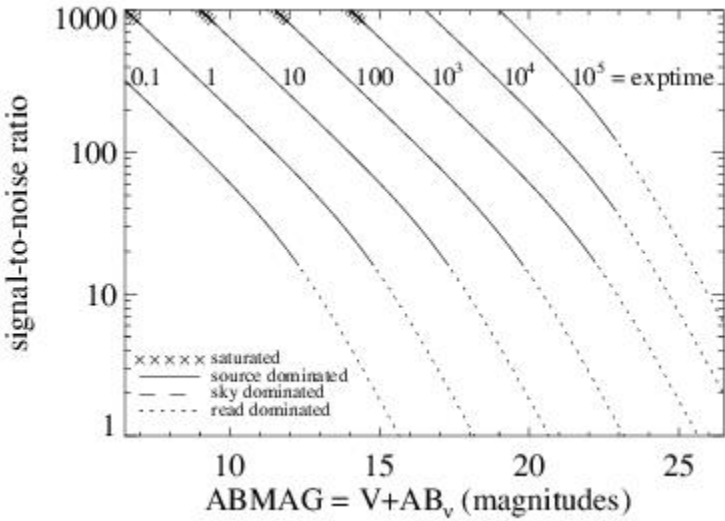
Figure A.51: Extended source S/N vs. V+AB$_\nu$ for the F469N filter, assuming high sky backgrounds and a source uniformly filling a 1 arcsec$^2$ aperture.
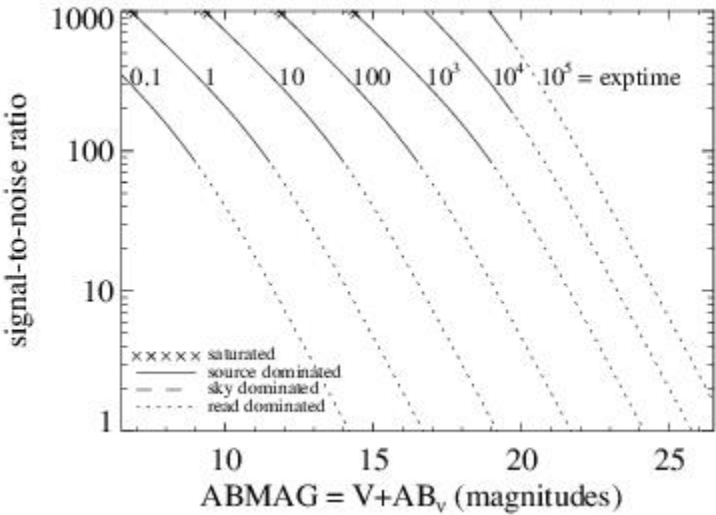
# UVIS F475W

**Description**
Sloan Digital Sky Survey $g'$ filter.

**Figure A.52: Integrated system throughput for F475W.**



System Throughput for F475W
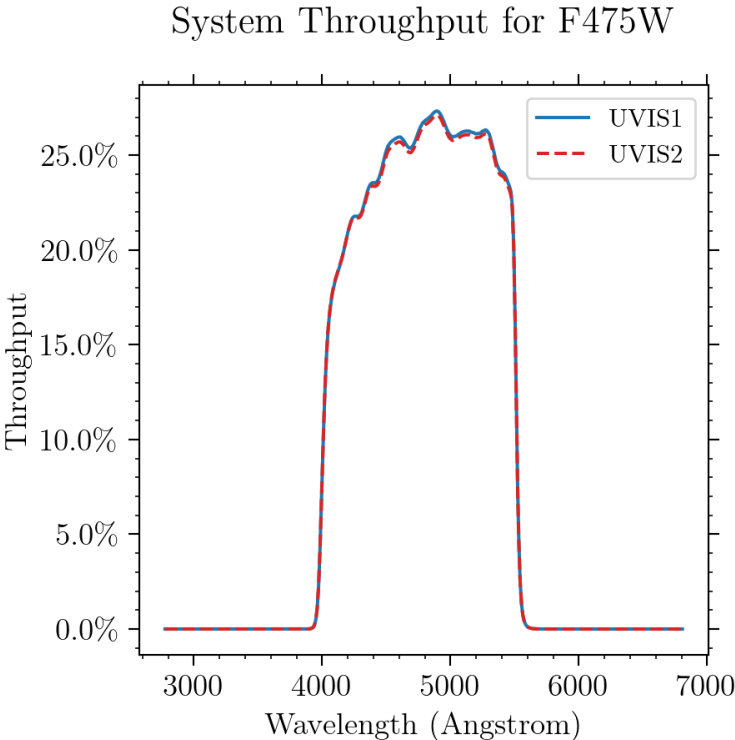
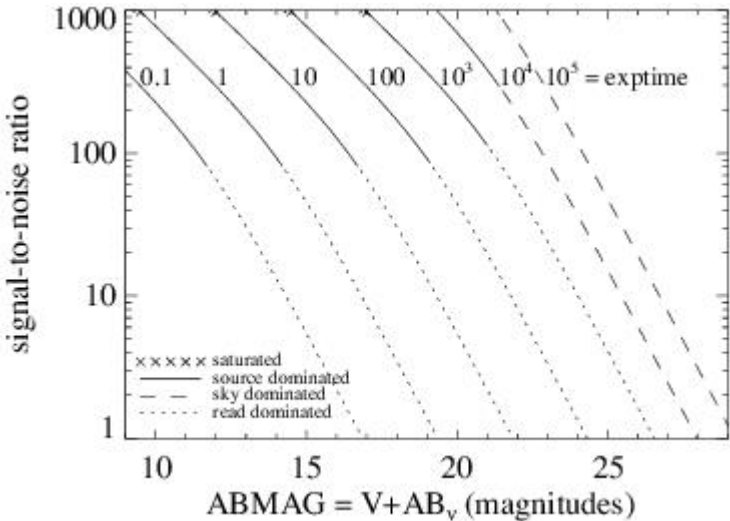**Figure A.53:** Point source S/N vs. V+AB$_\nu$ for the F475W filter, assuming high sky backgrounds and a 5 × 5 pixel aperture.
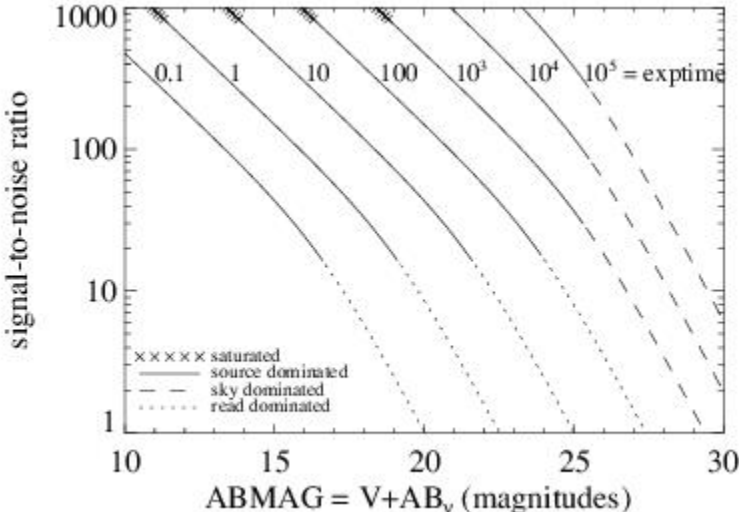
Figure A.54: Extended source S/N vs. V+AB$_\nu$ for the F475W filter, assuming high sky backgrounds and a source uniformly filling a 1 arcsec$^2$ aperture.
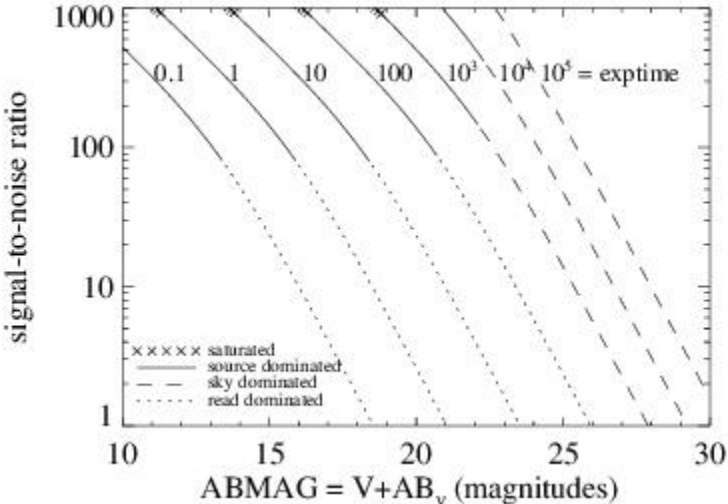
# UVIS F475X

**Description**
Extremely wide blue filter.

**Figure A.55: Integrated system throughput for F475X.**



System Throughput for F475X
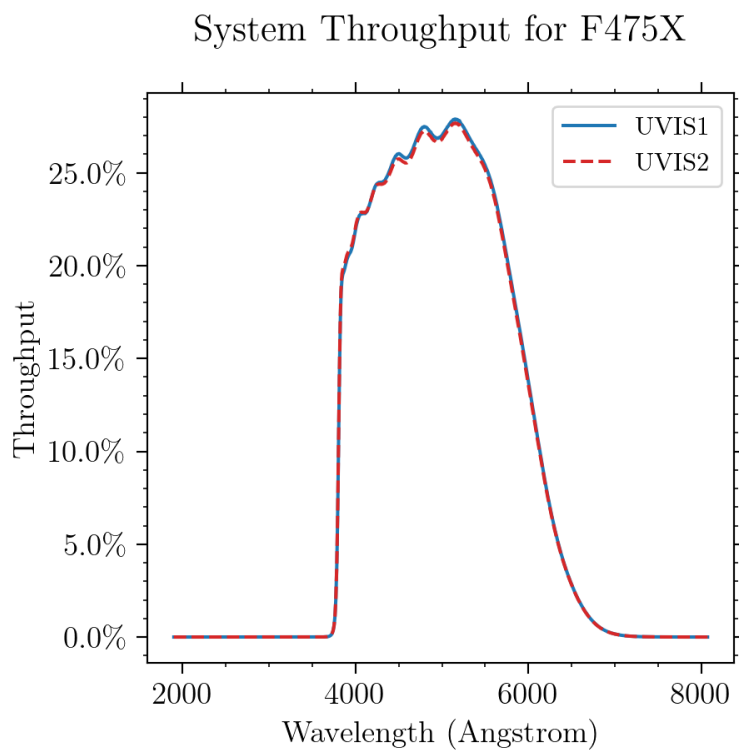
Figure A.56: Point source S/N vs. V+AB$_\nu$ for the F475X filter, assuming high sky backgrounds and a 5 × 5 pixel aperture.
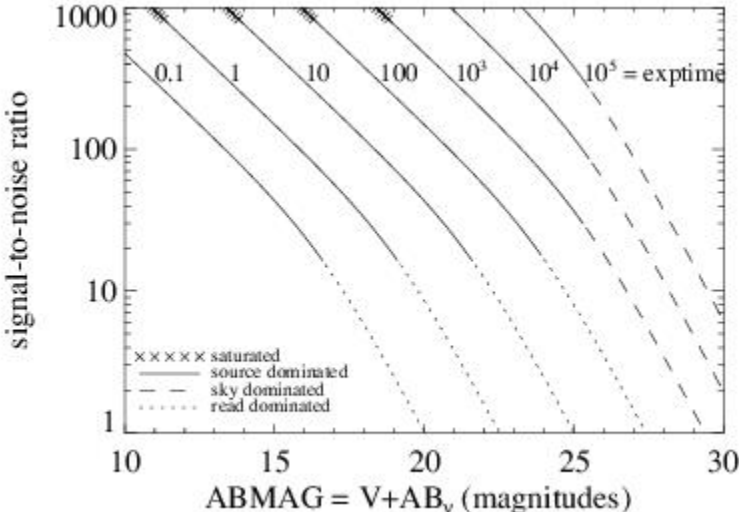
Figure A.57: Extended source S/N vs. V+AB$_\nu$ for the F475X filter, assuming high sky backgrounds and a source uniformly filling a 1 arcsec$^2$ aperture.
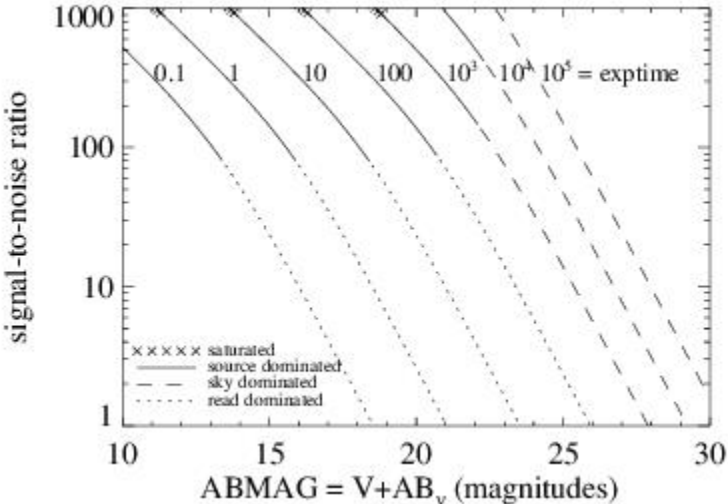
# UVIS F487N

**Description**
Hβ 4861 filter.

**Figure A.58: Integrated system throughput for F487N.**



System Throughput for F487N
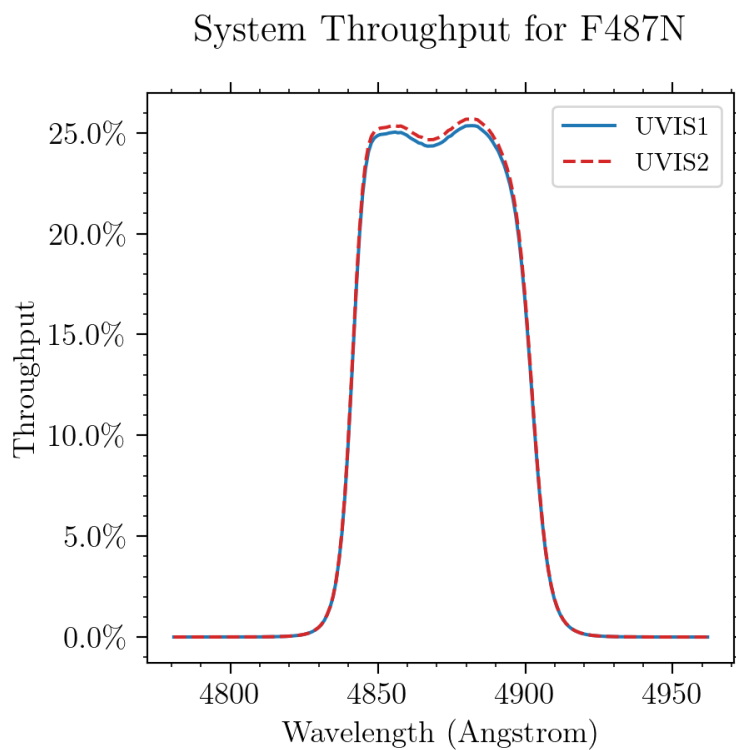
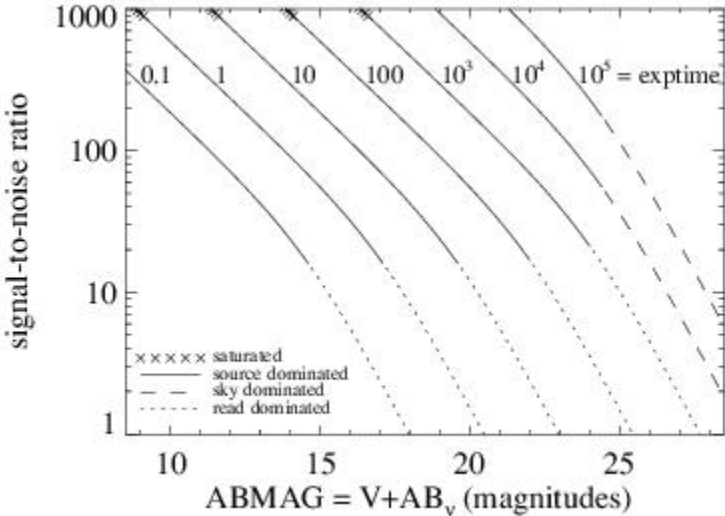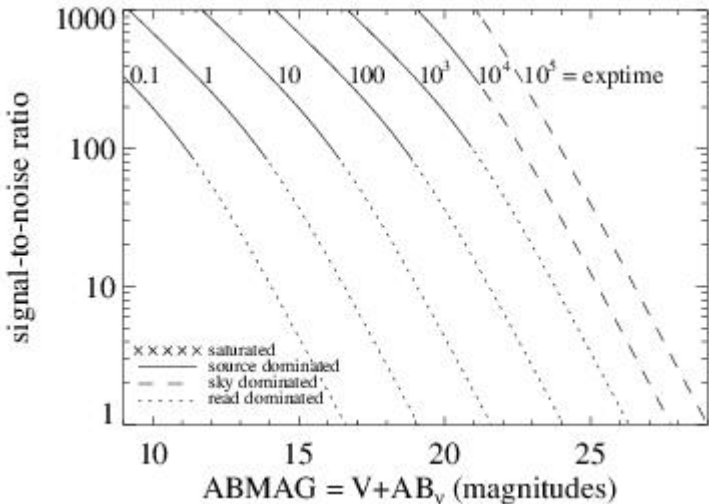Figure A.59: Point source S/N vs. V+AB$_\nu$ for the F487N filter, assuming high sky backgrounds and a 5 × 5 pixel aperture.
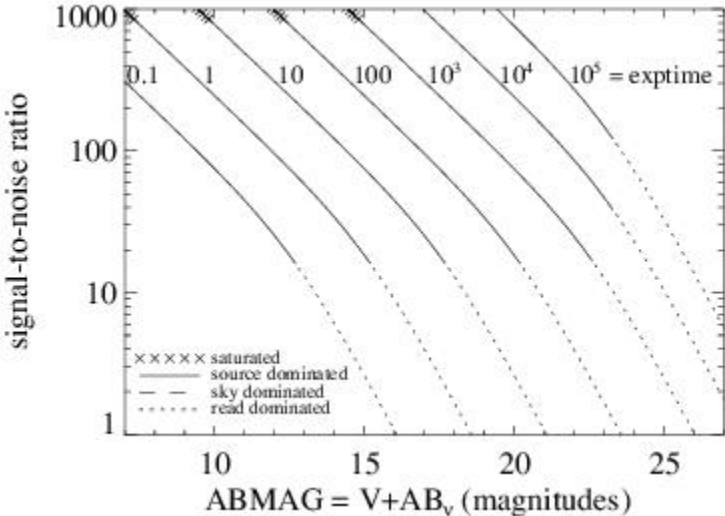
Figure A.60: Extended source S/N vs. V+AB$_{\nu}$ for the F487N filter, assuming high sky backgrounds and a source uniformly filling a 1 arcsec$^2$ aperture.
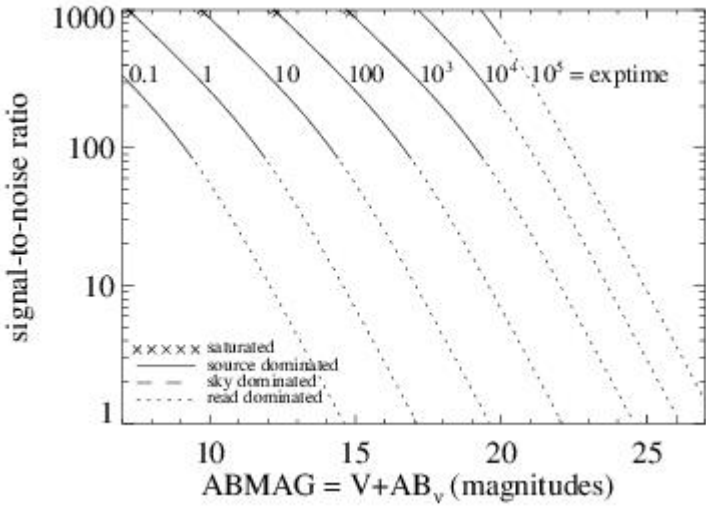
# UVIS F502N

**Description**
[O ɪɪɪ] 5007 filter.

**Figure A.61: Integrated system throughput for F502N.**



System Throughput for F502N
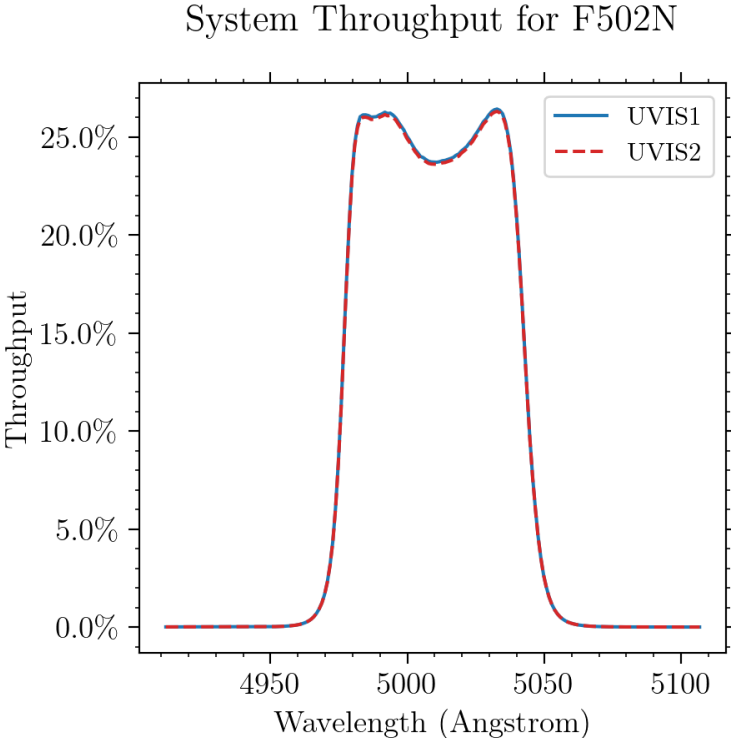
Figure A.62: Point source S/N vs. V+AB$_\nu$ for the F502N filter, assuming high sky backgrounds and a 5 × 5 pixel aperture.
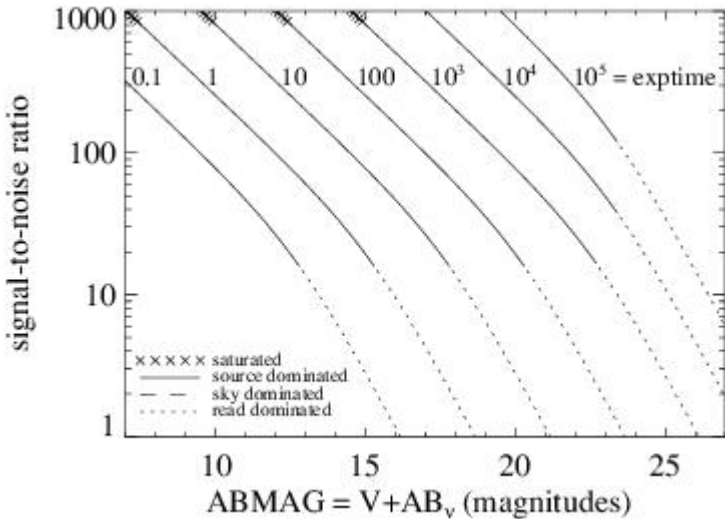
Figure A.63: Extended source S/N vs. V+AB$_\nu$ for the F502N filter, assuming high sky backgrounds and a source uniformly filling a 1 arcsec$^2$ aperture.
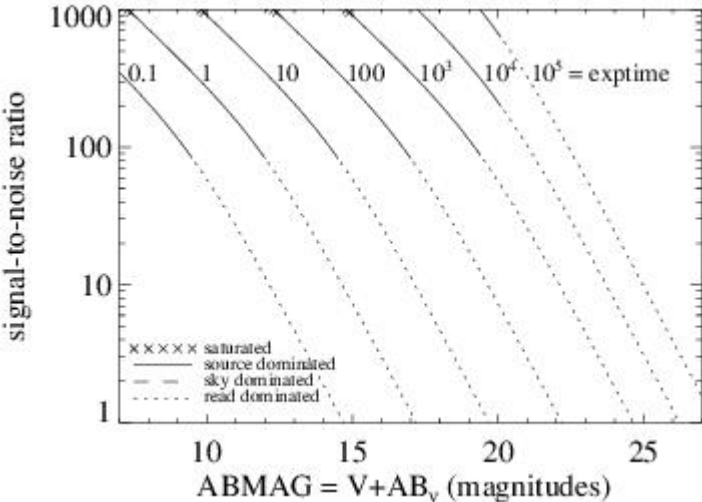
# UVIS F547M

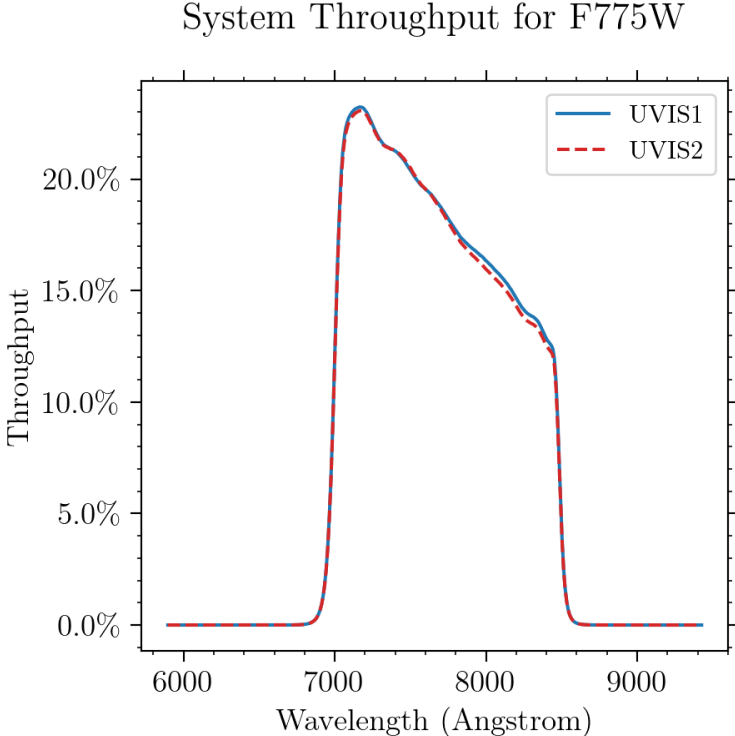**Description**
Strömgren *y* filter.

# System Throughput for F547M
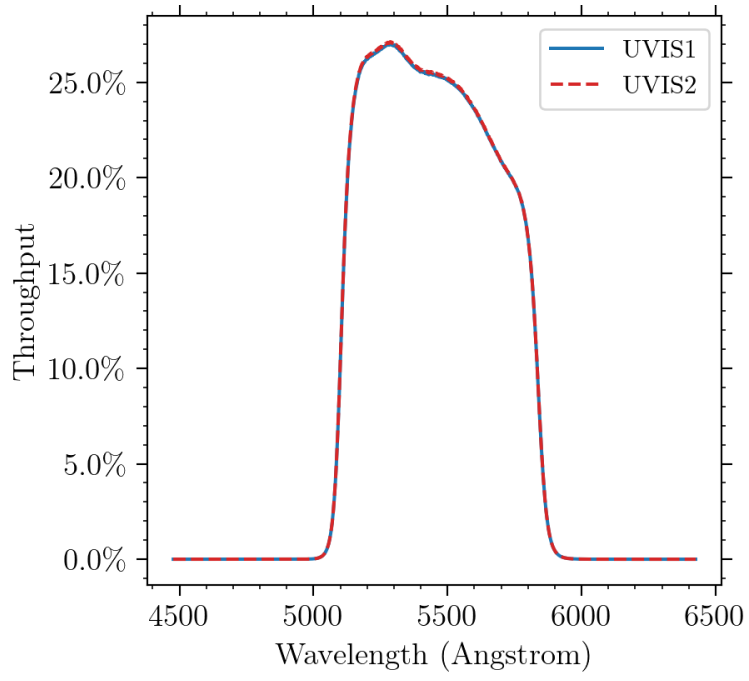
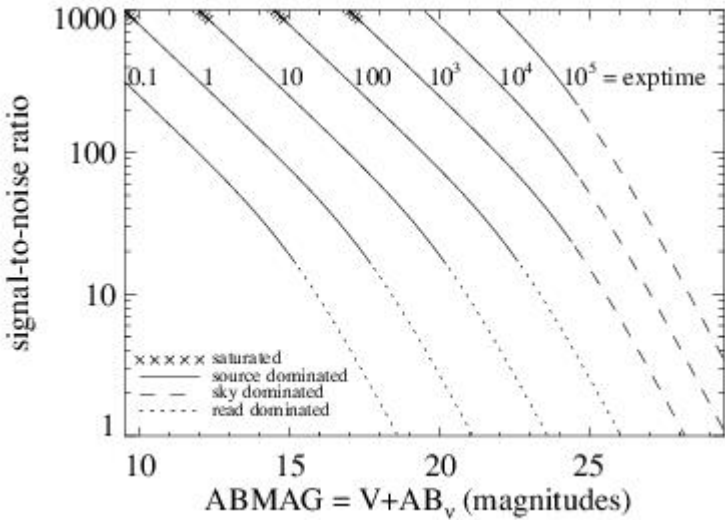Figure A.65: Point source S/N vs. V+AB$_\nu$ for the F547M filter, assuming high sky backgrounds and a 5 × 5 pixel aperture.
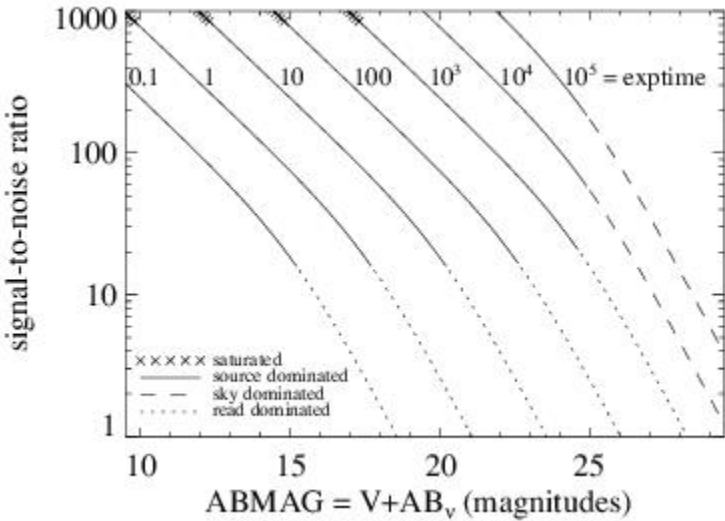
Figure A.66: Extended source S/N vs. V+AB$_\nu$ for the F547M filter, assuming high sky backgrounds and a source uniformly filling a 1 arcsec$^2$ aperture.
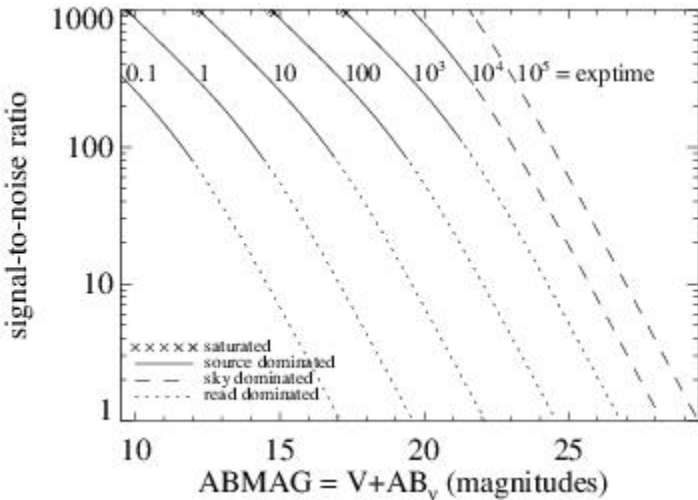
# UVIS F555W

**Description**
WFPC2 *V* filter.

**Figure A.67: Integrated system throughput for F555W.**



System Throughput for F555W
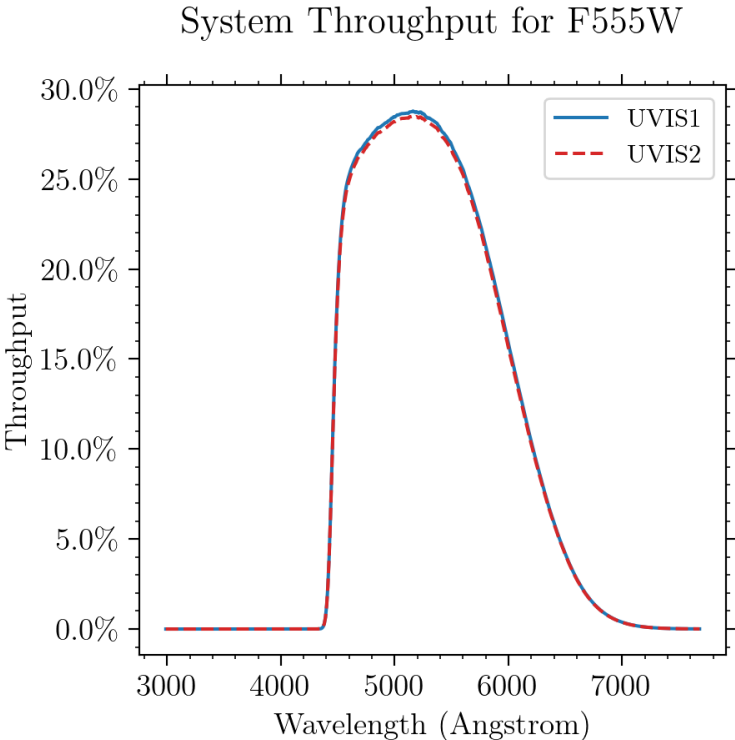
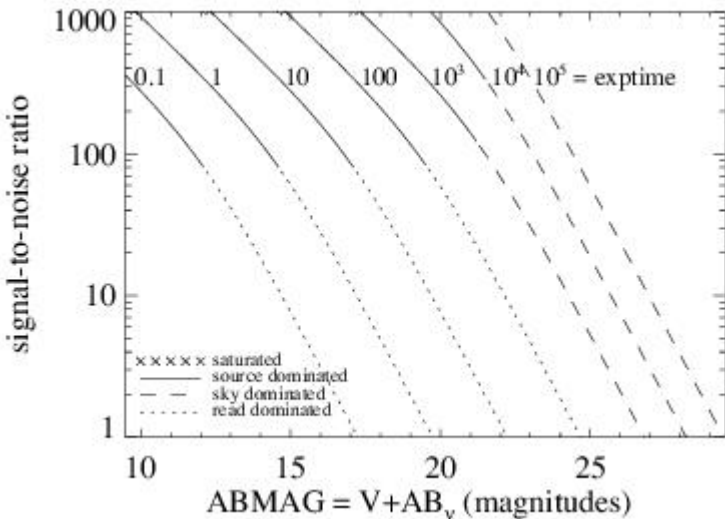Figure A.68: Point source S/N vs. V+AB$_\nu$ for the F555W filter, assuming high sky backgrounds and a 5 × 5 pixel aperture.
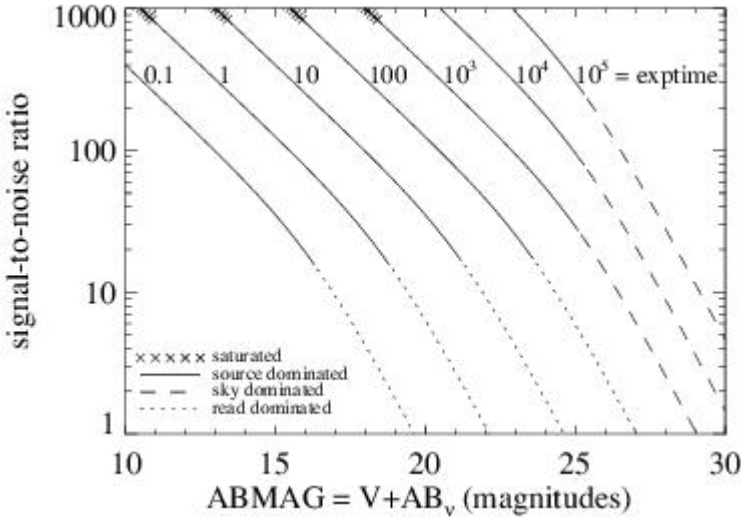
Figure A.69: Extended source S/N vs. V+AB$_\nu$ for the F555W filter, assuming high sky backgrounds and a source uniformly filling a 1 arcsec$^2$ aperture.
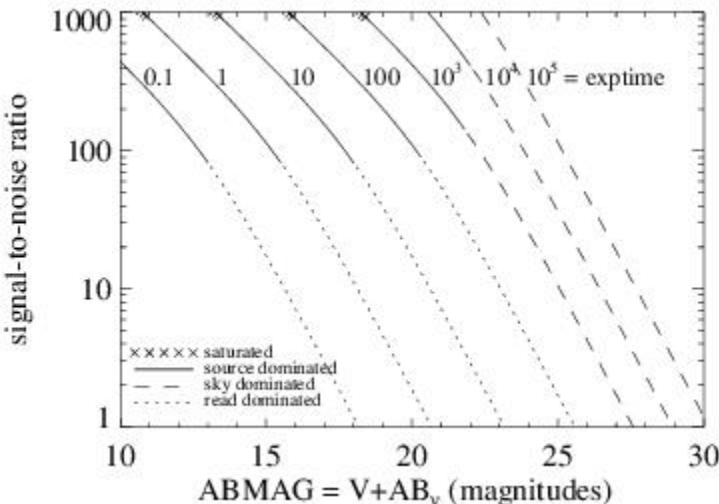
# UVIS F600LP

**Description**
Long-pass filter.

**Figure A.70: Integrated system throughput for F600LP.**
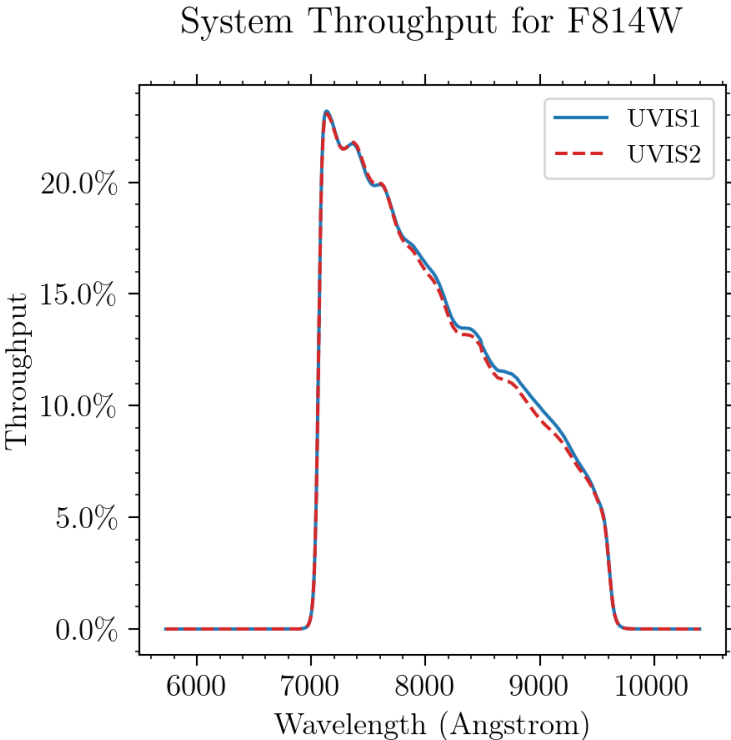


System Throughput for F600LP
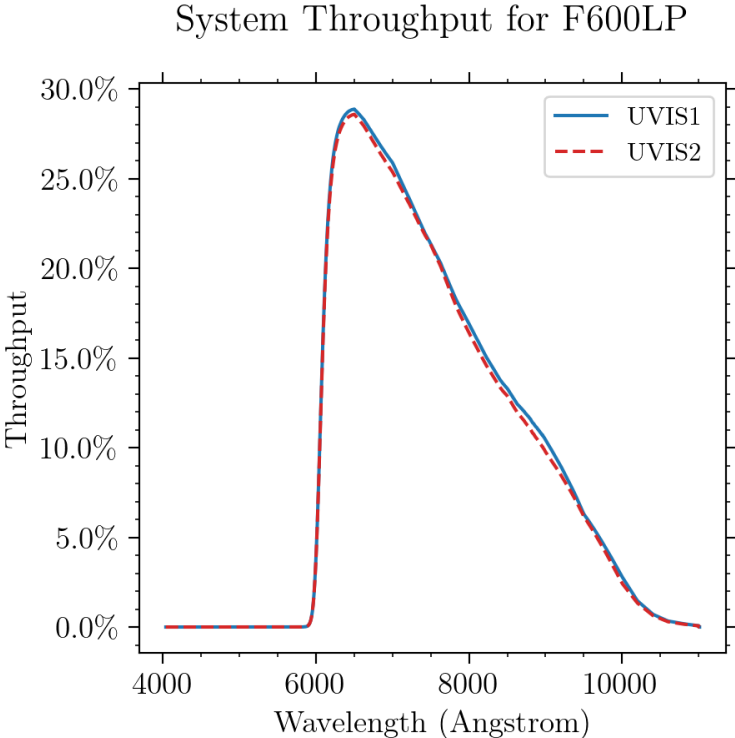
**Figure A.71:** Point source S/N vs. V+AB$_\nu$ for the F600LP filter, assuming high sky backgrounds and a 5 × 5 pixel aperture.
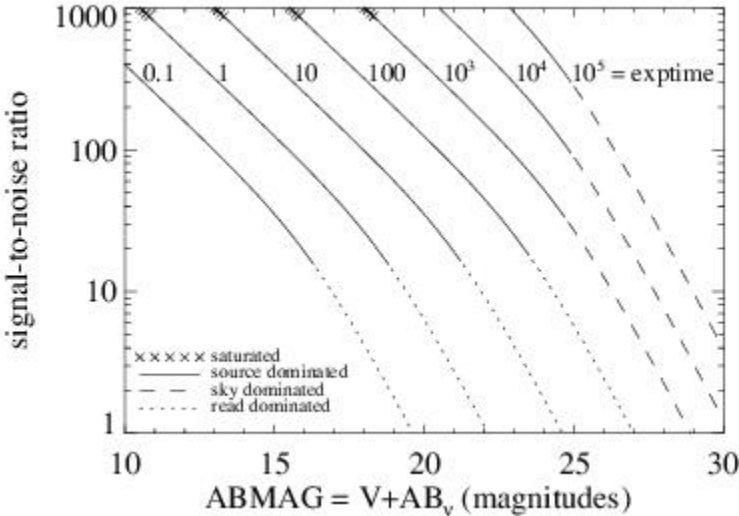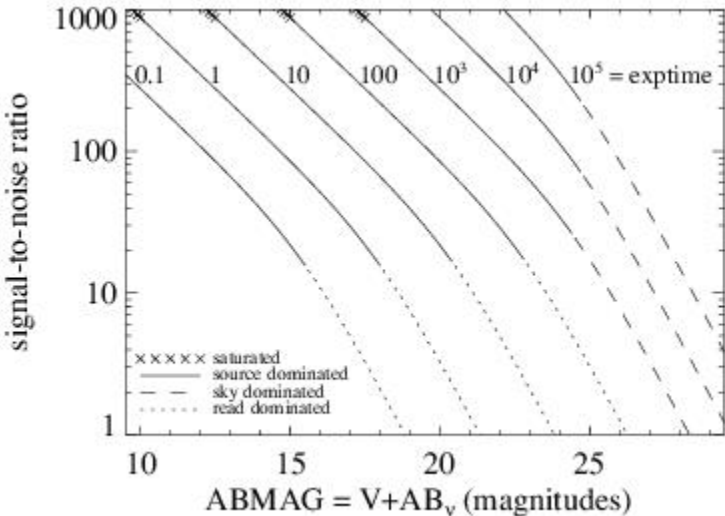
Figure A.72: Extended source S/N vs. V+AB$_\nu$ for the F600LP filter, assuming high sky backgrounds and a source uniformly filling a 1 arcsec$^2$ aperture.
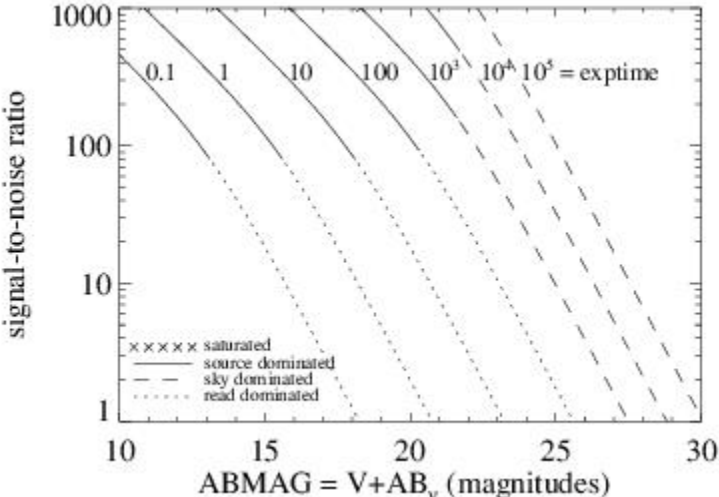
# UVIS F606W

**Description**
WFPC2 Wide *V* filter.

**Figure A.73: Integrated system throughput for F606W.**
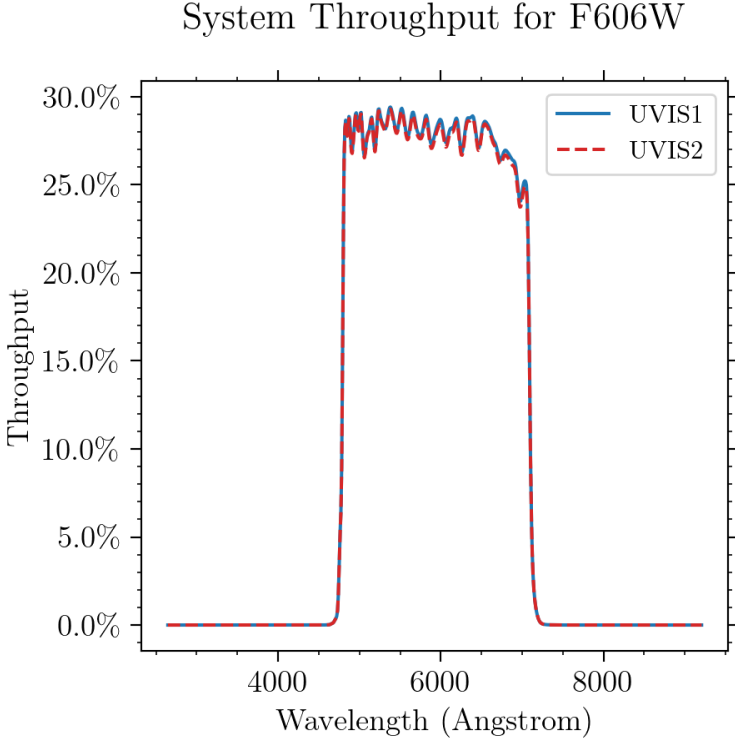
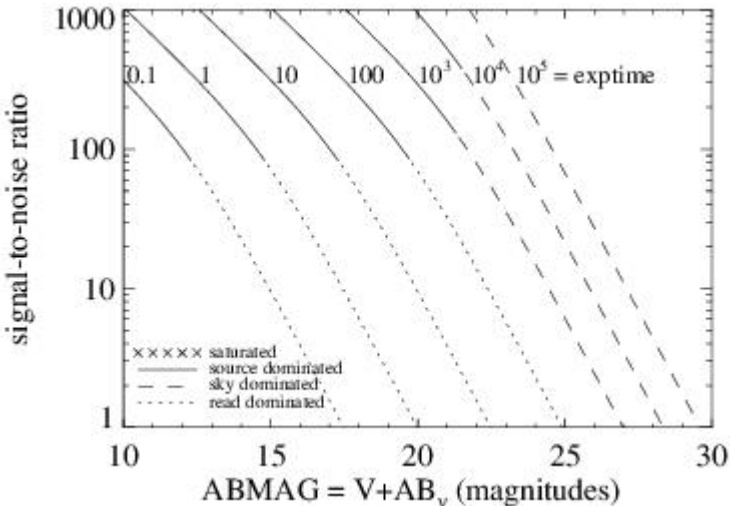Figure A.74: Point source S/N vs. V+AB$_\nu$ for the F606W filter, assuming high sky backgrounds and a 5 × 5 pixel aperture.
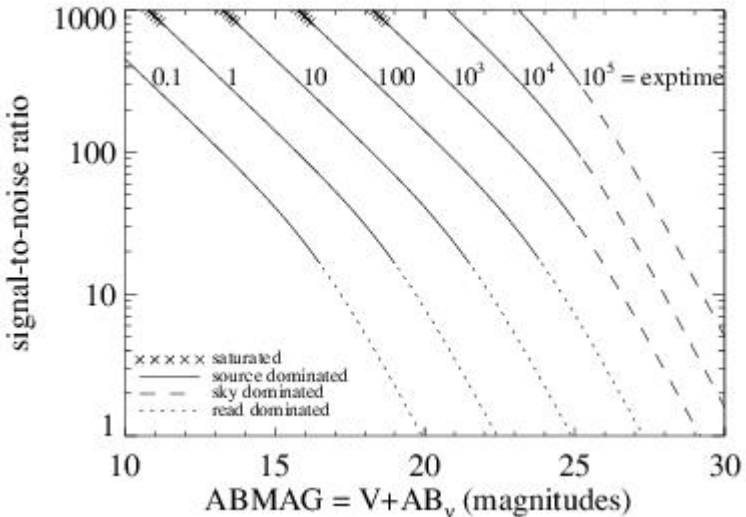
Figure A.75: Extended source S/N vs. V+AB$_\nu$ for the F606W filter, assuming high sky backgrounds and a source uniformly filling a 1 arcsec$^2$ aperture.
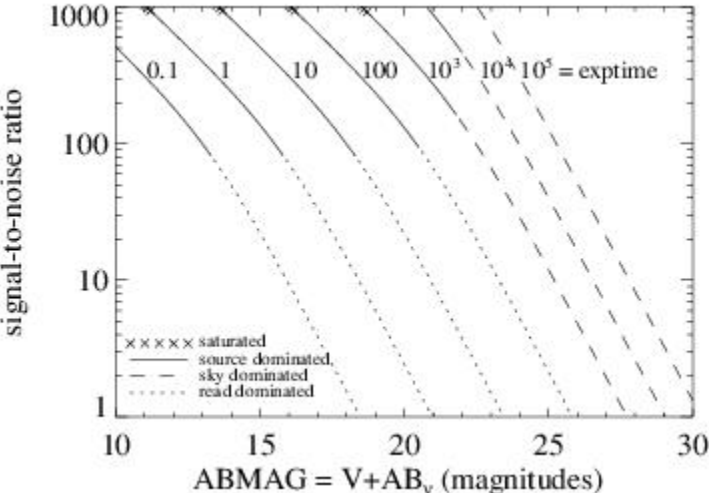
# UVIS F621M

**Description**
11% passband filter.

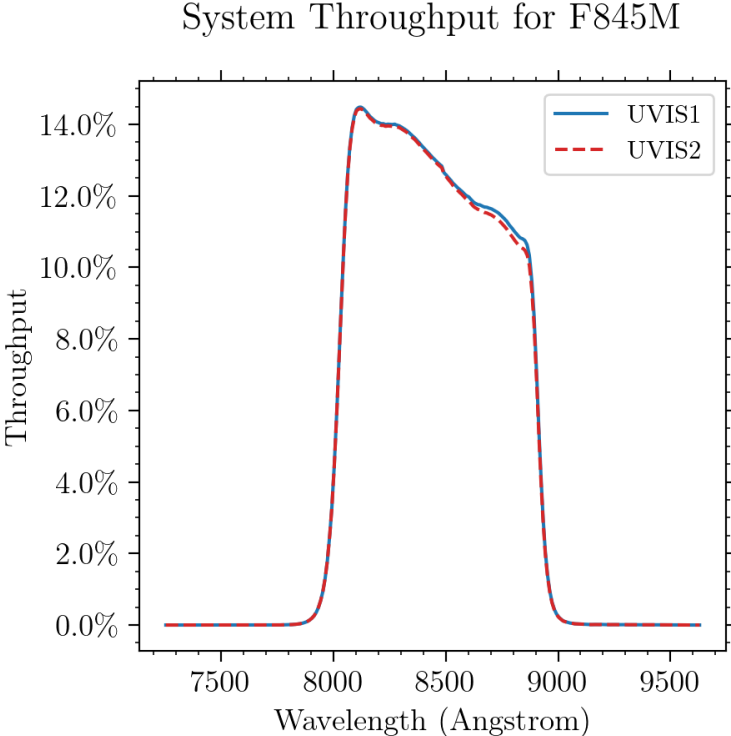**Figure A.76: Integrated system throughput for F621M.**



System Throughput for F621M
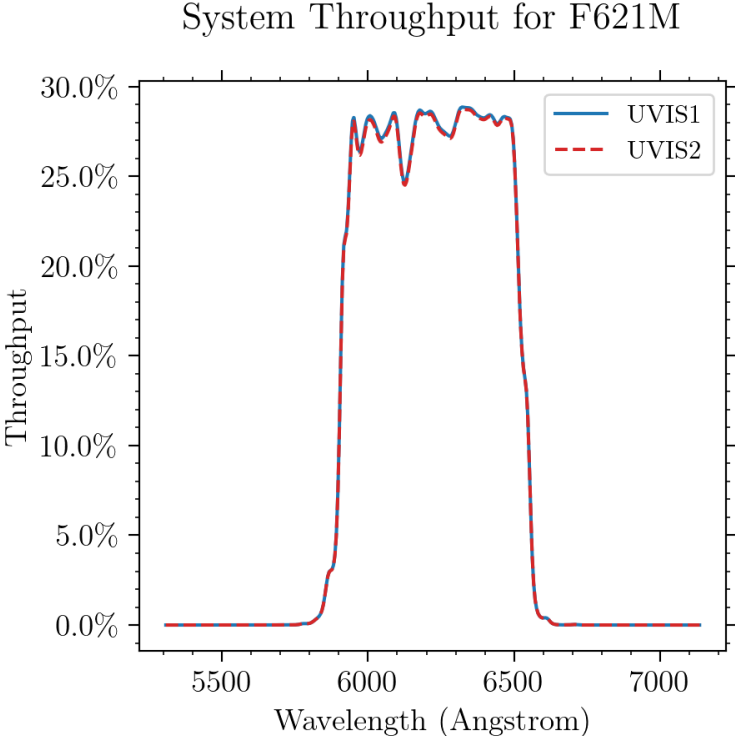
Figure A.77: Point source S/N vs. V+AB$_\nu$ for the F621M filter, assuming high sky backgrounds and a 5 × 5 pixel aperture.
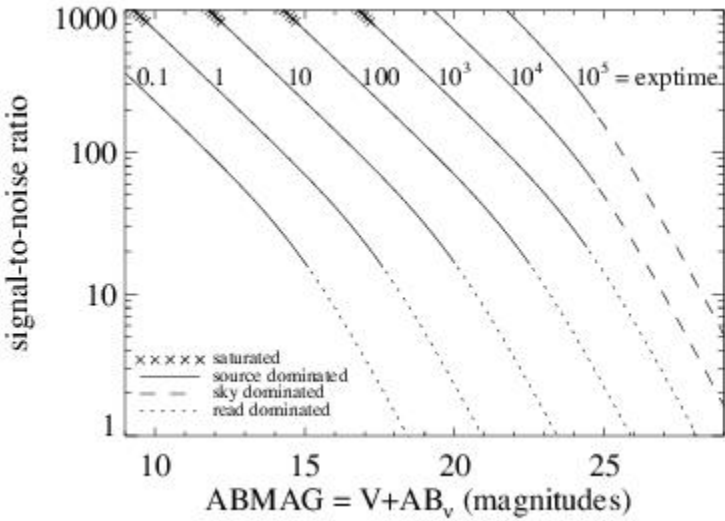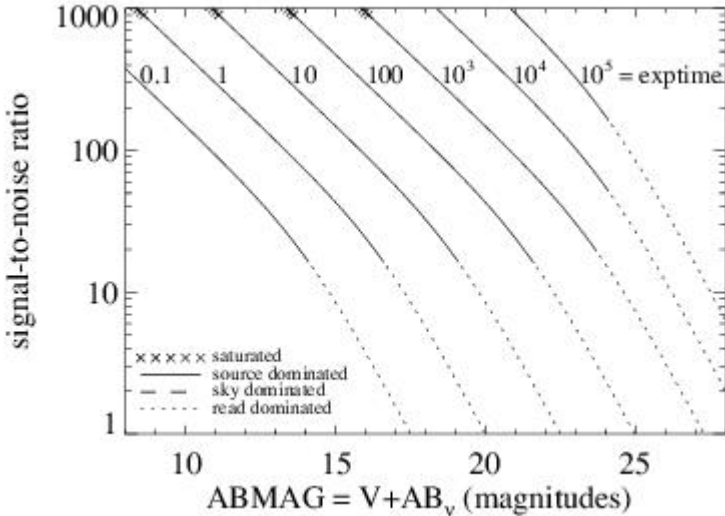
**Figure A.78:** Extended source S/N vs. V+AB$_\nu$ for the F621M filter, assuming high sky backgrounds and a source uniformly filling a 1 arcsec$^2$ aperture.
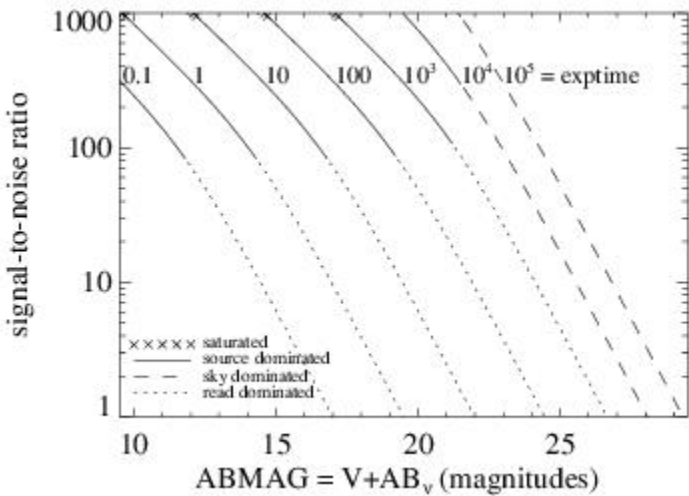
# UVIS F625W

**Description**
Sloan Digital Sky Survey *r'* filter.

**Figure A.79: Integrated system throughput for F625W.**



System Throughput for F625W
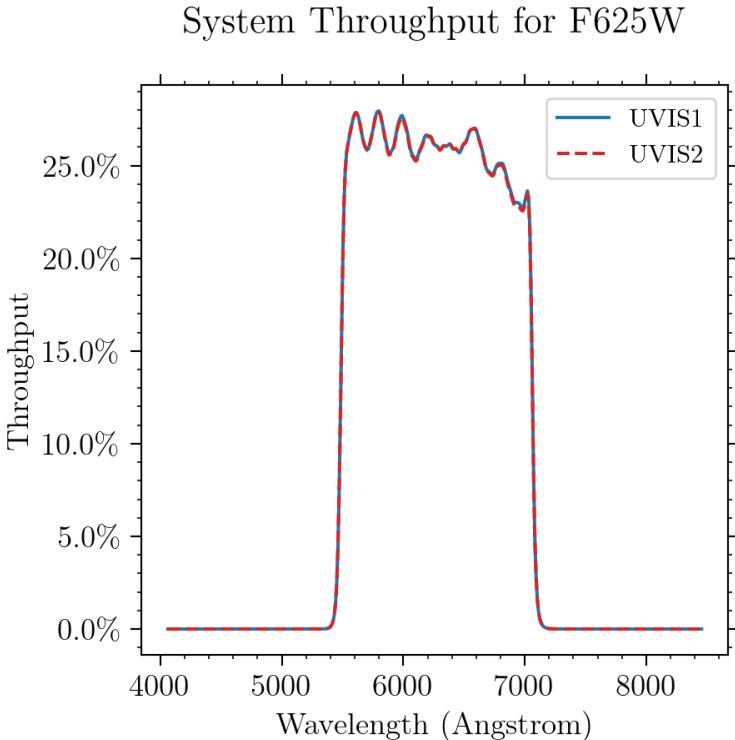
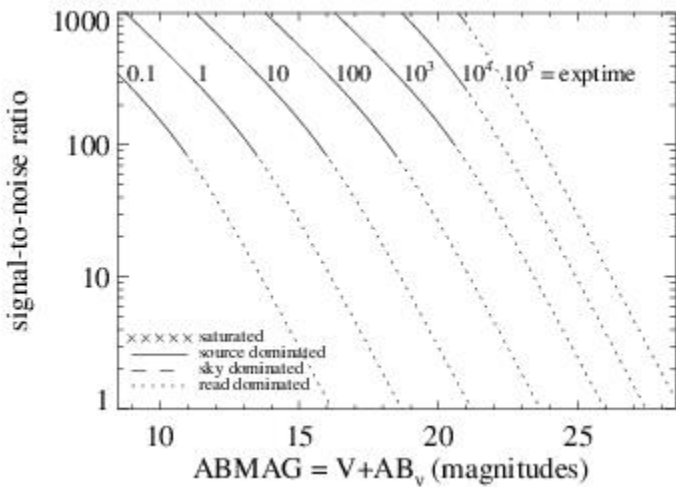Figure A.80: Point source S/N vs. V+AB$_\nu$ for the F625W filter, assuming high sky backgrounds and a 5 × 5 pixel aperture.
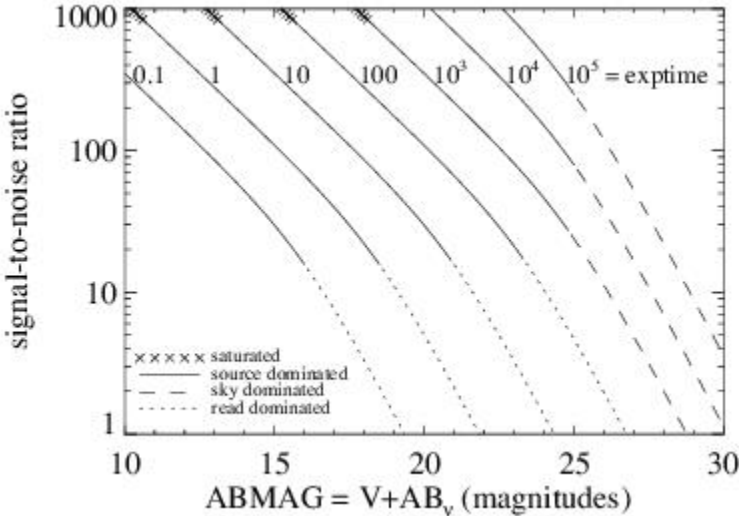
Figure A.81: Extended source S/N vs. V+AB$_\nu$ for the F625W filter, assuming high sky backgrounds and a source uniformly filling a 1 arcsec$^2$ aperture.

# UVIS F631N

**Description**
[O I] 6300 filter.

**Figure A.82: Integrated system throughput for F631N.**

**Figure A.83:** Point source S/N vs. V+AB$_\nu$ for the F631N filter, assuming high sky backgrounds and a 5 × 5 pixel aperture.

Figure A.84: Extended source S/N vs. V+AB$_\nu$ for the F631N filter, assuming high sky backgrounds and a source uniformly filling a 1 arcsec$^2$ aperture.

# UVIS F645N

**Description**
Continuum filter.
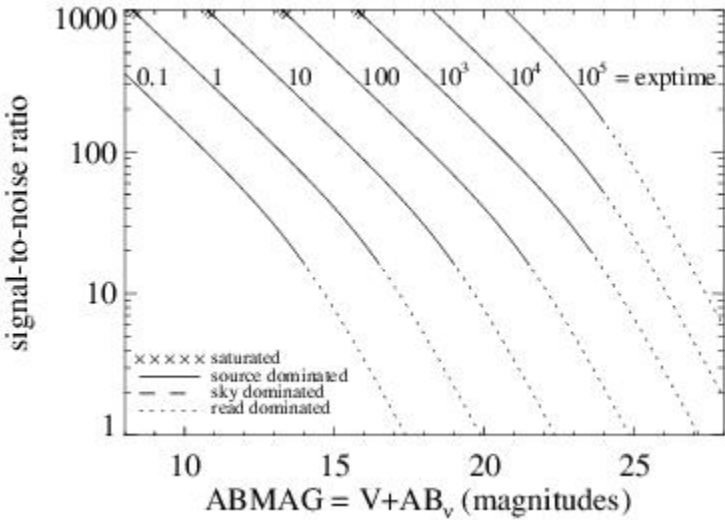
**Figure A.85: Integrated system throughput for F645N.**



System Throughput for F645N

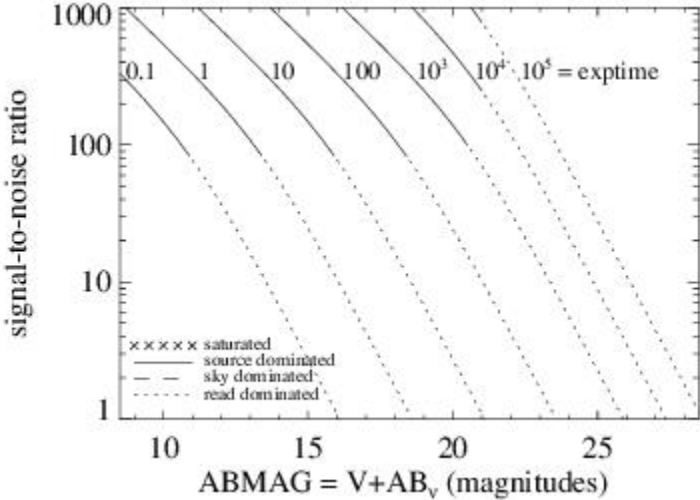Figure A.86: Point source S/N vs. V+AB$_\nu$ for the F645N filter, assuming high sky backgrounds and a 5 × 5 pixel aperture.

Figure A.87: Extended source S/N vs. V+AB$_\nu$ for the F645N filter, assuming high sky backgrounds and a source uniformly filling a 1 arcsec$^2$ aperture.

# UVIS F656N

**Description**
Hα 6562 filter.

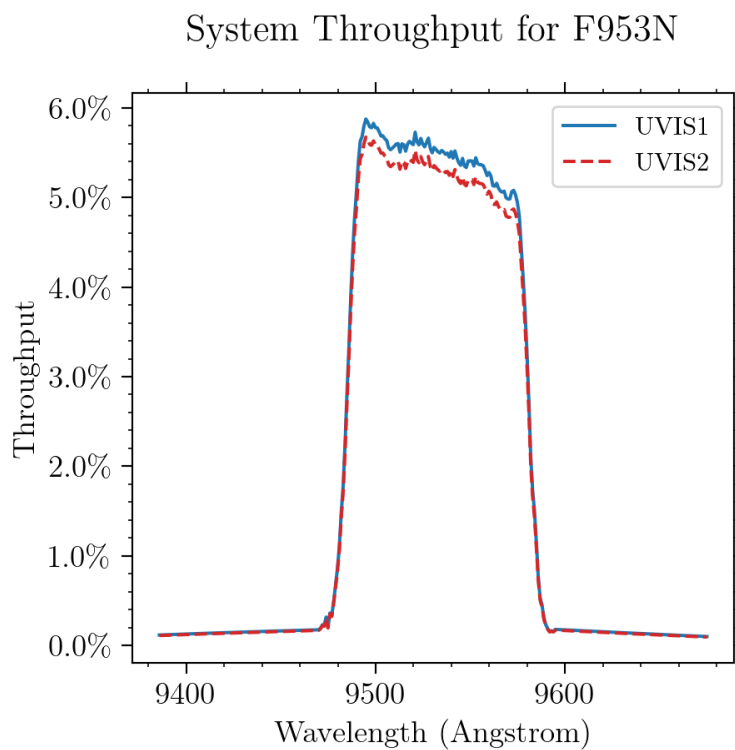**Figure A.88: Integrated system throughput for F656N.**



System Throughput for F656N

Figure A.89: Point source S/N vs. V+AB$_\nu$ for the F656N filter, assuming high sky backgrounds and a 5 × 5 pixel aperture.

Figure A.90: Extended source S/N vs. V+AB$_\nu$ for the F656N filter, assuming high sky backgrounds and a source uniformly filling a 1 arcsec$^2$ aperture.

# UVIS F657N

**Description**
Wide Hα + [N II] filter.

**Figure A.91: Integrated system throughput for F657N.**

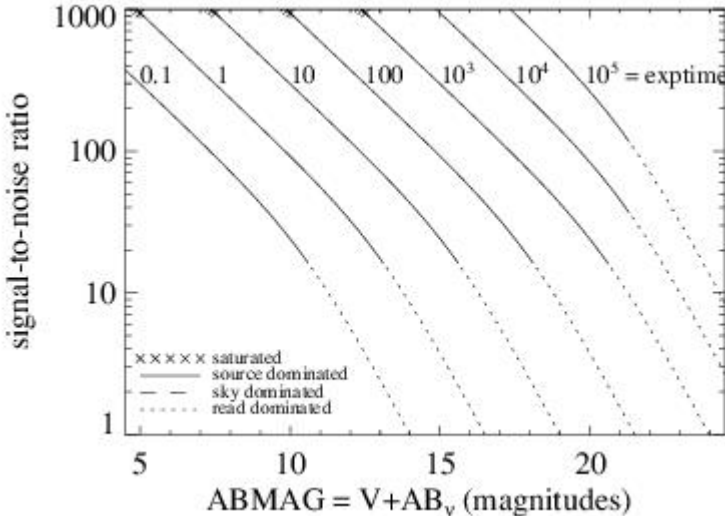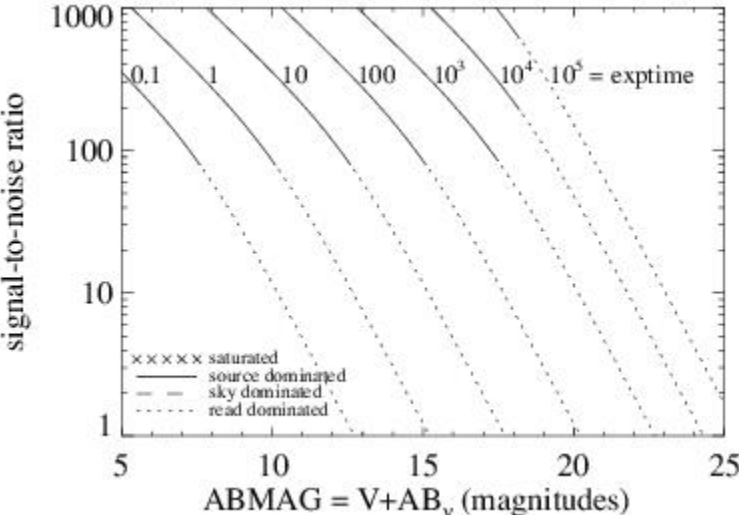**Figure A.92: Point source S/N vs. V+AB$_\nu$ for the F657N filter, assuming high sky backgrounds and a 5 × 5 pixel aperture.**

Figure A.93: Extended source S/N vs. V+AB$_\nu$ for the F657N filter, assuming high sky backgrounds and a source uniformly filling a 1 arcsec$^2$ aperture.

# UVIS F658N

**Description**
[N ɪɪ] 6583 filter.

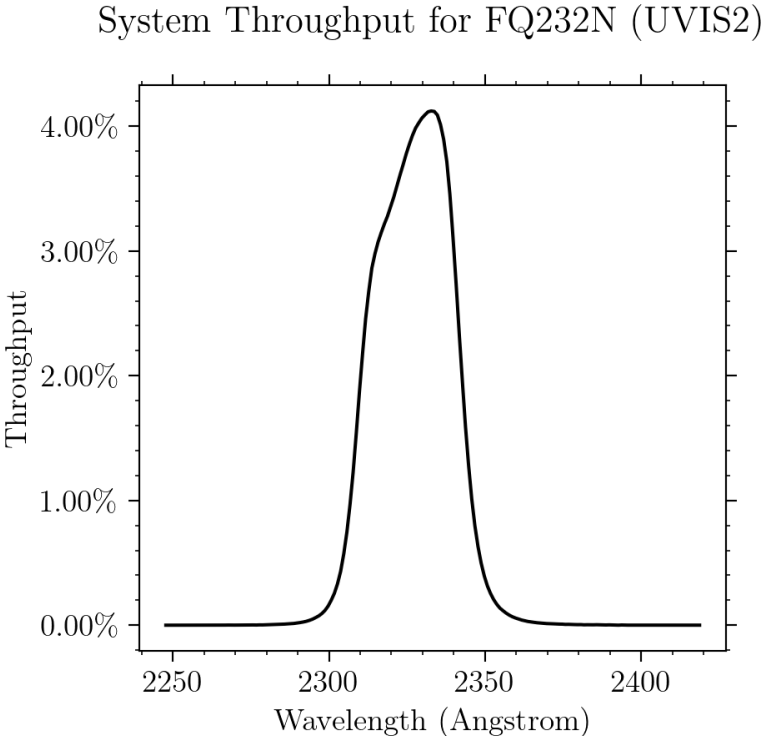**Figure A.94: Integrated system throughput for F658N.**



System Throughput for F658N

**Figure A.95: Point source S/N vs. V+AB$_\nu$ for the F658N filter, assuming high sky backgrounds and a 5 × 5 pixel aperture.**

Figure A.96: Extended source S/N vs. V+AB$_\nu$ for the F658N filter, assuming high sky backgrounds and a source uniformly filling a 1 arcsec$^2$ aperture.

# UVIS F665N

**Description**

*z* (Hα + [N ɪɪ]) filter.

**Figure A.97: Integrated system throughput for F665N.**



System Throughput for F665N

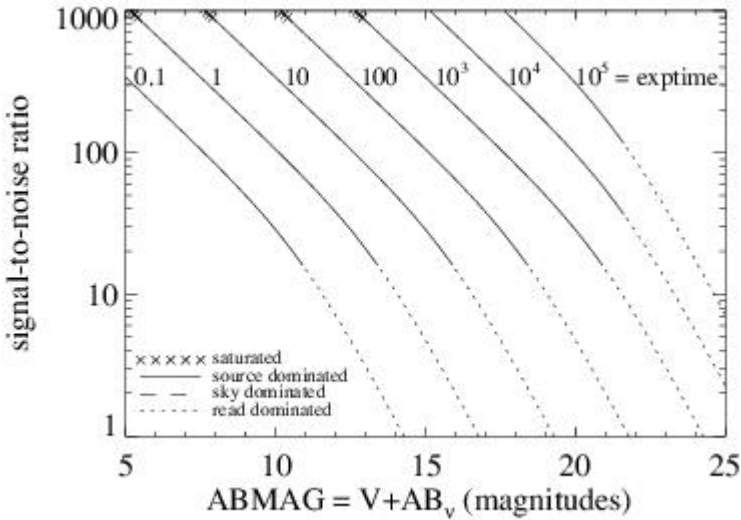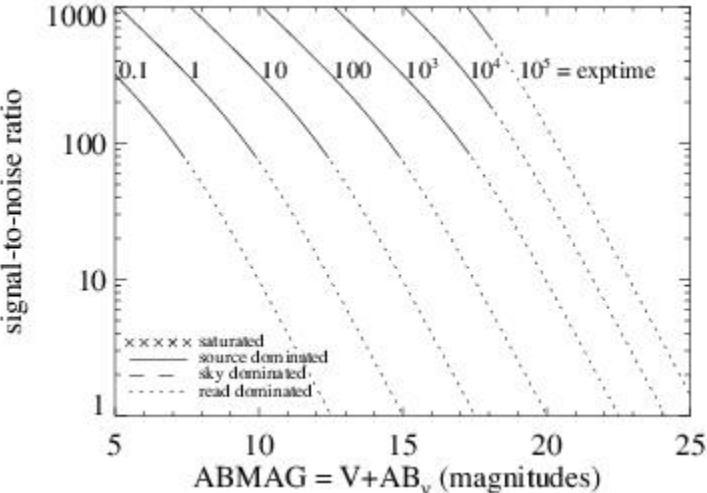Figure A.98: Point source S/N vs. V+AB$_\nu$ for the F665N filter, assuming high sky backgrounds and a 5 × 5 pixel aperture.

Figure A.99: Extended source S/N vs. V+AB$_\nu$ for the F665N filter, assuming high sky backgrounds and a source uniformly filling a 1 arcsec$^2$ aperture.

# UVIS F673N

**Description**
[S II] 6717/6731 filter.

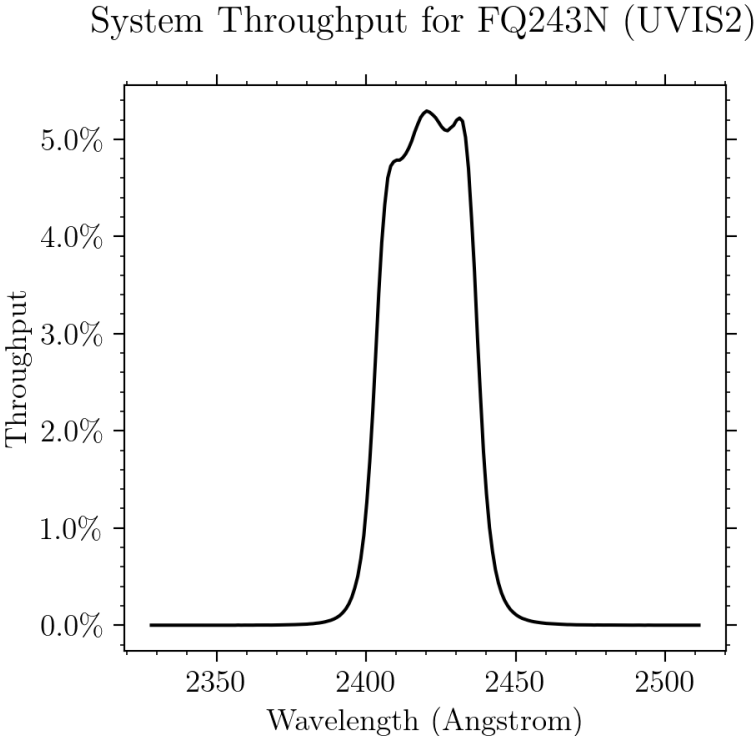**Figure A.100: Integrated system throughput for F673N.**



System Throughput for F673N

Figure A.101: Point source S/N vs. V+AB$_\nu$ for the F673N filter, assuming high sky backgrounds and a 5 × 5 pixel aperture.

Figure A.102: Extended source S/N vs. V+AB$_\nu$ for the F673N filter, assuming high sky backgrounds and a source uniformly filling a 1 arcsec$^2$ aperture.

# UVIS F680N

**Description**
*z* (Hα + [N ɪɪ]) filter.

**Figure A.103: Integrated system throughput for F680N.**

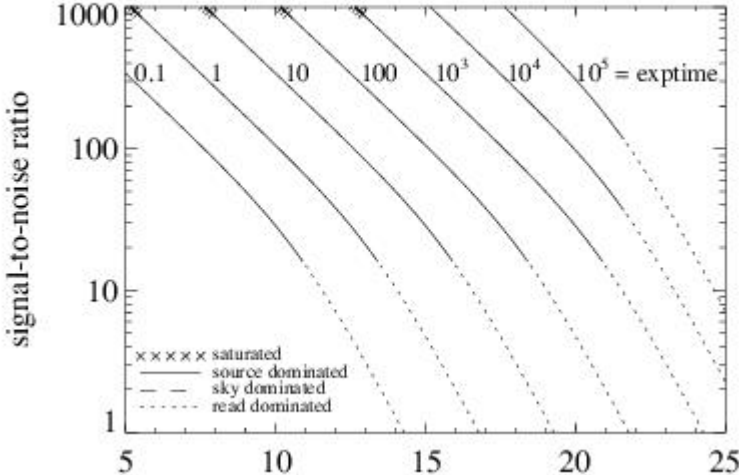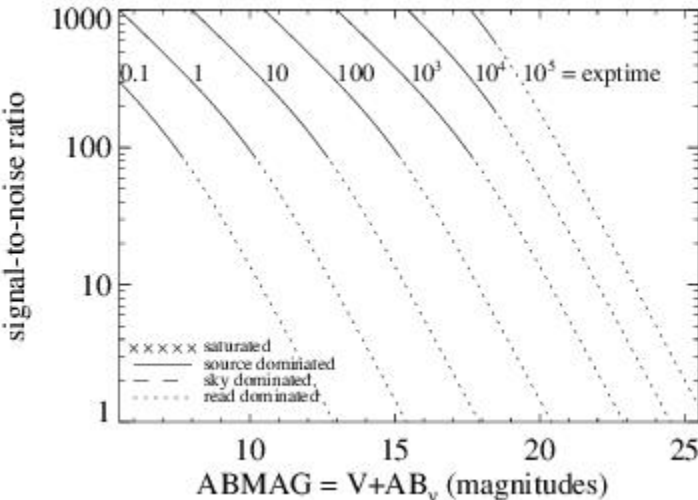Figure A.104: Point source S/N vs. V+AB$_\nu$ for the F680N filter, assuming high sky backgrounds and a 5 × 5 pixel aperture.

Figure A.105: Extended source S/N vs. V+AB$_\nu$ for the F680N filter, assuming high sky backgrounds and a source uniformly filling a 1 arcsec$^2$ aperture.

# UVIS F689M

**Description**
11% passband filter.

**Figure A.106: Integrated system throughput for F689M.**



System Throughput for F689M
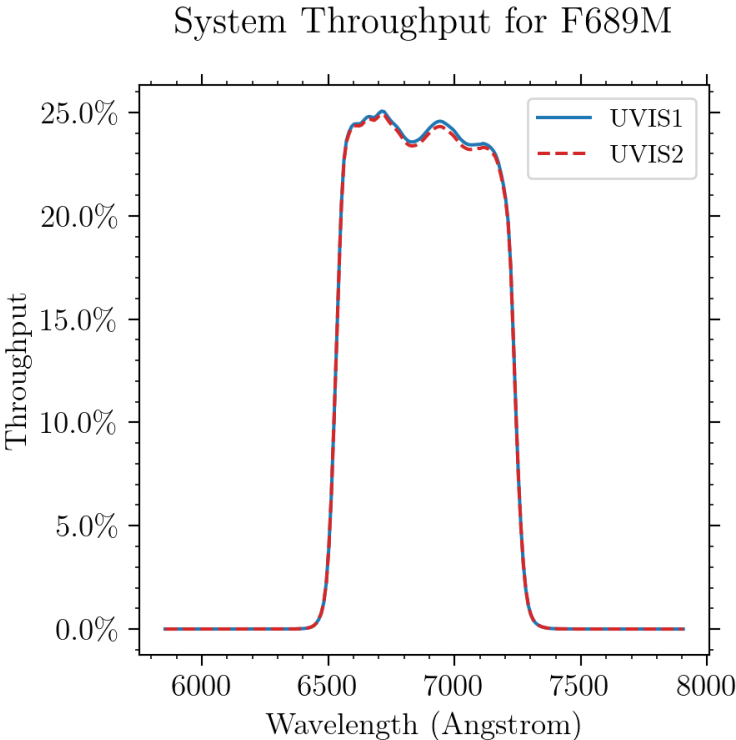
Figure A.107: Point source S/N vs. V+AB$_\nu$ for the F689M filter.Top curves are for low sky; bottom curves are for average sky.
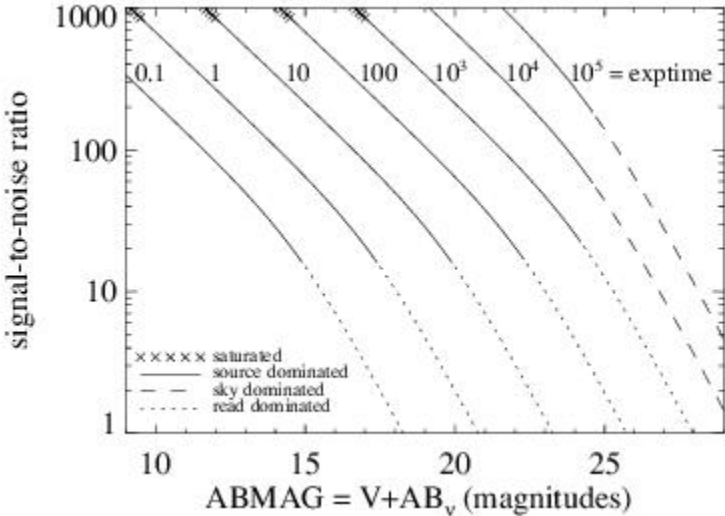
Figure A.108: Extended source S/N vs. V+AB$_\nu$ for the F689M filter, assuming high sky backgrounds and a source uniformly filling a 1 arcsec$^2$ aperture.

# UVIS F763M

**Description**
11% passband filter.

**Figure A.109:** Integrated system throughput for F763M.



System Throughput for F763M
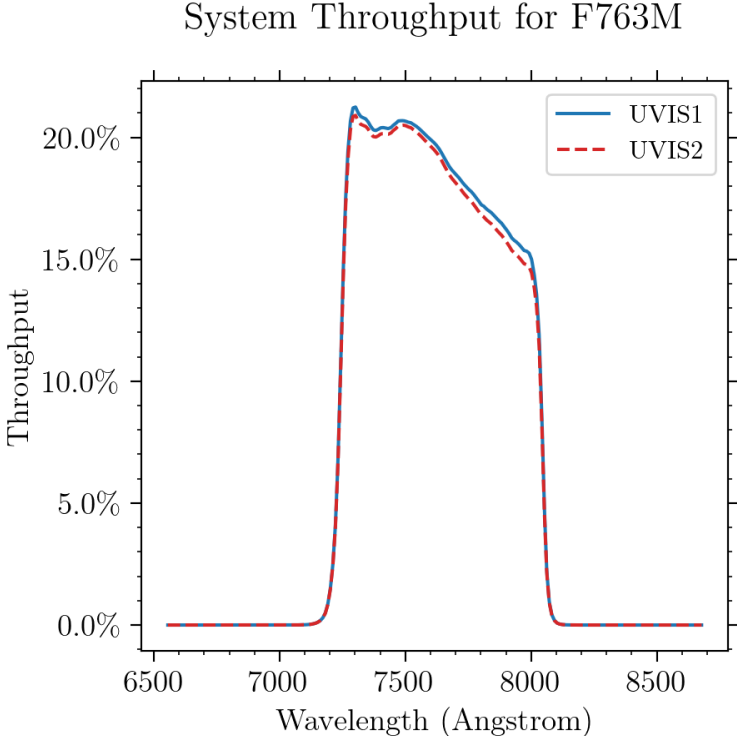
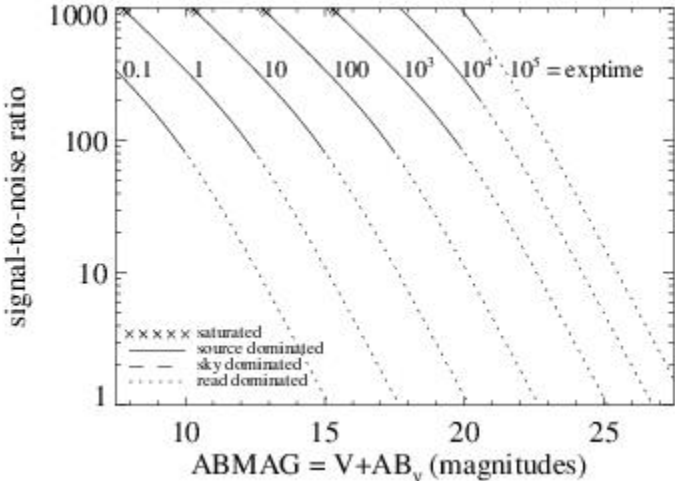Figure A.110: Point source S/N vs. V+AB$_\nu$ for the F763M filter.Top curves are for low sky; bottom curves are for average sky.

Figure A.111: Extended source S/N vs. V+AB$_\nu$ for the F763M filter, assuming high sky backgrounds and a source uniformly filling a 1 arcsec$^2$ aperture.

# UVIS F775W

**Description**
Sloan Digital Sky Survey *i* filter.
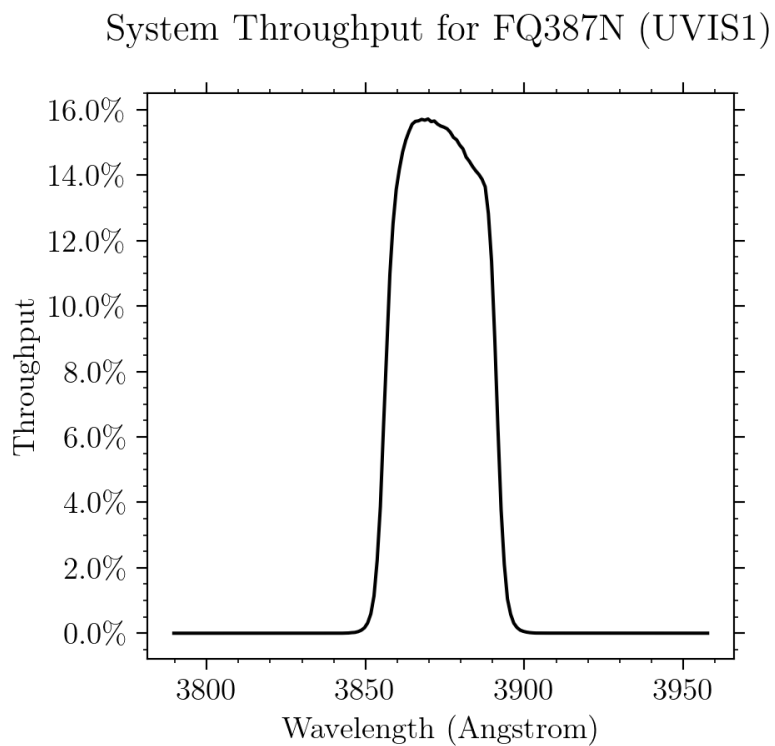
**Figure A.112: Integrated system throughput for F775W.**

Figure A.113: Point source S/N vs. V+AB$_\nu$ for the F775W filter, assuming high sky backgrounds and a 5 × 5 pixel aperture.

Figure A.114: Extended source S/N vs. V+AB$_\nu$ for the F775W filter, assuming high sky backgrounds and a source uniformly filling a 1 arcsec$^2$ aperture.

# UVIS F814W

**Description**
WFPC2 Wide *I* filter.

Figure A.115: Integrated system throughput for F814W.

Figure A.116: Point source S/N vs. V+AB$_\nu$ for the F814W filter, assuming high sky backgrounds and a 5 × 5 pixel aperture.
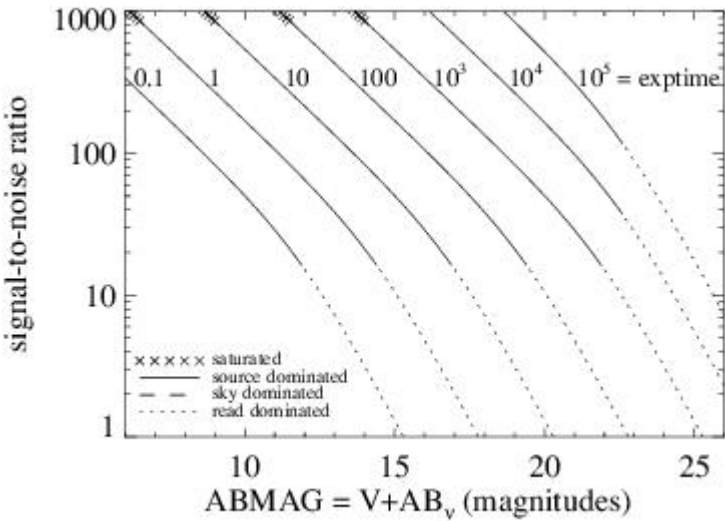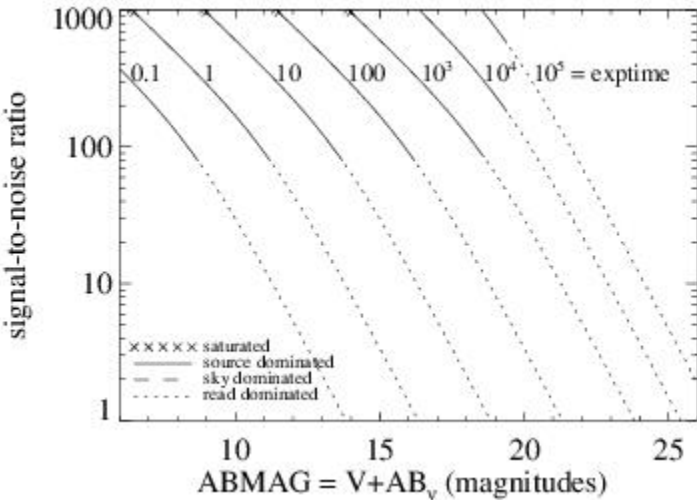
Figure A.117: Extended source S/N vs. V+AB$_\nu$ for the F814W filter, assuming high sky backgrounds and a source uniformly filling a 1 arcsec$^2$ aperture.

# UVIS F845M

**Description**
11% passband filter.

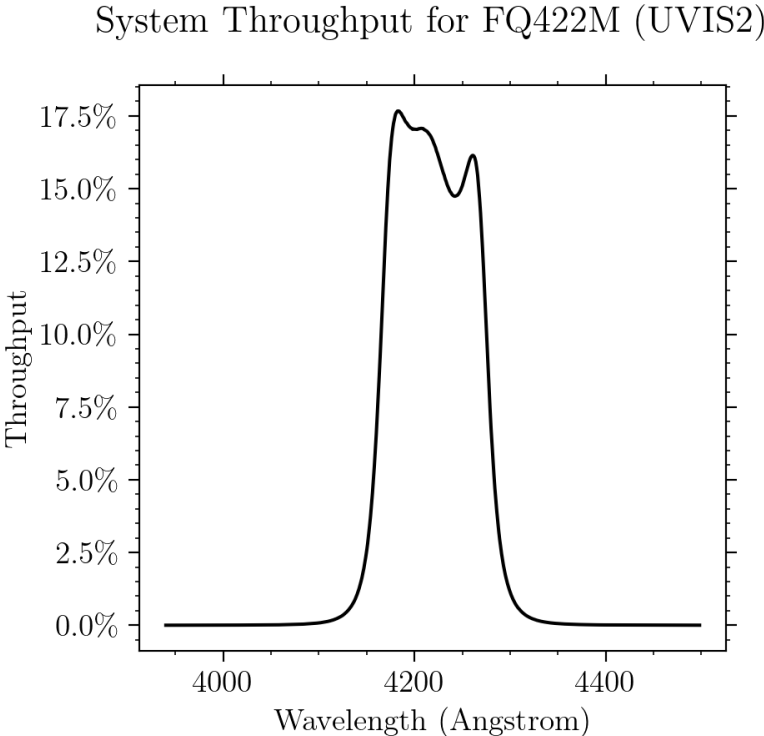**Figure A.118:** Integrated system throughput for F845M.



System Throughput for F845M

Figure A.119: Point source S/N vs. V+AB$_v$ for the F845M filter, assuming high sky backgrounds and a 5 × 5 pixel aperture.

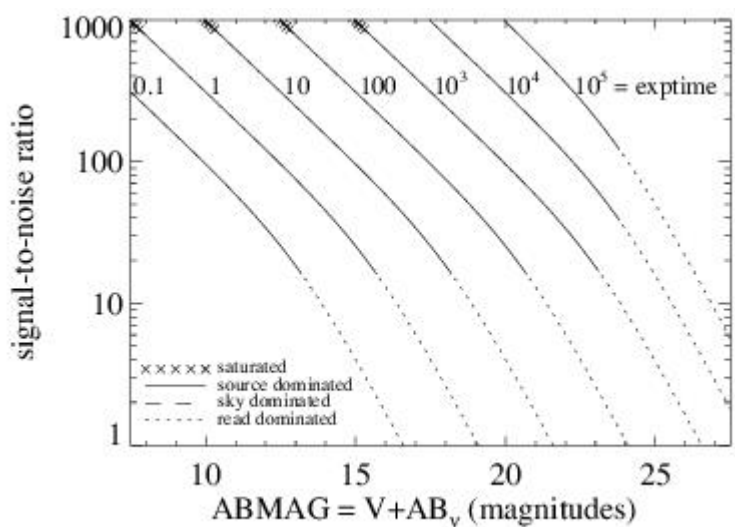Figure A.120: Extended source S/N vs. V+AB$_\nu$ for the F845M filter, assuming high sky backgrounds and a source uniformly filling a 1 arcsec$^2$ aperture.

# UVIS F850LP

Description
Sloan Digital Sky Survey *z'* filter.

**Figure A.121: Integrated system throughput for F850LP.**



System Throughput for F850LP
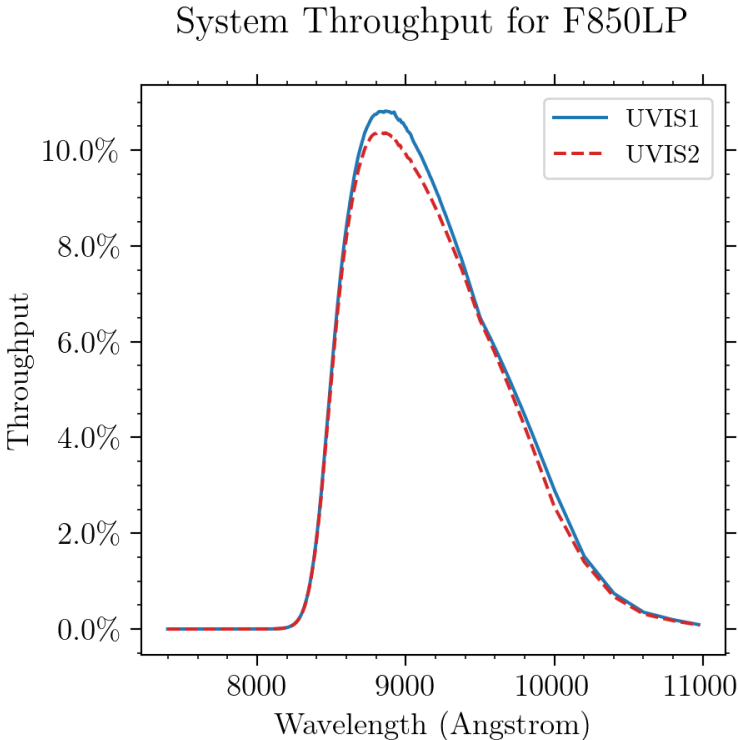
Figure A.122: Point source S/N vs. V+AB$_\nu$ for the F850LP filter.Top curves are for low sky; bottom curves are for average sky.
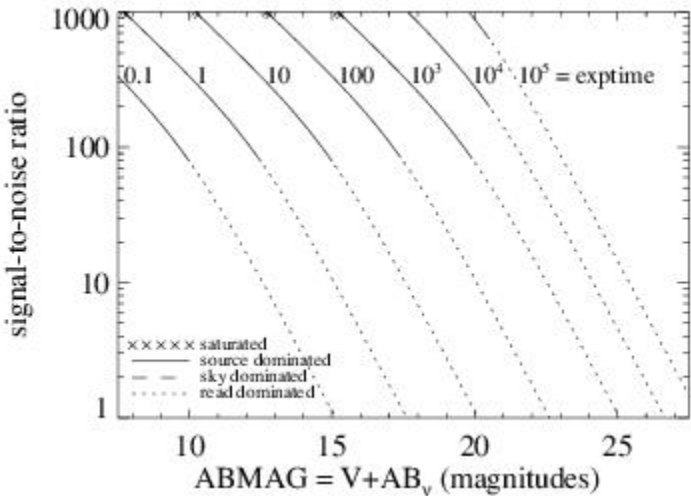
Figure A.123: Extended source S/N vs. V+AB$_\nu$ for the F850LP filter, assuming high sky backgrounds and a source uniformly filling a 1 arcsec$^2$ aperture.

# UVIS F953N

**Description**
[S ɪɪɪ] 9532 filter.

**Figure A.124: Integrated system throughput for F953N.**

Figure A.125: Point source S/N vs. V+AB$_\nu$ for the F953N filter, assuming high sky backgrounds and a 5 × 5 pixel aperture.

Figure A.126: Extended source S/N vs. V+AB$_\nu$ for the F953N filter, assuming high sky backgrounds and a source uniformly filling a 1 arcsec$^2$ aperture.

# UVIS FQ232N

**Description**
C ɪɪ] 2326 filter.

**Figure A.127: Integrated system throughput for FQ232N.**
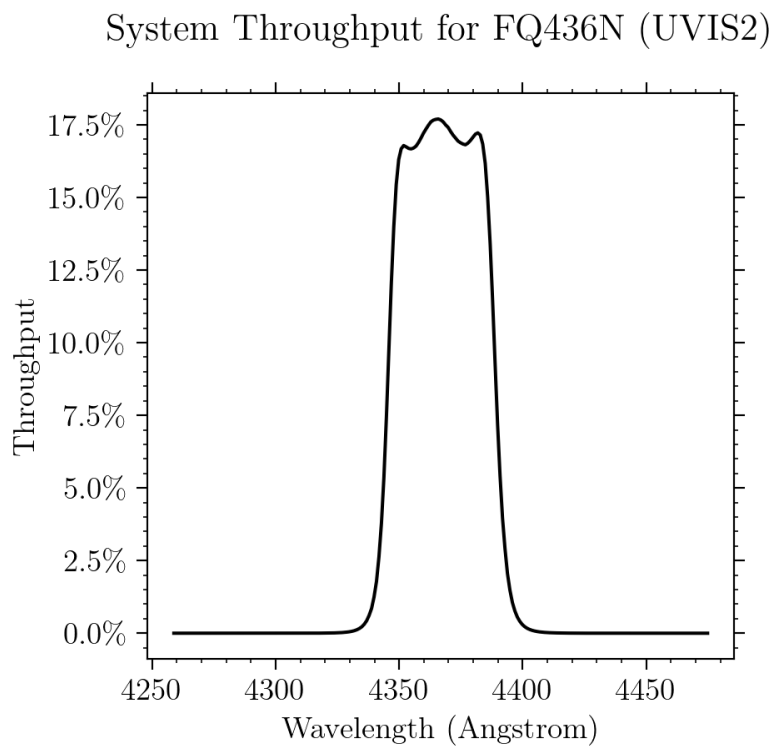


System Throughput for FQ232N (UVIS2)

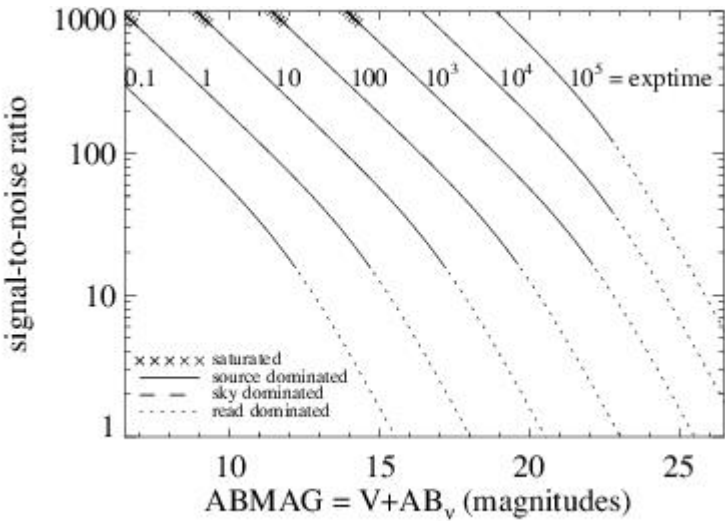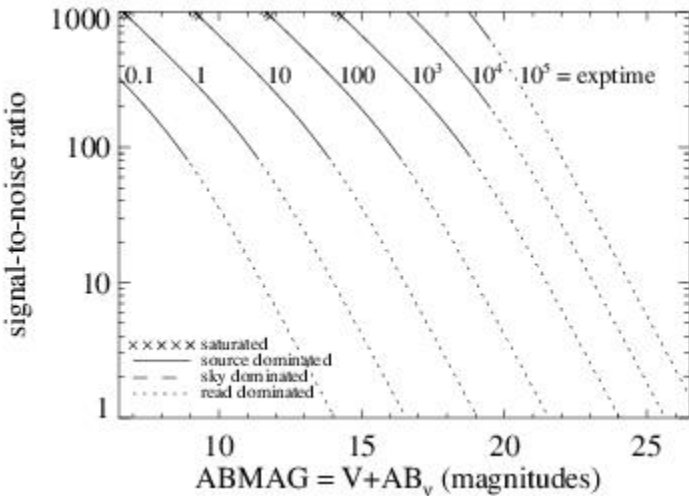Figure A.128: Point source S/N vs. V+AB$_\nu$ for the FQ232N filter, assuming high sky backgrounds and a 5 × 5 pixel aperture.

Figure A.129: Extended source S/N vs. V+AB$_\nu$ for the FQ232N filter, assuming high sky backgrounds and a source uniformly filling a 1 arcsec$^2$ aperture.

# UVIS FQ243N

**Description**
[Ne IV] 2425 filter.

**Figure A.130: Integrated system throughput for FQ243N.**



System Throughput for FQ243N (UVIS2)
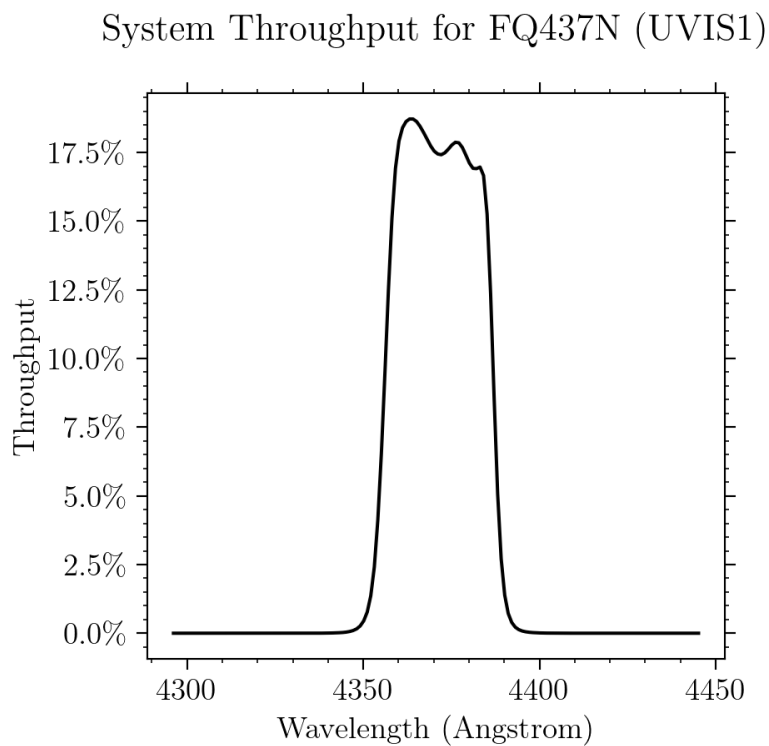
Figure A.131: Point source S/N vs. V+AB$_\nu$ for the FQ243N filter, assuming high sky backgrounds and a 5 × 5 pixel aperture.

Figure A.132: Extended source S/N vs. V+AB$_\nu$ for the FQ243N filter, assuming high sky backgrounds and a source uniformly filling a 1 arcsec$^2$ aperture.

# UVIS FQ378N

**Description**
$z$ ([O II] 3726) filter.

**Figure A.133:** Integrated system throughput for FQ378N.
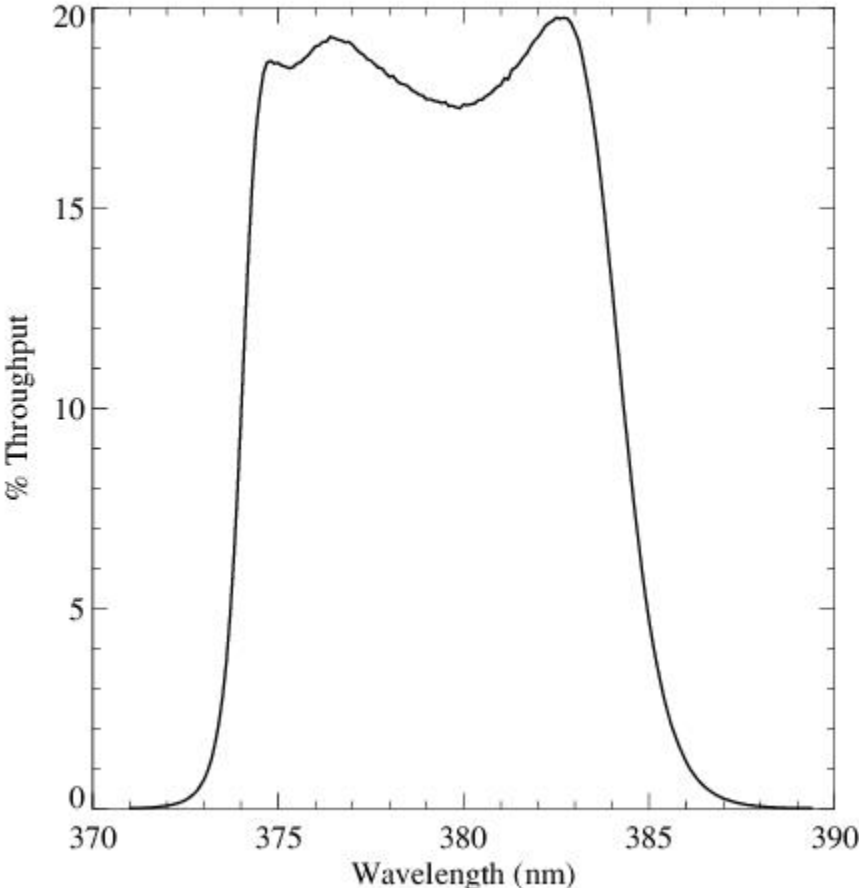
Figure A.134: Point source S/N vs. V+AB$_\nu$ for the FQ378N filter, assuming high sky backgrounds and a 5 × 5 pixel aperture.
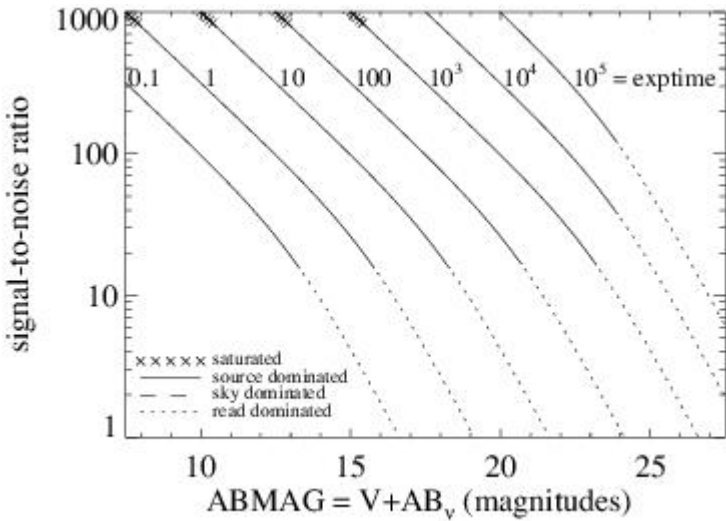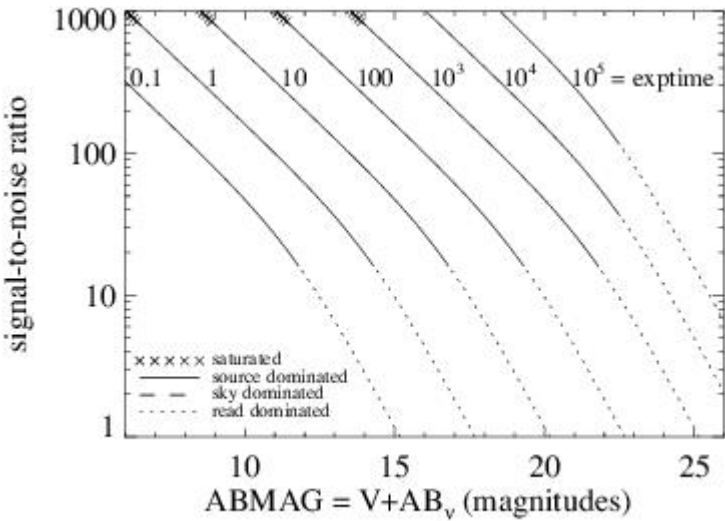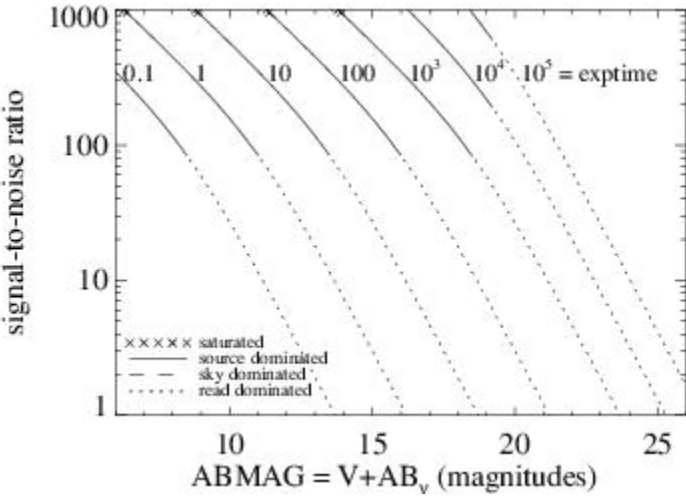
Figure A.135: Extended source S/N vs. V+AB$_\nu$ for the FQ378N filter, assuming high sky backgrounds and a source uniformly filling a 1 arcsec$^2$ aperture.

# UVIS FQ387N

**Description**
[Ne ɪɪɪ] 3868 filter.

**Figure A.136: Integrated system throughput for FQ387N.**



System Throughput for FQ387N (UVIS1)
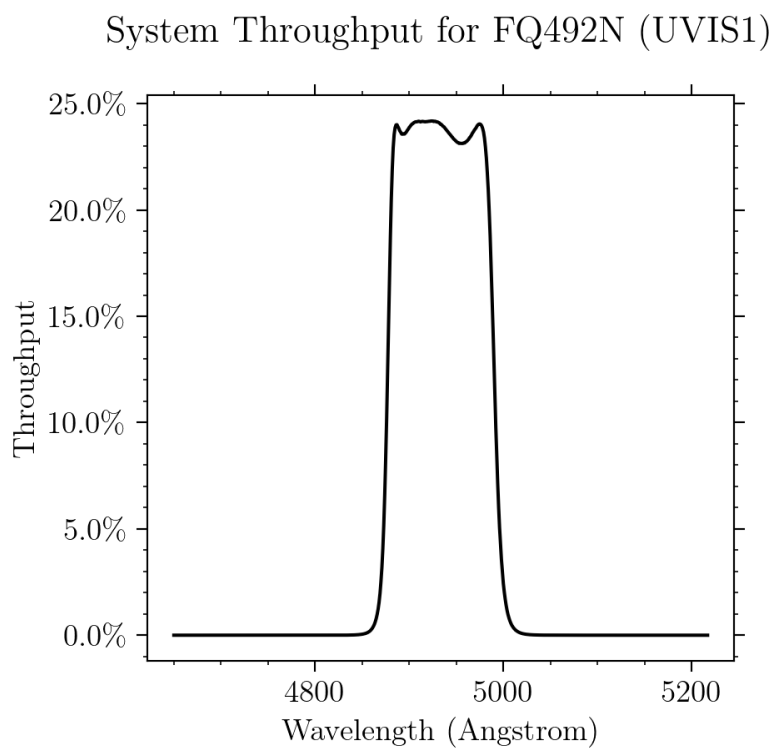
Figure A.137: Point source S/N vs. V+AB$_\nu$ for the FQ387N filter, assuming high sky backgrounds and a 5 × 5 pixel aperture.

Figure A.138: Extended source S/N vs. V+AB$_\nu$ for the FQ387N filter, assuming high sky backgrounds and a source uniformly filling a 1 arcsec$^2$ aperture.

# UVIS FQ422M

**Description**
Blue continuum filter.

**Figure A.139:** Integrated system throughput for FQ422M.

System Throughput for FQ422M (UVIS2)

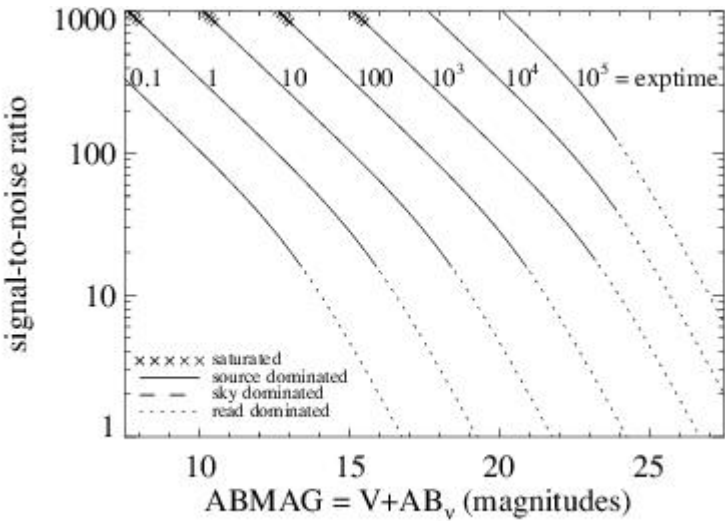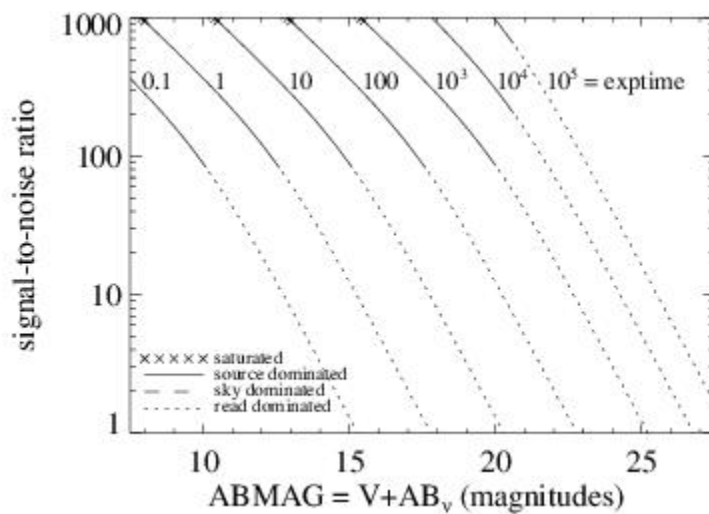Figure A.140: Point source S/N vs. V+AB$_\nu$ for the FQ422M filter, assuming high sky backgrounds and a 5 × 5 pixel aperture.

Figure A.141: Extended source S/N vs. V+AB$_\nu$ for the FQ422M filter, assuming high sky backgrounds and a source uniformly filling a 1 arcsec$^2$ aperture.

# UVIS FQ436N

**Description**
Hγ 4340 + [O iii] 4363 filter.

**Figure A.142:** Integrated system throughput for FQ436N.



System Throughput for FQ436N (UVIS2)
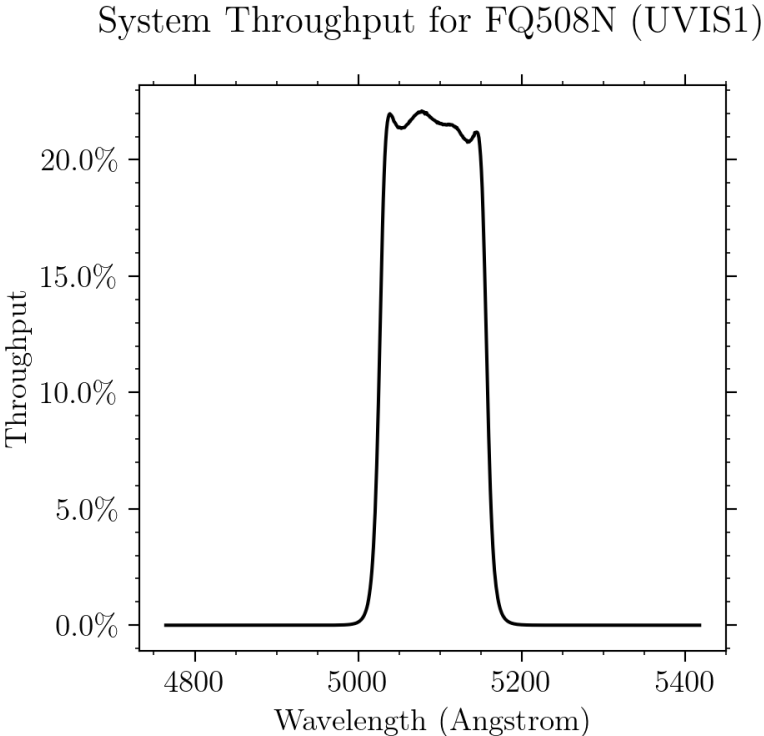
Figure A.143: Point source S/N vs. V+AB$_\nu$ for the FQ436N filter, assuming high sky backgrounds and a 5 × 5 pixel aperture.

Figure A.144: Extended source S/N vs. V+AB$_\nu$ for the FQ436N filter, assuming high sky backgrounds and a source uniformly filling a 1 arcsec$^2$ aperture.

# UVIS FQ437N

**Description**
[O III] 4363 filter.

**Figure A.145:** Integrated system throughput for FQ437N.



System Throughput for FQ437N (UVIS1)

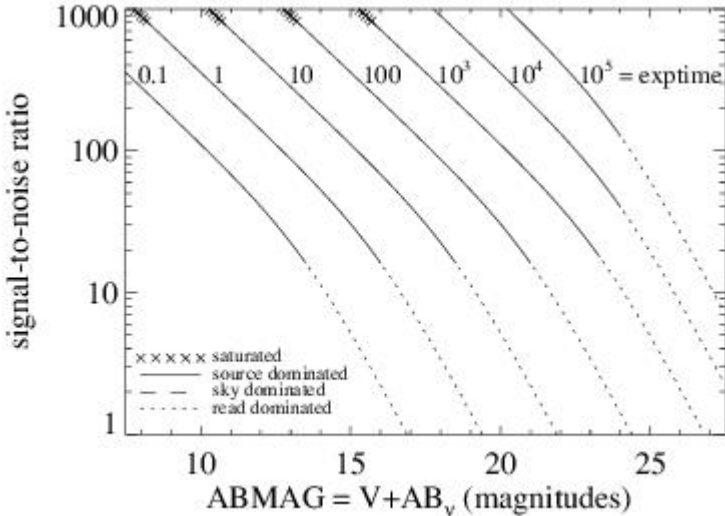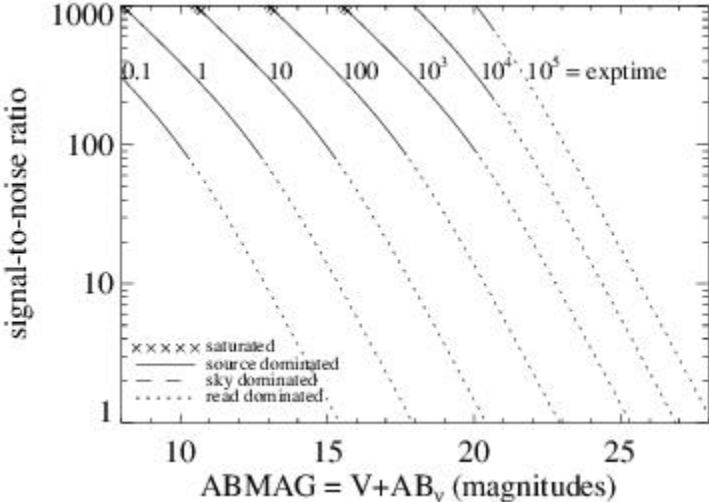Figure A.146: Point source S/N vs. V+AB$_\nu$ for the FQ437N filter, assuming high sky backgrounds and a 5 × 5 pixel aperture.

Figure A.147: Extended source S/N vs. V+AB$_\nu$ for the FQ437N filter, assuming high sky backgrounds and a source uniformly filling a 1 arcsec$^2$ aperture.

# UVIS FQ492N

**Description**

*z* (Hβ) filter.

**Figure A.148: Integrated system throughput for FQ492N.**



System Throughput for FQ492N (UVIS1)
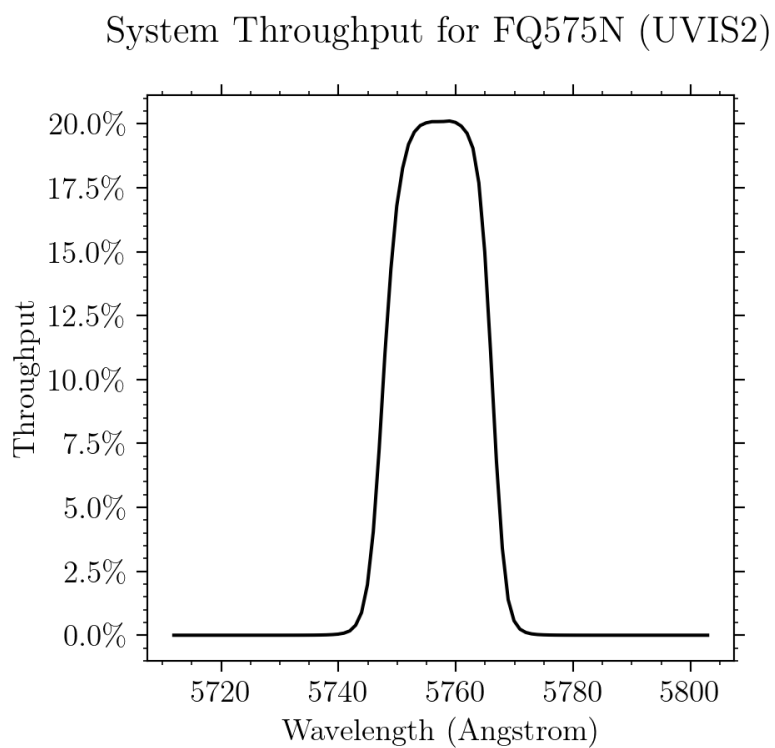
Figure A.149: Point source S/N vs. V+AB$_\nu$ for the FQ492N filter, assuming high sky backgrounds and a 5 × 5 pixel aperture.

Figure A.150: Extended source S/N vs. V+AB$_\nu$ for the FQ492N filter, assuming high sky backgrounds and a source uniformly filling a 1 arcsec$^2$ aperture.

# UVIS FQ508N

**Description**

*z* ([O III] 5007) filter.

**Figure A.151:** Integrated system throughput for FQ508N.



System Throughput for FQ508N (UVIS1)

Figure A.152: Point source S/N vs. V+AB$_\nu$ for the FQ508N filter, assuming high sky backgrounds and a 5 × 5 pixel aperture.
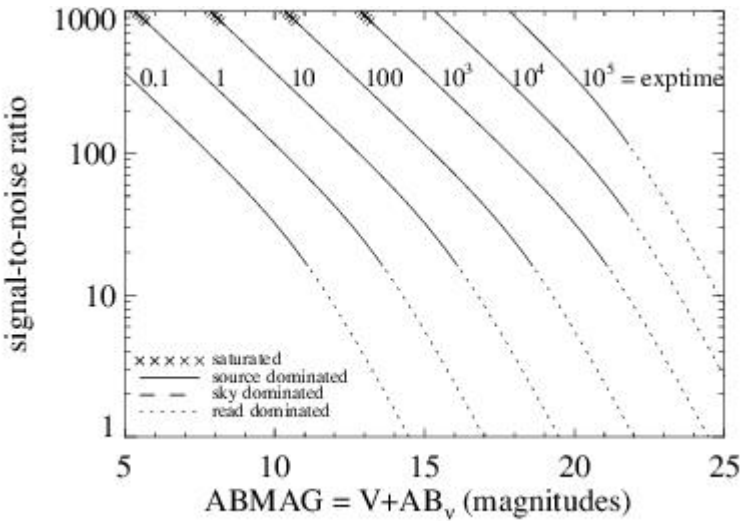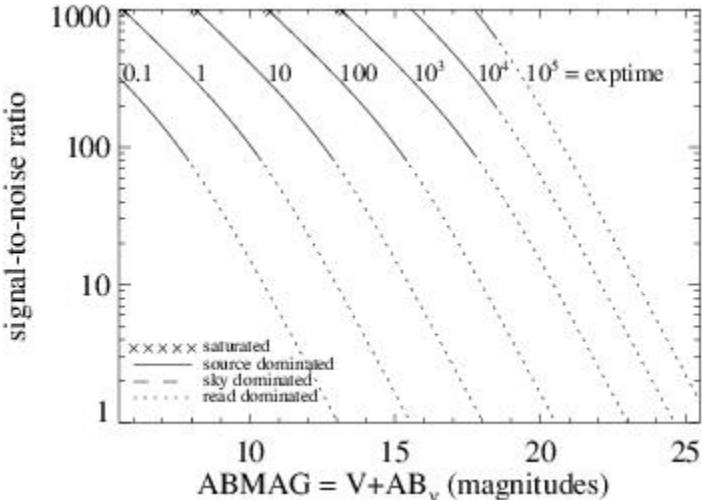
Figure A.153: Extended source S/N vs. V+AB$_\nu$ for the FQ508N filter, assuming high sky backgrounds and a source uniformly filling a 1 arcsec$^2$ aperture.

# UVIS FQ575N

**Description**
[N II] 5754 filter.

**Figure A.154: Integrated system throughput for FQ575N.**

System Throughput for FQ575N (UVIS2)

Figure A.155: Point source S/N vs. V+AB$_\nu$ for the FQ575N filter, assuming high sky backgrounds and a 5 × 5 pixel aperture.

**Figure A.156:** Extended source S/N vs. V+AB$_\nu$ for the FQ575N filter, assuming high sky backgrounds and a source uniformly filling a 1 arcsec$^2$ aperture.

# UVIS FQ619N

**Description**
$CH_4$ 6194 filter.

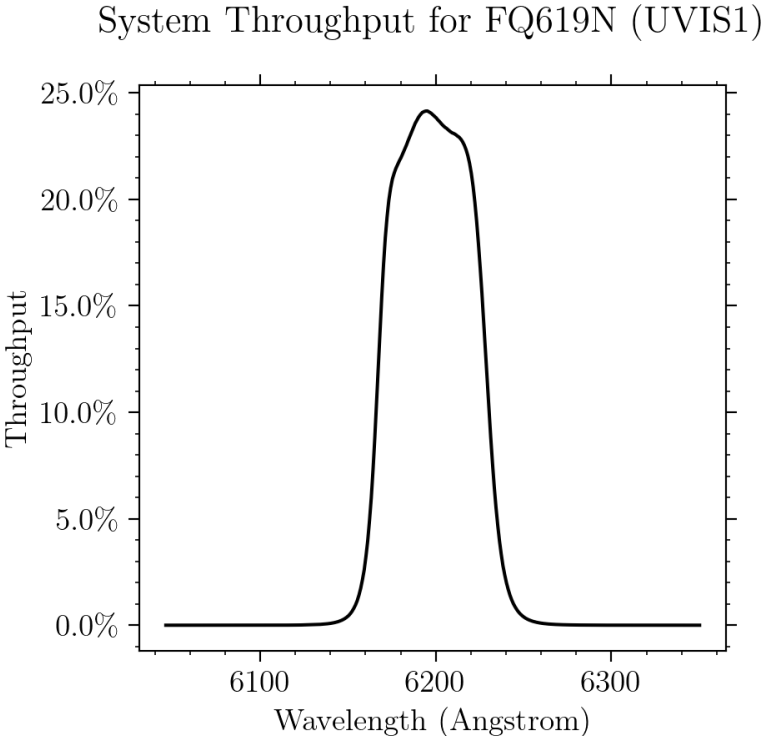**Figure A.157:** Integrated system throughput for FQ619N.



System Throughput for FQ619N (UVIS1)

Figure A.158: Point source S/N vs. V+AB$_\nu$ for the FQ619N filter, assuming high sky backgrounds and a 5 × 5 pixel aperture.
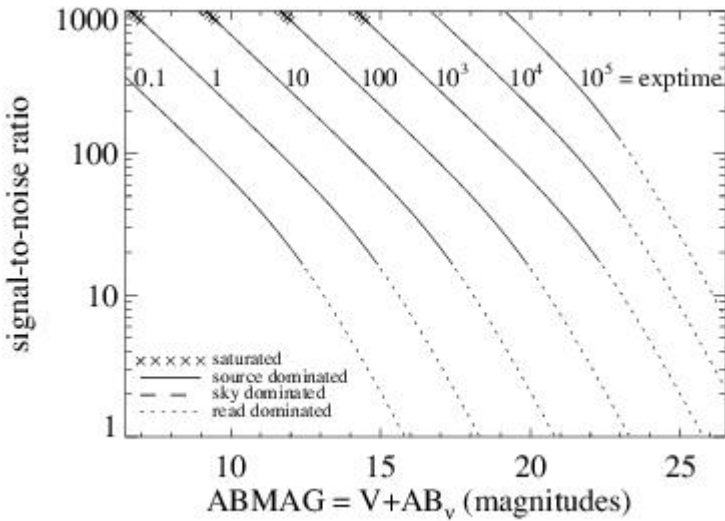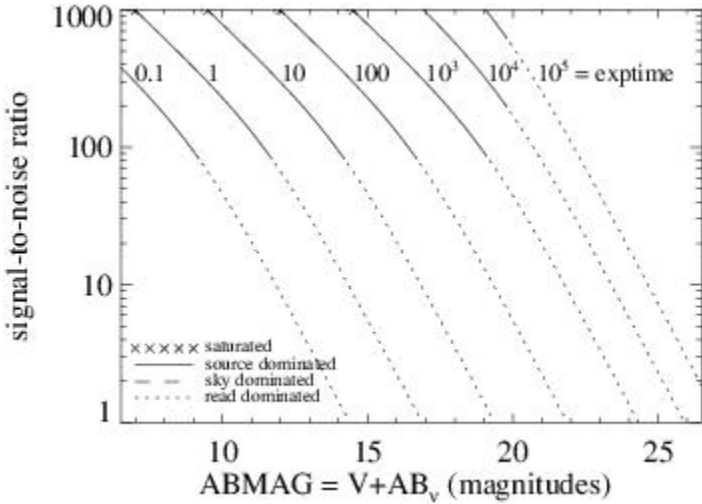
Figure A.159: Extended source S/N vs. V+AB$_\nu$ for the FQ619N filter, assuming high sky backgrounds and a source uniformly filling a 1 arcsec$^2$ aperture.

# UVIS FQ634N

**Description**
6194 continuum filter.

**Figure A.160:** Integrated system throughput for FQ634N.
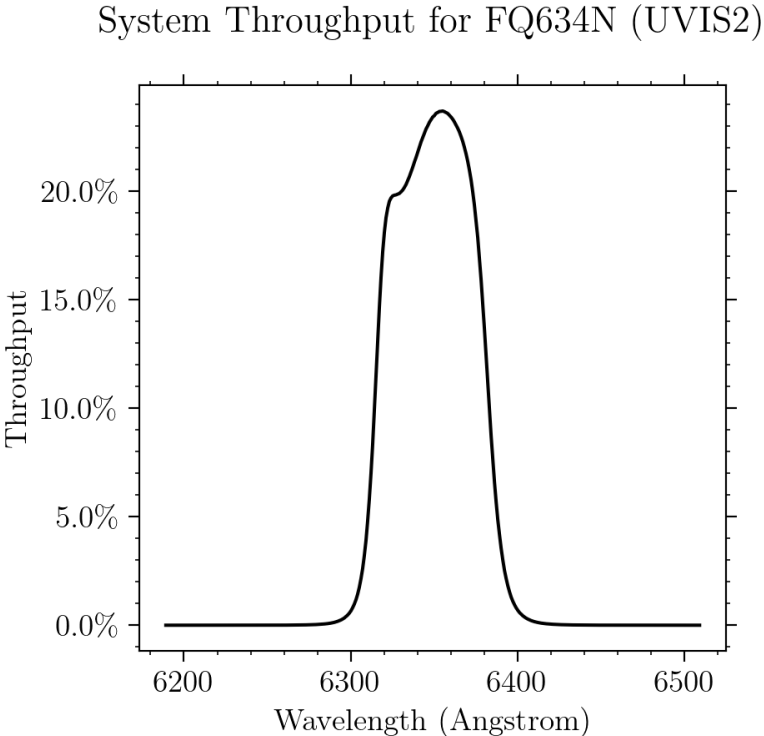


System Throughput for FQ634N (UVIS2)

Figure A.161: Point source S/N vs. V+AB$_\nu$ for the FQ634N filter, assuming high sky backgrounds and a 5 × 5 pixel aperture.

**Figure A.162:** Extended source S/N vs. V+AB$_v$ for the FQ634N filter, assuming high sky backgrounds and a source uniformly filling a 1 arcsec$^2$ aperture.

# UVIS FQ672N

**Description**
[S ɪɪ] 6717 filter.

**Figure A.163:** Integrated system throughput for FQ672N.



System Throughput for FQ672N (UVIS2)

Figure A.164: Point source S/N vs. V+AB$_\nu$ for the FQ672N filter, assuming high sky backgrounds and a 5 × 5 pixel aperture.
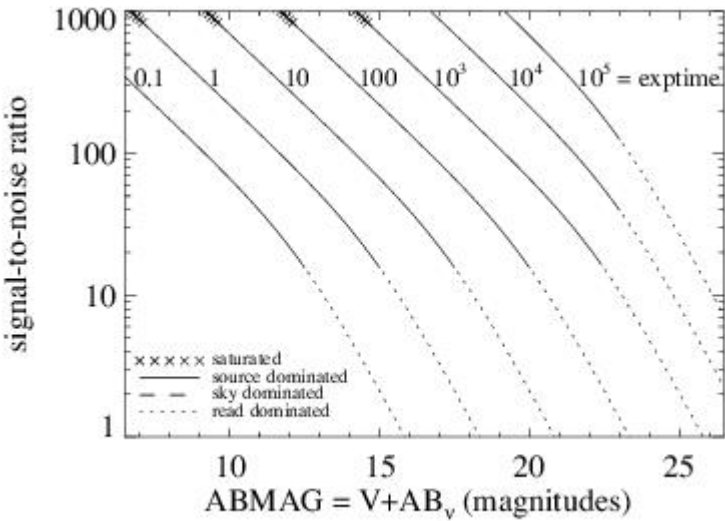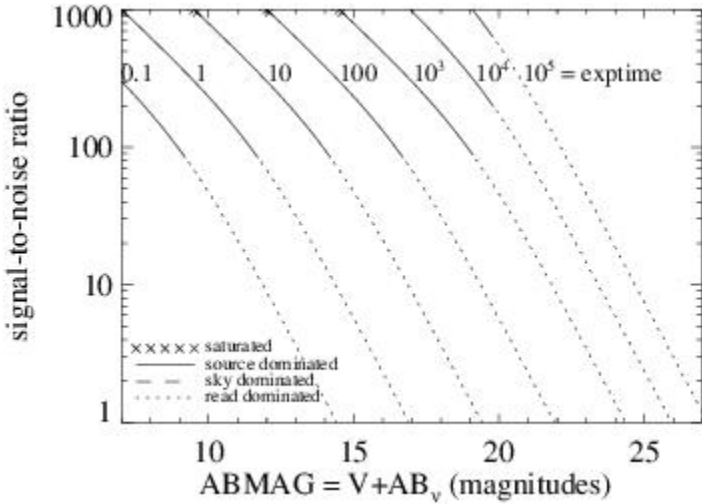
Figure A.165: Extended source S/N vs. V+AB$_\nu$ for the FQ672N filter, assuming high sky backgrounds and a source uniformly filling a 1 arcsec$^2$ aperture.

# UVIS FQ674N

**Description**
[S ɪɪ] 6731 filter.

**Figure A.166:** Integrated system throughput for FQ674N.
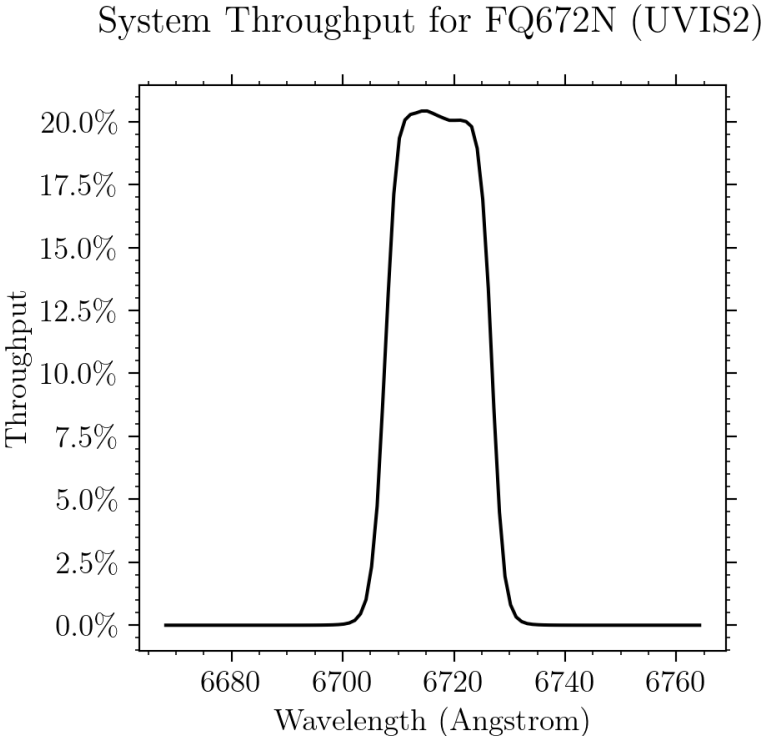
System Throughput for FQ674N (UVIS1)

Figure A.167: Point source S/N vs. V+AB$_\nu$ for the FQ674N filter, assuming high sky backgrounds and a 5 × 5 pixel aperture.

**Figure A.168:** Extended source S/N vs. V+AB$_\nu$ for the FQ674N filter, assuming high sky backgrounds and a source uniformly filling a 1 arcsec$^2$ aperture.

# UVIS FQ727N

**Description**
$CH_4$ 7270 filter.

**Figure A.169: Integrated system throughput for FQ727N.**

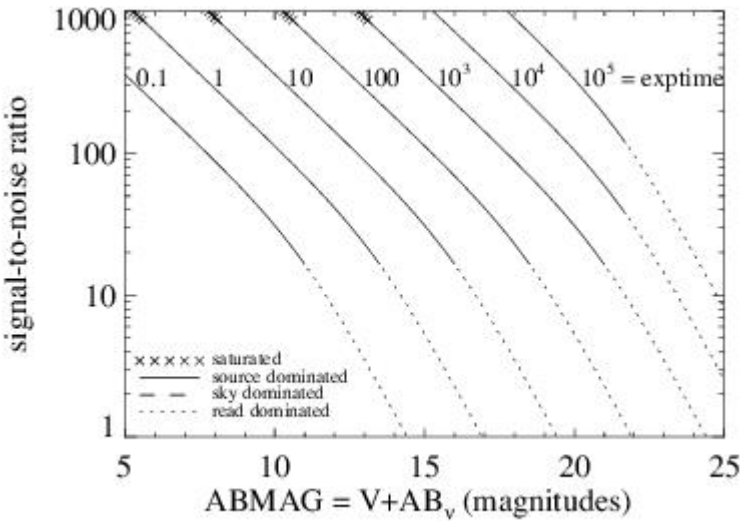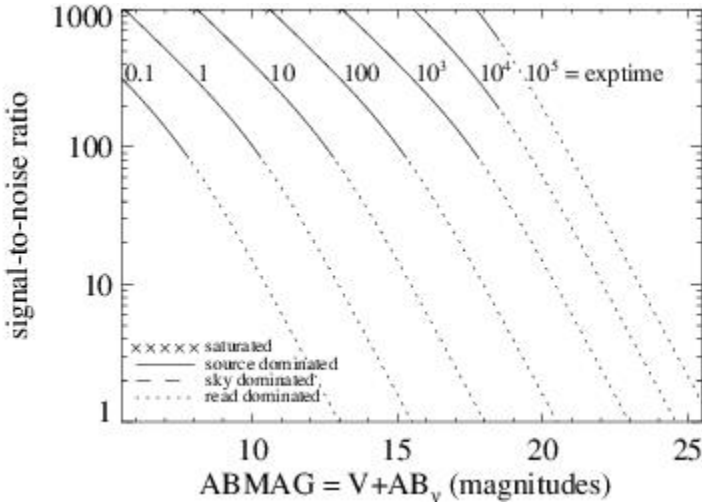Figure A.170: Point source S/N vs. V+AB$_\nu$ for the FQ727N filter, assuming high sky backgrounds and a 5 × 5 pixel aperture.

Figure A.171: Extended source S/N vs. V+AB$_\nu$ for the FQ727N filter, assuming high sky backgrounds and a source uniformly filling a 1 arcsec$^2$ aperture.

# UVIS FQ750N

**Description**
7270 continuum filter.

**Figure A.172: Integrated system throughput for FQ750N.**
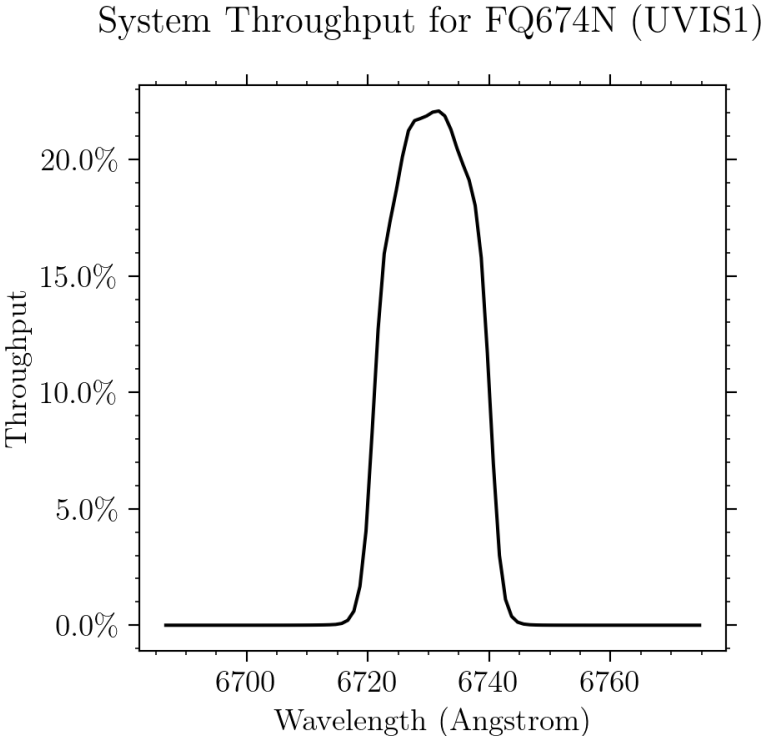


System Throughput for FQ750N (UVIS1)

Figure A.173: Point source S/N vs. V+AB$_v$ for the FQ750N filter, assuming high sky backgrounds and a 5 × 5 pixel aperture.

Figure A.174: Extended source S/N vs. V+AB$_\nu$ for the FQ750N filter, assuming high sky backgrounds and a source uniformly filling a 1 arcsec$^2$ aperture.

# UVIS FQ889N

**Description**

$CH_4$ 25 km-agt filter.

**Figure A.175:** Integrated system throughput for FQ889N.



System Throughput for FQ889N (UVIS1)

**Figure A.176:** Point source S/N vs. V+AB$_\nu$ for the FQ889N filter, assuming high sky backgrounds and a 5 × 5 pixel aperture.
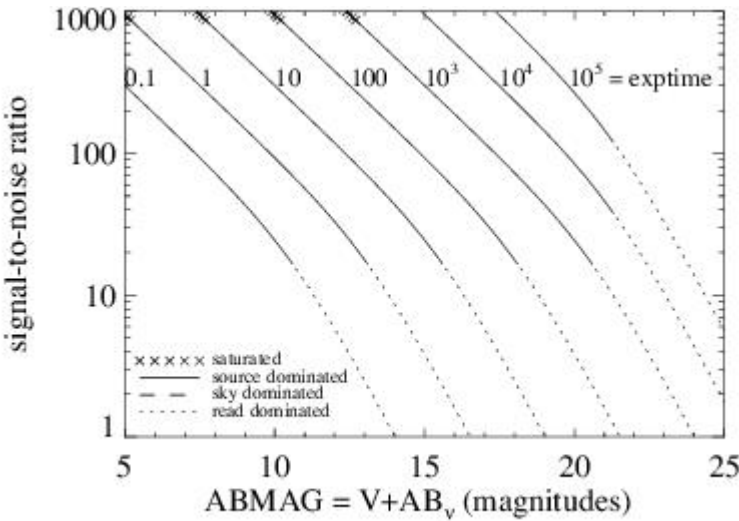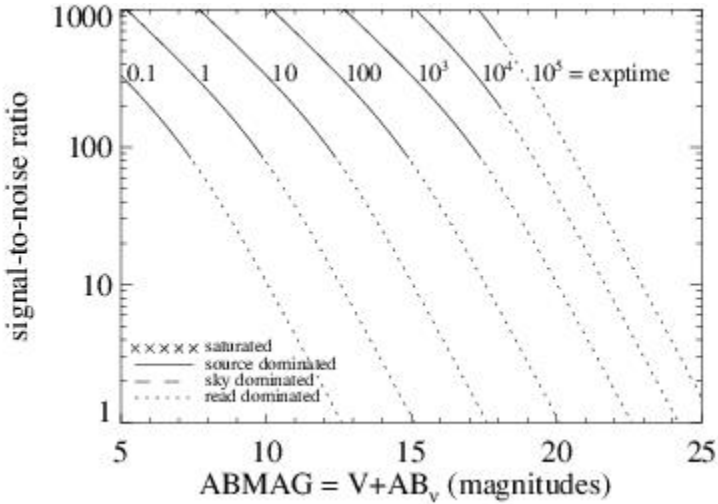
Figure A.177: Extended source S/N vs. V+AB$_\nu$ for the FQ889N filter, assuming high sky backgrounds and a source uniformly filling a 1 arcsec$^2$ aperture.

# UVIS FQ906N

**Description**
$CH_4$ 2.5 km-agt filter.

**Figure A.178:** Integrated system throughput for FQ906N.
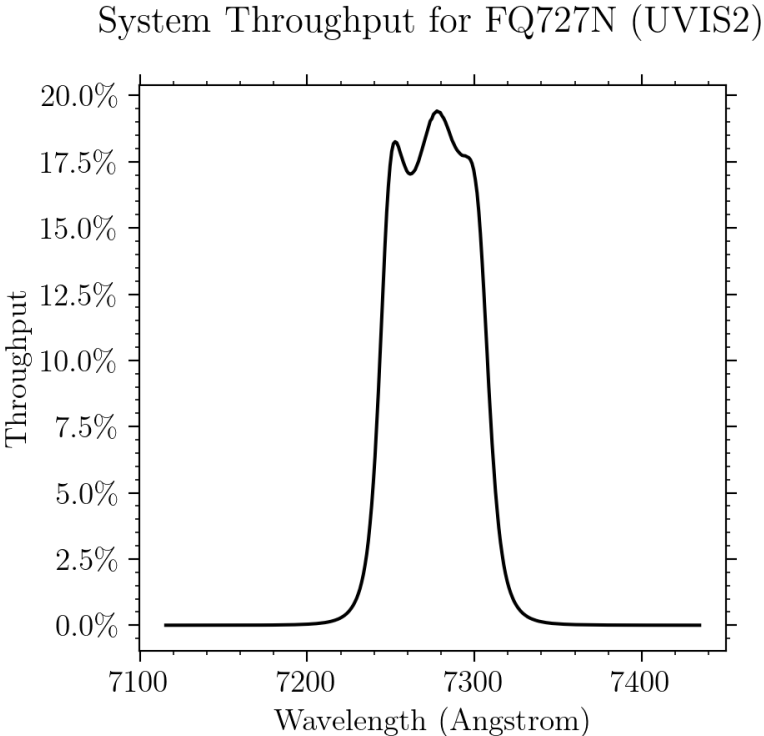


System Throughput for FQ906N (UVIS2)

Figure A.179: Point source S/N vs. V+AB$_\nu$ for the FQ906N filter, assuming high sky backgrounds and a 5 × 5 pixel aperture.

Figure A.180: Extended source S/N vs. V+AB$_\nu$ for the FQ906N filter, assuming high sky backgrounds and a source uniformly filling a 1 arcsec$^2$ aperture.

# UVIS FQ924N

## Description
$CH_4$ 0.25 km-agt filter.

**Figure A.181:** Integrated system throughput for FQ924N.



System Throughput for FQ924N (UVIS2)

Figure A.182: Point source S/N vs. V+AB$_\nu$ for the FQ924N filter, assuming high sky backgrounds and a 5 × 5 pixel aperture.
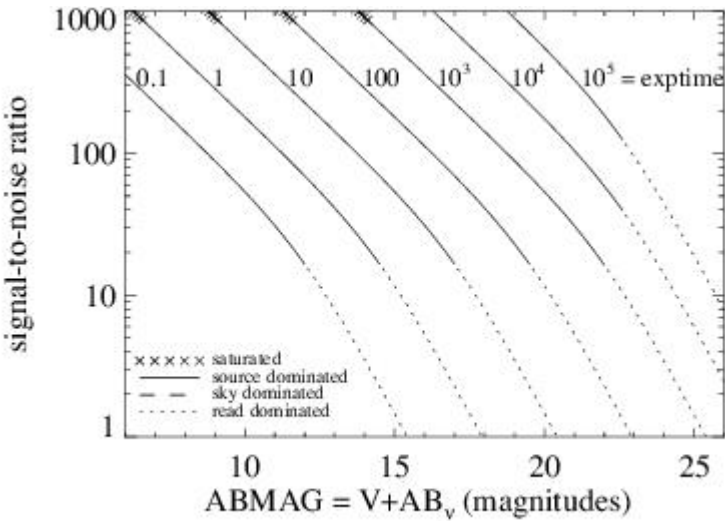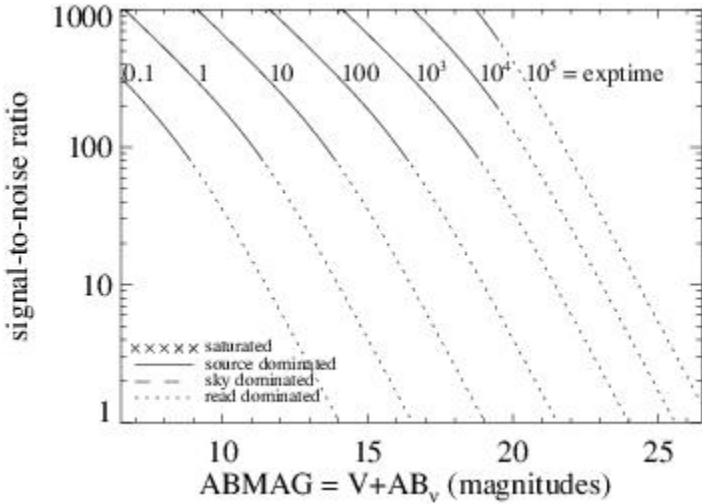
Figure A.183: Extended source S/N vs. V+AB$_v$ for the FQ924N filter, assuming high sky backgrounds and a source uniformly filling a 1 arcsec$^2$ aperture.

# UVIS FQ937N

**Description**
$CH_4$ 0.025 km-agt filter.

**Figure A.184:** Integrated system throughput for FQ937N.
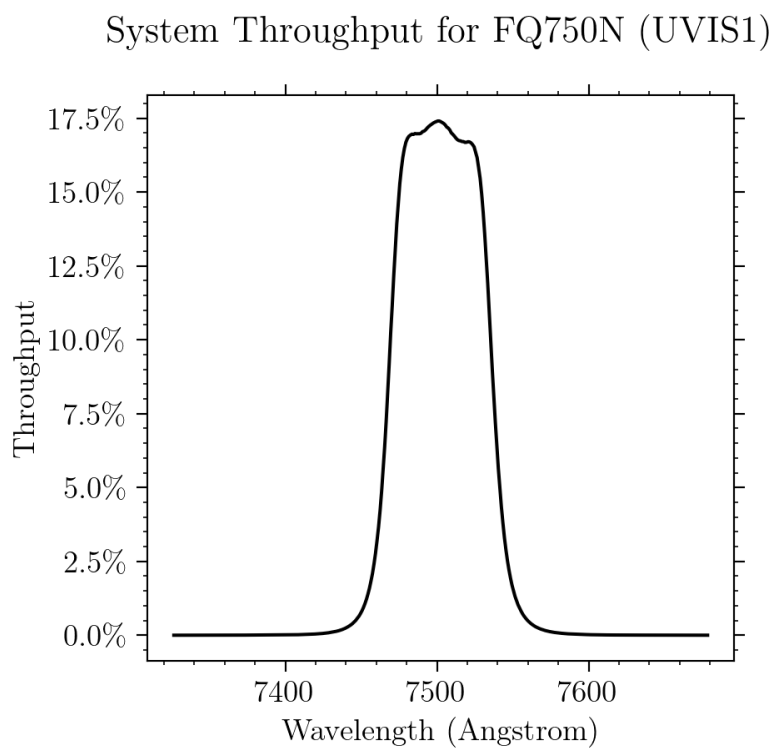


System Throughput for FQ937N (UVIS1)

Figure A.185: Point source S/N vs. V+AB$_\nu$ for the FQ937N filter, assuming high sky backgrounds and a 5 × 5 pixel aperture.

**Figure A.186:** Extended source S/N vs. V+AB$_\nu$ for the FQ937N filter, assuming high sky backgrounds and a source uniformly filling a 1 arcsec$^2$ aperture.

# IR F098M

**Description**
Blue grism reference filter.

**Figure A.187:** Integrated system throughput for F098M.



System Throughput for F098M

Figure A.188: Point source S/N vs. V+AB$_\nu$ for the F098M filter, assuming high sky backgrounds and a 3 × 3 pixel aperture.
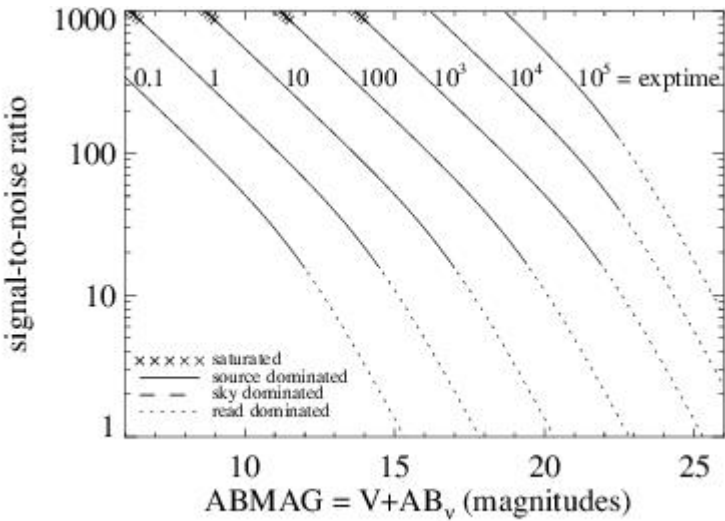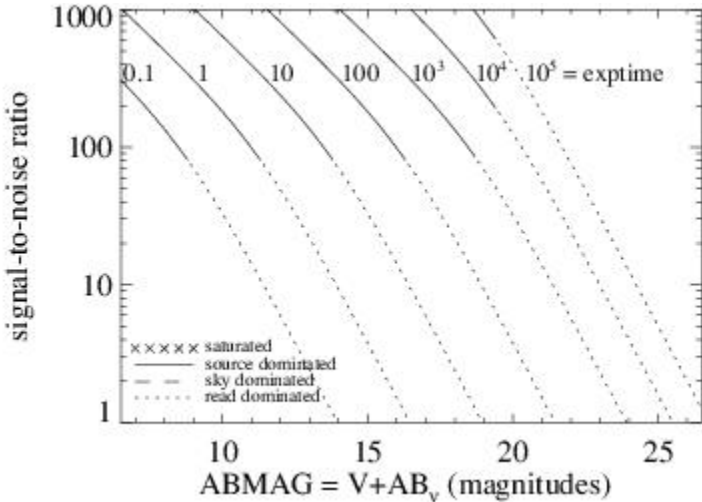
**Figure A.189:** Extended source S/N vs. V+AB$_\nu$ for the F098M filter, assuming high sky backgrounds and a source uniformly filling a 1 arcsec$^2$ aperture.

# IR F105W

**Description**
Wide *Y* filter.

**Figure A.190:** Integrated system throughput for F105W.

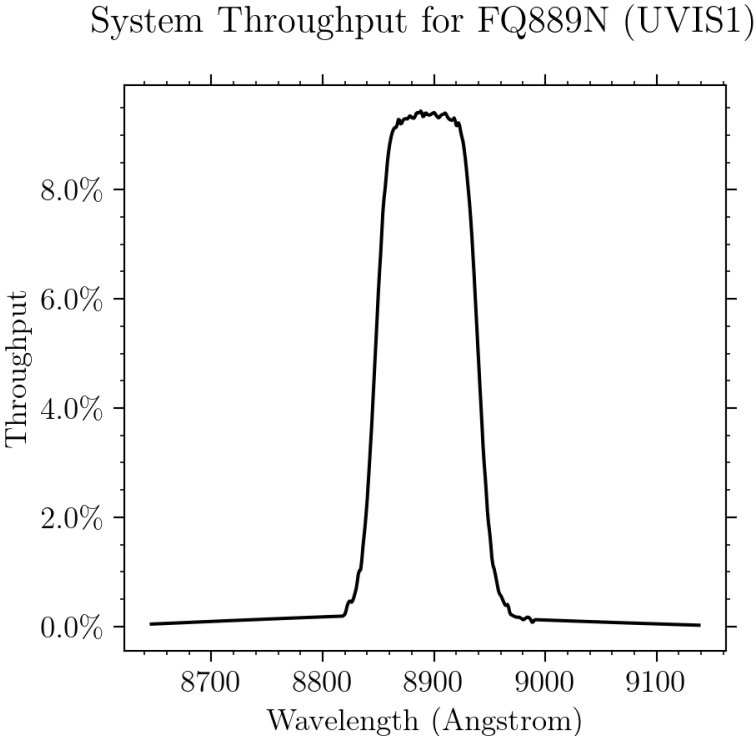**Figure A.191:** Point source S/N vs. V+AB$_\nu$ for the F105W filter, assuming high sky backgrounds and a 3 × 3 pixel aperture.

Figure A.192: Extended source S/N vs. V+AB$_\nu$ for the F105W filter, assuming high sky backgrounds and a source uniformly filling a 1 arcsec$^2$ aperture.

# IR F110W

**Description**
Wide *YJ* filter.

**Figure A.193:** Integrated system throughput for F110W.



System Throughput for F110W

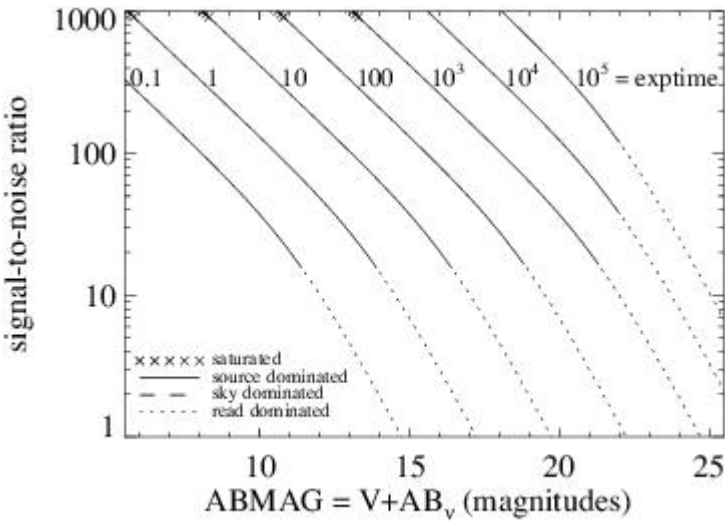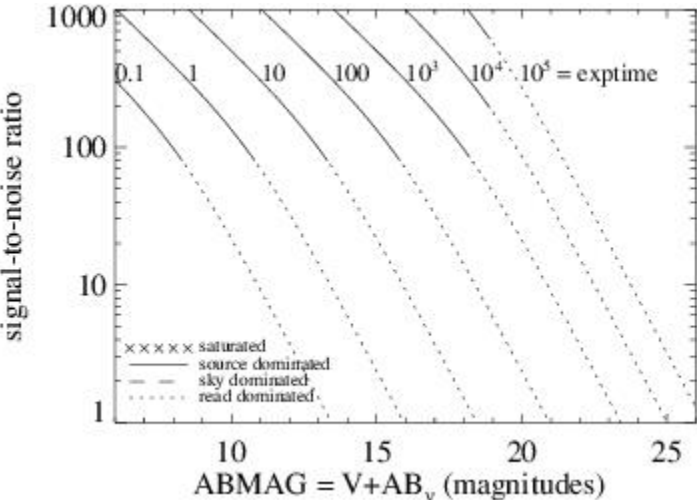Figure A.194: Point source S/N vs. V+AB$_\nu$ for the F110W filter, assuming high sky backgrounds and a 3 × 3 pixel aperture.

Figure A.195: Extended source S/N vs. V+AB$_\nu$ for the F110W filter, assuming high sky backgrounds and a source uniformly filling a 1 arcsec$^2$ aperture.

# IR F125W

**Description**
Wide *J* filter.

**Figure A.196: Integrated system throughput for F125W.**



System Throughput for F125W

Figure A.197: Point source S/N vs. V+AB$_\nu$ for the F125W filter, assuming high sky backgrounds and a 3 × 3 pixel aperture.

Figure A.198: Extended source S/N vs. V+AB$_\nu$ for the F125W filter, assuming high sky backgrounds and a source uniformly filling a 1 arcsec$^2$ aperture.

# IR F126N

**Description**
[Fe II] filter.

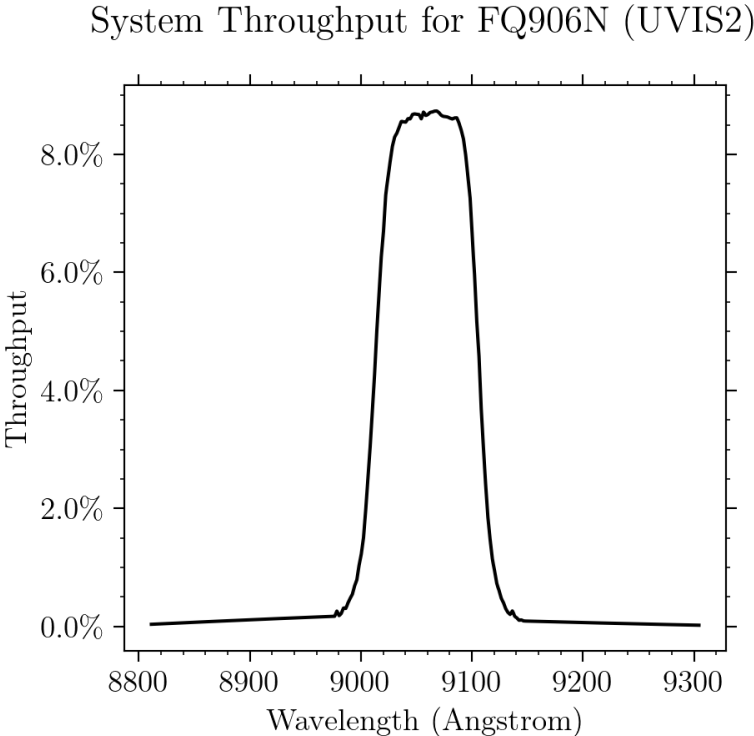**Figure A.199: Integrated system throughput for F126N.**



System Throughput for F126N

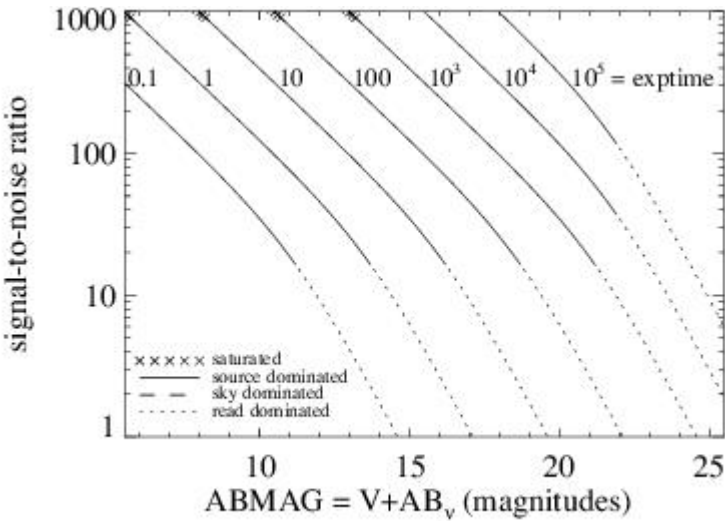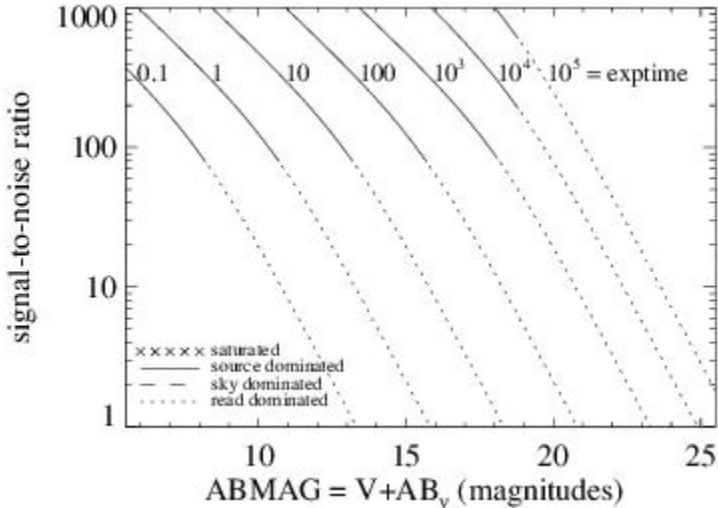Figure A.200: Point source S/N vs. V+AB$_\nu$ for the F126N filter, assuming high sky backgrounds and a 3 × 3 pixel aperture.

Figure A.201: Extended source S/N vs. V+AB$_\nu$ for the F126N filter, assuming high sky backgrounds and a source uniformly filling a 1 arcsec$^2$ aperture.

# IR F127M

**Description**
$H_2O/CH_4$ continuum filter.

**Figure A.202: Integrated system throughput for F127M.**



System Throughput for F127M

Figure A.203: Point source S/N vs. V+AB$_\nu$ for the F127M filter, assuming high sky backgrounds and a 3 × 3 pixel aperture.

Figure A.204: Extended source S/N vs. V+AB$_\nu$ for the F127M filter, assuming high sky backgrounds and a source uniformly filling a 1 arcsec$^2$ aperture.

# IR F128N

**Description**
Paschen β filter.

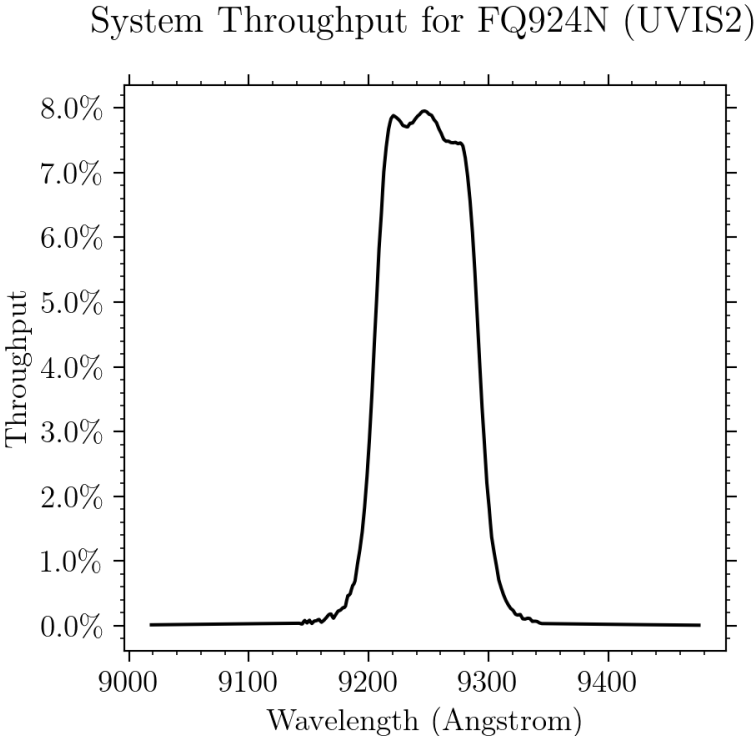**Figure A.205: Integrated system throughput for F128N.**



System Throughput for F128N

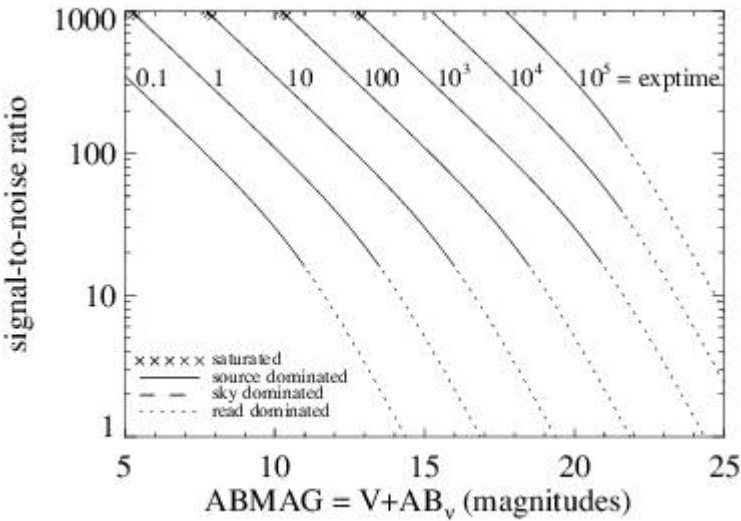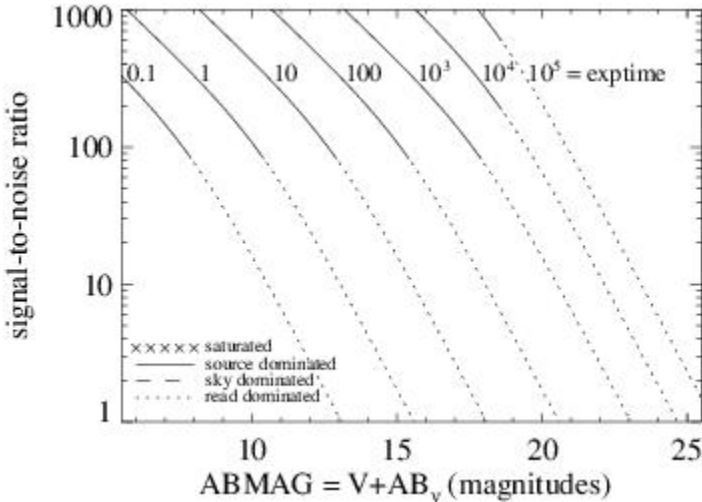Figure A.206: Point source S/N vs. V+AB$_\nu$ for the F128N filter, assuming high sky backgrounds and a 3 × 3 pixel aperture.

Figure A.207: Extended source S/N vs. V+AB$_\nu$ for the F128N filter, assuming high sky backgrounds and a source uniformly filling a 1 arcsec$^2$ aperture.
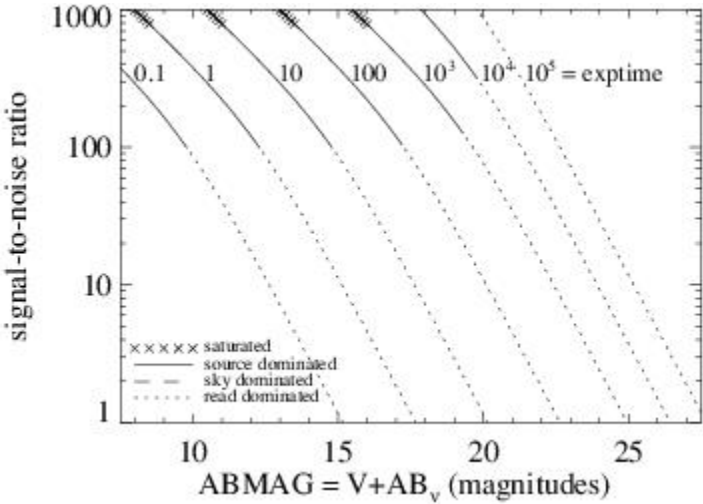
# IR F130N

**Description**
Paschen β continuum filter.

**Figure A.208: Integrated system throughput for F130N.**



System Throughput for F130N
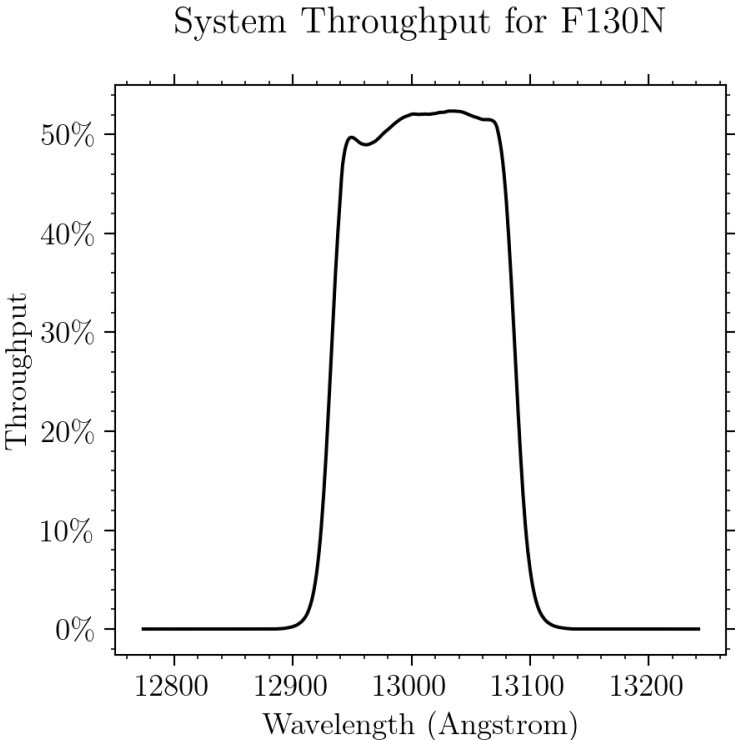
Figure A.209: Point source S/N vs. V+AB$_\nu$ for the F130N filter, assuming high sky backgrounds and a 3 × 3 pixel aperture.
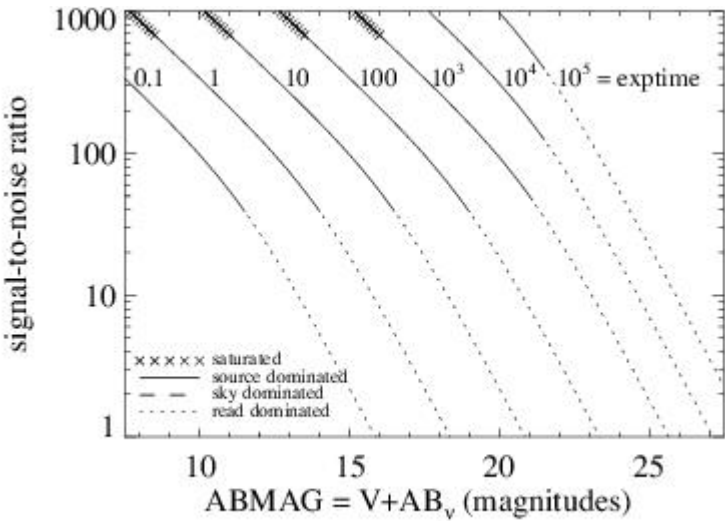
Figure A.210: Extended source S/N vs. V+AB$_\nu$ for the F130N filter, assuming high sky backgrounds and a source uniformly filling a 1 arcsec$^2$ aperture.
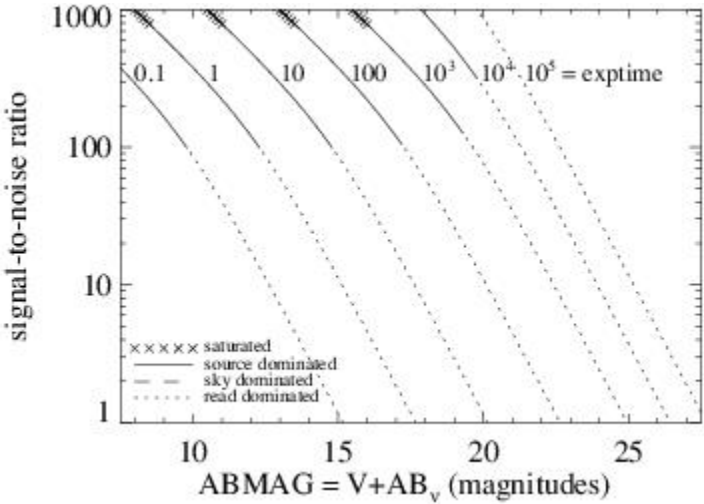
# IR F132N

Description
Paschen β (redshifted) filter.

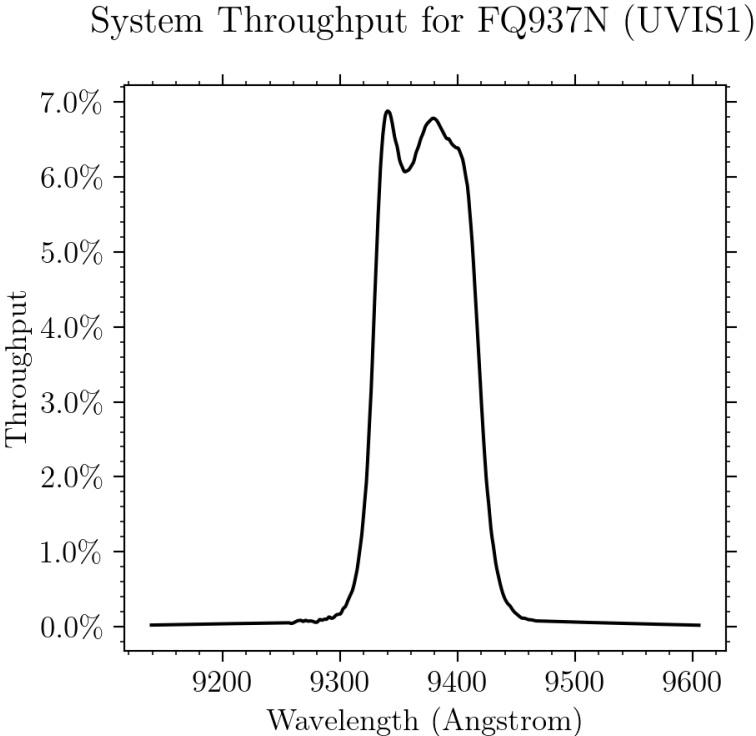**Figure A.211: Integrated system throughput for F132N.**



System Throughput for F132N
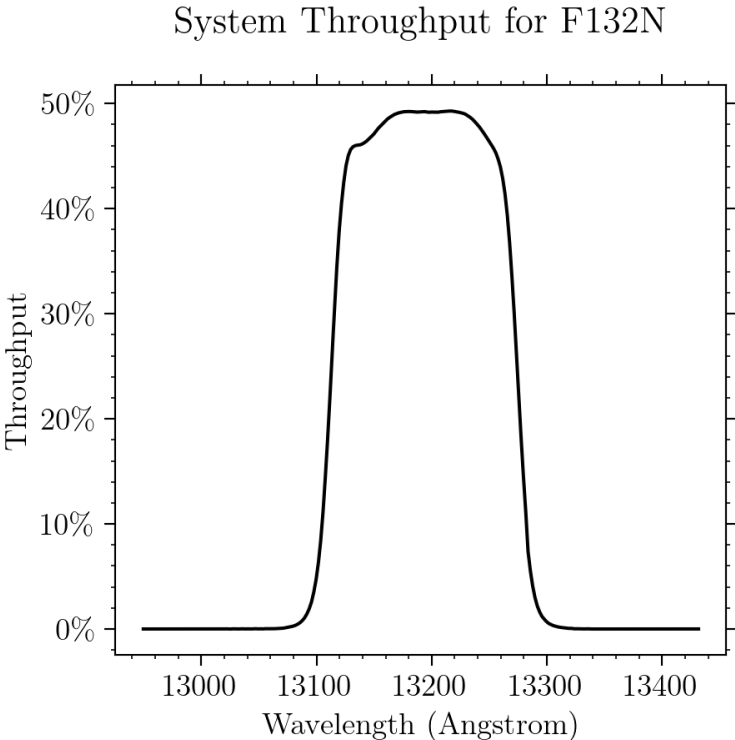
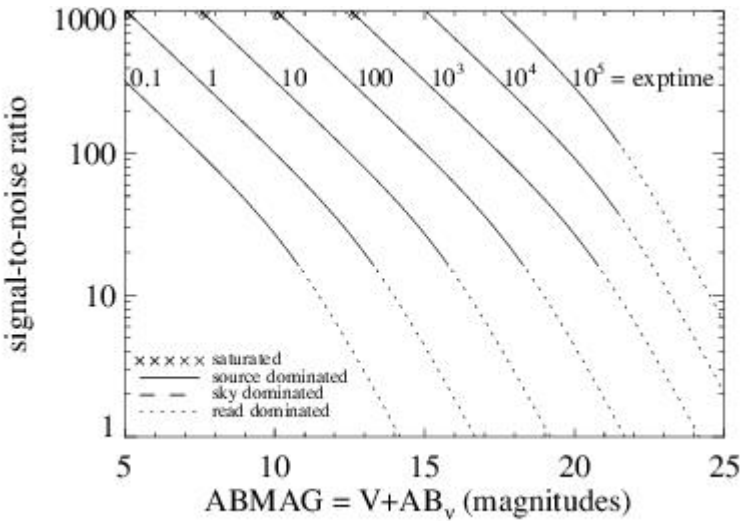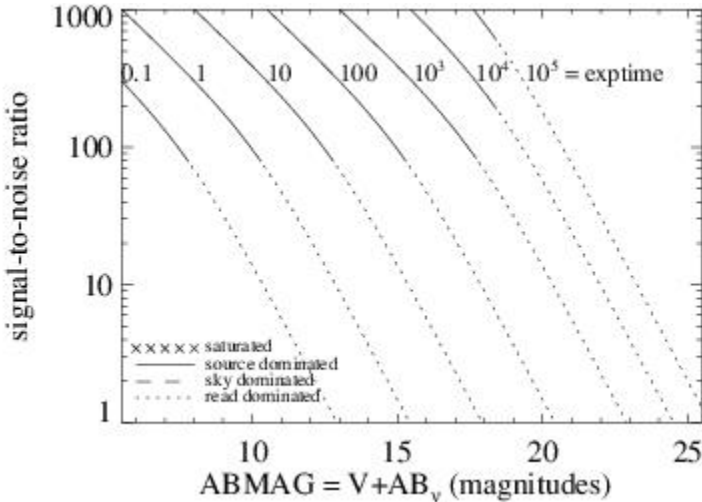Figure A.212: Point source S/N vs. V+AB$_\nu$ for the F132N filter, assuming high sky backgrounds and a 3 × 3 pixel aperture.
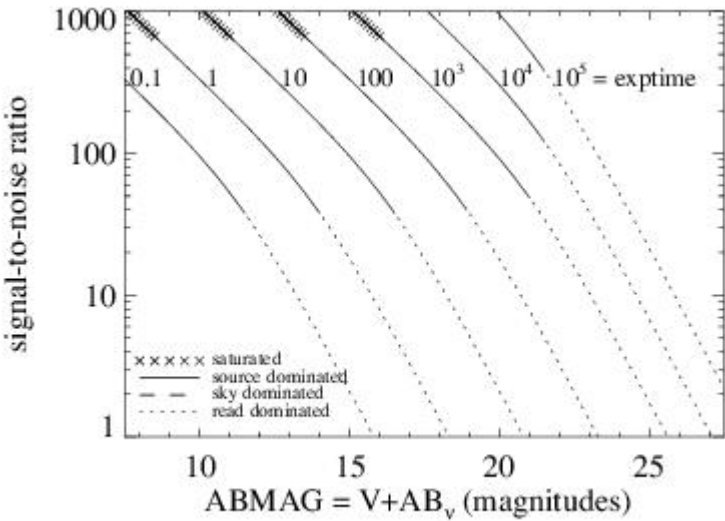
Figure A.213: Extended source S/N vs. V+AB$_\nu$ for the F132N filter, assuming high sky backgrounds and a source uniformly filling a 1 arcsec$^2$ aperture.
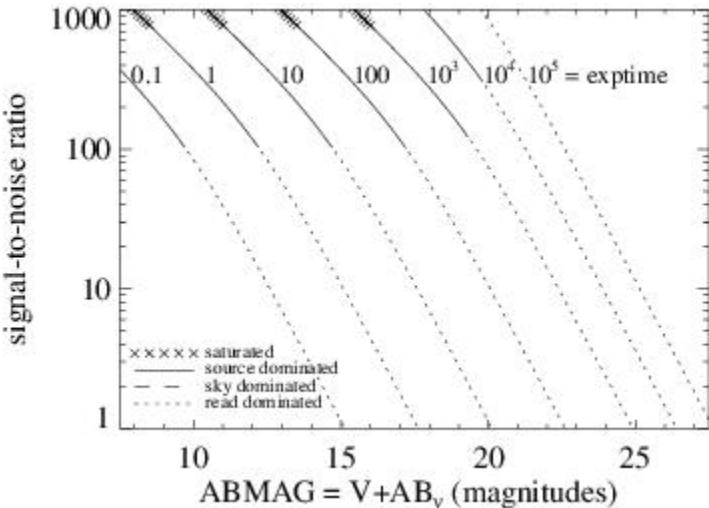
# IR F139M

**Description**
$H_2O/CH_4$ line filter.

**Figure A.214: Integrated system throughput for F139M.**



System Throughput for F139M
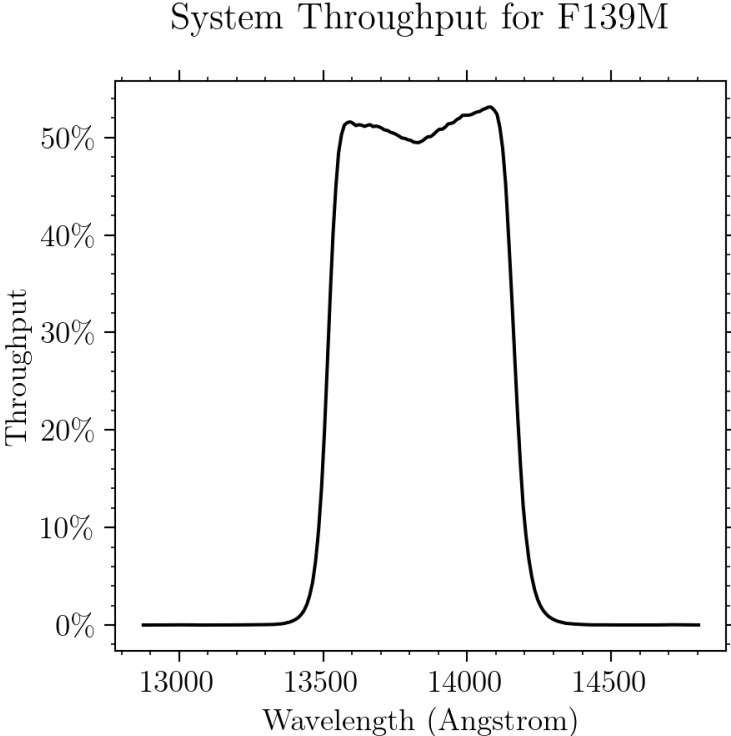
Figure A.215: Point source S/N vs. V+AB$_\nu$ for the F139M filter, assuming high sky backgrounds and a 3 × 3 pixel aperture.
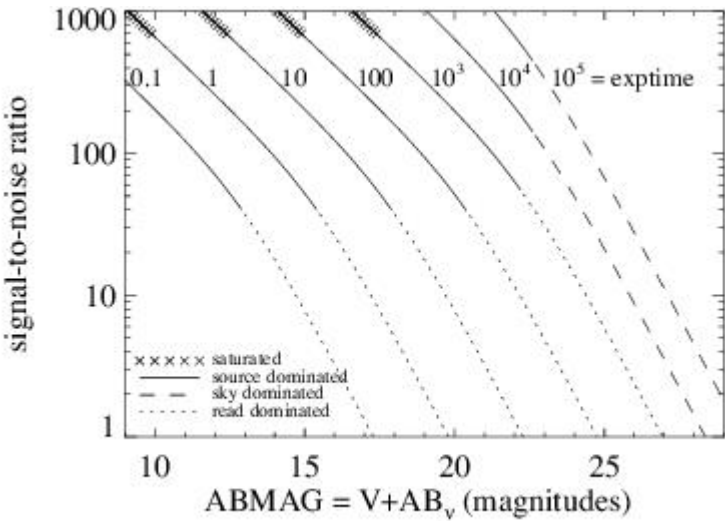
**Figure A.216:** Extended source S/N vs. V+AB$_\nu$ for the F139M filter, assuming high sky backgrounds and a source uniformly filling a 1 arcsec$^2$ aperture.
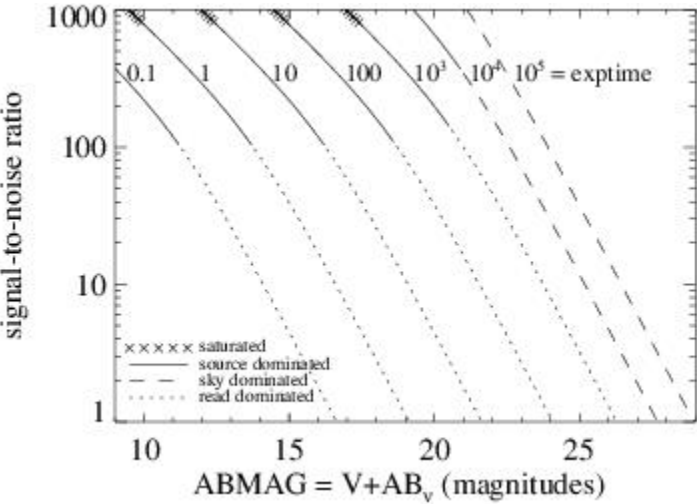
# IR F140W

**Description**
Wide *JH* gap; red grism reference filter.

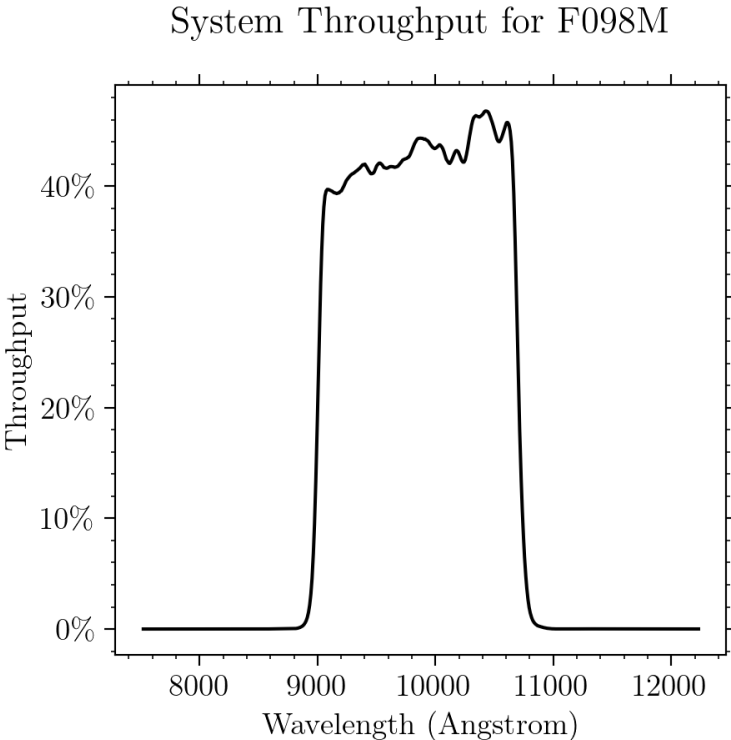**Figure A.217: Integrated system throughput for F140W.**



System Throughput for F140W
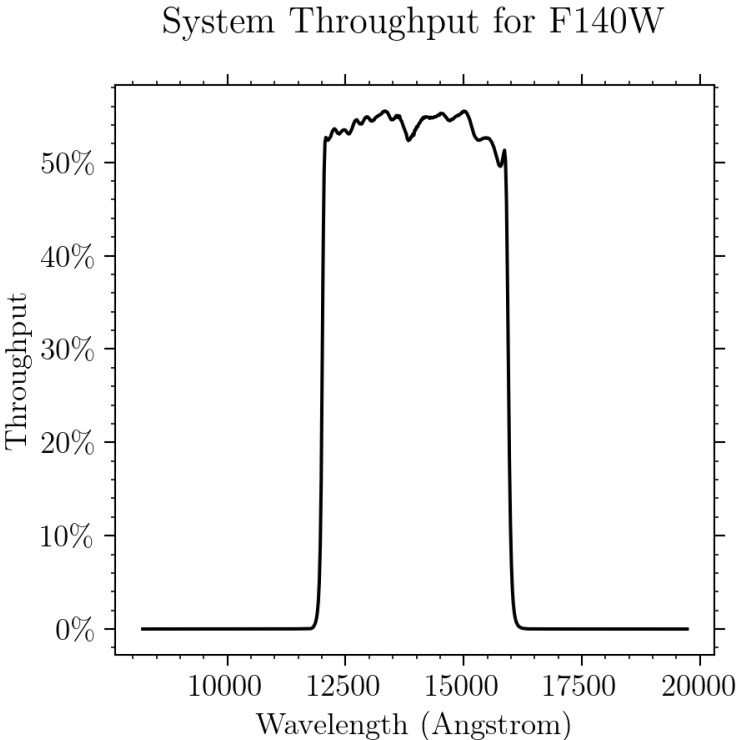
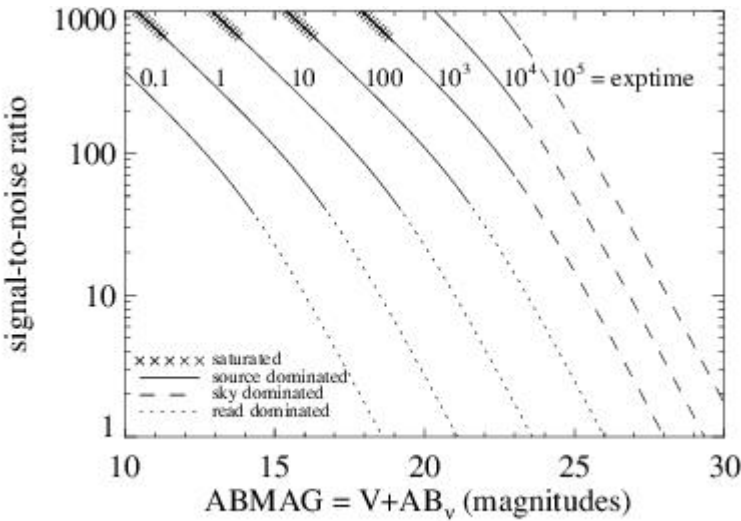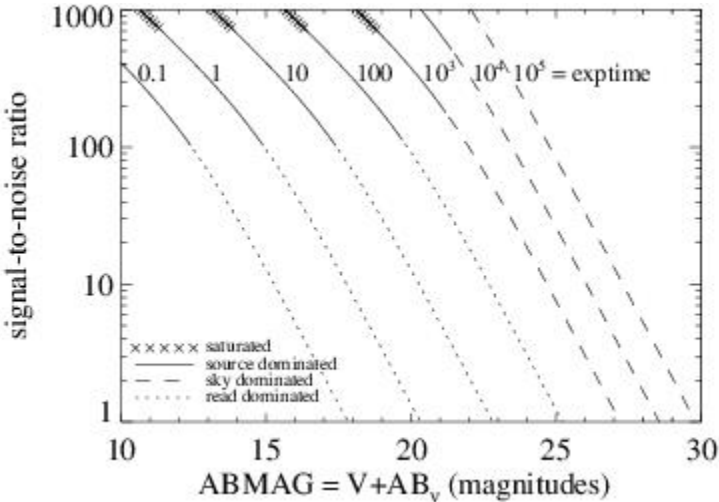Figure A.218: Point source S/N vs. V+AB$_\nu$ for the F140W filter, assuming high sky backgrounds and a 3 × 3 pixel aperture.
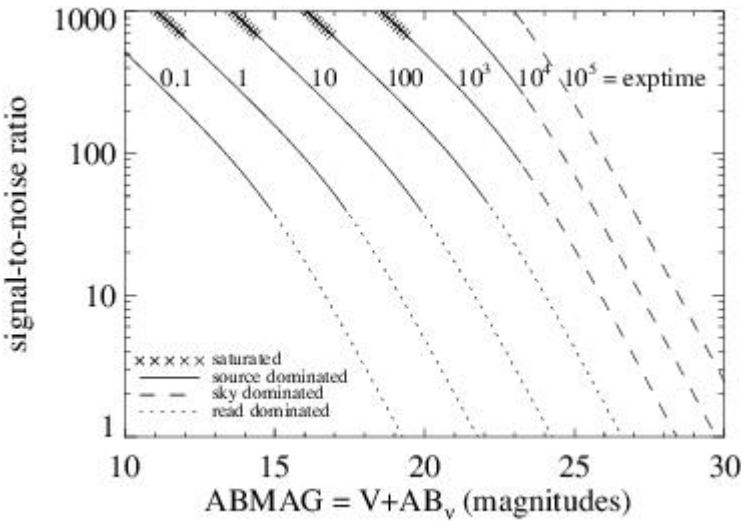
Figure A.219: Extended source S/N vs. V+AB$_\nu$ for the F140W filter, assuming high sky backgrounds and a source uniformly filling a 1 arcsec$^2$ aperture.
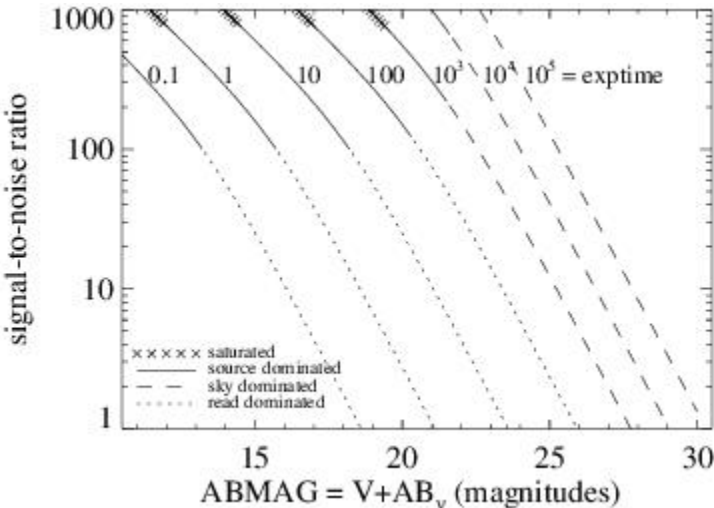
# IR F153M

**Description**

$H_2O$ and $NH_3$ filter.

**Figure A.220:** Integrated system throughput for F153M.



System Throughput for F153M
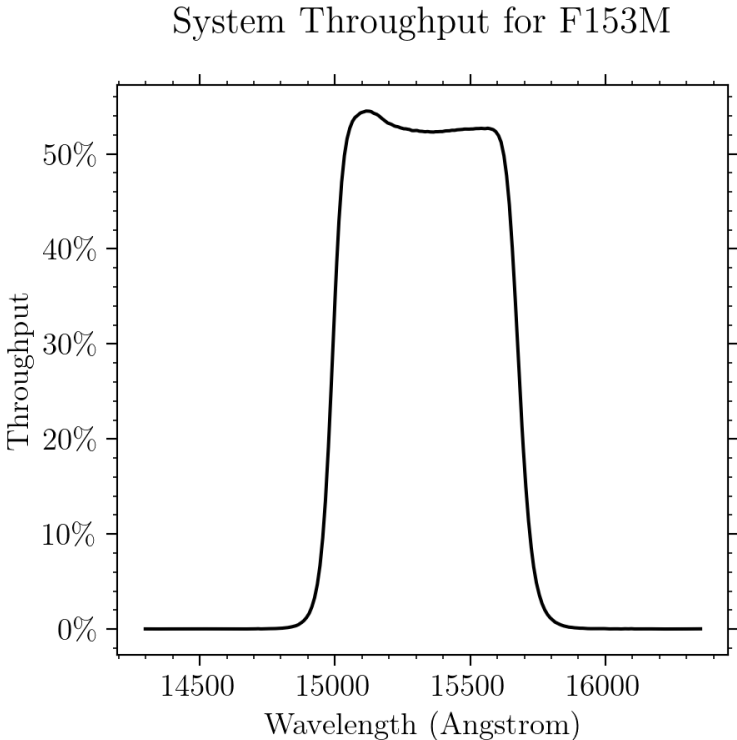
Figure A.221: Point source S/N vs. V+AB$_\nu$ for the F153M filter, assuming high sky backgrounds and a 3×3 pixel aperture.
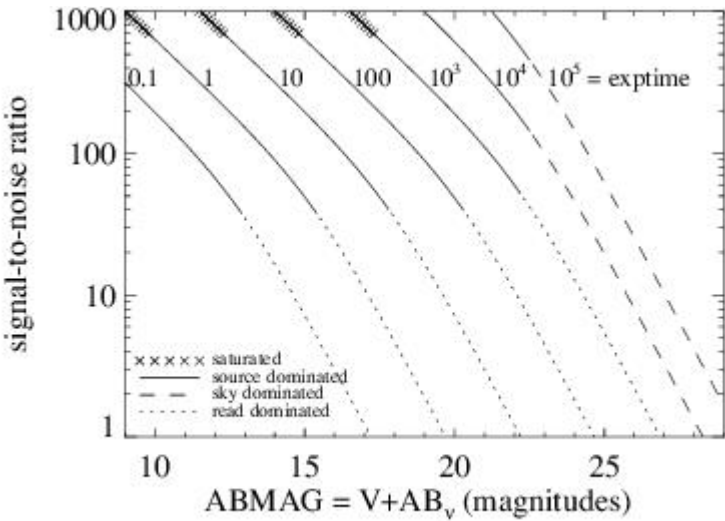
Figure A.222: Extended source S/N vs. V+AB$_\nu$ for the F153M filter, assuming high sky backgrounds and a source uniformly filling a 1 arcsec2aperture.
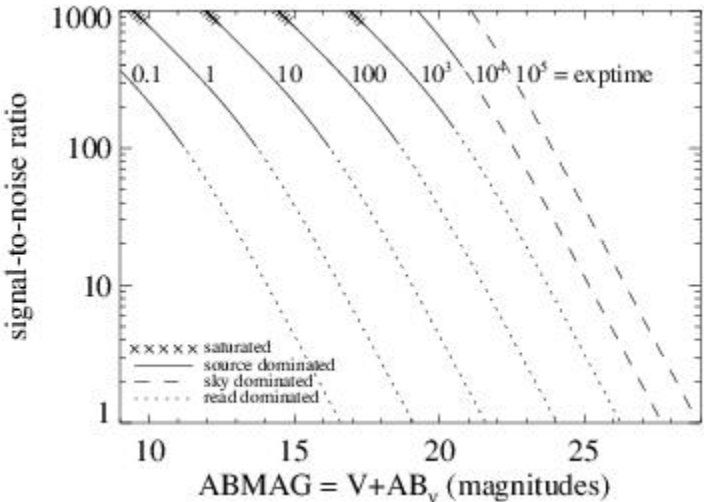
# IR F160W

**Description**
WFC3 *H* filter.

**Figure A.223:** Integrated system throughput for F160W.
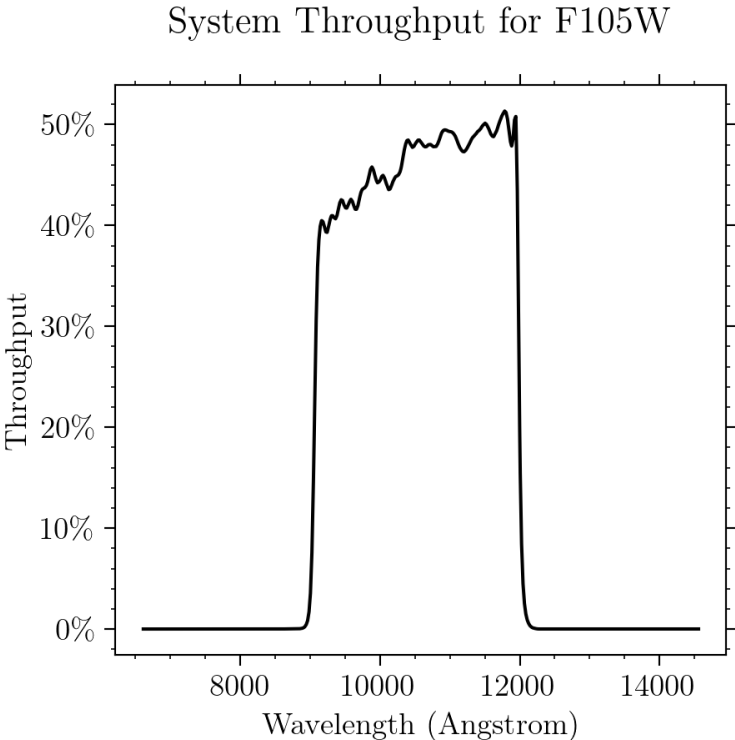


System Throughput for F160W
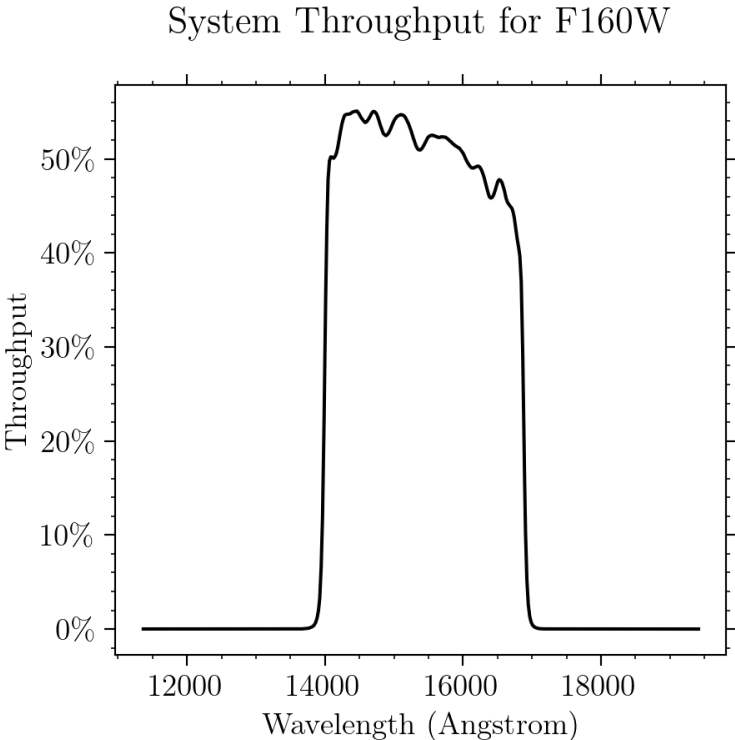
**Figure A.224:** Point source S/N vs. V+AB$_\nu$ for the F160W filter, assuming high sky backgrounds and a 3 × 3 pixel aperture.
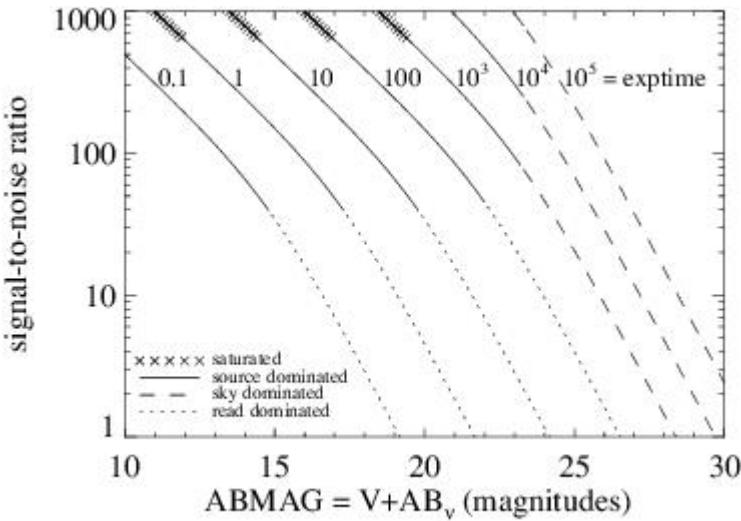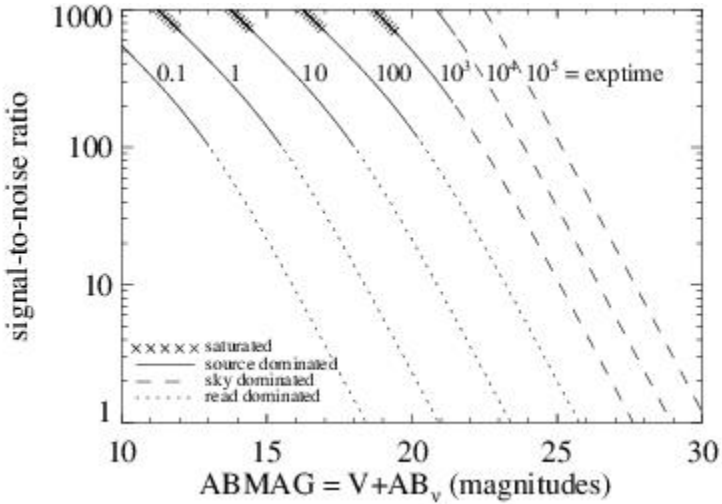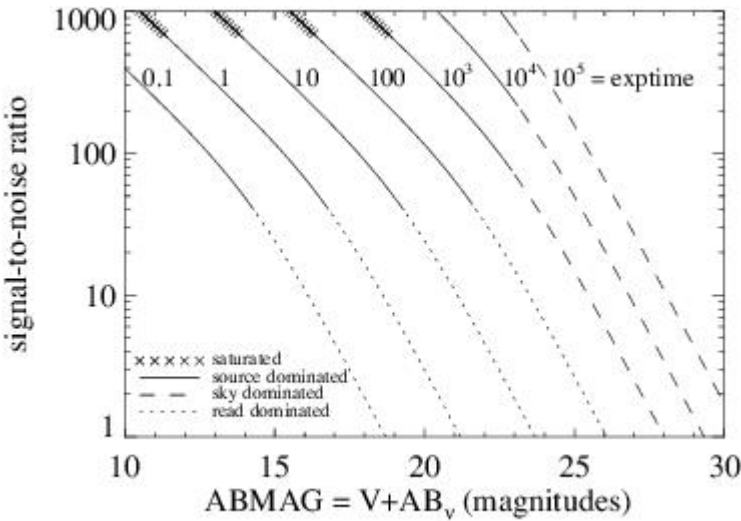
Figure A.225: Extended source S/N vs. V+AB$_\nu$ for the F160W filter, assuming high sky backgrounds and a source uniformly filling a 1 arcsec$^2$ aperture.
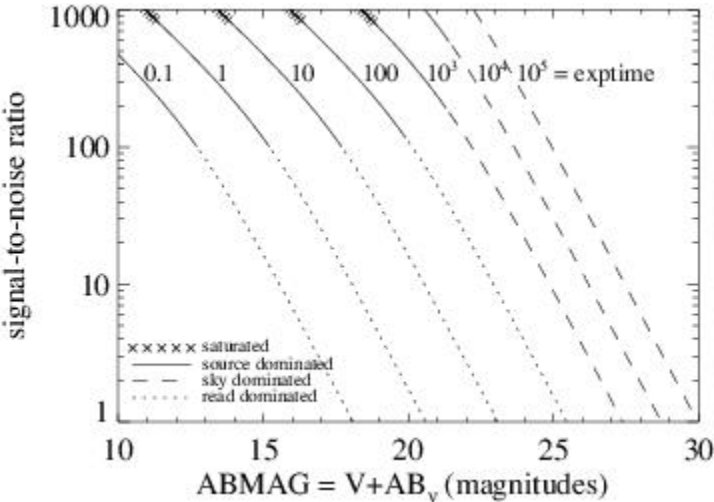
# IR F164N

**Description**
[Fe II] filter.

**Figure A.226:** Integrated system throughput for F164N.



System Throughput for F164N
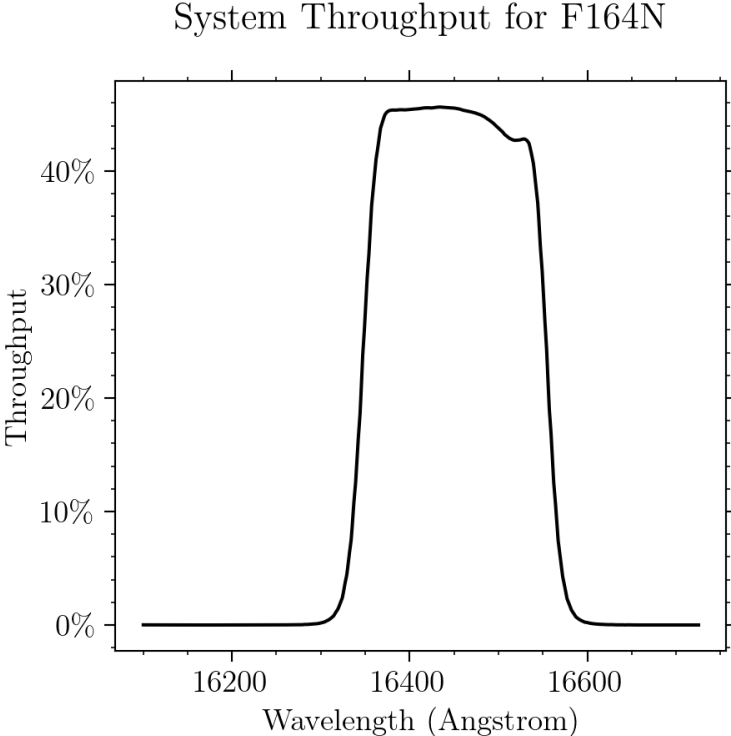
Figure A.227: Point source S/N vs. V+AB$_\nu$ for the F164N filter, assuming high sky backgrounds and a 3 × 3 pixel aperture.
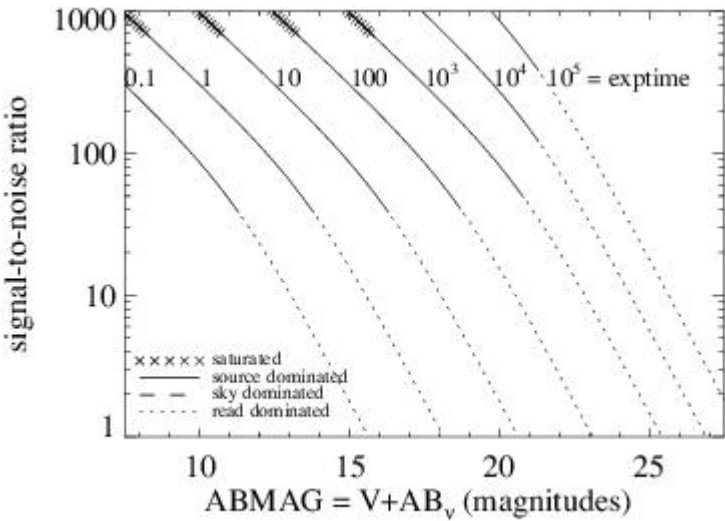
Figure A.228: Extended source S/N vs. V+AB$_\nu$ for the F164N filter, assuming high sky backgrounds and a source uniformly filling a 1 arcsec$^2$ aperture.
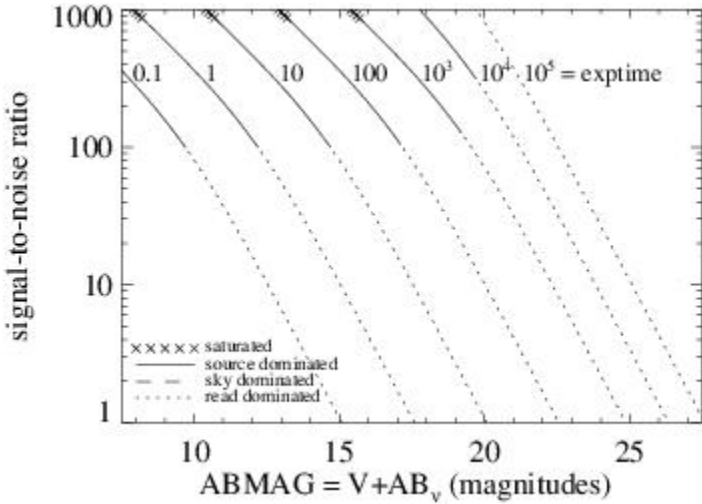
# IR F167N

**Description**
[Fe II] continuum filter.

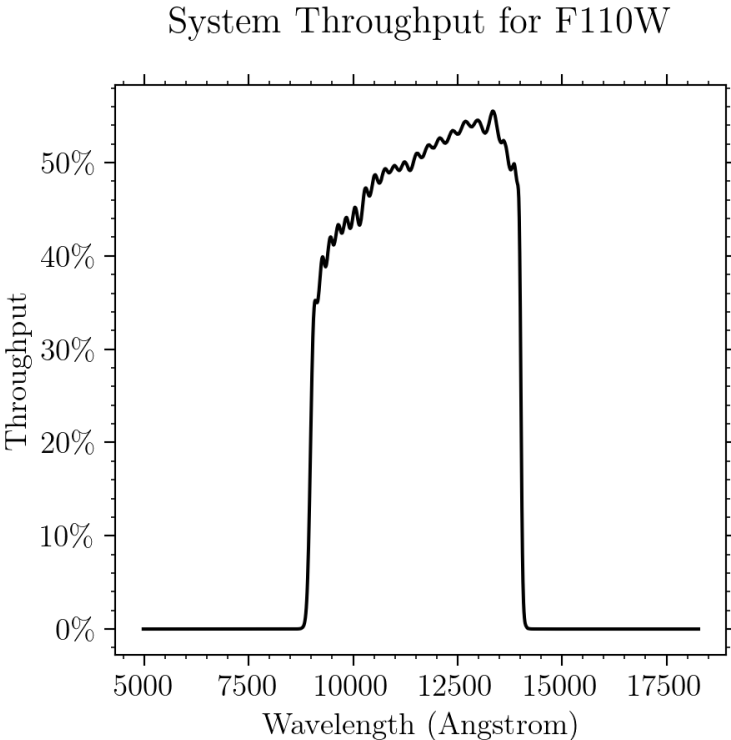**Figure A.229: Integrated system throughput for F167N.**



System Throughput for F167N
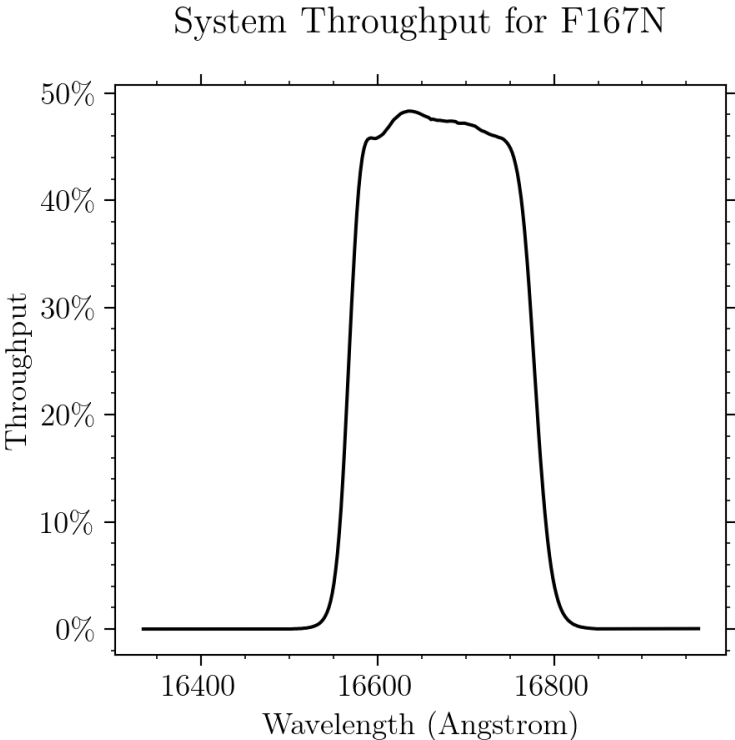
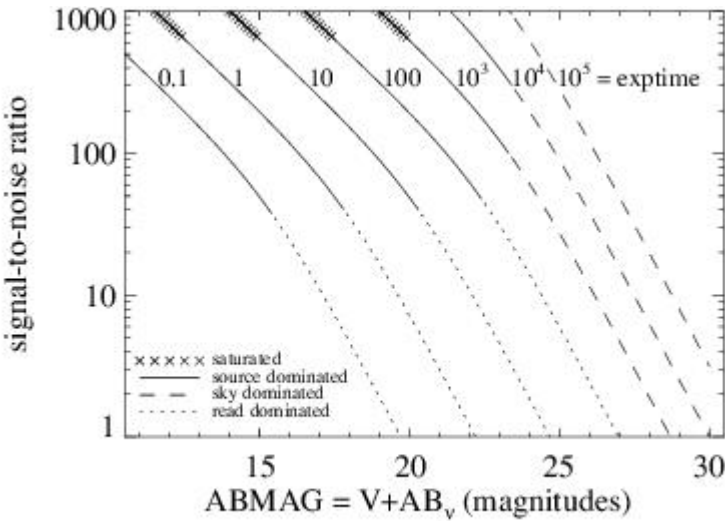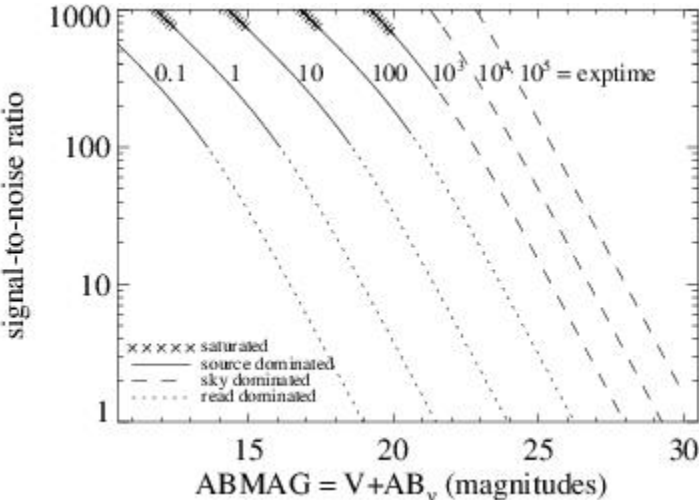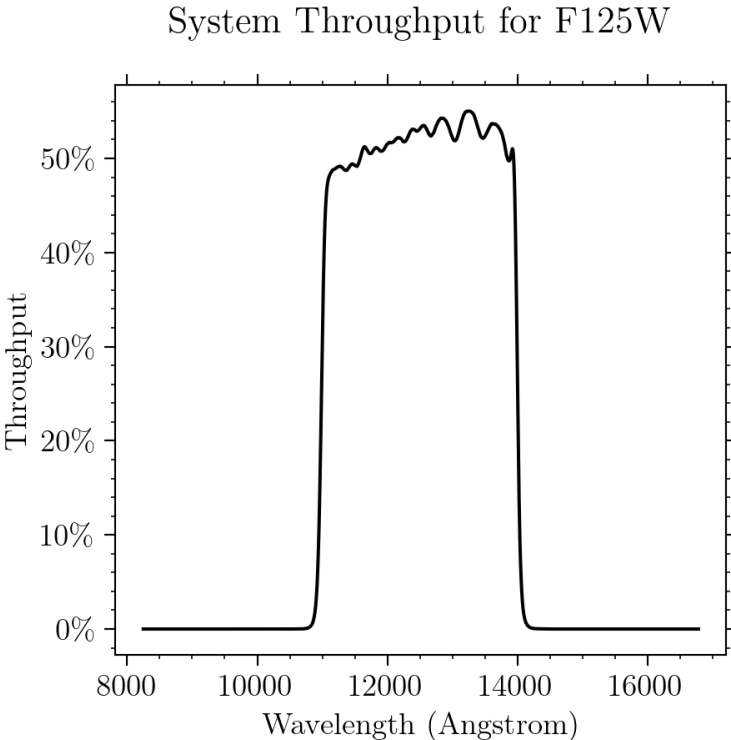Figure A.230: Point source S/N vs. V+AB$_\nu$ for the F167N filter, assuming high sky backgrounds and a 3 × 3 pixel aperture.
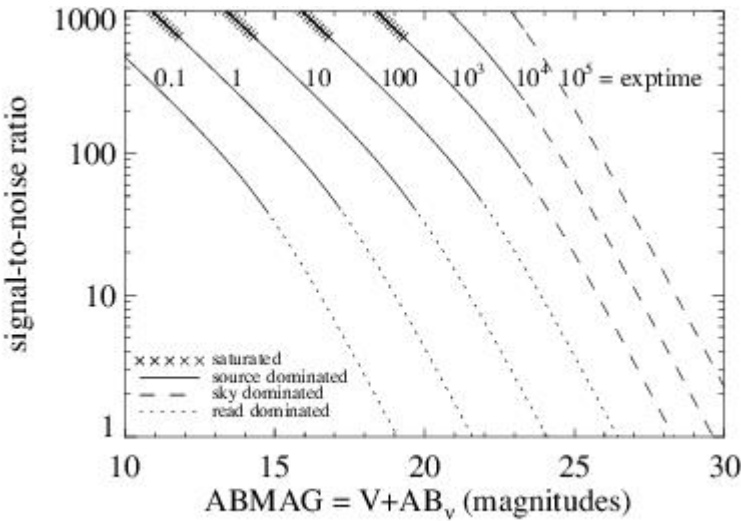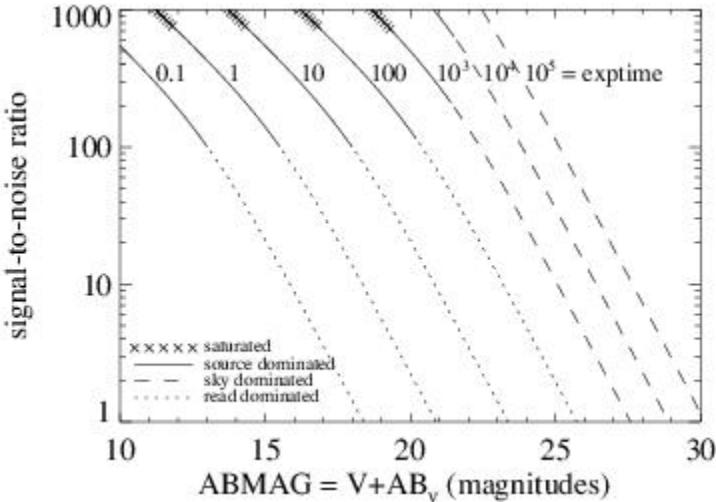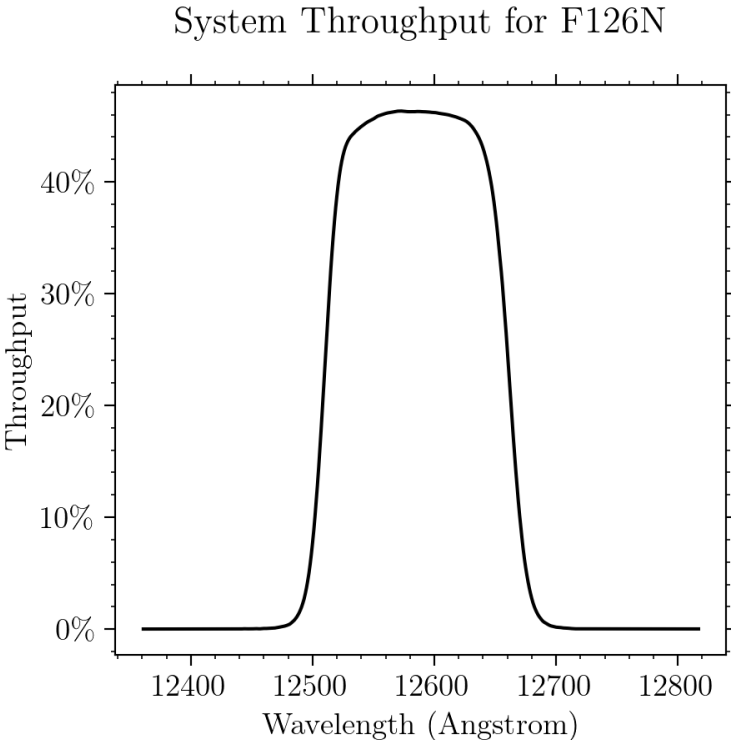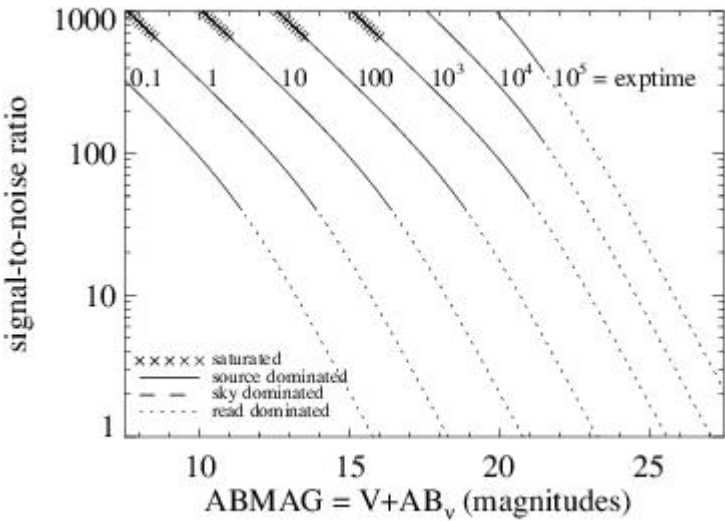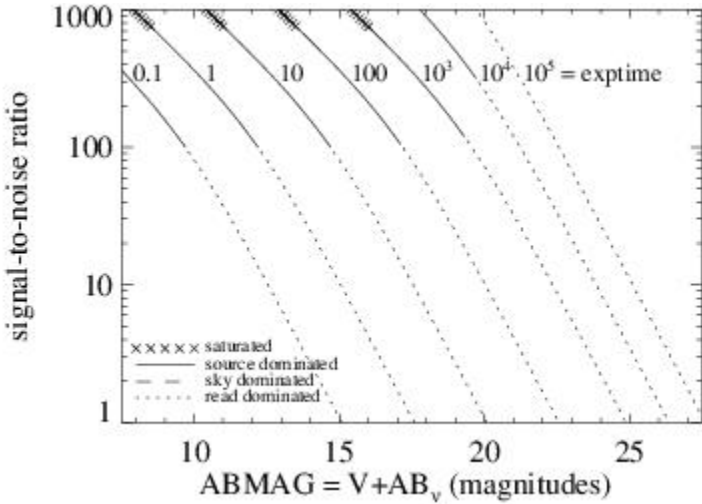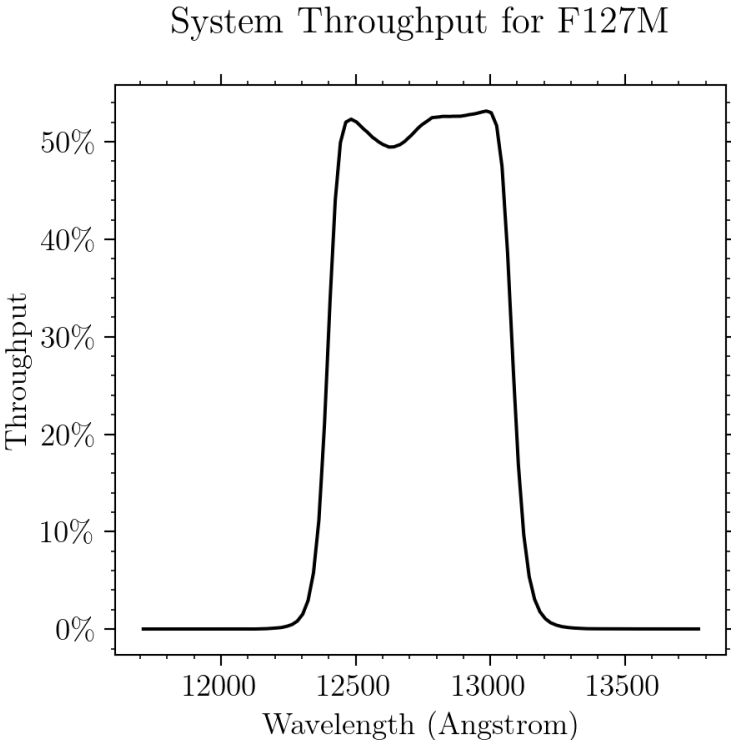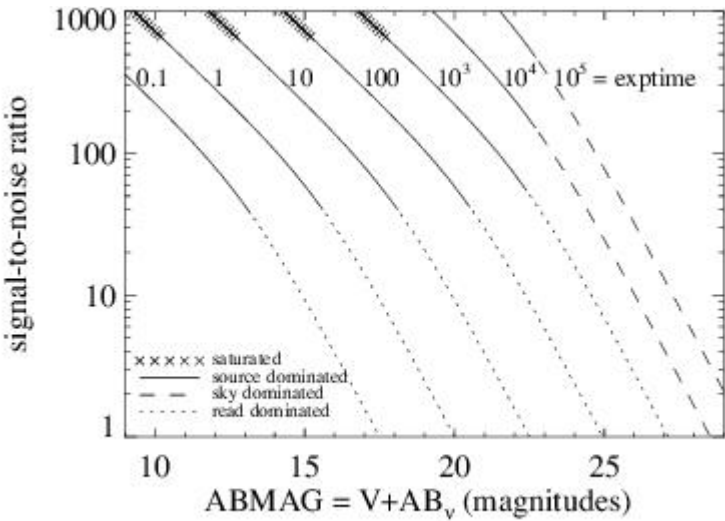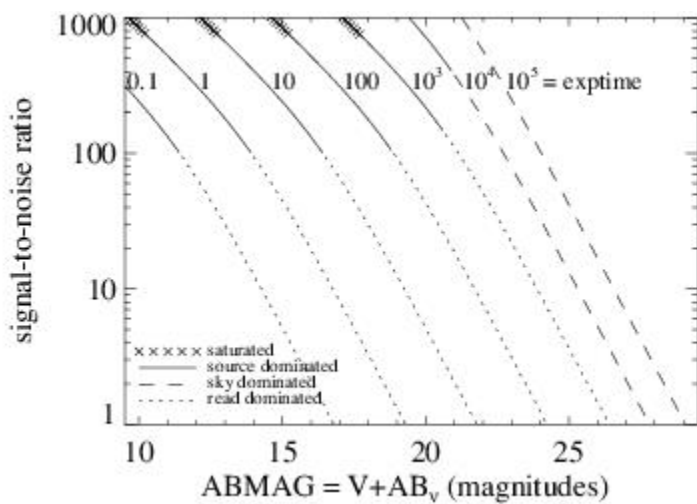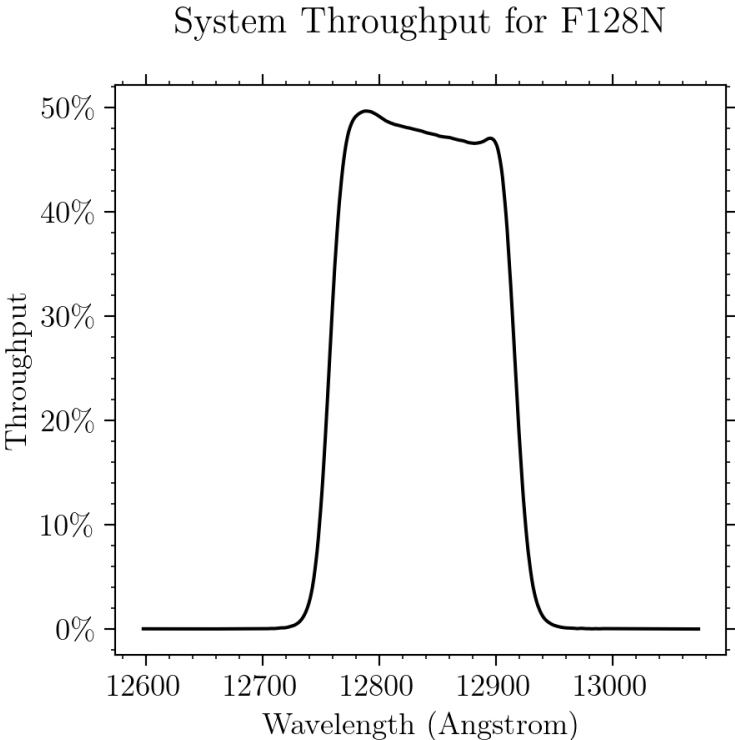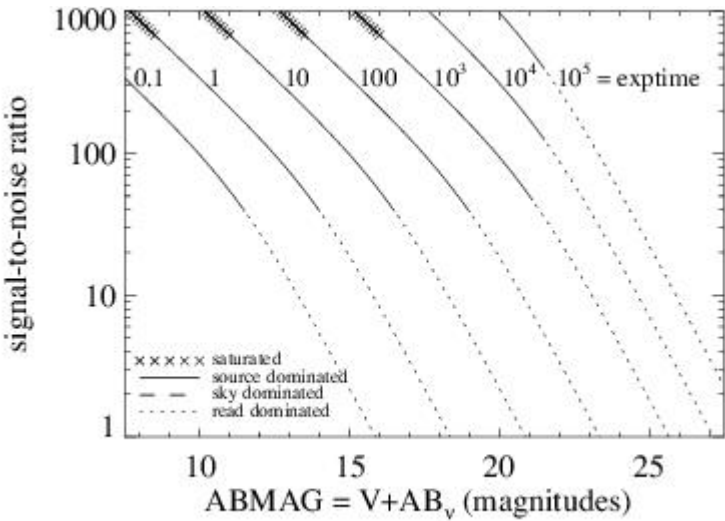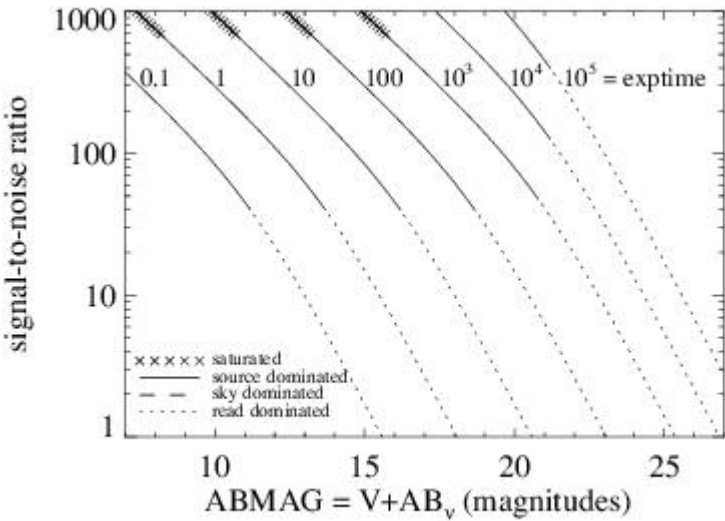
Figure A.231: Extended source S/N vs. V+AB$_\nu$ for the F167N filter, assuming high sky backgrounds and a source uniformly filling a 1 arcsec$^2$ aperture.
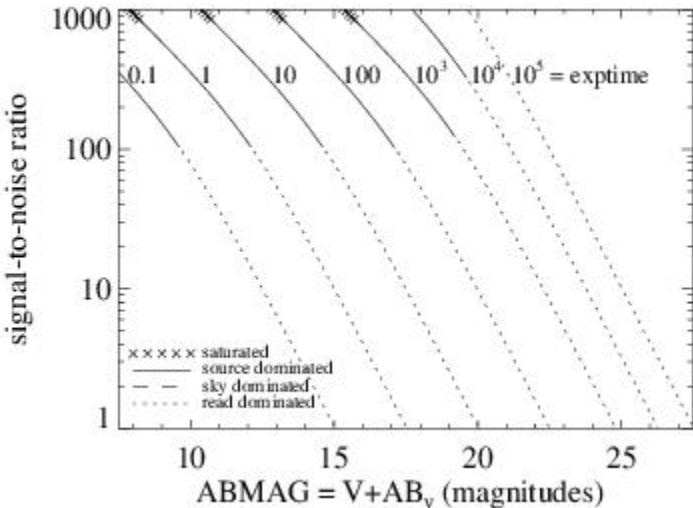
# Appendix B: Geometric Distortion

**Appendix Contents**

# B.1 Overview

WFC3 images exhibit significant geometric distortion, similar to that seen in ACS images. The required folding, with powered optics, of the light paths in both channels to fit within the instrument's optical-bench envelope results in substantial tilts of the focal surfaces with respect to the chief rays. The WFC3 UVIS detector is tilted at ~21° about one of its diagonals, producing a rhomboidal elongation of ~7%. The IR detector has a ~24° tilt about its *x*-axis, creating a rectangular elongation of ~10%.

If these were the only distortions they would not present much difficulty: their impacts on photometry, mosaicking, or dithering could be computed simply. More problematic, however, is the variation of plate scale across each detector. For the WFC3 UVIS and IR channels, this variation in plate scale amounts to a change of 3.5% in *x* and *y*, and 2% in *x* and 6% in *y*, respectively, over the full field. Hence the area on the sky covered by a pixel varies, by about 7% for the UVIS channel and about 8% for the IR channel. Allowance for this change in plate scale must be made in photometric reductions of WFC3 data that have not been corrected for distortion. Further details are available in WFC3 ISR 2010-08 and at the pixel area map section of the WFC3 website: http://www.stsci.edu/hst /instrumentation/wfc3/data-analysis/pixel-area-maps

Dithering and mosaicking are complicated by the fact that an integer pixel shift near the center of the detector translates into a non-integer displacement for pixels in other locations. Even this is not a fundamental difficulty, but implies some computational complexity in registering and correcting images. All of these considerations make it necessary to obtain accurate measurements of the distortions. The orientations of the WFC3 detector edges for both detectors are at approximately 45° with respect to the V2 and V3 coordinate axes of the telescope. Figure 2.2 shows the WFC3 apertures in the telescope's V2,V3 reference frame. For a telescope roll angle of zero this would correspond to an on-sky view with the V3 axis aligned with north and the V2 axis with east. See Section 6.2.2 of the *Phase II Proposal Instructions*, which gives detailed information on the relationship between detector coordinates, spacecraft coordinates, and ORIENT.

The first on-orbit measurements of the geometric distortion for the WFC3 detectors were made during SMOV (Servicing Mission Observatory Verification). Astrometric fields in 47 Tuc (NGC 104) and the LMC were observed with multiple offsets in programs 11444 (UVIS, filter F606W) and 11445 (IR, filter F160W). Geometric distortion solutions were derived from this data (WFC3 ISR 2009-33; WFC3 ISR 2009-34) and entered into IDCTAB files to support the use of MultiDrizzle to produce distortion-corrected images (MultiDrizzle has since been replaced by DrizzlePac). In the initial IDCTAB files, the solutions for filters F606W and F160W were applied to all UVIS and IR filters, respectively. Because there are small filter-dependent differences in distortion, exposures made with other filters during SMOV and in subsequent calibration programs observing Omega Centauri have been used to derive improved solutions for the more commonly used filters (WFC3 ISR 2012-07; WFC3 ISR 2018-10).

The distortion in both UVIS and IR has been found to be stable over the years (see WFC3 ISR 2019-09 for analysis of WFC3/UVIS in the F606W filter, and WFC3 ISR 2018-09 for analysis of WFC3/IR in the F160W filter). The relative displacement of stars in exposures made with different filters due to non-coplanarity of the filters is ~ 0.02 arcsec in most cases (WFC3 ISR 2010-12; WFC3 ISR 2012-01). Astrometric accuracy of the WFC3/UVIS distortion solutions has been improved by incorporating correction for the lithographic mask pattern of the detector (WFC3 ISR 2013-14). Further work on the lithographic mask pattern and filter-dependent fine scale structure has reduced astrometric errors to the level of ~1 mas for many of the UVIS filters (WFC3 ISR 2014-12). The WFC3/UVIS distortion solution for F606W was found to be stable and accurate to +/-2 mas over 5 years using a standard astrometric catalog of the central region of Omega Centauri created from exposures made at different centerings and roll angles (WFC3 ISR 2015-02). With 10 years of data, the WFC3/UVIS distortion solution for F606W was confirmed as stable, based on F606W images corrected with the current geometric solutions to the Gaia DR2 source catalogue in the central region of Omega Centauri (WFC3 ISR 2019-09). Preliminary results based on 14 years of UVIS data indicate that the X and Y scales changed by ~0.2 and 0.1 UVIS pixels respectively at the detector edge (2048 pixels; 2024). Should this be confirmed and shown to significantly impact science data calibration, time-dependent distortion solutions can be incorporated into the IDCTAB reference files.

Delivered IDCTABs with distortion solutions for WFC3/IR filters and WFC3/UVIS filters are listed in Table B.1. Any IR filter or UVIS filter not listed in the delivered IDCTABs is still using the solution derived for F160W and F606W, respectively. All UVIS filters listed in the table have accompanying NPOLFILE (Non-polynomial Offset) reference files available. The NPOLFILE reference files are the 2-D look-up-tables of the filter-dependent fine scale distortion (WFC3 ISR 2014-12; WFC3 ISR 2018-10).

Table B.1: IDCTAB (Instrument Distortion Correction Table) deliveries for the IR and UVIS filters

| WFC3 Channel Updated | Name of IDCTAB Reference File | Date of Delivery | Filters updated (later files include filters calibrated previously) |
|---|---|---|---|
| IR (current available version) | w3m18525i_idc.fits | Mar 2012 | **F105W, F110W, F125W, F140W, F098M, F139M, F153M** |
| UVIS | yas1621ai_idc.fits | Oct 2014 | F350LP, F850LP, F225W, F275W, F336W, F390W, F438W, F475W, F555W, F606W, F775W, F814W, F390M, F621M, F953N |
| UVIS | 1cl1823gi_idc.fits | Dec 2017 | F390M, F547M, F763M, F845M |
| UVIS (current available version) | 2731450pi_idc.fits | July 2018 | **F475W, F475X, F600LP, F280N, F343N, F373N, F395N, F469N, F487N, F502N, F631N, F645N, F656N, F658N, F665N, F680N** |

# B.2 UVIS Channel

Figure B.1 illustrates the shape of the UVIS channel field of view as projected onto the sky. As noted previously, its rhomboidal shape is due primarily to the diagonal tilt of the CCD focal plane with respect to the chief ray. The angle between the x- and y-axes is ~86.1°. The field diagonals are tilted slightly from the V2 and V3 axes. There is a ~1.2 arcsec gap between the two CCD chips. The crosses in the diagram indicate where points in the image would be located without non-linear distortion, and the vectors, scaled up by a factor of 10, indicate the actual locations of the points on the sky, including the non-linear distortion components.

The corner displacements are about 30 pixels, corresponding to 1.3 arcsec. The principal effect is the diagonal variation of scale. At the center of UVIS1 (CCD Chip 1), the scale in the x-direction is 0.0396 arcsec/pixel, and 0.0393 arcsec/pixel in the y-direction. For UVIS2 (CCD Chip 2), these scales are 0.0400 arcsec/pixel, and 0.0398 arcsec/pixel, respectively. Between the corner of the UVIS image nearest to Amp A and the diagonally opposite corner near Amp D, the overall scale increases by 3.5%. UVIS1 forms a slightly distorted rectangle 162 × 81 arcsec in size, while UVIS2 subtends 164× 81 arcsec.

The resulting variation of the projected pixel area on the sky requires corrections to photometry of point sources using images that have not been distortion-corrected. A contour plot of relative pixel size across the UVIS image, normalized at the photometric reference pixel, is shown in Figure B.2. The ratio of maximum to minimum pixel area over the detector is 1.074.

See the Pixel Area Maps webpage for FITS files of the pixel area maps for both CCDs, and a discussion of its normalization and application for photometry.

Figure B.1: Linear components (crosses) and non-linear components (vectors, magnified by 10) of geometric distortion on the WFC3/UVIS detector.



UVIS Distortion Map
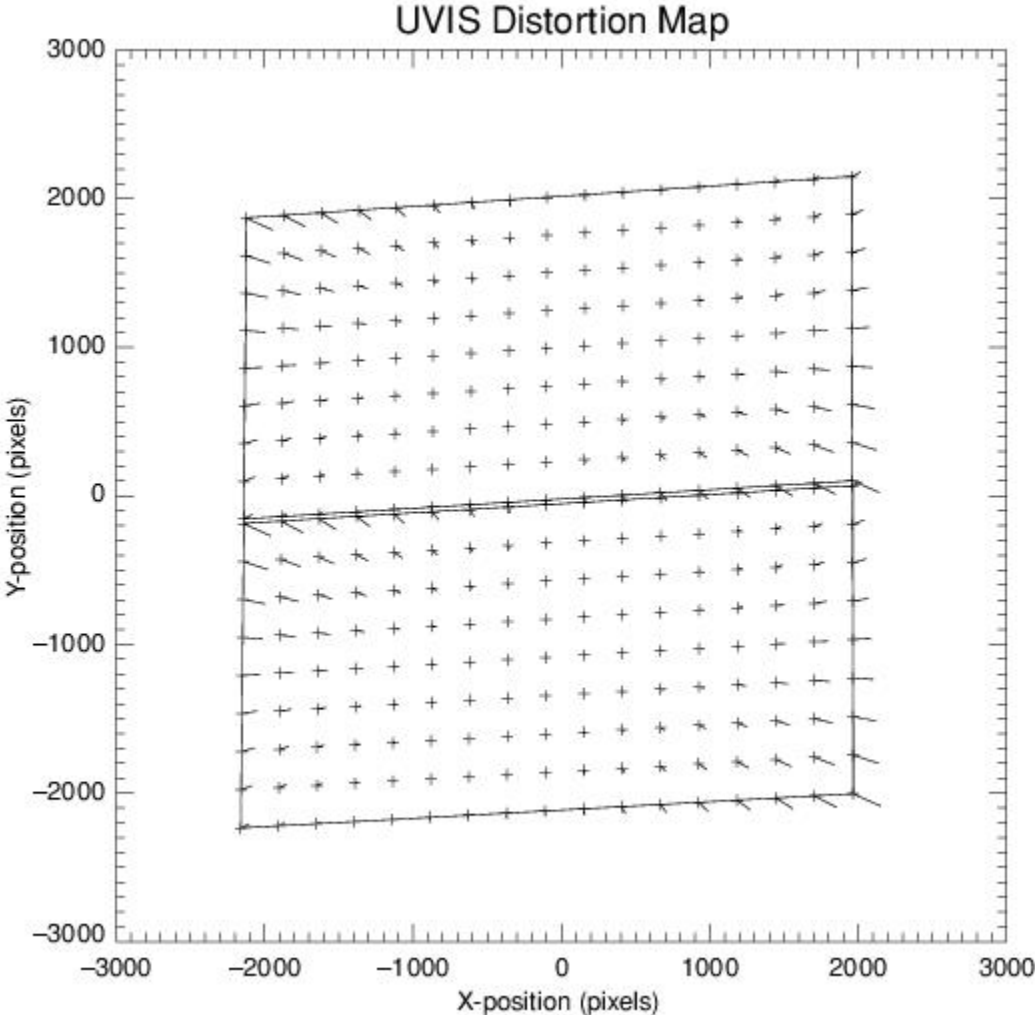
Figure B.2: Variation of the effective pixel area with position on the UVIS detector. Darker shading indicates pixels with smaller area. Contours are drawn at 1% increments.
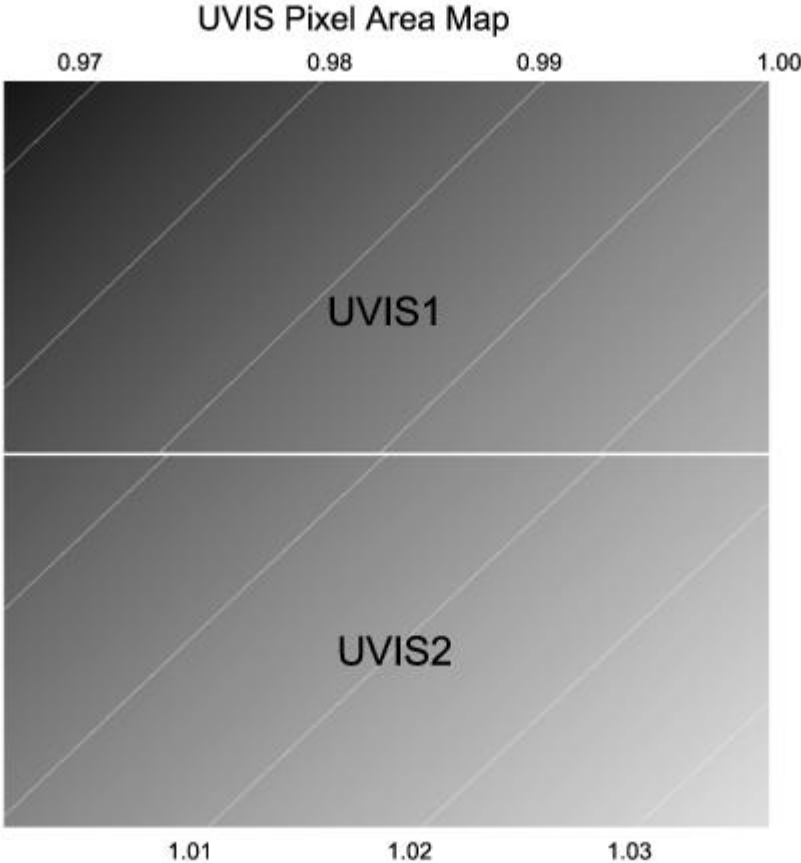
# B.3 IR Channel

The IR detector field of view is nominally concentric with the UVIS field, but subtends a somewhat smaller area on the sky, 136 × 123 arcsec. The detector tilt is about the x-axis (AXIS1 in Figure 7.1), so the projected aperture shape is nearly a rectangle, with the angle between the x- and y-axes on the sky nearly 90°, as shown by the outline in Figure B.3. At field center, the x- and y-scales are 0.135 and 0.121 arcsec/pixel, respectively. A vector plot of the deviation from linearity is given in Figure B.3. The deviations have been magnified by a factor of 10, as in Figure B.1. The largest deviation is 10 pixels, corresponding to about 1.4 arcsec.

**Figure B.3:** Linear components (crosses) and non-linear components (vectors, magnified by 10) of the geometric distortion on the WFC3/IR detector.
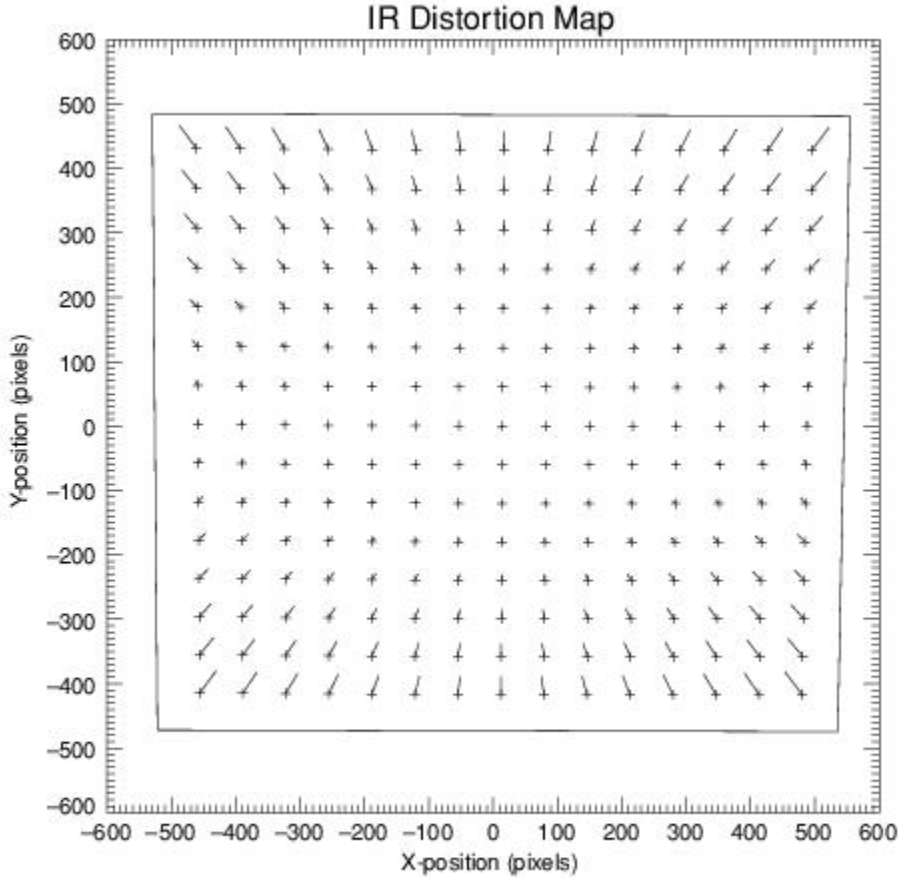


A map of the variation of pixel area across the IR detector to be used for correction of point-source photometry from images that have not been distortion-corrected (see the Pixel Area Maps webpage) is shown in Figure B.4. The ratio of maximum to minimum pixel area is 1.090.

Figure B.4: Variation of the effective pixel area with position on the IR detector. Darker shading indicates pixels with smaller area. Contours are drawn at 2% increments.



IR Pixel Area Map

1.02

1.00

0.98

0.96
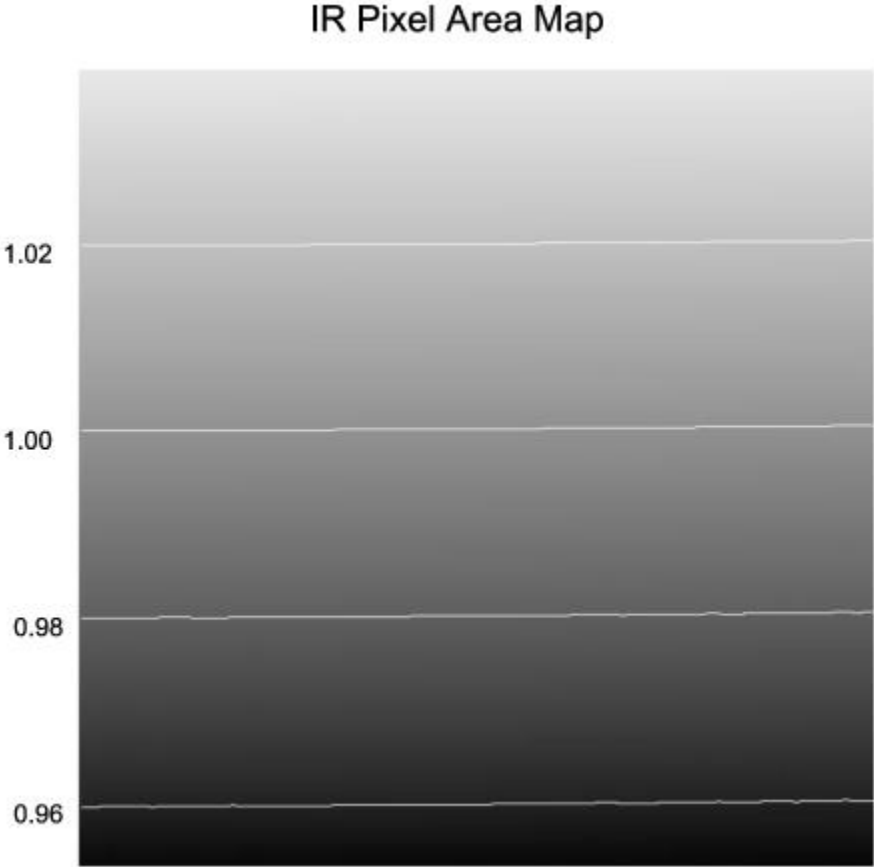
# Appendix C: Dithering and Mosaicking

**Appendix Contents**

# C.1 Why Mosaicking and Dithering are Needed

The sizes of telescope pointing offsets between successive exposures can be very different, depending on whether the purpose is "**mosaicking**" or "**dithering**." Mosaicking is done with the aim of increasing the area of sky covered by a particular set of exposures, usually with the goal of providing a seamless joining of contiguous frames. The angular offsets used when mosaicking are generally large, up to the size of the field of view. Only programs observing targets larger than the field of view of the detector need to use mosaicked exposures.

Dithering generally involves much smaller telescope offsets, often on the order of a few pixels in size. Most imaging programs are advised to use dithering for several reasons, including:

- removal of hot pixels and other detector blemishes (Section 6.10.2)
- improving sampling of the PSF (Sections 6.11.1 and 7.10.1)
- improving photometric accuracy by averaging over flat-fielding errors (Sections 5.4.3, 5.7.4, and 6.11.1)
- bridging over the gap between the chips in the UVIS channel (Section 5.2.2).

Dithered and mosaicked exposures can be combined using software included in *DrizzlePac*. Several documents provide examples of how to use this software, including the ReadTheDocs software documentation and the *DrizzlePac Handbook*.

WFC3 ISR 2015-04 describes a methodology for optimizing the parameter `pixfrac` and shows the results of tests conducted for the Frontier Fields program. WFC3 ISR 2015-09 shows how mosaic alignment can be achieved in a single step in DrizzlePac 2.0 by building up an expanded reference catalog, and uses the WFC3 observations of the Eagle Nebula (M16) as an example.

Instead of using DrizzlePac, WFC3 ISR 2014-23 describes the procedure by which the individual images in the Frontier Fields program were aligned using galaxies and provides the FORTRAN source code `hst2galign` that accomplishes the alignment. Further uses of `hst2galign` involving PSF-fitting and faint source location and photometry are discussed in WFC3 ISR 2014-24.

Note that it is sometimes necessary to use software like that in DrizzlePac to combine even CR-SPLIT or repeat exposures, when pointing drift causes slight misalignment of exposures and differences in how PSFs are pixelated, or when gradual changes in focus over the course of an orbit produce changes in the observed PSF.

In some programs, especially those observing time-variable phenomena, combining dithered exposures to correct for cosmic rays and transient bad pixels may be scientifically infeasible. In such cases, single-image based methods must be used. These methods use statistical properties of cosmic-ray brightness or sharpness to identify and interpolate across cosmic rays. Single-image cosmic ray rejection schemes are not available through the standard WFC3 calibration pipeline.

# C.2 WFC3 Patterns

A number of different types of patterns are available to support dithered and mosaicked WFC3 observations. The pre-defined patterns that have been implemented in APT are described in the *Phase II Proposal Instructions*, which are updated when the selection of a new cycle of proposals is announced. The pre-defined WFC3 patterns in effect in APT at the time of publication of this handbook are summarized here. Patterns not predefined in APT can still be executed by specifying POS TARGs on exposures in the Phase II proposal. WFC3 ISR 2016-14 and WFC3 ISR 2020-07 tabulate the necessary POS TARGs for compact patterns with up to 9 steps for WFC3/IR and WFC3/UVIS, respectively. WFC3 ISR 2023-05 tabulates the necessary POS TARGs for optimal patterns when using WFC3 and ACS simultaneously (i.e. one instrument as prime and the other in parallel). Those patterns are designed to preserve sub-pixel sampling as much as possible over the face of the detector, given the scale changes introduced by geometric distortion. Alternatively, observers can also develop custom Patterns within APT by starting with a Generic pattern and setting the required parameters as desired or by adjusting specific parameters within a pre-defined pattern.

Pre-defined WFC3 dither patterns designed to subsample pixels can optionally be selected as secondary patterns when WFC3 patterns with larger steps are selected as primary patterns. WFC3 patterns can also be added as secondary patterns to any of the generic pattern types (BOX, LINE, SPIRAL). When combining patterns, the smaller dither pattern should be the secondary pattern to minimize the time spent moving the telescope. Due to geometric distortion (Appendix B), a large mosaic step shifts some objects by an integer number of rows (or columns), and others by an integer plus some fraction of a pixel. The PSF is thus not evenly sampled in the overlap region of the two exposures, so a PSF-sampling dither should be added if spatial resolution is important.

Sets of exposures with offsets executed using patterns or POS TARGs are associated and combined automatically during pipeline processing, as long as the same guide stars have been used for all exposures. Pointings must be contained within a diameter ~130 arcsec or less (depending on the availability of guide stars in the region) to use the same guide stars. Note that the rms pointing repeatability is significantly less accurate if the same guide stars are not used for all exposures (Appendix B of the *DrizzlePac Handbook*).

The names and purposes of the patterns in effect in APT at the time of publication are given in Table C.1. Note that the initially-adopted names of patterns have been preserved for continuity, although they do not always correspond to the distinction between dither steps and mosaic steps outlined above. The small BOX dither patterns are designed to optimally sample the PSF when 4 steps are used. Since time constraints do not always permit visits to be broken into multiples of 4 steps, LINE dither patterns that optimally sample the PSF in 2 or 3 steps are also given. The BOX and LINE dither patterns are illustrated in WFC3 ISR 2010-09. A full discussion and illustrations of patterns that optimally sample the PSF for different numbers of steps are available in Section C.2 of the *DrizzlePac Handbook*. Note that PSF sampling generally produces a more significant improvement for IR images than for UVIS images (Section 6.6.1 and Section 7.6.1). The remainder of the patterns in Table C.1 are special-purpose mosaic patterns that are expected to be commonly needed. There are no pre-defined patterns to deal with specific features in flats—notably, the circular dead spot on the IR detector (WFC3 ISR 2008-08) and the UVIS "droplets" (WFC3 ISR 2008-10); however, patterns that can be used to mitigate the effects of these artifacts are discussed in WFC3 ISR 2010-09.

**Table C.1: Dithering and Mosaicking Patterns in APT for WFC3.**

| Pattern Name | Description |
|---|---|
| WFC3 IR Patterns | |

| | |
|---|---|
| WFC3-IR-DITHER-BLOB | Dithers over "blobs" (Section 7.9.6) |
| WFC3-IR-DITHER-BOX-MIN | Provides optimal 4-step sampling of the PSF. |
| WFC3-IR-DITHER-BOX-UVIS | Produces an IR mosaic (despite the name) covering approximately the same area as the UVIS-CENTER aperture. |
| WFC3-IR-DITHER-LINE | Provides optimal 2-step sampling of the PSF. |
| WFC3-IR-DITHER-LINE-3PT | Provides optimal 3-step sampling of the PSF. |
| **WFC3 UVIS Patterns** | |
| WFC3-UVIS-DITHER-BOX | Provides optimal 4-step sampling of the PSF; produces spacings of >1 column for removal of hot columns. |
| WFC3-UVIS-DITHER-LINE | Provides optimal 2-step sampling of the PSF; produces spacings of >1 column for removal of hot columns. |
| WFC3-UVIS-DITHER-LINE-3PT | Provides optimal 3-step sampling of the PSF; produces spacings of >1 column for removal of hot columns. |
| WFC3-UVIS-GAP-LINE | Dithers over the interchip gap. |
| WFC3-UVIS-MOS-BOX-LRG | Produces a mosaic that can generally be executed with a single set of guide stars. |
| WFC3-UVIS-MOS-DITH-LINE | Combines a primary gap-stepping pattern with an optional dither at each primary position. |
| WFC3-UVIS-MOSAIC-LINE | For full-frame UVIS with ACS/WFC in parallel; steps the gap on both detectors. |

The default specifications of the patterns are summarized in Table C.2. The equivalent POS TARG moves are summarized in Table C.3, along with the approximate number of pixels corresponding to these moves. The number of pixels was computed using only the linear distortion terms with coefficients measured at the center of each detector. This is an excellent approximation for small moves and for objects that remain in the central region of the detector (Figure B.1 and B.3 in Appendix B).

**Note that you can easily scale up the patterns in APT to make them larger; e.g., multiply the Point Spacing and Line Spacing of patterns with half-pixel sampling** (WFC3-IR-DITHER-BOX-MIN, WFC3-IR-DITHER-LINE, WFC3-UVIS-DITHER-BOX, WFC3-UVIS-DITHER-LINE) **by an odd number to preserve the half-pixel sampling** (this is equivalent to multiplying the POS TARGs and steps in pixels by that number). You may want to do this in the IR, for example, to achieve the recommended spacing of **at least 10 pixels** between positions for photometric repeatability (WFC3 ISR 2019-07) or to move a saturated persistence-generating core of a target by a greater distance than the minimal default distance.

As an example, for the WFC3-IR-DITHER-LINE, one would scale the 0.636" spacing x3 to preserve half-pixel sampling, making this ~15 pixels along the diagonal instead of the standard ~5 pixels.  This will help minimize the effect of self-persistence from bright stars taken in prior exposures from the same visit.

Be aware, however, that larger steps result in larger variations in sub-pixel sampling of the PSF over the face of the detector due to non-linear geometric distortion (WFC3 ISR 2016-14).

Table C.2: Default values of the parameters that define the WFC3 APT convenience patterns

| Pattern | No. of Points | Point Spacing (arcsec) | Line Spacing (arcsec) | Pattern Orient (degrees) | Angle between Sides (degrees) | Center Pattern |
|---|---|---|---|---|---|---|
| WFC3-IR-DITHER-BLOB | 2 | 5.183 | | 41.859 | | yes |
| WFC3-IR-DITHER-BOX-MIN | 4 | 0.572 | 0.365 | 18.528 | 74.653 | no |
| WFC3-IR-DITHER-BOX-UVIS | 4 | 23.020 | 35.212 | 0.713 | 89.287 | yes |
| WFC3-IR-DITHER-LINE | 2 | 0.636 | | 41.788 | | no |
| WFC3-IR-DITHER-LINE-3PT | 3 | 0.605 | | 41.788 | | no |
| | | | | | | |
| WFC3-UVIS-DITHER-BOX | 4 | 0.173 | 0.112 | 23.884 | 81.785 | no |
| WFC3-UVIS-DITHER-LINE | 2 | 0.145 | | 46.840 | | no |
| WFC3-UVIS-DITHER-LINE-3PT | 3 | 0.135 | | 46.840 | | no |
| WFC3-UVIS-GAP-LINE | 2 | 2.414 | | 85.759 | | yes |
| WFC3-UVIS-MOS-BOX-LRG | 4 | 79.400 | 77.500 | 5.550 | 95.300 | yes |
| WFC3-UVIS-MOS-DITH-LINE | | | | | | |

| primary pattern | 3 | 2.400 | | 85.754 | | yes |
|---|---|---|---|---|---|---|
| secondary pattern | 2 | 0.119 | | 33.606 | | no |
| WFC3-UVIS-MOSAIC-LINE | 2 | 3.264 | | 63.697 | | no |

Table C.3: Steps in arcsec in the POS TARG frame and in detector pixels for the WFC3 APT convenience patterns.

| Pattern Name | POS TARG X (arcsec) | POS TARG Y (arcsec) | x (pixels) | y (pixels) |
|---|---|---|---|---|
| WFC3-IR-DITHER-BLOB | -1.930<br>1.930 | -1.729<br>1.729 | -14.25<br>14.25 | -14.25<br>14.25 |
| WFC3-IR-DITHER-BOX-MIN | 0.000<br>0.542<br>0.339<br>-0.203 | 0.000<br>0.182<br>0.485<br>0.303 | 0.0<br>4.0<br>2.5<br>-1.5 | 0.0<br>1.5<br>4.0<br>2.5 |
| WFC3-IR-DITHER-BOX-UVIS | -11.071<br>11.947<br>11.071<br>-11.947 | -17.744<br>-17.457<br>17.744<br>17.457 | -81.7<br>88.2<br>81.7<br>-88.2 | -146.5<br>-144.2<br>146.5<br>144.2 |
| WFC3-IR-DITHER-LINE | 0.000<br>0.474 | 0.000<br>0.424 | 0.0<br>3.5 | 0.0<br>3.5 |
| WFC3-IR-DITHER-LINE-3PT | 0.000<br>0.451<br>0.902 | 0.000<br>0.403<br>0.806 | 0.00<br>3.33<br>6.67 | 0.00<br>3.33<br>6.67 |
| WFC3-UVIS-DITHER-BOX | 0.000<br>0.158<br>0.099<br>-0.060 | 0.000<br>0.070<br>0.165<br>0.095 | 0.0<br>4.0<br>2.5<br>-1.5 | 0.0<br>1.5<br>4.0<br>2.5 |
| WFC3-UVIS-DITHER-LINE | 0.000<br>0.099 | 0.000<br>0.106 | 0.0<br>2.5 | 0.0<br>2.5 |
| WFC3-UVIS-DITHER-LINE-3PT | 0.000<br>0.092<br>0.185 | 0.000<br>0.098<br>0.197 | 0.00<br>2.33<br>4.67 | 0.00<br>2.33<br>4.67 |
| WFC3-UVIS-GAP-LINE | -0.089<br>0.089 | -1.203<br>1.203 | -2.25<br>2.25 | -30.25<br>30.25 |
| WFC3-UVIS-MOS-BOX-LRG | -39.611<br>39.611<br>39.611<br>-39.611 | -42.120<br>-36.860<br>42.120<br>36.860 | -1000.0<br>1000.0<br>1000.0<br>-1000.0 | -997.0<br>-1001.0<br>997.0<br>1001.0 |

| | | | | |
|---|---|---|---|---|
| WFC3-UVIS-MOS-DITH-LINE | -0.178 | -2.393 | -4.5 | -60.2 |
| | -0.079 | -2.328 | -2.0 | -58.7 |
| | 0.000 | 0.000 | 0.0 | 0.0 |
| | 0.099 | 0.066 | 2.5 | 1.5 |
| | 0.178 | 2.393 | 4.5 | 60.2 |
| | 0.277 | 2.459 | 7.0 | 61.7 |
| WFC3-UVIS-MOSAIC-LINE | 0.000 | 0.000 | 0.0 | 0.0 |
| | 1.446 | 2.926 | 36.5 | 71.5 |

For the IR detector, the linear relation between POS TARGs and pixels is simply

$$\text{POS TARG X} = a_{11} * x$$
$$\text{POS TARG Y} = b_{10} * y$$

where $a_{11} \sim 0.1355$ arcsec/pixel and $b_{10} \sim 0.1211$ arcsec/pixel near the center of the detector. For the UVIS detector, there is a cross-term that takes into account the fact that the projected axes are not perpendicular:

$$\text{POS TARG X} = a_{11} * x$$
$$\text{POS TARG Y} = b_{11} * x + b_{10} * y$$

where $a_{11} \sim 0.0396$ arcsec/pixel, $b_{11} \sim 0.0027$ arcsec/pixel, and $b_{10} \sim 0.0395$ arcsec/ pixel near the center of the detector. This relationship is illustrated in Figure C.1.

The values of these coefficients were derived using optical models and apply to the centers of the detectors. On-orbit geometric distortion solutions give marginally different coefficients (WFC3 ISR 2010-09). The corresponding changes in pixel steps in small dithers are insignificant. The corresponding changes in pixel steps in large dithers or mosaic steps are inconsequential, since non-linear distortion makes the step size in pixels variable over the detector.

Figure C.1: Transformation between image x,y coordinates (in pixel units) and X,Y coordinates (in arcsec) in the POS TARG frame. See also Figure 6.1.
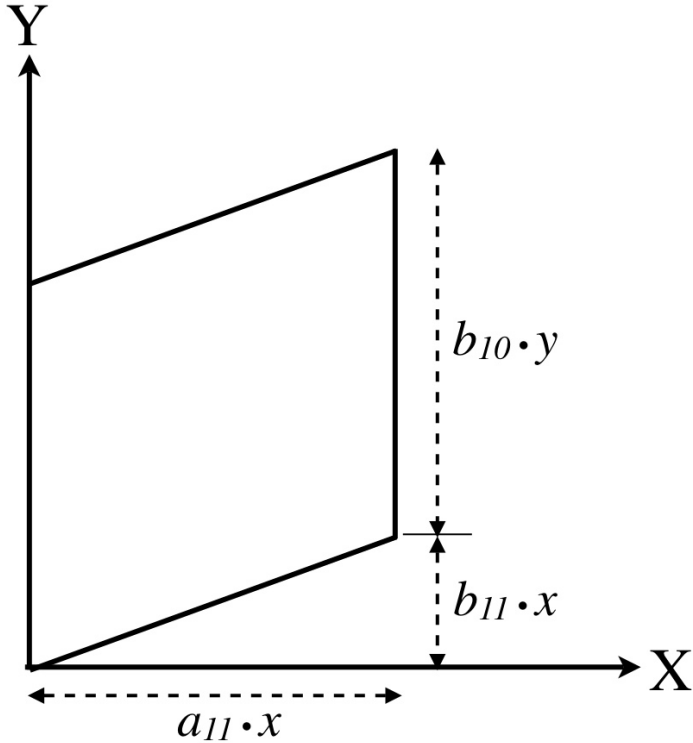
# Appendix D: Bright-Object Constraints and Image Persistence

**Appendix Contents**

# D.1 UVIS Channel

The UVIS channel's CCDs have no bright-object constraints. Overexposures on very bright targets do not have any adverse health and safety issues, nor do they affect subsequent exposures. As for any CCD, there can be some bleeding into adjacent rows and columns surrounding the bright object. This however is generally quite modest assuming the bright object is not itself the science target. From a scientific perspective, the largest problem with bright targets in the field is likely to arise from window or filter ghosts (see Section 6.5.3) or more rarely, scattered light (Section 6.10.6), effects that can be mitigated via dithering.

# D.2 IR Channel

The IR channel likewise has no bright-object constraints that are imposed due to instrument safety concerns. However, as discussed in Section 5.7.9 and Section 7.9.4, observers should bear in mind that there is a potential for image-persistence effects that could compromise observations made immediately following an exposure on a bright target. Such observations contain "afterglow" images at the location of the overexposed object, which gradually fades away over an interval of several hours.

Observers are able to be able to mitigate the effects of persistence from previous visits of other investigators. The Institute is minimizing the effects of persistence due to other observers as part of scheduling. We also provide estimates of the amount of persistence expected due to earlier exposures through MAST (as described in the *WFC3 Data Handbook*). These estimates allow the user to exclude regions of images that are affected by persistence and in some cases to subtract the persistence from an image.

However, observers are responsible for assuring that persistence within a visit (i.e. self-persistence) is not harmful to the science requirements of their own observations. Persistence is primarily a function of fluence, the total number of electrons accumulated by a pixel in an exposure. Very little persistence is observed when the fluence is less than about 35,000 electrons; thus, the best way to avoid self-persistence effects is to adopt an observing strategy that keeps fluence levels below that level. For example, an observing strategy involving a larger number of shorter exposures will result in less persistence than one with fewer longer exposures.

The WFC IR channel has a field of view seven times larger than NICMOS Camera 3 and also has higher sensitivity. This combination means that for WFC3/IR images it is often impossible to avoid saturating some portions of the image, especially since one is also constrained by the total volume of data that can be accumulated. In many cases this will not matter from a science perspective. For example, if your observing strategy involves small dithers and there are a few bright stars in the field, then persistence from earlier images will appear in the wings of the PSF of the bright star. Even if you have large dithers, you will probably not find persistence to be a major problem in the analysis, as long as you are willing to treat pixels with significant persistence as bad pixels.

Nevertheless, if you are planning a sequence of IR observations that may contain severely overexposed images, you may wish to estimate the degree of overexposure. Examples of types of observations for which this is commonly a problem are observations of regions in the Galactic plane or the LMC with large numbers of fairly bright stars, such as eta Car or 30 Dor. Significant amounts of persistence have also been observed in certain instances from globular clusters and nearby elliptical galaxies.

An IR observer might expect that the Two Micron All Sky Survey (2MASS) would be the appropriate catalog for examining the frequency of WFC3/IR saturation, but in fact the 2MASS catalog is generally not deep enough for this purpose. Although the depth of the survey varies across the sky, the faint limit is typically near 15th mag in J, H, and Ks (the formal Level 1 requirements on limiting magnitudes of the 2MASS catalog are J = 15.8, H = 15.1, and Ks = 14.3). Stars near this faint limit saturate the WFC3/IR detector in a relatively short time in both the medium and broad band filters. The STScI Guide Star Catalog (GSC), currently at version 2.3, generally goes much fainter (down to 22nd mag in V), but the extrapolation from the optical into the infrared depends on the accuracy of the spectral type implied by the optical colors and the assumed extinction (a large source of systematic errors along sightlines of high extinction).

As described in Chapter 9, the WFC3 Exposure Time Calculator (ETC) can be used to estimate the count rate in the central pixel for a given astronomical source. (Note that it is the rate for the central pixel and not the total count rate in an aperture that matters.) However, as a rough guideline, below we present tables of the count rates for two cases: a "hot star" with spectral type O3V, Teff = 45,000 K, [Fe/H] = 0, and log g = 4.0; and a "cool star" with spectral type M5V, Teff = 3500 K, [Fe/H] = 0, and log g = 5.0.

Tables D.1, D.2, D.3, and D.4 give the results for the cases where one normalizes to Johnson *J*, *K*, *V*, and Bessel *H*, as stated in the table captions. In each case a magnitude of 15 in the respective bandpass is assumed. The count rates are given in e⁻/s for the central pixel of a star centered in a WFC3/IR pixel. These tables give the most reliable results when normalizing to a ground-based bandpass that overlaps with the WFC3 bandpass, regardless of the assumed spectral energy distribution. However, when normalizing to Johnson *V*, one must know the underlying spectral energy distribution to high accuracy in order to predict the count rate in the WFC3/IR bandpasses.

The Bright Object Tool (BOT) in the Astronomer's Proposal Tool (APT) can provide a list of saturated objects for a potential WFC3/IR observation, given a Phase II proposal. Because the 2MASS survey is sufficiently deep for objects that would severely oversaturate the detector (by more than a factor of 100), the BOT uses 2MASS data where they are available, and the GSC2 where no 2MASS data are available. To use this feature, display a visit with the Aladin tool, loading the DSS image. Then, click on the BOT button in the main tool bar, which will bring up the Bright Object Tool. At this point you press the "Update 2MASS Display" button and stars likely to cause persistence problems are indicated in the Aladin Window, and can be looked at individually there, or shown as a list with the "Get Details…" button. The tool lists stars with different levels of saturation, computed using the time between pixel resets, which can be significantly longer than the exposure time for subarray exposures (WFC3 ISR 2011-09). One should probably be more concerned with the numbers of stars listed as saturated and their locations than with the crude categorization by saturation level, but keep in mind that extremely bright stars saturate not only the central pixel, but also pixels in the PSF wings.

One should be aware that neither the BOT nor other estimates based on star catalogs provide good information about persistence due to diffuse sources, e.g., a bright and extended galaxy nucleus. For that one can use the ETC, if one has an estimate of the surface brightness of the source.

*The best strategy to reduce the effects of persistence is to reduce the exposure times*. Two exposures of 350 seconds (SPARS25 with 15 full-frame readouts) will result in less persistence than one exposure of 700 seconds (SPARS50 with 15 full-frame readouts). If one cannot get short enough exposures (or enough readouts) with the full array and the science target does not fill all of the field, one should consider using a sub-array (see Section 7.7.4).

A second possibility if the program involves images that go to different depths is to place shallower exposures at the beginning of an orbit and deeper exposures at the end of an orbit. For example, if one is planning three 500 second exposures with a narrow band filter and one 500 second exposure through a broad band filter, one should almost always put the broad band filter last.

If neither of these strategies solves the problem, then one needs to very carefully examine dither patterns, and decide what is most important to the observing program. Sometimes, if persistence is isolated to one portion of the image, a line dither in the appropriate direction can limit the damage effects of persistence. Small dither patterns tend to keep bad pixels confined to small regions within the point spread function of the stars that cause persistence. On the other hand, these dither patterns do not cover enough area to step over IR blobs (Section 7.9.6). In some cases, one simply needs to decide which of these two problems it is more important to mitigate as part of planning an observation. An observer who cannot determine the best strategy for a program should consult the Contact Scientist of that program for advice.

Table D.1: Count Rates (e⁻/s) for source with J=15 renormalized to Johnson/J.

| WFC3 IR filter | Cool star[1] | Hot star[1] |
|---|---|---|
| F098M | 2542.9 | 1876.2 |
| F105W | 4541.3 | 3572.4 |
| F110W | 7610.7 | 6754.8 |
| F125W | 4570.8 | 4484.4 |
| F126N | 226.4 | 215.0 |
| F127M | 1108.7 | 1068.2 |
| F128N | 244.9 | 238.8 |
| F130N | 246.9 | 243.5 |
| F132N | 235.2 | 240.0 |
| F139M | 790.2 | 1030.2 |
| F140W | 5136.5 | 6336.3 |
| F153M | 749.4 | 1144.6 |
| F160W | 3021.0 | 4527.5 |
| F164N | 204.0 | 301.0 |
| F167N | 197.4 | 295.3 |

[1] Cool star has spectral type M5V; hot star has spectral type O3V. See text for full definition.

Table D.2: Count Rates (e⁻/s) for source with H=15 renormalized to Bessell/H.

| WFC3 IR filter | Cool star[1] | Hot star[1] |
|---|---|---|
| F098M | 1540.5 | 5141.9 |

| | | |
|---|---|---|
| F105W | 2751.2 | 7706.9 |
| F110W | 4610.7 | 10850.3 |
| F125W | 2769.1 | 4982.5 |
| F126N | 137.2 | 226.2 |
| F127M | 671.7 | 1065.4 |
| F128N | 148.3 | 229.7 |
| F130N | 149.6 | 224.8 |
| F132N | 142.5 | 210.3 |
| F139M | 478.7 | 744.7 |
| F140W | 3111.8 | 4652.4 |
| F153M | 454.0 | 554.7 |
| F160W | 1830.2 | 2202.0 |
| F164N | 123.6 | 112.3 |
| F167N | 119.6 | 104.0 |

[1] Cool star has spectral type M5V; hot star has spectral type O3V. See text for full definition.

Table D.3: Count Rates (e⁻/s) for source with K=15 renormalized to Johnson/K.

| WFC3 IR filter | Cool star[1] | Hot star[1] |
|---|---|---|
| F098M | 1402.6 | 5684.4 |
| F105W | 2504.9 | 8520.0 |
| F110W | 4197.8 | 11995.0 |
| F125W | 2521.2 | 5508.2 |
| F126N | 124.9 | 250.1 |
| F127M | 611.5 | 1177.8 |
| F128N | 135.1 | 253.9 |
| F130N | 136.2 | 248.5 |
| F132N | 129.7 | 232.4 |
| F139M | 435.9 | 823.3 |

| | | |
|---|---|---|
| F140W | 2833.2 | 5143.2 |
| F153M | 413.3 | 613.2 |
| F160W | 1666.3 | 2434.3 |
| F164N | 112.5 | 124.0 |
| F167N | 108.9 | 115.0 |

[1]Cool star has spectral type M5V; hot star has spectral type O3V. See text for full definition.

Table D.4: Count Rates (e⁻/s) for source with V=15 renormalized to Johnson/V.

| WFC3 IR filter | Cool star[1] | Hot star[1] |
|---|---|---|
| F098M | 52334.0 | 2291.8 |
| F105W | 93463.6 | 3435.0 |
| F110W | 156631.7 | 4836.1 |
| F125W | 94070.7 | 2220.8 |
| F126N | 4660.4 | 100.8 |
| F127M | 22818.0 | 474.8 |
| F128N | 5039.4 | 102.4 |
| F130N | 5081.7 | 100.2 |
| F132N | 4840.2 | 93.7 |
| F139M | 16262.9 | 331.9 |
| F140W | 105713.1 | 2073.6 |
| F153M | 15422.3 | 247.1 |
| F160W | 62174.0 | 981.5 |
| F164N | 4197.5 | 50.0 |
| F167N | 4062.2 | 46.4 |

[1]Cool star has spectral type M5V; hot star has spectral type O3V. See text for full definition.

# Appendix E: Reduction and Calibration of WFC3 Data

## Appendix Contents

# E.1 Overview

This appendix contains information regarding the processing and calibration of WFC3 data (Section E.2), the Servicing Mission Observatory Verification (SMOV) calibration plan (Section E.3), and the calibration plans for Cycles 17 through 32, as listed in Table E.1.

**Table E.1: Summary of WFC3 Calibration Plans**

| Cycle | Date Range | Section |
|---|---|---|
| Cycle 17 | August 2009 - November 2010 | Section E.4 |
| Cycle 18 | October 2010 - September 2011 | Section E.5 |
| Cycle 19 | October 2011 - October 2012 | Section E.6 |
| Cycle 20 | November 2012 - October 2013 | Section E.7 |
| Cycle 21 | November 2013 - October 2014 | Section E.8 |
| Cycle 22 | November 2014 - October 2015 | Section E.9 |
| Cycle 23 | November 2015 - October 2016 | Section E.10 |
| Cycle 24 | November 2016 - October 2017 | Section E.11 |
| Cycle 25 | November 2017 - October 2018 | Section E.12 |
| Cycle 26 | November 2018 - October 2019 | Section E.13 |
| Cycle 27 | November 2019 - October 2020 | Section E.14 |
| Cycle 28 | November 2020 - October 2021 | Section E.15 |
| Cycle 29 | November 2021 - October 2022 | Section E.16 |
| Cycle 30 | November 2022 - October 2023 | Section E.17 |
| Cycle 31 | November 2023 - October 2024 | Section E.18 |
| Cycle 32 | November 2024 - October 2025 | Section E.19 |

# E.2 The STScI Reduction and Calibration Pipeline

> E.2.1 Selected Pipeline History
> E.2.2 Processing Data
> E.2.3 Calibrating Data

In this section of the appendix, we summarize the basic reductions and calibrations that are performed in the STScI WFC3 calibration pipeline, `calwf3`. The material in this appendix is intended to provide only enough background to develop robust observing proposals. The *WFC3 Data Handbook* provides more detailed information needed for analyzing your data.

## E.2.1 Selected Pipeline History

In February 2016, the pipeline began to process WFC3 data with `calwf3` version 3.3, which incorporates two fundamental changes to the way UVIS exposures are calibrated and corrected. First, `calwf3` applies pixel-based CTE (Charge Transfer Efficiency) corrections. (Note that `calwf3` version 3.4, which added CTE corrections for subarray apertures, became operational in October 2016.) Second, photometric calibrations are determined and applied independently for each CCD chip. See WFC3 STAN issue 22 for a summary of the changes underlying and included in `calwf3` version 3.3. WFC3 ISR 2016-01 and WFC3 ISR 2016-02 provide a reference guide and cookbook for `calwf3` version 3.3, respectively. WFC3 ISR 2016-03 provides chip-dependent inverse sensitivities. WFC3 ISR 2016-04 describes the creation of chip-dependent flat fields, which included a correction for the effect of the crosshatch pattern in the UV filters on sensitivity calibrations, based on analysis presented in WFC3 ISR 2015-18 and described in Section 5.4.3. WFC3 ISR 2016-07 documents the changes in WFC3/UVIS component files used by **synphot** (Lim et al. 2016) and **pysynphot** (Lim, Diaz, & Laidler 2015) to simulate HST photometric measurements. Note that `pysynphot` was retired in 2022, and the currently-supported counterpart to `synphot` is **stsynphot** (see Lim et al. 2016 for observatory-specific functionality).

In late 2020, a new set of UVIS (as well as IR) inverse sensitivities, i.e. zeropoints, were derived to incorporate improvements to the HST CALSPEC models (Bohlin et al. 2020) as well as an increase in the Vega reference flux. As a consequence of the model adjustments, the standard white dwarf fluxes increase by ~2% for wavelengths in the range 0.15 - 0.4 micron and ~1.5% in the range 0.4 - 1.6 micron covered by both detectors. The updated UVIS calibration includes the new models as well as a correction for the time-dependent detector sensitivity (changes of ~ 0.1 - 0.2 %/year)  derived from over 10 years of monitoring data (WFC3 ISR 2021-04). The IR inverse sensitivity changes installed in late 2020 were primarily the result of the new models, although the new zeropoints also incorporate new IR flat fields in the calibration of the flux standards (WFC3 ISR 2020-10). For more information on the updated photometric calibration, see Calamida et al. (2022). The updated IR 'pixel to pixel' flats, computed by stacking deep exposures acquired over 10 years, correct for spatial sensitivity residuals up to 0.5% in the center of the detector and up to 2% at the edges (WFC3 ISR 2021-01). A new set of 'delta' flats available for six filters (F098M, F105W, F110W, F125W, F140W, and F160W) correct for low-sensitivity artifacts known as 'blobs', as new blobs appear over time ( WFC3 ISR 2021-10).

In December 2023, `calwf3` version 3.7.1 was released, which adopted a new method of UVIS full well saturation flagging that uses a two-dimensional array of pixel threshold values instead of a single scalar threshold per amplifier quadrant. While this change does not meaningfully affect science data (and thus users should not need to redownload/reprocess data accessed before the pipeline update), it does lay the foundation for the future delivery of a spatially-dependent saturation map that accounts for the variation in full well depth across the detectors (Section 5.4.5, specifically Figure 5.6). See the release notes for hstcal version 2.7.6 and WFC3 ISR 2023-08 for more information regarding this change to the pipeline.

## E.2.2 Processing Data

Science data taken by WFC3 are received from the Space Telescope Data Capture Facility and sent to the STScI data processing pipeline, where the data are unpacked, keyword values are extracted from the telemetry stream, and the science data reformatted and repackaged into uncalibrated FITS files by the generic conversion process. All WFC3 science data products are two-dimensional images that are stored in FITS image-extension files. Like ACS and STIS images, WFC3 UVIS channel exposures are stored as triplets of FITS image extensions, consisting of science (SCI), error (ERR), and data quality (DQ) arrays. There is one triplet of image extensions for each CCD chip used in an exposure. Full-frame exposures, using both chips, therefore have two triplets of SCI, ERR, and DQ extensions in a single FITS file. UVIS subarray exposures, which use only one CCD chip, have a single triplet of extensions in their FITS files. After the new Enhanced Pipeline Products code has been used to reprocess data, there will be a number of extensions past 6 related to the WCS (world coordinate system) and the astrometric solutions. Description of those products and their use is at https://outerspace.stsci.edu/pages/viewpage.action?spaceKey=HAdP&title=Improvements+in+HST+Astrometry.

WFC3 IR channel exposures use the NICMOS file structure, which are quintuplets of FITS image extensions, consisting of science (SCI), error (ERR), data quality (DQ), number of samples (SAMP), and integration time (TIME) arrays. There is one quintuplet of extensions for each of the non-destructive detector readouts that make up an IR exposure. Using the maximum number of readouts (16: from NSAMP=15 plus the zeroth read) in an IR exposure therefore results in a single FITS file containing a total of 80 image extensions.

## E.2.3 Calibrating Data

The uncalibrated ("RAW") FITS files are processed through `calwf3`, the software task that calibrates the data for individual exposures, producing calibrated FITS files. Exposures that are obtained as part of an associated set, such as dithered images, have `calwf3` calibration applied to the individual exposures before being processed as a set for the purpose of image combination. All calibrated images will be processed further with the DrizzlePac software for the purpose of removing geometric distortions from individual exposures and for combining associated exposures.

The FITS file name suffixes given to WFC3 raw and calibrated data products are described in Table E.2 and closely mimic the suffixes used by ACS and NICMOS. The initial input files to `calwf3` are the RAW files from generic conversion and the association (ASN) table, if applicable, for the complete observation set.

Most WFC3/UVIS RAW images first go through pixel-based CTE correction, producing a temporary, CTE-corrected RAW file with the suffix "RAC_TMP". The RAC_TMP and original RAW files have the same calibration steps applied, producing two sets of final calibrated products (one uncorrected and one corrected for CTE). For WFC3/UVIS images, a temporary file, with the suffix "BLV_TMP" (BLC_TMP for CTE products), is created by `calwf3` once bias levels have been subtracted and the overscan regions trimmed. This file is renamed using the "FLT" ("FLC" for CTE-corrected products) suffix after the remaining standard calibrations (dark subtraction, flat fielding, etc.) have been completed. For exposures taken as part of a UVIS CR-SPLIT or REPEAT-OBS set, a parallel set of processing is performed, using the BLV_TMP/BLC_TMP files as input to an image combination and cosmic ray rejection routine. The resulting CR-combined image, with a temporary file name suffix of "CRJ_TMP" ("CRC_TMP" for CTE products), then receives the remaining standard calibrations, after which it is renamed using the "CRJ" ("CRC" for CTE products) suffix.

## Table E.2: WFC3 File Name Suffixes.

| File Suffix | Description | Units |
|---|---|---|
| _RAW (_RAC_TMP) | Raw data (with CTE correction) | DN |
| _ASN | Association file for observation set | |
| _SPT | Telemetry and engineering data | |
| _TRL | Trailer file with processing log | |
| _BLV_TMP (_BLC_TMP) | Bias subtracted individual UVIS exposure (with CTE correction) | DN |
| _CRJ_TMP (_CRC_TMP) | Uncalibrated, CR-rejected combined UVIS image (with CTE correction) | DN |
| _IMA | Calibrated intermediate IR exposure | $e^-$/s |
| _FLT (_FLC) | Calibrated individual exposure (with CTE correction) | $e^-$ (UVIS) $e^-$/s (IR) |
| _CRJ (_CRC) | Calibrated, CR-rejected, combined UVIS image (with CTE correction) | $e^-$ |
| _DRZ | Calibrated, geometrically-corrected, dither-combined image | $e^-$/s |

Processing of WFC3/IR exposures results in an intermediate MULTIACCUM ("IMA") file, which is a file that has had all calibrations applied to all of the individual readouts of the IR exposure if the *CORR keywords were populated with PERFORM in the raw file (excluding DRIZCORR). This includes calibrations such as dark subtraction, linearity correction, and flat fielding (see below for list of calibration steps). A final step in `calwf3` processing of WFC3/IR exposures produces a combined image from the individual readouts, which is stored in an FLT output product file. *Note: we recommend observers inspect not only their FLT files but the IMA products as well.*

`calwf3` performs the following basic science data calibrations:

- Pixel-based CTE correction (UVIS only)
- Bad pixel flagging
- Bias level subtraction (UVIS); Reference pixel subtraction (IR)
- Bias image subtraction (UVIS); Zero-read subtraction (IR)
- Dark current subtraction
- Post-Flash subtraction
- Non-linearity correction
- Flat-field correction and gain calibration
- Shutter shading correction (UVIS only)
- Up-the-ramp fitting (IR only)
- Photometric calibration
- CR-SPLIT/REPEAT-OBS image combination

As noted in the list above, the details of some calibration steps differ for UVIS and IR exposures, while others do not apply at all. The process of bias subtraction, in particular, differs for UVIS and IR exposures. The UVIS channel CCDs include regions of overscan, which are used for measuring and subtracting the overall bias level from each CCD exposure. A bias reference image is also subtracted from each science exposure to remove spatial variations in the bias. For IR exposures, the reference pixels located around the perimeter of the detector are used to track and remove changes in the overall bias level between readouts, while the image from the initial ("zeroth") readout of the exposure is subtracted from all subsequent readouts to remove spatial bias structure.

UVIS shutter shading correction is in principle only necessary for very short duration exposures. Note, however, that testing has shown that the shading amounts to only a 0.2-0.3% variation across the field and therefore this step is not applied.

Up-the-ramp fitting is applied to IR exposures to determine a final signal rate for each pixel in the image. This process not only determines the best-fit rate from the individual readouts of the exposure, but also detects and removes effects due to cosmic-ray hits. This process is also capable of recovering a useful signal for pixels that go into saturation during the exposure by using only the non-saturated readouts to compute the fit.

WFC3 grism observations are handled in a special way by the pipeline. Grism observations require a special flat-fielding procedure, where the flat-field value for each pixel is based on the wavelength of the detected signal. Processing of grism images in `calwf3` therefore uses an "identity" flat-field reference image (an image filled with values of 1.0 at each pixel), which allows for the gain calibration part of the flat-fielding step to still be applied without actually flat-fielding the science image. Separate software packages are used to extract and calibrate one-dimensional spectra from WFC3 grism exposures (see Section 8.5). These packages are used to locate and extract spectra of individual sources from calibrated images and perform wavelength calibration, background subtraction, flat fielding, and absolute flux calibration for the extracted spectra.

Table E.3 shows the values assigned to pixels in the DQ arrays of calibrated images, which indicate anomalous conditions and are frequently used in downstream processes to reject a pixel value. If more than one data quality condition applies to a pixel, the sum of the values is used. Note that some flag values have different meanings for UVIS and IR images.

**Table E.3: WFC3 Data Quality Flags.**

| FLAG Value | Data Quality Condition | |
|---|---|---|
| | UVIS | IR |
| 0 | OK | OK |
| 1 | Reed-Solomon decoding error | Reed-Solomon decoding error |
| 2 | Data replaced by fill value | Data replaced by fill value |
| 4 | Bad detector pixel | Bad detector pixel |
| 8 | (unused) | Unstable in zero-read |
| 16 | Hot pixel | Hot pixel |
| 32 | Unstable pixel | Unstable pixel |
| 64 | Warm pixel | (Obsolete: Warm pixel) |
| 128 | Bad pixel in bias | Bad reference pixel |
| 256 | Full- well saturation | Full-well saturation |
| 512 | Bad or uncertain flat value | Bad or uncertain flat value |
| 1024 | Charge trap (sink pixel) | (unused) |
| 2048 | A-to-D saturation | Signal in zero-read |
| 4096 | Cosmic ray detected by AstroDrizzle | Cosmic ray detected by AstroDrizzle |
| 8192 | Cosmic ray detected during CR-SPLIT or REPEAT-OBS combination | Cosmic ray detected during up-the-ramp fitting |
| 16384 | Pixel affected by ghost or crosstalk (not used) | Pixel affected by crosstalk (not used) |

# E.3 The SMOV Calibration Plan

The Servicing Mission Observatory Verification (SMOV) plan for WFC3 was executed following the instrument's successful installation in HST in May, 2009. The calibration plan consisted of engineering, alignment, and calibration activities whose principal goal was to verify that the instrument would be ready for science at the beginning of Cycle 17 in August, 2009. WFC3's SMOV activities began on 25 May 2009 with the Activation Test. The first set of SMOV imaging data were acquired on 11 June 2009, and the last in the first week of September. Because of the short duration, only a critical subset of WFC3's imaging and spectroscopic modes were calibrated. All of the 44 activities are presented in Table E.4. The proposals and observation dates can be viewed by entering the Proposal ID into the HST Program Information webpage. Most of these activities have an associated Instrument Science Report, published in 2009 with the proposal number in the title, and are available on the WFC3 website at:
https://www.stsci.edu/hst/instrumentation/wfc3/documentation/instrument-science-reports-isrs.

**Table E.4: SMOV4 Calibration Programs.**

| Proposal ID | Title |
| --- | --- |
| 11454 | Activation Test |
| 11357 | Memory Test |
| 11358 | Sci Data Buffer Test |
| N/A | UVIS CCD Cooldown |
| N/A | IR Detector Cooldown |
| 11419 | UVIS Det Functional |
| 11420 | IR Det Functional |
| 11421 | CSM Test |
| 11422 | UVIS SOFA Test |
| 11529 | UVIS Spare Tungsten Lamp |
| 11423 | IR FSM Test |
| 11543 | IR Spare Tungsten Lamp |
| 11424 | UVIS Initial Alignment |
| 11425 | IR Initial Alignment |
| 11426 | UVIS Contam Monitor |
| 11427 | UVIS Shutter Test |
| 11428 | D2 Cal Lamp Test |
| N/A | UVIS TEC Performance |

| | |
|---|---|
| N/A | IR TEC Performance |
| 11431 | UVIS Hot Pixel Anneal |
| 11432 | UVIS Int Flats |
| 11433 | IR Int Flats |
| 11434 | UVIS Fine Alignment |
| 11435 | IR Fine Alignment |
| 11436 | UVIS Image Quality |
| 11437 | IR Image Quality |
| 11438 | UVIS PSF Wings |
| 11439 | IR PSF Wings |
| 11549 | UVIS & IR Pointing Stability |
| 11442 | FGS-UVIS Update |
| 11443 | FGS-IR Update |
| 11444 | UVIS Plate Scale |
| 11445 | IR Plate Scale |
| 11446 | UVIS Dark, Noise, Backgnd |
| 11447 | IR Dark, Noise, Backgnd |
| 11448 | UVIS SAA Passage |
| 11449 | IR SAA Passage |
| 11450 | UVIS Phot Zero Points |
| 11451 | IR Phot Zero Points |
| 11452 | UVIS Flat Field Uniformity |
| 11453 | IR Flat Field Uniformity |
| 11552 | IR Grisms |
| 11798 | UVIS PSF Core Modulation |
| 11808 | UVIS Bowtie Monitor |

# E.4 The Cycle 17 Calibration Plan

The Cycle 17 calibration plan was executed from August 2009 through November 2010. The calibration programs comprising this plan are listed in Table E.5. The proposals and observation dates can be viewed by entering the Proposal ID into the HST Program Information webpage. The initial plan provided improved photometric, spectroscopic, flat field, and geometric distortion values and additional on-orbit detector characterization. Supplemental programs, beginning with proposal ID 12087, were introduced mid-cycle to provide data needed to improve calibration in specific areas and to characterize problems or anomalies.

The results of these calibration programs have been documented in Instrument Science Reports on the WFC3 website at:
 http://www.stsci.edu/hst/instrumentation/wfc3/documentation/instrument-science-reports-isrs.

The overall Cycle 17 calibration plan is discussed in WFC3 ISR 2009-08, with more details available concerning the photometric calibration of WFC3 (WFC3 ISR 2009-05) and the detector monitoring campaign (WFC3 ISR 2009-07). Galactic cluster observations are a cornerstone of the Cycle 17 calibration effort (WFC3 ISR 2009-06).

Table E.5: Cycle 17 Calibration Programs.

| Proposal ID | Title |
| --- | --- |
| 11903 | UVIS Zero Points |
| 11904 | UVIS Droplets |
| 11905 | UVIS CCD Daily Monitor |
| 11906 | UVIS CCD Gain |
| 11907 | UVIS Contamination Monitor |
| 11908 | Bowtie Monitor |
| 11909 | UVIS Hot Pixel Anneal |
| 11911 | UVIS L-Flats & Geometric Distortion |
| 11912 | UVIS Internal Flats |
| 11913 | IR Filter Wedge Check |
| 11914 | UVIS Earth Flats |
| 11915 | IR Internal Flats |
| 11916 | IR Intrapixel Sensitivity |
| 11917 | IR Earth Flats |
| 11918 | UVIS Image Quality |
| 11919 | UVIS PSF Wings |

| 11920 | IR Image Quality |
|---|---|
| 11921 | IR PSF Wings |
| 11922 | UVIS Fringing |
| 11923 | UVIS Filter Wedge Check |
| 11924 | UVIS CTE Monitoring |
| 11925 | UVIS Linearity |
| 11926 | IR Zero Points |
| 11927 | IR Persistence |
| 11928 | IR L-Flats and Geometric Distortion |
| 11929 | IR Dark Monitor |
| 11930 | IR Gain |
| 11931 | IR Count Linearity |
| 11932 | IR Stray Light |
| 11933 | IR Rate-Dependent Non-Linearity |
| 11934 | UVIS G280 Flux Calibration |
| 11935 | UVIS G280 Wavelength Calibration |
| 11936 | IR Grism Flux Calibration |
| 11937 | IR Grism Wavelength Calibration |
| 11938 | UVIS Stray Light |
| 12087 | WFC3 IR subarray anomaly |
| 12088 | Tungsten lamp warm-up time |
| 12089 | Persistence - Part 2 |
| 12090 | WFC3/UVIS Photometric Calibration - The Spatial Stability of the Detector |
| 12091 | WFC3/UVIS Fringe Calibration - Part 2 |
| 12092 | UVIS Stray Light Characterization |
| 12093 | IR non-linearity calibration using subarrays |
| 12094 | WFC3/UVIS image skew |
| 12325 | Photometry with Spatial Scans |

# E.5 The Cycle 18 Calibration Plan

The Cycle 18 calibration plan is summarized in WFC3 ISR 2011-14. It was executed from October 2010 through September 2011. The calibration programs comprising this plan are listed in Table E.6. The proposals and observation dates can be viewed by entering the Proposal ID into the HST Program Information webpage. The Cycle 18 plan provides less frequent monitoring of characteristics that were demonstrated to be stable during Cycle 17. It places increased emphasis on characterizing IR persistence, measuring UVIS and IR flat fields, calibrating the IR grism, monitoring CTE on the UVIS detector, and quantifying the ability to do high contrast imaging on both detectors. It tests CTE mitigation procedures and the performance of spatial scans for high S/N IR observations.

The results of these calibration programs have been documented in Instrument Science Reports on the WFC3 website at:
 http://www.stsci.edu/hst/instrumentation/wfc3/documentation/instrument-science-reports-isrs.

## Table E.6: Cycle 18 Calibration Programs

| Proposal ID | Title |
| --- | --- |
| 12333 | UVIS&IR Zeropoint Stability Monitor |
| 12334 | UVIS & IR Photometric Calibration |
| 12335 | IR Color Transformation with asterisms |
| 12336 | Scan Enabled Photometry |
| 12337 | UVIS Flat Field Stability |
| 12338 | IR Flat Field Stability Monitor |
| 12339 | UVIS L-Flat Correction |
| 12340 | IR L-Flat Correction |
| 12341 | IR Blob Photometry Test |
| 12342 | UVIS Darks and Bias Monitor |
| 12343 | UVIS Anneal |
| 12344 | UVIS Bowtie Monitor |
| 12345 | UVIS Long Darks Test |
| 12346 | UVIS CCD Gain Stability Test |
| 12347 | UVIS Internal CTE Monitor: EPER |
| 12348 | UVIS Charge Injection Test |
| 12349 | IR Dark Monitor |
| 12350 | IR Gain Monitor |

| 12351 | IR Persistence Experiments |
|-------|---------------------------|
| 12352 | IR Non-linearity (full frame & subarrays) |
| 12353 | UVIS & IR Geometric Distortion Corrections |
| 12354 | High Contrast Imaging |
| 12355 | IR Grism Wavelength and LSF Calibration |
| 12356 | IR Grism Wavelength Calibration Stability Test |
| 12357 | IR Grism Flux Calibration Monitor |
| 12358 | IR Grism L-flat Correction and Independent 2-D Wavelength Solution |
| 12359 | UVIS Grism Wavelength Calibration |
| 12379 | UVIS CTE Monitor: Star Clusters |

# E.6 The Cycle 19 Calibration Plan

The Cycle 19 calibration plan was executed from October 2011 through October 2012. It is discussed in WFC3 ISR 2012-04.

The calibration programs comprising this plan are listed in Table E.7. The proposals and observation dates can be viewed by entering the Proposal ID into the HST Program Information webpage.

The Cycle 19 calibration plan was designed to:

- continue to maintain and update the standard reference files (biases, darks, IR non-linearity, UVIS and IR geometric distortion table)
- monitor the pixel-to-pixel response of both channels and the hysteresis (QE) offset
- validate the temporal and spatial photometric performance of the WFC3 channels
- characterize and model the persistence effects in the IR detector and verify the temporal behavior
- characterize and model the charge transfer efficiency (CTE) in the UVIS channel, including analysis and calibration of the post-flash option
- improve the wavelength and flux calibration over the whole detector for all the WFC3 grisms
- validate in-flight correction of the flat fields
- improve the accuracy of the absolute photometric calibration

The results of these calibration programs are being documented in Instrument Science Reports on the WFC3 website at:

http://www.stsci.edu/hst/instrumentation/wfc3/documentation/instrument-science-reports-isrs

Table E.7: Cycle 19 Calibration Programs

| Proposal ID | Title |
|---|---|
| 12687 | UVIS Anneal |
| 12688 | UVIS Bowtie Monitor |
| 12689 | UVIS CCD Daily Monitor |
| 12690 | UVIS CCD Gain Stability |
| 12691 | UVIS CTI Monitor (EPER) |
| 12692 | UVIS CTE Monitor (Star Clusters) |
| 12693 | UVIS Charge Injection |
| 12694 | IR Persistence Strength |
| 12695 | IR Dark Monitor |
| 12696 | IR Linearity Monitor |
| 12697 | IR Gain Monitor |
| 12698 | WFC3 Contamination & Stability Monitor |

| 12699 | WFC3 Photometric Calibration & Calibration Flux Ladder |
|---|---|
| 12700 | Extending the Range & Precision of the Count Rate non Linearity |
| 12701 | WFC3 PSF Wings |
| 12702 | IR Grisms: Flux/Trace Calibration & Stability |
| 12703 | IR Grisms: Wavelength Calibration & Stability |
| 12704 | UVIS Grism: Flux Calibration |
| 12705 | UVIS Grism: Wavelength Calibration & Stability |
| 12706 | UVIS Flare Wavelength Dependence |
| 12707 | UVIS Spatial Sensitivity |
| 12708 | IR Spatial Sensitivity |
| 12709 | UVIS & IR Moonlit Flats |
| 12710 | UVIS Bright Earth Flats |
| 12711 | UVIS Internal Flats |
| 12712 | IR Internal Flats |
| 12713 | Spatial Scanned L-flat Validation Pathfinder |
| 12714 | UVIS & IR Geometric Distortion |
| 12784 | Characterization of UVIS Traps Via Charge-Injected Biases |
| 12794 | Repeatability of High Precision Photometry and Astrometry in Spatially Scanned UVIS Data |
| 12798 | Bias, Dark, and Charge Injection (CI) for UVIS Binned mode |
| 12802 | WFC3 Post-Flash Characterization |
| 12803 | Guard Darks |
| 12808 | Characterization of UVIS Pixel-to-Pixel QE Variations Via Internal Flats |
| 13068 | WFC3 Blob Monitor Using Dark-Earth IR Flats |
| 13069 | WFC3 UVIS Post-Flash Calibration |
| 13103 | WFC3/UVIS Anneal |
| 13104 | UVIS Bowtie Monitor |
| 13105 | Characterization of UVIS Traps Via Charge-Injected Biases |

# E.7 The Cycle 20 Calibration Plan

The Cycle 20 calibration plan is summarized in WFC3 ISR 2013-05. It was executed from November 2012 through October 2013.

The calibration programs comprising this plan are listed in Table E.8. The proposals and observation dates can be viewed by entering the Proposal ID into the HST Program Information webpage.

The Cycle 20 calibration plan was designed to:

- continue to maintain and update the standard reference files (biases, darks, linearity, CTE traps)
- continue to monitor the instrument (throughput, gain, hysteresis, bad/hot pixels, filter transmission, IR blobs, grism calibration, CTE decline, stability of post-flash)
- improve photometric precision (CTE correction, IR flat fields, dynamic range)
- improve astrometric precision (spatial scans, DGEO files)
- enhance UV calibration (flat fields, post-flash and CTE correction)
- improve our understanding of IR persistence, IR blobs and the CSM, anomalous QE in CCD pixels

The results of these calibration programs will be documented in Instrument Science Reports on the WFC3 website at:
http://www.stsci.edu/hst/instrumentation/wfc3/documentation/instrument-science-reports-isrs

## Table E.8: Cycle 20 Calibration Programs

| Proposal ID | Title |
|---|---|
| 13071 | UVIS Anneal |
| 13072 | UVIS Bowtie Monitor |
| 13073 | UVIS CCD Daily Monitor A |
| 13074 | UVIS CCD Daily Monitor B |
| 13075 | UVIS CCD Daily Monitor C |
| 13076 | UVIS CCD Daily Monitor D |
| 13077 | IR Dark Monitor |
| 13078 | UVIS Post-Flash Monitor |
| 13079 | IR Linearity Monitor |
| 13080 | IR Gain Monitor |
| 13081 | Guard Dark for MCT Programs |
| 13082 | UVIS CTI Monitor (EPER) |
| 13083 | UVIS CTE Monitor (star clusters) |
| 13084 | Characterization of UVIS Traps with CI |

| 13085 | Line 10 CI Bias |
|---|---|
| 13086 | IR Persistence Behaviors as Function of Saturation Time |
| 13087 | IR Persistence Model Tests |
| 13088 | WFC3 Contamination & Stability Monitor |
| 13089 | WFC3 UVIS & IR Photometry |
| 13090 | UVIS Grism: Flux Calibration |
| 13091 | UVIS Grism: Wavelength Calibration |
| 13092 | IR Grisms: Flux Calibration |
| 13093 | IR Grisms: Wavelength Calibration |
| 13094 | IR Grism -1 Order Calibration |
| 13095 | UVIS L-Flat via Spatial Scans |
| 13096 | UVIS Flat Field Validation |
| 13097 | UVIS Internal Flats |
| 13098 | IR Internal Flats |
| 13099 | IR Earth Flats |
| 13100 | UVIS & IR Geometric Distortion |
| 13101 | High Precision Astrometry |
| 13168 | UVIS CCD Gain Stability |
| 13169 | CCD Anomalous QE pixels |
| 13499 | WFC3 Blob Monitor Using Dark-Earth IR Flats |

# E.8 The Cycle 21 Calibration Plan

The Cycle 21 calibration plan is summarized in WFC3 ISR 2014-07. It was executed from November 2013 through October 2014.

The calibration programs comprising this plan are listed in Table E.9. The proposals and observation dates can be viewed by entering the Proposal ID into the HST Program Information webpage.

The Cycle 21 calibration plan was designed to:

- continue to maintain and update the standard reference files (biases, darks, linearity, CTE traps)
- continue to monitor the instrument (throughput, gain, hysteresis, bad/hot pixels, filter transmission, IR blobs, grism calibration, CTE decline, stability of post-flash)
- improve photometric precision (CTE correction, IR flat fields, dynamic range, IR persistence)
- improve astrometric precision (spatial scans, DGEO files)
- enhance UV calibration (flat fields, post-flash and CTE correction)
- improve our understanding of IR persistence, IR blobs and the CSM, anomalous QE in CCD pixels

The results of these calibration programs will be documented in Instrument Science Reports on the WFC3 website at:
http://www.stsci.edu/hst/instrumentation/wfc3/documentation/instrument-science-reports-isrs

### Table E.9: Cycle 21 Calibration Programs

| Proposal ID | Title |
|---|---|
| 13554 | UVIS anneal |
| 13555 | UVIS bowtie monitor |
| 13556 | UVIS CCD daily monitor A |
| 13557 | UVIS CCD daily monitor B |
| 13558 | UVIS CCD daily monitor C |
| 13559 | UVIS CCD un-flashed monitor |
| 13560 | UVIS post-flash monitor |
| 13561 | UVIS CCD gain stability |
| 13562 | IR dark monitor |
| 13563 | IR linearity monitor |
| 13564 | IR gain monitor |
| 13565 | UVIS CTI monitor (EPER) |
| 13566 | UVIS CTE monitor (star cluster) |
| 13567 | CTE characterization with post-flashed darks |

| 13568 | Characterization of the charge-level dependence of CTE losses |
|---|---|
| 13569 | Characterization of UVIS traps with CI |
| 13570 | UVIS & IR geometric distortion |
| 13571 | High precision astrometry |
| 13572 | IR persistence model tests |
| 13573 | Trapping mitigation in spatial scan observations of exosolar planets |
| 13574 | WFC3 contamination & stability monitor |
| 13575 | WFC3 UVIS & IR photometry |
| 13576 | IR grisms: cross check sensitivity function of hot and cool stars |
| 13577 | UVIS grisms: flux calibration |
| 13578 | UVIS grisms: wavelength calibration |
| 13579 | IR grisms: flux calibration |
| 13580 | IR grisms: wavelength calibration |
| 13581 | IR grisms: sky characterization |
| 13582 | Calibration of the IR grism wavelength ZPs |
| 13583 | UV flats spatial scan |
| 13584 | UV flat field validation |
| 13585 | CCD anomalous QE pixels |
| 13586 | UVIS internal flats |
| 13587 | IR internal flats |
| 13588 | CSM monitor with earth flats |
| 13624 | Monitoring Persistence after scanned grism observations |
| 13625 | Characterizing persistence following scanned grism observations |
| 13627 | Timing verification for spatial scan observations |

# E.9 The Cycle 22 Calibration Plan

The Cycle 22 calibration plan is summarized in WFC3 ISR 2015-07. It was executed from November 2014 through October 2015.

The calibration programs comprising this plan are listed in Table E.10. The proposals and observation dates can be viewed by entering the Proposal ID into the HST Program Information webpage.

The Cycle 22 calibration plan was designed to:

- maintain and update the standard reference files (biases, darks, linearity CTE traps, UVIS anomalous QE pixels)
- monitor the health of the instrument (throughput, gain, hysteresis, bad/hot pixels, wavelength and flux stability of grisms; filter transmission, number of IR blobs, CTE decline, stability of the post-flash LED, state of the CSM)
- improve astrometric precision (in narrow and medium band filters, and with spatial scan)
- improve the characterization of persistence in IR observations

The results of these calibration programs will be documented in Instrument Science Reports on the WFC3 website at:
http://www.stsci.edu/hst/instrumentation/wfc3/documentation/instrument-science-reports-isrs

## Table E.10: Cycle 22 Calibration Programs

| Proposal ID | Title |
|---|---|
| 14000 | UVIS Anneal |
| 14001 | UVIS Bowtie Monitor |
| 14002 | UVIS Daily Monitor A |
| 14003 | UVIS Daily Monitor B |
| 14004 | UVIS Daily Monitor C |
| 14005 | UVIS Unflashed Monitor |
| 14006 | UVIS Post-Flash Monitor |
| 14007 | UVIS CCD Gain Stability |
| 14008 | IR Dark Monitor |
| 14009 | IR Linearity Monitor |
| 14010 | IR Gain Monitor |
| 14011 | UVIS CTI Monitor (EPER) |
| 14012 | UVIS CTE Monitor (Star cluster) |
| 14013 | UVIS CTE in subarrays |

| 14014 | UVIS Traps with CI |
|-------|--------------------|
| 14015 | Refining IR Persistence Model |
| 14016 | Short term IR Persistence |
| 14017 | Persistence after Worst Actors |
| 14018 | UVIS Contam Monitor |
| 14019 | UVIS Shutter Characterization |
| 14020 | Photometric Repeatability |
| 14021 | UVIS & IR Photometry Zero Points |
| 14022 | IR Observations of Red CALSPEC Stars |
| 14023 | IR Grism wavelength Calibration stability |
| 14024 | IR Grisms flux and trace calibration stability |
| 14025 | UVIS Grism wavelength Calibration stability |
| 14026 | UVIS Grisms flux and trace calibration stability |
| 14027 | UVIS Pixel variations via int-flat monitor |
| 14028 | UVIS Internal Flats |
| 14029 | IR Internal Flats |
| 14030 | CSM monitor Earth Flats |
| 14031 | Astrometric Validation of UVIS Filters |
| 13929 | High precision calibration of UVIS Geometric distortion |

# E.10 The Cycle 23 Calibration Plan

The Cycle 23 calibration plan was executed from November 2015 through October 2016.

The calibration programs comprising this plan are listed in Table E.11. The proposals and observation dates can be viewed by entering the Proposal ID into the HST Program Information webpage.

The Cycle 23 calibration plan was designed to:

- maintain and update the standard reference files (biases, darks, linearity, CTE traps, UVIS anomalous QE pixels, post-flash)
- monitor the health of the instrument (throughput, gain, hysteresis, bad/hot pixels, wavelength and flux stability of grisms; filter transmission, number of IR blobs, CTE decline, stability of the post-flash LED, state of the CSM)
- improve astrometric precision (in narrow and medium band filters, and with spatial scan)
- improve the characterization of persistence in IR observations

The results of these calibration programs will be documented in Instrument Science Reports on the WFC3 website at:
http://www.stsci.edu/hst/instrumentation/wfc3/documentation/instrument-science-reports-isrs

Table E.11: Cycle 23 Calibration Programs

| Proposal ID | Title |
|---|---|
| 14366 | UVIS Anneal |
| 14367 | UVIS Bowtie Monitor |
| 14368 | UVIS Daily Monitor A |
| 14369 | UVIS Daily Monitor B |
| 14370 | UVIS Daily Monitor C |
| 14371 | UVIS Unflashed Monitor |
| 14372 | UVIS Post-Flash Monitor |
| 14373 | UVIS CCD Gain Stability |
| 14374 | IR Dark Monitor |
| 14375 | IR Linearity Monitor |
| 14376 | IR Gain Monitor |
| 14377 | UVIS CTI Monitor (EPER) |
| 14378 | UVIS CTE Monitor (Star cluster) |
| 14379 | UVIS Traps with CI |
| 14380 | IR Persistence: Amplitude Variations |

| | |
|---|---|
| 14381 | IR Persistence: Improve the Position Dependent Model |
| 14382 | UVIS Contamination and Stability Monitor |
| 14383 | UVIS Shutter Characterization |
| 14384 | UVIS & IR Photometry Zero Points |
| 14385 | IR Grisms: Wavelength Calibration |
| 14386 | IR Grisms: Trace and Flux Calibration |
| 14387 | UVIS Grism Wavelength Calibration Stability |
| 14388 | -1st Order Grism Calibration in IR Grisms |
| 14389 | UVIS Pixel Variations Via Int-flat Monitor |
| 14390 | UVIS Internal Flats |
| 14391 | IR Internal Flats |
| 14392 | CSM monitor Earth Flats |
| 14393 | Astrometric Calibration of All Remaining UVIS Filters |
| 14394 | Time Dependence of X-CTE & Astrometry |

# E.11 The Cycle 24 Calibration Plan

The Cycle 24 calibration plan was executed from November 2016 through October 2017. The individual programs are listed in Table E.12 and are described in more detail on the WFC3 Calibration Plan webpage. In the Cycle 24 Calibration section, a similar table contains direct links to the Phase II programs and observation dates. This information may alternately be accessed via the HST Program Information webpage by entering the Proposal ID.

The WFC3 Cycle 24 section also links to a PDF presentation summarizing WFC3 usage and comparing the Cycle 24 plan with the prior cycle. This document contains more details on the calibration justification and in many cases includes supporting figures with the latest results from regular monitoring.

The Cycle 24 calibration plan was designed to:

- maintain and update the standard reference files (biases, darks, linearity, CTE traps, UVIS anomalous QE pixels, post-flash)
- monitor the health of the instrument (throughput, gain, hysteresis, bad/hot pixels, sink pixels, CTE decline, stability of the post-flash LED, filter transmission, wavelength and flux stability of grisms, number of IR blobs, state of the CSM)
- test the precision of the IR count rate non-linearity correction for faint targets and determine whether a wavelength-dependent correction is required
- improve the precision of the UVIS contamination monitor by making use of spatially scanned observations of photometric standards
- re-evaluate the 2013 UVIS pixel-based CTE model and verify that the recommended post-flash level has not changed

The results of these calibration programs will be documented in Instrument Science Reports on the WFC3 website at:
http://www.stsci.edu/hst/wfc3/documents/ISRs/

## Table E.12: Cycle 24 Calibration Programs

| Proposal ID | Title |
|---|---|
| 14529 | UVIS Anneal |
| 14530 | UVIS Bowtie Monitor |
| 14531 | UVIS Daily Monitor A |
| 14532 | UVIS Daily Monitor B |
| 14533 | UVIS Daily Monitor C |
| 14534 | UVIS Unflashed Monitor |
| 14535 | UVIS Post-Flash Monitor |
| 14536 | UVIS CCD Gain Stability |
| 14537 | IR Dark Monitor |

| 14538 | IR Linearity Monitor |
|---|---|
| 14539 | IR Gain Monitor |
| 14540 | UVIS CTI Monitor (EPER) |
| 14541 | UVIS CTE Monitor (Star cluster) |
| 14542 | UVIS Traps with CI |
| 14815 | UVIS Contamination and Stability Monitor |
| 14543 | IR Grisms: Wavelength Calibration |
| 14544 | IR Grisms: Trace and Flux Calibration |
| 14545 | UVIS Grism Wavelength Calibration Stability |
| 14546 | UVIS Pixel-to-Pixel QE Variations Via Internal Flats |
| 14547 | UVIS Internal Flats |
| 14548 | IR Internal Flats |
| 14549 | CSM monitor Earth Flats |
| 14550 | WFC3 Astrometric Scale Monitoring |
| 14868[1] | Improved Precision, Wavelength Dependence of the IR Count Rate Non-Linearity |
| 14870[1] | IR Zeropoint Linearity |
| 14871[1] | Improving the CALSPEC model for GRW+70D5824 |
| 14878[1] | UVIS Contamination Using Spatial Scans |
| 14879[1] | UVIS Sink Pixel Map Update |
| 14880[1] | UVIS CTE Model Re-characterization |
| 14881[1] | UVIS CTE Pixel-Based Model Evaluation |
| 14882 | UVIS Shutter Monitoring |
| 14883 | WFC3 UVIS & IR Photometry |

[1]New programs this cycle; others are routine monitors.

# E.12 The Cycle 25 Calibration Plan

The Cycle 25 calibration plan was executed from November 2017 through October 2018. The individual programs are listed in Table E.13 and are described in more detail on the WFC3 Calibration Plan webpage. Following the link to Cycle 25 Calibration, a similar table may be found with direct links to the phase II programs and observation dates. This information may alternately be accessed via the HST Program Information webpage by entering the Proposal ID.

The WFC3 Cycle 25 section also links to a PDF presentation summarizing WFC3 usage and comparing the Cycle 25 plan with the prior cycle. This document contains more details on the calibration justification and in many cases includes supporting figures with the latest results from regular monitoring.

The Cycle 25 calibration plan was designed to:

- maintain and update the standard reference files (biases, darks, linearity, CTE traps, UVIS anomalous QE pixels, post-flash)
- monitor the health of the instrument (throughput, gain, hysteresis, bad/hot pixels, sink pixels, CTE decline, stability of the post-flash LED, filter transmission, wavelength and flux stability of grisms, number of IR blobs, state of the CSM)
- improve the precision of the UVIS contamination monitor by using spatially scanned observations of photometric standards
- quantify color terms for the UVIS filters and recheck the photometric calibration at the center of the detector
- test a strategy to mitigate IR persistence using the calibration lamps to fill charge traps prior to obtaining science observations

The results of these calibration programs will be documented in Instrument Science Reports on the WFC3 website at:

http://www.stsci.edu/hst/instrumentation/wfc3/documentation/instrument-science-reports-isrs

Table E.13: Cycle 25 Calibration Programs.

| Program ID | Title |
|---|---|
| 14978 | WFC3 UVIS Anneal |
| 14979 | WFC3 UVIS Bowtie Monitor |
| 14980 | WFC3 UVIS CCD Daily Monitor (darks & biases) (Part 1) |
| 14981 | WFC3 UVIS CCD Daily Monitor (darks & biases) (Part 2) |
| 14982 | WFC3 UVIS CCD Daily Monitor (darks & biases) (Part 3) |
| 14983 | WFC3 UVIS CCD Un-flashed Monitor |
| 14984 | WFC3 UVIS Post-flash Monitor |
| 14985 | WFC3 UVIS CCD Gain Stability |
| 14986 | WFC3 IR Dark Monitor |

| | |
|---|---|
| 14987 | WFC3 IR Linearity Monitor |
| 14988 | WFC3 IR Gain Monitor |
| 14989 | WFC3 UVIS CTI monitor (EPER) |
| 14990 | WFC3 UVIS CTE monitor (star cluster) |
| 14991 | WFC3 Characterization of UVIS traps with CI |
| 14992 | WFC3 UVIS & IR photometry |
| 14993 | WFC3 IR grisms wavelength calibration |
| 14994 | WFC3 IR grisms flux/trace calibration |
| 14995 | WFC3 UVIS grism wavelength calibration |
| 14996 | WFC3 UVIS Pixel-to-Pixel QE Variations via Internal Flats |
| 14997 | WFC3 UVIS Internal Flats |
| 14998 | WFC3 IR Internal Flats |
| 14999 | WFC3 CSM monitor with Earth Flats |
| 15000 | WFC3 Astrometric scale monitoring |
| 15397 | UVIS shutter monitoring |
| 15398 | UVIS contamination monitor (staring and scans) |
| 15399[1] | UVIS Supplemental Photometry: Color Terms & Revisiting M512 |
| 15400[1] | Mitigating Persistence for Time-Series Observations |

[1]New programs this cycle; others are routine monitors.

# E.13 The Cycle 26 Calibration Plan

The Cycle 26 calibration plan was executed from November 2018 through October 2019. The individual programs are listed in Table E.14 and are described in more detail on the WFC3 Calibration Plan webpage. Following the link to Cycle 26 Calibration, a similar table may be found with direct links to the phase II programs and observation dates. This information may alternately be accessed via the HST Program Information webpage by entering the Proposal ID.

The WFC3 Cycle 26 section also links to a PDF presentation summarizing WFC3 usage and comparing the Cycle 26 plan with the prior cycle. This document contains more details on the calibration justification and in many cases includes supporting figures with the latest results from regular monitoring.

The Cycle 26 calibration plan was designed to:

- Maintain and update the standard reference files (biases, darks, linearity, CTE traps, UVIS anomalous QE pixels, post-flash)
- Monitor the health of the instrument (throughput, gain, hysteresis, bad/hot pixels, sink pixels, CTE decline, stability of the post-flash LED, filter transmission, state of the CSM, number of IR blobs, wavelength and flux stability of the grisms)
- Support new initiatives and obtain supplemental (non-routine) calibration data

In this cycle, two new calibration programs will supplement the standard monitoring data. These programs (15585, 15581) were designed to:

- Cross-calibrate the HST focus values derived from the OTA Focus monitor (based on UVIS /F410M observations) with the focus values derived empirically from the WFC3/UVIS PSF database, which has many more F606W observations
- Characterize the decay of IR persistence at short time-scales (t <300 sec), where the observed residual signal deviates from the current power-law model

The results of these calibration programs will be documented in Instrument Science Reports on the WFC3 website at:
http://www.stsci.edu/hst/instrumentation/wfc3/documentation/instrument-science-reports-isrs

## Table E.14: The Cycle 26 Calibration Programs

| Program ID | Title |
|---|---|
| 15567 | WFC3 UVIS Anneal |
| 15568 | WFC3 UVIS Bowtie Monitor |
| 15569 | WFC3 UVIS CCD Daily Monitor (Darks and Biases) Part 1 |
| 15570 | WFC3 UVIS CCD Daily Monitor (Darks and Biases) Part 2 |
| 15571 | WFC3 UVIS CCD Daily Monitor (Darks and Biases) Part 3 |
| 15572 | WFC3 UVIS CCD Unflashed (CTE) Monitor |
| 15573 | WFC3 UVIS Post-flash Monitor |

| | |
|---|---|
| 15574 | WFC3 UVIS CCD Gain Stability |
| 15575 | WFC3 UVIS CTI Monitor (EPER) |
| 15576 | WFC3 UVIS CTE Monitor (star cluster) |
| 15577 | WFC3 Characterization of UVIS traps with Charge Injection |
| 15578 | WFC3 IR Dark Monitor |
| 15579 | WFC3 IR Linearity Monitor |
| 15580 | WFC3 IR Gain Monitor |
| 15581 | WFC3 Short-term IR Persistence |
| 15582 | WFC3 UVIS & IR Photometry |
| 15583 | WFC3 UVIS Contamination Monitor (staring and scans) |
| 15584 | WFC3 UVIS Shutter Monitoring |
| 15585 | WFC3 Focus Cross-Calibration |
| 15586 | WFC3 IR Grism Wavelength Calibration |
| 15587 | WFC3 IR Grism Flux/trace Calibration |
| 15588 | WFC3 UVIS Grism Wavelength Calibration |
| 15589 | WFC3 UVIS Pixel-to-Pixel QE Variations via Internal Flats |
| 15590 | WFC3 UVIS Internal Flats |
| 15591 | WFC3 IR Internal Flats |
| 15592 | WFC3 CSM Monitor with Earth Flats |
| 15593 | WFC3 Astrometric Scale Monitoring |

# E.14 The Cycle 27 Calibration Plan

The Cycle 27 calibration plan was executed from November 2019 through October 2020. The individual programs are listed in Table E.15 and are described in more detail on the WFC3 Calibration Plan webpage. Following the link to Cycle 27 Calibration, a similar table may be found with direct links to the phase II programs and observation dates. This information may alternately be accessed via the HST Program Information webpage by entering the Proposal ID.

The WFC3 Cycle 27 section also links to a PDF presentation summarizing WFC3 usage and comparing the Cycle 27 plan with the prior cycle. This document contains more details on the calibration justification and in many cases includes supporting figures with the latest results from regular monitoring.

The Cycle 27 calibration plan was designed to:

- Maintain and update the standard reference files (biases, darks, linearity, CTE traps, UVIS anomalous QE pixels, post-flash)
- Monitor the health of the instrument (throughput, gain, hysteresis, bad/hot pixels, sink pixels, CTE decline, stability of the post-flash LED, filter transmission, state of the CSM, number of IR blobs, wavelength and flux stability of the grisms)
- Support new initiatives and obtain supplemental (non-routine) calibration data

In this cycle, two standard monitoring programs have been restructured from Cycle 26. These programs (16021, 16030) were designed to:

- Quantify losses in the UVIS sensitivity using spatial scans (previously called 'UVIS Contamination Monitor')
- Monitor the 'UVIS and IR Photometric Calibration' via staring mode observations of HST standards

Five new calibration programs will supplement the standard monitoring. These programs (16020, 16022, 16023, 16029, 16031) were designed to:

- Measure the stability of the tungsten lamp output immediately after turn-on
- Refine the UVIS grism wavelength calibration across the entire detector with better 2D sampling
- Finalize the flux calibration of the UVIS grism with similar spatial sampling as for the wavelength calibration
- Recheck the optimal UVIS background level to mitigate CTE losses
- Check for time dependent sensitivity in the IR detector grisms and filters

The results of these calibration programs will be documented in Instrument Science Reports on the WFC3 website at:
http://www.stsci.edu/hst/instrumentation/wfc3/documentation/instrument-science-reports-isrs

## Table E.15: The Cycle 27 Calibration Programs

| Program ID | Title |
|---|---|
| 15712 | WFC3 UVIS Anneal |
| 15713 | WFC3 UVIS Bowtie Monitor |
| 15714 | WFC3 UVIS CCD Daily Monitor (Darks and Biases) Part 1 |

| 15715 | WFC3 UVIS CCD Daily Monitor (Darks and Biases) Part 2 |
|---|---|
| 15716 | WFC3 UVIS CCD Daily Monitor (Darks and Biases) Part 3 |
| 15717 | WFC3 UVIS CCD Unflashed (CTE) Monitor |
| 15718 | WFC3 UVIS Post-flash Monitor |
| 15719 | WFC3 UVIS CCD Gain Stability |
| 15720 | WFC3 UVIS CTI Monitor (EPER) |
| 15721 | WFC3 UVIS CTE Monitor (star cluster) |
| 15722 | WFC3 Characterization of UVIS traps with Charge Injection |
| 15723 | WFC3 IR Dark Monitor |
| 15724 | WFC3 IR Linearity Monitor |
| 15725 | WFC3 IR Gain Monitor |
| 15726 | WFC3 UVIS Shutter Monitoring |
| 15727 | WFC3 IR Grism Wavelength Calibration |
| 15728 | WFC3 IR Grism Flux/trace Calibration |
| 15729 | WFC3 UVIS Pixel-to-Pixel QE Variations via Internal Flats |
| 15730 | WFC3 UVIS Internal Flats |
| 15731 | WFC3 IR Internal Flats |
| 15732 | WFC3 CSM Monitor with Earth Flats |
| 15733 | WFC3 Astrometric Scale Monitoring |
| 16020 | WFC3 Tungsten Lamp Warmup |
| 16021 | WFC3 UVIS Time Dependent Sensitivity |
| 16022 | WFC3 UVIS Grism Wavelength Calibration |
| 16023 | WFC3 UVIS Grism Flux Calibration |
| 16029 | WFC3 UVIS Background Check |
| 16030 | WFC3 UVIS & IR Photometry Monitor |
| 16031 | IR Time Dependent Sensitivity |

# E.15 The Cycle 28 Calibration Plan

The Cycle 28 calibration plan was executed from November 2020 through October 2021. The individual programs are listed in Table E.16 and are described in more detail on the WFC3 Calibration Plan webpage. Following the link to Cycle 28 Calibration, a similar table may be found with direct links to the phase II programs and observation dates. This information may alternately be accessed via the HST Program Information webpage by entering the Proposal ID.

The WFC3 Cycle 28 section also links to a PDF presentation summarizing WFC3 and comparing the Cycle 28 plan with the prior cycle. This document contains more details on the calibration justification and in many cases includes supporting figures with the latest results from regular monitoring.

The Cycle 28 calibration plan was designed to:

- Maintain and update the standard reference files (biases, darks, linearity, CTE traps, UVIS anomalous QE pixels, post-flash)
- Monitor the health of the instrument (throughput, gain, hysteresis, bad/hot pixels, sink pixels, CTE decline, stability of the post-flash LED, filter transmission, state of the CSM, number of IR blobs, wavelength and flux stability of the grisms)
- Support new initiatives and obtain supplemental (non-routine) calibration data

In this cycle, the IR Grism Flux Monitor (program 16408) has been modified to:

- Quantify sensitivity losses in the IR grisms by supplementing the annual GD153 data with two additional WD standards

Five new calibration programs will supplement the standard monitoring. These programs (16439, 16440, 16441, 16512, 16518) were designed to:

- Check whether IR filters are losing sensitivity similar to the grisms by repeating prior scanned observations of M35
- Recheck the optimal background (post-flash) level, as CTE losses continue to grow
- Measure the impact of CTE on very faint stars
- Test for changes in the F110W sensitivity with time by leveraging off of prior observations of the M4 cluster.
- Check the UVIS focus cross-calibration from F410M to F606W for 'despace' values below 2 microns.

The results of these calibration programs will be documented in Instrument Science Reports on the WFC3 website at:
http://www.stsci.edu/hst/instrumentation/wfc3/documentation/instrument-science-reports-isrs

## Table E.16: The Cycle 28 Calibration Programs

| Program ID | Title |
|---|---|
| 16414 | WFC3 UVIS Anneal |
| 16393 | WFC3 UVIS Bowtie Monitor |
| 16394 | WFC3 UVIS CCD Daily Monitor Part 1 |
| 16395 | WFC3 UVIS CCD Daily Monitor Part 2 |

| | |
|---|---|
| 16396 | WFC3 UVIS CCD Daily Monitor Part 3 |
| 16397 | WFC3 UVIS CCD Unflashed (CTE) Monitor |
| 16398 | WFC3 UVIS Post-flash Monitor |
| 16399 | WFC3 UVIS CCD Gain Stability |
| 16400 | WFC3 UVIS CTI Monitor (EPER) |
| 16401 | WFC3 UVIS CTE Monitor (Star Cluster) |
| 16402 | WFC3 UVIS Traps with Charge Injection |
| 16403 | WFC3 IR Dark Monitor |
| 16404 | WFC3 IR Linearity Monitor |
| 16405 | WFC3 IR Gain Monitor |
| 16406 | WFC3 UVIS Shutter Monitoring |
| 16415 | WFC3 UVIS and IR Photometry |
| 16416 | WFC3 UVIS Time Dependent Sensitivity |
| 16407 | WFC3 IR Grism Wavelength Calibration |
| 16408 | WFC3 IR Grism Flux Calibration |
| 16409 | WFC3 UVIS Pixel-to-Pixel QE Variations via Int Flats |
| 16410 | WFC3 UVIS Internal Flats |
| 16411 | WFC3 IR Internal Flats |
| 16412 | WFC3 CSM Monitor with Earth Flats |
| 16413 | WFC3 Astrometric Scale Monitoring |
| 16439 | WFC3 IR Time Dependent Sensitivity |
| 16440 | WFC3 UVIS CTE: A Completely Direct Approach to Model Pinning |
| 16441 | Understanding How CTE Affects the Faintest Point Sources in WFC3/UVIS |
| 16512 | WFC3/IR Time-Dependent Sensitivity in Staring Mode (Clusters) |
| 16518 | WFC3 Focus Cross-Calibration |

# E.16 The Cycle 29 Calibration Plan

The Cycle 29 calibration plan was executed from November 2021 through October 2022. The individual programs are listed in Table E.17 and are described in more detail on the WFC3 Calibration Plan webpage. Following the link to Cycle 29 Calibration, a similar table may be found with direct links to the phase II programs and observation dates. This information may alternately be accessed via the HST Program Information webpage by entering the Proposal ID.

The WFC3 Cycle 29 section also links to a PDF presentation summarizing WFC3 usage and comparing the Cycle 29 plan with the prior cycle. This document contains more details on the calibration justification and in many cases includes supporting figures with the latest results from regular monitoring.

The Cycle 29 calibration plan was designed to:

- Maintain and update the standard reference files (biases, darks, linearity, CTE traps, UVIS anomalous QE pixels, post-flash)
- Monitor the health of the instrument (throughput, gain, hysteresis, bad/hot pixels, sink pixels, CTE decline, stability of the post-flash LED, filter transmission, state of the CSM, number of IR blobs, wavelength and flux stability of the grisms)
- Support new initiatives and obtain supplemental (non-routine) calibration data

Four new calibration programs will supplement the standard monitoring. These programs (16861, 16862, 16863, 16864) were designed to:

- Test for changes in the IR filter sensitivity with wavelength by leveraging off of prior observations of stellar clusters
- Explore a new method for measuring CTE losses based on long darks with flash levels the 20-50 electron background range
- Measure the impact of CTE losses on extended sources by comparing with early inflight observations
- Improve table-based CTE corrections for photometry and astrometry for backgrounds between 5 and 30 electrons

The results of these calibration programs will be documented in Instrument Science Reports on the WFC3 website at:
http://www.stsci.edu/hst/instrumentation/wfc3/documentation/instrument-science-reports-isrs

## Table E.17: The Cycle 29 Calibration Programs

| ID | Program |
|---|---|
| 16564 | WFC3 UVIS Anneal |
| 16565 | WFC3 UVIS Bowtie Monitor |
| 16566 | WFC3 UVIS CCD Daily Monitor Part 1 |
| 16567 | WFC3 UVIS CCD Daily Monitor Part 2 |
| 16568 | WFC3 UVIS CCD Daily Monitor Part 3 |
| 16569 | WFC3 UVIS CCD Unflashed (CTE) Monitor |

| | |
|---|---|
| 16570 | WFC3 UVIS Post-flash Monitor |
| 16571 | WFC3 UVIS CCD Gain Stability |
| 16572 | WFC3 UVIS CTI Monitor (EPER) |
| 16573 | WFC3 UVIS CTE Monitor (star cluster) |
| 16574 | WFC3 Characterization of UVIS traps with Charge Injection |
| 16575 | WFC3 IR Dark Monitor |
| 16576 | WFC3 IR Linearity Monitor |
| 16577 | WFC3 IR Gain Monitor |
| 16578 | WFC3 UVIS Shutter Monitoring |
| 16579 | WFC3 UVIS and IR Photometry |
| 16580 | WFC3 Time Dependent Sensitivity |
| 16581 | WFC3 UVIS Grism Wavelength Calibration |
| 16582 | WFC3 IR Wavelength Calibration |
| 16583 | WFC3 IR Flux/Trace Monitor |
| 16584 | WFC3 UVIS Pixel-to-Pixel QE Variations via Internal Flats |
| 16585 | WFC3 UVIS Internal Flats |
| 16586 | WFC3 IR Internal Flats |
| 16587 | WFC3 CSM Monitor with Earth Flats |
| 16588 | WFC3 Astrometric Scale Monitoring |
| 16861 | Testing a New Method for Pinning Down CTE Losses |
| 16862 | Supplemental Empirical CTE Calibrations for Photometry and Astrometry |
| 16863 | CTE Evaluation of Resolved Objects |
| 16864 | WFC3/IR Time-Dependent Sensitivity in Staring Mode (Clusters) |

# E.17 The Cycle 30 Calibration Plan

The Cycle 30 calibration plan was executed from November 2022 through October 2023. The individual programs are listed in Table E.18 and are described in more detail on the WFC3 Calibration Plan webpage. Following the link to Cycle 30 Calibration, a similar table may be found with direct links to the phase II programs and observation dates. This information may alternately be accessed via the HST Program Information webpage by entering the Proposal ID.

The WFC3 Cycle 30 section also links to a PDF presentation summarizing WFC3 usage and comparing the Cycle 30 plan with the prior cycle. This document contains more details on the calibration justification and in many cases includes supporting figures with the latest results from regular monitoring.

The Cycle 30 calibration plan was designed to:

- Maintain and update the standard reference files (biases, darks, linearity, CTE traps, UVIS anomalous QE pixels, post-flash)
- Monitor the health of the instrument (throughput, gain, hysteresis, bad/hot pixels, sink pixels, CTE decline, stability of the post-flash LED, filter transmission, state of the CSM, number of IR blobs, wavelength and flux stability of the grisms)
- Support new initiatives and obtain supplemental (non-routine) calibration data

Four new calibration programs will supplement the standard monitoring. These programs (17261, 17262, 17265, 17271) were designed to:

- Track any changes in the IR sensitivity using repeated scan mode observations of M35
- Measure the non-repeatability of the mechanical shutter using repeated short exposures of a bright spectrophotometric standard with the UVIS grism
- Provide users with faint-source CTE-loss curves for backgrounds between 30 e- and 100 e-
- Investigate the UVIS EE and PSF spatial structure at radii greater than 150 pixels using saturated exposures of a white dwarf standard

The results of these calibration programs will be documented in Instrument Science Reports on the WFC3 website at:
http://www.stsci.edu/hst/instrumentation/wfc3/documentation/instrument-science-reports-isrs

## Table E.18: The Cycle 30 Calibration Programs

| ID | Program |
|-------|---------|
| 16967 | WFC3 UVIS Anneal |
| 16982 | WFC3 UVIS Post-flash Monitor |
| 17002 | WFC3 UVIS Bowtie Monitor |
| 17003 | WFC3 UVIS CCD Daily Monitor Part 1 |
| 17004 | WFC3 UVIS CCD Daily Monitor Part 2 |
| 17005 | WFC3 UVIS CCD Daily Monitor Part 3 |
| 17006 | WFC3 UVIS CCD Unflashed (CTE) Monitor |

| 17007 | WFC3 UVIS CCD Gain Stability |
|--------|-------------------------------|
| 17008 | WFC3 UVIS CTI Monitor (EPER) |
| 17009 | WFC3 UVIS CTE Monitor (star cluster) |
| 17010 | WFC3 Characterization of UVIS traps with Charge Injection |
| 17011 | WFC3 IR Dark Monitor |
| 17012 | WFC3 IR Linearity Monitor |
| 17013 | WFC3 IR Gain Monitor |
| 17014 | WFC3 UVIS Shutter Monitoring |
| 17015 | WFC3 UVIS and IR Photometry |
| 17016 | WFC3 Time Dependent Sensitivity |
| 17017 | WFC3 IR Wavelength Calibration |
| 17018 | WFC3 IR Flux/Trace Monitor |
| 17019 | WFC3 UVIS Pixel-to-Pixel QE Variations via Internal Flats |
| 17020 | WFC3 UVIS Internal Flats |
| 17021 | WFC3 IR Internal Flats |
| 17022 | WFC3 CSM Monitor with Earth Flats |
| 17023 | WFC3 Astrometric Scale Monitoring |
| 17258 | HST Cycle 30 Focus & Optical Monitor |
| 17259 | WFC3 UVIS CTE Internal Monitor |
| 17260 | WFC3 IR Time-Dependent Sensitivity: Clusters |
| 17261 | WFC3 IR Time-Dependent Sensitivity: Scans |
| 17262 | WFC3 UVIS Faint-Source CTE Characterization |
| 17265 | WFC3 Shutter Timing Jitter and FLASH with UVIS grism |
| 17271 | WFC3 UVIS Deep PSFs |

# E.18 The Cycle 31 Calibration Plan

The Cycle 31 calibration plan is being executed from November 2023 through October 2024. The individual programs are listed in Table E.19 and are described in more detail on the WFC3 Calibration Plan webpage. In the Cycle 31 Calibration section, a similar table contains direct links to the Phase II programs and observation dates. This information may alternately be accessed via the HST Program Information webpage by entering the Proposal ID.

The WFC3 Cycle 31 section also links to a PDF presentation summarizing WFC3 usage in the latest cycle and comparing the current plan with the prior cycle. This document contains more details on the calibration justification and in many cases includes supporting figures with the latest results from regular monitoring.

The Cycle 31 calibration plan was designed to:

- Maintain and update the standard reference files (biases, darks, linearity, CTE traps, UVIS anomalous QE pixels, post-flash)
- Monitor the health of the instrument (throughput, gain, hysteresis, bad/hot pixels, sink pixels, CTE decline, stability of the post-flash LED, filter transmission, state of the CSM, number of IR blobs, wavelength and flux stability of the grisms)
- Support new initiatives and obtain supplemental (non-routine) calibration data

One new calibration program will supplement the standard monitoring, and is designed to:

- Track changes in the IR sensitivity using repeated scan mode observations of M35.

The results of these calibration programs will be documented in Instrument Science Reports on the WFC3 website at:
http://www.stsci.edu/hst/instrumentation/wfc3/documentation/instrument-science-reports-isrs

Table E.19: The Cycle 31 Calibration Programs

| 17345 | WFC3 UVIS Anneal |
|-------|------------------|
| 17346 | WFC3 UVIS Bowtie Monitor |
| 17347 | WFC3 UVIS CCD Daily Monitor Part 1 |
| 17348 | WFC3 UVIS CCD Daily Monitor Part 2 |
| 17349 | WFC3 UVIS CCD Daily Monitor Part 3 |
| 17350 | WFC3 UVIS CCD Unflashed (CTE) Monitor |
| 17351 | WFC3 UVIS Post-flash Monitor |
| 17352 | WFC3 UVIS CCD Gain Stability |
| 17353 | WFC3 UVIS CTI Monitor (EPER) |
| 17354 | WFC3 UVIS CTE Monitor (star cluster) |
| 17355 | WFC3 Characterization of UVIS traps with Charge Injection |

| | |
|---|---|
| 17356 | WFC3 UVIS CTE Internal Monitor |
| 17357 | WFC3 IR Dark Monitor |
| 17358 | WFC3 IR Linearity Monitor |
| 17359 | WFC3 IR Gain Monitor |
| 17360 | WFC3 UVIS Shutter Monitoring |
| 17361 | WFC3 UVIS and IR Photometry |
| 17362 | WFC3 Time Dependent Sensitivity |
| 17363 | WFC3 IR Time Dependent Sensitivity in Clusters |
| 17364 | HST Focus and Optical Montior |
| 17365 | WFC3 UVIS Grism Wavelength Calibration |
| 17366 | WFC3 IR Grism Wavelength Calibration |
| 17367 | WFC3 IR Flux/Trace Monitor |
| 17368 | WFC3 UVIS Pixel-to-Pixel QE Variations via Internal Flats |
| 17369 | WFC3 UVIS Internal Flats |
| 17370 | WFC3 IR Internal Flats |
| 17371 | WFC3 CSM Monitor with Earth Flats |
| 17372 | WFC3 Astrometric Scale Monitoring |
| 17586 | WFC3 IR Time-Dependent Sensitivity: Spatial Scans |

# E.19 The Cycle 32 Calibration Plan

The Cycle 32 calibration plan is being executed from November 2024 through October 2025. The individual programs are listed in Table E.20 and are described in more detail on the WFC3 Calibration Plan webpage. In the Cycle 32 Calibration section, a similar table contains direct links to the Phase II programs and observation dates. This information may alternately be accessed via the HST Program Information webpage by entering the Proposal ID.

The WFC3 Cycle 32 Calibration section also links to a PDF presentation summarizing WFC3 usage in the latest cycle and comparing the current plan with the prior cycle. This document contains more details on the calibration justification and in many cases includes supporting figures with the latest results from regular monitoring.

The Cycle 32 calibration plan was designed to:

- Maintain and update the standard reference files (biases, darks, linearity, CTE traps, UVIS anomalous QE pixels, post-flash).
- Monitor the health of the instrument (throughput, gain, hysteresis, bad/hot pixels, sink pixels, CTE decline, stability of the post-flash LED, filter transmission, state of the CSM, number of IR blobs, wavelength and flux stability of the grisms).
- Support new initiatives and obtain supplemental (non-routine) calibration data.

The results of these calibration programs will be documented in Instrument Science Reports on the WFC3 website at:
http://www.stsci.edu/hst/instrumentation/wfc3/documentation/instrument-science-reports-isrs

## Table E.20: The Cycle 32 Calibration Programs

| | |
|---|---|
| 17665 | WFC3 UVIS Anneal |
| 17666 | WFC3 UVIS Bowtie Monitor |
| 17667 | WFC3 UVIS CCD Daily Monitor Part 1 |
| 17668 | WFC3 UVIS CCD Daily Monitor Part 2 |
| 17669 | WFC3 UVIS CCD Daily Monitor Part 3 |
| 17670 | WFC3 UVIS CCD Unflashed (CTE) Monitor |
| 17671 | WFC3 UVIS Post-flash Monitor |
| 17672 | WFC3 UVIS CCD Gain Stability |
| 17673 | WFC3 UVIS CTI Monitor (EPER) |
| 17674 | WFC3 UVIS CTE Monitor (star cluster) |
| 17675 | WFC3 Characterization of UVIS traps with Charge Injection |
| 17676 | WFC3 UVIS CTE Internal Monitor |
| 17677 | WFC3 IR Dark Monitor |

| | |
|---|---|
| 17678 | WFC3 IR Linearity Monitor |
| 17679 | WFC3 IR Gain Monitor |
| 17680 | WFC3 UVIS Shutter Monitoring |
| 17681 | WFC3 UVIS and IR Photometry |
| 17682 | WFC3 Time Dependent Sensitivity |
| 17683 | WFC3 IR Time Dependent Sensitivity in Clusters |
| 17684 | WFC3 IR Time-Dependent Sensitivity: Spatial Scans |
| 17685 | HST Focus and Optical Monitor |
| 17686 | WFC3 UVIS Grism Wavelength Calibration |
| 17687 | WFC3 IR Grism Wavelength Calibration |
| 17688 | WFC3 IR Flux/Trace Monitor |
| 17689 | WFC3 UVIS Pixel-to-Pixel QE Variations via Internal Flats |
| 17690 | WFC3 UVIS Internal Flats |
| 17691 | WFC3 IR Internal Flats |
| 17692 | WFC3 CSM Monitor with Earth Flats |
| 17693 | WFC3 Astrometric Scale Monitoring |

# Glossary

The following terms and acronyms are used in this Handbook.

| | |
|---|---|
| *ADU* | Analog-to-digital Unit |
| *ADC* | Analog-to-digital Converter |
| *ABMAG* | $-2.5 \log (F_\nu) - 48.60$ where $F_\nu$ is the flux from the source in erg cm$^{-2}$ sec$^{-1}$ Hz$^{-1}$ |
| *AB$_\nu$* | Correction to ABMAG to account for the fact that the source spectrum is not constant in $F_\nu$ (ABMAG=V+AB$_\nu$) |
| *ACS* | Advanced Camera for Surveys |
| *APT* | Astronomer's Proposal Tool |
| *aXe* | Spectroscopic data extraction software (deprecated and replaced by `hstaxe`) |
| *BOP* | Bright Object Protection |
| *calwf3* | WFC3 calibration pipeline software |
| *CCD* | Charge Coupled Device; a solid-state, photon counting device |
| *CDS* | Correlated Double Sampling |
| *COS* | Cosmic Origins Spectrograph |
| *CfP* | Call for Proposals |
| *CR* | Cosmic ray |
| *CR-SPLIT* | Division of a CCD exposure into shorter exposures to be used for cosmic ray rejection |
| *CSM* | Channel select mechanism |
| *CTE* | Charge Transfer Efficiency |
| *CVZ* | Continuous Viewing Zone |
| *DCL* | Detector Characterization Laboratory at NASA/GSFC |
| *DN* | Data Number |
| *DQ* | Data Quality |
| *EE* | Encircled energy |
| *ETC* | Exposure Time Calculator; ETCs are Web-based tools which can be accessed through the WFC3 ETC webpage |
| *FET* | Field-effect Transistor |
| *FGS* | Fine Guidance Sensors |

| | |
|---|---|
| *FITS* | Flexible Image Transport System, the standardized astronomical data format (see [NASA/GSFC documentation](#)) |
| *FOV* | Field of View |
| *FPA* | Focal-Plane Array |
| *FSM* | Filter select mechanism |
| *FWHM* | Full width at half maximum |
| *GO* | General Observer |
| *GSC* | Guide Star Catalog |
| *GSFC* | NASA's Goddard Space Flight Center |
| *Help Desk* | Facility for getting help on *HST* related topics: [http://hsthelp.stsci.edu](http://hsthelp.stsci.edu) or [help@stsci.edu](mailto:help@stsci.edu) |
| *HRC* | High Resolution Channel of ACS (non-operational) |
| *HST* | Hubble Space Telescope |
| *hstaxe* | Grism exposure analysis software (replaced aXe) |
| *IPT* | Integrated Product Team |
| *IR* | Infrared |
| *IRAF* | Image Reduction and Analysis System, the environment in which -STSDAS operated; deprecated in 2018 (see [article](#) in [STScI Newsletter Volume 35, Issue 03](#)) |
| *ISR* | Instrument Science Report |
| *K* | Degree Kelvin |
| *MAST* | Barbara A. Mikulski Archive for Space Telescopes, an [online-accessible data archive](#) hosting data from missions including HST |
| *MBE* | Molecular-beam Epitaxial |
| *MPP* | Multi Pinned Phased, a CCD mode that reduces dark current rate. |
| *MTF* | Modulation Transfer Function |
| *MUX* | Multiplexer |
| *NICMOS* | Near-Infrared Camera and Multi-Object Spectrograph |
| *NUV* | Near ultraviolet (~2000–4000 Å) |
| *OTA* | Optical Telescope Assembly |
| *PASP* | Publications of the Astronomical Society of the Pacific |

| | |
|---|---|
| *Phase ɪ* | A proposal for observing time on *HST.* |
| *Phase ɪɪ* | An approved *HST* proposal; includes precise detail of how program is to be executed |
| *PI* | Principal investigator |
| *POM* | Pick-off Mirror |
| *PRF* | Pixel Response Function |
| *PSF* | Point-spread function |
| *PyRAF* | IRAF version implemented in the Python language; deprecated as of 2018 (see note in IRAF entry) |
| *QE* | Quantum efficiency |
| *ramp* | A sequence of non-destructive readouts comprising a single IR exposure |
| *rms* | Root mean square |
| *SAA* | South Atlantic anomaly |
| *SBC* | Solar-Blind Channel of ACS |
| *SDSS* | Sloan Digital Sky Survey |
| *SED* | Spectral-energy Distribution |
| *SIAF* | Science Instrument Aperture File |
| *SM4* | Servicing Mission 4 |
| *SMOV* | Servicing Mission Observatory Verification |
| *SNR* | Signal-to-noise ratio |
| *SOFA* | Selectable Optical Filter Assembly |
| *SOC* | Scientific Oversight Committee |
| *ST-ECF* | Space Telescope European Coordinating Facility |
| *STIS* | Space Telescope Imaging Spectrograph |
| *STScI* | Space Telescope Science Institute |
| *STSDAS* | Space Telescope Science Data Analysis System, IRAF software for data analysis and calibration formerly used to process *HST* data; unsupported as of 2018 (see note in IRAF entry) |
| `stsynphot` | HST-specific synthetic photometry software package (designed to complement synphot); see `stsynphot` User's Guide, Lim et al. (2016) |
| `synphot` | Synthetic photometry software package; see `synphot` User's Guide, Lim et al. (2016) |

| | |
|---|---|
| *TAC* | Telescope Allocation Committee |
| *TEC* | Thermal Electric Coolers |
| *TV* | Thermal Vacuum (ground tests done before WFC3 was installed on HST) |
| *UV* | Ultraviolet |
| *UVIS* | Ultraviolet and Visual (CCD channel of WFC3) |
| *WFC* | Wide-Field Channel of ACS |
| *WFC3* | Wide Field Camera 3 |
| *WF/PC-1* | Wide Field Planetary Camera-1. Original on-axis HST camera |
| *WFPC2* | Wide Field Planetary Camera-2. Replacement for WF/PC installed during first servicing mission of December 1993 |